Examining *Para*-Substituted Derivatives of Pyridine to Improve Catalytic Efficiency and Understanding of the SABRE Hyperpolarisation Process

Emma Victoria Stanbury

PhD

University of York

Chemistry

June 2020

Abstract

The insensitivity of magnetic resonance techniques can be overcome through the use of hyperpolarisation methods such as Signal Amplification by Reversible Exchange (SABRE). SABRE utilises an iridium catalyst to transfer the latent magnetisation of *para*hydrogen to a substrate by reversible binding. In this thesis, we present a comprehensive quantitative study of substrate-iridium ligation effects and evaluate the role of the substrate in SABRE catalysis. A range of *para*-substituted pyridines were selected to probe the relationship between their electronic properties and SABRE efficiency. These substrates reacted to form $[Ir(H)_2(SIMes)(substrate)_3]Cl$ as the key SABRE-active species. The lifetimes of these complexes were assessed via exchange spectroscopy and longer catalyst residence times were clearly linked to short substrate T_1 times in solution. SABRE efficiency was shown to be optimal where the rate of substrate dissociation was 6.69 s^{-1} and the T_1 was 6.42 s, as an enhancement of 767 ± 8-fold was observed. These data illustrate that SABRE performance is explicitly linked to substrate exchange and relaxation.

The substrates, 4-hydroxypyridine and isoniazid, were also examined and found to form novel *bis*-substituted iridium complexes. 4-Hydroxypyridine readily tautomerizes to 4-pyridone resulting in the unusual SABRE-active species; $[IrCl(H)_2(SIMes)(\kappa\text{-}O\text{-}4\text{-pyridone})(\kappa\text{-}N\text{-}4\text{-hydroxypyridine})]$. The 4-pyridone tautomer ligates to iridium via the oxygen atom in the keto group and lies *trans* to hydride. This ligand undergoes rapid substrate dissociation (18.31 s^{-1} at 270 K) resulting in low levels of hyperpolarisation (−31±1-fold). Isoniazid was found to form the SABRE-active species $[Ir(H)_2(SIMes)(\kappa\text{-}N\text{-isonicotinylhydrazide})(\text{isonicotinyl-}\kappa\text{-}O\text{-}\kappa\text{-}N\text{-hydrazide}]Cl$, where the substrate ligand *trans* to hydride ligates to iridium via the pyridine nitrogen. The second substrate ligand chelates to iridium via the terminal nitrogen and the oxygen in the hydrazide functional group. This complex undergoes slow substrate dissociation (0.04 s^{-1} at 280 K) and yields high polarisation levels (−696±17-fold). This work could broaden the scope of the SABRE method in the future.

Chapter 1 Contents

Abstract 3

Table of Figures 11

Acknowledgements 32

Declaration 33

Abbreviations 34

Chapter 1 Introduction 37

1.1 Nuclear Magnetic Resonance 37

1.1.1 Nuclear Spin 37

1.2 The Sensitivity Problem 38

1.3 Hyperpolarisation 40

1.3.1 Optical Pumping 41

1.3.2 Dynamic Nuclear Polarisation 42

1.4 *Para*hydrogen Induced Polarisation 46

1.4.1 Spin Isomers of Hydrogen 47

1.4.2 Generating *Para*hydrogen 48

1.4.3 PASADENA & ALTADENA 50

1.4.4 Applications of PHIP 52

1.5 Signal Amplification by Reversible Exchange 53

1.5.1 The SABRE Mechanism 53

1.5.2 SABRE Substrates of Interest 60

1.5.3 Catalyst Design 63

1.5.4 Biocompatibility of SABRE 67

1.5.5 Exchange in the SABRE-Active Species 69

1.5.6 Relaxation Effects in the SABRE-Active Species 71

1.5.7 Long Lived States 74

1.6 Thesis Aims 75

1.7 References 77

Chapter 2 Comparison of Experimental Methods for SABRE Hyperpolarisation . 85

2.1 Observation of the Chemical Process of SABRE via NMR 85

2.1.1 Field for Polarisation Transfer in the SABRE Hyperpolarisation Process 91

2.2 The Manual Shaking Method 93

2.2.1 Polarisation Transfer Using the Magnetic Stray Field 95

2.2.2 The Impact of Different Experimenters 98

2.2.3 Effect of *Para*hydrogen dissolution Time (Shake Time) on Signal Enhancement 100

2.3 The Automated Flow System 102

2.3.1 Effect of *Para*hydrogen Dissolution Time (Bubble Time) on Signal Enhancement 103

2.4 Handheld Magnetic Array 105

2.4.1 Design of the Handheld Magnetic Array 106

2.4.2 Effect of *Para*hydrogen Dissolution Time (Shake Time) on Signal Enhancement 108

2.5 Comparison of SABRE Methods 109

2.6 Summary 112

2.7 References 114

Chapter 3 SABRE Optimisation for a Series of *Para*-Substituted Pyridines 116

3.1 The Substrates 116

3.1.1 Substituent Effects in Pyridine 116

3.2 Formation of the SABRE Pre-Catalyst: [Ir(COD)(SIMes)(sub)]Cl 124

3.2.1 Formation of [Ir(COD)(SIMes)(sub)]Cl with 4-Pyridinecarboxaldehyde 125

3.3 Formation of the SABRE-Active Species: $[Ir(H)_2(SIMes)(sub)_3]Cl$ 127

3.3.1 Formation of $[Ir(H)_2(SIMes)(sub)_3]Cl$ with 4-Pyridinecarboxaldehyde 129

3.3.2 SABRE Enhancements in $[Ir(H)_2(SIMes)(sub)_3]Cl$ 131

3.4 Chemical Exchange in $[Ir(H)_2(SIMes)(sub)_3]Cl$ 138

3.4.1 Using the Rate of Substrate Dissociation to Determine the Gibbs Free Energy 140

3.5 Measuring the Pseudo $^4J_{HH}$ Coupling in $[Ir(H)_2(SIMes)(sub)_3]Cl$ 149

3.6 Relaxation Effects $[Ir(H)_2(SIMes)(sub)_3]Cl$ 154

3.6.1 T_1 and Hyperpolarised T_1 Measurements 154

3.6.2 Effect of Catalyst Deuteration atthe NHC 156

3.6.3 Optimum Rate of Dissociation for SABRE 158

3.7 Exploring the Effect of Catalyst Modifications on Iridium-Substrate Ligation 159

3.7.1 Gibbs Free Energy in $[Ir(H)_2(NHC)(sub)_3]Cl$ 161

3.7.2 Relaxation Effects in $[Ir(H)_2(NHC)(sub)_3]Cl$ 163

3.7.3 Enhancement in $[Ir(H)_2(NHC)(sub)_3]Cl$ 165

3.8 Summary 168

3.9 References 172

Chapter 4 SABRE Optimisation for Oxygen-Bound Pyridines 175

4.1 The Substrates 175

4.1.1 4-Hydroxypyridine 175

4.1.2 Isoniazid 182

4.2 Formation of the SABRE pre-catalyst 183

4.2.1 [Ir(COD)(SIMes)(4-Hydroxypyridine)]Cl 184

4.2.2 [Ir(COD)(SIMes)(Isoniazid)]Cl 189

4.3 Formation of the SABRE-Active Catalyst 194

4.3.1 [IrCl(H)$_2$(SIMes)(κ-O-4-pyridone)(κ-N-4-hydroxypyridine)] 195

4.3.2 [Ir(H)$_2$(SIMes)(κ-N-isonicotinylhydrazide)(isonicotinyl-κ-O-κ-N-hydrazide]Cl 198

4.3.3 SABRE Enhancements in the SABRE-Active Catalyst 204

4.4 Diffusion Ordered Spectroscopy in the SABRE-Active Catalyst 207

4.4.1 [Ir(H)$_2$(SIMes)(4-methylpyridine)$_3$]Cl 212

4.4.2 [IrCl(H)$_2$(SIMes)(κ-O-4-pyridone)(κ-N-4-hydroxypyridine)] 216

4.4.3 [Ir(H)$_2$(SIMes)(κ-N-isonicotinylhydrazide)(isonicotinyl-κ-O-κ-N-hydrazide]Cl 219

4.5 Ligand exchange within these SABRE-active catalysts 222

4.5.1 Gibbs Free Energy 224

4.6 Relaxation Effects in the SABRE-Active Catalyst 227

4.6.1 T_1 Relaxation Measurements 227

4.7 Summary 229

4.8 References 234

Chapter 5 Conclusions and Further Work 237

5.1 Further Work 240

5.2 References 241

Chapter 6 Experimental 243

6.1 Instrumentation 243

6.1.1 Nuclear Magnetic Resonance 243

6.1.2 *Para*hydrogen Rig 247

6.1.3 Flow System 248

6.1.4 Fourier Transform Infrared (FTIR) 250

6.2 General Experimental Procedures 250

6.2.1 Synthesis of [IrCl(COD)(NHC)] and Isotopically Labelled Substrates . 250
6.2.2 NMR Samples 251
6.2.3 Manual Shaking Method 251
6.2.4 Flow System 252
6.2.5 Calculating SABRE Enhancements 252
6.2.6 Measuring pK_a 253
6.2.7 Exchange Spectroscopy 256
6.2.8 T_1 Relaxation Measurements 264
6.2.9 Hyperpolarised T_1 Measurements 265
6.3 Diffusion Ordered Spectroscopy 268
6.4 References 270
Appendix A 272
Manual Shaking Method Using the Stray Field of the Spectrometer 272
Automated Flow System 272
Manual Shaking Using a Handheld Magnetic Array 272
Appendix B 273
Measuring the pK_a for the substrates in Chapter 3 273
Characterisation of Substrates for the Substrates in Chapter 3 283
4-Chloropyridine 283
4-Methylpyridine 284
4-Methoxypyridine 284
4-Pyridinecarboxaldehyde 284
Characterisation of [Ir(COD)(SIMes)(sub)]Cl for the Substrates in Chapter 3 285
[Ir(COD)(SIMes)(4-chloropyridine)]Cl 285
[Ir(COD)(SIMes)(4-methylpyridine)]Cl 286
[Ir(COD)(SIMes)(4-methoxypyridine)]Cl 287

[Ir(COD)(SIMes)(4-pyridinecarboxaldehyde)]Cl 288

Characterisation of $[Ir(H)_2(SIMes)(sub)_3]Cl$ for the Substrates in Chapter 3 289

$[Ir(H)_2(SIMes)(4\text{-chloropyridine})_3]Cl$.....289

$[Ir(H)_2(SIMes)(4\text{-methylpyridine})_3]Cl$.....290

$[Ir(H)_2(SIMes)(4\text{-methoxypyridine})_3]Cl$.....291

$[Ir(H)_2(SIMes)(4\text{-pyridinecarboxaldehyde})_3]Cl$ 292

Enhancements in $[Ir(H)_2(SIMes)(sub)_3]Cl$ for the Substrates in Chapter 3 293

Exchange in $[Ir(H)_2(SIMes)(sub)_3]Cl$ for the Substrates in Chapter 3 293

Variation in enhancement factor with temperature used to calculate optimum rates of substrate dissociation 294

Measuring the $^4J_{HH}$ Coupling in $[Ir(H)_2(SIMes)(sub)_3]Cl$ 295

Relaxation effects in $[Ir(H)_2(SIMes)(sub)_3]Cl$ for the substrates in chapter 3 299

T_1 graphs for $[Ir(H)_2(SIMes)(sub)_3]Cl$ 299

T_1 graphs for $[Ir(H)_2(d_{22}\text{-SIMes})(sub)_3]Cl$ 305

T_1 graphs at optimum SABRE temperature.....307

Changing the NHC for the substrates in chapter 3 308

Gibbs Free Energy 308

Relaxation Effects.....309

Enhancement 315

Appendix C 315

Enhancements in $[IrCl(H)_2(SIMes)(\kappa\text{-O-4-pyridone})(\kappa\text{-N-4-hydroxypyridine})]$ and $[Ir(H)_2(SIMes)(\kappa\text{-N-isonicotinylhydrazide})(\text{isonicotinyl-}\kappa\text{-O-}\kappa\text{-N-hydrazide})]Cl$ 315

Diffusion Ordered Spectroscopy in $[Ir(H)_2(SIMes)(4\text{-methylpyridine})_3]Cl$, $[IrCl(H)_2(SIMes)(\kappa\text{-O-4-pyridone})(\kappa\text{-N-4-hydroxypyridine})]$ and $[Ir(H)_2(SIMes)(\kappa\text{-N-isonicotinylhydrazide})(\text{isonicotinyl-}\kappa\text{-O-}\kappa\text{-N-hydrazide})]Cl$ 315

$[Ir(H)_2(SIMes)(4\text{-methylpyridine})_3]Cl$.....315

$[IrCl(H)_2(SIMes)(\kappa\text{-O-4-pyridone})(\kappa\text{-N-4-hydroxypyridine})]$ 323

[$Ir(H)_2$(SIMes)(κ-N-isonicotinylhydrazide)(isonicotinyl-κ-O-κ-N-hydrazide]Cl. 329

Exchange in [$IrCl(H)_2$(SIMes)(κ-O-4-pyridone)(κ-N-4-hydroxypyridine)] and [$Ir(H)_2$(SIMes)(κ-N-isonicotinylhydrazide)(isonicotinyl-κ-O-κ-N-hydrazide]Cl 333

Relaxation Effects in [$IrCl(H)_2$(SIMes)(4-hydroxypyridine$)_2$] and [$Ir(H)_2$(SIMes)(Isoniazid$)_2$]Cl 334

Free Substrate (no catalyst) 334

Free Substrate 335

Bound Substrate *Trans* to Hydride 336

Bound Substrate *Trans* to NHC 337

Bibliography 339

Table of Figures

Figure 1 - The Larmor Precession.....37
Figure 2 - The Boltzmann Distribution of Spins at Thermal Equilibrium Where ΔE = energy difference between the two states, γ = gyromagnetic ratio, h = Planck's constant & B_0 = magnetic field strength. 39
Figure 3 - The Boltzmann Distribution at Thermal Equilibrium vs Hyperpolarised. Adapted with permissions from L. Frydman, et *al*.[19] 40
Figure 4 - a) Experimental setup for SEOP experiments. Adapted with permissions from Raftery *et al*.[29] b) Inside the pumping cell. Adapted with permissions from Walker *et al*.[13] c) Electronic transitions that occur between the Rb and Xe atoms in the pumping cell. Adapted with permissions from T. Pietrass et *al*.[26] 42
Figure 5 - Mechanism for polarisation transfer via the Solid Effect in DNP. Adapted with permissions from A. B. Barnes et *al.*[39] 43
Figure 6 - Mechanism for polarisation transfer for the cross effect in DNP. Adapted with permissions from A. B. Barnes et *al.*[39] 44
Figure 7 - Thermal Mixing mechanism for polarisation transfer in DNP. Adapted with permissions from A. B. Barnes et *al.*[39] 45
Figure 8 - Hydrogenation of acrylonitrile to propionitrile using *p*-H_2. a) ^{1}H spectrum of acrylonitrile under Boltzman conditions b) ^{1}H spectrum of *para*-hydrogenated propionitrile. The blue antiphase peaks are the *p*-H_2 derived protons in the product. Spectra a) and b) are reprinted with permissions from C. R. Bowers et *al.*[44] 47
Figure 9 - The Four Spin States of Dihydrogen. 48
Figure 10 - Schematic of the *p*-H_2 Generator. Adapted from S. B. Duckett et *al.*[46]...49
Figure 11 - a) *o*-H_2 enrichment as a function of temperature. Population of the *ortho* state has been quantified using the integral of the proton signal of hydrogen, b) *p*-H_2 enrichment as a function of temperature. Figure has been adapted with permissions from P. M. Richardson et *al.*[50].....50
Figure 12 - The energy levels of an AX spin system, where the population of each spin state is represented by line thickness. The transitions between energy levels and the corresponding NMR signals are shown, for a negative value of $J_{AX.}$ [14] Figure adapted with permissions from J. Natterer et *al.*[14] 51

Figure 13 - a) Comparison of the thermal ^{1}H-NMR spectrum (top) compared to the hyperpolarised ^{1}H spectrum for a sample of 6 nmol pyridine. The top spectrum has been magnified 128 times so that the ^{1}H resonances can be compared to the hyperpolarised spectrum. b) Hyperpolarised ^{1}H decoupled ^{13}C spectrum after refocusing for a 6 nmol sample of pyridine. c) Hyperpolarised ^{1}H decoupled ^{15}N spectrum with refocusing for a sample contains 25 nmol of ^{15}N-labelled pyridine. Figure adapted with permissions from R. W. Adams et *al.*[64] 53
Figure 14 - Schematic diagram of the SABRE process. The curved blue arrow indicates hydrogen exchange with the free *p*-H_2 in the excess solution. The curved pink arrow indicates substrate exchange with the non-polarised free substrate material. The blue/pink arrow indicates polarisation transfer from *p*-H_2 to the substrate. In the ^{1}H-NMR spectra shown, the black is the thermal, non-hyperpolarised spectrum which has been magnified 32 times and the pink spectrum is the hyperpolarised spectra. 54
Figure 15 - Full SABRE mechanism illustrating formation of the SABRE species: [Ir(COD)(NHC)(sub)]Cl and [Ir(H)$_2$(NHC)(sub)$_3$]Cl 55
Figure 16 - SABRE couplings according to an AA'BB' system 56
Figure 17 - Representation of the LAC approach to SABRE. Adapted with permissions from Buljubasich *et al*.[75] 57
Figure 18 - Schematic Diagram of the SABRE-Relay Polarisation Process 62
Figure 19 - Structure of the SABRE-Active Species formed from Crabtrees catalyst 63
Figure 20 - SABRE-active species containing IMes based NHC ligands 65
Figure 21 – SABRE-Active species based on the pincer based catalyst,[120] the phenolate-substituted NHC[123] and COE based complex.[124] The latter rapidly forms a non-SABRE active CH activation product which is shown. 66
Figure 22 - Catalyst modifications for water soluble iridium SABRE catalysts 69
Figure 23 - Ligand Exchange pathways. a) Illustrated the dissociative substrate exchange pathway, b) shows the associative H_2 exchange pathway. Image adapted with permissions from D. A. Barskiy et *al*.[139] The methanol adduct was adapted with permissions from L. S. Lloyd et *al.*[65] 71
Figure 24 - a) Plot of the T_1 value at the H-5 resonance of methyl nicotinate and 2 of its deuterated analogues. The graph compares the T_1 in the absence of the catalyst

and in the presence of IMes. b) Plot of the T_1 value at the H-5 resonance of methyl-4,6-d_2-nicotinate as a function of the catalyst IMes and corresponding deuterated analogues for the free substrate, the equatorially bound substrate (*trans* to hydride) and the axially bound substrate (*trans* to the NHC). Image created using data from P. J. Rayner et *al.*[80] 73
Figure 25 - Pyridazine (a) and associated derivatives and isotopalogues (b-c). Figure adapted with permissions from S. S. Roy et *al*.[151] 75
Figure 26 - The SABRE active species $[Ir(H)_2(SIMes)(sub)_3]Cl$ 86
Figure 27 - Stacked ^{1}H-NMR spectra for [Ir(COD)(SIMes)(sub)]Cl (bottom) and $[Ir(H)_2(SIMes)(sub)_3]Cl$ (top). Formation of the SABRE active species, $[Ir(H)_2(SIMes)(sub)_3]Cl$ is indicated by the appearance of extra substrate peaks (shown in pink) alongside the hydride peak shown in blue (top spectra). The disappearance of COD related peaks (shown in green in the bottom spectra) indicates that the SABRE precatalyst, [Ir(COD)(SIMes)(sub)]Cl has been consumed. ^{1} H NMR spectra collected on a 300 MHz spectrometer at 298 K using a sample containing [IrCl(COD)(SIMes)] (5 mM), 4-methylpyridine (50 mM), methanol-d_4 (0.6 mL) (bottom spectra) with addition of pH$_2$ (4 bar) (top spectra). 88
Figure 28 - Standard ^{1}H 90° pulse used for SABRE experiments 89
Figure 29 - ^{1}H NMR spectra collected for the SABRE active species $[Ir(H)_2(SIMes)(sub)_3]Cl$ under thermal conditions (no pH$_2$, black spectra) compared to hyperpolarised spectra (pink) in the presence of pH$_2$ (4 bar). The thermal spectrum (black) has been magnified 32 times so that it can be visually compared to the hyperpolarised spectrum. ^{1}H NMR spectra was measured on a 400 MHz spectrometer at 298 K using the one-shot pulse sequence depicted in Figure 28 and a sample containing the SABRE precatalyst [IrCl(COD)(SIMes)] (5 mM), methanol-d4 (0.6 mL) and the substrate 4-methylpyridine (50 mM) under 4 bar of pH$_2$. The hyperpolarised spectrum was collected using the manual shaking method. The sample was then left in the spectrometer for 10 minutes after hyperpolarisation before the thermal spectra was acquired. The equations for calculation of enhancement and percentage hyperpolarisation are also included. 91
Figure 30 – a) series of hyperpolarised ^{1}H NMR spectra as a function of field strength in the SABRE active species $[Ir(H)_2(SIMes)(sub)_3]Cl$ where the resonances at the *ortho*

proton are shown in pink and the *meta* resonances are shown in black. The hyperpolarised ^{1}H NMR spectra was collected using the automated flow system using the pulse sequence shown in Figure 28 where the field strength was varied over 0-130 G in 10 G increments. This was measured on a 400 MHz spectrometer at 298 K using a sample of [IrCl(COD)(SIMes)] (5 mM), 4-methylpyridine (50 mM), methanol-d_4 (0.6 mL) under a pH$_2$ atmosphere of 4 bar. b) The signal enhancement calculated at the *ortho* proton in the free substrate plotted as a function of polarisation transfer field (PTF) 92
Figure 31 – Schematic diagram describing the manual shaking method. 1) 4 bar pH$_2$ is added to an NMR tube fitted with a Young's tap containing the SABRE active species, 2) The sample is shaken within the stray field of the spectrometer to allow for polarisation transfer from the pH$_2$ to the target substrate via the *J*-coupled network, 3) The sample is quickly transferred into the spectrometer for acquisition using the one-shot pulse sequence described in Figure 28, 4) Hyperpolarised spectrum is generated and enhancement and polarisation can be calculated by comparing to the thermal spectrum and using the calculations shown in Figure 2994
Figure 32 - Schematic diagram of a nuclear magnetic spectrometer adapted with permissions from M. H. Levitt et *al.*[16] 95
Figure 33 - Diagram of a solenoid coil. Arrows are used to show the direction of the magnetic field. As the field is more concentrated in the centre, this is where the NMR sample is placed. 96
Figure 34 – Stray field plots for the two spectrometers used for SABRE experiments where A is the narrow bore spectrometer and b is the wide bore spectrometer. Reproduced with permission from the NMR magnet system folder. 97
Figure 35 – Box plot showing the enhancement factor as a function of experimenter utilising the manual shaking method. The coloured portions indicate the 25% and 75% quartiles, the whiskers the minimum and maximum enhancement values, the median line the mid-point of the data and the square the mean. Samples contained the SABRE precatalyst [IrCl(COD)(SIMes)] (5 mM), substrate (50 mM) dissolved in methanol-d_4 (0.6 mL) and in the presence of pH$_2$ (4 bar). Samples were shaken for 10 seconds in the stray field of the spectrometer at approximately 60 G at 298 K..... 99

Figure 36 – Box plots showing the ^{1}H signal enhancement at the *ortho* proton, plotted as a function of shake time for a sample containing [Ir(COD)(SIMes)(sub)]Cl (5 mM) with the substrate 4-methylpyridine (50 mM) and pH$_2$ (4 bar) in methanol-d_4. Green is used to represent the narrow bore instrument a) and purple the wide bore instrument b). The sample was manually shaken at approximately 60 G using the stray field of the 400 MHz spectrometers at 298 K. The coloured portions indicate the 25% and 75% quartiles, the whiskers the minimum and maximum enhancement values, the median line the mid-point of the data, the square the mean and the diamonds show any outliers in the data. 101
In general, the data in Figure 37 indicates that the average enhancements (indicated by the squares) at the *ortho*-proton position are slightly higher when measured on spectrometer a. For example, an average enhancement of −891 ± 18-fold was observed on instrument a compared to −842 ± 43-fold on b. However, the whiskers show that the highest enhancement was observed using instrument b, where a 10 second shake time induced an enhancement of −973-fold. This compares to a maximum of 935-fold on a. Generally, larger variations were observed using instrument b compared to a. This is indicated by the whiskers which illustrate the maximum and minimum enhancement values. For example, for a 5 second shake time, the minimum enhancement was −74-fold and the largest was −801-fold. The 5 second shake time also induced a large variation in results on a, this is highlighted by the presence of data anomalies at −556-fold and −767-fold. Henceforth it is difficult to reproduce enhancements when shaking for such a short period of time. 101
Figure 38 – Schematic diagram of the automated flow probe. 1) A sample of [Ir(H)$_2$(SIMes)(sub)$_3$]Cl in methanol-d_4 is contained in a flow cell where pH$_2$ (4 bar) is bubbled through the solution, 2) The hyperpolarised sample is transferred into the spectrometer via a nitrogen flow, 3) The hyperpolarised spectrum is acquired using the one-shot pulse sequence described in Figure 28, 4) The sample is transferred from the spectrometer back to the flow cell using a nitrogen flow. Image adapted with permissions from R. E. Mewis et *al.*[6] 102
Figure 39 – Box plot showing the ^{1}H NMR signal enhancement plotted as a function of bubble time for the *ortho* proton resonance in the free substrate for the SABRE active species [Ir(H)$_2$(SIMes)(sub)$_3$]Cl (5 mM) containing the substrate 4-

methylpyridine (50 mM). Measurements collected on the 400 MHz narrow bore instrument a) are shown in green and those collected on the 400 MHz wide bore instrument b) are shown in purple. Hyperpolarised measurements were taken using the flow method shown in Figure 38 at 298 K and the pulse sequence shown in Figure 28. The coloured portions indicate the 25% and 75% quartiles, the whiskers the minimum and maximum enhancement values, the median line the mid-point of the data, the square the mean and the diamonds show any outliers in the data. 104
Figure 40 shows the variation in the ^{1}H signal enhancement at the *ortho* proton as a function of the *p*-H_2 bubble time. If we first consider the average signal enhancements, the data generally follows the same pattern as the manual shaking method whereby larger enhancements were observed on spectrometer a. However, the largest average signal enhancement of −264-fold corresponding to a 15 second bubble time was observed on instrument b. This compares to −227-fold on instrument a which resulted from a 10 second bubble time. Furthermore, the largest calculated enhancement of −410-fold was observed on b for a 25 second bubble time. In Figure 41, this is shown as an outlier (indicated by the diamond) as the remaining data points ranged from −40-fold to −126-fold. Figure 42 clearly shows that there is a larger variation in signal enhancements using spectrometer b. This is highlighted by the larger box plots, for example a 10 second bubble time induced enhancements ranging from −0.6-fold to −399-fold (illustrated by the whiskers). Additionally, more anomalies were observed in the data using NMR b (shown by the diamonds). Henceforth, the data collected using spectrometer b is shown to be less reproducible compared to a. It was expected that the signal enhancements generated on both instruments would be very reproducible as this SABRE method is fully automated and all experimental parameters (e.g. sample transfer time, *p*-H_2 pressure etc) were constant for both spectrometers. It is possible that the larger variation in data is caused by solvent evaporation in the sample. This could be induced by the sample being shuttled between the spectrometer and the flow cell a number of times via a nitrogen flow. However if this were the case, it would be expected that the error would increase with bubble time. . Interestingly, the variation in data across the different bubble times is minimal for a. For example, the lowest average enhancement of −193-fold was observed for a 5s bubble time, compared to −227-

fold for a 10 second bubble time. This suggests that the shake/bubble time does not influence the enhancement as much as the field strength, transfer time or shake/bubble intensity. 104
Figure 43 – Schematic diagram describing the use of the handheld magnetic array. 1) 4 bar pH$_2$ is added to SABRE active species in an NMR tube fitted with a young's tap, 2) The sample is placed inside the handheld magnetic array, 3) The handheld magnetic array containing the sample is shaken to allow for polarisation transfer into the substrate, 4) the sample is removed from the handheld magnetic array and transferred into the spectrometer for detection 106
Figure 44 – The hand-held shaker adapted with permissions from P. M. Richardson et *al.*[5] 106
Figure 45 – Photo of the hand-held shaker and corresponding magnetic field profile measured along the central axis of the cylinder. Image taken with permission from P. M. Richardson et *al.*[5].....107
Figure 46 – ^{1}H signal enhancement plotted as a function of shake time for the *ortho* proton in the free substrate for SABRE active species [Ir(H)$_2$(SIMes)(sub)$_3$]Cl containing the substrate 4-methylpyridine. The green represent measurements taken on the narrow bore 400 MHz spectrometer a, and the purple are used for the wide bore 400 MHz spectrometer b. Hyperpolarised measurements were collected using the 60 G handheld magnetic array in Figure 43 at 298 K. The coloured portions indicate the 25% and 75% quartiles, the whiskers the minimum and maximum enhancement values, the median line the mid-point of the data, the square the mean and the diamonds show any outliers in the data. 108
Figure 47 illustrates the variation in ^{1}H signal enhancement at the *ortho* proton as a function of shake time. The largest average enhancement was observed for a shake time of 10 seconds. On spectrometer a this shake time induced a signal enhancement of −497-fold compared to −339-fold on spectrometer b. Furthermore, larger enhancements were observed on instrument a compared to b. If the individual data points are considered, the largest enhancement was −564-fold on a compared to −410-fold on NMR b (outlieing data point for a 5 second shake time). 108
If the average signal enhancements are considered, there was less variation overall in the data using the handheld magnetic array. For example, on NMR a, the minimum

average enhancement was −442-fold (15 second shake time) compared to the maximum of −497-fold (10 second shake time). However, if the individual data points are considered, the minimum measurement was −387-fold (15 second shake time) compared to −564-fold (10 second shake time). On NMR b, the lowst average signal enhancement was −339-fold (7 and 10 second shake times) compared to the maximum signal enhancement of −365-fold (5 second shake time). Considering the individual measurements, the lowest signal enhancement was −279-fold (10 second shake time) and the highest was 396-fold (15 second shake time). This lower variation in data suggests that the sample shake time is less important compared to the polarisation transfer field and the transfer time. As the field has been kept constant at 63 G, this means that it is the difference in transfer time that has contributed to the lower enhancements observed on b compared to a.It is clear that this method is less reproducible than both the manual shaking method using the stray field of the spectrometer and the automated flow system. This can be observed by the number of data anomalies shown in Figure 48 for both spectrometers. The lower reproducibility can also be attributed to the differences in transfer time between measurements as the sample must be removed from the shaker before being dropped into the spectrometer for acquisition. 109
The effect of *p*-H_2 dissolution time has been compared to the ^{1}H signal enhancements for each method. This was observed by plotting the shake time or the bubble time as a function of signal enhancement. In order to compare the methods directly, the ^{1}H signal enhancements for each method have been plotted for a 10 second shake time for spectrometers a and b, this is shown in Figure 49. 109
Figure 50 – Signal enhancement plotted as a function of SABRE methodfor the *ortho* proton in the free substrate 4-methylpyridine in the SABRE-active species $[Ir(H)_2(SIMes)(sub)_3]Cl$. This is shown for a *p*-H_2 dissolution time of 10 seconds. Plot a) in green compares the signal enhancements measured on the 400 MHz narrow bore instrument a Plot b) compares the signal enhancements measured on the 400 MHz wide bore instrument b. The manual shaking method is is labelled ‘M.S’, the handheld magnetic array is labelled ‘H.M.A’ and the automated flow system is labelled ‘A.F’. All measurements were collected at 298 K using a sample of [Ir(COD)(SIMes)(sub)]Cl (5 mM), 4-methylpyridine (50 mM) and *p*H_2 (4 bar) in

methanol-d_4. c) Enhancement Factor as a function of SABRE method adapted from Richardson *et al*.[5] with permissions. These measurements were collected at 298 K using a sample of [Ir(COD)(IMes)(sub)]Cl (5 mM), 4-methylpyridine (50 mM) and pH$_2$ (4 bar) and a 10 second p-H$_2$ dissolution time.....110
Box plots a) and b) in Figure 51 compare the ^{1}H signal enhancements for a 10 second shake time for each SABRE methods on spectrometers a (graph a) and b (graph b). The manual shaking method using the stray field of the spectrometer is indicated by 'M.S', the handheld magnetic array by 'H.M.A' and the automated flow system by 'A.F'. Both plots a) and b) show that the largest signal enhancements were measured using the manual shaking method. On NMR a, this generated a average enhancement of – 891-fold compared to −497-fold using the handheld magneti array and −227-fold using the automated flow system. If the individual measurements are considered, the largest enhancement was −935-fold using the manual shaking method. Similarly, on NMR b, the largest enhancements were also observed using the manual shaking method. This induced an average enhancement of −842-fold, however the largest individual measurement was −974-fold which is larger than the maximum observed on NMR b. An average enhancement of −339-fold was observed using the handheld magnetic array and −135-fold using the automated flow system. A larger variation in the data was generated by spectrometer b compared to a. This is clearly observed by the large box plot using the automated flow method. Larger variations were also observed with the manual shaking method and the handheld magnetic array. For example, the data ranged from −714-fold to −974 fold for the manual shaking method. On NMR a, the data ranged from −832-fold to −935-fold. This difference in reproducibility is attributed to the longer transfer time induced when using instrument b. A longer transfer time means that hyperpolarisation can be lost before the data can be acquired. Furthermore, as results were found to be more reproducible using NMR a compared to b, this was used for all the SABRE experiments in the remainder of this thesis.....110
Figure 52 – Resonance structures for pyridine.....116
Figure 53 – comparison of the effect of a) electron withdrawing groups (EWG) and b) electron donating groups (EDG) in the *para* position of pyridine on the metal-ligand interaction.....118

Figure 54 - The chemical structures of the para-substituted pyridines substrates chosen for this study. 119
Figure 55 – The two forms of the substituted pyridine in solution with methanol and hydrochloric acid (HCl) used to control the pH of the solution 120
Figure 56 – Chemical shift as a function of pH for 4-chloropyridine in methanol-d_4. HCl was used to reach low pH values and KOH was added to achieve high pH. The data points have been fitted using Equation 14. 123
Figure 57 – ^{1}H-NMR spectra showing the SABRE precatalyst [Ir(COD)(SIMes)(sub)]Cl for the substrate 4-methylpyridine. The sample was prepared by adding [IrCl(COD)(SIMes)] (4 mM) to 4-methylpyridine (40 Mm) in methanol-d_4. The sample was measured at 235 K and 500 MHz. 124
Figure 58 - ^{1}H-NMR spectrum for [Ir(COD)(SIMes)(4-pyridinacarboxaldehyde)]Cl in methanol-d_4 measured at 500 MHz and 263 K. Black indicates the presence of the free aldehyde conformation and the orange highlights the bound and free hemiacetal conformation. 126
Figure 59 – ^{1}H-NMR spectra for the SABRE-active species [Ir(H)$_2$(SIMes)(sub)$_3$]Cl for 4-methylpyridine. The sample was prepared using [IrCl(COD)(SIMes)] (4 mM), 4-methylpyridine (40 mM) and *p*-H$_2$ (4 bar) in methanol-d_4. The sample was measured at 235 K and 500 MHz. 128
Figure 60 - ^{1}H-NMR Spectrum of [Ir(H)$_2$(SIMes)(sub)$_3$]Cl in methanol-d_4 at 500 MHz and 263 K. Black indicates the presence of the free aldehyde conformation and the orange highlights the bound and free hemiacetal conformation. 130
Figure 61 – Thermal ^{1}H-NMR spectrum under Boltzmann conditions (black) compared to a hyperpolarised spectrum where the sample was shaken for 10 s in the stray field (65 G) of the spectrometer (400 MHz) (pink). These were measured using a sample containing 4-methylpyridine (40 mM), [IrCl(COD)(SIMes)] (4 mM) and *p*-H$_2$ (4 bar) in methanol-d_4 (0.6 mL). 132
Figure 62 – Thermal ^{1}H-NMR spectrum under Boltzmann conditions (black) compared to a hyperpolarised spectrum where the sample was shaken for 10 s in the stray field (65 G) of the spectrometer (400 MHz) (orange). These were measured using a sample containing 4-pyridinecarboxaldehyde (40 mM), [IrCl(COD)(SIMes)] (4 mM) and *p*-H$_2$ (4 bar) in methanol-d_4 (0.6 mL). 133

Figure 63 – Enhancements at the *ortho* proton resonance in the free substrate as a function of substrate p*K*a for the SABRE-active species; $[Ir(H)_2(SIMes)(sub)_3]Cl$ for each of the substrates tested. The enhancements were observed using the manual shaking method. The experiment was repeated five times and the ^1H signal enhancements at the *ortho* proton were averaged. The error bars indicate the standard error of the experiment. 134
Figure 64 – Structures for deuterated isotopologue of IMes. Image adapted from Rayner *et al*. *Proceedings of the National Academy of Sciences*, 2017. 136
Figure 65 – Enhancements at the *ortho* proton resonance in the free substrate as a function of substrate pK_a for the SABRE-active species for the four substrates. SIMes is indicated by the darker colour and d_{22}-SIMes by the lighter colour. The enhancements were observed using the manual shaking method. The experiment was repeated five times and the ^1H signal enhancements at the *ortho* proton were averaged. The error bars indicate the standard error of the experiment. 137
Figure 66 – The dissociation constant (k_d) as a function of temperature for the SABRE active species for each of the substrates shown. The error bars indicate the error associated with k_d calculated using the Jacknife method described in Chapter 6, Section 6.2.7.2 Associated errors in the calculation of k_d. A table of the associated errors can be found in Appendix B. 139
Figure 67 – Eyring-Polanyi plot for the three substrates where $\ln(k_d/T)$ is plotted against 1/T. The data have been fitted according to the equation y = mx + c. These are indicated on the graph alongside the corresponding substrate. 141
Figure 68 – Gibbs free energy ($\Delta G^{\neq}_{298K}$) as a function of the substrate pK_a for the SABRE-active species for the substrates shown. 143
Figure 69 – The modified flow cell used to study the temperature dependence of SABRE 146
Figure 70 – Enhancement factor plotted as a function of temperature for the SABRE active species for each of the substrates shown. 147
Figure 71 - Enhancement plotted as a function of the $\Delta G^{\neq}$ value at 298 K using the manual shaking method (left) and the optimum temperature for SABRE using the automated flow system (right) 149

Figure 72 - Pulse sequence for the selective 1D-COSY experiment. Adapted with permissions from P. J. Rayner et *al*. [28] 151
Figure 73 - the relative integral of the *ortho* proton in the equatorially bound substrate as a function of the delay time (d4). The data has been fitted to a sine function and the oscillation maxima has been indicated. The example shown is for $[Ir(H)_2(SIMes)(4\text{-methylpyridine})_3]Cl$. 152
Figure 74 - The long range hydride-substrate coupling, $^4J_{HH}$, as a function of the Gibbs free energy ($\Delta G^{\neq}_{298K}$) for each of the substrates indited 153
Figure 75 – T_1 as a function of $\Delta G^{\neq}_{298K}$ for the SABRE active species for the substrates shown. The graph shows the T_1 at the *ortho*-proton in the free material (dark colour) compared to the *ortho*-proton in the substrate bound *trans* to the hydride (medium colour) and the *ortho*-proton in the substrate bound *trans* to the NHC (light colour). The error bars indicate the fitting error for the T_1 curves shown in Appendix B. ... 155
Figure 76 – T_1 as a function of $\Delta G^{\neq}_{298K}$ for the SABRE active species, $[Ir(H)_2(SIMes)(sub)_3]Cl$, for the substrates shown. The graph compares the T_1 at the *ortho*-proton when SIMes is used as the NHC (darker colour) to the *ortho*-proton in the substrate when d_{22}-SIMes is used as the NHC (lighter colour). The errors in the T_1 values are calculated from fitting the T_1 curves shown in Appendix B. 157
Figure 77 – T_1 values at the *ortho*-proton in the free substrate for the substrates shown as a function of the optimum SABRE temperatures shown in Table 8. 159
Figure 78 – Basic structure for the NHC ligand 159
Figure 79 – Structures of the NHCs; SIMes, ITBXy and $IMes^{Cl}$, including the TEP and $\%V_{bur}$ values. 161
Figure 80 – The Gibbs free energy $\Delta G^{\neq}_{298K}$ as a function of the NHC in the SABRE active species, $[Ir(H)_2(NHC)(sub)_3]Cl$ for the substrates shown. 162
Figure 81 – T_1 as a function of the NHC in the SABRE active species, $[Ir(H)_2(NHC)(sub)_3]Cl$ for the substrates shown. The T_1 is for the *ortho*-proton in the free substrate. The errors in the T_1 values are calculated from fitting the T_1 curves shown in Appendix B. 164
Figure 82 - Radiation dampening observed during repeating manual shaking using the stray field of the spectrometer, with 4-methylpyridine, ITBXy and 99% *p*-H_2 165
Figure 83 - Plot of enhancements against *p*-H_2 percentage 166

Figure 84 – Enhancement factor as a function of the NHC in the SABRE active species, $[Ir(H)_2(NHC)(sub)_3]Cl$ for the substrates shown. The enhancements were observed using the manual shaking method. The experiment was repeated five times and the ^1H signal enhancements at the *ortho* proton were averaged. The error bars indicate the standard error of the experiment.....167
Figure 85 - Variation in enhancement factor with [*p*-H_2] for ITBXy and its deuterated isotopologue d_{34}-ITBXy.....168
Figure 86 - Tautomerism of 4-hydroxpyridine to 4-pyridone.....176
Figure 87 - FTIR spectra of 4-hydroxypyridine solid (black), dissolved in dichloromethane-d_2 (red) and dissolved in methanol-d_4 (blue). Solid FTIR was measured where a <1 mg of substrate was placed directly onto the diamond crystal. Solution FTIR was measured using the diamond fibre optic probe submersed into a vial containing the sample. 178
Figure 88 - ^1H NMR spectra as a function of temperature for a solution of 4-hydroxypyridine in dichloromethane-d_2. The enol tautomer is represented by the resonances highlighted in teal and the keto tautomer is indicated by the purple resonances. The darker colour represents the *ortho* ^1H resonance and the lighter colour the *meta* ^1H resonance. The samples were measured on the 500 MHz spectrometer.....179
Figure 89 - plot of ln(keto/enol) as a function of 1/T according to the linear form of the Van't Hoff equation in Equation 17 181
Figure 90 - Metal complexes formed with isoniazid. a) adapted with permissions from B. Bottari et *al.* [18] b) adapted with permissions from T. Stringer et *al.* [19] c) adapted with permissions from O. Akinyele et *al.* [20] 183
Figure 91 - Schematic diagram of the formation of the SABRE precatalyst [Ir(COD)(SIMes)(sub)]Cl with the substrate 4-hydroxypyridine 184
Figure 92 - ^1H NMR spectra of the SABRE precatalyst; [Ir(COD)(SIMes)(4-hydroxypyridine)]Cl. The sample contained [IrCl(COD)(SIMes)] (5 mM) and 4-hydroxypyridine (50 mM) dissolved in methanol-d_4 (0.6 mL). The NMR spectrum was acquired at 235 K and 500 MHz. 185
Figure 93 - $^{15}N/^1H$ HMQC NMR spectrum of a solution containing [IrCl(COD)(SIMes)] (5 mM) and ^{15}N-labelled 4-hydroxypyridine (50 mM) in methanol-d_4 at 9.4 T and 253

K. The purple highlighted resonance indicates the ^{15}N-labelled pyridine nitrogen in the bound 4-hydroxypyridine in the SABRE precatalyst; [Ir(COD)(SIMes)(sub)]Cl..186
Figure 94 - ^{1}H NMR spectra as a function of temperature for a solution of 4-hydroxypyridine (40 mM) and [IrCl(COD)(SIMes)]Cl (4 mM) in dichloromethane-d_2. The enol tautomer is represented by the resonances highlighted in teal and the keto tautomer is indicated by the purple resonances. Only the resonances at the *ortho* proton are shown. These spectra were measured on a 500 MHz spectrometer. ..187
Figure 95 - plot of ln(keto/enol) as a function of 1/T according to the linear form of the Van't Hoff equation in Equation 1 189
Figure 96 - Schematic diagram for the formation of the SABRE precatalst [Ir(COD)(SIMes)(sub)]Cl for the substrate isonaizid showing the major and minor forms. The major species binds to the iridium via the oxygen in the hydrazide group and the minor binds via the pyridine nitrogen. 190
Figure 97 - ^{1}H NMR spectrum of the SABRE precatalyst [Ir(COD)(SIMes)(isoniazid)]Cl. Sample initially contained [IrCl(COD)(SIMes)(sub)] (5 mM) and isoniazid (50 mM) in methanol-d_4 (0.6 mL) and was measured at 500 MHz and 235 K. 191
Figure 98 - ^{1}H/^{15}N HMQC NMR spectrum of a solution of [IrCl(COD)(SIMes)] (5 mM) and isoniazid (50 mM) in methanol-d_4 at 9.4 T and 263 K. 193
Figure 99 - ^{15}N NMR spectrum of the SABRE precatalyst [Ir(COD)(SIMes)(isoniazid)]Cl with i^{15}N-labelled labelled isoniazid. ^{15}N NMR spectrum measured at 40.56 MHz and 263 K. The strong signals are due to the free ligand 194
Figure 100 - Schematic diagram showing the formation of the SABRE-active species [IrCl(H)$_2$(SIMes)(κ-O-4-pyridone)(κ-N-4-hydroxypyridine)] from the precatalyst [Ir(COD)(SIMes)(4-hydroxypyridine)]Cl.....195
Figure 101 - ^{1}H NMR spectrum of the SABRE-active species [IrCl(H)$_2$(SIMes)(κ-O-4-pyridone)(κ-N-4-hydroxypyridine)] . Sample contains [IrCl(COD)(SIMes)] (5 mM), 4-hydroxpyridine (50 mM) and *p*-H$_2$ (4 bar) dissolved in methanol-d_4 (0.6 mL) in a young's tap NMR tube. Sample was measured at 500 MHz and 235 K. 195
Figure 102 - ^{1}H/^{13}C -HMQC NMR spectrum of [IrCl(H)$_2$(SIMes)(κ-O-4-pyridone)(κ-N-4-hydroxypyridine)]. Sample containing [IrCl(COD)(SIMes)] (5 mM), 4-hydroxypyridine (50 mM) and *p*-H$_2$ (4 bar) dissolved in methanol-d_4 measured at 11.74 T at 235 K. Resonance for the keto carbon shown at 180 ppm (^{13}C)/7.35 ppm (^{1}H) is highlighted

in lilac and resonance for the enol carbon shown at 164 ppm (^{13}C)/7.69 ppm (^{1}H) highlighted in purple. 197
Figure 103 –^{1}H/^{15}N -HMQC of [IrCl(H)$_2$(SIMes)(κ-O-4-pyridone)(κ-N-4-hydroxypyridine)]. Sample containing [IrCl(COD)(SIMes)] (5 mM), 4-hydroxypyridine (50 mM) and *p*-H$_2$ (4 bar) dissolved in methanol-*d*$_4$ measured at 500 MHz (^{1}H) and 51 MHz (^{15}N) at 235 K. Resonance for the nitrogen in the keto tautomer shown at 215 ppm (^{15}N)/7.35 ppm (^{1}H) is highlighted in lilac and the resonance for the nitrogen in the enol form is shown at 148.8 ppm (^{15}N)/7.69 ppm (^{1}H) highlighted in purple...198
Figure 104 - Schematic diagram showing the formation of the SABRE-active species [Ir(H)$_2$(SIMes)(κ-N-isonicotinylhydrazide)(isonicotinyl-κ-O-κ-N-hydrazide]Cl from the pre-catalyst [Ir(COD)(SIMes)(sub)]Cl. 199
Figure 105 - ^{1}H NMR spectra of the SABRE-active catalyst formed upon the reaction of [IrCl(COD)(SIMes)] (5 mM) with isoniazid (50 mM) and *p*-H$_2$ (4 bar) in methanol-*d*$_4$ (0.6 mL). Spectra measured at 500 MHz and 235 K. 199
Figure 106 – ^{1}H/^{15}N-HMQC NMR spectrum of the product formed when [IrCl(COD)(SIMes)] (5 mM), isoniazid (50 mM) and *p*-H$_2$ (4 bar) react together in methanol-*d*$_4$ (0.6 mL), measured at 500 MHz (^{1}H) and 51 MHz (^{15}N) and 235 K. The ^{15}N resonance of the pyridine bound isoniazid ligand is highlighted at 261.1 ppm (^{15}N)/8.07 ppm (^{1}H) in light blue and the resonance for the chelate bound isoniazid is shown at 311 ppm (^{15}N)/8.81 ppm (^{1}H) in dark blue. 201
Figure 107 – ^{1}H/^{13}C-HMQC NMR spectrum of the product formed when [IrCl(COD)(SIMes)] (5 mM), isoniazid (50 mM) and *p*-H$_2$ (4 bar) react in methanol-*d*$_4$ (0.6 mL). Measured at 500 MHz (^{1}H) and 125 MHz (^{13}C) and 235 K. The ^{13}C resonance of pyridine bound isoniazid is highlighted at 165 ppm (^{13}C)/8.07 ppm (^{1}H) in light blue and the resonance for the chelate bound isoniazid is shown at 170 ppm (^{13}C)/8.81 ppm (^{1}H) in dark blue. 202
Figure 108 – ^{15}N NMR spectrum of ^{15}N labelled isoniazid measured at 41 MHz and 298 K for a sample containing [IrCl(COD)(SIMes) (5 mM), isoniazid (50 mM) and *p*-H$_2$ (4 bar) in methanol-*d*$_4$ (0.6 mL). ^{15}N resonances for the pyridine bound hydrazide nitrogen atoms are highlighted in light blue while those for the chelate bound form are shown in dark blue. 203

Figure 109 - Thermal ^{1}H-NMR spectrum under Boltzmann conditions (black) compared to a hyperpolarised spectrum where the sample was shaken for 10 s in the stray field (65 G) of the spectrometer (400 MHz) (purple = 4-hydroxypyridine, blue = isoniazid). These spectra were measured using a sample containing the substrate (40 mM), [IrCl(COD)(SIMes)] (4 mM) and *p*-H_2 (4 bar) in methanol-d_4 (0.6 mL). The thermal spectrum has been magnified 8 times for 4-hydroxypyridine and 16 times for isoniazid in the stacked spectra. The enhancements at the *ortho* and *meta* resonances have been calculated. 205
Figure 110 – ^{1}H NMR signal Enhancement factor as a function of substrate enhancement for the SABRE-Active species containing 4-methylpyridine, 4-hydroxypyridine and isoniazid in methanol-d_4 measured at 400 MHz and 298 K. . 206
Figure 111 - Suggested dimer structures for the SABRE active species for (a) 4-hydroxypyridine and (b) isoniazid 207
Figure 112 - The PFG-SE pulse sequence 210
Figure 113 - Signal intensity as a function of the gradient strength. The data has been plotted according to Equation 21. The delays used for δ and Δ have been indicated alongside the calculated diffusion coefficient (D) 211
Figure 114 - 2D DOSY spectra of [Ir(H)$_2$(SIMes)(4-methylpyridine)$_3$]Cl. Sample contained [IrCl(COD)(SIMes)] (5 mM), 4-methylpyridine (50 mM)), *p*-H_2 (4 bar absolute) dissolved in methanol-d_4 (0.6 mL) measured at 400 MHz and 298 K. This figure is used for illustrative purposes only. 213
Figure 115 - 2D DOSY ^{1}H NMR spectra of [Ir(H)$_2$(SIMes)(4-methylpyridine)$_3$]Cl. Sample contained [IrCl(COD)(SIMes)] (5 mM), 4-methylpyridine (50 mM)), p-H_2 (4 bar) dissolved in methanol-d4 (0.6 mL) measured at 400 MHz and 273 K. This figure is used for illustrative purposes only. 214
Figure 116 - 2D DOSY ^{1}H NMR spectra of [IrCl(H)$_2$(SIMes)(κ-O-4-pyridone)(κ-N-4-hydroxypyridine)] . Sample contained [IrCl(COD)(SIMes)] (5 mM), 4-hydroxypyridine (50 mM) and p-H2 (4 bar) dissolved in methanol-d4 (0.6 mL) measured at 400 MHz and 298 K. This figure is used for illustrative purposes only. 217
Figure 117 – 2D DOSY ^{1}H NMR spectra of [IrCl(H)$_2$(SIMes)(κ-O-4-pyridone)(κ-N-4-hydroxypyridine)]. Sample contained [IrCl(COD)(SIMes)] (5 mM), 4-hydroxypyridine

(50 mM) and *p*-H_2 (4 bar) dissolved in methanol-d_4 (0.6 mL) measured at 400 MHz and 253 K. This figure is used for illustrative purposes only. 218
Figure 118 - 2D DOSY ^{1}H NMR spectra of [Ir(H)$_2$(SIMes)(κ-N-isonicotinylhydrazide)(isonicotinyl-κ-O-κ-N-hydrazide]Cl Sample contained [IrCl(COD)(SIMes)] (5 mM), isoniazid (50 mM) and p-H2 (4 bar) dissolved in methanol-d4 (0.6 mL) measured at 400 MHz and 298 K. This figure is used for illustrative purposes only. 220
Figure 119 – 2D DOSY ^{1}H NMR spectra of [Ir(H)$_2$(SIMes)(κ-N-isonicotinylhydrazide)(isonicotinyl-κ-O-κ-N-hydrazide]Cl. Sample contained [IrCl(COD)(SIMes)] (5 Mm), isoniazid (50 Mm) and p-H2 (4 bar) dissolved in methanol-d4 (0.6 Ml) measured at 400 MHz and 273 K. This figure is used for illustrative purposes only. 221
Figure 120 – Rate of ligand dissociation (k_d) as a function of temperature for the complexes form when [IrCl(COD)(SIMes)]Cl (5 mM), the indicated substrate (50 Mm) and *p*-H_2 (4 bar) are probed in methanol-d_4 (0.6 mL) at 500 MHz. Data points corresponding to isoniazid are shown in blue squares, 4-hydroxypyridine are represented by purple circles and 4-methylpyridine are shown by pink triangles. The error bars indicate the error associated with k_d calculated using the Jacknife method described in Chapter 6, Section 6.2.7.2 Associated errors in the calculation of k_d. A table of the associated errors can be found in Appendix C. 223
Figure 121 - Eyring polanyi plot for the SABRE-active species containing 4-hydroxypyridine, isoniazid and 4-methylpyridine. 225
Figure 122 – Gibbs free energy as a function of substrate in the SABRE-active species. 226
Figure 123 – Comparison of the *Ortho*H T_1 values for 4-hydroxypyridine (purple) and isoniazid (blue). The T_1 for the substrate without catalyst was measured using at 40 mM in methanol-d_4. The T_1 in the presence of catalyst was measured using a sample containing [IrCl(COD)(SIMes)] (4 mM), substrate (40 mM) and *p*-H_2 (4 bar) in methanol-d_4. All measurements were taken at 298 K and 400 MHz. The error bars indicate the fitting error for the T_1 curves shown in Appendix C. 228
Figure 124 - hmqcgpqf pulse sequence 244
Figure 125 - zgig pulse sequence 244

Figure 126 - standard zg pulse sequence 245
Figure 127 - selnogp pulse sequence 245
Figure 128 - selcogp pulse sequence 246
Figure 129 - ledbpgp2s pulse sequence 246
Figure 130 - invrec pulse sequence 247
Figure 131 – Schematic diagram of the automated flow probe. 1) A sample of $[Ir(H)_2(SIMes)(sub)_3]Cl$ in methanol-d_4 is contained in a flow cell where pH_2 (4 bar) is bubbled through the solution, 2) The hyperpolarised sample is transferred into the spectrometer via a nitrogen flow, 3) The hyperpolarised spectrum is acquired using the one-shot pulse sequence described in Figure 28, 4) The sample is transferred from the spectrometer back to the flow cell using a nitrogen flow. Image adapted with permissions R. E. Mewis, K. D. Atkinson, M. J. Cowley, S. B. Duckett, G. G. Green, R. A. Green, L. A. Highton, D. Kilgour, L. S. Lloyd, J. A. Lohman and D. C. Williamson, *Magn. Reson. Chem.*, 2014, 52, 358-369.[6] 249
Figure 132 – The modified flow cell used to study the temperature dependence of SABRE 250
Figure 133 - The two forms of the substituted pyridine in solution with methanol and hydrochloric acid (HCl) used to control the pH of the solution 254
Figure 134 - Exchange species for substrate dissociation in $[Ir(H)_2(NHC)(substrate)_3]Cl$. The asterix, *, is used to denote the ^1H resonance that is selectively excited. 257
Figure 135 - Movement of excited signal from the bound substrate to the free substrate over time 259
Figure 136 - Percentage signal intensity as a function of the delay time. The diamond and square markers are used to signify the experimental data set and the lines the simulation. Dark blue represents the bound substrate and the light blue signifies the free substrate. 259
Figure 137 - Table showing how the uncertainties are generated using the Jackknife method alongside the experimental data set. 260
Figure 138 - Eyring plot where ln(2kd/T) is plotted as a function of 1/T. The data is fitted using a linear fit of the form y = mx + c. 262

Figure 139 - Summary output from the linear regression analysis from the Eyring plot shown in Figure 1. Red is used to indicate numbers relevant to the gradient and blue indicates those related to the intercept. In the equations, R = gas constant and T = temperature (K).....263
Figure 140 - The magnetisation (M_{XY}) for a spin ½ nuclei as a function of time (τ) after exposure of the system to a magnetic field. M_0 is the magnetisation at thermal equilibrium and T_1 is the spin-lattice/longitudinal relaxation time.....265
Figure 141 - Single-shot hyperpolarised T_1 variable flip angle pulse sequence 266
Figure 142 - Signal intensity as a function of the gradient strength. The data has been plotted according to Equation 21. The delays used for δ and Δ have been indicated alongside the calculated diffusion coefficient (D) 270
Figure 143 - *Ortho* ^{1}H resonance in 4-Chloropyridine 273
Figure 144 - *Meta* ^{1}H resonance in 4-chloropyridine.....274
Figure 145 - *Ortho* ^{1}H resonance in 4-pyridinecarboxaldehyde 275
Figure 146 - *Meta* ^{1}H resonance in 4-pyridinecarboxaldehyde 276
Figure 147 - *Para* ^{1}H resonance in 4-pyridinecarboxaldehyde 277
Figure 148 - *Ortho* ^{1}H resonance in 4-methylpyridine.....278
Figure 149 - *Meta* ^{1}H resonance in 4-methylpyridine.....279
Figure 150 - *Para* ^{1}H resonance in 4-methylpyridine.....280
Figure 151 - *Ortho* ^{1}H resonance in 4-methoxypyridine.....281
Figure 152 - *Meta* ^{1}H resonance in 4-methoxypyridine.....282
Figure 153 - *Para* ^{1}H resonance in 4-methoxypyridine.....283
Figure 154 – Oscillation frequency for 4-chloropyridine.....295
Figure 155 - 4-methylpyridine.....296
Figure 156 - 4-methoxypyridine.....297
Figure 157 - 4-pyridinecarboxaldehyde 298
Figure 158 - T_1 for 4-chloropyridine.....299
Figure 159 - T_1 for 4-methylpyridine.....300
Figure 160 - T_1 for 4-methoxypyridine.....300
Figure 161 - T_1 for 4-pyridinecarboxaldehyde 301
Figure 162 - 4-chloropyridine.....301
Figure 163 - 4-methylpyridine.....302

Figure 164 - 4-pyridinecarboxaldehyde 302
Figure 165 - 4-chloropyridine 303
Figure 166 - 4-methylpyridine 303
Figure 167 - 4-methoxypyridine 304
Figure 168 - 4-pyridinecarboxaldehyde 304
Figure 169 - T_1 for substrate 4-chloropyridine 309
Figure 170 - T_1 for substrate 4-methylpyridine 310
Figure 171 - T_1 for substrate 4-methoxypyridine 310
Figure 172 - T_1 for substrate 4-pyridinecarboxaldehyde 311
Figure 173 - A single-shot pulse sequence for measuring the lifetime of hyperpolarisation 312
Figure 174 - Hyperpolarised T_1 for substrate 4-chloropyridine 313
Figure 175 - T_1 for substrate 4-methylpyridine 313
Figure 176 - T_1 for substrate 4-methoxypyridine 314
Figure 177 - T_1 for substrate 4-pyridinecarboxaldehyde 314
Figure 178 - *ortho*H enhancement factor for different substrate concentrations for the substrates in Chapter 4 315
Figure 179 - Free substrate 316
Figure 180 - *Trans* to H^- 317
Figure 181 - *Trans* to NHC 318
Figure 182 – SIMes 319
Figure 183 - Free substrate 320
Figure 184 - *Trans* to H^- 321
Figure 185 - *Trans* to NHC 322
Figure 186 – SIMes 323
Figure 187 - Free Substrate 324
Figure 188 – SIMes 325
Figure 189 - Free substrate 326
Figure 190 - Nitrogen bound substrate 327
Figure 191 - Oxygen bound substrate 328
Figure 192 – SIMes 329
Figure 193 - Free substrate 330

Figure 194 - Chelate bound substrate.....331
Figure 195 - Pyridine bound substrate.....332
Figure 196 - SIMes.....333
Figure 197 - dissociation constant (k_d).....333
Figure 198 - dissociation constant (k_d) and associated errors calculated using the Jackknife method for the substrates in Chapter 4.....334
Figure 199 - 4-hydroxypyridine.....334
Figure 200 - isoniazid.....335
Figure 201 - 4-hydroxypyridine.....335
Figure 202 - isoniazid.....336
Figure 203 - 4-hydroxypyridine (oxygen bound).....336
Figure 204 - isoniazid (nitrogen bound).....337
Figure 205 - 4-hydroxypyridine (nitrogen bound).....337
Figure 206 - isoniazid (chelate bound).....338

Acknowledgements

Firstly I would like to thank my supervisor Professor Simon Duckett for all his support and advice throughout my PhD. He encouraged me to publish a first author paper and had faith in me when I did not believe in myself.

I would also like to thank the Duckett research group for their support, encouragement, help and advice throughout my research. I would particularly like to thank Peter Richardson, not only for helping me conduct many of my experiments whilst I was pregnant and unable to, but for keeping me sane and constantly making me laugh. I would like to thank my office mates (and friends!) Peter Rayner, Peter Richardson, Jenny, Olga, Liz, Barby, Kate and Rhianna for distracting me from writing with drinks, dinners, trips away and plenty of laughter! I'd like to thank Vicky and Richard for all their technical support and always answering my questions, no matter how stupid they may seem. Thank you also to Peter Rayner and Phil Norcott for the synthesis of the metal complexes and isotopically labelled substrates.

Lastly and most importantly, I'd like to thank my family. Mum and dad thank you for your never-ending love, support and encouragement. Mum thank you for all the times you've taken James so that I can focus on writing and making sure I'm fed and taken care of. Dad thank you for always being on the other end of the phone with your advice and reassurance. Harry and Katie thank you for taking absolutely zero interest in my research and always making me laugh. I'd also like to thank my partner's parents, Alan and Wendy for their support.

My partner Sam, without you this thesis probably would have never made it onto paper. Thank you for your continuous encouragement to achieve my goals. Finally, my son James, thank you for keeping mummy laughing and smiling throughout this difficult time (especially writing during a worldwide pandemic and lockdown!). I hope that this shows you that even when everything is against you, you can make the impossible, possible.

Declaration

I declare that this thesis is a presentation of original work and I am the sole author. This work has not previously been presented for an award at this, or any other, University. All sources are acknowledged as References.

Abbreviations

A.F	Automated Flow System
ALTADENA	Adiabatic Longitudinal Transport After Dissociation Engenders Net Alignment
COA	Cyclooctane
COD	1,5-Cyclooctadiene
COE	Cyclooctene
DNP	Dynamic Nuclear Polarisation
DOSY	Diffusion-Ordered Spectroscopy
EXSY	Exchange Spectroscopy
FID	Free Induction Decay
FTIR	Fourier Transform InfraRed Spectroscopy
$\Delta G^{\neq}$	Gibbs free energy
$\Delta H^{\neq}$	Enthalpy
H.M.A	Handheld magnetic array
HMQC	Heteronuclear Multiple Quantum Coherence
HyperT_1	Hyperpolarised lifetime or T_1

IMes	1,3-Bis(2,4,6-trimethylphenyl)-imidiazol-2-ylidene
IMes^{Cl}	1,3-Bis(2,4,6-trimethylphenyl)-4,5-dichloroimidazol-2-ylidine
ITBXy	1,3-Bis(4-*tert*-butyl-2,6-dimethylphenyl)imidazole-2-ylidine
K_a	Ionisation constant
k_d	Dissociation rate constant
LLS	Long-lived states
M.S	Manual shaking method using the stray field of the spectrometer
MRI	Magnetic Resonance Imaging
NMR	Nuclear Magnetic Resonance
***o*-H_2**	*Ortho*hydrogen
OP	Optical Pumping
PASADENA	*Para*hydrogen And Synthesis Allows Dramatically Enhanced Nuclear Alignement
***p*-H_2**	*para*hydrogen
PHIP	*Para*hydrogen Induced Polarisation
PTF	Polarisation transfer field
$\Delta S^{\neq}$	Entropy

SABRE	Signal Amplification by Reversible Exchange
SEOP	Spin Exchange Optical Pumping
SIMes	1,3-Bis(2,4,6-trimethylphenyl)-4,5-dihydroimidazol-2-ylidene
TEP	Toleman Electronic Parameter
T_1	Longitudinal Relaxation Time
$\%V_{bur}$	Percentage buried volume

Chapter 1 Introduction

1.1 Nuclear Magnetic Resonance

1.1.1 Nuclear Spin

NMR is observed through the fundamental property of nuclear spin, which is defined by the quantum number, I. All elements possess this fundamental property but they can only be observed via NMR if I is larger than zero. If I is equal to zero, they are termed 'NMR silent' and cannot be probed by NMR. However, almost all of the elements in the periodic table have at least one isotope which is NMR active, but the most commonly exploited elements for NMR are: ^{1}H, ^{13}C, and ^{15}N.

Spinning nuclei possess angular momentum, P, and charge, Ω. The motion of this charge gives rise to an associated magnetic moment, μ. When these small magnetic moments are placed in an external magnetic field, they align themselves relative to the field in a discrete number of orientations.[1]

For a spin of magnetic quantum number, I, there are 2I+1 possible spin states. For example, ^{1}H has a spin quantum number, I = ½, therefore it has two possible orientations. These are, +½ (α) or −½ (β), where α is parallel to the magnetic field (B_0) and β is antiparallel to B_0. As B_0 is a static field, it imposes a torque on the spinning nuclei meaning it traces a circular path about the applied magnetic field. This is called the Larmor precession and is depicted in Figure 1.[2] The rate of this precession depends on the field strength and the gyromagnetic ratio (the ratio of the magnetic moment to the angular momentum).[3, 4]

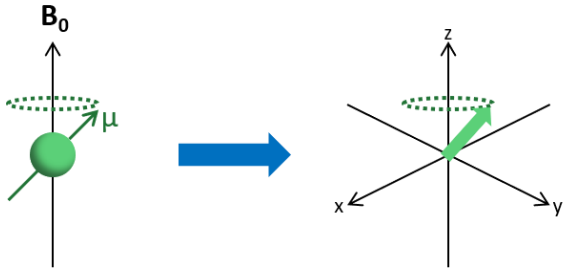

Figure 1 - The Larmor Precession

One description of nuclear magnetic resonance states that it is observed when the nucleus changes its spin state after irradiation via radio waves, the frequency of which must match that of the Larmor Precession (Equation 1).

$$\Delta E = h\nu = \frac{h\gamma B_0}{2\pi}$$

Equation 1, where h = Planck's constant, ν = resonant frequency, γ = gyromagnetic ratio, B_0= field strength

Equation 1 shows that the rate of precession is dependent on the field strength and the gyromagnetic ratio (constant relative to the nucleus of interest).

Modern NMR methods utilise radiofrequency (rf) pulses to induce magnetisation differences between the energy levels. This rf pulse creates a weak oscillating magnetic field which is dependent on the magnetic field strength of the spectrometer and the resonant frequency of the nuclei under observation. The precession of the nuclear spins about B_0 generates a voltage in the detection coil of the spectrometer. This precession occurs at the intrinsic Larmor frequency of the nuclei. A second, resonant RF pulse then flips the spins into the transverse (xy) plane, allowing detection by the spectrometer. Modern pulsed NMR methods have been well described in the literature.[5]

1.2 The Sensitivity Problem

The limiting factor of NMR is its inherent sensitivity. If we consider an assortment of similar spin ½ nuclei, in the absence of a magnetic field, the spin states are degenerate. However, once a magnetic field is applied, they may orient themselves along the field (α) or against the field (β) (where I = ½). The spins in the parallel state are lower in energy than those in the antiparallel orientation and therefore there is an excess of spins in the α state (Figure 2).

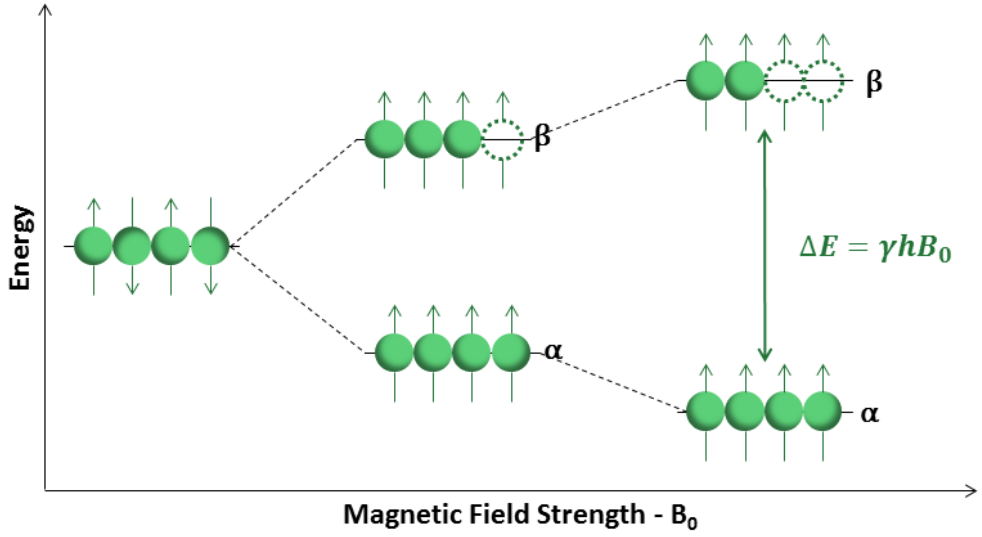

Figure 2 - The Boltzmann Distribution of Spins at Thermal Equilibrium Where ΔE = energy difference between the two states, γ = gyromagnetic ratio, h = Planck's constant & B_0 = magnetic field strength.

The distribution of the spins amongst the α and β states is determined by the Boltzmann Distribution (Equation 2).[6]

$$\frac{N_\alpha}{N_\beta} = e^{\frac{\Delta E}{k_B T}}$$

Equation 2 , where N_α = number of nuclei in the α state, N_β = number of nuclei in the β state, ΔE = energy difference between the two states, k_B = Boltzmann constant & T = temperature

According to Equation 2, the population between the two states is miniscule, for example, only 1 in 31, 000 ^{1}H nuclei are detected in a 400 MHz spectrometer at 298 K. Although this population difference can be extended by lowering the temperature or using a larger magnet, this only imposes minute differences. For instance, the world's largest magnet in operation is 1020 MHz and was developed by JEOL Resonance in Japan.[7] However, even at this high magnetic field only 1 in 15, 000 ^{1}H molecules are detected. It is for this reason that there is a requirement for techniques which magnify this population difference and hence increase sensitivity.

1.3 Hyperpolarisation

The term 'hyperpolarisation' is used to describe any method which has been designed to enhance the sensitivity of the NMR experiment. There are 3 principal techniques which are employed for this; Dynamic Nuclear Polarisation (DNP),[8-10] Optical Pumping[11-13] and *Para*hydrogen Induced Polarisation (PHIP).[14-16] Although these techniques adopt different approaches they are based on the same principle; to increase the population of the α spin state by greatly increasing the energy difference between the spin states α and β.[17, 18]

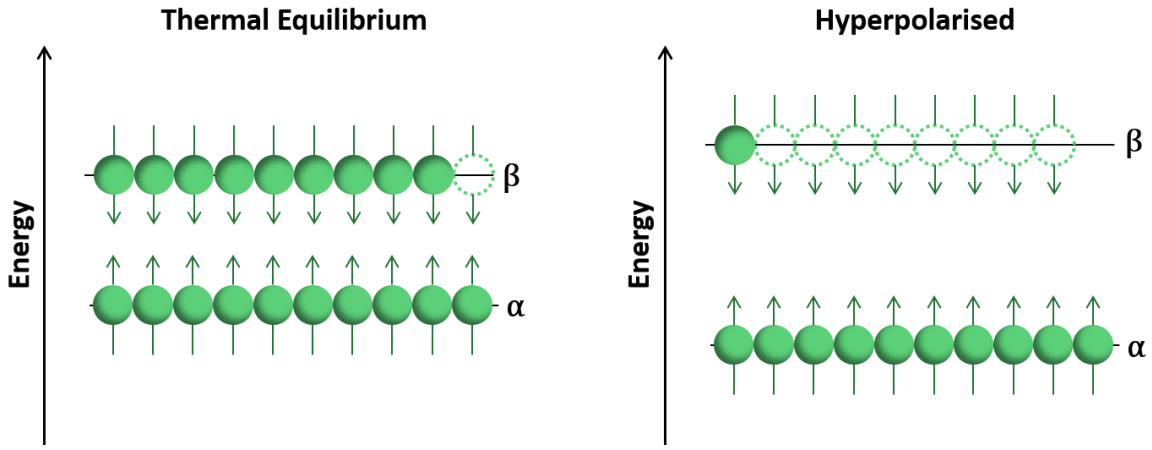

Figure 3 - The Boltzmann Distribution at Thermal Equilibrium vs Hyperpolarised. Adapted with permissions from L. Frydman, et *al*.[19]

Increasing the sensitivity of the NMR experiment via hyperpolarisation is important because it allows for the detection of low concentration analytes in solution. Potentially, this could be used for the characterisation of mixtures, reaction intermediates or impurities that were not previously visible under thermal conditions (without hyperpolarisation).[155, 156]

One of the most important applications of hyperpolarisation is its application to magnetic resonance imaging (MRI). MRI is a diagnostic tool used for the clinical diagnosis of disease by creating 3-dimensional images of anatomy and physiological processes within the body.[20-22] In NMR, protons can be used to produce a spectrum of a molecule/compound, in MRI, protons are used to image different tissue types in

the body. Generating these detailed images of the body can take a long time (15-90 minutes is typical) which can be uncomfortable for the patient. Therefore coupling hyperpolarisation techniques with MRI could reduce patient scan times as detailed images could be generated in seconds rather than minutes or hours.[23] Furthermore, hyperpolarisation methods could be used to highlight specific abnormalities to aid in the early diagnoses of disease (see section 1.3.2).[24] There are three main hyperpolarisation techniques: spin exchange optical pumping (SEOP, often referred to as optical pumping, OP), dynamic nuclear polarisation (DNP) and *para*hydrogen induced polarisation (PHIP). SEOP and DNP utilise unpaired electrons for the hyperpolarisation of NMR-active nuclei, whereas PHIP employs the singlet state of hydrogen, *para*hydrogen.

1.3.1 Optical Pumping

In 1966, Kastler was awarded the Noble Prize in physics for the development of optical pumping in alkali atoms.[11, 25] This hyperpolarisation method uses light to excite electrons within a system which is then transferred to the nuclear spins of NMR-active nuclei of interest. Typically the NMR-active nuclei of interest are helium (^{3}He) and xenon (^{129}Xe) which have widespread applications in both NMR spectroscopy and MRI. Due to their chemical inertness, they are ideal probes for surfaces with porous structures and have been used clinically for the imaging of lungs and other organs in the human body.[13, 26, 27]

To achieve non-Boltzmann nuclear spin polarisation, a vapour of alkali atoms is first irradiated with circularly polarised light. Rubidium (Rb) is commonly used as the alkali metal as the energy required for excitation (794.7 nm) can be generated by titanium sapphire lasers or high power diode lasers.[26] The electronic ground state of Rb ($5^2S_{½}$) and the corresponding excited state ($5^2P_{½}$) are split into two spin states, one with spin up and the other spin down. Irradiation with circularly polarised light induces transitions from −½ ground spin state to the +½ excited spin state. Relaxation into either of the ground states occurs with equal probability due to collisional mixing in the excited state.[26] As the −½ spin state is continuously depleted due to optical

pumping, polarisation builds up in the +½ spin state (Figure 4c). When xenon (Xe) is introduced, collisions between Xe and Rb atoms lead to the formation of Van der Waals pairs. The lifetime of these pairs allows for spin exchange to occur via hyperfine interactions (Figure 4b).[13] The pumping cell is held within a small magnetic field provided by either the fringe field of the superconducting magnet or using NMR coils. This exposes the degeneracy of the nuclear spin states of xenon, allowing for polarisation build-up. The magnetic field also prevents spin lattice relaxation of the polarised xenon gas. Chemically inert nitrogen (N_2) is also introduced to the pumping cell to quench reabsorption of photons emitted in a radiative decay process.

The polarised xenon gas nuclei exhibit much larger NMR signals compared to thermal Boltzmann conditions. Polarisation levels of >65% Xe has been observed using a high-powered (210 Watt) laser diode array system.[28] Whilst large polarisations are observed using this technique, it can only be applied to noble gases which limits its applications.

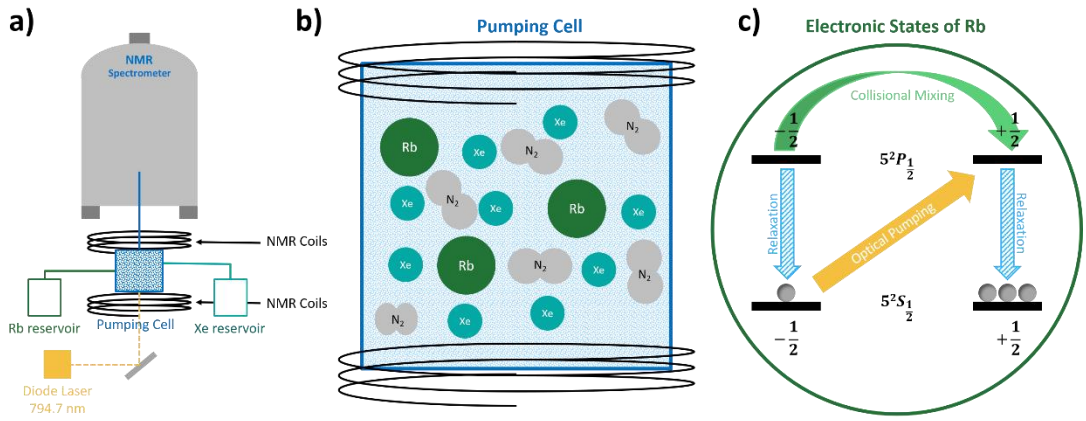

Figure 4 - a) Experimental setup for SEOP experiments. Adapted with permissions from Raftery *et al*.[29] b) Inside the pumping cell. Adapted with permissions from Walker *et al*.[13] c) Electronic transitions that occur between the Rb and Xe atoms in the pumping cell. Adapted with permissions from T. Pietrass et *al*.[26]

1.3.2 Dynamic Nuclear Polarisation

Similarly to optical pumping, dynamic nuclear polarisation (DNP) employs the high polarisation of electrons. In this technique the source of electrons are typically exogenous stable free radicals.[30, 31] There are four mechanisms of polarisation transfer from electrons to nuclear spins in DNP; the Overhauser effect,[32] the solid

effect,[33, 34] the cross effect[35, 36] and thermal mixing.[9] The dominant mechanism is dictated by the number of unpaired electrons involved. The solid effect is typically observed for a single electron, the cross effect for paired electrons and thermal mixing for extended networks of electron spins.[37]

The solid effect is a two spin process involving an electron spin (s) and a nuclear spin (I), as shown in Figure 5.[38] Forbidden zero quantum and double quantum transitions become slightly allowed when they are driven by microwave irradiation. Positive enhancements are observed for zero quantum transitions and negative enhancements for double quantum transitions.

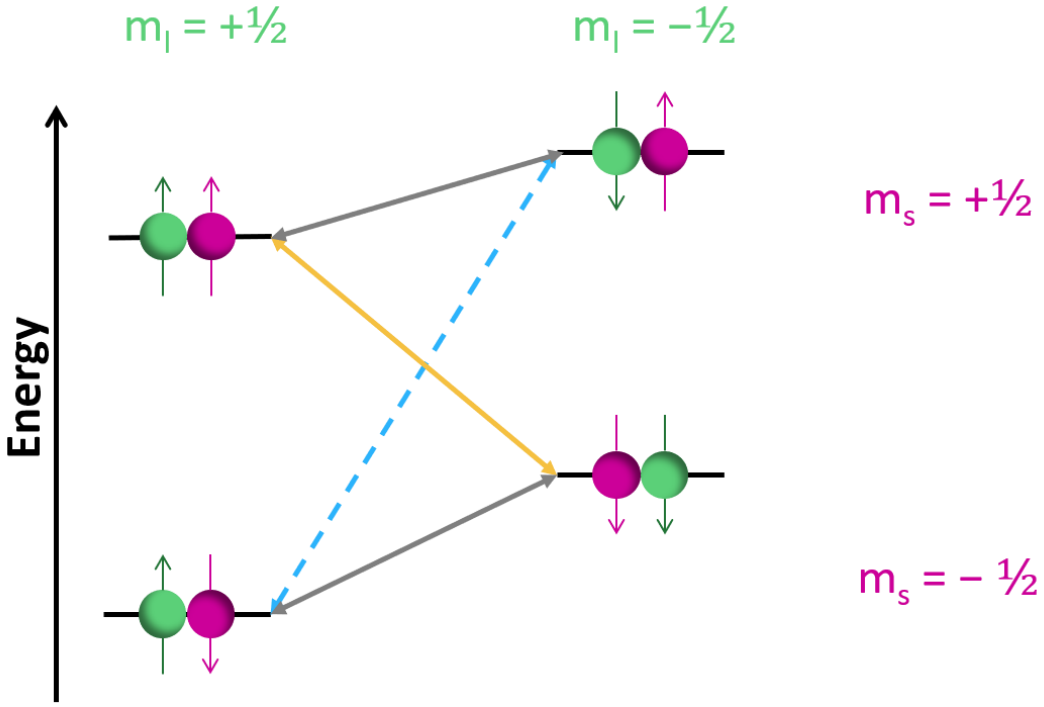

Figure 5 - Mechanism for polarisation transfer via the Solid Effect in DNP. Adapted with permissions from A. B. Barnes et *al.*[39]

The cross effect dominates when a biradical containing two coupled electrons also couple to a nuclear spin (Figure 6). Microwave irradiation then saturates transitions between states resulting in hyperpolarisation of specific nuclear spin states.[40]

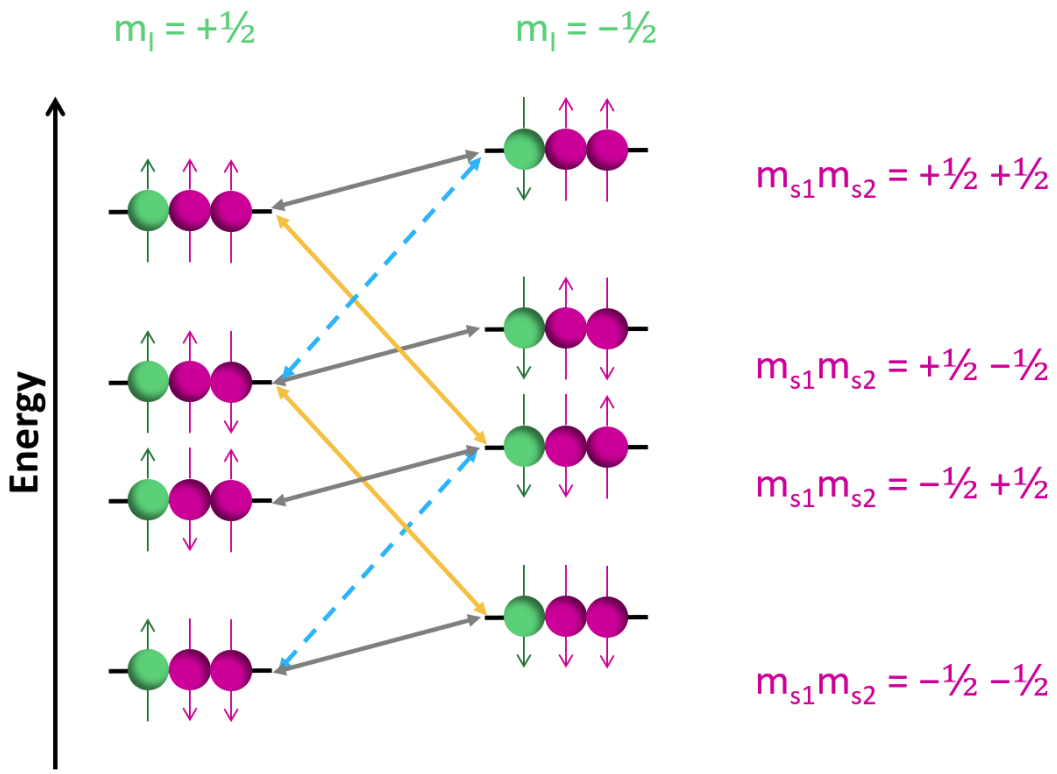

Figure 6 - Mechanism for polarisation transfer for the cross effect in DNP. Adapted with permissions from A. B. Barnes et *al.*[39]

Thermal mixing is an extension of the cross effect where couplings among electrons induce manifolds of states (Figure 7).[39] Overlap between these manifolds maximises electron nuclear transfer. This mechanism requires a high concentration of *para*magnets (electrons) which can cause broadening of NMR signals.

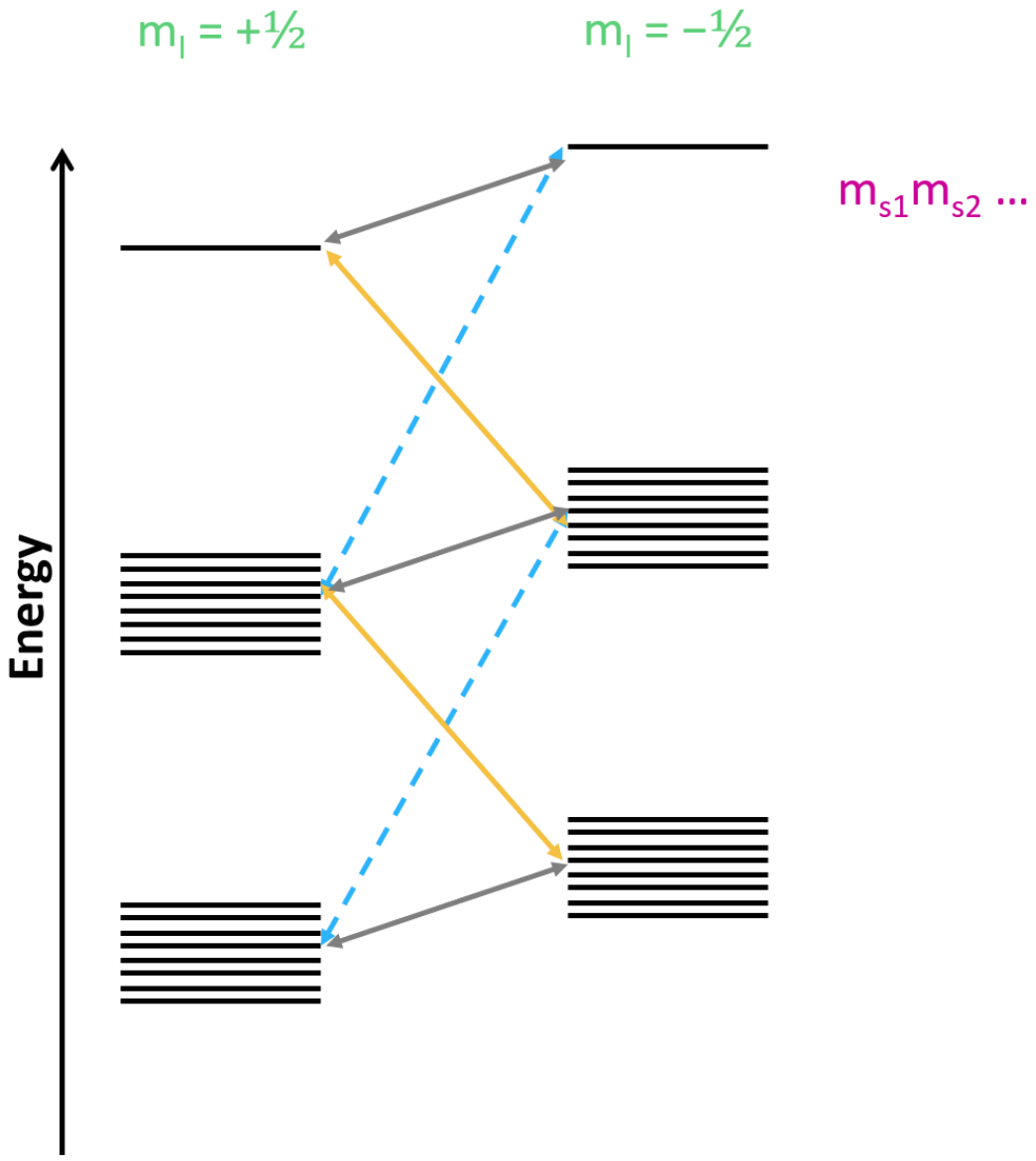

Figure 7 - Thermal Mixing mechanism for polarisation transfer in DNP. Adapted with permissions from A. B. Barnes et *al.*[39]

DNP can be conducted in both solids and liquids, but to be effective it is necessary that the radical is homogeneously distributed within the sample.[10] In liquid or dissolution DNP, nuclear polarisation is preserved during the transition from solid-liquid state. First, the free stable radical and target molecule (typically ^{13}C-enriched) is dissolved into a glass forming solvent (glycerol/glycol) and then placed into a high magnetic field. The compound is cryogenically cooled (<3 K) and then irradiated with microwaves.[41] Addition of the glass forming agent prevents crystallisation and produces an amorphous solid upon cooling.[10] After polarisation transfer, the sample

is rapidly warmed to room temperature before transfer into the NMR spectrometer for detection. This hyperpolarisation technique has yielded polarisation levels of 64 %.[42] Furthermore, performing DNP in this way enables real-time investigation of *in-vivo* metabolism via MRI. The enhanced sensitivity provided by DNP means that the kinetics of conversion of metabolites into other cell metabolites can be integrated with traditional MRI methods. The most famous example of this is the use of ^{13}C-pyruvate which has been used to observe the evolution of tumour cells. However, the main drawback of this technique is that hyperpolarisation of the target molecule can take hours. Furthermore, once hyperpolarised, the target molecule can only be used once as the hyperpolarisation is limited by the substrates T_1 which is typically on the order of a few seconds to minutes.[42]

1.4 *Para*hydrogen Induced Polarisation

*Para*hydrogen induced polarisation (PHIP), is a hyperpolarisation technique that employs *para*hydrogen (*p*-H_2) for the enhanced detection of a target substrate. This is achieved using a metal catalyst which catalyses the incorporation of *p*-H_2 into the substrate via hydrogenation reactions. PHIP was first observed in 1987 by

Weitekamp and co-workers via *para*-hydrogenation of acrylonitrile to propionitrile using Wilkinson's catalyst [$RhCl(PPh_3)_3$] (see Figure 8).[43, 44]

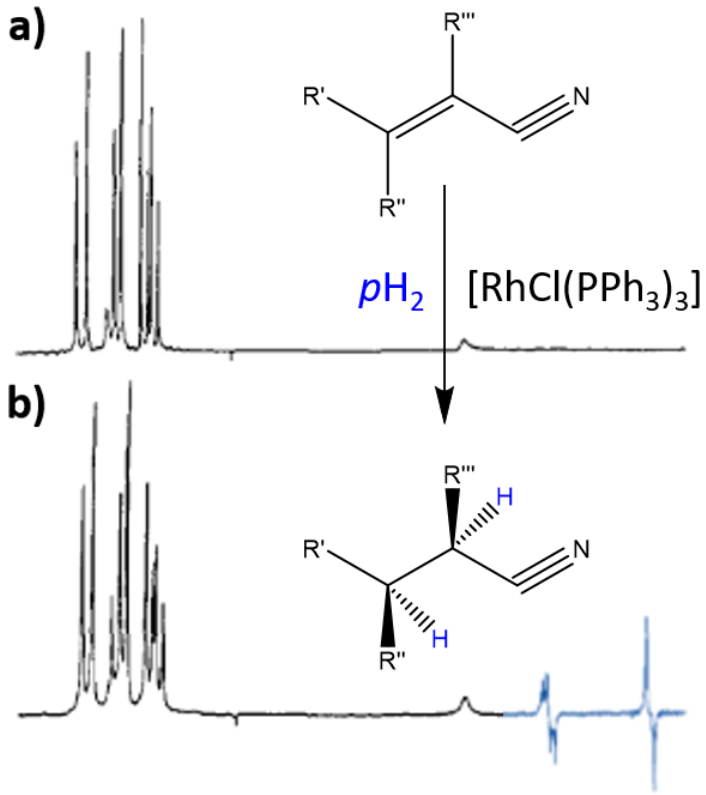

Figure 8 - Hydrogenation of acrylonitrile to propionitrile using *p*-H_2. a) ^1H spectrum of acrylonitrile under Boltzman conditions b) ^1H spectrum of *para*-hydrogenated propionitrile. The blue antiphase peaks are the *p*-H_2 derived protons in the product. Spectra a) and b) are reprinted with permissions from C. R. Bowers et *al.*[44]

1.4.1 Spin Isomers of Hydrogen

PHIP utilises *p*-H_2, the singlet state of hydrogen as the source of polarisation. Molecular hydrogen is comprised of two hydrogen atoms bound through a single, covalent bond. The nucleus of both these atoms possesses a spin, rendering it NMR active. There are four allowed spin configurations of hydrogen (Figure 9) which constitute the two spin isomers of hydrogen; *ortho*hydrogen (*o*-H_2) and *p*-H_2.

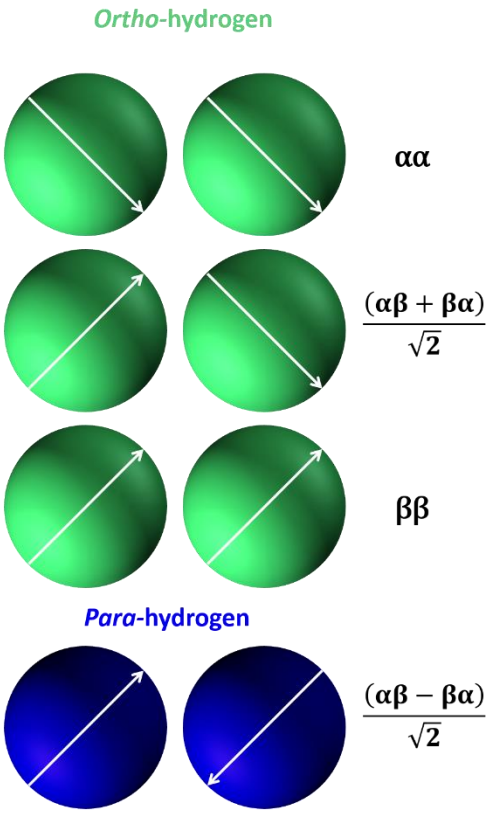

Figure 9 - The Four Spin States of Dihydrogen.

The first three spin configurations are triply degenerate where the spins are aligned parallel (↑↑ or ↓↓) so that there is a net component of spin in either the z direction or the x-y plane.[45] This triplet state is known as *o*-H_2 and is symmetric with respect to the exchange of nuclei. The final configuration is recognised as *p*-H_2 where the spins are antiparallel (↑↓) so that there is no net spin in either direction, it is also antisymmetric with respect to the exchange of nuclei.[46] It is important to note that symmetric nuclear states (*ortho*) occupy odd rotational states and antisymmetric nuclear states (*para*) occupy even rotational states. It is for this reason that *p*-H_2 is considered more stable as its lowest rotational state has *J*=0 compared to *J*=1 for *o*-H_2. This difference in energy leads to a Boltzmann distribution among the isomers, where *p*-H_2 is favoured at low temperatures.

1.4.2 Generating *Para*hydrogen

Interconversion between the *ortho*- and *para*- states of hydrogen is symmetry forbidden. However, conversion can occur in the presence of a paramagnetic

material. To produce *p*-H_2 enriched gas, hydrogen is cooled in the presence of a silica or iron (II) chloride interconversion catalyst (Figure 10).[46] Once the desired level of *p*-H_2 enrichment has been achieved, the gas is heated in the absence of catalyst for use at room temperature. This can then be stored at room temperature for long periods of time.[47-49]

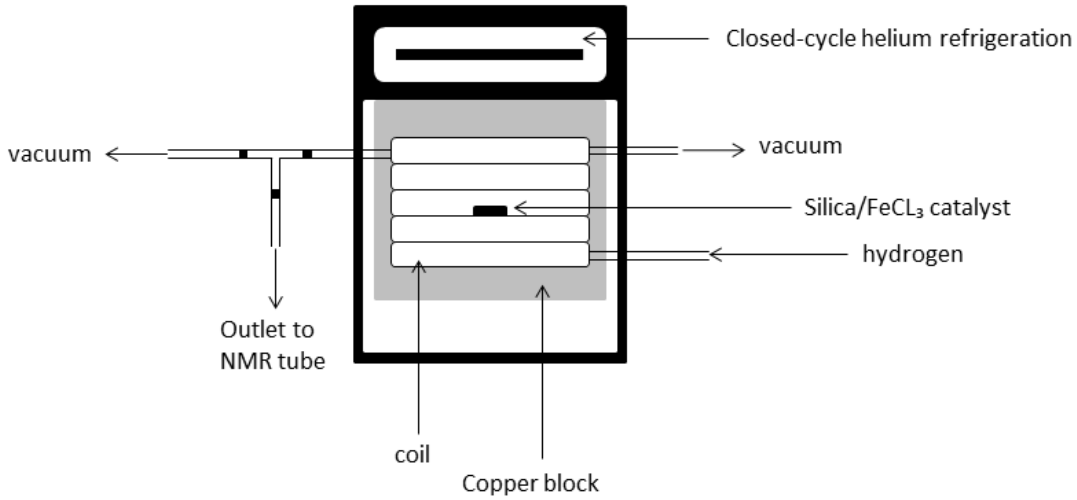

Figure 10 - Schematic of the *p*-H_2 Generator. Adapted from S. B. Duckett et *al.*[46]

The level of *p*-H_2 enrichment depends on the conversion temperature (see Figure 11). For example, at room temperature, the populations of the *ortho* and *para* states is governed by Boltzmann statistics, such that 75 % is *o*-H_2 and the remaining 25% is *p*-H_2.[50] If the temperature is cooled to 30 K, the percentage of *p*-H_2 increases to 75%.

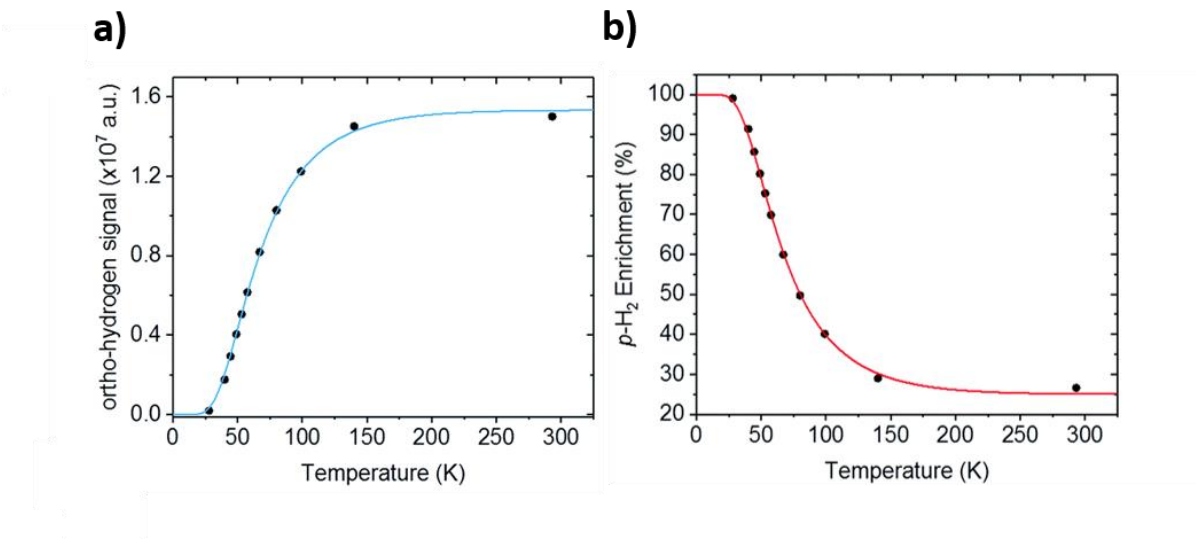

Figure 11 - a) *o*-H_2 enrichment as a function of temperature. Population of the *ortho* state has been quantified using the integral of the proton signal of hydrogen, b) *p*-H_2 enrichment as a function of temperature. Figure has been adapted with permissions from P. M. Richardson et *al.*[50]

1.4.3 PASADENA & ALTADENA

P-H_2 is NMR silent, therefore, to unlock its latent polarisation, the symmetry must be broken. In PHIP this is achieved by transfer to an unsaturated substrate via hydrogenation. The hydrogenated product contains the *p*-H_2 derived protons which occupy magnetically inequivalent sites.

There are two main types of hydrogenative PHIP: PASADENA (*para*hydrogen and synthesis allow dramatically enhanced nuclear alignment) where the hydrogenation reaction and NMR detection occurs at high magnetic field (> 1 T) and ALTADENA (adiabatic longitudinal transport after dissociation engenders net alignment) where the hydrogenation reaction occurs at low magnetic field (< 10mT) and the hydrogenation product is transferred to high magnetic field for detection.[51]

The magnetic field of hydrogenation is based on the homonuclear spin-spin or *J*-coupling of the nascent *p*-H_2 derived hydrogen atoms in the hydrogenated product.[52] In ALTADENA, the *J*-coupling is strong, however, in PASADNA, the *J*-coupling is weak. This means that the difference in chemical shift between the *p*-H_2 derived protons is much larger than the corresponding *J*-coupling (in Hz). As the chemical shift depends on the magnetic field, adjusting this allows for the desired *J*-coupling regime to be

realised. ALTADENA is typically associated with a faster rate of hydrogenation and a more reactive hydrogenation catalyst.[53]

In an AX-spin system there are 4 spin states: αα, αβ, βα and ββ (see Figure 12). Under thermal conditions, microscopic differences between populations of these energy states arises from the Boltzmann factor (approx. 10^{-5}) hence it appears that all four states are equally populated. This means that four transitions are possible. In PASADENA, only the αβ and βα states are populated, resulting in a larger population difference compared to the Boltzmann distribution. Again, four transitions are possible, however, 2 antiphase doublets are observed as either spin may undergo absorption or emission with equal probability. In ALTADENA, the spin system is generated at low field, therefore it becomes strongly coupled.[14] Consequently, once the sample is measured at high field, either the αβ or βα states are populated. This means that only two transitions are possible, yielding two singlets in the ^{1}H-NMR experiment.

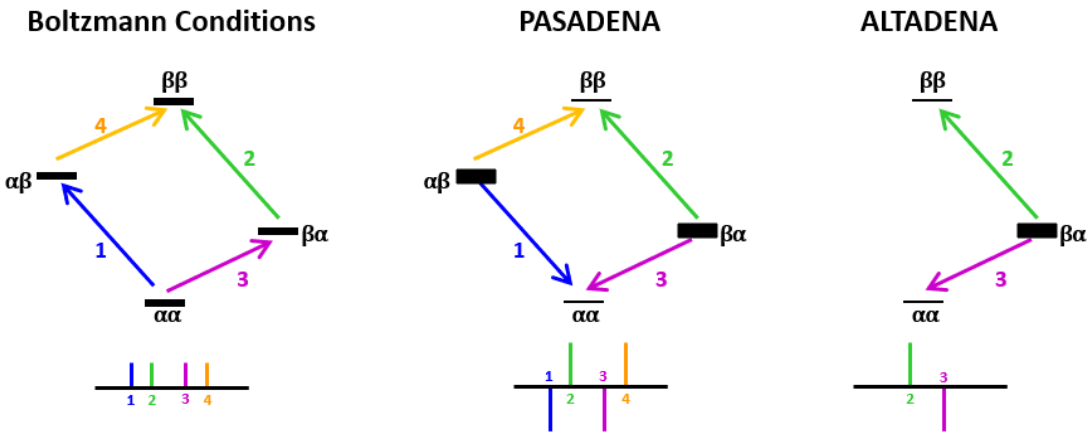

Figure 12 - The energy levels of an AX spin system, where the population of each spin state is represented by line thickness. The transitions between energy levels and the corresponding NMR signals are shown, for a negative value of J_{AX}.[14] Figure adapted with permissions from J. Natterer et *al.*[14]

PHIP can also be applied to heteronuclei whereby the polarisation is transferred from ^{1}H to the heteronuclei via an INEPT (insensitive nuclei enhancement by polarisation transfer) pulse sequence. This has been reported for ^{13}C, ^{15}N, ^{31}P, ^{195}Pt, ^{103}Rh and ^{29}Si-NMR.[54-56]

1.4.4 Applications of PHIP

PHIP hyperpolarisation typically involves the *para*-hydrogenation of an unsaturated molecule. This limits the application of PHIP to substrates that contain an unsaturated precursor as the hydrogenated product is hyperpolarised. In 2015, Cavallari *et al*.[57] presented a modification of this hyperpolarisation method termed PHIP-SAH, where SAH = side arm hydrogenation. This technique has been used to hyperpolarise a number of carboxylic acids by functionalisation with an unsaturated alcohol (side arm) followed by hydrogenation of this moiety by *p*-H_2. Hyperpolarisation transfer from the *p*-H_2 spin order to the ^{13}C carboxylate signal then ensues. The hydrogenated alcohol side arm can subsequently be removed by hydrolysis. PHIP-SAH has allowed the hyperpolarisation of a number of biologically relevant molecules, widening the applicability of PHIP. The most valuable application is the hyperpolarisation of [1-^{13}C]-pyruvate, an unsaturated metabolite which thus far had only been successfully polarised via DNP. Hyperpolarised [1-^{13}C]-pyruvate has been the subject of intense scrutiny as a potential imaging probe for the assessment of prostate cancer in humans.[58] Furthermore, [1-^{13}C]-pyruvate could be applied to *in vivo* studies of metabolism in diseases such as cancer, heart failure and stroke.[59] Whilst DNP is an effective hyperpolarisation method, achieving polarisation levels exceeding 64%, it is an expensive and time consuming process. Hyperpolarisation via PHIP-SAH is a cost-effective method which does not require any specialist equipment. Hyperpolarisation of [1-^{13}C]-pyruvate via this technique has yielded polarisation levels of 5%, however this could be improved by optimisation of the *para*-hydrogenation reaction, polarisation transfer and *p*-H_2 purity.[60] Despite these advances in PHIP, the target molecule cannot be rehyperpolarised as hyperpolarisation requires hydrogenation. There is a non-hydrogenative form of PHIP, called signal amplification by reversible exchange (SABRE) that achieves hyperpolarisation of a target molecule without chemically changing it. This means that substrates can be continuously rehyperpolarised using this technique.

1.5 Signal Amplification by Reversible Exchange

SABRE is a non-hydrogenative form of PHIP where *p*-H_2 enhances the NMR response of a substrate but is not chemically incorporated into the molecule.[61-63] This phenomenon is observed when a metal catalyst reversibly binds both *p*-H_2 and substrate molecules thereby facilitating polarisation transfer. SABRE was first reported in 2009 by Duckett *et al*.[64] when pyridine was hyperpolarised using an iridium dihydride complex of the form $[Ir(H)_2(PCy_3)(pyridine)_3][BF_4]$. A 550-fold increase in signal was observed in the resulting ^{1}H-NMR spectrum and enhanced signals were also observed using ^{13}C and ^{15}N-NMR methods (Figure 13).

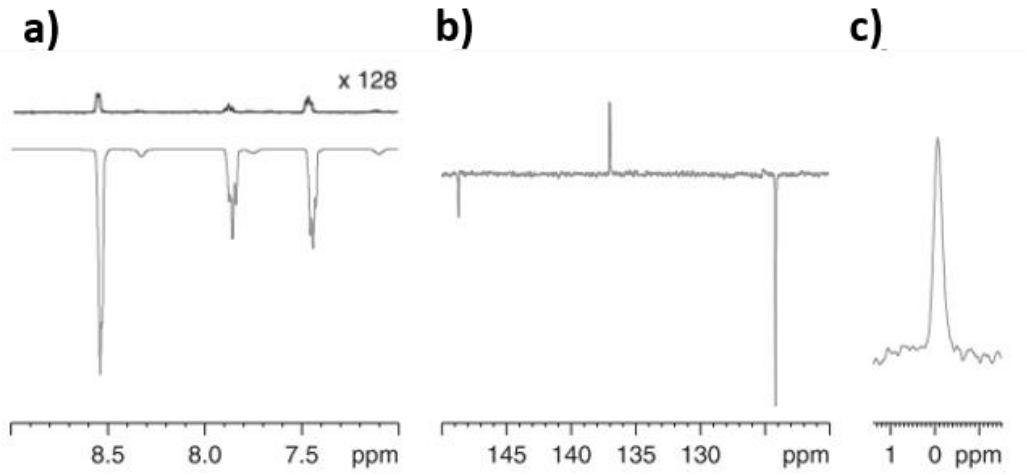

Figure 13 - a) Comparison of the thermal ^{1}H-NMR spectrum (top) compared to the hyperpolarised ^{1}H spectrum for a sample of 6 nmol pyridine. The top spectrum has been magnified 128 times so that the ^{1}H resonances can be compared to the hyperpolarised spectrum. b) Hyperpolarised ^{1}H decoupled ^{13}C spectrum after refocusing for a 6 nmol sample of pyridine. c) Hyperpolarised ^{1}H decoupled ^{15}N spectrum with refocusing for a sample contains 25 nmol of ^{15}N-labelled pyridine. Figure adapted with permissions from R. W. Adams et *al.*[64]

1.5.1 The SABRE Mechanism

1.5.1.1 Chemical Process

SABRE is a catalytic process whereby two hydrogen atoms, derived from *p*-H_2,and the target molecule (substrate) are brought together through the temporary formation of a scalar coupled network which is facilitated by an inorganic catalyst.[63, 65-68] SABRE catalysis requires the formation of a complex with two *cis* hydrides in the same plane as the substrate. Subsequently, the spontaneous transfer of spin order from the *p*-H_2

derived hydride ligands to the substrate can occur.[69] Dynamic exchange between the hydride ligands and free *p*-H_2 and the substrate ligands with free substrate present then ensues. As the free substrate and free *p*-H_2 are in excess in solution, these exchange processes allow for polarisation build-up in solution, yielding SABRE enhanced NMR spectra. This process is illustrated in Figure 13.

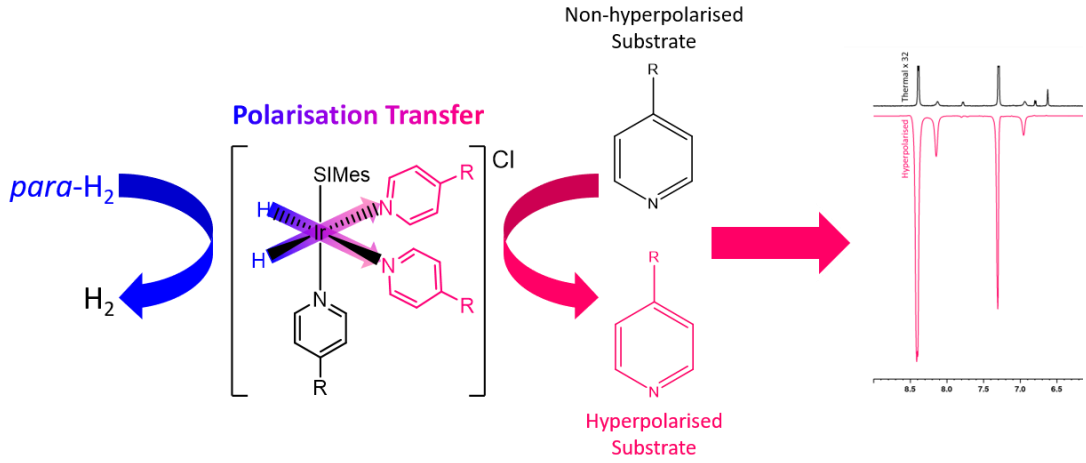

Figure 14 - Schematic diagram of the SABRE process. The curved blue arrow indicates hydrogen exchange with the free *p*-H_2 in the excess solution. The curved pink arrow indicates substrate exchange with the non-polarised free substrate material. The blue/pink arrow indicates polarisation transfer from *p*-H_2 to the substrate. In the ^{1}H-NMR spectra shown, the black is the thermal, non-hyperpolarised spectrum which has been magnified 32 times and the pink spectrum is the hyperpolarised spectra.

Typically, the SABRE precatalyst is a square planar iridium complex containing an *N*-heterocyclic carbene (NHC), chloride and cyclooctadiene (COD) (see section 1.5.3 Catalyst Design). Addition of the substrate displaces the chloride ligand to form a 16-electron square planar species: [Ir(COD)(NHC)(substrate)]Cl (see Figure 15). Once this complex formation has been confirmed by NMR characterisation experiments, *p*-H_2 is added. Hydrogenation of the COD ligand to form cyclooctane then ensues.[70] As the substrate and *p*-H_2 are in excess, they promote formation of an 18-electron octahedral complex where the axial sites are normally occupied by the NHC ligand and a substrate ligand. The equatorial plane then contains two substrate ligands which lie *trans* to two *p*-H_2 derived hydride ligands.[66, 71-73]

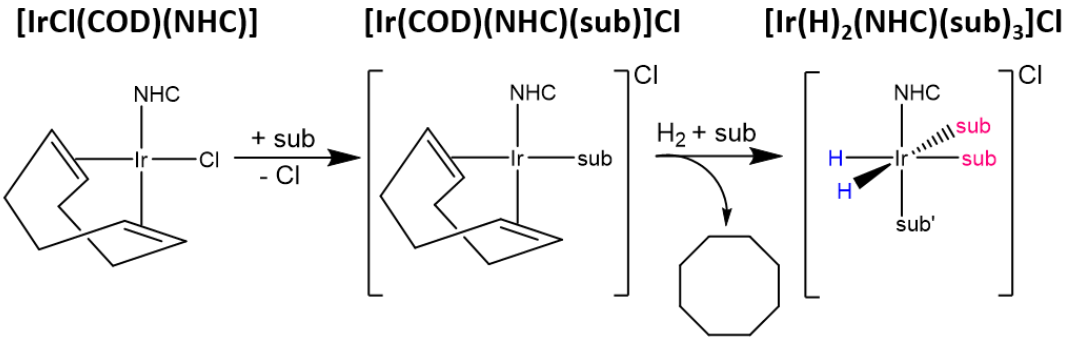

Figure 15 - Full SABRE mechanism illustrating formation of the SABRE species: [Ir(COD)(NHC)(sub)]Cl and $[Ir(H)_2(NHC)(sub)_3]Cl$

1.5.1.2 Mechanism of Polarisation Transfer

SABRE employs the singlet state of hydrogen, *p*-H_2 for the enhanced detection of a target molecule.[17, 52] The hydrogen atoms in *p*-H_2 are both chemically and magnetically equivalent and therefore they have no magnetic moment meaning it is NMR silent.[44, 74] In order to make the magnetisation visible, the symmetry of the *p*-H_2 molecule must be broken. This can be realised by coupling *p*-H_2 to a 3rd nucleus which can result in two chemically equivalent but magnetically inequivalent protons.[75] In SABRE this condition is achieved as the SABRE-active species, such as $[Ir(H)_2(NHC)(sub)_3]Cl$, consists of two hydride ligands bound *trans* to two substrate ligands within the equatorial plane and form a scalar coupling network (see Figure 15). For polarisation transfer to occur from the *p*-H_2 derived hydrides to the substrate nuclei of interest, the chemical shift difference between the hydrides and the substrate nuclei must equal the dominant *J*-coupling in the network.[76] Typically this is the hydride-hydride coupling which is of the order of 10 Hz.[63] This resonance condition can be satisfied at low magnetic fields of ~65 G for the ^{1}H hyperpolarisation of *N*-heterocycles such as pyridine.[64]

The SABRE-active species shown in Figure 16 can be modelled as a 4 spin system where the *p*-H_2 hydrides are represented by AA' and the ^{1}H nuclei of the substrate by BB' (see Figure 16).[77] In this network, the spins can couple to each other in different ways, giving rise to the couplings; $J_{AA'}$, $J_{BB'}$, J_{AB}, $J_{A'B'}$, $J_{A'B}$ and $J_{AB'}$. As the molecule has C_s symmetry, $J_{AB} = J_{A'B'}$ and $J_{A'B} = J_{AB'}$.[75, 77, 78]

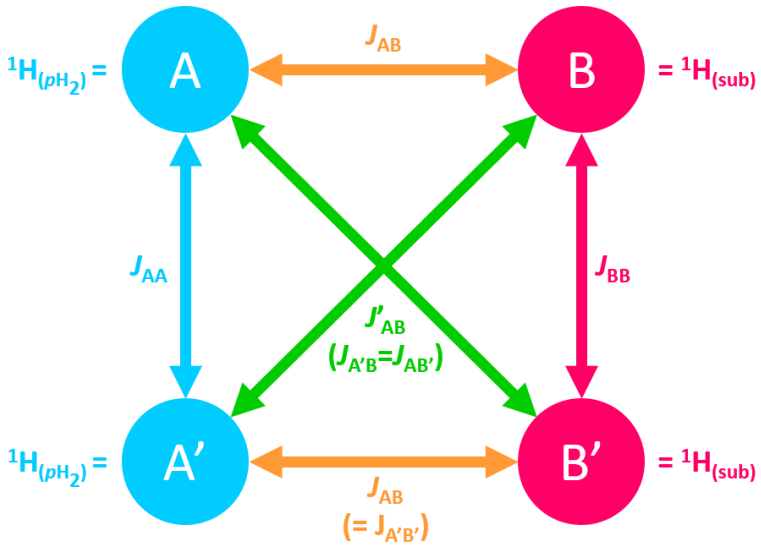

Figure 16 - SABRE couplings according to an AA'BB' system

Whilst there are a number of different methods for deriving the magnetic field at which polarisation transfer occurs, here the level-anticrossing (LAC) approach will be considered.[77-79] In order to do this, we must also acknowledge the eigenstates of both pairs of protons:

$$|T_{+1}\rangle = |\alpha\alpha\rangle$$
$$|T_0\rangle = \frac{1}{\sqrt{2}}|\alpha\beta\rangle + |\beta\alpha\rangle$$
$$|T_{-1}\rangle = |\beta\beta\rangle$$
$$|S\rangle = \frac{1}{\sqrt{2}}|\alpha\beta\rangle - |\beta\alpha\rangle$$

Equation 3 - The eigenstates of the AA' and BB' spin pairs

When *p*-H_2 is considered, only the AA'-singlet state is populated, which is NMR silent. This population must be transferred to the AA'-triplet state in order to observe NMR signal. Furthermore, if the couplings J_{AB} and J'_{AB} are identical, the *p*-H_2 protons, AA', remain magnetically equivalent and therefore transfer to the AA'-triplet cannot occur. If these couplings are different ($J_{AB} - J'_{AB} \neq 0$), the AA'-singlet and AA'-triplet experience a level anticrossing where they approach each other but do not cross (Figure 17).[75, 78]

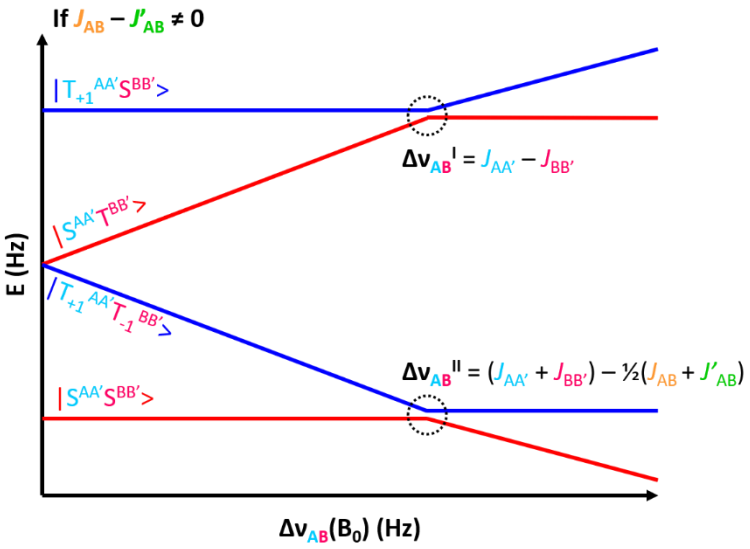

Figure 17 - Representation of the LAC approach to SABRE. Adapted with permissions from Buljubasich *et al.*[75]

At specific magnetic fields (B_0), different sets of these energy levels in the AA'BB' system experience anticrossing which permits efficient polarisation transfer from the *p*-H_2 (AA') to the substrate protons of interest (BB') (Equation 4).

$$B_{0(Transfer)} = \frac{\Delta\nu}{\gamma_A(1-\sigma_A) - \gamma_B(1-\sigma_B)}$$

Equation 4 - Where Δν = the Larmor frequencies shown in Figure 17 for specific LAC interactions, γ = gyromagnetic ratio ($MHzT^{-1}$) and σ = chemical shielding ($\delta = 10^6 \times (\sigma_{ref} - \sigma_{sample})$).

Where polarisation transfer to ^1H nuclei is targeted, the gyromagnetic ratios of A and B are equivalent (γ for ^1H = 42.58 $MHzT^{-1}$).[4] Therefore, the matching condition is determined by the chemical shift difference between A and B. For *N*-heterocycles such as pyridine, this polarisation transfer field ($B_{0(Transfer)}$ or PTF) is satisfied at approximately 65 G (6.5 mT).[75]

Whilst the proton is the most popular SABRE nuclei of interest, SABRE has successfully been used for the hyperpolarisation of ^{13}C, ^{15}N, ^{19}F, ^{29}Si, ^{31}P and ^{129}Sn.[77, 80-85] Hyperpolarisation of these nuclei can either proceed via indirect intramolecular transfer from hyperpolarised ^1H resonances or via the direct polarisation of the heteronuclei of interest by coupling to the hydride ligands in the SABRE catalyst.

The SABRE hyperpolarisation of ^{15}N was first reported by Theis *et al*.[77] ^{15}N magnetic resonance is predicted to be more useful for *in vivo* SABRE experiments due to the longer signal lifetimes, the lack of background signal and facile chemical shift discrimination.[86] This contrasts to ^{1}H nuclei which rapidly depolarises due to short signal lifetimes and must compete with the background signal within the body. Furthermore, even if high polarisation levels are observed in ^{1}H nuclei, significant losses will be induced during preparation, *in vivo* administration, circulation and tissue penetration in SABRE-MRI.[86] However, ^{15}N nuclei are low in natural abundance, therefore this technique typically requires ^{15}N isotopic enrichment of the target analyte which can be expensive. Furthermore, ^{15}N nuclei have a lower gyromagnetic ratio compared to ^{1}H (≈ 1:10) which results in low detection sensitivity.[87]

The SABRE-SHEATH (SABRE in shield enables alignment transfer to heteronuclei) method, as it was later named, was utilised for the hyperpolarisation of ^{15}N in pyridine. In order to transfer polarisation from the *p*-H_2 derived hydrides to the ^{15}N nucleus, a polarisation transfer field of 0.4 μT was required. This method induced a polarisation of 10%, corresponding to an enhancement of 30,000-fold at 9.4 T.[17]

1.5.1.2.1 High Field SABRE

SABRE enhancements depend on polarisation transfer from *p*-H_2 to the substrate nuclei of interest. It has previously been discussed (section 1.5.1.2 Mechanism of Polarisation Transfer) that this occurs at low magnetic fields which satisfy the resonance condition for polarisation transfer (see above). For ^{1}H nuclei, this method can be performed in a number of ways: either via manual shaking of the sample using the stray field of the NMR magnet, manual shaking using a handheld magnetic array or an automated flow system.[76] These methods are described in more detail in Chapter 2. However, these approaches, which require the sample to be moved between low field and high field (where detection occurs) are problematic as the polarisation transfer field must be optimised for each class of substrate.

Theis *et al*.[88] proposed the use of low power continuous wave (cw) pulses for coherent polarisation transfer from *p*-H_2 to the substrate. This method can be used at any magnetic field provided the *p*-H_2 are chemically equivalent but magnetically inequivalent. Furthermore, the cw-power must match the sum of the hydride-hydride and ^{15}N-^{15}N coupling ($\gamma B_1 = 2\pi(J_{HH} \pm J_{NN})$. This hyperpolarisation strategy is termed LIGHT-SABRE, where LIGHT = low-irradiation generation of high tesla-SABRE and can be performed on any modern high-resolution NMR spectrometer. Hyperpolarisation via this method yielded a ^{15}N enhancement of 480-fold for a 2.5 mM sample of pyridine in a single shot experiment.

Pravdivtsev *et al*.[89] demonstrated the use of RF fields for high field SABRE. They showed that the application of a RF field enables rapid transfer of the *p*-H_2 spin order (within 1s), therefore removing the need for field cycling methods. For successful polarisation transfer, the amplitude and frequency of the RF field must be carefully set to enable modelling of low-field conditions at high magnetic field. However, lower enhancements were observed in this method compared to the magnetic field cycling approach. For example, a ^{1}H enhancement of 100-fold was observed for a range of heterocyclic substrates at 4.7 T.

ADAPT-SABRE, where ADAPT = alternating delays achieve polarisation transfer, is another high field SABRE method.[90] This method has been used for the hyperpolarisation of other spin ½ heteronuclei such as ^{13}C, ^{15}N, ^{19}F and ^{31}P. SABRE hyperpolarisation of these nuclei is technically demanding as the optimal field for polarisation transfer is weaker than the Earth's magnetic field. This method was exemplified using ^{15}N nuclei and was shown to be faster and more robust than the magnetic field cycling approach. For example signals that were 3 orders of magnitude larger than the thermal signals were achieved for ^{15}N within 2 seconds of RF pulsing. Polarisation transfer via ADAPT-SABRE is achieved by alternate pulse and delay on the ^{15}N nuclei.

There are a number of advantages of high-field SABRE over the magnetic field cycling approach. For example, RF-SABRE is capable of generating continuous

hyperpolarisation with high efficiency.[89] Furthermore, ADAPT-SABRE allows for constant field shuttling and is inherently simple as it can be easily augmented for the hyperpolarisation of spin ½ nuclei in any SABRE-active species.[90] Moreover, LIGHT-SABRE, RF-SABRE and ADAPT-SABRE all prevent unnecessary signal losses during transport as the sample is maintained within the spectrometer for the entirety of the experiment. However, these methods induce smaller enhancements compared to the magnetic field cycling approach. This indicates that magnetic field cycling induces efficient transfer of the spin order of *p*-H_2 compared to high-field SABRE. Additionally, these high-field approaches are harder to transfer to *in vivo* SABRE-MRI applications.

1.5.2 SABRE Substrates of Interest

1.5.2.1 Pyridine and its Derivatives

The most commonly exploited substrates for SABRE are pyridine and its derivatives.[72] Pyridine is an example of a simple heterocycle analogous to benzene - a highly conjugated system with 6 π electrons delocalised across the ring.[91] Pyridine is known to be more reactive than benzene towards nucleophiles and exhibits properties comparable to tertiary amines.[92] This is due to the nitrogen atom containing a lone pair of electrons which occupy the same plane as the ring.[93] It is this geometry which makes it easily accessible for donation to metals when forming metal complexes.

In SABRE, the substrate is required to reversibly bind to the iridium catalyst. Pyridine is capable of 'soft' binding where it weakly coordinates to the metal centre.[91] It is this mechanism of association/dissociation which allows for polarisation to be built up in the solution. The substrate must be bound to the catalyst long enough for sufficient magnetisation to be transferred from the *p*-H_2 before dissociation, thus enabling a new substrate molecule to bind to the metal for polarisation. If the substrate does not bind for long enough, then insufficient polarisation can be transferred to the solution. However, if it binds for too long, then relaxation effects takeover as coordination to iridium promotes relaxation.[94]

In addition to the electronic considerations of using pyridine as a SABRE substrate, it was also selected due to its vital role in many biologically relevant molecules. Pyridine

rings are a motif used in common pharmaceuticals, ranging from anti-viral to anti-cancer treaments.[95] This is particularly important for the application of SABRE in clinical MRI, where pyridine-like molecules could be used as MRI contrast agents. For example, pyrimidine, an anti-cancer agent,[96, 97] has previously been examined as a SABRE candidate, where total signal enhancements of −2300-fold were observed.[84]

1.5.2.2 Biologically Relevant Substrates

SABRE has also successfully been used for the hyperpolarisation of biologically relevant molecules including: nicotinic acid, nicotinamide, vitamin B_3, pyruvate and isoniazid.[80, 98, 99] Pyruvate was also hyperpolarised using the SABRE-active complex $[Ir(H)_2(\eta^2\text{-pyruvate})(DMSO)(IMes)]$ where DMSO (dimethoxy sulfoxide) is used as a co-ligand to overcome poor pyruvate-iridium ligation. It was demonstrated that hyperpolarisation was possible in a 70:30 solvent mixture of D_2O:ethanol-d_6; which is more suitable for biological applications.[100] Without optimisation of the SABRE system, ^{13}C polarisation levels of 2% were observed.[101, 102] Therefore modifying the catalyst, the co-ligand or increasing the *p*-H_2 pressure could induce polarisation levels comparable to DNP methods which are currently used in the clinic for hyperpolarised MRI.

1.5.2.3 Diazirines

Diazirines have been proposed as an attractive class of potential molecular tags for molecular imaging by Shen *et al*.[103] Diazirines can be incorporated into a variety of biologically relevant small molecules, metabolites and biomolecules. Furthermore, they are known to be both biocompatible and stable under acidic and basic conditions.[104] $^{15}N_2$-labelled diazirines yielded ^{15}N enhancements of 15,000-fold via the complex $[Ir(H)_2(IMes)(diazirine)_2(Lewis\ Base)]Cl$ or $[Ir(H)_2(IMes)(diazirine)(Lewis\ Base)_2]Cl$. The Lewis base is required to generate the SABRE-active species for polarisation transfer as without it, hyperpolarisation is observed. Hyperpolarisation of ^{15}N-diazirine-containing choline derivatives demonstrates potential application within biologically relevant molecules.

1.5.2.4 SABRE-RELAY via Proton Exchange

In 2018, Iali *et al.*[105, 106] reported the direct polarisation of amines via the SABRE-active species $[Ir(H)_2(IMes)(RNH_2)_3]Cl$ which has previously been used to catalyse hydrogenation reactions. Hyperpolarisation of a number of primary amines was noted to induce the subsequent polarisation of residual water within the solvent. This process was termed SABRE-RELAY via proton exchange where the ammonia is utilised as the hyperpolarisation transfer agent. Hyperpolarisation is first transferred to ammonia (or another primary amine) via the SABRE catalyst $[Ir(H)_2(IMes)(RNH_2)_3]Cl$. The hyperpolarised proton of the amine is then transferred to the analyte via proton exchange. This method has vastly expanded the substrate range amenable to SABRE, allowing the polarisation of amines, amides, carboxylic acids, alcohols, phosphates and carbonates. For example, direct polarisation of free amine yielded an enhancement of 10- to 120-fold per ^1H resonance. This polarisation was then transferred to propanol where an enhancement between 250- and 500-fold for the OH resonance was observed. Polarisation was then transferred into the aliphatic ^1H resonances of propanol, inducing enhancements of 650- and 790-fold.

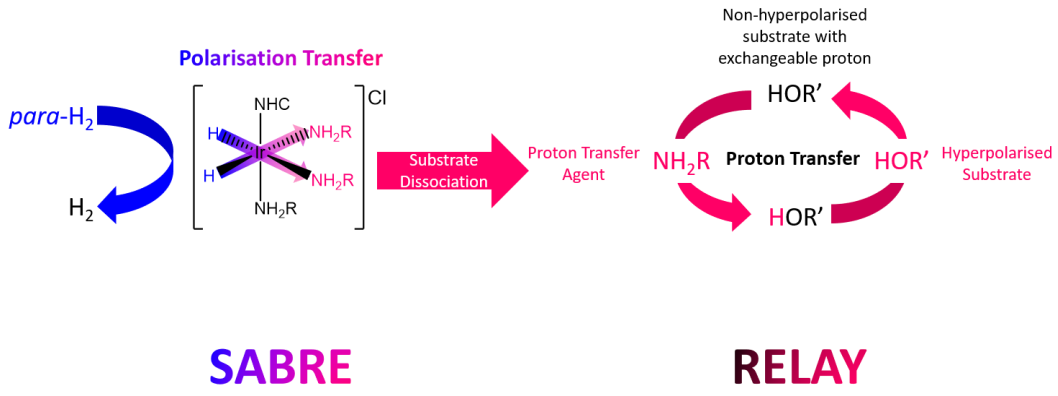

Figure 18 - Schematic Diagram of the SABRE-Relay Polarisation Process

This method has also been used for the hyperpolarisation of glucose and fructose allowing the tautomeric composition of these to be determined.[107] For example, a ^{13}C enhancement of 250-fold was yielded at 9.4 T for both glucose and fructose, corresponding to a polarisation of 0.02%. This allowed for the rapid quantification of the distribution between isomers, taking just 15 seconds. Quantification using standard (thermal) NMR techniques would have taken 18 hours.

1.5.3 Catalyst Design

1.5.3.1 Crabtrees Catalyst

The polarisation transfer catalyst initially used for SABRE is derived from Crabtree's catalyst, $[Ir(COD)(PCy_3)(py)]PF_6$ which is a well-known hydrogenation catalyst (Figure 19).[108-110] The SABRE-active complex of this, $[Ir(H)_2(PCy_3)(pyridine)_3]PF_6$, induced signal enhancements in excess of 100-fold in ^1H, ^{13}C and ^{15}N NMR spectra.[64] Experimental studies have demonstrated that sterically bulky phosphine ligands such as PCy_3, deliver the highest levels of hyperpolarisation.[111] The SABRE-active complex $[Ir(H)_2(PCy_3)(pyridine)_3]BF_4$ induced signal enhancements of 110-fold in the ^1H, 116-fold in ^{13}C and 128 in ^{15}N hyperpolarised spectra of free pyridine.

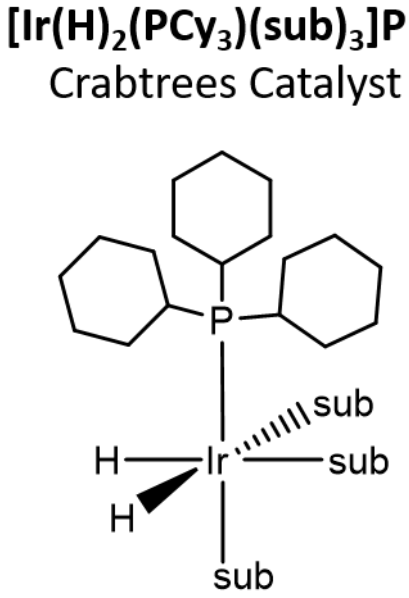

Figure 19 - Structure of the SABRE-Active Species formed from Crabtrees catalyst

1.5.3.2 N-Heterocyclic Carbenes

Evidence has suggested that *N*-heterocyclic carbene-metal catalysts surpass phosphine-based metal catalysts in both activity and scope.[112] This is due to their higher electron donating power and steric bulk which offers lower stability to the complex but rapid formation and exchange.[65] This is driven by donation from the nitrogen lone pairs into the formally empty p(π) orbital of the carbene atom.[113] Additional stabilisation can also be provided by substitution at the carbene nitrogen

atoms. Furthermore, related *N*-heterocyclic carbene complexes have been shown to be excellent catalysts for the hydrogenation of olefins.[114]

N-heterocyclic carbenes were first reported in SABRE in 2011 by Cowley *et al*.[73] Where the square planar complex [IrCl(COD)(IMes)] was utilised as the SABRE pre-catalyst for the enhancement of pyridine. Here, 1,3-bis(2,4,6-trimethyl-phenyl)imidazole-2-yilidene (IMes) was employed as the NHC. The SABRE-active species $[Ir(H)_2(IMes)(py)_3]Cl$ (Figure 20) was confirmed by NMR spectroscopy and mass spectrometry methods. This catalyst delivered an 8100-fold increase in ^{1}H-NMR signal strength relative to non-hyperpolarised pyridine at 127.74 MHz. Substitution at the nitrogen atoms in the carbenes and its effect on SABRE efficiency has been thoroughly explored by various groups. For example, the introduction of chloride to the imidazolium backbone in IMes yields a 78% increase in net polarisation of the ^{1}H resonances in methyl 4,6-d_2-nicotinate compared to IMes. These substitution effects are discussed in more detail in Chapter 3 (section 3.7 Exploring the Effect of Catalyst Modifications on Iridium-Substrate Ligation). [65, 115-117] Whilst IMes and its derivatives are the most popular SABRE catalysts for the ^{1}H, ^{13}C and ^{15}N hyperpolarisation of pyridine-based substrates, it struggles to catalyse the hyperpolarisation of *ortho*-substituted pyridines or other bulkier substrates. Wong *et al.*[118] illustrated the behaviour of asymmetric NHC-based catalysts and how these can be used to improve the SABRE efficiency of sterically encumbered substrate ligands. These asymmetric ligands contained 1 mesityl arm to maintain steric congestion, and a smaller substituent bound to the second imidazole nitrogen atom (Figure 20). Pyridine and 3,4-lutidine were shown to have poor SABRE activity which was attributed to slow ligand loss due to reduced steric bulk at the NHC relative to IMes. Conversely, 3,5-lutidine was shown to enhance under SABRE conditions where a 258-fold ^{1}H enhancement was observed at the *ortho* resonance.

Colell *et al*.[119] have recently expanded on modifications of the catalyst ligand sphere for the hyperpolarisation of sterically demanding substrates such as provitamin B_6 and caffeine using the NHC ligand PHOX (2-(2-(diphenylphosphanyl)phenyl)-4,5-dihydrooxazole) (Figure 20). This complex has previously been used for the asymmetric hydrogenation of olefins. This complex yielded ^{15}N enhancements of

1000-fold and ^{19}F enhancements of 30-fold at 8.5 T in the biologically relevant molecules provitamin B_6 and caffeine.

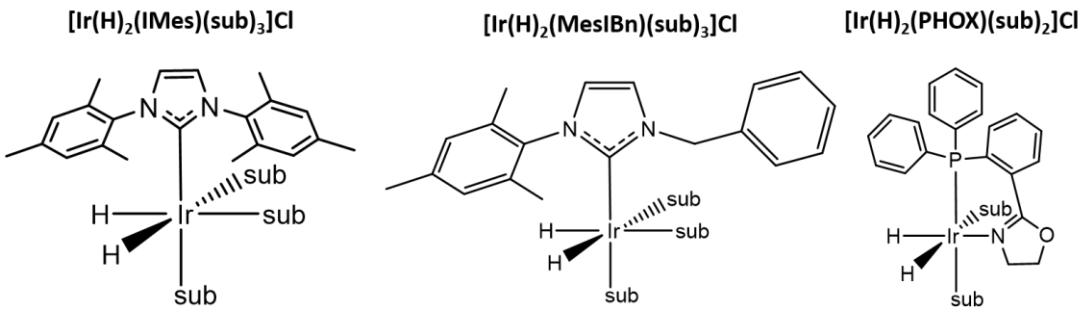

Figure 20 - SABRE-active species containing IMes based NHC ligands

1.5.3.3 Alternative Ligands

In 2015, Holmes *et al*.[120] discussed the use of a pincer-based catalyst for SABRE catalysis. Cyclometalated phosphine-based pincer complexes (Figure 21) had previously been shown to be efficient catalysts for dehydrogenation reactions and the reduction of carbon dioxide.[121] They were also shown to have a unique set of properties capable of enhancing the reactivity, stability and reaction selectivity of the metal catalyst.[122] They were shown to enable efficient polarisation transfer into a single substrate molecule as three of the iridium coordination sites are blocked by the pincer ligand. This pincer complex yielded a ^1H enhancement of 12.3-fold at the *ortho* proton in pyridine. Interestingly, both the ^1H nuclei in the pyridine within the pincer arm and the pyridine ligand hyperpolarised under SABRE conditions. Isotopic labelling of the protons (to ^2H) in the pincer arm prevented polarisation wastage, increasing catalytic efficiency by 35%. However, this pincer complex yields smaller enhancements compared to IMes as polarisation is transferred to a single substrate molecule.

Ruddlesden *et al*.[123] have also controlled SABRE catalysis via a bidentate phenoxide derivative of the NHC IMes. They reported on the use of a pendant alkoxide ligand which binds to iridium via the carbon of the imidazole group and the oxygen of the phenoxide arm. This forms the SABRE active species $[Ir(H)_2(\kappa\text{-}C,O\text{-}IMesPhen)(sub)_3]$ (Figure 21) which was shown to undergo pyridine and hydrogen exchange. Formation

of this complex took five days, however it yielded SABRE enhancements of pyridine, quinoline and nicotine in non-polar solvents. For example, a 500-fold enhancement was observed for the *ortho* protons in pyridine. Whilst this complex allows the SABRE catalytic cycle to be controlled, the enhancements are far inferior to those demonstrated using IMes based catalysts.

In 2016, Iali *et al*.[124] reported a cyclooctene based iridium catalyst for the successful hyperpolarisation of pyridine, nicotinamide, nicotine, 5-aminopyrimidine and 3,5-lutidine. The SABRE-active catalyst, $[IrCl(H)_2(COE)(sub)_2]$ (Figure 21) was shown to be highly effective for hyperpolarisation in aprotic solvents. The COE ligand was proven to bind to iridium in an η^2 fashion and is much simpler than NHC ligands and therefore easier to employ for SABRE catalysis. However, this complex rapidly undergoes C-H bond activation which has been shown to quench SABRE catalysis, thus preventing further hyperpolarisation.[118]

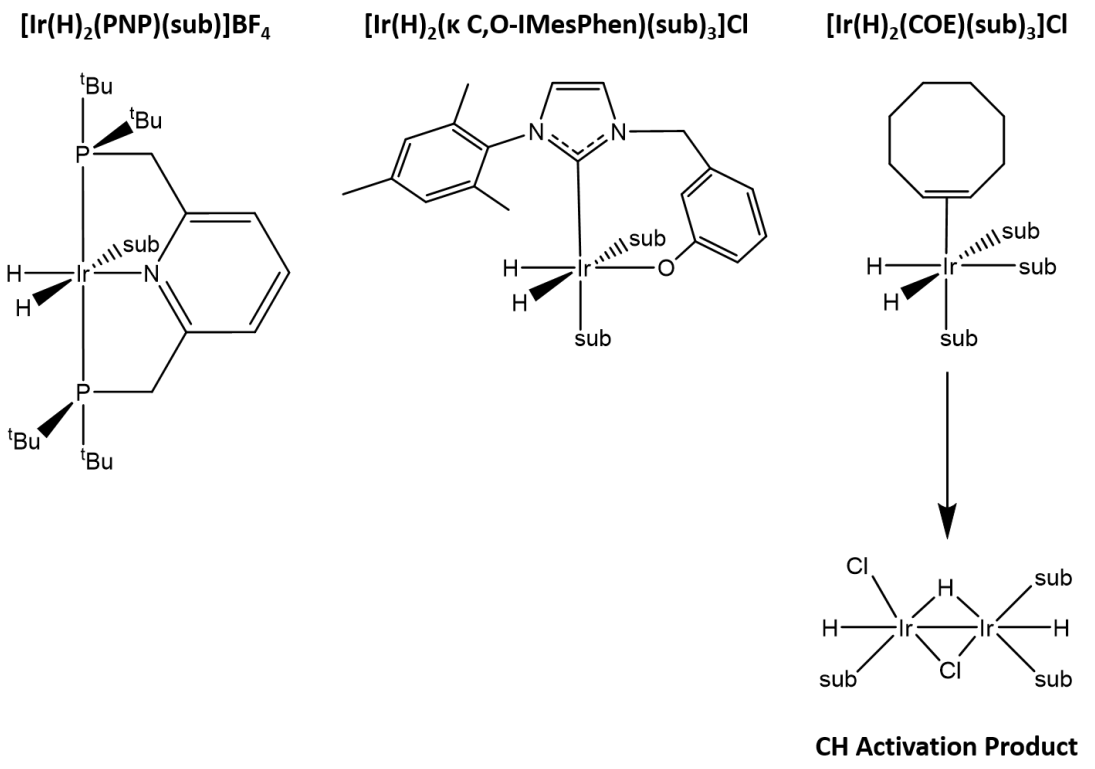

Figure 21 – SABRE-Active species based on the pincer based catalyst,[120] the phenolate-substituted NHC[123] and COE based complex.[124] The latter rapidly forms a non-SABRE active CH activation product which is shown.

1.5.4 Biocompatibility of SABRE

The majority of SABRE studies have been conducted in methanol-d_4.[125] However, this solvent is not biologically compatible and therefore alternative solvents are required for use in clinical MRI. Cyclotoxicity studies of the solvent composition demonstrated that the most biocompatible solvent mixture is a 30:70 ratio of ethanol-d_6:D_2O.[126] The main cause of SABRE toxicity arises from the iridium catalyst, as this was shown to be the dominant factor in cell death, even at low concentrations. Manoharan *et al*.[100] demonstrated a biocompatible bolus of <2 ppm iridium catalyst content which is below the limit for intravenous administration. Therefore the concentrations typically used for SABRE experiments (≈ 5mM) are not suitable for clinical use.[127, 128] This can be negated by catalyst removal methods via catalyst deactivation,[129] removal by ion exchange chromatography[126] or biphasic catalysis,[98] catalyst capture using solid phase scavengers and filtration[130] or heterogenous methods combined with filtration.[131-133]

In 2015, Mewis *et al*.[129] reported that the SABRE catalyst could be deactivated using 2,2'-bipyridine (bpy). Addition of bpy to $[Ir(H)_2(IMes)(substrate)_3]Cl$ lead to the partial displacement of the substrate, thus effectively quenching the active catalyst. A further benefit of bpy was that it extended the lifetime of the hyperpolarised signal such that the potential for SABRE in clinical MRI was increased. Removal of the SABRE catalyst using SiO_2 microparticles functionalised with 3-mercaptopropyl or 2-mercaptoethyl sulfide moieties has also been reported.[134] This method was utilised alongside the ^{15}N-SABRE hyperpolarisation of metronidazole. Addition of the functionalised SiO_2 microparticles was shown to be successful as the catalyst could no longer hyperpolarise the ^{15}N spins in the sample. High ^{15}N signal enhancements of >100,000-fold at 9.4 T were recorded, corresponding to nuclear polarisation levels of 34%.

Water soluble catalysts for SABRE polarisation have also been extensively reported (Figure 22).[116, 135, 136] Fekete *et al*.[116] reported the synthesis of $[Ir(H)_2(IMes)(MeCN(py)(X)]BF_4$, where X = di-*para*-sulfonated triphenylphosphine

(*p*tppds), mono-*meta*-sulfonated triphenylphosphine (*m*tppms) or *meta*-tri-sulfonated triphenylphosphine (*m*tppts). However these complexes yielded very low enhancements of 3-hydroxypyridine. A second class of these catalysts were suggested where the carbene was functionalised to include water-soluble azolium salts, however this also induced small signal enhancements. Shi *et al.*[135] expanded on these water-soluble catalysts in 2016. They described two synthetic approaches using iridium-based catalysts for SABRE. The first utilised a novel catalyst where PEGylation was employed at the NHC ligand. This complex was shown to be soluble in water, however SABRE efficiency was 50% lower than in ethanol solutions. The second strategy employed a novel di-iridium complex precursor where the COD ligand was replaced by CODDA (1,2-dihydroxy-3,7-cyclooctadiene). This complex was dissolved and activated with *p*-H_2 (1 atm) in water and yielded enhancements of 32-fold for the ^{1}H resonances of pyridine. Spannring *et al*.[136] have also reported that changes at the NHC can lead to the observation of SABRE in D_2O. They synthesised the SABRE precatalyst [IrCl(COD)(IDEG)], where IDEG=1,3-bis(3,4,5-tris(diethyleneglycol)(benzyl)imidiazole-2-ylidene). Activation and hyperpolarisation was achieved in D_2O and resulted in ^{1}H signal enhancements of nicotinamide, pyridine, methylnicotinate and *N*-methylnicotinamide at 7 T. ^{15}N enhancements of approximately 1000-fold at 7 T were also yielded for ^{15}N-pyridine, however catalyst removal would still be necessary to create a biocompatible bolus for *in vivo* injection.[137]

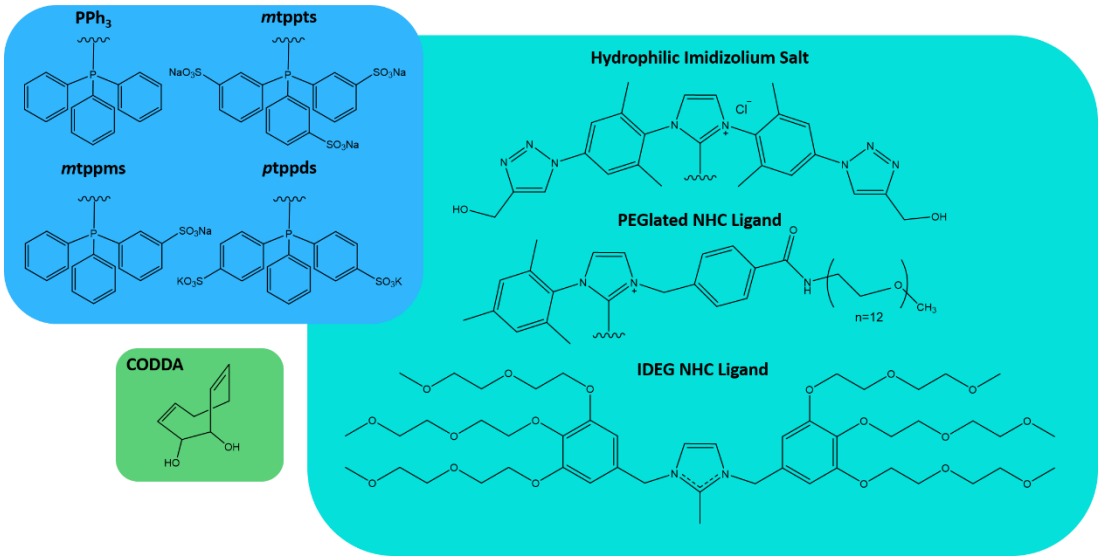

Figure 22 - Catalyst modifications for water soluble iridium SABRE catalysts

The most promising advancement towards biocompatible SABRE is the investigation of biphasic solutions using CASH-SABRE, where CASH = catalyst separated hyperpolarisation.[98] In this technique, chloroform-*d* and D_2O were used as the solvent mixture which are immiscible. The catalyst was then dissolved in the organic phase (chloroform-*d*) along with the substrate. Shaking of the sample then ensued, causing emulsification of the two phases, phase separation then occurred over 60 s. The two phases were then analysed where the catalyst was found in the organic layer and the hyperpolarised substrate was found in the aqueous layer. ^{1}H signal gains of up to 3000-fold were yielded per ^{1}H resonance at 9.4 T for pyrazine, 5-methyl-pyrimidine, 4,6-dimethyl nicotinamide and pyridazine.

1.5.5 Exchange in the SABRE-Active Species

1.5.5.1 Exchange Pathways

In SABRE, hyperpolarization is transferred from the *p*-H_2 to the bound substrate through the temporary formation of a scalar, *J*-coupled network, facilitated by the iridium centre.[64] As the ligation between the iridium and the nitrogen substrate is labile, the bound substrate can exchange with the 'free' excess substrate in solution.[138] Hydrogen exchange between the bound *p*-H_2 derived hydrides and *p*-H_2 in solution occurs concurrently with this process.[65] For SABRE efficiency to be

optimal, it is essential that these two exchange process allow for sufficient polarisation to be transferred before dissociation occurs. Furthermore, higher substrate exchange rates only result in larger signal enhancements if the polarisation transfer process is fast enough. Contrastingly, if the exchange rate is too slow, insufficient polarisation can be built-up in solution and decay occurs due to relaxation processes.[115]

SABRE exchange pathways have been extensively scrutinised as these processes are critical to the level of SABRE enhancement achieved. In 2011, Cowley *et al*.[73] used DFT calculations alongside experimental calculations of ligand and hydride exchange pathways via exchange spectroscopy (EXSY). These experiments revealed that substrate loss via the ligand bound *trans* to the NHC (IMes) did not occur on the timescale of the NMR experiment. Therefore ligand exchange is driven by the substrate bound *trans* to the hydride. Using the Eyring-Polanyi equation, they established that substrate exchange is a dissociative process (S_N1 reaction). This was indicated by a positive value of entropy ($\Delta S^{\neq}$) and supported by the fact that increasing substrate concentration did not significantly alter the observed exchange rate. Conversely it was found that H_2 exchange was dependent on the concentrations of both *p*-H_2 and the substrate. For example, H_2 exchange was directly proportional to H_2 concentration but inversely proportional to substrate concentration.[70] Consequently, H_2 exchange was shown to be an associative process (S_N2 reaction).

These findings were confirmed by Lloyd *et al*.[65] and Barskiy *et al*.[79] The former established that substrate loss proceeds via formation of the 16 electron species $[Ir(H)_2(NHC)(sub)_2]Cl$. However formation of this intermediate also provides a route for the solvent to bind to iridium via $[Ir(H)_2(NHC)(MeOH)(sub)_2]Cl$ (Figure 23). Although this complex is highly reactive, it is present in low concentrations and therefore plays a minimal role in SABRE. Formation of this species was confirmed by the ^1H resonances for the hydrides which were observed at −23.44 ppm and −25.49 ppm. The former is known to bind to iridium *trans* to the nitrogen bound substrate and the latter was found to lie *trans* to the oxygen bound methanol. The formation of this complex also provides a route to H/D exchange leading to the formation of $[Ir(H)(D)(NHC)(sub)_3]Cl$ which reduces the SABRE effect. Barskiy *et al*.[79, 139] concluded

that both substrate and hydrogen exchange require formation of the intermediate $[Ir(H)_2(NHC)(sub)_2]Cl$.

As substrate loss leads to the build-up of the hyperpolarised substrate in solution, there must be an optimal rate constant that allows for sufficient polarisation to be transferred prior to substrate dissociation. Barskiy *et al.*[79] used computational methods to calculate that the optimum rate constant for substrate dissociation is 4.5 s^{-1} for pyridine-based substrates. This value was also supported by Rayner *et al.*[117] where the largest SABRE enhancements were observed for catalysts where the ligand loss rate was 4 s^{-1}.

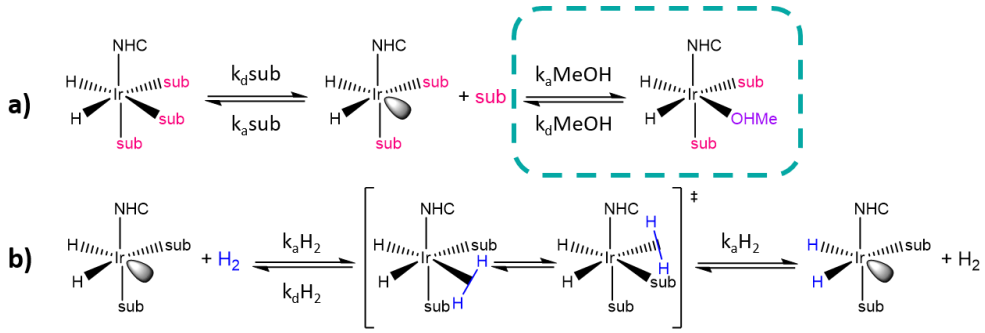

Figure 23 - Ligand Exchange pathways. a) Illustrated the dissociative substrate exchange pathway, b) shows the associative H_2 exchange pathway. Image adapted with permissions from D. A. Barskiy et *al.*[139] The methanol adduct was adapted with permissions from L. S. Lloyd et *al.*[65]

The rate of substrate and hydrogen dissociation determines the level of hyperpolarisation that is built up into the excess solution. The rate of relaxation determines how long the substrate remains hyperpolarised.

1.5.6 Relaxation Effects in the SABRE-Active Species

Relaxation quantifies the mechanisms that allow nuclear spins to lose energy and drop from the excited state to the ground state non-radiatively.[140] Two forms of relaxation exist; spin-lattice relaxation and spin-spin relaxation. In spin-lattice relaxation, the spins of a nucleus are permitted to flip between the energy levels, thus establishing the Boltzmann population difference essential to the NMR experiment. As the nuclei return to the equilibrium state, the energy released is dissipated into the surroundings (the 'lattice').[6] The process of spin-lattice relaxation

is necessary to understanding how molecules behave in NMR and is characterised by a time, T_1 (spin-lattice relaxation time).

There are several different relaxation mechanisms, however for spin $\frac{1}{2}$ nuclei the most dominant mechanism arises from dipole-dipole interactions. Nuclei with low gyromagnetic ratios, such as ^{13}C and ^{15}N have longer relaxation times compared to ^{1}H, particularly if the heteronuclei is not attached to a proton.[141] For example, relaxation decay constants of up to 20 minutes have been observed for ^{13}N nuclei in diazirines.[142, 143] Whilst the lifetime of the proton permits the imaging of some metabolic processes, it is vastly shorter than those associated with other molecular imaging modalities, for example, the ^{18}F positron emission tomography (PET) signal decays in ≈ 2 hours.[144] In MRI, T_1 weighted images are used for imaging the brain as the T_1 between grey and white matter is significantly different.[145]

It has been discussed that SABRE can be utilised to enhance the detection of a target nuclei within a substrate. The SABRE phenomenon is observed via an iridium catalyst that facilitates polarisation transfer from the *p*-H_2 derived hydrides to the substrate nuclei of interest. The formation of this SABRE-active species is temporary as the substrate and hydride ligands undergo exchange processes. Signal enhancements are then observed via the build-up of the hyperpolarised substrate in the excess solution. Whilst the catalyst provides a route to polarisation build-up, it also provides a route to polarisation depletion via relaxation mechanisms.[81]

The SABRE-active species $[Ir(H)_2(NHC)(sub)_3]Cl$ acts as a polarisation transfer catalyst by redistributing the magnetisation at a molecular level. Therefore it was predicted that the equilibrium process of hyperpolarisation operates in both directions and therefore could provide a route to enhanced rate of signal relaxation. This was proved using experimental methods by Lloyd *et al*.[65] in 2014. The ^{1}H substrate T_1 values were determined in the presence of catalyst and with and without the presence of H_2 gas. It was established that the free substrate T_1 was significantly affected by the presence of $[Ir(COD)(NHC)(sub)]Cl$ and $[Ir(H)_2(NHC)(sub)_3]Cl$. This dramatic increase in T_1 efficiency was attributed to the formation of these catalysts and the reversible ligation of the substrate. It was concluded that the presence of the

catalyst in solution reduces the steady-state level of hyperpolarisation as it takes several seconds for the sample to move from the position where polarisation transfer occurs (eg. outside the NMR magnet) to the final position where high field measurement occurs.

It was proposed that the effect of the catalyst on the substrate T_1 could be mitigated by deuteration of the NHC ligand and the substrate, thus increasing bound T_1 times such that higher free substrate T_1 values could be achieved.[69, 80, 146-148] For example, deuteration of IMes to form the isotopologue d_{22}-IMes was shown to increase the T_1 by 21% for each proton in the substrate methyl-4,6-d_2-nicotnate.[80]

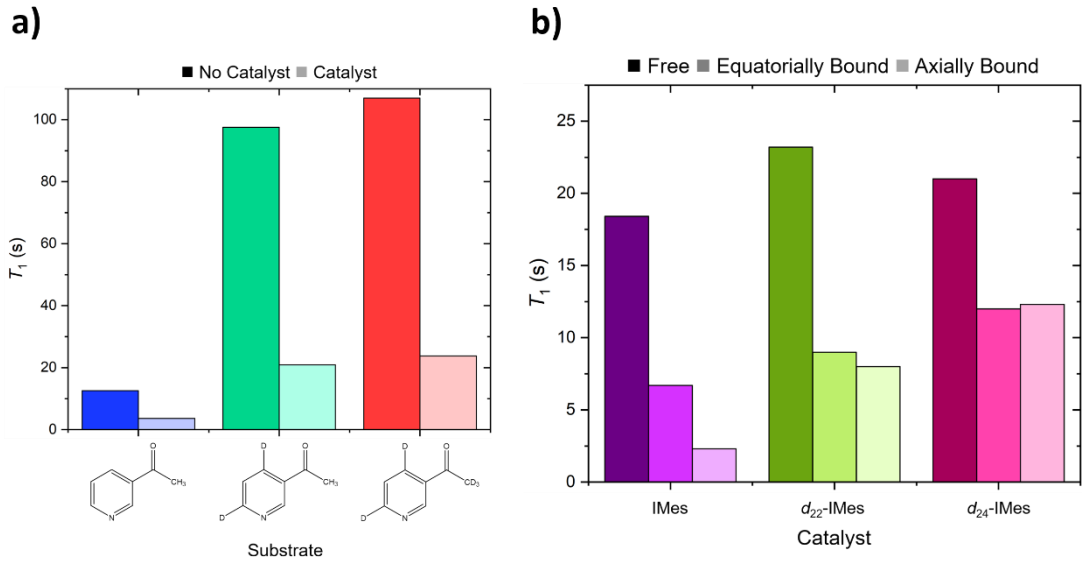

Figure 24 - a) Plot of the T_1 value at the H-5 resonance of methyl nicotinate and 2 of its deuterated analogues. The graph compares the T_1 in the absence of the catalyst and in the presence of IMes. b) Plot of the T_1 value at the H-5 resonance of methyl-4,6-d_2-nicotinate as a function of the catalyst IMes and corresponding deuterated analogues for the free substrate, the equatorially bound substrate (*trans* to hydride) and the axially bound substrate (*trans* to the NHC). Image created using data from P. J. Rayner et *al.*[80]

Figure 24 a) clearly illustrates the T_1 effect induced by the catalyst as the T_1 in the absence is much larger compared to when the catalyst is added. Figure 24 b) highlights the positive influence of deuteration of the catalyst on the substrate T_1. For example, the d_{22}-IMes isotopologue extended the T_1 of the H-5 resonance in methyl-4,6-d_2-nicotinate for the free substrate. Furthermore, graph b) also demonstrates the influence of binding to catalyst compared to the free substrate in

the presence of the catalyst. For example, the bound substrate T_1 values are substantially lower than the free substrate T_1.

Other methods to reduce the T_1 effect of the catalyst include quenching of the catalyst by addition of a chelate, or the conversion of SABRE-derived hyperpolarisation into long lived states.[143, 149-151]

1.5.7 Long Lived States

The lifetime of the hyperpolarised substrate is typically on the order of seconds, however for advancement of SABRE towards integration with MRI, hyperpolarisation must survive transfer to a diagnostically relevant region of the body.[151] This means that the hyperpolarisation lifetime must be on the order of minutes to be considered suitable for *in vivo* MRI. Selective deuteration at the carbene ligand and the substrate has been shown to extend hyperpolarisation lifetimes. For example, selective deuteration of nicotinamide was shown to induce a 75% increase in the substrate T_1 to 25.1 s.[80] Whilst the T_1 is significantly improved, it is not sufficiently long enough for integration with MRI. A second technique for extending the lifetime of hyperpolarised substrates via SABRE, is the use of long-lived states (LLS) which have been suggested as potential clinical imaging probes.[152] Such states were first reported in 2004 by Levitt *et al.*[153] who demonstrated that non-magnetic singlet states between two spin ½ nuclei that are magnetically inequivalent have lifetimes much longer than T_1. LLS have been prepared under PHIP and applied to ^{15}N SABRE hyperpolarisation via SABRE-SHEATH.[143, 154]

For ^{1}H LLS to be created, the substrate must contain a coupled ^{1}H pair that resonate at a similar frequency but are magnetically inequivalent. This has been illustrated by Roy *et al*.[151] using the substrate pyridazine. Pyridazine contains 4 protons in 2 proton resonance environments (Figure 25). The protons H-4 and H-5 are magnetically equivalent and therefore to create the LLS, the symmetry between these two protons must be broken. This was achieved by modifications at the α-proton sites shown in Figure 25. The most successful of these modifications was structure 3, where one α-^{1}H site was replaced with a methyl group and the remaining site was deuterated, this

gave an LLS of 255 s. The storage of the created LLS was then explored, where the sample was either retained in the NMR spectrometer without intervention, kept in the spectrometer with a spin-lock applied or removed from the magnet and placed in a 10 mT field. The most effective storage strategy was the latter example which allowed for the successful detection of magnetisation 15 minutes post-creation. Thus, this technique provides a suitable route for SABRE integration with *in vivo* MRI methods.

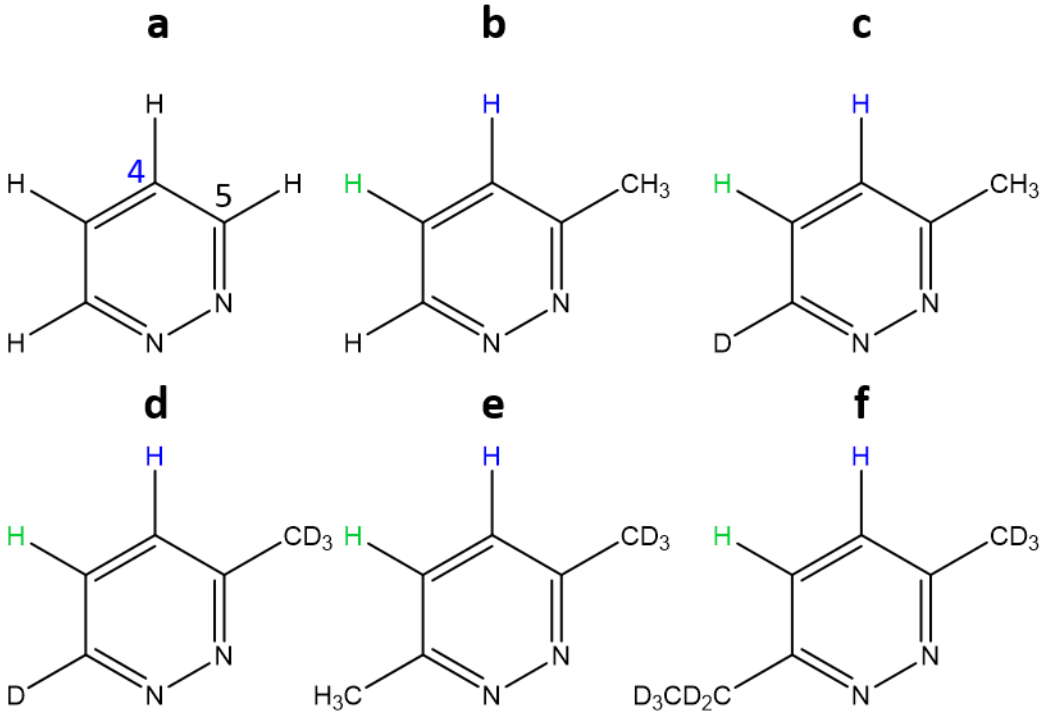

Figure 25 - Pyridazine (a) and associated derivatives and isotopalogues (b-c). Figure adapted with permissions from S. S. Roy et *al.*[151]

1.6 Thesis Aims

NMR is inherently insensitive. This is due to the small population difference between states as defined by the Boltzmann distribution that NMR probes. This population difference can be enhanced by hyperpolarisation methods such as: optical pumping (OP), dynamic nuclear polarisation (DNP), hydrogenative *para*hydrogen induced polarisation (PHIP) and non-hydrogenative PHIP (SABRE). Hyperpolarisation techniques have allowed for the detection of low concentration analytes in solution via NMR. This has been used for the characterisation of mixtures, reaction

intermediates or impurities that are not visible under thermal conditions.[155, 156] Applying hyperpolarisation techniques to MRI is critical for the reduction in patient scan times,[23] to highlight specific abnormalities to aid in the early diagnosis of disease, or for the observation of disease metabolites.[24] DNP has already been coupled with MRI to aid in the clinical diagnosis of prostate cancer via the hyperpolarisation of [1-^{13}C]-pyruvate. Despite yielding large polarisation levels of 64 %,[42] this technique requires costly equipment which also demands specialist training. Furthermore hyperpolarisation of the target molecule can take hours and once hyperpolarised can only be used once. SABRE provides a quick and cheap alternative to DNP. It also has the ability to re-hyperpolarise a substrate without chemically modifying it.[61] Additionally, it has been used to hyperpolarise a number of heteronuclei including: ^{1}H, ^{13}C, ^{15}N, ^{19}F, ^{29}Si, ^{31}P and ^{129}Sn.[77, 80-85]

SABRE employs an iridium catalyst and *p*-H_2 for the hyperpolarisation of a target molecule (substrate). Large signal enhancements are observed whereby the latent polarisation of *p*-H_2 is transferred into the substrate nuclei of interest. Polarisation transfer occurs via the *J*-coupled network which is facilitated by the iridium catalyst which holds the *p*-H_2 derived hydrides in the same plane as the substrate. Substrate and *p*-H_2 exchange then occurs with the excess substrate and *p*-H_2 allowing for hyperpolarisation to be refreshed and then built up into the surrounding solution. The research detailed in this thesis focuses on the role of the substrate in the SABRE hyperpolarisation method and is aimed at advancing catalytic efficiency and understanding of the hyperpolarisation process. This was achieved by the completion of the following objectives:

1. Hyperpolarisation of a series of *para*-substituted pyridine derivatives using the SABRE pre-catalyst [IrCl(COD)(SIMes)]Cl.
2. Complete characterisation of the SABRE species [Ir(COD)(SIMes)(substrate)]Cl and [Ir(H)$_2$(SIMes)(substrate)$_3$]Cl where the latter is the SABRE-active catalyst. This included the characterisation of novel SABRE-active species: [IrCl(H)$_2$(SIMes)(κ-O-4-pyridone)(κ-N-4-

hydroxypyridine)] and [Ir(H)$_2$(SIMes)(κ-N-isonicotinylhydrazide)(isonicotinyl-κ-O-κ-N-hydrazide]Cl.

3. Analysis of the exchange pathways in the SABRE-active species and optimisation of these parameters to improve catalytic efficiency in the hyperpolarisation process. Furthermore, to use this information to understand the consequences of the strength of the substrate-iridium ligation on SABRE performance.
4. Investigation of the relaxation methods and their impact on SABRE efficiency. Moreover, how the strength of the substrate-iridium ligation effects substrate relaxation.

A number of *para*-substituted pyridine derivatives were selected in order to assess ligation effects to the iridium catalyst. The pK_a of these substrates was measured and it was assumed that increasing the basicity at the pyridine nitrogen would increase the strength of the pyridine-iridium association. This would be assessed using rates of exchange and the rate of relaxation. Furthermore, to improve catalytic efficiency within the SABRE process by optimising these parameters. Full characterisation of each of the SABRE-active species has also allowed the identification of novel species.

A summary of the research conducted in the Chapters 2,3 and 4 is provided in Chapter 5 including the scope for further study.

1.7 References

1. T. D. W. Claridge, *High-Resolution NMR Techniques in Organic Chemistry*, Elsevier Science, 2016.
2. E. L. Hahn, *Phys. Rev.*, 1950, **77**, 297-299.
3. C. Kittel, *Phys. Rev.*, 1949, **76**, 743.
4. P. Vigoureux and G. B. B. M. Sutherland, *Proceedings of the Royal Society of London. Series A. Mathematical and Physical Sciences*, 1962, **270**, 72-89.
5. D. I. Hoult and B. Bhakar, *Concepts in Magnetic Resonance*, 1997, **9**, 277-297.
6. P. J. Hore, *Nuclear Magnetic Resonance (Oxford Chemistry Primers)*, Oxford University Press, USA, 1995.
7. K. Hashi, S. Ohki, S. Matsumoto, G. Nishijima, A. Goto, K. Deguchi, K. Yamada, T. Noguchi, S. Sakai, M. Takahashi, Y. Yanagisawa, S. Iguchi, T. Yamazaki, H. Maeda, R. Tanaka, T. Nemoto, H. Suematsu, T. Miki, K. Saito and T. Shimizu, *J. Magn. Reson.*, 2015, **256**, 30-33.

8. A. Abragam and M. Goldman, *Rep. Prog. Phys.*, 1978, **41**, 395-467.
9. R. Wind, M. Duijvestijn, C. Van Der Lugt, A. Manenschijn and J. Vriend, *Prog. Nucl. Magn. Reson. Spec.*, 1985, **17**, 33-67.
10. J. H. Ardenkjaer-Larsen, B. Fridlund, A. Gram, G. Hansson, L. Hansson, M. H. Lerche, R. Servin, M. Thaning and K. Golman, *Proc. Natl. Acad. Sci. U. S. A.*, 2003, **100**, 10158-10163.
11. A. Kastler, *J. Opt. Soc. Am.*, 1957, **47**, 460-465.
12. R. Tycko and J. A. Reimer, *J. Phys. Chem.*, 1996, **100**, 13240-13250.
13. T. G. Walker and W. Happer, *Rev. Mod. Phys.* , 1997, **69**, 629-642.
14. J. Natterer and J. Bargon, *Prog. Nucl. Magn. Reson. Spec.*, 1997, **31**, 293-315.
15. S. B. Duckett and D. Blazina, *Eur. J. Inorg. Chem.*, 2003, DOI: 10.1002/ejic.200300119, 2901-2912.
16. S. B. Duckett and R. E. Mewis, *Acc. Chem. Res.*, 2012, **45**, 1247-1257.
17. B. M. Goodson, B. Kidd, J.-B. Hövener, L. Schröder, T. Theis, N. Whiting and E. Y. Chekmenev, 2018.
18. P. Nikolaou, B. M. Goodson and E. Y. Chekmenev, *Chem. Eur. J.*, 2015, **21**, 3156-3166.
19. L. Frydman, *Nat. Chem.*, 2009, **1**, 176-178.
20. A. Filler, 2009.
21. J. C. Richardson, R. W. Bowtell, K. Mäder and C. D. Melia, *Adv. Drug Delivery Rev.*, 2005, **57**, 1191-1209.
22. J. F. Schenck, *Medical physics*, 1996, **23**, 815-850.
23. M. L. Hirsch, N. Kalechofsky, A. Belzer, M. Rosay and J. G. Kempf, *J. Am. Chem. Soc.*, 2015, **137**, 8428-8434.
24. S. E. Day, M. I. Kettunen, F. A. Gallagher, D. E. Hu, M. Lerche, J. Wolber, K. Golman, J. H. Ardenkjaer-Larsen and K. M. Brindle, *Nat. Med. (N. Y., NY, U. S.)*, 2007, **13**, 1382-1387.
25. A. Kastler, *J. Phys. Radium*, 1950, **11**, 255-265.
26. T. Pietrass, *Colloid Surf. A-Physicochem. Eng. Asp.*, 1999, **158**, 51-57.
27. N. J. Stewart, G. Norquay, P. D. Griffiths and J. M. Wild, *Magn. Reson. Med.*, 2015, **74**, 346-352.
28. A. L. Zook, B. B. Adhyaru and C. R. Bowers, *J. Magn. Reson.*, 2002, **159**, 175-182.
29. D. Raftery, L. Reven, H. Long, A. Pines, P. Tang and J. Reimer, *J. Phys. Chem.*, 1993, **97**, 1649-1655.
30. J. Ardenkjaer-Larsen, S. Bowen, J. Raagaard Petersen, O. Rybalko, M. Vinding, M. Ullisch and N. Chr. Nielsen, *Cryogen-Free dissolution Dynamic Nuclear Polarization polarizer operating at 3.35 T, 6.70 T and 10.1 T*, 2018.
31. J. N. Dumez, *Magn. Reson. Chem.*, 2017, **55**, 38-46.
32. A. W. Overhauser, *Phys. Rev.*, 1953, **92**, 411-415.
33. A. Abragam and W. G. Proctor, *C. R. Acad. Sci.*, 1958, **246**.
34. B. Corzilius, *Phys. Chem. Chem. Phys.*, 2016, **18**, 27190-27204.
35. D. S. Wollan, *Phys. Rev. B*, 1976, **13**, 3671.
36. D. S. Wollan, *Phys. Rev. B*, 1976, **13**, 3686.
37. A. B. Barnes, G. De Paëpe, P. C. A. van der Wel, K. N. Hu, C. G. Joo, V. S. Bajaj, M. L. Mak-Jurkauskas, J. R. Sirigiri, J. Herzfeld, R. J. Temkin and R. G. Griffin, *Appl. Magn. Reson.*, 2008, **34**, 237-263.

38. T. V. Can, Q. Z. Ni and R. G. Griffin, *J. Magn. Reson.*, 2015, **253**, 23-35.
39. A. B. Barnes, G. D. Paepe, P. C. van der Wel, K. N. Hu, C. G. Joo, V. S. Bajaj, M. L. Mak-Jurkauskas, J. R. Sirigiri, J. Herzfeld, R. J. Temkin and R. G. Griffin, *Appl. Magn. Reson.*, 2008, **34**, 237-263.
40. Y. Lee, *Appl. Spectrosc. Rev.*, 2016, **51**, 210-226.
41. H. Gutte, A. E. Hansen, H. H. Johannesen, A. E. Clemmensen, J. H. Ardenkjær-Larsen, C. H. Nielsen and A. Kjær, *Am. J. Nucl. Med. Mol. Im*, 2015, **5**, 548-560.
42. H. Jóhannesson, S. Macholl and J. H. Ardenkjaer-Larsen, *J. Magn. Reson.*, 2009, **197**, 167-175.
43. C. R. Bowers and D. P. Weitekamp, *Phys. Rev. Lett.*, 1986, **57**, 2645-2648.
44. C. R. Bowers and D. P. Weitekamp, *J. Am. Chem. Soc.*, 1987, **109**, 5541-5542.
45. J. Y. C. Chen, unpublished work.
46. S. B. Duckett and N. J. Wood, *Coord. Chem. Rev.*, 2008, **252**, 2278-2291.
47. C. Terenzi, S. Bouguet-Bonnet and D. Canet, *J. Chem. Phys.*, 2017, **146**, 154203.
48. B. Feng, A. M. Coffey, R. D. Colon, E. Y. Chekmenev and K. W. Waddell, *J. Magn. Reson.*, 2012, **214**, 258-262.
49. E. Bartholomé, *Zeitschrift für Elektrochemie und angewandte physikalische Chemie*, 1935, **41**, 812-812.
50. P. M. Richardson, R. O. John, A. J. Parrott, P. J. Rayner, W. Iali, A. Nordon, M. E. Halse and S. B. Duckett, *Phys. Chem. Chem. Phys.*, 2018, **20**, 26362-26371.
51. R. Zhou, W. Cheng, L. M. Neal, E. W. Zhao, K. Ludden, H. E. Hagelin-Weaver and C. R. Bowers, *Phys. Chem. Chem. Phys.*, 2015, **17**, 26121-26129.
52. J. B. Hovener, A. N. Pravdivtsev, B. Kidd, C. R. Bowers, S. Gloggler, K. V. Kovtunov, M. Plaumann, R. Katz-Brull, K. Buckenmaier, A. Jerschow, F. Reineri, T. Theis, R. V. Shchepin, S. Wagner, P. Bhattacharya, N. M. Zacharias and E. Y. Chekmenev, *Angew. Chem. Int. Ed.*, 2018, **57**, 11140-11162.
53. R. U. Kirss, T. C. Eisenschmid and R. Eisenberg, *J. Am. Chem. Soc.*, 1988, **110**, 8564-8566.
54. T. C. Eisenschmid, J. McDonald, R. Eisenberg and R. G. Lawler, *J. Am. Chem. Soc.*, 1989, **111**, 7267-7269.
55. S. B. Duckett, C. L. Newell and R. Eisenberg, *J. Am. Chem. Soc.*, 1993, **115**, 1156-1157.
56. J. Barkemeyer, M. Haake and J. Bargon, *J. Am. Chem. Soc.*, 1995, **117**, 2927-2928.
57. E. Cavallari, C. Carrera, T. Boi, S. Aime and F. Reineri, *J. Phys. Chem. B*, 2015, **119**, 10035-10041.
58. J. Kurhanewicz, D. B. Vigneron, K. Brindle, E. Y. Chekmenev, A. Comment, C. H. Cunningham, R. J. DeBerardinis, G. G. Green, M. O. Leach and S. S. Rajan, *Neoplasia*, 2011, **13**, 81-97.
59. E. Cavallari, C. Carrera, G. Di Matteo, O. Bondar, S. Aime and F. Reineri, *Frontiers in Oncology*, 2020, **10**.
60. E. Cavallari, C. Carrera, S. Aime and F. Reineri, *J. Magn. Reson.*, 2018, **289**, 12-17.
61. K. D. Atkinson, M. J. Cowley, S. B. Duckett, P. I. Elliott, G. G. Green, J. Lopez-Serrano, I. G. Khazal and A. C. Whitwood, *Inorg. Chem.*, 2009, **48**, 663-670.

62. H. Zeng, J. Xu, J. Gillen, M. T. McMahon, D. Artemov, J.-M. Tyburn, J. A. B. Lohman, R. E. Mewis, K. D. Atkinson, G. G. R. Green, S. B. Duckett and P. C. M. van Zijl, *J. Magn. Reson.*, 2013, **237**, 73-78.
63. R. W. Adams, S. B. Duckett, R. A. Green, D. C. Williamson and G. G. Green, *J. Chem. Phys.*, 2009, **131**, 194505.
64. R. W. Adams, J. A. Aguilar, K. D. Atkinson, M. J. Cowley, P. I. Elliott, S. B. Duckett, G. G. Green, I. G. Khazal, J. Lopez-Serrano and D. C. Williamson, *Science*, 2009, **323**, 1708-1711.
65. L. S. Lloyd, A. Asghar, M. J. Burns, A. Charlton, S. Coombes, M. J. Cowley, G. J. Dear, S. B. Duckett, G. R. Genov, G. G. R. Green, L. A. R. Highton, A. J. J. Hooper, M. Khan, I. G. Khazal, R. J. Lewis, R. E. Mewis, A. D. Roberts and A. J. Ruddlesden, *Catal. Sci. Technol.*, 2014, **4**, 3544-3554.
66. M. J. Cowley, S. B. Duckett and G. Green, *Abstr. Pap. Am. Chem. Soc.*, 2010, **240**.
67. N. Eshuis, R. L. Aspers, B. J. van Weerdenburg, M. C. Feiters, F. P. Rutjes, S. S. Wijmenga and M. Tessari, *J. Magn. Reson.*, 2016, **265**, 59-66.
68. N. Eshuis, N. Hermkens, B. J. A. van Weerdenburg, M. C. Feiters, F. Rutjes, S. S. Wijmenga and M. Tessari, *J. Am. Chem. Soc.*, 2014, **136**, 2695-2698.
69. M. Fekete, O. W. Bayfield, S. B. Duckett, S. Hart, R. E. Mewis, N. Pridmore, P. J. Rayner and A. Whitwood, *Inorg. Chem.*, 2013, **52**, 13453-13461.
70. K. M. Appleby, R. E. Mewis, A. M. Olaru, G. G. R. Green, I. J. S. Fairlamb and S. B. Duckett, *Chem. Sci.*, 2015, **6**, 3981-3993.
71. L. S. Lloyd, R. W. Adams, M. Bernstein, S. Coombes, S. B. Duckett, G. G. Green, R. J. Lewis, R. E. Mewis and C. J. Sleigh, *J. Am. Chem. Soc.*, 2012, **134**, 12904-12907.
72. E. B. Ducker, L. T. Kuhn, K. Munnemann and C. Griesinger, *J. Magn. Reson.*, 2012, **214**, 159-165.
73. M. J. Cowley, R. W. Adams, K. D. Atkinson, M. C. Cockett, S. B. Duckett, G. G. Green, J. A. Lohman, R. Kerssebaum, D. Kilgour and R. E. Mewis, *J. Am. Chem. Soc.*, 2011, **133**, 6134-6137.
74. M. Haake, J. Barkemeyer and J. Bargon, *J. Phys. Chem.*, 1995, **99**, 17539-17543.
75. L. Buljubasich, M. B. Franzoni, H. W. Spiess and K. Munnemann, *J. Magn. Reson.*, 2012, **219**, 33-40.
76. P. M. Richardson, S. Jackson, A. J. Parrott, A. Nordon, S. B. Duckett and M. E. Halse, *Magn. Reson. Chem.*, 2018, **56**, 641-650.
77. T. Theis, M. L. Truong, A. M. Coffey, R. V. Shchepin, K. W. Waddell, F. Shi, B. M. Goodson, W. S. Warren and E. Y. Chekmenev, *J. Am. Chem. Soc.*, 2015, **137**, 1404-1407.
78. A. N. Pravdivtsev, A. V. Yurkovskaya, H. M. Vieth, K. L. Ivanov and R. Kaptein, *Chem. Phys. Chem.*, 2013, **14**, 3327-3331.
79. D. A. Barskiy, A. N. Pravdivtsev, K. L. Ivanov, K. V. Kovtunov and I. V. Koptyug, *Phys. Chem. Chem. Phys.*, 2016, **18**, 89-93.
80. P. J. Rayner, M. J. Burns, A. M. Olaru, P. Norcott, M. Fekete, G. G. R. Green, L. A. R. Highton, R. E. Mewis and S. B. Duckett, *Proc. Natl. Acad. Sci. U. S. A.*, 2017, **114**, E3188-E3194.

81. R. E. Mewis, K. D. Atkinson, M. J. Cowley, S. B. Duckett, G. G. Green, R. A. Green, L. A. Highton, D. Kilgour, L. S. Lloyd, J. A. Lohman and D. C. Williamson, *Magn. Reson. Chem.*, 2014, **52**, 358-369.
82. A. M. Olaru, T. B. R. Robertson, J. S. Lewis, A. Antony, W. Iali, R. E. Mewis and S. B. Duckett, *ChemistryOpen*, 2017, **7**, 97-105.
83. S. S. Roy, K. M. Appleby, E. J. Fear and S. B. Duckett, *J. Phys. Chem. Lett.*, 2018, **9**, 1112-1117.
84. A. M. Olaru, A. Burt, P. J. Rayner, S. J. Hart, A. C. Whitwood, G. G. R. Green and S. B. Duckett, *Chem Commun (Camb)*, 2016, **52**, 14482-14485.
85. P. J. Rayner, P. M. Richardson and S. B. Duckett, *Angew. Chem.*, 2020, **132**, 2732-2736.
86. M. L. Truong, T. Theis, A. M. Coffey, R. V. Shchepin, K. W. Waddell, F. Shi, B. M. Goodson, W. S. Warren and E. Y. Chekmenev, *J.Phys.Chem.C.*, 2015, **119**, 8786-8797.
87. I. V. Skovpin, A. Svyatova, N. Chukanov, E. Y. Chekmenev, K. V. Kovtunov and I. V. Koptyug, *Chem. Eur. J.*, 2019, **25**, 12694-12697.
88. T. Theis, M. Truong, A. M. Coffey, E. Y. Chekmenev and W. S. Warren, *J. Magn. Reson.*, 2014, **248**, 23-26.
89. A. N. Pravdivtsev, A. V. Yurkovskaya, H.-M. Vieth and K. L. Ivanov, *J. Phys. Chem. B*, 2015, **119**, 13619-13629.
90. S. S. Roy, G. Stevanato, P. J. Rayner and S. B. Duckett, *J. Magn. Reson.*, 2017, **285**, 55-60.
91. V. Boekelheide, *J. Am. Chem. Soc.*, 1961, **83**, 4680-4680.
92. T. Gilchrist, *New York*, 1997.
93. D. J. Brown, *The Chemistry of Heterocyclic Compounds, Pyridine Metal Complexes*, John Wiley & Sons, 2009.
94. E. V. Stanbury, P. M. Richardson and S. B. Duckett, *Catal. Sci. Technol.*, 2019, **9**, 3914-3922.
95. A. A. Altaf, A. Shahzad, Z. Gul, N. Rasool, A. Badshah, B. Lal and E. Khan, *J. Drug Des. Med. Chem*, 2015, **1**, 1-11.
96. M. MacCoss and M. Robins, in *The Chemistry of antitumour agents*, Springer, 1990, pp. 261-298.
97. R. Kaur, P. Kaur, S. Sharma, G. Singh, S. Mehndiratta, P. MS Bedi and K. Nepali, *Recent Pat. Anti-Cancer Drug Discovery*, 2015, **10**, 23-71.
98. W. Iali, A. M. Olaru, G. G. R. Green and S. B. Duckett, *Chemistry*, 2017, **23**, 10491-10495.
99. A. M. Olaru, M. J. Burns, G. G. R. Green and S. B. Duckett, *Chem. Sci.* , 2017, **8**, 2257-2266.
100. A. Manoharan, P. J. Rayner, M. Fekete, W. Iali, P. Norcott, V. Hugh Perry and S. B. Duckett, *Chem. Phys. Chem.*, 2019, **20**, 285-294.
101. B. J. Tickner, J. S. Lewis, R. O. John, A. C. Whitwood and S. B. Duckett, *Dalton Trans.*, 2019, **48**, 15198-15206.
102. W. Iali, S. S. Roy, B. J. Tickner, F. Ahwal, A. J. Kennerley and S. B. Duckett, *Angew. Chem. Int. Ed.*, 2019, **58**, 10271-10275.
103. K. Shen, A. W. J. Logan, J. F. P. Colell, J. Bae, G. X. Ortiz Jr., T. Theis, W. S. Warren, S. J. Malcolmson and Q. Wang, *Angew. Chem. Int. Ed.*, 2017, **56**, 12112-12116.

104. A. L. MacKinnon and J. Taunton, *Current Protocols in Chemical Biology*, 2009, **1**, 55-73.
105. M.-L. Yuan, J.-H. Xie, S.-F. Zhu and Q.-L. Zhou, *ACS Catalysis*, 2016, **6**, 3665-3669.
106. Y. Sato, Y. Kayaki and T. Ikariya, *Organometallics*, 2016, **35**, 1257-1264.
107. P. M. Richardson, W. Iali, S. S. Roy, P. J. Rayner, M. E. Halse and S. B. Duckett, *Chem. Sci.*, 2019, **10**, 10607-10619.
108. Y. Xu, D. M. P. Mingos and J. M. Brown, *Chem. Commun.*, 2008, 199-201.
109. R. H. Crabtree, H. Felkin and G. E. Morris, *J. Organomet. Chem.*, 1977, **141**, 205-215.
110. R. H. Crabtree, M. F. Mellea, J. M. Mihelcic and J. M. Quirk, *J. Am. Chem. Soc.*, 1982, **104**, 107-113.
111. K. D. Atkinson, M. J. Cowley, P. I. Elliott, S. B. Duckett, G. G. Green, J. Lopez-Serrano and A. C. Whitwood, *J. Am. Chem. Soc.*, 2009, **131**, 13362-13368.
112. S. Díez-González and S. P. Nolan, *Coord. Chem. Rev.*, 2007, **251**, 874-883.
113. C. Boehme and G. Frenking, *J. Am. Chem. Soc.*, 1996, **118**, 2039-2046.
114. L. D. Vázquez-Serrano, B. T. Owens and J. M. Buriak, *Chem. Commun.*, 2002, DOI: 10.1039/B208403A, 2518-2519.
115. B. J. van Weerdenburg, S. Gloggler, N. Eshuis, A. H. Engwerda, J. M. Smits, R. de Gelder, S. Appelt, S. S. Wymenga, M. Tessari, M. C. Feiters, B. Blumich and F. P. Rutjes, *Chem. Commun.*, 2013, **49**, 7388-7390.
116. M. Fekete, C. Gibard, G. J. Dear, G. G. Green, A. J. Hooper, A. D. Roberts, F. Cisnetti and S. B. Duckett, *Dalton Trans.*, 2015, **44**, 7870-7880.
117. P. J. Rayner, P. Norcott, K. M. Appleby, W. Iali, R. O. John, S. J. Hart, A. C. Whitwood and S. B. Duckett, *Nat Commun*, 2018, **9**, 4251.
118. C. M. Wong, M. Fekete, R. Nelson-Forde, M. R. D. Gatus, P. J. Rayner, A. C. Whitwood, S. B. Duckett and B. A. Messerle, *Catal. Sci. Technol.*, 2018, **8**, 4925-4933.
119. J. Colell, A. W. Logan, Z. Zhou, J. R. Lindale, R. Laasner, R. Shchepin, E. Chekmenev, V. Blum, W. S. Warren and S. J. Malcolmson, *Chem. Commun.*, 2020.
120. A. J. Holmes, P. J. Rayner, M. J. Cowley, G. G. R. Green, A. C. Whitwood and S. B. Duckett, *Dalton Trans.*, 2015, **44**, 1077-1083.
121. M. E. van der Boom and D. Milstein, *Chem. Rev. (Washington, DC, U. S.)*, 2003, **103**, 1759-1792.
122. C. J. Moulton and B. L. Shaw, *Journal of the Chemical Society, Dalton Transactions*, 1976, DOI: 10.1039/DT9760001020, 1020-1024.
123. A. J. Ruddlesden, R. E. Mewis, G. G. Green, A. C. Whitwood and S. B. Duckett, *Organometallics*, 2015, **34**, 2997-3006.
124. W. Iali, G. G. R. Green, S. J. Hart, A. C. Whitwood and S. B. Duckett, *Inorg. Chem.*, 2016, **55**, 11639-11643.
125. R. E. Mewis, *Magn. Reson. Chem.*, 2015, **53**, 789-800.
126. A. Manoharan, P. J. Rayner, W. Iali, M. J. Burns, V. H. Perry and S. B. Duckett, *ChemMedChem*, 2018, **13**, 352-359.
127. K. S. Egorova and V. P. Ananikov, *Organometallics*, 2017, **36**, 4071-4090.
128. N. G. Anderson, *Practical Process Research and Development: A Guide for Organic Chemists*, Elsevier Science, 2012.

129. R. E. Mewis, M. Fekete, G. G. Green, A. C. Whitwood and S. B. Duckett, *Chem. Commun.*, 2015, **51**, 9857-9859.
130. D. A. Barskiy, L. A. Ke, X. Li, V. Stevenson, N. Widarman, H. Zhang, A. Truxal and A. Pines, *J. Phys. Chem. Lett.*, 2018, **9**, 2721-2724.
131. F. Shi, A. M. Coffey, K. W. Waddell, E. Y. Chekmenev and B. M. Goodson, *Angew. Chem. Int. Ed.*, 2014, **53**, 7495-7498.
132. K. V. Kovtunov, L. M. Kovtunova, M. E. Gemeinhardt, A. V. Bukhtiyarov, J. Gesiorski, V. I. Bukhtiyarov, E. Y. Chekmenev, I. V. Koptyug and B. M. Goodson, *Angew. Chem. Int. Ed.*, 2017, **56**, 10433-10437.
133. F. Shi, A. M. Coffey, K. W. Waddell, E. Y. Chekmenev and B. M. Goodson, *J. Phys. Chem. C.*, 2015, **119**, 7525-7533.
134. B. E. Kidd, J. L. Gesiorski, M. E. Gemeinhardt, R. V. Shchepin, K. V. Kovtunov, I. V. Koptyug, E. Y. Chekmenev and B. M. Goodson, *J. Phys. Chem. C.*, 2018, **122**, 16848-16852.
135. F. Shi, P. He, Q. A. Best, K. Groome, M. L. Truong, A. M. Coffey, G. Zimay, R. V. Shchepin, K. W. Waddell, E. Y. Chekmenev and B. M. Goodson, *J. Phys. Chem. C.*, 2016, **120**, 12149-12156.
136. P. Spannring, I. Reile, M. Emondts, P. P. M. Schleker, N. K. J. Hermkens, N. G. J. van der Zwaluw, B. J. A. van Weerdenburg, P. Tinnemans, M. Tessari, B. Blümich, F. P. J. T. Rutjes and M. C. Feiters, *Chem. Eur. J.*, 2016, **22**, 9277-9282.
137. P. J. Rayner and S. B. Duckett, *Angew. Chem. Int. Ed.*, 2018, **57**, 6742-6753.
138. M. J. Cowley, R. W. Adams, K. D. Atkinson, M. C. R. Cockett, S. B. Duckett, G. G. R. Green, J. A. B. Lohman, R. Kerssebaum, D. Kilgour and R. E. Mewis, *J. Am. Chem. Soc.*, 2011, **133**, 6134-6137.
139. D. A. Barskiy, S. Knecht, A. V. Yurkovskaya and K. L. Ivanov, *Prog. Nucl. Magn. Reson. Spec.*, 2019, **114-115**, 33-70.
140. J. A. Iggo, *NMR spectroscopy in Inorganic Chemistry*, Oxford University Press New York, 1999.
141. W. S. Warren, E. Jenista, R. T. Branca and X. Chen, *Science*, 2009, **323**, 1711-1714.
142. D. A. Barskiy, R. V. Shchepin, C. P. N. Tanner, J. F. P. Colell, B. M. Goodson, T. Theis, W. S. Warren and E. Y. Chekmenev, *Chem. Phys. Chem.*, 2017, **18**, 1493-1498.
143. T. Theis, G. X. Ortiz, Jr., A. W. Logan, K. E. Claytor, Y. Feng, W. P. Huhn, V. Blum, S. J. Malcolmson, E. Y. Chekmenev, Q. Wang and W. S. Warren, *Sci. Adv.*, 2016, **2**, e1501438.
144. M. M. Alauddin, *Am. J. Nucl. Med. Mol. Im*, 2012, **2**, 55-76.
145. Y. J. Lin and A. P. Koretsky, *Magn. Reson. Med.*, 1997, **38**, 378-388.
146. R. E. Mewis, R. A. Green, M. C. Cockett, M. J. Cowley, S. B. Duckett, G. G. Green, R. O. John, P. J. Rayner and D. C. Williamson, *J. Phys. Chem. B*, 2015, **119**, 1416-1424.
147. P. Norcott, P. J. Rayner, G. G. R. Green and S. B. Duckett, *Chemistry*, 2017, **23**, 16990-16997.
148. M. Fekete, P. J. Rayner, G. G. R. Green and S. B. Duckett, *Magn. Reson. Chem.*, 2017, **55**, 944-957.
149. S. S. Roy, P. Norcott, P. J. Rayner, G. G. R. Green and S. B. Duckett, *Chemistry*, 2017, **23**, 10496-10500.

150. S. S. Roy, P. J. Rayner, P. Norcott, G. G. R. Green and S. B. Duckett, *Phys. Chem. Chem. Phys.*, 2016, **18**, 24905-24911.
151. S. S. Roy, P. Norcott, P. J. Rayner, G. G. Green and S. B. Duckett, *Angew. Chem. Int. Ed.*, 2016, **55**, 15642-15645.
152. I. Marco-Rius, M. C. Tayler, M. I. Kettunen, T. J. Larkin, K. N. Timm, E. M. Serrao, T. B. Rodrigues, G. Pileio, J. H. Ardenkjaer-Larsen and M. H. Levitt, *NMR Biomed.*, 2013, **26**, 1696-1704.
153. M. Carravetta, O. G. Johannessen and M. H. Levitt, *Phys. Rev. Lett.*, 2004, **92**, 153003.
154. M. B. Franzoni, L. Buljubasich, H. W. Spiess and K. Münnemann, *J. Am. Chem. Soc.*, 2012, **134**, 10393-10396.
155. O. Torres, B. Procacci, M. E. Halse, R. W. Adams, D. Blazina, S. B. Duckett, B. Eguillor, R. A. Green, R. N. Perutz and D. C. Williamson, *J. Am. Chem. Soc.*, 2014, **136**, 10124-10131.
156. O. Semenova, P. M. Richardson, A. J. Parrott, A. Nordon, M. E. Halse and S. B. Duckett, *Anal. Chem.*, 2019, **91**, 6695-6701.

Chapter 2 Comparison of Experimental Methods for SABRE Hyperpolarisation

SABRE experiments can be performed using three different methods: manual shaking (using the stray field of the spectrometer), the automated flow system and manual shaking using a handheld magnetic array. In this chapter, these methods will be compared and contrasted according to the magnitude of signal enhancement and reproducibility of the method. This was achieved by varying the *p*-H_2 dissolution time across these three methods and calculating the respective ^{1}H signal enhancements. It was established that none of these methods can generate both reproducible and large signal enhancements; signal enhancements are either large with high error (not very reproducible) or low enhancements that are highly reproducible. The impact and the importance of this trade-off between the magnitude of the signal enhancement and the reproducibility is also considered.

2.1 Observation of the Chemical Process of SABRE via NMR

SABRE is a hyperpolarisation technique which employs *p*-H_2 and an iridium catalyst for the enhanced detection of a target molecule (substrate). The SABRE-active species is usually an octahedral complex of the form $[Ir(H)_2(NHC)(sub)_3]Cl$, where the axial positions are occupied by an *N*-heterocycle (NHC) and a substrate ligand.[1-3] The other two substrate molecules lie in the equatorial plane with the *p*-H_2 derived hydrides in a *cis* configuration (Figure 26). As the substrate and the hydrides are held within the same plane, the non-equilibrium spin order of hydrogen can be transferred to the substrate, as described in the introduction.[4]

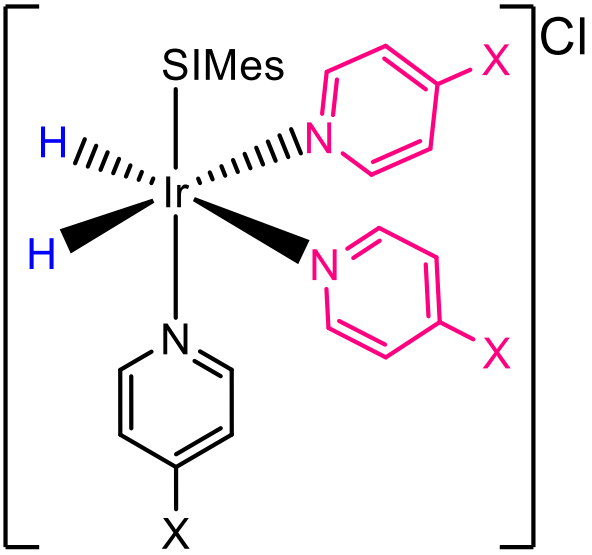

Figure 26 - The SABRE active species $[Ir(H)_2(SIMes)(sub)_3]Cl$

The hyperpolarised response of the species in Figure 26 can be detected using three different methods; manual shaking using the stray field of the spectrometer,[1] manual shaking using a handheld magnetic array[5] or an automated flow system.[6] Each of these will be discussed in more detail in this chapter. Formation of the SABRE active catalyst of type $[Ir(H)_2(SIMes)(sub)_3]Cl$ begins with the reaction of the precatalyst [IrCl((COD)(SIMes)] with the substrate in a methanol solution under a pressure of hydrogen. Practically, this typically involves the preparation of a 5 mM solution of [IrCl(COD)(SIMes)] in methanol (0.6 mL). To this, the target substrate (50 mM) is added. This addition causes the displacement of the chloride ligand and forms [Ir(COD)(SIMes)(sub]Cl. The sample is then degassed to ensure complete removal of any oxygen in the sample. This step is critical as oxygen is *para*magnetic, therefore it can catalyse the interconversion of *p*-H_2 back to thermal equilibrium, significantly reducing, if not preventing substrate polarisation.[7] The presence of oxygen may also decrease the relaxation time (T_1) of the substrate and promote degradation of the SABRE-active species which is air-sensitive. *P*-H_2 (4 bar) is then added, causing the solution to become colourless, suggesting formation of the SABRE-active species $[Ir(H)_2(SIMes)(sub)_3]Cl$, which can be characterised via different analytical methods including NMR, mass spectrometry and infrared spectroscopy.[1] Usually, this is indicated by the disappearance of all COD related peaks and the appearance of a single hydride peak at approximately −23 ppm (see Figure 27 for more details).

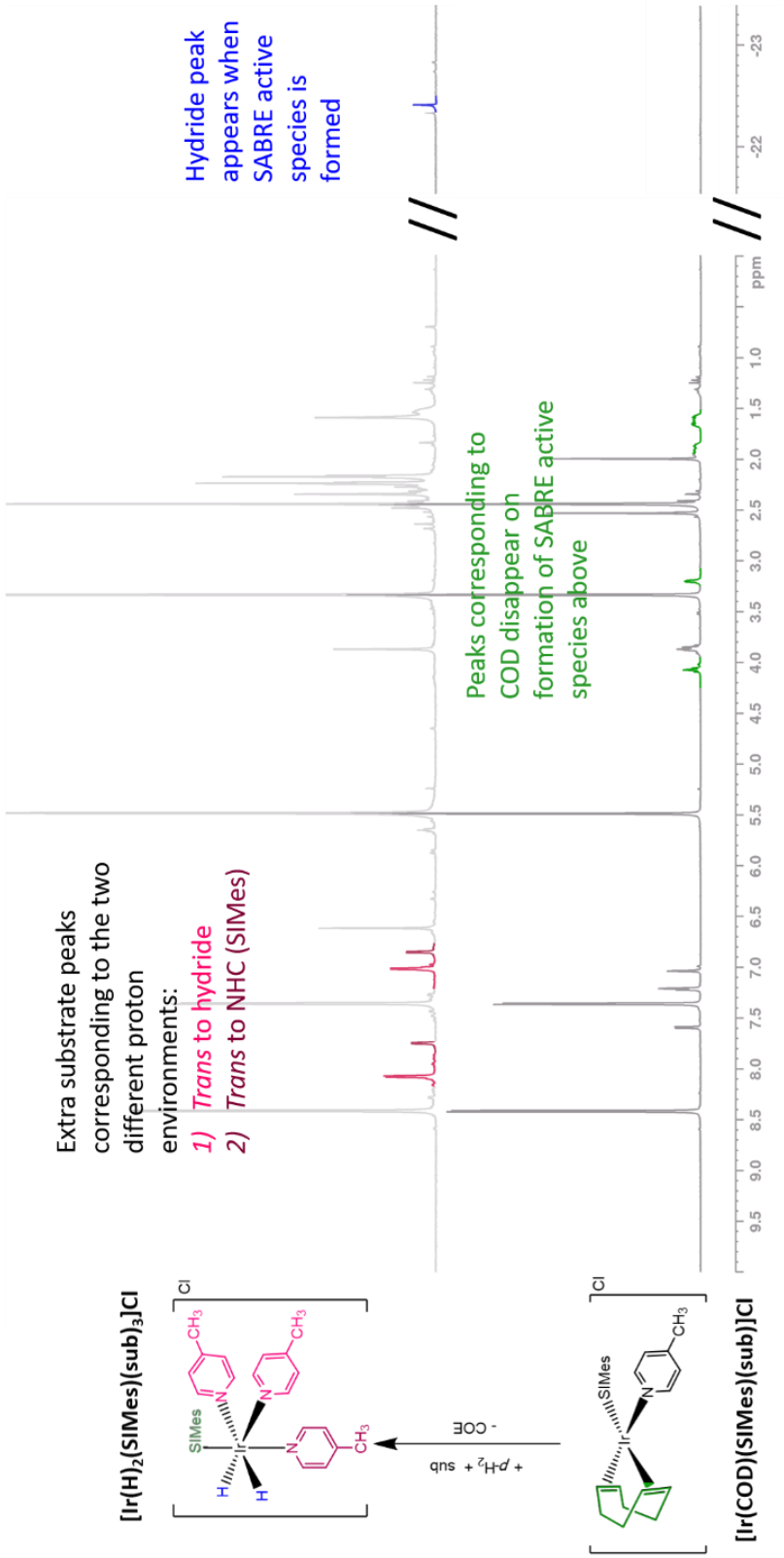

Figure 27 - Stacked ^{1}H-NMR spectra for [Ir(COD)(SIMes)(sub)]Cl (bottom) and [Ir(H)$_2$(SIMes)(sub)$_3$]Cl (top). Formation of the SABRE active species, [Ir(H)$_2$(SIMes)(sub)$_3$]Cl is indicated by the appearance of extra substrate peaks (shown in pink) alongside the hydride peak shown in blue (top spectra). The disappearance of COD related peaks (shown in green in the bottom spectra) indicates that the SABRE precatalyst, [Ir(COD)(SIMes)(sub)]Cl has been consumed. ^{1}H NMR spectra collected on a 300 MHz spectrometer at 298 K using a sample containing [IrCl(COD)(SIMes)] (5 mM), 4-methylpyridine (50 mM), methanol-d_4 (0.6 mL) (bottom spectra) with addition of pH$_2$ (4 bar) (top spectra).

Figure 27 compares the ^{1}H-NMR spectra for the SABRE precatalyst [Ir(COD)(SIMes)(4-methylpyridine)]Cl (bottom) and the SABRE-active catalyst [Ir(H)$_2$(SIMes)(4-methylpyridine)$_3$]Cl (top) which is formed upon addition of *p*-H$_2$ to the precatalyst. Firstly it is noted that the resonances for the CH in COD highlighted in green at 4.07 and 3.21 ppm in the bottom spectra are shown to disappear alongside the CH$_2$ resonances at 1.91 and 1.62 ppm when [Ir(COD()(SIMes)(sub)]Cl is consumed. Secondly, additional substrate peaks are observed in the spectra for [Ir(H)$_2$(SIMes)(sub)$_3$]Cl (top). These are shown in pink at 8.12, 7.80, 6.96 and 6.81 ppm indicating the presence of the octahedral complex containing two different substrate environments. One of these contains two substrate ligands *trans* to the hydrides and the other one substrate ligand *trans* to the NHC in a 2:1 ratio. Finally, the hydride resonance is highlighted in blue at -22.4 ppm. The formation of the SABRE active species is described in more detail in the introductory chapter.

SABRE experiments are performed using a standard approach one-shot (1 scan) proton experiment with a 90° pulse, recycling delay (d1) value of 1 µs and a receiver gain (RG) of 1 (see Figure 28).[1] The lifetime of the hyperpolarised signal is dictated by the T_1 value of the substrate as relaxation destroys hyperpolarisation.[8] The T_1 at the *ortho* proton for the substrate used in this chapter (4-methylpyridine) is 6.50 s. Therefore, a short recycling delay (d1) value ensures a minimal amount of hyperpolarisation is lost before acquisition. The hyperpolarised signal is significantly larger than the non-hyperpolarised (thermal) spectrum and therefore a short RG value is used to prevent clipping of the NMR signal.

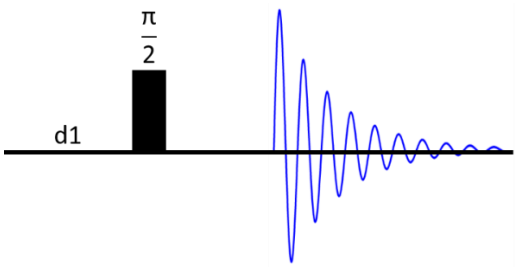

Figure 28 - Standard ^{1}H 90° pulse used for SABRE experiments

It is also important to acquire a spectrum under thermal polarisation (i.e. no *p*-H_2) to compare to the hyperpolarised spectrum and calculate the signal gain. This 'thermal' spectrum is usually acquired under exactly the same conditions and includes the same sample used for the hyperpolarised measurements. It is essential that the same conditions are applied for the thermal spectrum so that the two spectra are directly comparable. For example if different samples were used then there may be minute differences in substrate concentration meaning that the calculated signal enhancement is unreliable. An example of a thermal and hyperpolarised spectrum is depicted below in Figure 29 for the SABRE-active species, $[Ir(H)_2(SIMes)(sub)_3]Cl$ containing the substrate 4-methylpyridine. The thermal spectrum is shown in black and has been magnified 32 times so that it can be seen on the same scale as the hyperpolarised spectrum shown in pink. The ^1H resonances for the three different proton environments (*ortho*, *meta* and *para*) on the substrate have been highlighted on the spectrum. The largest level of hyperpolarisation is observed in the *ortho* proton resonance, followed by the *meta* proton resonance and finally the *para* proton resonance. The *ortho* signal enhancement is larger than the *meta* and the *para* resonances because it is situated closer to the hydrides from which polarisation is transferred within the active complex and therefore exhibits the largest propagating spin-spin coupling.[9] The signal enhancement (ε) is calculated by dividing the integrals of the thermal equilibrated spectrum by the integrals of the hyperpolarised spectrum (Figure 29).[1] The example shown in Figure 29 corresponds to a signal enhancement of −600-fold at the *ortho* proton, although signal enhancements of >10,000-fold have been observed using this method.[10] This signal enhancement can then be converted to percentage polarisation (% P) using Equation 5 where, ε is the signal enhancement, γ is the gyromagnetic ratio in $rads^{-1}T^{-1}$, B_0 is the field strength in T, $\hbar$ is the reduced Planck's constant in Js, k_B is the Boltzmann constant in $m^2kgs^{-2}K^{-1}$ and T is the temperature in K.

$$\% P = \varepsilon \frac{\gamma B_0 \hbar}{2 k_B T}$$

Equation 5

The *ortho* proton enhancement in Figure 29 is equivalent to a percentage polarisation of 1.93%.

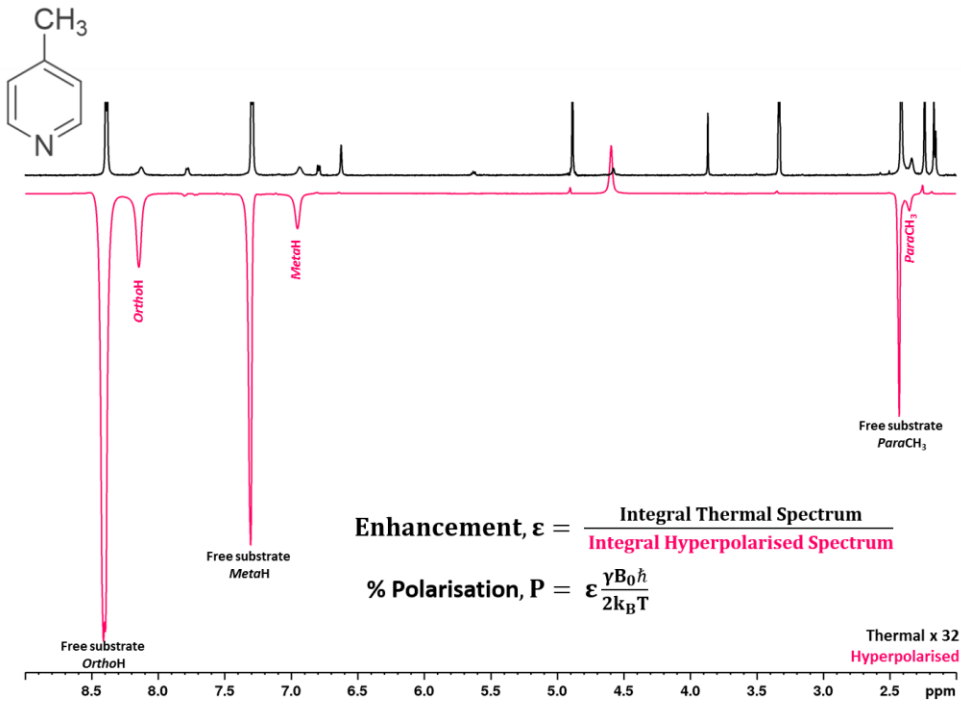

Figure 29 - ^{1}H NMR spectra collected for the SABRE active species [Ir(H)$_2$(SIMes)(sub)$_3$]Cl under thermal conditions (no *p*H$_2$, black spectra) compared to hyperpolarised spectra (pink) in the presence of *p*H$_2$ (4 bar). The thermal spectrum (black) has been magnified 32 times so that it can be visually compared to the hyperpolarised spectrum. ^{1}H NMR spectra was measured on a 400 MHz spectrometer at 298 K using the one-shot pulse sequence depicted in Figure 28 and a sample containing the SABRE precatalyst [IrCl(COD)(SIMes)] (5 mM), methanol-d4 (0.6 mL) and the substrate 4-methylpyridine (50 mM) under 4 bar of *p*H$_2$. The hyperpolarised spectrum was collected using the manual shaking method. The sample was then left in the spectrometer for 10 minutes after hyperpolarisation before the thermal spectra was acquired. The equations for calculation of enhancement and percentage hyperpolarisation are also included.

2.1.1 Field for Polarisation Transfer in the SABRE Hyperpolarisation Process

SABRE employs *p*-H$_2$ for the enhanced detection of a target molecule or substrate. The latent polarisation is then unlocked by coupling the *p*-H$_2$ to a 3rd nucleus. This breaks the symmetry of the *p*-H$_2$ molecule allowing the polarisation to flow to the substrate nuclei of interest via the *J*-coupling of the catalyst. However, for optimum polarisation transfer the chemical shift difference between the hydrides and the substrate nuclei must equal the dominant *J*-coupling in the network. In the SABRE catalysis that serves as the basis of this thesis ([Ir(H)$_2$(SIMes)(substrate)$_3$]Cl) this is

the hydride-hydride coupling. This resonance condition is satisfied at low magnetic field of approximately 65 G for the ^{1}H hyperpolarisation of substrate such as pyridine. More detail of this process can be found in Chapter 1, Section 1.5.1.2 Mechanism of Polarisation Transfer.

To demonstrate the effect of polarisation transfer field on SABRE efficiency, an example of a PTF plot is shown in Figure 30. At 0 G the signal enhancement was −15-fold, this rose to −247-fold at 70 G before decreasing at higher magnetic fields. Therefore polarisation transfer is most efficient at 70 G for 4-methylpyridine, which is the substrate used for all the experiments throughout this chapter.

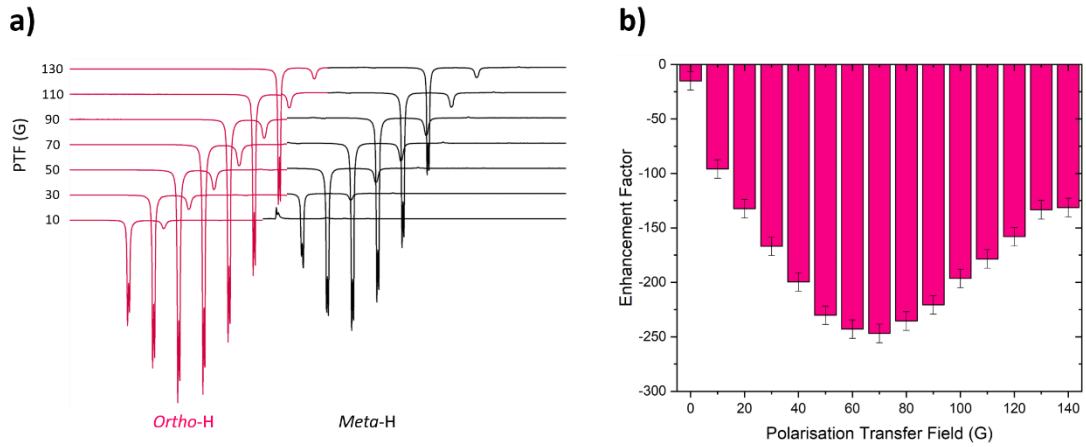

Figure 30 – a) series of hyperpolarised ^{1}H NMR spectra as a function of field strength in the SABRE active species [Ir(H)$_2$(SIMes)(sub)$_3$]Cl where the resonances at the *ortho* proton are shown in pink and the *meta* resonances are shown in black. The hyperpolarised ^{1}H NMR spectra was collected using the automated flow system using the pulse sequence shown in Figure 28 where the field strength was varied over 0-130 G in 10 G increments. This was measured on a 400 MHz spectrometer at 298 K using a sample of [IrCl(COD)(SIMes)] (5 mM), 4-methylpyridine (50 mM), methanol-d_4 (0.6 mL) under a pH$_2$ atmosphere of 4 bar. b) The signal enhancement calculated at the *ortho* proton in the free substrate plotted as a function of polarisation transfer field (PTF)

There are three main methods for performing SABRE. The first is a manual shaking approach which uses the stray field of the superconducting magnet to provide the polarisation transfer field (PTF) necessary for SABRE to occur. The second employs a handheld shaker consisting of a Halbach array of solid-state magnets providing the required PTF.[5] The final method is a fully automated flow system where the polarisation transfer field is provided by a chamber containing a copper coil which can generate controlled magnetic environments between −150 G and 150 G.[6] The

flow and the shaker methods both afford homogenous magnetic fields essential for polarisation transfer. However, as the shake and drop approach relies on the stray field of the magnet, the polarisation transfer step may not occur at the optimum field for polarisation transfer.

2.2 The Manual Shaking Method

When SABRE was first published in 2009,[3] the phenomenon was observed through what was termed the 'shake and drop' approach. This is a manual technique whereby the SABRE sample is shaken vigorously within the stray field of the magnet (at approximately 65 G for ^{1}H) before being dropped into the spectrometer for subsequent acquisition (Figure 31). Shaking the sample promotes dissolution of *p*-H_2 gas in the headspace of the NMR tube to form the SABRE-active species, $[Ir(H)_2(SIMes)(sub)_3]Cl$ (see Figure 26).

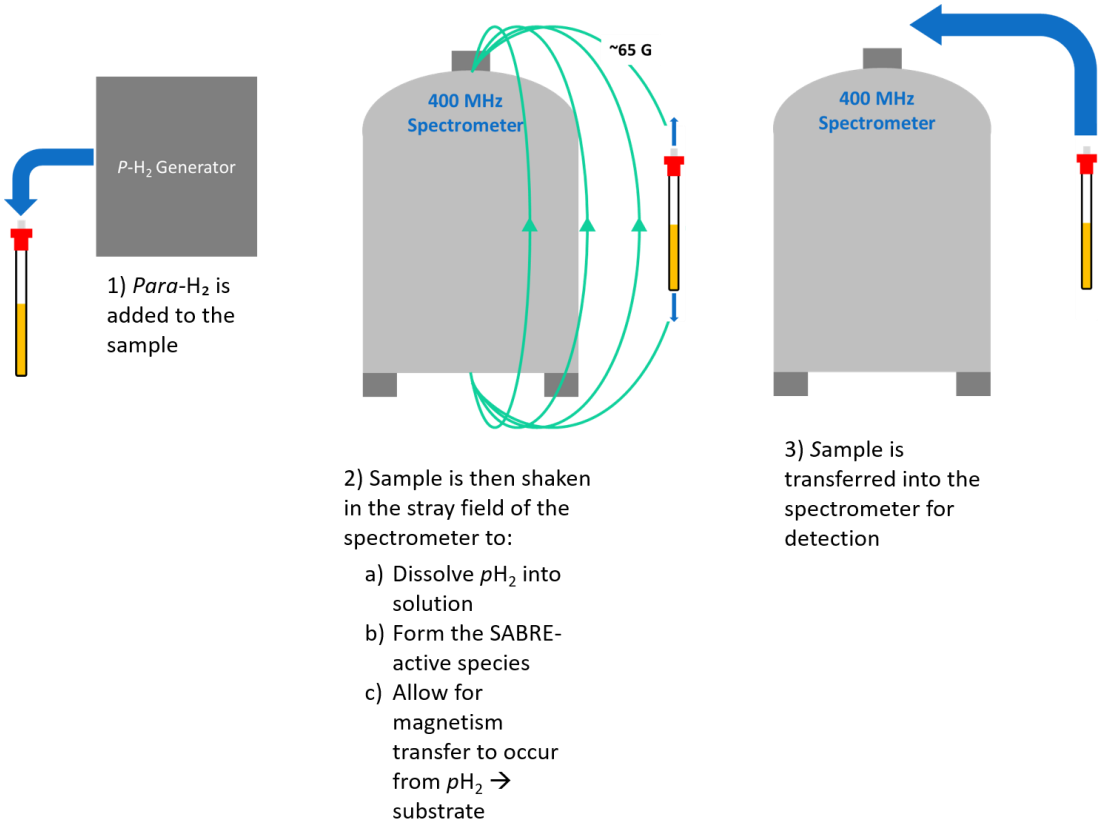

Figure 31 – Schematic diagram describing the manual shaking method. 1) 4 bar pH_2 is added to an NMR tube fitted with a Young's tap containing the SABRE active species, 2) The sample is shaken within the stray field of the spectrometer to allow for polarisation transfer from the pH_2 to the target substrate via the *J*-coupled network, 3) The sample is quickly transferred into the spectrometer for acquisition using the one-shot pulse sequence described in Figure 28, 4) Hyperpolarised spectrum is generated and enhancement and polarisation can be calculated by comparing to the thermal spectrum and using the calculations shown in Figure 29

This method is quick and simple to perform. However, the approach is susceptible to several variables including: field strength, shake time, shake intensity (usually dependent on the user) and transfer time. This means that results produced using the shake and drop method are associated with significant errors. For example, as shown in Figure 30, the impact of the polarisation transfer field is significant. In the manual shaking method, the stray field of the magnet provides the PTF. Whilst the distance from the magnet has been accurately measured using a Gaussmeter it is difficult to maintain shaking of the sample within this area. If the sample is not shaken

within the required PTF then the calculated signal enhancement may not be optimum.

2.2.1 Polarisation Transfer Using the Magnetic Stray Field

In order to observe SABRE hyperpolarisation of a sample, a polarisation transfer field is required. In the shake and drop approach this is achieved by shaking the sample within the stray field of the NMR spectrometer.

In order to appreciate the stray field of the magnet, it is necessary to first acknowledge the set-up of the hardware in an NMR spectrometer (see Figure 32).

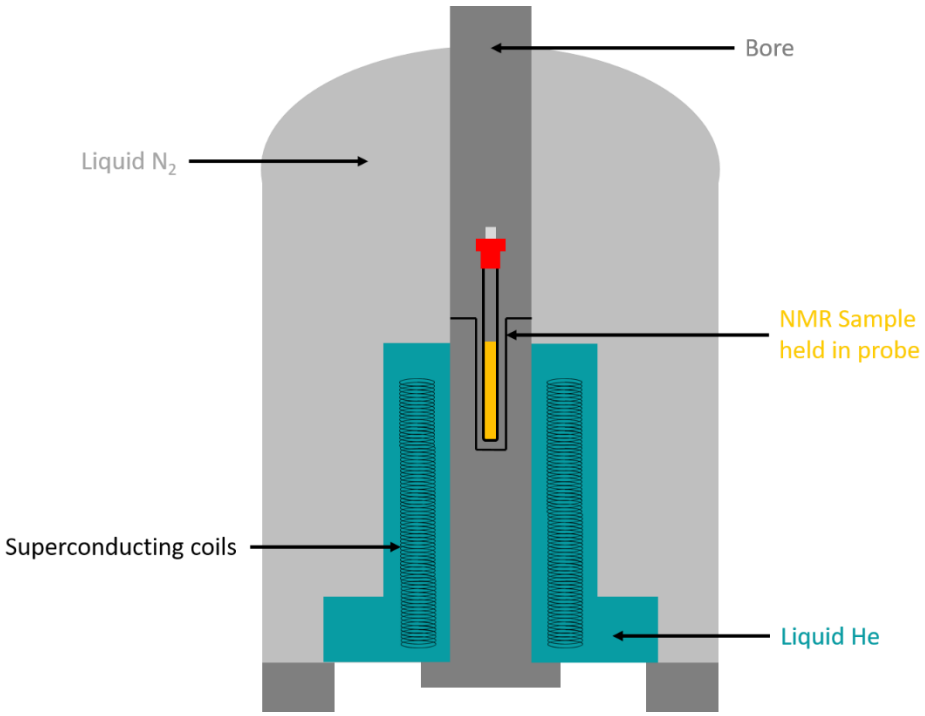

Figure 32 - Schematic diagram of a nuclear magnetic spectrometer adapted with permissions from M. H. Levitt et *al.*[16]

As described previously, observation of NMR depends on the splitting of spin states in a molecule which is promoted when a magnetic field is applied (see Chapter 1.2). Therefore, the most important component of the NMR spectrometer is the superconducting coil as it is this that provides the large magnetic field necessary to observe magnetic resonance spectroscopy. In order to maintain the homogeneity of such large magnetic fields and prevent electrical resistance, the superconducting coil

is immersed in liquid helium which is then further insulated via a reservoir of liquid nitrogen. Through the centre of the superconducting coil is the bore of the spectrometer where the probe is placed containing the sample. The probe is designed such that the sample is held at the point of maximum field within the superconducting coils.[16] Different probes are selected according to the nuclei under scrutiny for the NMR experiment or whether imaging is required.

A superconducting coil or solenoid is depicted in Figure 33. The magnetic field of the solenoid can be calculated according to Ampère's Law:

$$B_0 = \mu \frac{NI}{l}$$

Equation 6

Where B_0 is the magnetic field, μ is the magnetic permeability ($\mu = k\mu_0$ where k = permeability of the sample, μ_0 = magnetic permeability in free space), N is the number of turns in the solenoid, I is the current and l is the length of the solenoid.

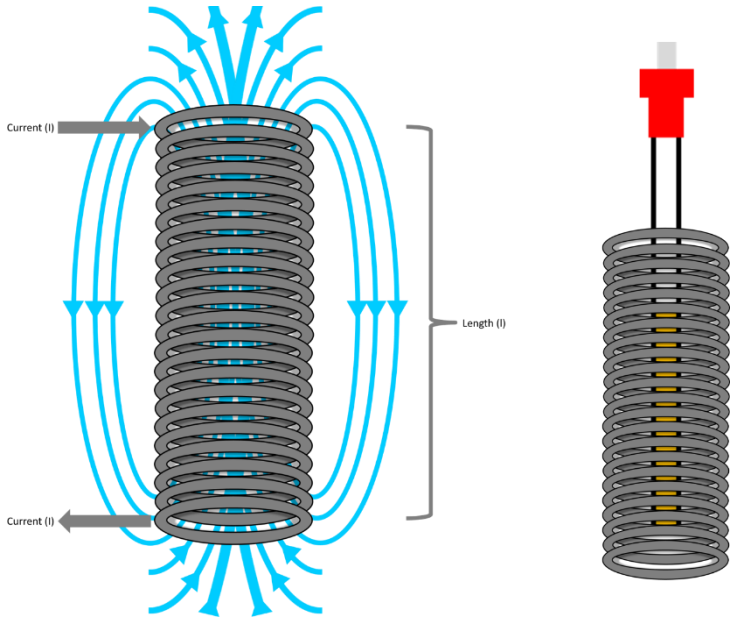

Figure 33 - Diagram of a solenoid coil. Arrows are used to show the direction of the magnetic field. As the field is more concentrated in the centre, this is where the NMR sample is placed.

The design of a solenoid is such that the magnetic field is both concentrated and homogenous in the centre of the coil whereas the field outside is weak and divergent.[17] This explains why there is commonly a stray field outside of the NMR magnet. The strength of the stray field depends on the distance from the spectrometer and how well the magnet is shielded.

There are two spectrometers used in York for SABRE experiments, both of which are 400 MHz. One is a narrow bore instrument and the other is a wide bore instrument. The wide bore instrument means that an imaging probe can be inserted for magnetic resonance imaging experiments. Due to the differences in bore size, each spectrometer has a different stray field profile (see Figure 34).

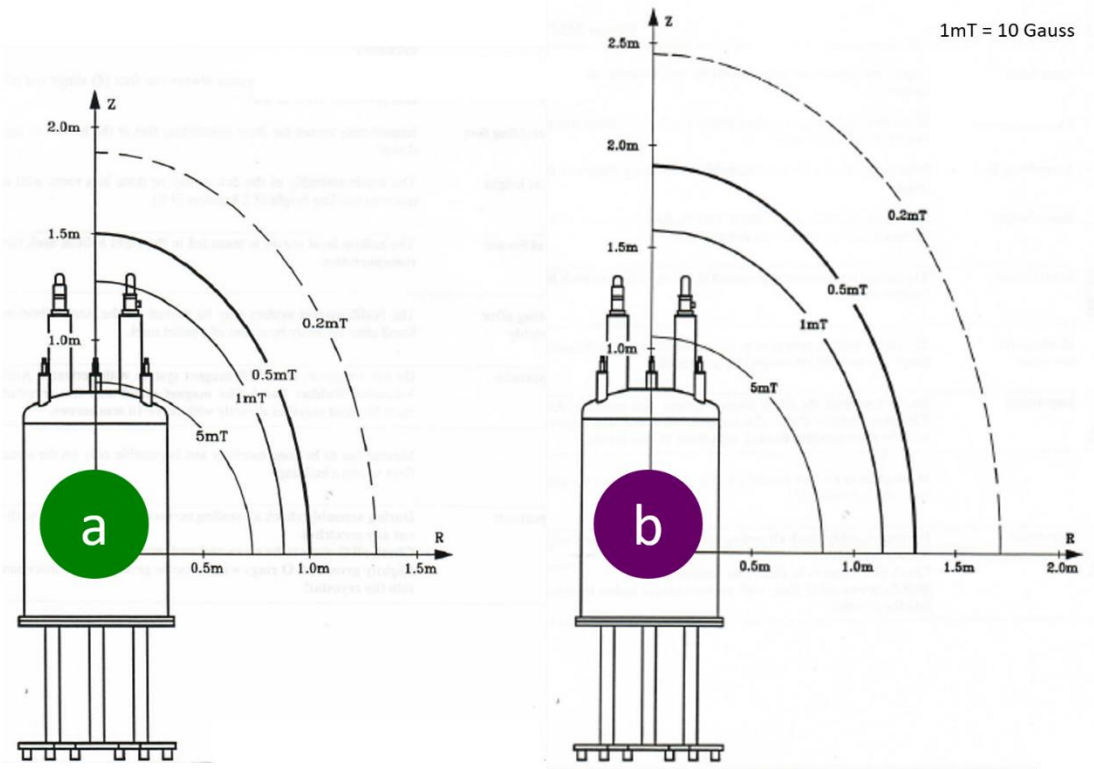

Figure 34 – Stray field plots for the two spectrometers used for SABRE experiments where A is the narrow bore spectrometer and b is the wide bore spectrometer. Reproduced with permission from the NMR magnet system folder.

The stray field plots for both spectrometers (Figure 34) show that the 65 G field required for the SABRE hyperpolarisation of ^{1}H nuclei is closer to the spectrometer in the narrow bore instrument (**a**) compared to the wide bore instrument (**b**).

Furthermore, the field lines in spectrometer **a** are closer together compared to **b**. The implication of this is that when performing SABRE experiments using the manual shaking approach, it is possible to cross these field lines when using instrument **a**. This means that polarisation is not transferred at the correct field and hence SABRE enhancements may be lower (see Figure 30). However, transfer of the sample into the spectrometer for detection is 1-2 s quicker when using instrument **a** compared to **b** as shaking occurs closer to the spectrometer.

2.2.2 The Impact of Different Experimenters

As mentioned previously, the manual shaking method is susceptible to a number of different variables, including: the experimenter, shake time, shake intensity, transfer time and the field at which the sample is shaken (see above). In particular, the shake intensity and transfer time can vary between experimenters, thus leading to different signal enhancements and associated standard errors. This means that experimenters cannot directly compare SABRE results using the manual shaking method as it has been reported that a ±20% variation is common between different experimenters due to differences in physical height, the rate and angle of shake and transfer times into the spectrometer.[6]

To illustrate the effect of using different experimenters on SABRE efficiency, a sample of $[Ir(H)_2(SIMes)(sub)_3]Cl$ was shaken by two different experimenters in the stray field of the spectrometer at approximately 60 G for 10 seconds. The results of this experiment are shown in Figure 35 below. The data shows that the signal enhancements calculated for experimenter 2 are larger than for experimenter 1. For example for , experimenter 1 achieved an average signal enhancement of −495 ± 22-fold compared to −767 ± 8-fold for experimenter 2. Furthermore, the enhancements calculated for experimenter 2 were more consistent compared to experimenter 1. This is indicated by the box plot in Figure 35, where there is a greater variability in the data collected for experimenter 1. For example, the minimum and maximum enhancements were −465-fold and −548-fold for experimenter 1 compared to −745-fold and −791-fold for experimenter 2.There are a number of possible reasons for

these variations in signal enhancements yielded by the two experimenters. For example, experimenter 2 is larger in stature compared to experimenter 1 and therefore shaking may be slightly more vigorous allowing for more *p*-H_2 to be dissolved into solution. There may be slight differences in transfer times as experimenter 2 was able to drop the sample into the spectrometer for detection without the use of a step as in the case of experimenter 1. Finally, experimenter 2 has performed more SABRE experiments using the manual shaking method than experimenter 1 and is therefore more comfortable applying this method.

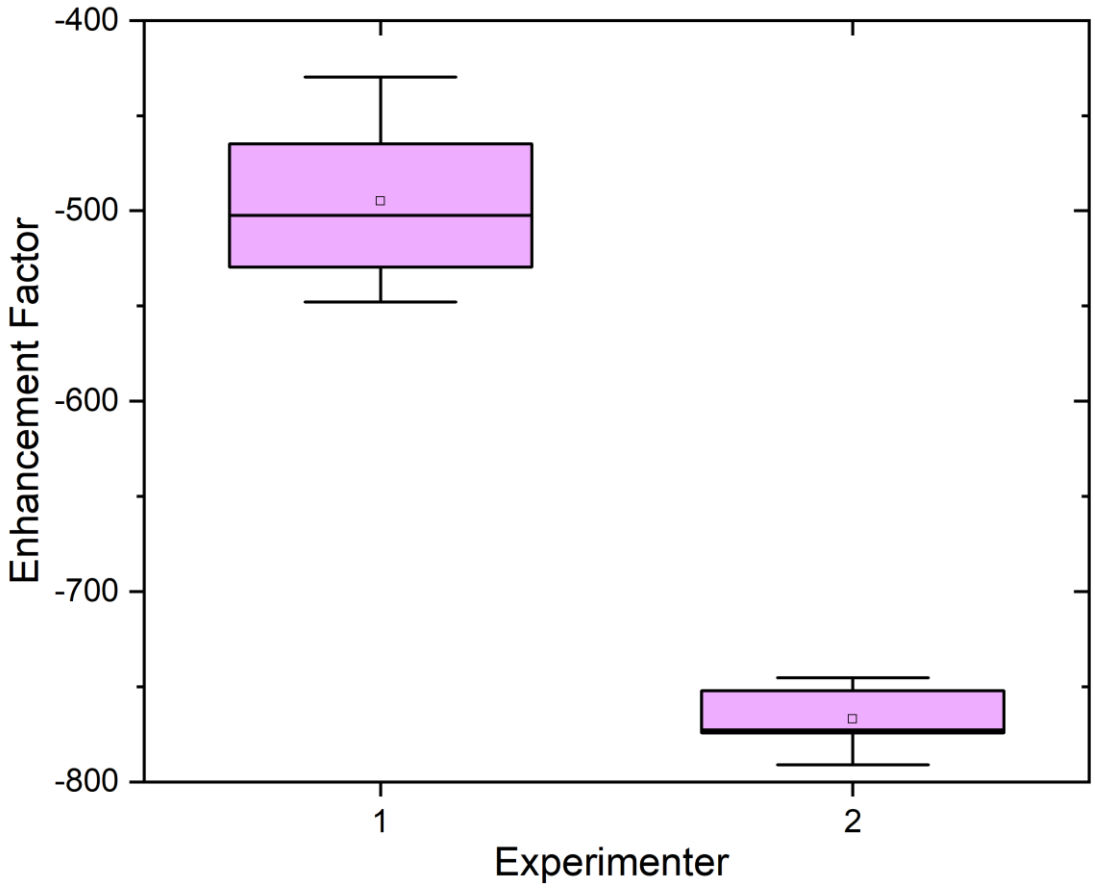

Figure 35 – Box plot showing the enhancement factor as a function of experimenter utilising the manual shaking method. The coloured portions indicate the 25% and 75% quartiles, the whiskers the minimum and maximum enhancement values, the median line the mid-point of the data and the square the mean. Samples contained the SABRE precatalyst [IrCl(COD)(SIMes)] (5 mM), substrate (50 mM) dissolved in methanol-d_4 (0.6 mL) and in the presence of pH_2 (4 bar). Samples were shaken for 10 seconds in the stray field of the spectrometer at approximately 60 G at 298 K.

2.2.3 Effect of *Para*hydrogen dissolution Time (Shake Time) on Signal Enhancement

Although the manual shaking method garners impressive enhancement factors, a crucial problem with this approach is the lack of reproducibility. Enhancement factors can also be influenced by shake time, the field strength and the NMR spectrometer used for the experiments, especially as each spectrometer has a different field profile (Figure 34).

The impact of shake time using the manual shaking method was assessed using a sample of 4-methylpyridine (50 mM) and [IrCl(COD)(SIMes)] (5 mM) in methanol-d_4 (0.6 mL), forming [Ir(COD)(SIMes)(sub)]Cl. The sample was then degassed using a freeze-pump-thaw procedure using a dry ice acetone bath. *P*-H_2 (99%) was then added to the sample to encourage formation of the SABRE-active species; $[Ir(H)_2(SIMes)(sub)_3]Cl$. Once formed, the SABRE response of this species was measured as a function of shake time. To do this, the sample was shaken within 65 ± 5 G (measured with a Hirst GM08 series gaussmeter) of the stray field of the spectrometer and the shake time was varied from 5-15 seconds.

The sample was shaken five times for each shake time in order to average the signal enhancements effectively assess the reproducibility of each measurement.[18] Although signal enhancements were generated at the *ortho*, *meta* and *para*-proton environments, only the *ortho* enhancements are considered. This is because these signal enhancements are the largest as they receive direct polarisation transfer from the *p*-H_2. This experiment was repeated on both 400 MHz Bruker AVANCE III NMR spectrometers (**a** & **b**) to check consistency between spectrometers.

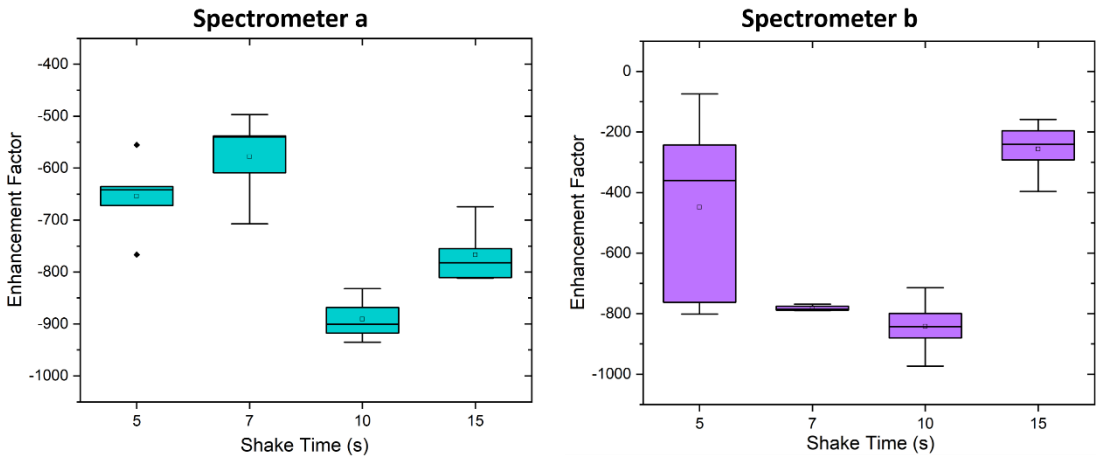

Figure 36 – Box plots showing the ^{1}H signal enhancement at the *ortho* proton, plotted as a function of shake time for a sample containing [Ir(COD)(SIMes)(sub)]Cl (5 mM) with the substrate 4-methylpyridine (50 mM) and pH_2 (4 bar) in methanol-d_4. Green is used to represent the narrow bore instrument a) and purple the wide bore instrument b). The sample was manually shaken at approximately 60 G using the stray field of the 400 MHz spectrometers at 298 K. The coloured portions indicate the 25% and 75% quartiles, the whiskers the minimum and maximum enhancement values, the median line the mid-point of the data, the square the mean and the diamonds show any outliers in the data.

In general, the data in Figure 37 indicates that the average enhancements (indicated by the squares) at the *ortho*-proton position are slightly higher when measured on spectrometer **a**. For example, an average enhancement of −891 ± 18-fold was observed on instrument **a** compared to −842 ± 43-fold on **b**. However, the whiskers show that the highest enhancement was observed using instrument **b**, where a 10 second shake time induced an enhancement of −973-fold. This compares to a maximum of 935-fold on **a**. Generally, larger variations were observed using instrument **b** compared to **a**. This is indicated by the whiskers which illustrate the maximum and minimum enhancement values. For example, for a 5 second shake time, the minimum enhancement was −74-fold and the largest was −801-fold. The 5 second shake time also induced a large variation in results on **a**, this is highlighted by the presence of data anomalies at −556-fold and −767-fold. Henceforth it is difficult to reproduce enhancements when shaking for such a short period of time.

There are a number of variables that could be to blame for this increased variance of data on **b**; the field at which the sample is shaken or the transfer time – the time between shaking the sample, dropping it into the spectrometer and acquiring the NMR signal. Instrument **b** is a wide bore instrument therefore the field lines are more

spaced apart compared to **a** (Figure 34). This means that maintaining shaking at 65 G on **b** is easier. Practically, **b** is situated further away from the computer from which it is controlled, therefore the transfer time is a couple of seconds longer compared to **a**. Longer transfer times mean that hyperpolarisation is lost before a spectrum can be acquired, therefore this could explain why the average enhancements on instrument **b** are lower than instrument **a**. Furthermore, the transfer time is more likely to be varied across different measurements.

2.3 The Automated Flow System

As described in the previous section, the shake and drop method was seen to induce large differences between measurements due its vulnerability to a large number of variables,[6] an automated polariser and sample delivery system was designed in collaboration with Bruker (Figure 38).

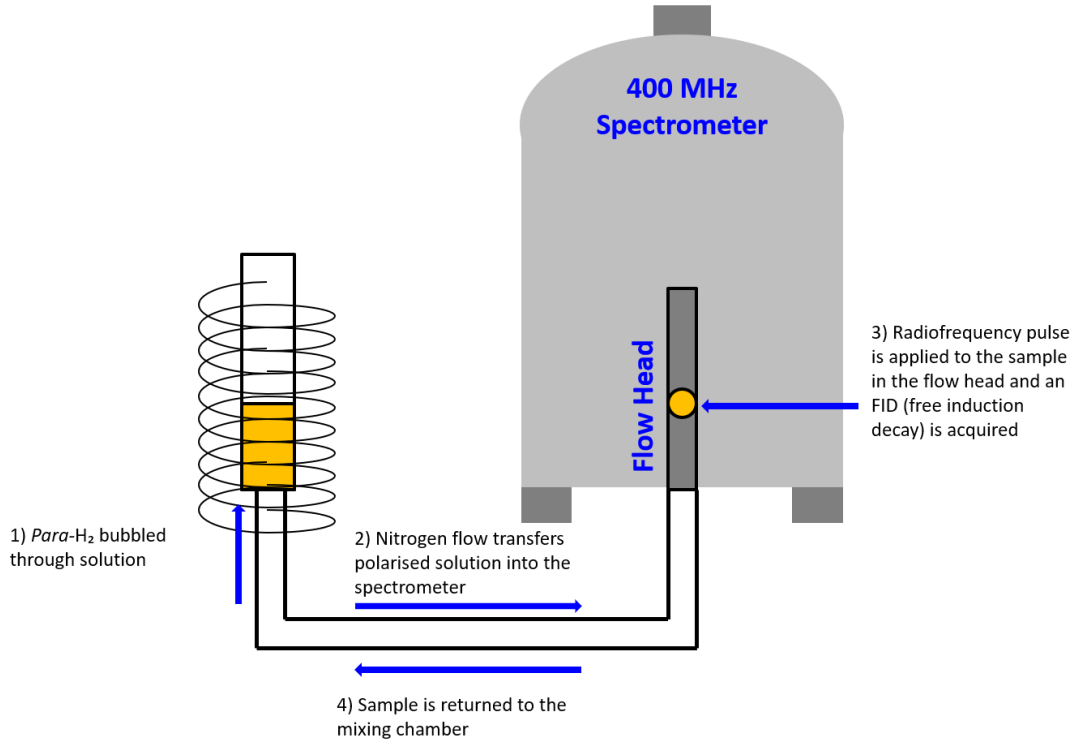

Figure 38 – Schematic diagram of the automated flow probe. 1) A sample of $[Ir(H)_2(SIMes)(sub)_3]Cl$ in methanol-d_4 is contained in a flow cell where pH_2 (4 bar) is bubbled through the solution, 2) The hyperpolarised sample is transferred into the spectrometer via a nitrogen flow, 3) The hyperpolarised spectrum is acquired using the one-shot pulse sequence described in Figure 28, 4) The sample is transferred

from the spectrometer back to the flow cell using a nitrogen flow. Image adapted with permissions from R. E. Mewis et *al.*[6]

The flow system briefly comprises of a *p*-H_2 generator which electrolyses water to produce hydrogen. The hydrogen is then cooled to 38 K in the presence of an activated charcoal catalyst to provide 92% *p*-H_2. The generator is then connected to a flow cell containing the sample solution and a porous frit through which *p*-H_2 can be bubbled at the base of the chamber. This is surrounded by a copper coil which is used to generate a controlled magnetic environment between −150 G and 150 G. This sample chamber is then connected to a flow probe located within the spectrometer.[6] When conducting a SABRE experiment, *p*-H_2 is first bubbled through the sample solution and the resulting hyperpolarised solution is pneumatically transferred into the spectrometer using a nitrogen flow. A radiofrequency (RF) pulse is then applied to the sample in the flow head and an FID is required. Finally the sample is shuttled back to the preparation chamber where fresh *p*-H_2 can be bubbled through the solution and the process repeated.[6]

Results performed on the flow probe are more reproducible as the potential for human error has been removed. However, the observed enhancements are generally much lower than those gained using the shake and drop method. This occurs because the bubbling of *p*-H_2 is generally less vigorous than shaking the sample, therefore less *p*-H_2 is dissolved into the solution. Furthermore, transfer times may be slower meaning that some of the hyperpolarisation has been lost before the signal has been acquired.

2.3.1 Effect of *Para*hydrogen Dissolution Time (Bubble Time) on Signal Enhancement

To assess the magnitude of signal enhancements and the reproducibility of the automated flow system (compared to the manual shaking method), the ^{1}H signal enhancements were measured for a number of different *p*-H_2 dissolution times (bubble time). To do this, a sample containing 4-methylpyridine (50 mM) and [IrCl(COD)(SIMes)] (5mM) was dissolved in 3 mL methanol-d_4 and placed in the sample chamber shown in Figure 38. *P*-H_2 was bubbled through the solution to

promote formation of the SABRE-active species; $[Ir(H)_2(SIMes)(sub)_3]Cl$. Once activated, the SABRE response was measured as a function of bubble time which was varied from 5-30 seconds. Each measurement was repeated five times in order to assess the reproducibility of the experiment (Figure 39).

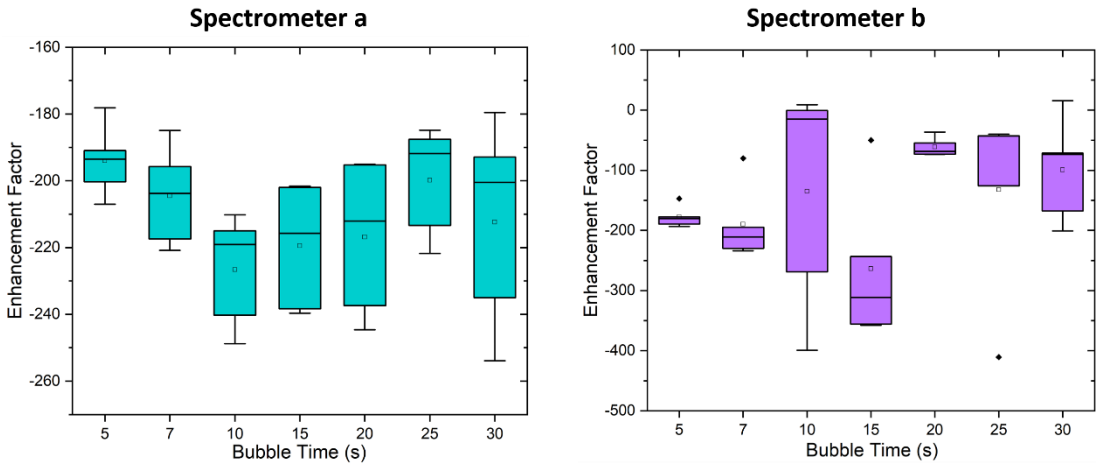

Figure 39 – Box plot showing the ^1H NMR signal enhancement plotted as a function of bubble time for the *ortho* proton resonance in the free substrate for the SABRE active species $[Ir(H)_2(SIMes)(sub)_3]Cl$ (5 mM) containing the substrate 4-methylpyridine (50 mM). Measurements collected on the 400 MHz narrow bore instrument a) are shown in green and those collected on the 400 MHz wide bore instrument b) are shown in purple. Hyperpolarised measurements were taken using the flow method shown in Figure 38 at 298 K and the pulse sequence shown in Figure 28. The coloured portions indicate the 25% and 75% quartiles, the whiskers the minimum and maximum enhancement values, the median line the mid-point of the data, the square the mean and the diamonds show any outliers in the data.

Figure 40 shows the variation in the ^1H signal enhancement at the *ortho* proton as a function of the *p*-H_2 bubble time. If we first consider the average signal enhancements, the data generally follows the same pattern as the manual shaking method whereby larger enhancements were observed on spectrometer **a**. However, the largest average signal enhancement of −264-fold corresponding to a 15 second bubble time was observed on instrument **b**. This compares to −227-fold on instrument **a** which resulted from a 10 second bubble time. Furthermore, the largest calculated enhancement of −410-fold was observed on **b** for a 25 second bubble time. In Figure 41, this is shown as an outlier (indicated by the diamond) as the remaining data points ranged from −40-fold to −126-fold. Figure 42 clearly shows that there is a larger variation in signal enhancements using spectrometer **b**. This is highlighted by the larger box plots, for example a 10 second bubble time induced enhancements ranging from −0.6-fold to −399-fold (illustrated by the whiskers).

Additionally, more anomalies were observed in the data using NMR **b** (shown by the diamonds). Henceforth, the data collected using spectrometer **b** is shown to be less reproducible compared to **a**. It was expected that the signal enhancements generated on both instruments would be very reproducible as this SABRE method is fully automated and all experimental parameters (e.g. sample transfer time, *p*-H_2 pressure etc) were constant for both spectrometers. It is possible that the larger variation in data is caused by solvent evaporation in the sample. This could be induced by the sample being shuttled between the spectrometer and the flow cell a number of times via a nitrogen flow. However if this were the case, it would be expected that the error would increase with bubble time. . Interestingly, the variation in data across the different bubble times is minimal for **a**. For example, the lowest average enhancement of −193-fold was observed for a 5s bubble time, compared to −227-fold for a 10 second bubble time. This suggests that the shake/bubble time does not influence the enhancement as much as the field strength, transfer time or shake/bubble intensity.

2.4 Handheld Magnetic Array

In 2018, Richardson *et al*.[5] designed and implemented a hand-held shaker to be used for SABRE experiments on a 43 MHz benchtop spectrometer. As the benchtop spectrometer has no stray field, manual shaking experiments had to be performed using the stray field of the 400 MHz spectrometer. The implication of this was that a large transfer time was involved and hence lower enhancements were observed. To combat this, a hand-held magnetic array (shaker) was developed to simulate the PTF required for SABRE experiments. Samples were made according to the same procedure detailed in section 0. Once *p*-H_2 was added the sample was then placed into the shaker and shaken for approximately 10 seconds. The sample was subsequently removed and transferred into the spectrometer for acquisition. The main advantage of this method is that the PTF remains constant throughout shaking. For example, it was noted that a 600% increase in total polarisation was noted compared to the flow method and a 25% increase compared to the traditional shake and drop approach. The reproducibility of these experiments was also assessed, it

was observed that the handheld magnetic array induced a standard deviation of 5.8 % compared to 9.1 % for the shake and drop and 4.6 % for the flow.

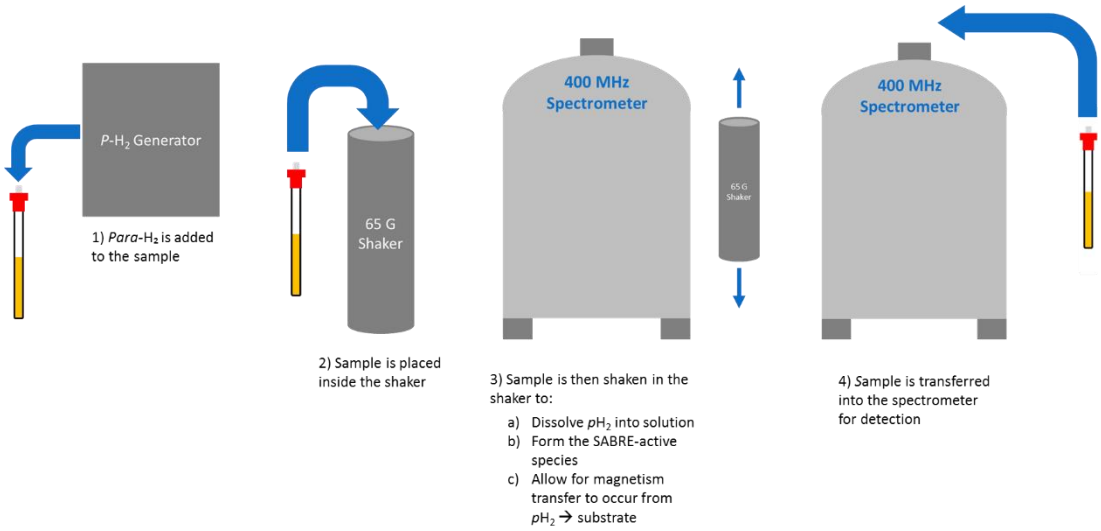

Figure 43 – Schematic diagram describing the use of the handheld magnetic array. 1) 4 bar pH_2 is added to SABRE active species in an NMR tube fitted with a young's tap, 2) The sample is placed inside the handheld magnetic array, 3) The handheld magnetic array containing the sample is shaken to allow for polarisation transfer into the substrate, 4) the sample is removed from the handheld magnetic array and transferred into the spectrometer for detection

2.4.1 Design of the Handheld Magnetic Array

This shaker device is comprised of a number of solid-state magnets arranged in a Halbach[19] design to generate a homogeneous field of B_X (Figure 44).[5]

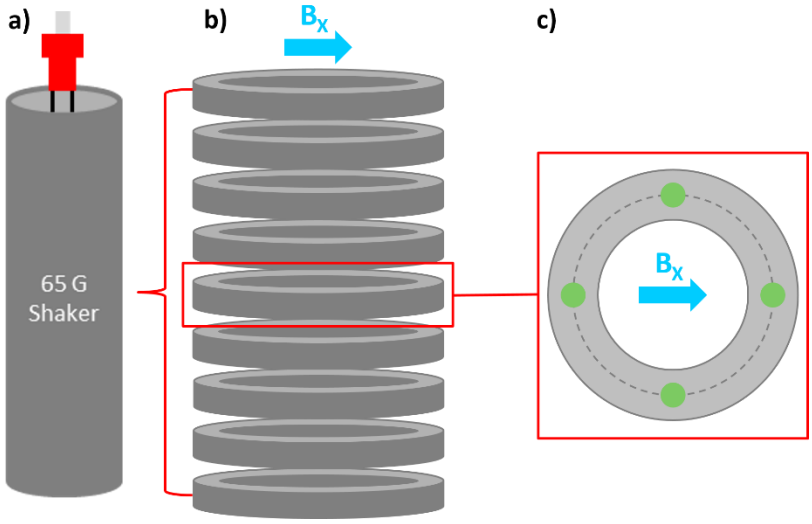

Figure 44 – The hand-held shaker adapted with permissions from P. M. Richardson et *al.*[5]

Figure 44 shows the handheld shaker (a) which is comprised of a number of rings (b). A cross section of one of these rings is shown in Figure 44c where magnets (shown in green) are placed at a fixed distance from the centre of the ring. The magnets are arranged such that they generate a homogenous field of B_X transverse to the long axis of the cylinder, and thus the NMR sample. This magnetic field is controlled by the number of magnets, their distance from the centre of the ring and the spacing between the rings shown in Figure 44c.

A number of these hand-held shakers have been developed, each with different magnetic fields of B_X. The advantage of this is that experimenters can now perform SABRE experiments quickly and easily on nuclei other than proton. For example, direct polarisation transfer via SABRE into ^{13}C nuclei occurs at 2.5 mG[20] and ^{15}N at 2 mG.[12] Before, these SABRE experiments would have required use of the flow method, as the PTF is controlled by the user. Magnetic field profiles for each of the manual shakers have been generated, where B_X is measured throughout the length of the shaker. Figure 45 shows the field profile for the 60 G shaker, where the red line demonstrates the average field of 60.6 G.

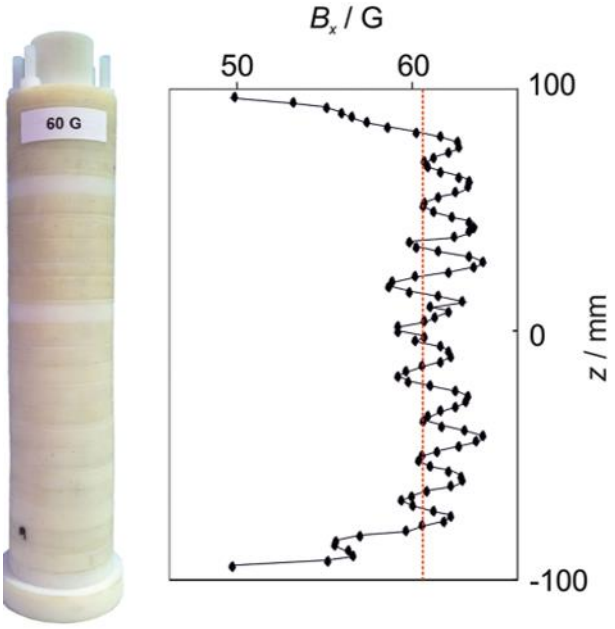

Figure 45 – Photo of the hand-held shaker and corresponding magnetic field profile measured along the central axis of the cylinder. Image taken with permission from P. M. Richardson et *al.*[5]

2.4.2 Effect of *Para*hydrogen Dissolution Time (Shake Time) on Signal Enhancement

The shake time was Shake time was assessed in a similar way to the manual shaking approach described in Section 2.2 The Manual Shaking Method. A sample of 4-methylpyridine and [IrCl(COD)(SIMes)] was dissolved in methanol-d_4. *P*-H_2 was then added and the sample placed in the shaker. This was then shaken for 5/7/10/15 s before being removed and dropped into the spectrometer for acquisition. Again, this process was repeated five times to calculate the average enhancement and the standard error.

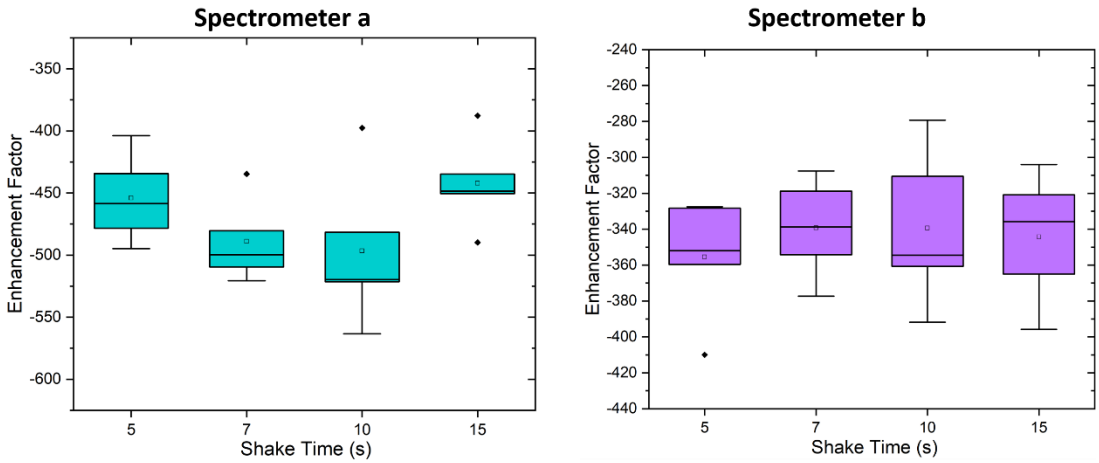

Figure 46 – ^{1}H signal enhancement plotted as a function of shake time for the *ortho* proton in the free substrate for SABRE active species $[Ir(H)_2(SIMes)(sub)_3]Cl$ containing the substrate 4-methylpyridine. The green represent measurements taken on the narrow bore 400 MHz spectrometer a, and the purple are used for the wide bore 400 MHz spectrometer b. Hyperpolarised measurements were collected using the 60 G handheld magnetic array in Figure 43 at 298 K. The coloured portions indicate the 25% and 75% quartiles, the whiskers the minimum and maximum enhancement values, the median line the mid-point of the data, the square the mean and the diamonds show any outliers in the data.

Figure 47 illustrates the variation in ^{1}H signal enhancement at the *ortho* proton as a function of shake time. The largest average enhancement was observed for a shake time of 10 seconds. On spectrometer **a** this shake time induced a signal enhancement of −497-fold compared to −339-fold on spectrometer **b**. Furthermore, larger enhancements were observed on instrument **a** compared to **b**. If the individual data points are considered, the largest enhancement was −564-fold on **a** compared to −410-fold on NMR **b** (outlieing data point for a 5 second shake time).

If the average signal enhancements are considered, there was less variation overall in the data using the handheld magnetic array. For example, on NMR **a**, the minimum average enhancement was −442-fold (15 second shake time) compared to the maximum of −497-fold (10 second shake time). However, if the individual data points are considered, the minimum measurement was −387-fold (15 second shake time) compared to −564-fold (10 second shake time). On NMR **b**, the lowst average signal enhancement was −339-fold (7 and 10 second shake times) compared to the maximum signal enhancement of −365-fold (5 second shake time). Considering the individual measurements, the lowest signal enhancement was −279-fold (10 second shake time) and the highest was 396-fold (15 second shake time). This lower variation in data suggests that the sample shake time is less important compared to the polarisation transfer field and the transfer time. As the field has been kept constant at 63 G, this means that it is the difference in transfer time that has contributed to the lower enhancements observed on **b** compared to **a**.It is clear that this method is less reproducible than both the manual shaking method using the stray field of the spectrometer and the automated flow system. This can be observed by the number of data anomalies shown in Figure 48 for both spectrometers. The lower reproducibility can also be attributed to the differences in transfer time between measurements as the sample must be removed from the shaker before being dropped into the spectrometer for acquisition.

2.5 Comparison of SABRE Methods

The effect of *p*-H_2 dissolution time has been compared to the ^{1}H signal enhancements for each method. This was observed by plotting the shake time or the bubble time as a function of signal enhancement. In order to compare the methods directly, the ^{1}H signal enhancements for each method have been plotted for a 10 second shake time for spectrometers **a** and **b**, this is shown in Figure 49.

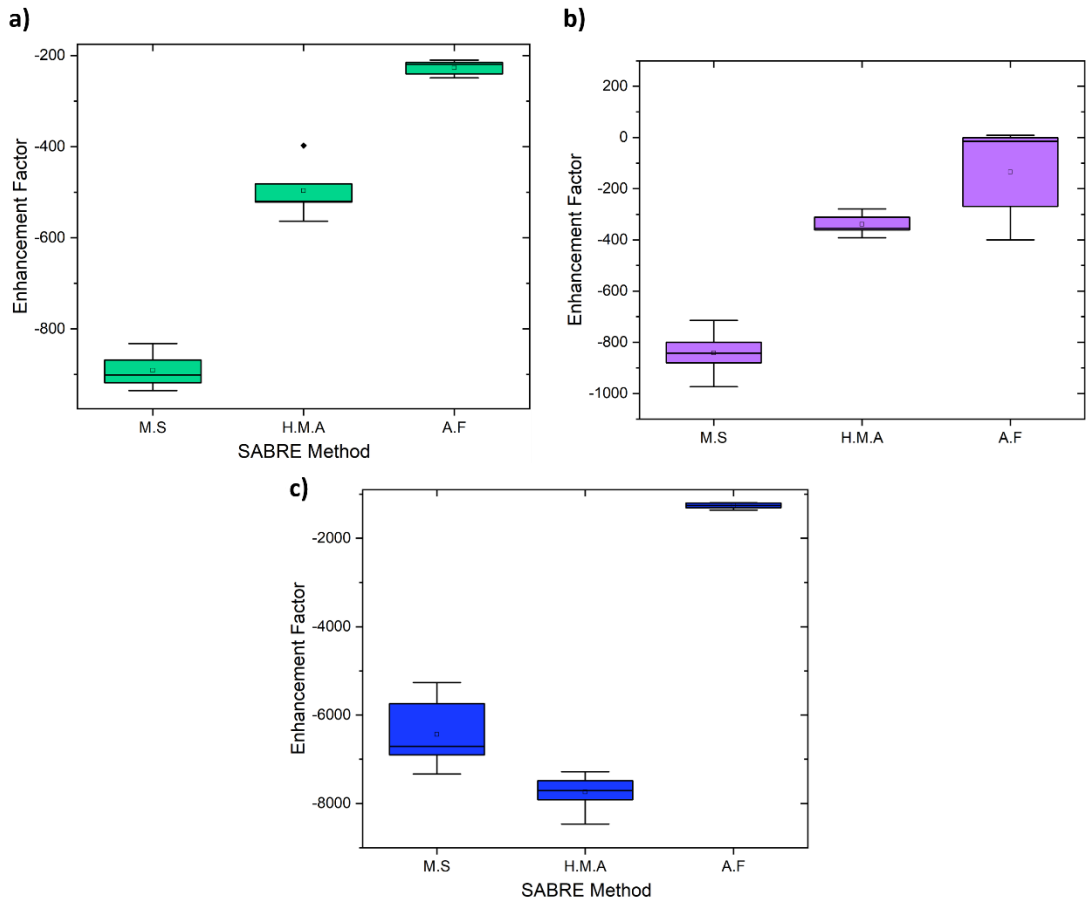

Figure 50 – Signal enhancement plotted as a function of SABRE methodfor the *ortho* proton in the free substrate 4-methylpyridine in the SABRE-active species $[Ir(H)_2(SIMes)(sub)_3]Cl$. This is shown for a *p*-H_2 dissolution time of 10 seconds. Plot a) in green compares the signal enhancements measured on the 400 MHz narrow bore instrument a Plot b) compares the signal enhancements measured on the 400 MHz wide bore instrument b. The manual shaking method is is labelled 'M.S', the handheld magnetic array is labelled 'H.M.A' and the automated flow system is labelled 'A.F'. All measurements were collected at 298 K using a sample of [Ir(COD)(SIMes)(sub)]Cl (5 mM), 4-methylpyridine (50 mM) and *p*H_2 (4 bar) in methanol-d_4. c) Enhancement Factor as a function of SABRE method adapted from Richardson *et al*.[5] with permissions. These measurements were collected at 298 K using a sample of [Ir(COD)(IMes)(sub)]Cl (5 mM), 4-methylpyridine (50 mM) and *p*H_2 (4 bar) and a 10 second *p*-H_2 dissolution time.

Box plots a) and b) in Figure 51 compare the ^1H signal enhancements for a 10 second shake time for each SABRE methods on spectrometers **a** (graph a) and **b** (graph b). The manual shaking method using the stray field of the spectrometer is indicated by 'M.S', the handheld magnetic array by 'H.M.A' and the automated flow system by 'A.F'. Both plots a) and b) show that the largest signal enhancements were measured using the manual shaking method. On NMR **a**, this generated a average enhancement of – 891-fold compared to −497-fold using the handheld magneti array and −227-fold using the automated flow system. If the individual measurements are considered, the largest enhancement was −935-fold using the manual shaking method. Similarly,

on NMR **b**, the largest enhancements were also observed using the manual shaking method. This induced an average enhancement of −842-fold, however the largest individual measurement was −974-fold which is larger than the maximum observed on NMR **b**. An average enhancement of −339-fold was observed using the handheld magnetic array and −135-fold using the automated flow system. A larger variation in the data was generated by spectrometer **b** compared to **a**. This is clearly observed by the large box plot using the automated flow method. Larger variations were also observed with the manual shaking method and the handheld magnetic array. For example, the data ranged from −714-fold to −974 fold for the manual shaking method. On NMR **a**, the data ranged from −832-fold to −935-fold. This difference in reproducibility is attributed to the longer transfer time induced when using instrument **b**. A longer transfer time means that hyperpolarisation can be lost before the data can be acquired. Furthermore, as results were found to be more reproducible using NMR **a** compared to **b**, this was used for all the SABRE experiments in the remainder of this thesis.

The fact that larger enhancements are observed using the manual shaking method is interesting because the homogeneous field of the handheld magnetic array has been shown to be capable of inducing enhancements 25% larger than using the stray field of the spectrometer.[5] This compares to a 44% increase using the stray field of the spectrometer on NMR **a** compared to the handheld magnetic array. It is important to note that although the handheld magnetic array removes the variability in the polarisation transfer field it does not remove other forms of human error such as; sample transfer time and shake intensity (which will also be user dependent). In this case, it was established that shaking of the sample was less vigorous and therefore less *p*-H_2 was dissolved into solution. Furthermore, the transfer time was longer as the sample must first be removed from the shaker before being dropped into the spectrometer, meaning that some of the polarisation is lost before data acquisition.

The data in graph **c)** was adapted from Richardson *et al*.[5] where the three SABRE methods were compared for a sample containing $[Ir(H)_2(IMes)(sub)_3]Cl$ where the substrate was 4-methylpyridine. It is important to note that the different NHC means

that larger enhancements were observed and so the data is not directly comparable to the data in graphs **a)** and **b)**. Furthermore, a different experimenter conducted the measurements in graph **c)** compared to graphs **a)** and **b)**. However, it was observed that the handheld magnetic array yielded the largest signal enhancements compared to the automated flow system and the manual shaking method using the stray field. This contrasts with the data in graphs **a)** and **b)** where the manual shaking method produced the largest enhancements. This may be a consequence of the experimenter in **c)** being more familiar with this method and therefore capable of achieving much larger signal enhancements. Personally, I found the handheld magnetic array difficult to use and therefore shaking was not as intense as the manual shaking method. Furthermore, the transfer times were longer using the handheld magnetic array which contributed to the smaller signal enhancements observed using this method. This inconsistency is apparent when the error bars are considered. For example, whilst the automated flow method induces the smallest error in graphs **a)** and **c)**, this is followed by the handheld magnetic array and the manual shaking method in graph **c)**. However in graph **a)** the manual shaking method was more reliable than when the handheld magnetic array was used. The experimenter in graph **c)** was more experienced in using the handheld magnetic array and therefore was more comfortable using the device leading to more consistency between results.

2.6 Summary

In this chapter we have presented three methods utilised in house for SABRE experiments: the manual shaking method using the stray field of the spectrometer,, the automated flow system and the handheld magnetic array method. Each method has its own advantages and disadvantages, for instance, manual shaking using the stray field of the spectrometer produces significant signal enhancements however it is susceptible to a number of variables meaning that these results are prone to large errors. Conversely, the automated flow and handheld magnetic array methods are highly reproducible but do not produce enhancements comparable to the manual shaking method. Large enhancements are preferable when analysing mixtures or assessing compounds present in low concentrations, such as impurities or reaction

intermediates. In MRI terms, this means that small drug quantities are easily observable. Furthermore, large enhancements would result in much shorter scan times. However, reproducibility is also essential so that different experimenters can effectively compare results (within the error). Additionally, in the proceeding chapters of this thesis, reproducibility is fundamental when comparing the SABRE activity of alternative substrates (see Chapter 3).

The first method described was the manual shaking method using the stray field of the spectrometer. This is a manual technique whereby the sample containing the SABRE species $[Ir(H)_2(SIMes)(sub)_3]Cl$, and *p*-$H_2$ is shaken in the stray field of the magnet (~65 G) before being dropped into the spectrometer for acquisition. Due to the crude nature of this technique, it is susceptible to a number of different variables including; field strength, shake time and transfer time. Although efforts were made to reduce these variables, the average standard error in these experiments was 29-fold compared to 18-fold for the handheld magnetic array and 7-fold for the automated flow system. Despite this, enhancements were 70% larger compared to the flow system and 44% larger compared to the handheld magnetic array.

The flow system comprises of a mixing chamber containing the SABRE pre-catalyst surrounded by a copper coil. *P*-H_2 is then bubbled through the solution whilst the copper coil generates a controlled magnetic environment (~65 G) around the sample. The hyperpolarised sample is then transferred into the spectrometer via a nitrogen flow for NMR detection. The flow system is fully automated, meaning that the field strength, bubble time and transfer time are carefully controlled by the user. Henceforth, the flow system is highly reproducible compared to the manual techniques. Unfortunately, this method is unable to replicate the high enhancements of the manual shaking method using the stray field of the spectrometer. For example, a 10 second bubble time produced an average signal enhancement of −227 ± 8-fold compared to −897 ± 18-fold for the manual shaking method. This has been attributed to the fact that shaking the sample promotes more effective dissolution of the *p*-H_2 into solution compared to bubbling.

Finally, a handheld magnetic array was introduced as a solution to the low reproducibility of the shake and drop method. In this technique, the sample is shaken in a hand-held shaker rather than the stray field of the magnet. The handheld magnetic array has been designed such that the field remains constant throughout the sample for the duration of the shake. Despite this, the handheld magnetic array method is still susceptible to variations in shake and transfer times. Henceforth the average standard error for the handheld magnetic array (18-fold) is lower than the manual shaking method (29-fold) but higher than the flow system (8-fold). Furthermore, whilst the handheld magnetic array has been shown to induce a 25% increase in enhancements compared to the manual shaking method using the stray field of the spectrometer,[5] in these experiments, enhancements were 56% lower.

Whilst it has been established that reproducibility is an important factor in the proceeding chapters of this thesis, most results were generated using the manual shaking method using the stray field of the spectrometer. This is because this method is much quicker and simple to implement compared to the flow system. For example, the comparison of different NHC/substrate combinations (see Chapter 3) involved a number of samples which could be analysed in one afternoon using the manual shaking method compared to a number of days using the flow where only one-two samples could be tested per day. Although the handheld magnetic array displays an improvement in the reproducibility, this method was not developed until the research in the subsequent chapters was in the later stages.

2.7 References

1. R. W. Adams, J. A. Aguilar, K. D. Atkinson, M. J. Cowley, P. I. Elliott, S. B. Duckett, G. G. Green, I. G. Khazal, J. Lopez-Serrano and D. C. Williamson, *Science*, 2009, **323**, 1708-1711.
2. R. W. Adams, S. B. Duckett, R. A. Green, D. C. Williamson and G. G. Green, *J. Chem. Phys.*, 2009, **131**, 194505.
3. K. D. Atkinson, M. J. Cowley, S. B. Duckett, P. I. Elliott, G. G. Green, J. Lopez-Serrano, I. G. Khazal and A. C. Whitwood, *Inorg. Chem.*, 2009, **48**, 663-670.
4. P. J. Rayner and S. B. Duckett, *Angew. Chem. Int. Ed.*, 2018, **57**, 6742-6753.
5. P. M. Richardson, S. Jackson, A. J. Parrott, A. Nordon, S. B. Duckett and M. E. Halse, *Magn. Reson. Chem.*, 2018, **56**, 641-650.

6. R. E. Mewis, K. D. Atkinson, M. J. Cowley, S. B. Duckett, G. G. Green, R. A. Green, L. A. Highton, D. Kilgour, L. S. Lloyd, J. A. Lohman and D. C. Williamson, *Magn. Reson. Chem.*, 2014, **52**, 358-369.
7. L. Frydman, *Nat Chem*, 2009, **1**, 176-178.
8. P. J. Rayner, M. J. Burns, A. M. Olaru, P. Norcott, M. Fekete, G. G. R. Green, L. A. R. Highton, R. E. Mewis and S. B. Duckett, *Proc. Natl. Acad. Sci. U. S. A.*, 2017, **114**, E3188-E3194.
9. D. A. Barskiy, K. V. Kovtunov, I. V. Koptyug, P. He, K. A. Groome, Q. A. Best, F. Shi, B. M. Goodson, R. V. Shchepin, A. M. Coffey, K. W. Waddell and E. Y. Chekmenev, *J. Am. Chem. Soc.*, 2014, **136**, 3322-3325.
10. L. S. Lloyd, A. Asghar, M. J. Burns, A. Charlton, S. Coombes, M. J. Cowley, G. J. Dear, S. B. Duckett, G. R. Genov, G. G. R. Green, L. A. R. Highton, A. J. J. Hooper, M. Khan, I. G. Khazal, R. J. Lewis, R. E. Mewis, A. D. Roberts and A. J. Ruddlesden, *Catal. Sci. Technol.*, 2014, **4**, 3544-3554.
11. L. Buljubasich, M. B. Franzoni, H. W. Spiess and K. Munnemann, *J. Magn. Reson.*, 2012, **219**, 33-40.
12. T. Theis, M. L. Truong, A. M. Coffey, R. V. Shchepin, K. W. Waddell, F. Shi, B. M. Goodson, W. S. Warren and E. Y. Chekmenev, *J. Am. Chem. Soc.*, 2015, **137**, 1404-1407.
13. A. N. Pravdivtsev, A. V. Yurkovskaya, H. M. Vieth, K. L. Ivanov and R. Kaptein, *Chem. Phys. Chem.*, 2013, **14**, 3327-3331.
14. D. A. Barskiy, A. N. Pravdivtsev, K. L. Ivanov, K. V. Kovtunov and I. V. Koptyug, *Phys. Chem. Chem. Phys.*, 2016, **18**, 89-93.
15. P. Vigoureux and G. B. B. M. Sutherland, *Proceedings of the Royal Society of London. Series A. Mathematical and Physical Sciences*, 1962, **270**, 72-89.
16. M. H. Levitt, *Spin Dynamics: Basics of Nuclear Magnetic Resonance*, Wiley, 2013.
17. C. P. Bean, *Rev. Mod. Phys.* , 1964, **36**, 31-+.
18. B. Efron, *Biometrika*, 1981, **68**, 589-599.
19. K. Halbach, *Nuclear Instruments & Methods*, 1980, **169**, 1-10.
20. D. A. Barskiy, R. V. Shchepin, C. P. N. Tanner, J. F. P. Colell, B. M. Goodson, T. Theis, W. S. Warren and E. Y. Chekmenev, *Chem. Phys. Chem.*, 2017, **18**, 1493-1498.

Chapter 3 SABRE Optimisation for a Series of *Para*-Substituted Pyridines

3.1 The Substrates

In SABRE, substrates are required to reversibly bind to the iridium metal centre as it is this association/dissociation that after polarisation transfer allows subsequent build-up of a hyperpolarised reagent in solution.[1] The most commonly exploited substrates for SABRE are *N*-heterocycles such as pyridine and its derivatives.[2] Pyridine rings contain a lone pair centred on the nitrogen atom which can be involved in different interactions including the metal-ligand interaction in organometallic chemistry.[3] As pyridine is considered a common and relatively strong σ-donor ligand,[4] it is capable of 'soft' binding, meaning it weakly coordinates to a metal centre. This makes pyridine an excellent candidate for SABRE as it can associate and dissociate from the iridium SABRE catalyst on a suitable timescale to allow polarisation transfer. Furthermore, pyridine rings feature heavily throughout nature[5, 6] and play a vital role in drug motifs.[7-9] Henceforth, hyperpolarisation of these molecules paves the way for their use as MRI contrast agents.

3.1.1 Substituent Effects in Pyridine

As pyridine is an aromatic system, its reactivity can be influenced by substituents around the ring. This effect is clear when the resonance structures of pyridine are considered (Figure 52).

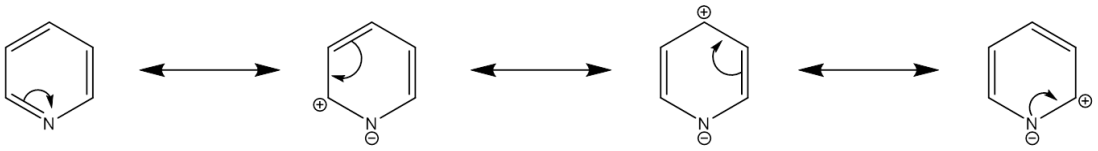

Figure 52 – Resonance structures for pyridine.

The resonance structures predict a partial positive charge on positions 2, 4 and 6 and a net negative charge on the nitrogen atom.[10] This means that substituents in both the *ortho* and *para* positions have the greatest influence on the behaviour of

pyridine. Substituents can be classed as either electron donating or electron withdrawing. According to Hęclik and Dobrowolski, substituents are classed as sEDA (σ electron donor-acceptor) if they affect the σ orbitals in the plane of the pyridine ring which includes the lone pair on the nitrogen. [11, 12] If they affect the π orbitals which form the conjugated π electron system they are classed as pEDA (π electron donor-acceptor). It was observed that an increase in σ donating ability increases the negative charge on the lone pair but decreases the electron population of the π valence orbitals on the nitrogen in both the *ortho* and *para* positions in pyridine. Conversely, an increase in π donation in these positions increases the electron population of the π valence orbitals but decreases the σ population at the nitrogen lone pair.

In 2007, Palusiak *et al*.[4] investigated a number of *para* substituted pyridines and their effect on $Cr(CO)_5$-pyridine complexes. It was found that electron withdrawing groups stabilised the Cr-N bond whilst electron donating groups weakened the bond. This was shown by shorter bond lengths in complexes containing electron withdrawing groups (such as aldehydes) due to removal of electron density from the π-system of the pyridine ring. Therefore, to stabilise the M-L interaction, π back-donation occurs from the metal to the ligand (Figure 53a). Electron donating groups such as methyoxy however, increase the electron density within the conjugated system. This destabilizes the bond as the metal cannot back-donate into the π-system (see Figure 53).[11, 13]

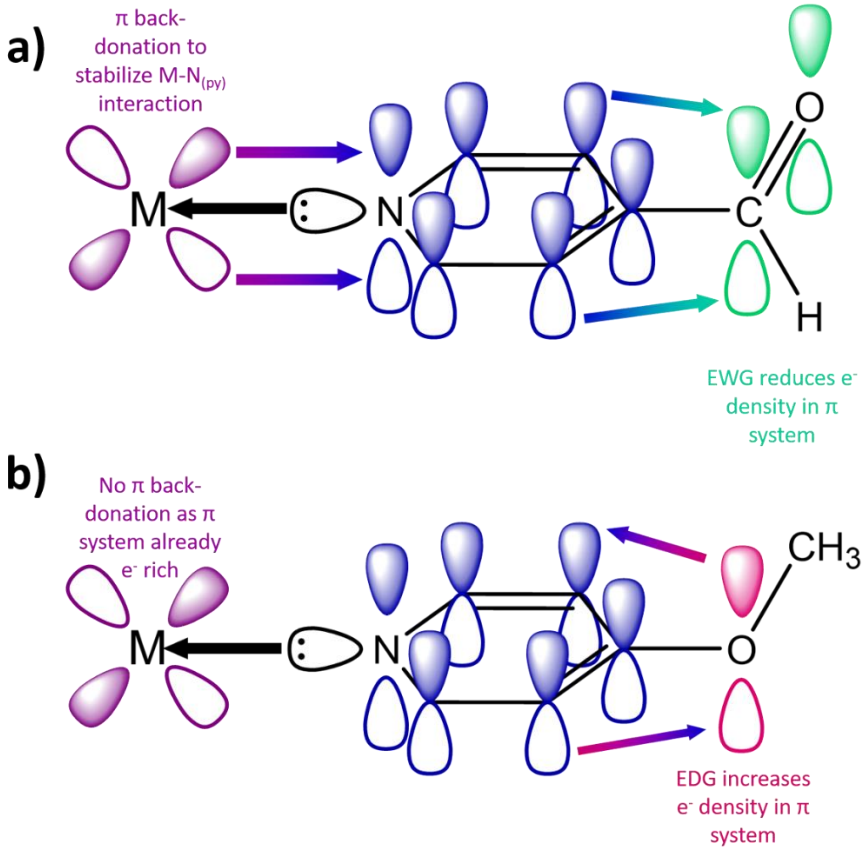

Figure 53 – comparison of the effect of a) electron withdrawing groups (EWG) and b) electron donating groups (EDG) in the *para* position of pyridine on the metal-ligand interaction.

Evidently the ligation of pyridine to a metal centre can be influenced by subsitutents in the *ortho* and *para* positions of the pyridine ring. As SABRE efficiency is heavily reliant on the rate of substrate dissociation, if the substrate dissociates too slowly, hyperpolarisation can be lost through relaxation effects as the association to the metal is too strong.[14, 15] This is because binding to the iridium centre promotes relaxation. Whereas if substrate ligation is too weak, insufficient polarisation can be transferred before dissociation occurs. This means that SABRE efficiency could be controlled via substitution at the *ortho* and/or *para* positions of pyridine. Shchepin *et al*.[16] have briefly compared the effect of methyl substituents in the *ortho* and *para* positions on the ^{15}N hyperpolarisation of substituted pyridine. Whilst they observed ^{15}N enhancements in the *para* substituted equivalent, the *ortho* substituted derivative resulted in no detectable hyperpolarisation. It was assumed that the steric hindrance from the *ortho* substituent critically altered the timescale of the SABRE

exchange process such that magnetism was insufficiently transferred to the nuclei of interest.

In this chapter, a range of *para*-substituted pyridines were employed to study the affect of iridium-substrate ligation on SABRE efficiency. *Para*-substituted pyridines were chosen in order to study the electronic contribution, while minimising the steric impact of the functional group change on the SABRE catalyst. In order to directly compare the functionality in these substrates, their corresponding pK_a values were determined. It was anticipated that substrates with high pK_a would form strong iridium-substrate ligations and those with low pK_a values would form weaker associations. The substrates selected for this study were 4-chloropyridine, 4-methylpyridine, 4-methoxypyridine and 4-pyridinecarboxaldehyde (see Figure 54), with corresponding literature pK_a values of 3.83,[17] 6.03,[17-19] 6.55[17] and 4.84[18, 19].

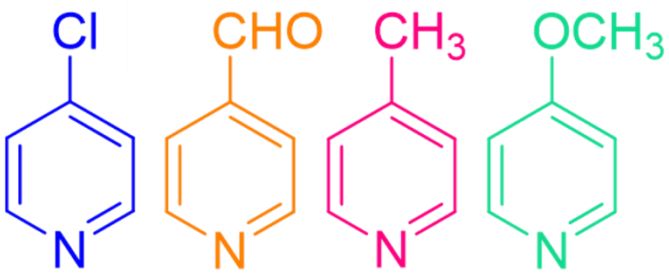

Figure 54 - The chemical structures of the para-substituted pyridines substrates chosen for this study.

3.1.1.1 Measuring pKa Values

The pK_a values of each of the substrates displayed in Figure 54 were measured via NMR using the method first described by Handloser *et al.*[19] In this method the substituted pyridines were dissolved in methanol with added hydrochloric acid (HCl). HCl was used to control the pH of the solution and its addition means that two forms of the substituted pyridine exist in solution (Figure 55).

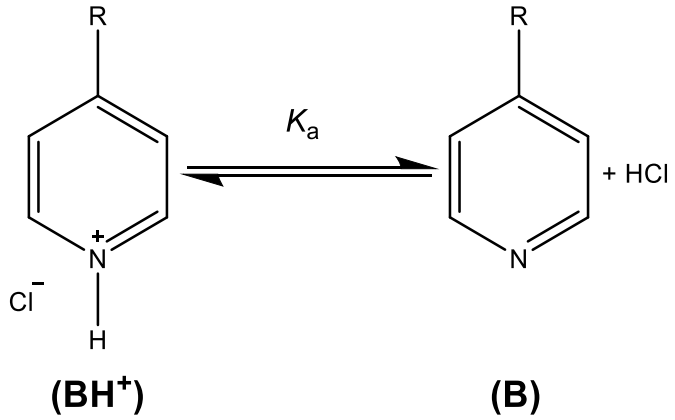

Figure 55 – The two forms of the substituted pyridine in solution with methanol and hydrochloric acid (HCl) used to control the pH of the solution

The ionisation constant, K_a, of these substituted pyridine acids can be described by:

$$K_a = \frac{[\mathrm{HCl}][\mathrm{B}]}{[\mathrm{BH^+}]}$$

Equation 7

The pK_a can then be written as:

$$\mathrm{p}K_\mathrm{a} = \mathrm{pH} + \log\left(\frac{[\mathrm{BH^+}]}{[\mathrm{B}]}\right)$$

Equation 8

In NMR, the concentrations of each form can be substituted for the fractional populations ($x_\mathrm{B}$and $x_{\mathrm{BH^+}}$), therefore Equation 8 becomes:

$$\mathrm{p}K_a = \mathrm{pH} + \log\left(\frac{x_{\mathrm{BH^+}}}{x_\mathrm{B}}\right)$$

Equation 9

The expected chemical shift (δ) for each of the two forms of the substituted pyridine would be different due to the proton in the charged case shifting the resonance downfield. However, NMR cannot detect chemical change that occurs on a faster

timescale than the NMR experiment itself, therefore there is only one observed peak which accounts for both forms. The location of this peak reflects the weighted average of the relative populations and chemical shift of the pure acidic and pure basic forms. If the chemical shift of the protonated form (i.e. in strong acidic conditions, δ_A) and the deprotonated form (i.e. in strong basic conditions, δ_B) are known then the measured chemical shift (δ_m) can be described by Equation 10.

$$\delta_m = x_{BH^+}\delta_{BH^+} + x_B\delta_B$$

Equation 10

As $x_B$and x_{BH^+} are fractional populations, they must sum to 1, therefore the proportion of the deprotonated form can be expressed as in Equation 11.

$$x_B = 1 - x_{BH^+}$$

Equation 11

The relative population of the protonated form can then be calculated using Equation 12 by substituting Equation 11 into Equation 10.

$$x_{BH^+} = \frac{\delta_m - \delta_B}{\delta_A - \delta_B}$$

Equation 12

Analogously, the fractional population of the deprotonated form can be expressed as in Equation 13.

$$x_B = \frac{\delta_A - \delta_m}{\delta_A - \delta_B}$$

Equation 13

Finally, substituting Equation 12 and Equation 13 into Equation 9 and rearranging provides an expression for the measured chemical shift as a function of pH in the form of Equation 14.

$$\delta_{\mathrm{m}} = \frac{\delta_{\mathrm{A}} 10^{\mathrm{p}K_{\mathrm{a}} - \mathrm{pH}} + \delta_B}{1 + 10^{\mathrm{p}K_{\mathrm{a}} - \mathrm{pH}}}$$

Equation 14

Therefore, it is possible to measure the chemical shift of a molecule by NMR for solutions of different pH levels and fit the data using Equation 14 to determine the pK_a for the molecule.

The pK_a values of the four target molecules 4-chloropyridine, 4-pyridinecarboxaldehyde, 4-methylpyridine and 4-methoxypyridine were measured in methanol-d_4 in order to mimic the conditions of hyperpolarisation experiments. For each substrate, two bulk samples were created each containing 10 mL solvent, 150 mg substrate and 40 µL of trimethylsilanol (TMSO). TMSO was added as a reference to ensure there was no drift in chemical shift over time or sample pH. To one bulk solution, drops of 1.0 M (and 0.1 M for fine tuning) hydrochloric acid (in methanol-d_4) were added to obtain low pH levels. Potassium hydroxide (in methanol-d_4) were added to the other bulk solution to reach high pH levels. The pH values of the solutions were determined using a benchtop pH sensor (Mettler Toledo) which was calibrated prior to each sample using the two-point calibration sequence using buffers at pH 4 and pH 7. For each sample, a range of pH values were measured and subsequently an aliquot was extracted and placed into NMR tubes for analysis. It should be noted that whilst pH is usually only relevant in water, it was measured in methanol-d_4. This is because all measurements in this chapter were taken in methanol-d_4.

The chemical shifts were determined from a simple pulse and acquire using a 90° pulse. For each substrate, all the proton resonances present were analysed. The data was then fitted with Equation 14 using a least squares regression algorithm where

the parameters δ_A, δ_B and pK_a were permitted to be free in the fitting routine. These values were determined for each resonance on the substrate and are shown in Figure 56 for 4-chloropyridine. The pK_a values determined for each substrate are shown in Table 1.

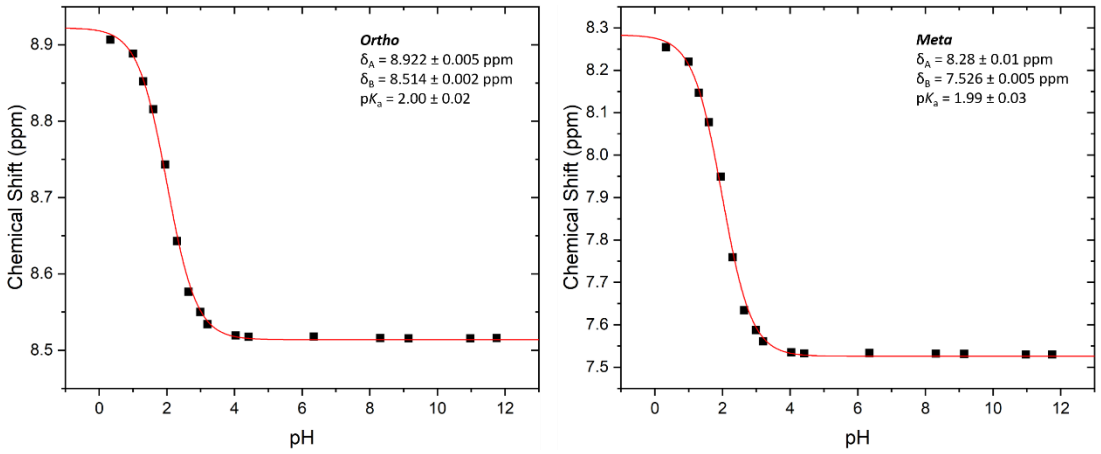

Figure 56 – Chemical shift as a function of pH for 4-chloropyridine in methanol-d_4. HCl was used to reach low pH values and KOH was added to achieve high pH. The data points have been fitted using Equation 14.

Substrate	Literature pK_a	Measured pK_a
4-Chloropyridine	3.83	2.00 ± 0.02
4-pyridinecarboxaldehyde	4.84	3.12 ± 0.04
4-methylpyridine	6.03	4.02 ± 0.02
4-methoxypyridine	6.55	4.89 ± 0.03

Table 1 - Table of the literature pK_a values[17, 18] compared to those measured at the *ortho* proton resonance for each of the substrates. Note that the literature values are in water whilst the measured values were taken in methanol-d_4.

Whilst the measured pK_a values are slightly lower than the literature values, they maintain the same trend where the 4-chloropyridine has the lowest pK_a value and the 4-methoxypyridine the highest value. The difference here is attributed to the use of methanol rather than H_2O which was used in the literature values. Methanol-d_4 was used for the measured values as it was important to use the solvent used for all the subsequent measurements in this chapter.

3.2 Formation of the SABRE Pre-Catalyst: [Ir(COD)(SIMes)(sub)]Cl

The initial step for formation of the active SABRE catalyst involves the reaction of the substrate with [IrCl(COD)(NHC)]. Upon this addition, the chloride ligand is displaced by the substrate to form the SABRE pre-catalyst [Ir(COD)(NHC)(sub)]Cl. This 16-electron, square planar species has been seen to form for each of the substrates discussed in this chapter. The [Ir(COD)(SIMes)(sub)]Cl complex has been fully characterised via ^{1}H, ^{13}C and ^{15}N NMR, full details of which can be found in Appendix B, an example characterisation data set for the species formed using 4-methylpyridine is shown below.

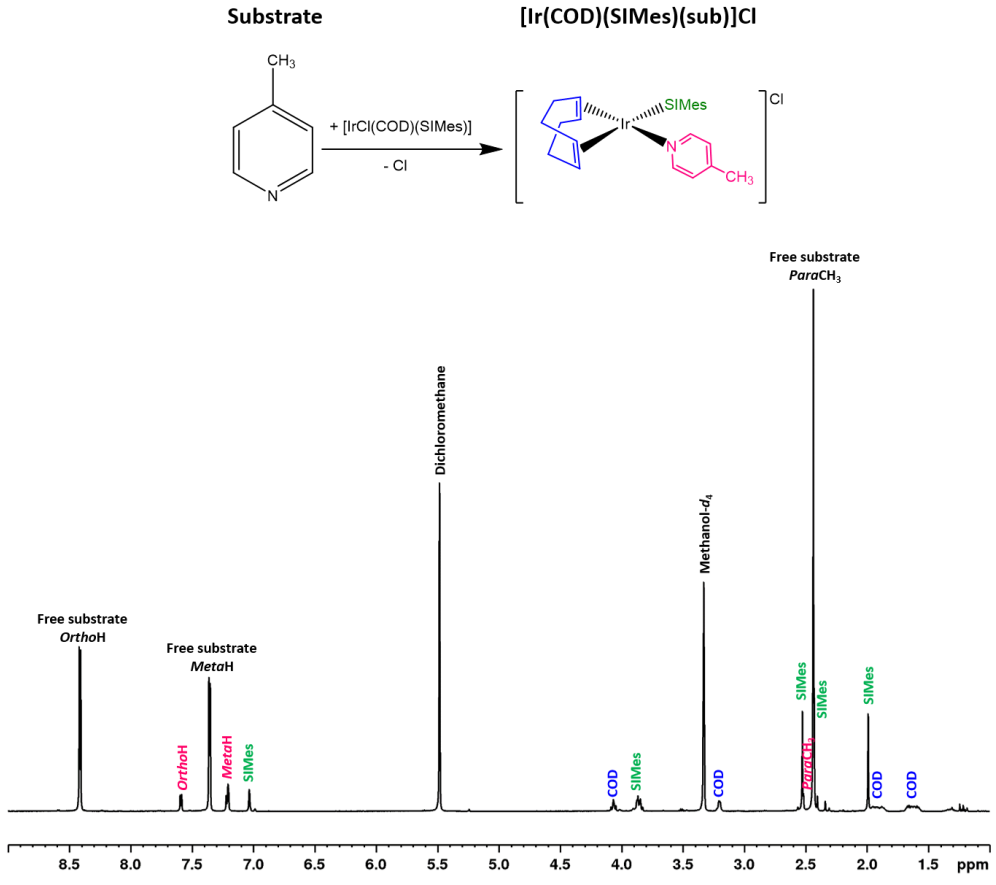

Figure 57 – ^{1}H-NMR spectra showing the SABRE precatalyst [Ir(COD)(SIMes)(sub)]Cl for the substrate 4-methylpyridine. The sample was prepared by adding [IrCl(COD)(SIMes)] (4 mM) to 4-methylpyridine (40 Mm) in methanol-d_4. The sample was measured at 235 K and 500 MHz.

Position	^{1}H-NMR	^{13}C-NMR	^{15}N-NMR

OrthoH^{Free}	8.415 J_{HH} = 6.1 Hz	148.4	288.1
MetaH^{Free}	7.359 J_{HH} = 6.1 Hz	125.4	-
CH_3^{Free}	2.439	19.8	-
Position	**^{1}H-NMR**	**^{13}C-NMR**	**^{15}N-NMR**
orthoH^{sub}	7.593 J_{HH} = 6.5 Hz	150.4	232.8
metaH^{sub}	7.223	126.4	
$CH^{Ar,Mes}$	7.208 7.035	136.0 129.4	
N-CH_2-CH_2-N	3.862	52.14	
CH^{COD}	4.068 3.206	64.4 83.0	
orthoCH_3^{Mes}	2.439 2.433	19.9	
CH_3^{Sub}	2.528	18.2	
paraCH_3^{Mes}	1.992	17.1	
CH_2^{COD}	1.904 1.624	32.2 28.8	

Table 2 – NMR Resonances for [Ir(COD)(SIMes)(4-Methylpyridine)]Cl in methanol-d_4. ^{1}H at 500 MHz, ^{13}C at 125 MHz and ^{15}N at 41 MHz at 235 K.

3.2.1 Formation of [Ir(COD)(SIMes)(sub)]Cl with 4-Pyridinecarboxaldehyde

Upon addition of 4-pyridinecarboxaldehyde to methanol-d_4, the methyl hemiacetal forms predominantly in solution (see Appendix B). It is this form that binds to the iridium catalyst [IrCl(COD)(SIMes)] in this initial step. However, in the excess solution or 'free substrate' there is a small quantity of the carboxaldehyde present (seen in black in

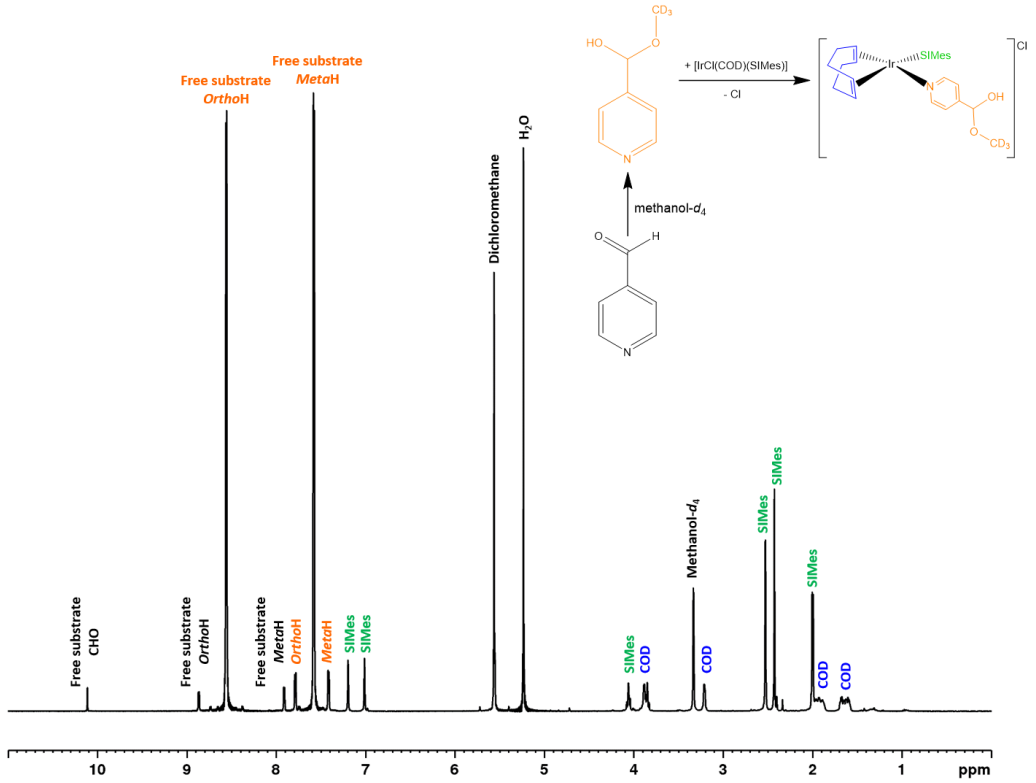

Figure 58).

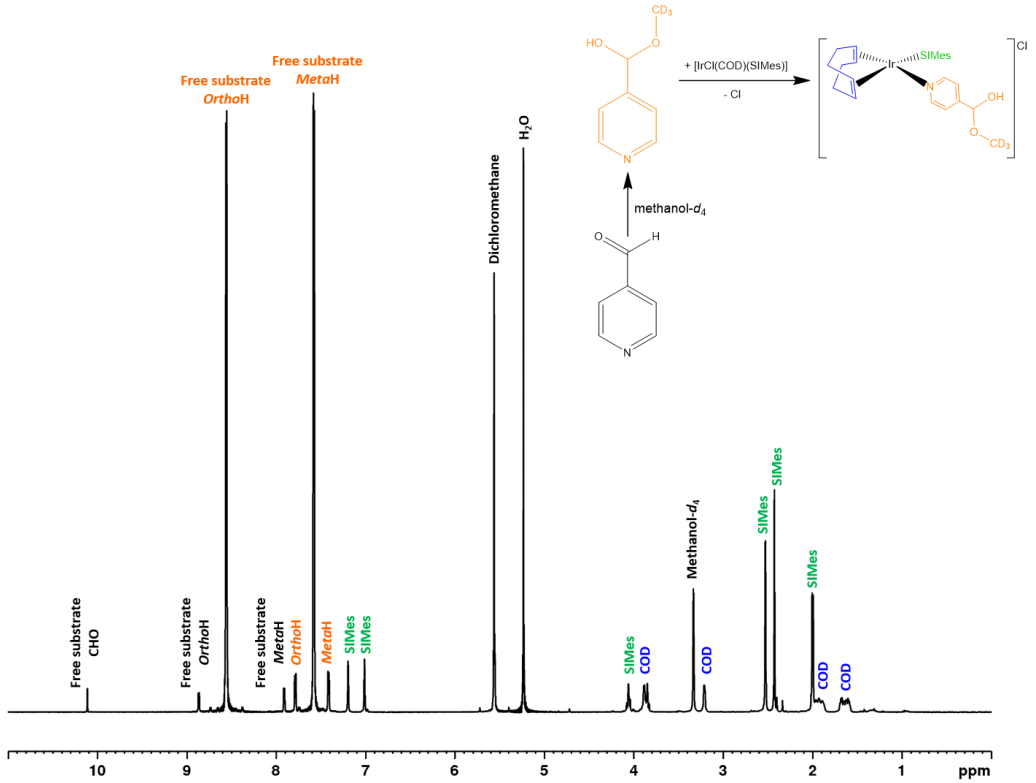

Figure 58 - ^{1}H-NMR spectrum for [Ir(COD)(SIMes)(4-pyridinacarboxaldehyde)]Cl in methanol-d_4 measured at

500 MHz and 263 K. Black indicates the presence of the free aldehyde conformation and the orange highlights the bound and free hemiacetal conformation.

Position	^{1}H-NMR	^{13}C-NMR	^{15}N-NMR
*Ortho*H^{Free}	8.571 J_{HH} = 6.1 Hz	148.5	294.8
*Meta*H^{Free}	7.602 J_{HH} = 6.1 Hz	121.8	-
OH**C**CD$_3$^{Free}	-	151.6	-
Position	**^{1}H-NMR**	**^{13}C-NMR**	**^{15}N-NMR**
*ortho*H^{sub}	7.769 J_{HH} = 6.5 Hz	151.4	239.9
*meta*H^{sub}	7.418 J_{HH} = 6.5 Hz	122.8	
OH**C**CD$_3$	-	151.9	
CH^{Ar,Mes}	7.202 7.012	129.4	
N-CH$_2$-CH$_2$-N	4.061 3.844	52.2	
CH^{COD}	3.886 3.210	64.6 83.1	
*ortho*CH$_3$^{Mes}	2.526 2.429	19.8	
*para*CH$_3$^{Mes}	1.998	17.2	
CH$_2$^{COD}	1.908 1.639	32.1 28.8	

Table 3 - NMR Resonances for [Ir(COD)(SIMes)(4-pyridinecarboxaldehyde)]Cl in methanol-d4. 1H at 500 MHz, 13C at 125 MHz and 15N at 41 MHz at 235 K.

The presence of the hemiacetal form is confirmed by the absence of a carbonyl ^{13}C resonance which would usually be found at 180 ppm (see following chapter).[20] Instead the ^{13}C resonance at the hemiacetal group is found at 151.9 ppm. This is close to the equivalent resonance in the free substrate at 151.6 ppm.

3.3 Formation of the SABRE-Active Species: [Ir(H)$_2$(SIMes)(sub)$_3$]Cl

Once the complex [Ir(COD)(SIMes)(sub)]Cl has formed, hydrogen is added to promote hydrogenation of the COD ligand. As the hydrogen and substrate are both

in excess, they both bind into the catalyst to form the SABRE-active complex, $[Ir(H)_2(SIMes)(sub)_3]Cl$. These species have been characterised for each of the four substrates discussed in this chapter. In all cases, the *tris*-substituted species forms where two substrate ligands lie in the equatorial plane of the iridium complex, *trans* to the hydride ligands, and one in the axial position *trans* to the NHC (SIMes). Full NMR characterisation for the SABRE-active species for each of the substrates can be found in Appendix B although characterisation for 4-methylpyridine is shown below.

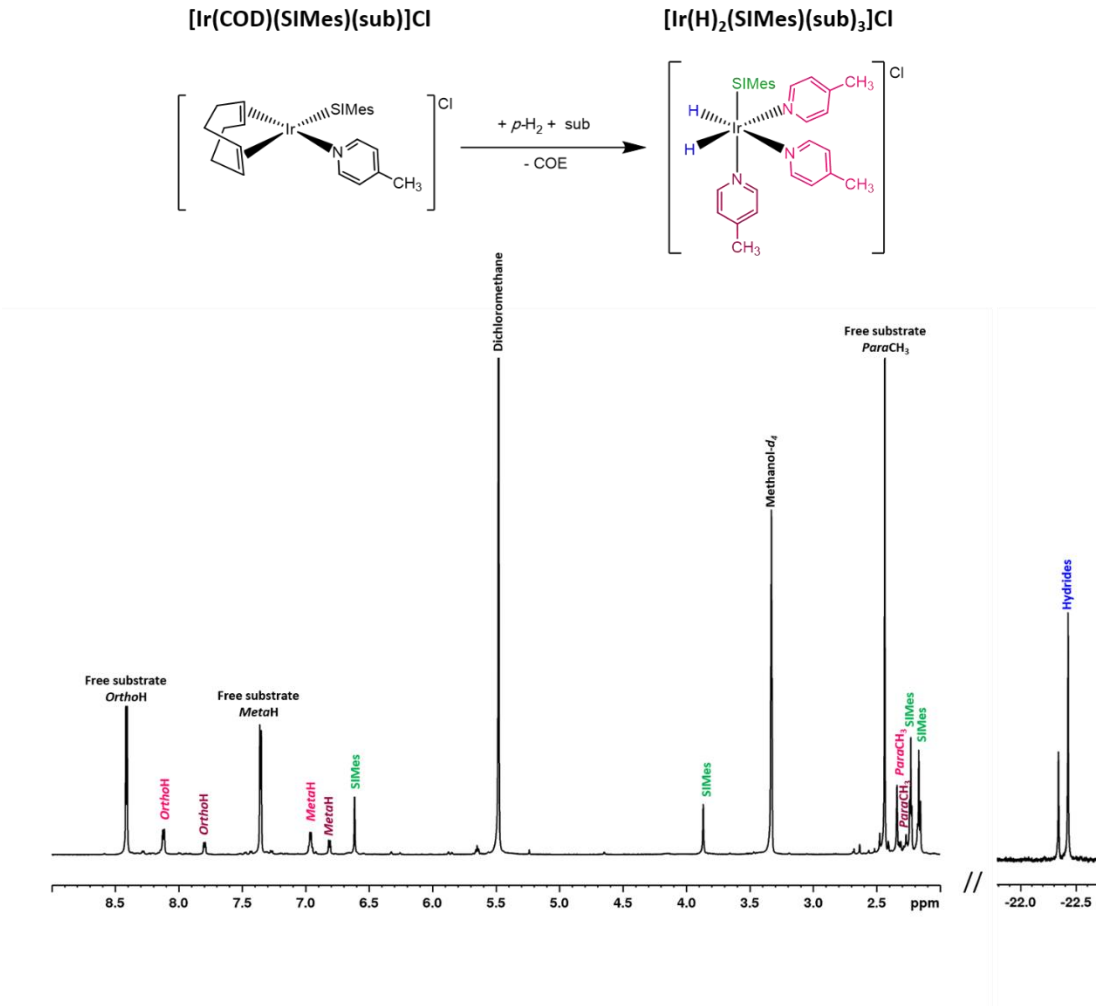

Figure 59 – ^{1}H-NMR spectra for the SABRE-active species $[Ir(H)_2(SIMes)(sub)_3]Cl$ for 4-methylpyridine. The sample was prepared using [IrCl(COD)(SIMes)] (4 mM), 4-methylpyridine (40 mM) and *p*-H_2 (4 bar) in methanol-d_4. The sample was measured at 235 K and 500 MHz.

Position	^{1}H-NMR	^{13}C-NMR	^{15}N-NMR

OrthoH^{Free}	8.413 J_{HH} = 6.0 Hz	149.3	288.1
MetaH^{Free}	7.357 J_{HH} = 6.0 Hz	125.3	-
CH_3^{Free}	2.439	19.8	-
Position	**^{1}H-NMR**	**^{13}C-NMR**	**^{15}N-NMR**
orthoH^{sub} (*trans* to H^-)	8.121 J_{HH} = 5.9 Hz	153.6	247.2
orthoH^{sub} (*trans* to NHC)	7.799 J_{HH} = 5.5 Hz	154.2	233.1
metaH^{sub} (*trans* to H^-)	6.963 J_{HH} = 5.9 Hz	125.9	
metaH^{sub} (*trans* to NHC)	6.814 J_{HH} = 5.5 Hz	125.9	
$CH^{Ar,Mes}$	6.616	128.5	
N-CH_2-CH_2-N	3.869	50.5	
orthoCH_3^{Mes}	2.235	19.83	
CH_3^{Sub} (*trans* to H^-)	2.170	17.67	
CH_3^{Sub} (*trans* to NHC)	2.343	19.52	
paraCH_3^{Mes}	2.157	19.36	
H^-	-22.43	-	

Table 4 – NMR resonances for $[Ir(H)_2(SIMes)(4\text{-Methylpyridine})_3]Cl$ in methanol-d_4 at 500 MHz spectrometer and 235 K

3.3.1 Formation of $[Ir(H)_2(SIMes)(sub)_3]Cl$ with 4-Pyridinecarboxaldehyde

Upon hydrogen addition to the complex [Ir(COD)(SIMes)(sub)]Cl, where sub = 4-pyridinecarboxaldehyde, it is the hemiacetal form that binds to the iridium catalyst. Resonances are observed for the 4-pyridinecarboxaldehyde equivalent which is present in small quantities in the free solution (Figure 60).

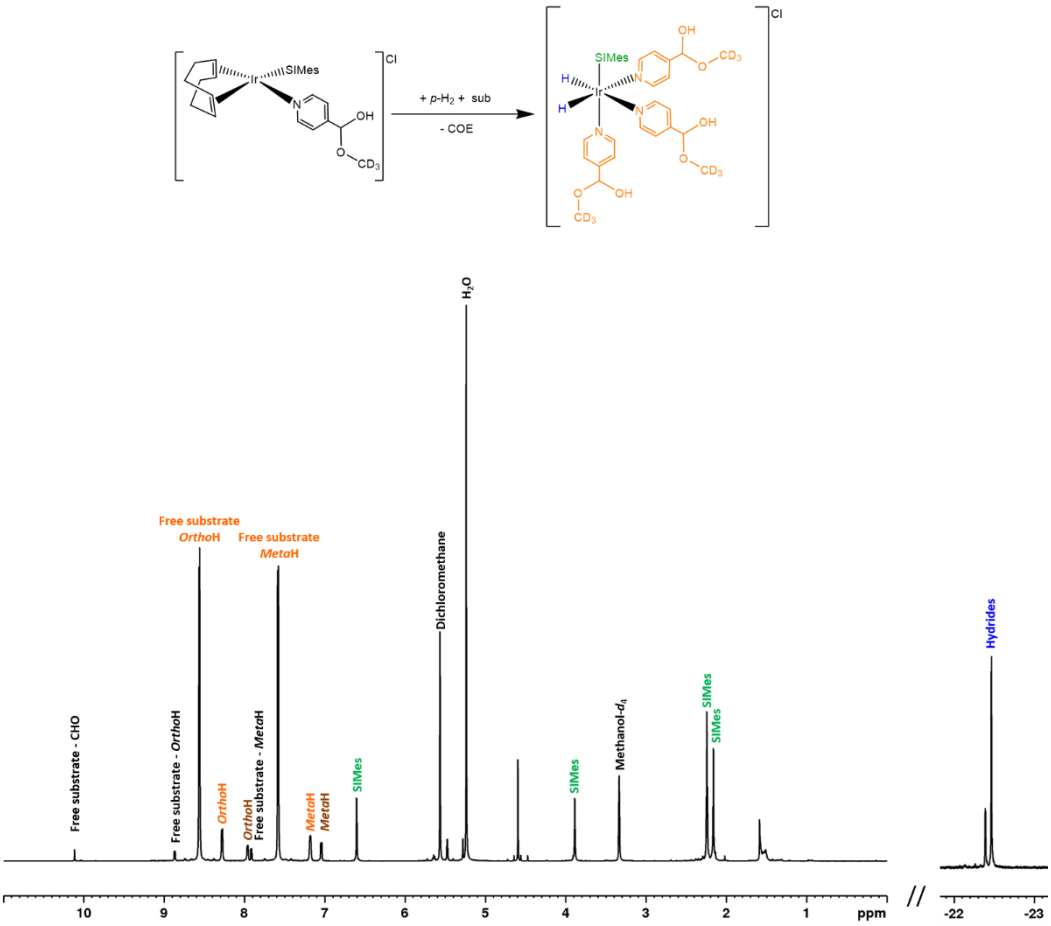

Figure 60 - ^{1}H-NMR Spectrum of [Ir(H)$_2$(SIMes)(sub)$_3$]Cl in methanol-d_4 at 500 MHz and 263 K. Black indicates the presence of the free aldehyde conformation and the orange highlights the bound and free hemiacetal conformation.

Position	^{1}H-NMR	^{13}C-NMR	^{15}N-NMR
*Ortho*H^{Free}	8.563 J_{HH} = 4.2 Hz	148.5	295.3
*Meta*H^{Free}	7.594 J_{HH} = 4.2 Hz	121.8	
OH**C**CD$_3$^{Free}	-	151.6	
Position	**^{1}H-NMR**	**^{13}C-NMR**	**^{15}N-NMR**
*ortho*H^{sub} (*trans* to H$^-$)	8.28	150.0	254.4
*ortho*H^{sub} (*trans* to NHC)	7.97	150.6	240.1
*meta*H^{sub} (*trans* to H$^-$)	7.18	122.53	
*meta*H^{sub} (*trans* to NHC)	7.04	122.59	

$OH\mathbf{C}CD_3$ (*trans* to H^-)	-	154.0
$OH\mathbf{C}CD_3$ (*trans* to NHC)	-	154.7
$CH^{Ar,Mes}$	6.60	128.62
$N\text{-}CH_2\text{-}CH_2\text{-}N$	3.89	50.39
orthoCH_3^{Mes}	2.24	17.86
paraCH_3^{Mes}	2.16	19.69
H^-	-22.39	-

Table 5 - NMR Resonances for $[Ir(H)_2(SIMes)(4\text{-pyridinecarboxaldehyde})_3]Cl$ in methanol-d_4. ^1H at 500 MHz, ^{13}C at 125 MHz and ^{15}N at 41 MHz at 243 K.

3.3.2 SABRE Enhancements in $[Ir(H)_2(SIMes)(sub)_3]Cl$

Once the SABRE-active species, $[Ir(H)_2(SIMes)(sub)_3]Cl$ has been formed, the sample is ready for hyperpolarised NMR detection. For SABRE to occur, *p*-H_2 is added to the sample resulting in *p*-H_2 derived hydride ligands as a product of chemical exchange. Once bound to the iridium, *p*-H_2 can transfer its non-equilibrium spin order to the NMR-active nuclei of the substrate via the *J*-coupling network.[21] As the *p*-H_2 and substrate are both in excess, they continuously exchange with their bound equivalents allowing for the hyperpolarised substrate to be built up into the solution. An example of the hyperpolarised spectrum is shown in Figure 61. The largest signals in the hyperpolarised spectrum arise from the substrate in solution and the smaller signals from the substrate bound *trans* to hydride. To calculate the enhancement, the hyperpolarised spectrum is compared to the thermal (non-hyperpolarised) spectrum obtained under identical conditions. In the case below, the hyperpolarised spectrum corresponds to an enhancement of −494-fold at the *ortho* proton for the complex $[Ir(H)_2(SIMes)(4\text{-methylpyridine})_3]Cl$ (Figure 63).

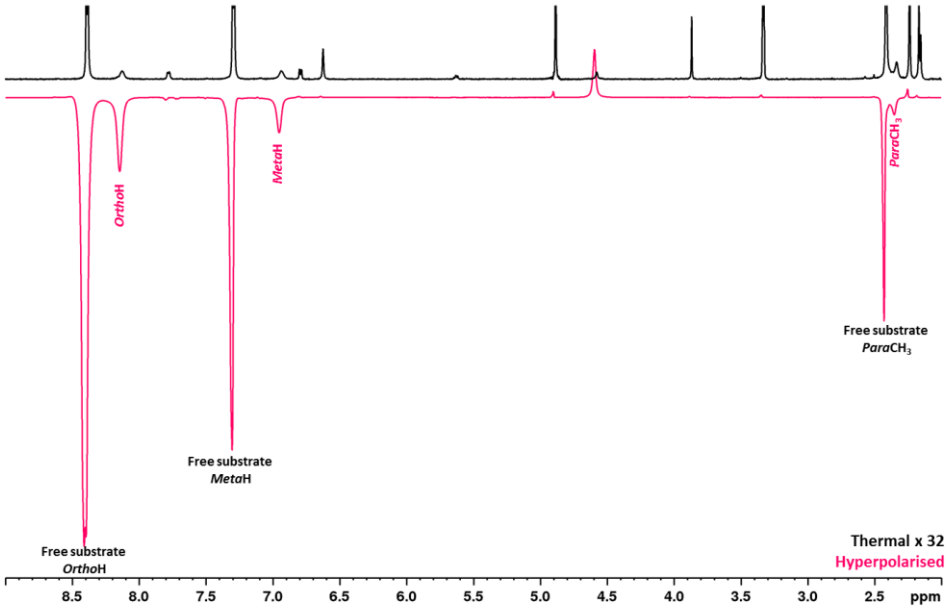

Figure 61 – Thermal ^{1}H-NMR spectrum under Boltzmann conditions (black) compared to a hyperpolarised spectrum where the sample was shaken for 10 s in the stray field (65 G) of the spectrometer (400 MHz) (pink). These were measured using a sample containing 4-methylpyridine (40 mM), [IrCl(COD)(SIMes)] (4 mM) and *p*-H_2 (4 bar) in methanol-d_4 (0.6 mL).

Hyperpolarised signal enhancements similar to that exhibited in Figure 61 were detected for each of the four substrates discussed in this chapter. However, it is important to note that as the 4-pyridinecarboxaldehyde binds to iridium as the hemiacetal form, it is this form that hyperpolarises. Interestingly, the free resonances of 4-pyridinecarboxaldehyde, which are present in low quantities, are also seen to hyperpolarise (see Figure 62). Furthermore, as the proton in the OH of the hemiacetal group is exchangeable, it exchanges with the solvent OH peak, also causing this to hyperpolarise under SABRE conditions (Figure 62). This effect appears similar to the SABRE-RELAY hyperpolarisation method described in Chapter 1, Section 1.5.2.4 SABRE-RELAY via Proton Exchange. However, for the purpose of this thesis this 'proton exchange' effect was not explored as it was not relevant to the study in this Chapter.

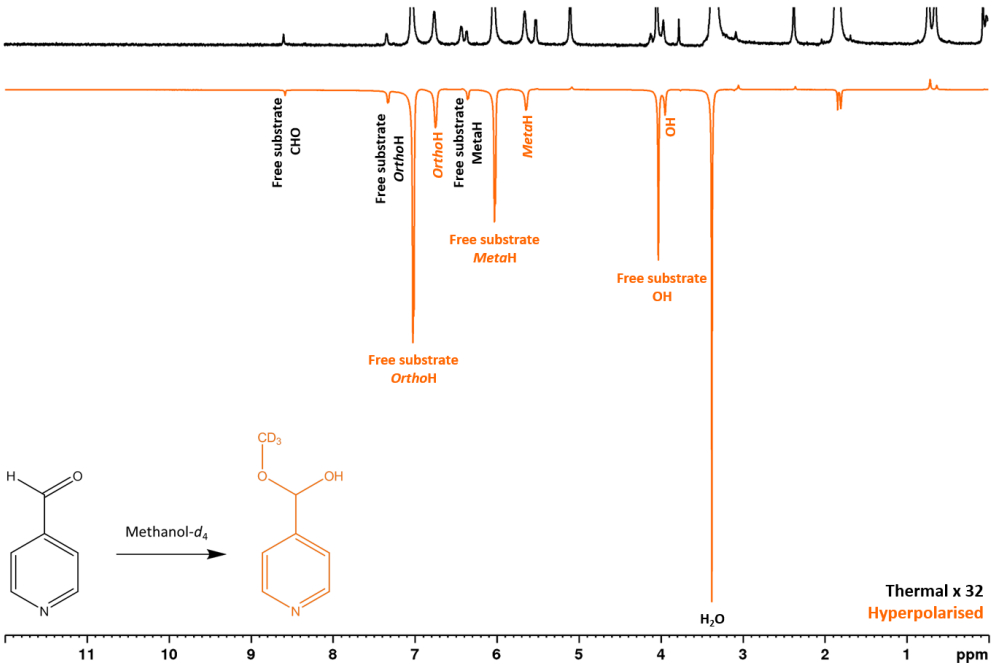

Figure 62 – Thermal ^{1}H-NMR spectrum under Boltzmann conditions (black) compared to a hyperpolarised spectrum where the sample was shaken for 10 s in the stray field (65 G) of the spectrometer (400 MHz) (orange). These were measured using a sample containing 4-pyridinecarboxaldehyde (40 mM), [IrCl(COD)(SIMes)] (4 mM) and *p*-H_2 (4 bar) in methanol-d_4 (0.6 mL).

The SABRE responses of the four substrates were measured using the manual shaking method using the stray field of the spectrometer, described in Chapter 2.2 The Manual Shaking Method.

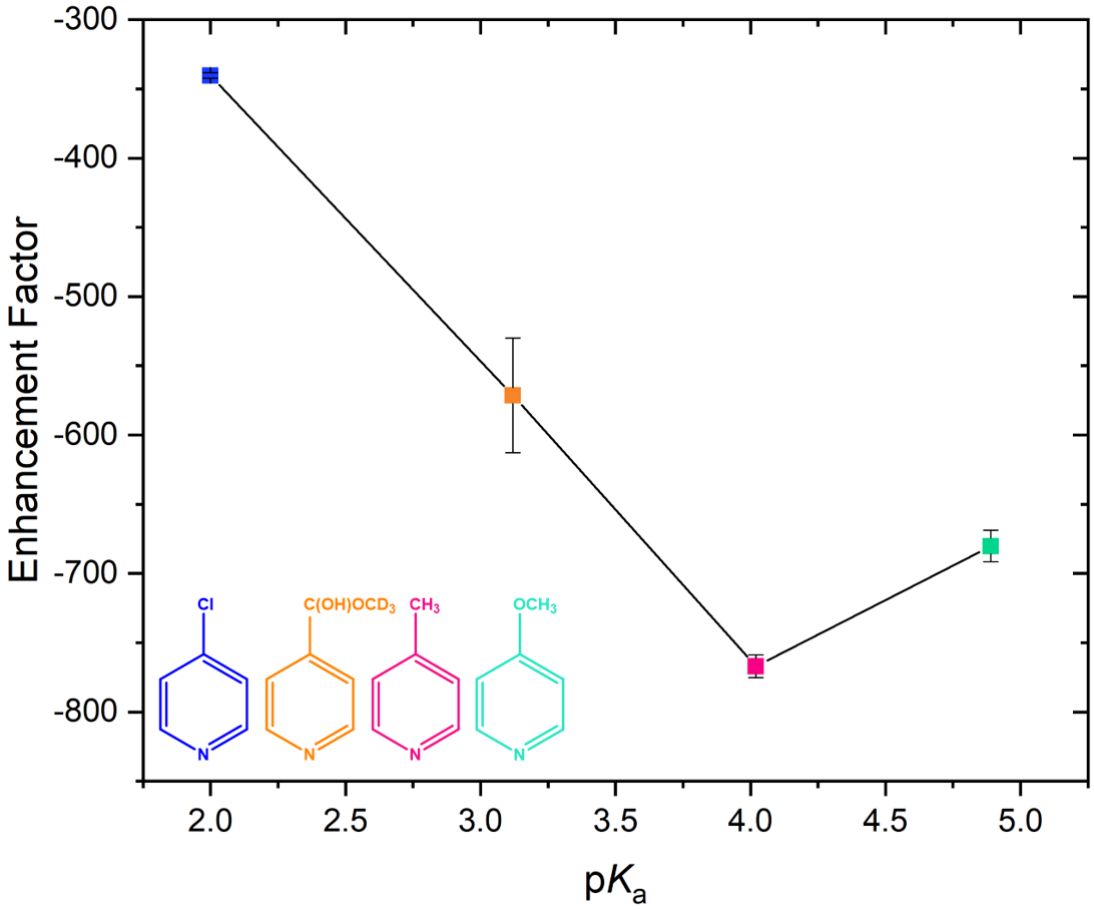

Figure 63 – Enhancements at the *ortho* proton resonance in the free substrate as a function of substrate p*K*a for the SABRE-active species; $[Ir(H)_2(SIMes)(sub)_3]Cl$ for each of the substrates tested. The enhancements were observed using the manual shaking method. The experiment was repeated five times and the ^1H signal enhancements at the *ortho* proton were averaged. The error bars indicate the standard error of the experiment.

The smallest *ortho* signal enhancement of −340 ± 2-fold was observed for the SABRE complex containing 4-chloropyridine. As this substrate has the lowest (and most acidic) pK_a value of 2.00 it is assumed that 4-chloropyridine weakly associates to the iridium centre. This means that a lesser amount of polarisation is transferred to the substrate before it dissociates into solution, allowing a non-hyperpolarised substrate from the excess solution to bind for subsequent polarisation transfer. The substrate with the highest (most basic) pK_a, 4-methoxypyridine yielded an enhancement of −680 ± 11-fold. In this case, it is predicted that 4-methoxypyridine forms much stronger associations to the metal centre. Association to iridium promotes relaxation, meaning that any hyperpolarisation transferred is lost before the substrate ligand dissociated into solution.[15] 4-Methylpyridine yielded the largest enhancement of −767 ± 8-fold. It seems that in this case, the substrate is bound in

such a way to allow for sufficient polarisation transfer before dissociation. Furthermore, the binding does not allow for the polarisation to be destroyed via relaxation.

3.3.2.1 Effect of Catalyst Deuteration at the NHC

Deuterating the NHC on the iridium catalyst has been seen to significantly improve SABRE enhancements of nicotinamide (and ^{2}H-labelled analogues),[15] pyrazinamide and isoniazid.[22] In 2017, Rayner *et al*.[15] reported a 250% increase in enhancement factor for a deuterated isotopologue of nicotinamide (methyl-4,6-d_2-nicotnate) when d_{22}-IMes was used, corresponding to enhancements of −7712-fold (at H-2) and −6368-fold (at H-5). d_{22}-IMes was also seen to extend the T_1 value by 21% for each proton in methyl-4,6-d_2-nicotnate compared to non-deuterated IMes. The fully deuterated analogue; d_{24}-IMes was also assessed, however this led to smaller increases in both T_1 (12% increase at both H-2 and H-5) and enhancement (−5952-fold for H-2 and −5280-fold for H-5). The difference between these two isotopologues is the deuteration of the imidazolydine backbone (Figure 64). This modification to the deuterated analogue (d_{24}-IMes) is thought to lead to a much smaller resonance condition for polarisation transfer to occur. As the SABRE experiments were performed using the manual shaking method using the stray field of the spectrometer, it was difficult to maintain an exact polarisation transfer field and henceforth magnetism transfer from *p*-H_2 to the substrate was inefficient, leading to smaller enhancements.

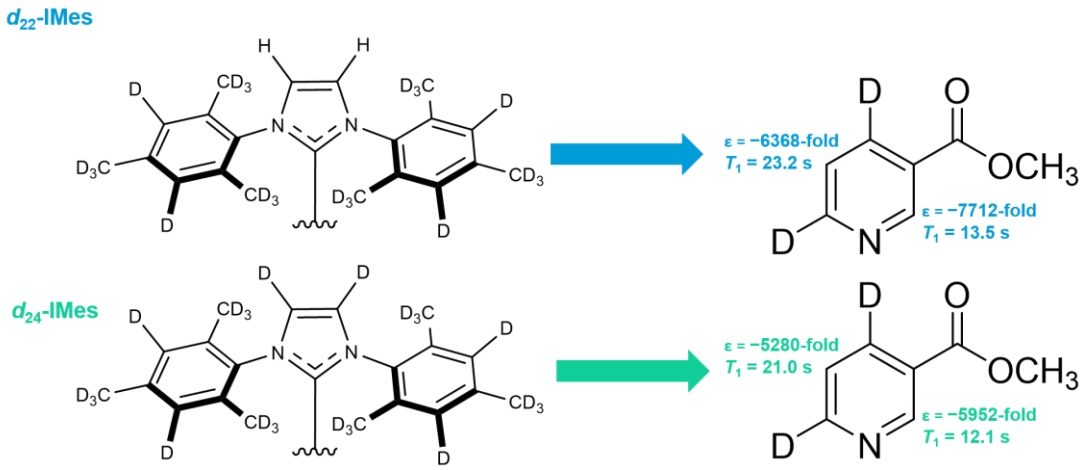

Figure 64 – Structures for deuterated isotopologue of IMes. Image adapted from Rayner *et al*. *Proceedings of the National Academy of Sciences*, 2017.

Norcott *et al*.[22] also used d_{22}-IMes to improve the SABRE efficiency for a number of tuberculosis drug scaffolds. They observed a −4200-fold enhancement for a partially deuterated isotopologue of pyrazinamide which corresponds to a 10% increase in enhancement factor compared to the non-deuterated form of IMes. Furthermore, they noted an 11% increase in the T_1 value for d_{22}-IMes compared to IMes.

Based on this research, it was thought that using the deuterated isotopologue of SIMes (d_{22}-SIMes) would also result in larger SABRE enhancements and longer T_1 values (see Section 3.6.2 Relaxation Effects in $[Ir(H)_2(SIMes)(sub)_3]Cl$, Deuteration of the NHC).

The SABRE enhancements were measured using the manual shaking method using the stray field of the spectrometer described in Chapter 2.2.

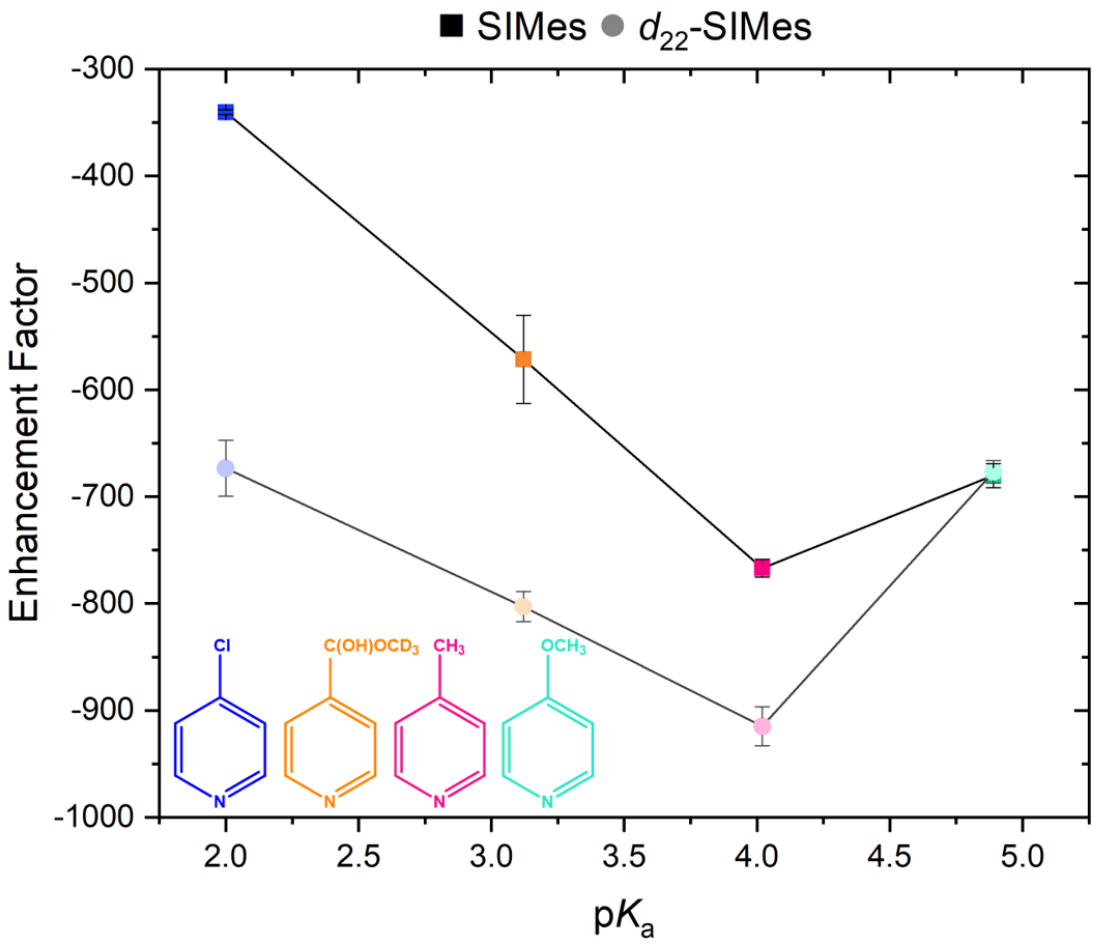

Figure 65 – Enhancements at the *ortho* proton resonance in the free substrate as a function of substrate pK_a for the SABRE-active species for the four substrates. SIMes is indicated by the darker colour and d_{22}-SIMes by the lighter colour. The enhancements were observed using the manual shaking method. The experiment was repeated five times and the ^{1}H signal enhancements at the *ortho* proton were averaged. The error bars indicate the standard error of the experiment.

The SABRE signal enhancements for both the deuterated SIMes and non-deuterated SIMes are shown in Figure 65. These data points show that using the d_{22}-SIMes catalyst results in much larger enhancements for the 4-chloropyridine, 4-methylpyridine and 4-pyridinecarboxaldehyde. The largest increase of 50% was observed for 4-chloropyridine compared to 29% for 4-pyridinecarboxaldehyde and 16% for 4-methylpyridine. The enhancements for d_{22}-SIMes follow a similar trend to those with SIMes, as the largest enhancement was achieved with 4-methylpyridine (−915 ± 18-fold). However, with the deuterated form the next largest enhancement was observed for 4-pyridinecarboxaldehyde (−803 ± 14-fold) compared to 4-methoxypyridine (−677 ± 10-fold). Furthermore, the difference induced by using the d_{22}-SIMes was negligible for 4-methoxypyridine.

3.4 Chemical Exchange in $[Ir(H)_2(SIMes)(sub)_3]Cl$

In SABRE, the strength of the substrate-iridium association contributes towards how much hyperpolarised substrate lies in the solution and therefore the level of signal enhancement. The rate at which the substrate dissociates from the metal centre can be measured using NMR exchange spectroscopy (EXSY) (see Chapter6, Section 6.2.7 Exchange Spectroscopy).[23]

According to the Arrhenius equation (Equation 15), the exchange rate (k) is dependent on temperature. At high temperatures, exchange occurs rapidly whereas at lower temperatures, rate of exchange is much slower.

$$k = Ae^{\frac{-Ea}{RT}}$$

Equation 15 – The Arrhenius Equation, where k = rate of exchange, E_a = activation energy, R = universal gas constant and T = temperature.

Because of this, the rate of dissociation (k_d) was measured at different temperatures, the range of which was dependent on the substrate under investigation. For example, observable substrate dissociation can be monitored from 255-295K for 4-methylpyridine compared to 250-300K for 4-pyridinecarboxaldehyde. Outside of these ranges, substrate dissociation was not observed within the timescale of the EXSY experiment. The dissociation constant calculated for all substrates has been plotted against the temperature (see Figure 66).

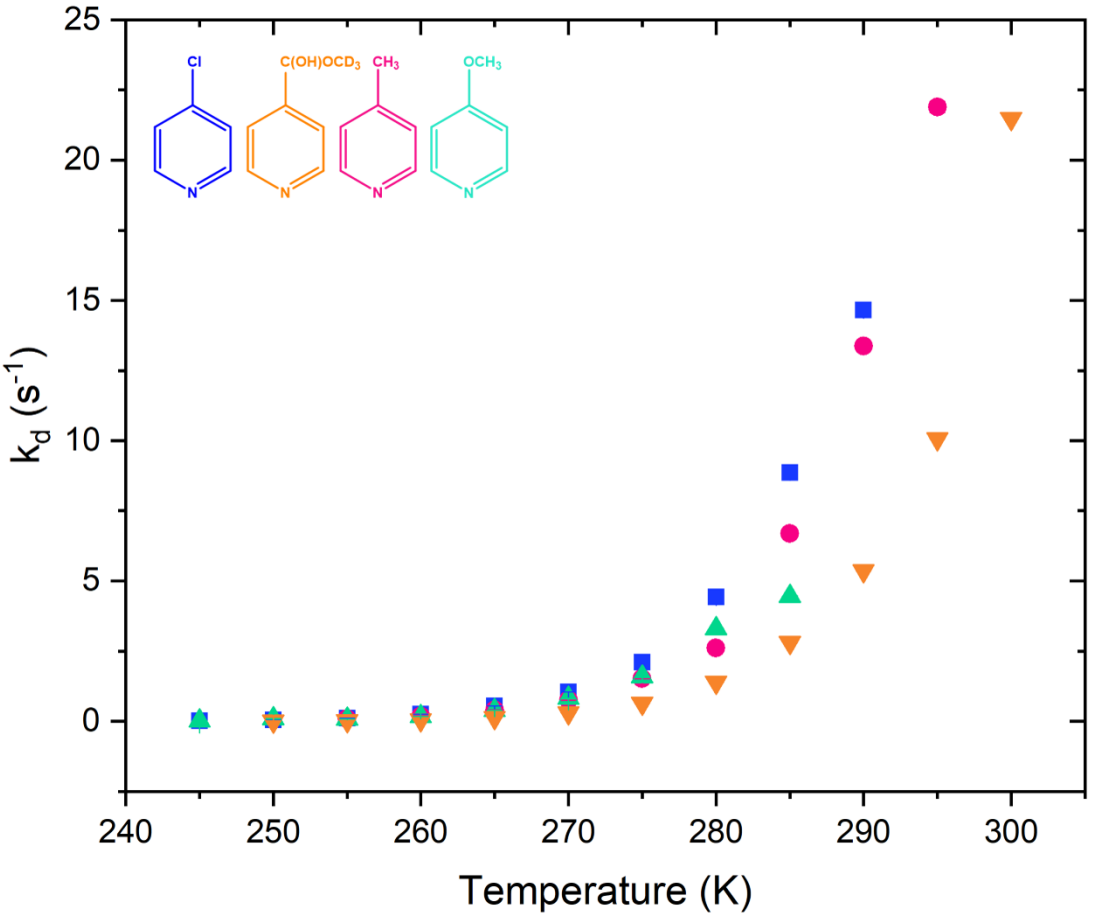

Figure 66 – The dissociation constant (k_d) as a function of temperature for the SABRE active species for each of the substrates shown. The error bars indicate the error associated with k_d calculated using the Jacknife method described in Chapter 6, Section 6.2.7.2 Associated errors in the calculation of k_d. A table of the associated errors can be found in Appendix B.

Figure 66 illustrates the exchange rates at different temperatures for each of the substrates. It clearly shows that the exchange rate increases with temperature regardless of the substrate used. 4-chloropyridine has the fastest exchange rate of 8.88 ± 4.42 × 10^{-4} s^{-1} at 285 K, compared to 2.80 ± 2.05 × 10^{-4} s^{-1} for 4-pyridinecarboxaldehyde, 6.69 ± 3.67 × 10^{-3} s^{-1} for 4-methylpyridine and 4.46 ± 1.23 × 10^{-2} s^{-1} for 4-methoxypyridine. As 4-chloropyridine has the lowest pK_a (2.00) out of the three substrates, it was hypothesised that this substrate would form weaker associations to the metal centre and therefore exchange on a much faster timescale compared to the other three substrates. It was expected that the rate of dissociation would become slower as the substrate pK_a increased, however 4-pyridinecarboxaldehyde (pKa = 3.12) has the slowest rate of dissociation. This suggests that 4-pyridinecarboxaldehyde has the strongest association to the metal

centre in the SABRE-active catalyst out of all the substrates in the series. This theory can be explored in more detail if the Gibbs free energy of dissociation is calculated which allows us to understand the binding potential between the substrate and the metal centre more confidently.

3.4.1 Using the Rate of Substrate Dissociation to Determine the Gibbs Free Energy

The Gibbs free energy of dissociation ($\Delta G^{\neq}_{d}$) can be used to define the strength of the association between the substrate and the metal centre. For example, as 4-chloropyridine has been shown to dissociate from the metal centre faster than the other substrates (Figure 66), it was assumed that its corresponding $\Delta G^{\neq}_{d}$ value would be the lowest.

In order to determine $\Delta G^{\neq}_{d}$, the enthalpy ($\Delta H^{\neq}_{d}$) and entropy ($\Delta S^{\neq}_{d}$) of dissociation must first be established (see Chapter 6.2.7.1.1). To do this an Eyring plot of $\frac{1}{T}$ against $\ln\frac{k}{T}$ was generated (Figure 67). From this, the enthalpy can be determined from the gradient: $\left(-\frac{\Delta H^{\neq}}{R}\right)$ and the entropy from the intercept: $\ln\left(\frac{k_B}{h}+\frac{\Delta S^{\neq}}{R}\right)$. The results of these calculations are shown in Table 6.

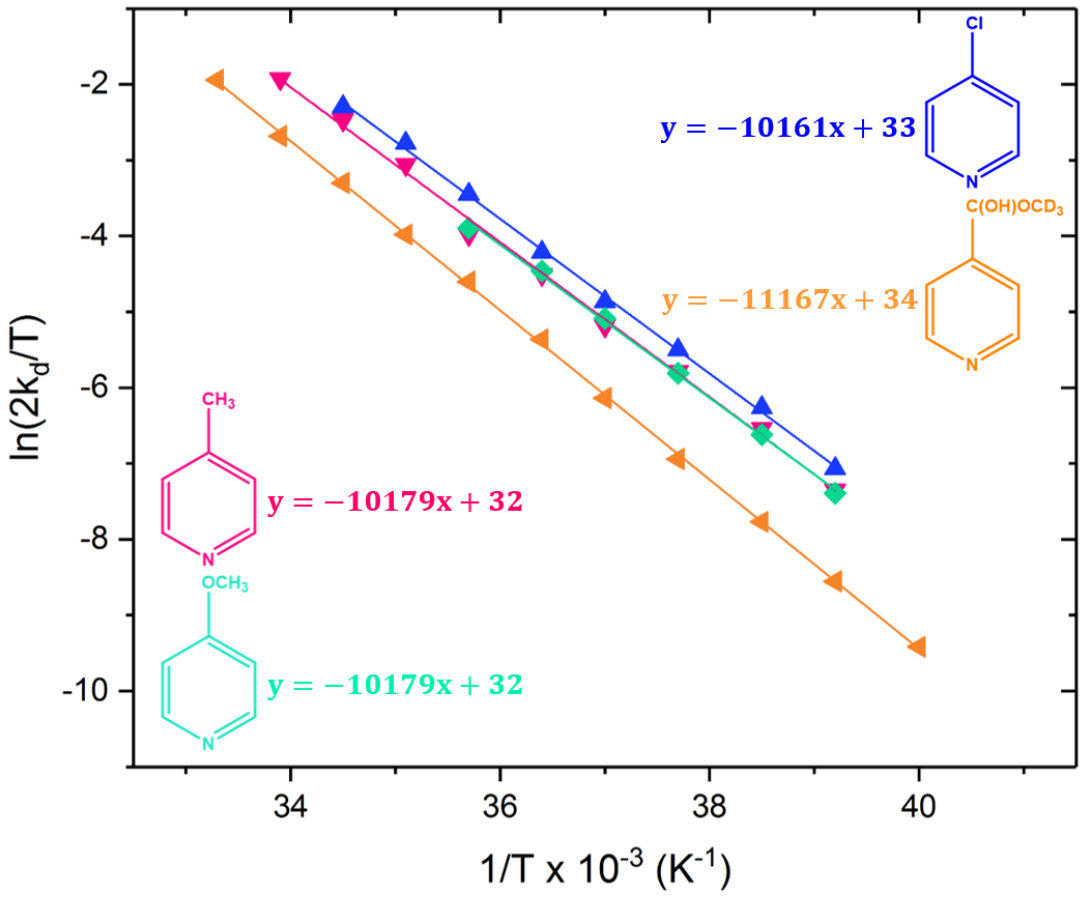

Figure 67 – Eyring-Polanyi plot for the three substrates where ln(k_d/T) is plotted against 1/T. The data have been fitted according to the equation y = mx + c. These are indicated on the graph alongside the corresponding substrate.

***p*-substituent**	**Cl**	**CHO**	**CH_3**	**OCH_3**
pK_a	2.00	3.12	4.02	4.89
$\Delta H^{\neq}$ (kJmol^{-1})	84.48 ± 2.57	92.84 ± 1.06	84.63 ± 3.59	83.93 ± 4.79
$\Delta S^{\neq}$ (JK^{-1}mol^{-1})	75.18 ± 9.45	95.30 ± 3.86	73.18 ± 13.09	70.42 ± 17.93
$\Delta G^{\neq}_{298K}$ (kJmol^{-1})	62.08 ± 0.01	64.44 ± 0.01	62.82 ± 0.01	62.94 ± 0.01

Table 6 – Calculated enthalpy and entropy of dissociation ($\Delta H^{\neq}$ & $\Delta S^{\neq}$) for the four substrates. $\Delta H^{\neq}$ is calculated from the gradient (m) and $\Delta S^{\neq}$ is calculated from the intercept (c) using the straight-line equations shown in Figure 59 above. $\Delta H^{\neq}$ & $\Delta S^{\neq}$ weresubsequently used to calculate the Gibbs free energy of dissociation. The calculations for the errors in $\Delta H^{\neq}$, $\Delta S^{\neq}$ & $\Delta G^{\neq}$ are explained in Chapter 6, Section 6.2.7.3 Calculation of Gibbs free energy and associated errors.

The enthalpy ($\Delta H^{\neq}$) of this process reflects the bond strength of the catalyst. Table 6 shows that the $\Delta H^{\neq}$ value does not link directly to the pK_a of the substrate. For example, 4-methoxypyridine has the lowest $\Delta H^{\neq}$ value of 83.93 ± 4.79 kJmol^{-1} compared to 4-pyridinecarboxaldehyde which has the highest value of 92.84 ± 1.06 kJmol^{-1}. This suggests that 4-pyridinecarboxaldehyde forms the strongest bond to the iridium catalyst and 4-methoxypyridine the weakest. The entropy ($\Delta S^{\neq}$) indicates the level of disorder or freedom on approaching the transition state in the catalyst for ligand dissociation. The data for $\Delta S^{\neq}$ follows a similar pattern to the $\Delta H^{\neq}$ values, where 4-methoxypyridine has the lowest value of $\Delta S^{\neq}$ (70.42 ± 17.93 JK^{-1}mol^{-1}) and 4-pyridinecarboxaldehyde has the highest $\Delta S^{\neq}$ value (95.30 ± 3.86 JK^{-1}mol^{-1}). These positive values confirm the dissociative nature of this process but are linked to solvation and the original bond length. The longer this bond, the greater the level of initial freedom and consequently the smaller the gain on reaching the loss point. This implies that 4-pyridinecarboxaldehyde gains the most freedom, compared to the other substrates, upon dissociation.

The Gibbs free energy for ligand loss was calculated at 298 K using the $\Delta H^{\neq}$ and $\Delta S^{\neq}$ values of Table 6 according to Equation 16.

$$\Delta G^{\neq} = \Delta H^{\neq} - T\Delta S^{\neq}$$

Equation 16

These $\Delta G^{\neq}$ values were then plotted as a function of substrate p*K*a as detailed in Figure 68. It was expected that higher substrate pK_a would result in higher values of $\Delta G^{\neq}_{298K}$ as the Ir-N(sub) bond is stronger and therefore more thermodynamic energy is required for dissociation to occur. Conversely, the lower the pK_a, the weaker the Ir-N(sub) bond and therefore the lower the $\Delta G^{\neq}_{298K}$. The experimental results are shown in Figure 68.

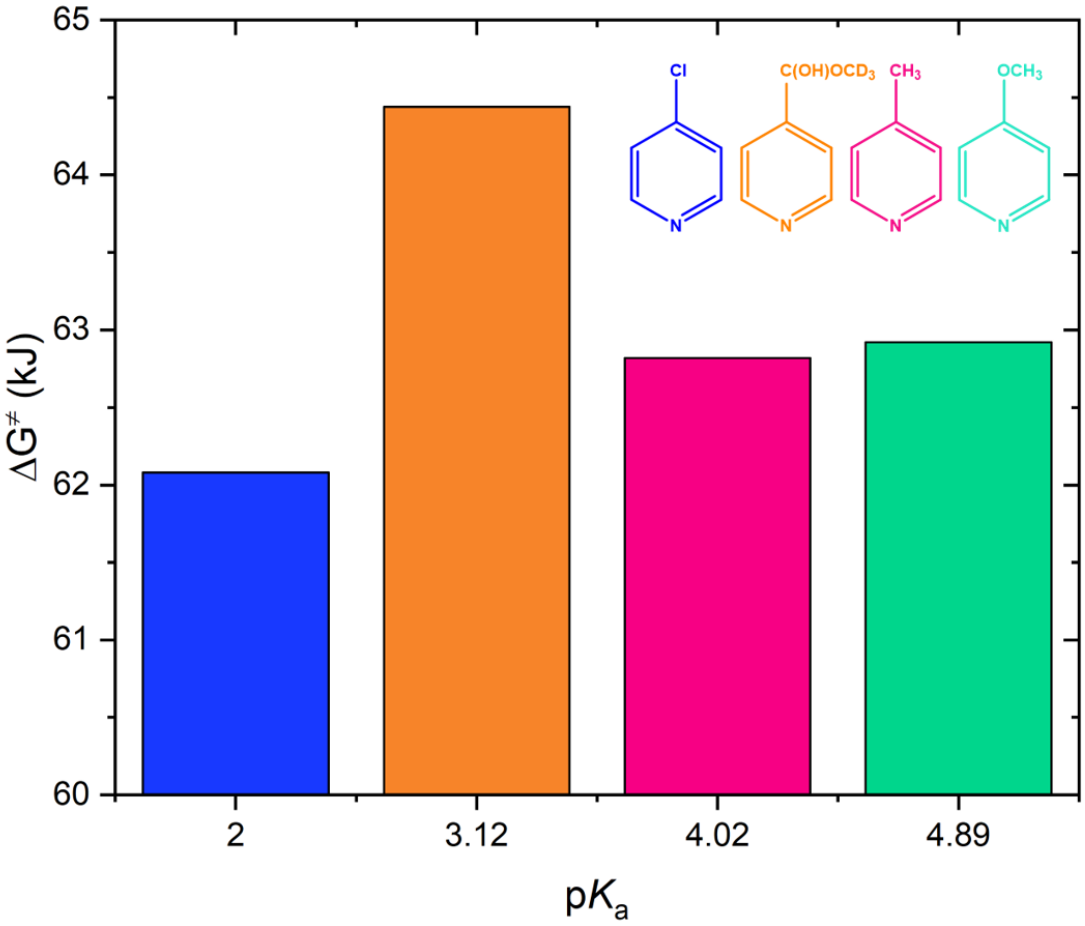

Figure 68 – Gibbs free energy ($\Delta G^{\neq}_{298K}$) as a function of the substrate pK_a for the SABRE-active species for the substrates shown.

According to Figure 68 4-chloropyridine has the lowest value of $\Delta G^{\neq}$ (62.08 kJ) while 4-pyridinecarboxaldehyde has the highest (64.44 kJ) but there is no clear link to pK_a. These data confirm the rate of exchange is much slower for 4-pyridinecarboxaldehyde compared to the other substrates. If p*K*a were the true indicator 4-methoxypyridine would have the highest $\Delta G^{\neq}_{298K}$ value. However, the stronger associations observed with 4-pyridinecarboxaldehyde may result from the fact that the hemiacetal group is an electron withdrawing group. Consequently, it removes electron density from the π-system of the pyridine ring, therefore, to stabilise the interaction between the metal and the ligand, π-back donation occurs from the metal centre to the pyridine ligand. This is usually observed by short M-L bond distances as reported by Palusiak *et al.*[4] and Malecki *et al.*[24] Therefore it is important to note that π-effects are an important consideration of bonding which is not revealed through pK_a. It would appear however that the expected progression in

entropy effects confirm that all of these substrates exhibit similar steric behaviour and that solvation differences are insignificant.

3.4.1.1 Optimum Rate of Dissociation for SABRE

In 2011, Cowley *et al*.[25] investigated the thermodynamic and kinetic behaviour of the SABRE-active species $[Ir(H)_2(IMes)(pyridine)_3]Cl$. They analysed the SABRE efficiency at different temperatures and noted that warming of the sample to 318 K reduced the signal enhancement. They measured the exchange rate for pyridine to be ~11.4 s^{-1} at 298 K. In 2014, Lloyd *et al*.[26] conducted a study into NHC effects where they also explored chemical exchange in the SABRE active species for a number of different NHC ligands. As part of this study, they explored the effect of temperature on SABRE efficiencies which they correlated to their respective rates of substrate dissociation. In 2016, Barskiy *et al.*[27] used computational methods to calculate an optimum dissociation rate for SABRE, which they found to be 4.5 s^{-1} in systems where J_{AB}-$J_{A'B}$ = 1 Hz (e.g. N-heterocycles such as pyridine). Furthermore, in 2018 Rayner *et al*.[28] compared the SABRE efficiency of a range of iridium catalysts with different NHC ligands. They found that the best performing catalysts exhibited an exchange rate of approximately 4 s^{-1}.

The rates of substrate dissociation for each of the four substrates have been measured at different temperatures (Section 3.4 Exchange in $[Ir(H)_2(SIMes)(sub)_3]Cl$). If SABRE efficiency is optimal at 4.5 s^{-1}, the enhancements of 4-chloropyridine would be larger at 281 K, compared to 288 K for 4-pyridinecarboxaldehyde where their respective k_d values approach the optimal value. Based on this theory, the optimum temperature for SABRE enhancements can be calculated by rearranging the fitting for the k_d curves shown in Section 3.4, Figure 66 (see Table 7).

***p*-substituent**	**Cl**	**CH_3**	**OCH_3**	**CHO**
$\Delta G^{\neq}_{298K}$ ($kJmol^{-1}$)	62.08	62.82	62.94	64.44

pK_a	2.00	4.02	4.89	3.12
$y = Ae^{BX}$	$y = 4\times10^{-13}e^{0.1069x}$	$y = 4\times10^{-17}e^{0.1389x}$	$y = 5\times10^{-17}e^{0.1377x}$	$y = 4\times10^{-19}e^{0.1522x}$
Optimum Temp. (K)	281.1	282.7	285.0	288.2

Table 7 – Optimum temperature calculated from the exponential equations fitted to the rate data in Figure 66 using the optimum rate of 4.5 s^{-1}. Substrates are ordered according to their $\Delta G^{\neq}_{298K}$ values calculated in Table 6

Table 7 compares the optimum temperatures for SABRE catalysis calculated from the optimal exchange rate of 4.5 s^{-1}. The substrates are ordered according to their $\Delta G^{\neq}_{298K}$ values calculated in Table 6 to show that the higher the value of Gibbs Free Energy, the higher the calculated optimum temperature for SABRE efficiency.

In previous studies, the effect of temperature has been investigated using the manual shaking method using the stray field of the spectrometer.[25, 26] However, as previously mentioned (Chapter 2, Section 2.2 The Manual Shaking Method), this method is susceptible to a large number of variables which results in large errors and low reproducibility. Performing a temperature study using this technique involves immersing the sample in a water bath, removing to shake for 10 s and then placing the sample in the spectrometer which is set to the same temperature as the water bath. As the sample is not maintained at the same temperature throughout the experiment, this method is associated with a large random error.

In this experiment, the SABRE efficiency was studied using the highly reproducible, automated flow system described in Chapter 2.3.[29, 30] The flow cell was modified such that the sample chamber was surrounded by a water jacket (Figure 69) connected to a variable temperature water bath which is capable of reaching temperatures between 277-373 K, although this range could be extended using alternative coolants.

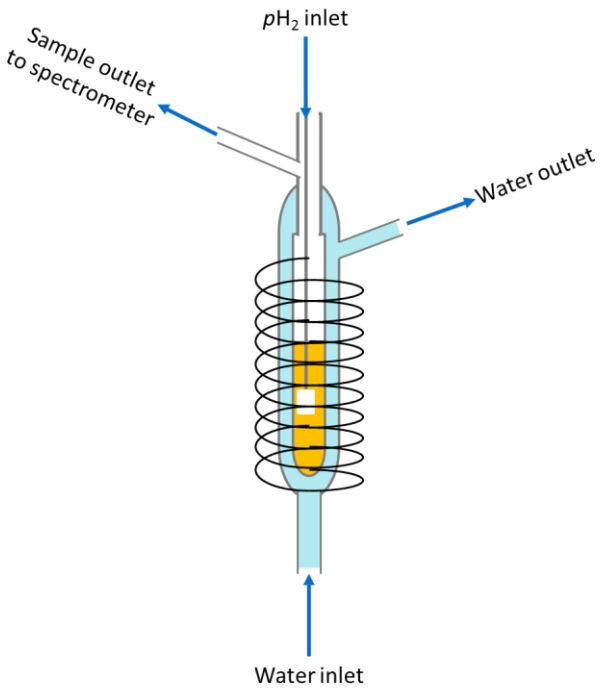

Figure 69 – The modified flow cell used to study the temperature dependence of SABRE

For this experiment, temperatures were measured in 5 K increments over 280-300 K, the data was then empirically fitted using a Gauss distribution curve to predict the optimum temperature for SABRE (Figure 70).

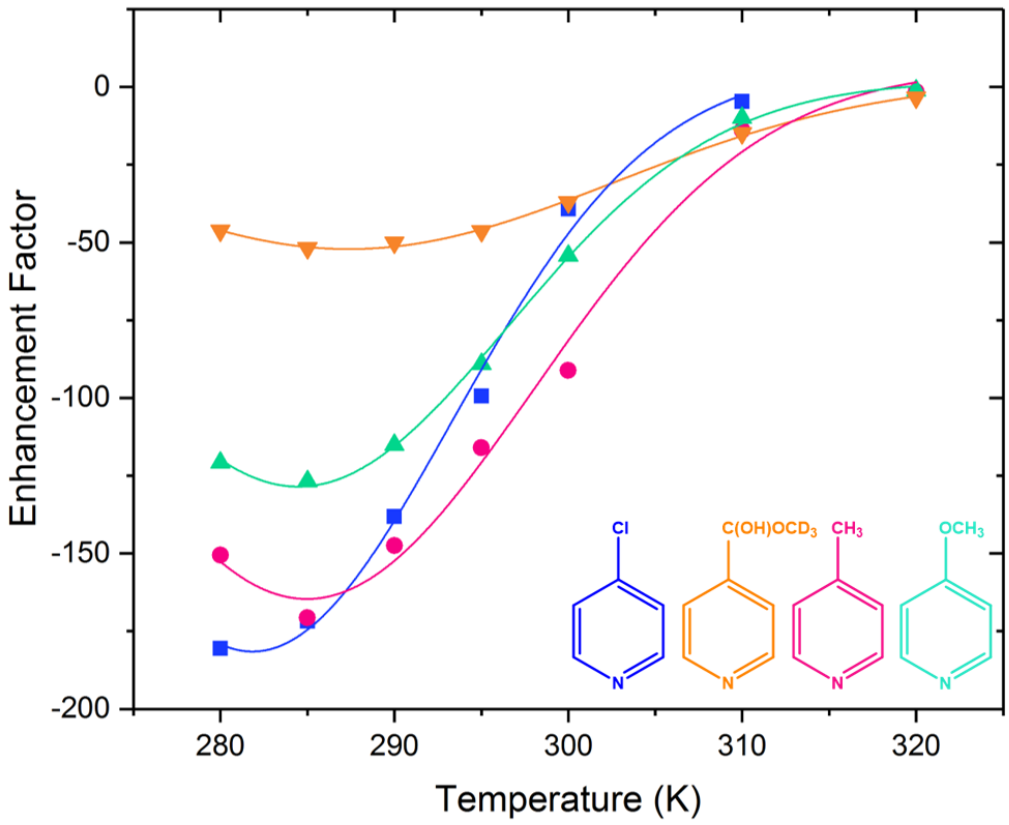

Figure 70 – Enhancement factor plotted as a function of temperature for the SABRE active species for each of the substrates shown.

***p*-substituent**	**Cl**	**CH_3**	**OCH_3**	**CHO**
$\Delta G^{\neq}$	62.08	62.82	62.94	64.44
pK_a	2.00	4.02	4.89	3.12
Predicted Temp from *Table 7* (K)	281.1	282.7	285.0	288.2
Predicted Temp from *Figure 70* (K)	281.8 ± 1.5	285.0 ± 1.2	284.5 ± 0.4	287.4 ± 0.4
Corresponding k_d (s^{-1})	4.86 ± 0.79	6.23 ± 1.01	5.15 ± 0.25	3.96 ± 0.25
Corresponding $\Delta G^{\neq}$ ($kJmol^{-1}$)	63.29 ± 0.01	63.77 ± 0.01	64.31 ± 0.01	65.45 ± 0.01

Table 8 – The optimal temperature for SABRE predicted using an empirical fit to the data shown in Figure 70 and the corresponding kd calculated using the exponential equations shown in Table 7. The errors in the optimum temperature predicted from Figure 70 are calculated from the gaussian fits shown in Figure 70. The error in the corresponding kd is calculated using error propagation. The error in ΔG≠ is calculated using the method described in Chapter 6, Section 6.2.7.3 Calculation of Gibbs free energy and associated errors.

Table 8 shows that the measured temperatures for optimal SABRE efficiency are within 1 K of those predicted using an optimal exchange rate of 4.5 s^{-1} (Table 7) apart from 4-methylpyridine. Furthermore, it is clear that the optimal temperature for SABRE response increases with pK_a. According to the Arrhenius equation (Equation 15), exchange rate is temperature dependent, therefore the higher the temperature, the faster the rate of substrate dissociation. This means that the stronger the iridium-substrate ligation, the higher the temperature required for optimum SABRE efficiency (e.g. 4-pyridinecarboxaldehyde). The optimum temperature could then be used to calculate the corresponding rate of dissociation. For example, for 4-chloropyridine, the maximum enhancement was predicted at occur at 282 K, from the fitting in Figure 70, where the expected rate is 4.86 ± 0.79 s^{-1}. For the other substrates investigated the corresponding maxima were seen at 286 K for 4-methylpyridine, 285 K for 4-methoxypyridine and 287 K for 4-pyridinecarboxaldehyde where the analogous ligand exchange rates are 6.23 ± 1.01 s^{-1} (4-methylpyridine), 5.15 ± 0.25 s^{-1} (4-methoxypyridine) and 3.96 ± 0.25 s^{-1} (4-pyridinecarboxaldehyde). This result strengthens the hypothesis that optimum SABRE hyperpolarisation transfer occurs when the exchange rate is around 4-5 s^{-1}, there is also likely to be other factors which affect this number, such as the spin-lattice relaxation values. Whilst these values are all close in range to the predicted 4.5 s^{-1} they are statistically different from one another.

If the $\Delta G^{\neq}$ values are considered at these temperatures, they can be plotted against the associated enhancement values and compared to those at 298 K (see Section 3.4.1).

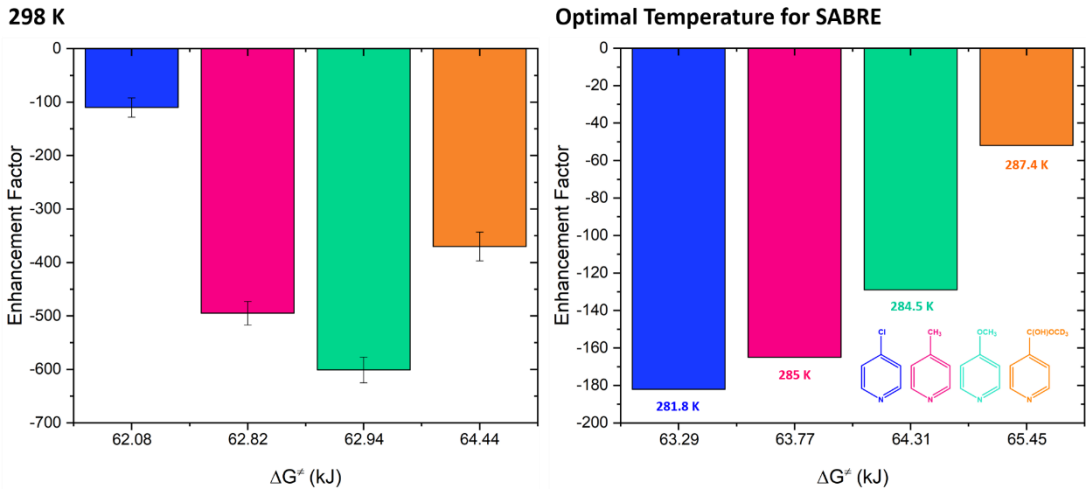

Figure 71 - Enhancement plotted as a function of the ΔG≠ value at 298 K using the manual shaking method (left) and the optimum temperature for SABRE using the automated flow system (right)

Figure 71 shows that the highest SABRE response was detected for 4-chloropyridine at the optimal SABRE temperature. The corresponding ΔG≠ value for this substrate is 63.29 kJ. At 298 K, the largest enhancement is observed for 4-methoxypyridine where the associated ΔG≠ value is 62.94 kJ. This suggests that SABRE enhancements are largely controlled by the strength of the ligation between the substrate and the iridium in the SABRE active catalyst. Furthermore, it appears that, for the substrates tested in this chapter, this ligation is optimal when the ΔG≠ value is between 62.94 and 63.29 kJ.

3.5 Measuring the Pseudo $^4J_{HH}$ Coupling in $[Ir(H)_2(SIMes)(sub)_3]Cl$

A further indication of the strength of the iridium-substrate ligation is the pseudo transfer coupling constant. Stronger ligations are usually indicated by stronger coupling constants between the *p*-H_2 derived hydride ligands and the substrate protons.

As described previously (Chapter 1, Section 1.5.1.2 Mechanism of Polarisation Transfer), polarisation is transferred via the *J*-coupled network between the hydride and substrate ligands within the equatorial plane.[31] This occurs in the first instance as the H-H scalar coupling between the hydride ligands determines the position of

the level anti-crossing (LAC) point.[32] This is the magnetic field at which maximum polarisation transfer occurs between the hydrides and the substrate protons. In SABRE, this transfer occurs at a low magnetic field, typically 60 G.[27] Polarisation transfer is driven by the long-range hydride-substrate couplings within the iridium complex.

The rate of polarisation transfer is associated with the creation of spin-order on the substrate. This is linked to $1/2J_{HH}$, which corresponds to the coupling between the hydride and the polarisation receptor (substrate). In 2016 Eshuis *et al*.[33] suggested that the hydride-substrate $^4J_{HH}$ coupling is 1.2 Hz in pyridine-like substrates. These measurements were conducted on complexes containing inequivalent hydrides and therefore the spin system is described as AX_2. Recently, Barskiy *et al*.[34] proposed that this coupling is usually below 1 Hz, whilst the coupling between the two hydrides is on the order of 5-10 Hz. For complexes of the type $[Ir(H)_2(SIMes)(sub)_3]Cl$ as used here, the spin system is actually of the $[AX_2]_2$ and hence the determination of $^4J_{HH}$ less appropriate. Nonetheless, the build-up of polarisation through transfer between the hydride and substrate protons can be monitored for these complexes, in this section, we will refer to these measurements as the pseudo $^4J_{HH}$ coupling constant.

The pseudo transfer coupling constants were measured using a series of selective 1D-COSY experiments conducted at high field and low temperature in order to quantify the corresponding oscillation frequency. This method has previously been described by Rayner *et al*.[28] where the hydride resonance in the SABRE-active species $[Ir(H)_2(SIMes)(sub)_3]Cl$ is selectively excited using the pulse sequence shown in Figure 72.

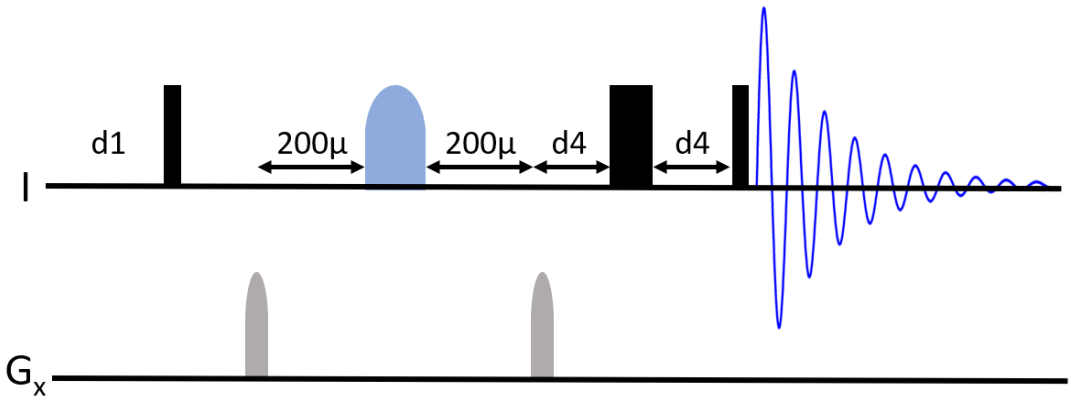

Figure 72 - Pulse sequence for the selective 1D-COSY experiment. Adapted with permissions from P. J. Rayner et *al*. [28]

The delay constant (d_4) was varied over 15 increments between 0.0078 and 0.021 s. The relative integral values at the *ortho* proton in the equatorially bound substrate were plotted and fitted according to a sine function to give the delay constant maxima. An example of this is shown in Figure 73 for the substrate 4-methylpyridine.

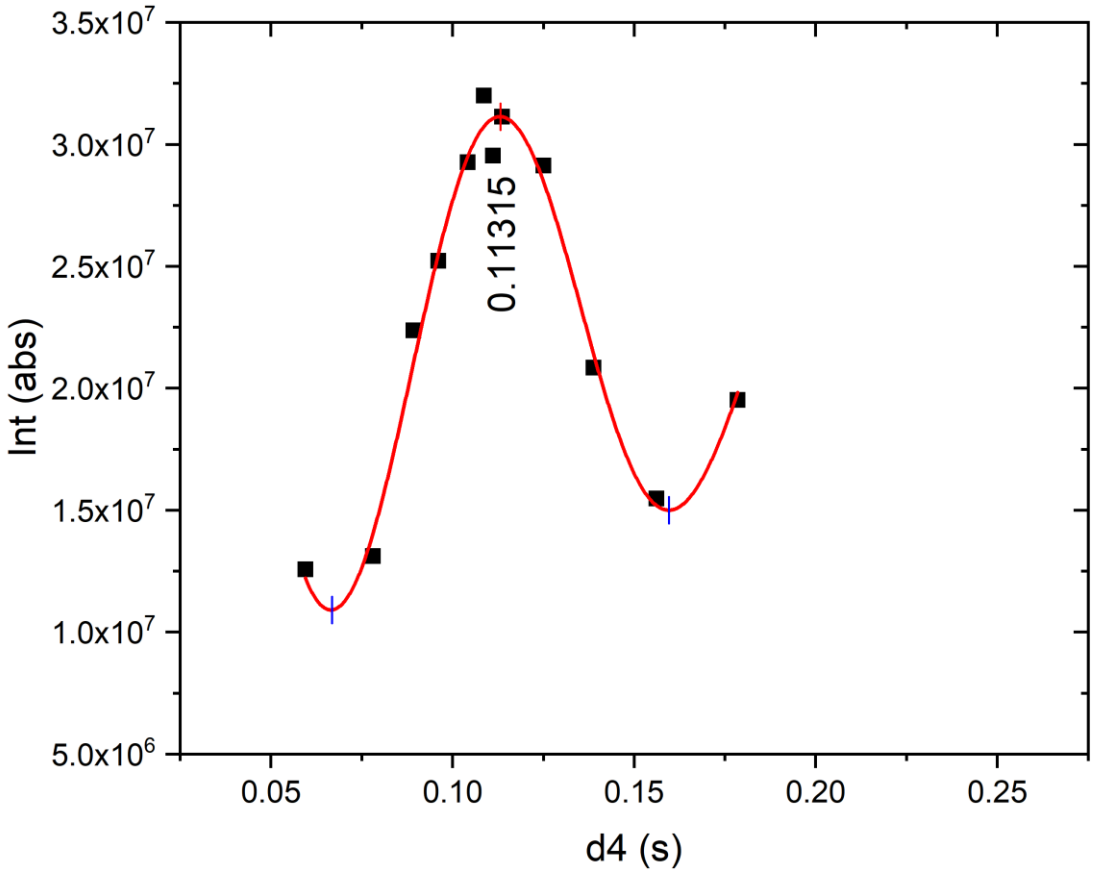

Figure 73 - the relative integral of the *ortho* proton in the equatorially bound substrate as a function of the delay time (d4). The data has been fitted to a sine function and the oscillation maxima has been indicated. The example shown is for $[Ir(H)_2(SIMes)(4\text{-methylpyridine})_3]Cl$.

The pseudo-transfer coupling was then calculated by taking the reciprocal of the delay constant maxima and multiplying this by two. For the example shown in in Figure 73, this corresponds to a pseudo-transfer coupling of 1.11 Hz. This effective coupling has been calculated for each of the substrates discussed in this chapter and the values are shown in Table 9.

***p*-substituent**	**Cl**	**CH_3**	**OCH_3**	**CHO**
$\Delta G^{\neq}_{298K}$ (kJmol^{-1})	62.08	62.82	62.94	64.44
pK_a	2.00	4.02	4.89	3.12
Pseudo Transfer Coupling (Hz)	1.05	1.11	1.24	1.38

Table 9 - Table comparing the $^4J_{HH}$ values to the corresponding $\Delta G^{\neq}_{298K}$ and pK_a values of the substrate

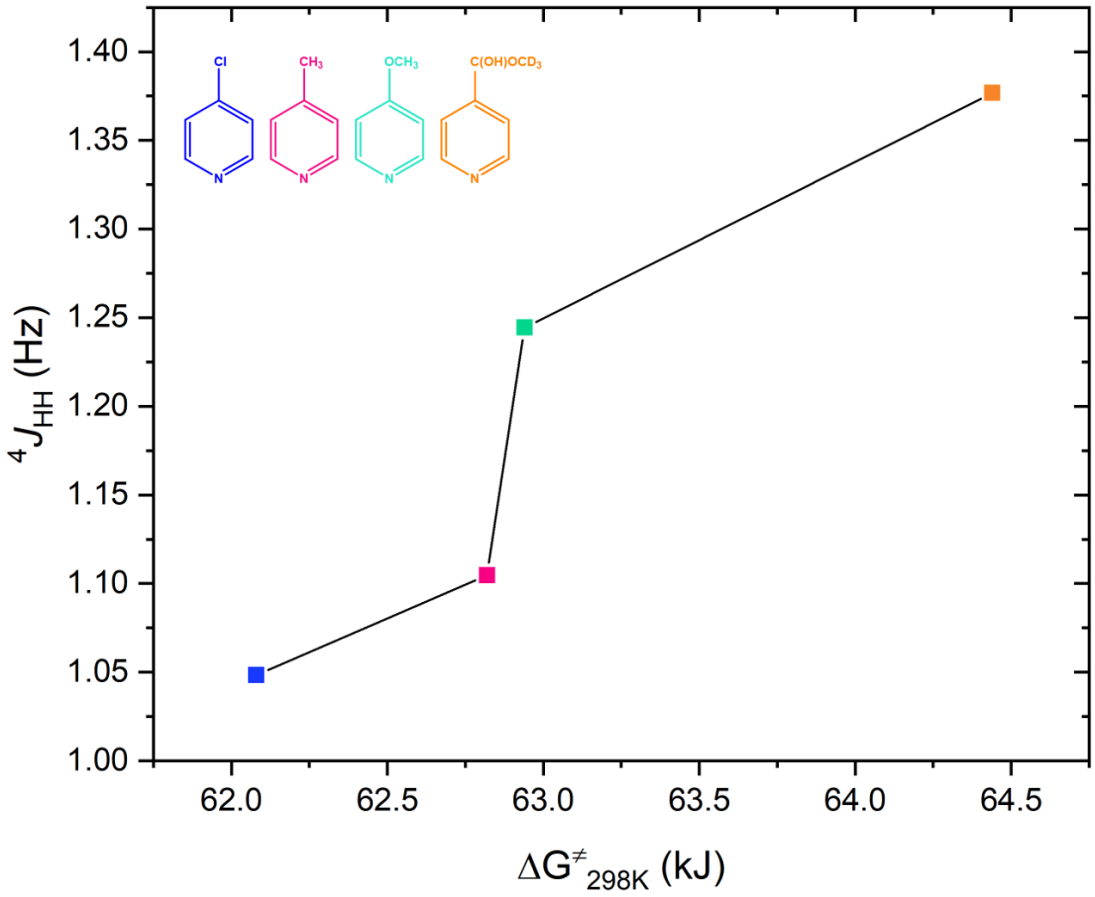

Figure 74 - The long range hydride-substrate coupling, $^4J_{HH}$, as a function of the Gibbs free energy ($\Delta G^{\neq}_{298K}$) for each of the substrates indited

Figure 74 displays the pseudo-transfer coupling constants as a function of the $\Delta G^{\neq}_{298K}$ values calculated in the previous section. The stronger the substrate-iridium ligation, the larger the value of pseudo-transfer coupling. For example, 4-pyridinecarboxaldehyde has the largest value of $\Delta G^{\neq}_{298K}$ at 64.44 kJ and the largest corresponding value of $^4J_{HH}$ of 1.38 Hz. The larger this pseudo hydride-substrate coupling, the more efficient the polarisation transfer into the substrate. However, the enhancements shown in Figure 63, show that whilst 4-pyridinecarboxaldehyde has the largest $^4J_{HH}$ value, it yields an enhancement of −571 ± 41-fold. This compares to 4-methylpyridine which yields the largest enhancement of −767 ± 8-fold but has a transfer coupling constant of 1.11 Hz. This information suggests that another effect such as relaxation must be an important consideration of SABRE efficiency.

These calculated values are comparable to those suggested by Eshuis and Barskiy above.[33, 34] However, the delay maxima values are similar to those measured by

Rayner *et al*.[28] where a maxima of 0.116 s was quoted for the SABRE-active species [Ir(H)$_2$(IMes)(methyl-4,6-d_2-nicotinate)$_3$]Cl. This corresponds to a $^4J_{HH}$ value of 1.07 Hz, which is similar to those found in Table 9.

3.6 Relaxation Effects [Ir(H)$_2$(SIMes)(sub)$_3$]Cl

As described previously in Chapter 1 (Section 1.5.6 Relaxation Effects in the SABRE-Active Species), ligation to iridium promotes relaxation. Therefore, the T_1 relaxation value can indicate the strength of the iridium-substrate ligation. It is hypothesised that the stronger the substrate associates to the metal centre, the faster the rate of relaxation and therefore smaller the T_1 value.

3.6.1 T_1 and Hyperpolarised T_1 Measurements

T_1 and hyperpolarised T_1 measurements were collected according to the methods described in Chapter 6, Section 6.2.7.2.1 T_1 Relaxation Measurements. These values were calculated at both the *ortho* and *meta* protons for each of the three substrates previously discussed in this section at 298 K. However, only the T_1 values at the *ortho* protons are discussed as this resonance exhibits higher enhancement levels and receives more direct polarisation. In order to prove that ligation to the metal promotes relaxation, the T_1s for the free substrate in solution have been compared

to those bound *trans* to the NHC and *trans* to the hydride in the SABRE-active complex (Figure 75).

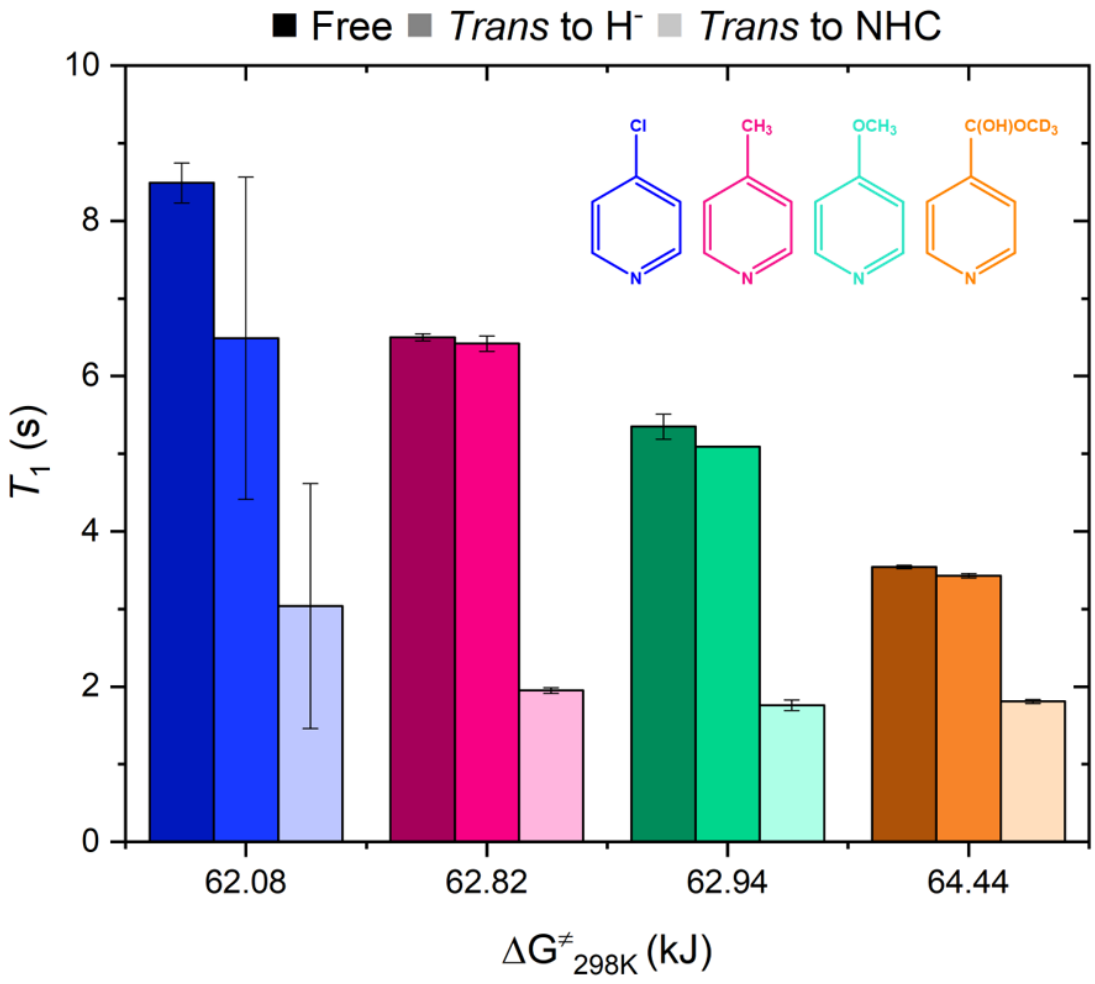

Figure 75 – T_1 as a function of $\Delta G^{\neq}_{298K}$ for the SABRE active species for the substrates shown. The graph shows the T_1 at the *ortho*-proton in the free material (dark colour) compared to the *ortho*-proton in the substrate bound *trans* to the hydride (medium colour) and the *ortho*-proton in the substrate bound *trans* to the NHC (light colour). The error bars indicate the fitting error for the T_1 curves shown in Appendix B.

***p*-substituent**	**Cl**	**CH_3**	**OCH_3**	**CHO**
$\Delta G^{\neq}_{298K}$	62.08	62.82	62.94	64.44
pK_a	2.00	4.02	4.89	3.12
HyperT_1 (s)	8.86	7.70	5.60	4.85
Free$_{(cat)}$ T_1(s)	8.49 ± 0.26	6.50 ± 0.04	5.35 ± 0.16	3.54 ± 0.02
Trans to H$^-$ T_1 (s)	6.49 ± 2.08	6.42 ± 0.10	5.09	3.43 ± 1.58
Trans to NHC T_1 (s)	3.04 ± 1.58	1.95 ± 0.04	1.76 ± 0.07	1.81 ± 0.03

Table 10 – Comparison of the T_1 and Hyperpolarised T_1 values at the *ortho* proton for each of the four substrates. The errors in the T_1 values are calculated from fitting the T_1 curves shown in Appendix B.

As predicted, Figure 75 demonstrates that as the substrate $\Delta G^{\neq}_{298K}$ increases, the T_1 value decreases due to longer residence times on the catalyst. This contributes to the lower ^1H enhancements shown in Figure 63 for 4-pyridinecarboxaldehyde compared to 4-methylpyridine and 4-methoxypyridine. The T_1 values of the substrate bound *trans* to the NHC are shown to be shorter than those of the equatorially bound substrate (*trans* to hydride). This is due to the strong iridium-substrate ligation with does not exchange on the timescale of the T_1 NMR experiment.[14, 15] The T_1 values of the equatorial substrate bound *trans* to hydride are similar to those of the free substrate as they exchange with one another, meaning they are a weighted average.[26, 29, 35]

3.6.2 Effect of Catalyst Deuteration atthe NHC

The use of deuterated NHCs has been shown to decrease the rate of relaxation, and thus increase the T_1 value (see Section 3.3.2.1 SABRE Enhancements in $[Ir(H)_2(SIMes)(sub)_3]Cl$, Effect of Catalyst Deuteration at the NHC),[15, 22] therefore the T_1 values for d_{22}-SIMes were also measured and compared to the non-deuterated NHC.

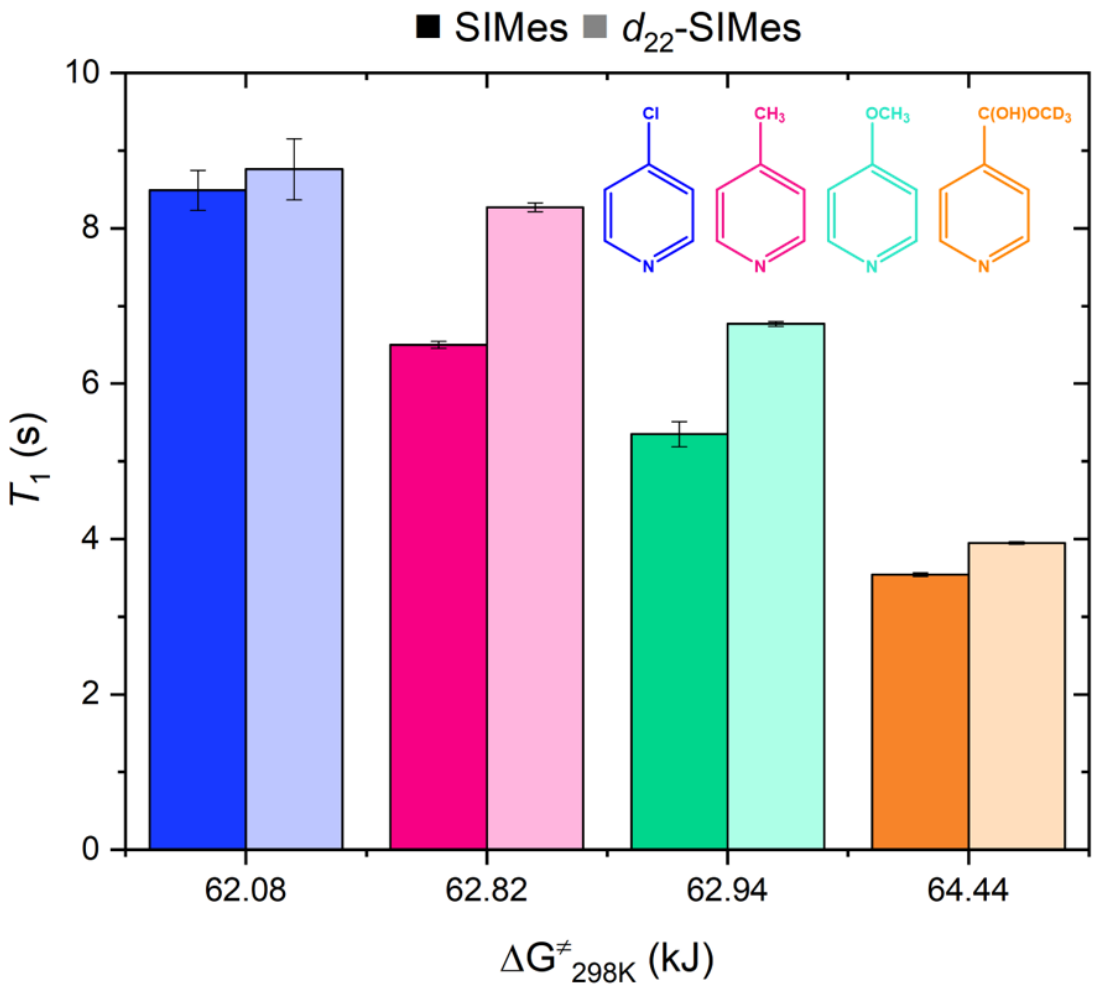

Figure 76 – T_1 as a function of $\Delta G^{\neq}_{298K}$ for the SABRE active species, $[Ir(H)_2(SIMes)(sub)_3]Cl$, for the substrates shown. The graph compares the T_1 at the *ortho*-proton when SIMes is used as the NHC (darker colour) to the *ortho*-proton in the substrate when d_{22}-SIMes is used as the NHC (lighter colour). The errors in the T_1 values are calculated from fitting the T_1 curves shown in Appendix B.

***p*-substituent**	**Cl**	**CH_3**	**OCH_3**	**CHO**
$\Delta G^{\neq}_{298K}$ (kJmol^{-1})	62.08	62.82	62.94	64.44
pK_a	2.00	4.02	4.89	3.12
T_1 SIMes (s)	8.49 ± 0.26	6.50 ± 0.04	5.35 ± 0.16	3.54 ± 0.02
T_1 d_{22}-SIMes (s)	8.76 ± 0.39	8.27 ± 0.06	6.77 ± 0.03	3.95 ± 0.02

Table 11 – T_1 values at the *ortho* proton in the free substrate for d^{22}-SIMes and SIMes for each of the four substrates. The errors in the T_1 values are calculated from fitting the T_1 curves shown in Appendix B.

As predicted, the data shows that the deuterated analogue of SIMes extends the T_1 value for the substrate in the SABRE mixture (Table 11). d_{22}-SIMes significantly increases the T_1 value for both 4-methylpyridine and 4-methoxypyridine. For these

substrates, a 21% increase is induced in the T_1 which is comparable to the increases observed by Rayner *et al*.[15] with d_{22}-IMes for a deuterated form of nicotinamide (21% increase). The T_1 values of 4-pyridinecarboxaldehyde and 4-chloropyridine are also lengthened, but to a lesser extent to the other substrates as a 10% increase is noted for the former compared to 3% for the latter. These smaller increases in T_1 lifetimes may be a result of their respective rates of substrate dissociation.

3.6.3 Optimum Rate of Dissociation for SABRE

Binding to iridium is known to promote relaxation of the substrate protons and so this may contribute to the differences in k_d predicted in Table 8 (see Section 3.4.1.1 Exchange in $[Ir(H)_2(SIMes)(sub)_3]Cl$, Optimum Rate of Dissociation for SABRE). To test this, the effective T_1 values for the four substrates were measured at the optimal temperatures of 281.8 K (4-chloropyridine), 285 K (4-methylpyridine), 284.5 K (4-methoxypyridine) and 287.4 K (4-pyridinecarboxaldehyde) shown in Table 8. For 4-chloropyridine, the T_1 was measured to be 5.63 ± 0.07s, compared to 4.07 ± 0.07s (4-methylpyridine), 3.3 ± 0.3s (4-methoxypyridine) and 2.6 ± 0.2s (4-pyridinecarboxaldehyde). If the T_1 values are plotted against the enhancement factor both determined at their respective optimum temperatures (Figure 77), it is clear that once the rate of dissociation is removed from consideration, the T_1 becomes the dominant factor dictating the level of enhancement. For example, larger enhancements are observed for longer T_1 values (4-chloropyridine). These data points can be fitted using a single exponential; therefore, beyond this point (4-chloropyridine) the level of enhancement will be less sensitive to changes in the T_1 value. This would suggest that beyond this point the enhancement could be controlled by a number of different variables including: p-H_2 concentration or the rate of hydrogen exchange.

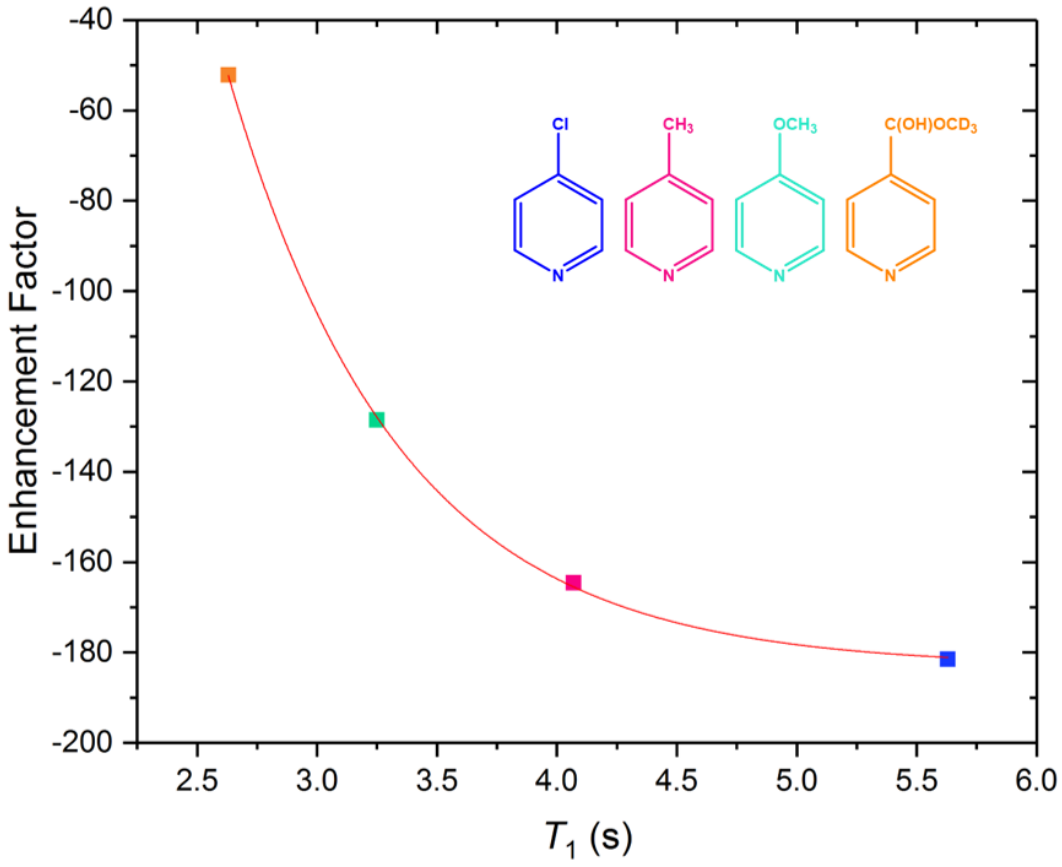

Figure 77 – T_1 values at the *ortho*-proton in the free substrate for the substrates shown as a function of the optimum SABRE temperatures shown in Table 8.

3.7 Exploring the Effect of Catalyst Modifications on Iridium-Substrate Ligation

Modifications at the NHC in the SABRE catalyst have been shown to influence the SABRE efficiency of a number of substrates.[26, 28, 36] In 2013, van Weerdenburg *et al*.[36] investigated the impact of different functionalities on the arms of the central imidazole ring (Figure 78).

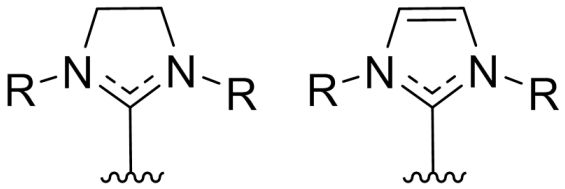

Figure 78 – Basic structure for the NHC ligand

They quantified the steric and electronic effects of various aliphatic and aromatic R-groups on the buried volume (%V_{bur}) and the Tolman Electronic Parameter (TEP). They reported that aromatic R-groups provided better SABRE enhancements. Additionally, they found that unsaturated ligands have less steric bulk compared to their respective saturated counterparts and yield much higher signal enhancements. The following year, Lloyd *et al*.[26] expanded on this research and reported that the larger the R-group (and the larger the steric bulk), the faster the rate of substrate dissociation. Consequently, they identified that the more sterically-encumbered NHCs cause elongation of the Ir-py bonds, resulting in smaller Ir-py bond energies ($\Delta H^{\neq}$) and a smaller release in entropy ($\Delta S^{\neq}$) on reaching the transition state required for substrate dissociation. Both groups found that optimum rates of substrate dissociation are achieved when mesityl groups are attached to the imidazole (1,3-bis(2,4,6-trimethyl phenyl)imidazole - IMes and 1,3-bis(2,4,6-trimethylphenyl)-4,5-dihydroimidazol-2-ylidene – SIMes), however the largest enhancements were observed for the unsaturated analogue, IMes.

In 2018, Rayner *et al*.[28] further expanded this research area by modifying the functionality at the *ortho*, *meta* and *para* positions on the mesityl ring along with altering the substituents on the imidazolium backbone and comparing them to IMes for the substrate methyl-4,6-d_2-nicotinate. They found that introducing strongly electron donating groups (such as *tert*-butyl) in the *para* position of the mesityl ring resulted in a higher rate of substrate dissociation. They suggested that these groups increase the electron density on the metal centre, stabilizing the intermediate complex leading to faster iridium-substrate dissociation (Figure 79). Furthermore, the addition of chloro-containing substituents on the imidazole ring significantly slows ligand association as they pull electron density away from the metal centre (Figure 79).

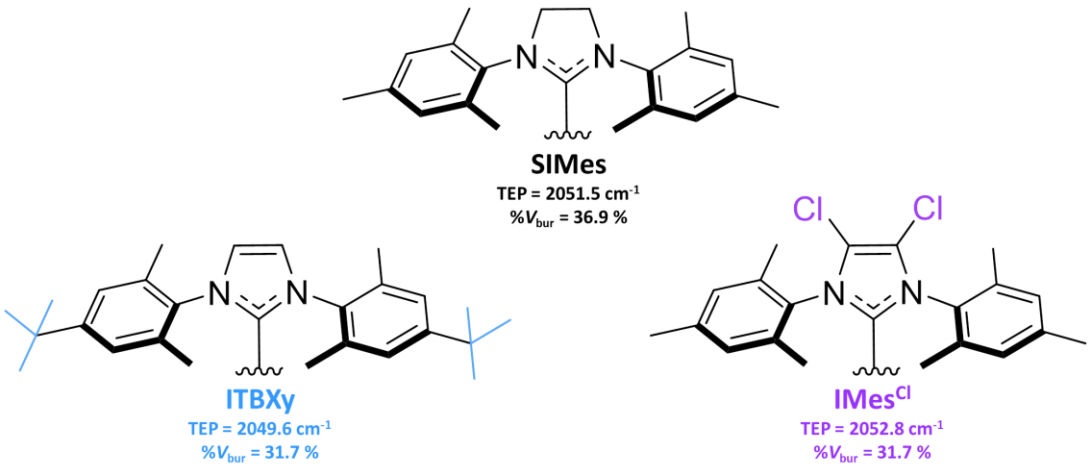

Figure 79 – Structures of the NHCs; SIMes, ITBXy and IMes^{Cl}, including the TEP and %V_{bur} values.

In this section, the effect of changing the NHC was explored in order to identify whether similar behaviours were observed in terms of enhancement, k_d and T_1. The NHCs chosen for this investigation were 1,3-bis(4-*tert*-butyl-2,6-dimethylphenyl)imidazole-2-ylidine (ITBXy) and 1,3-bis(2,4,6-trimethylphenyl)-4,5-dichloroimidazol-2-ylidine (IMes^{Cl}) (see Figure 79).

It was hypothesised that ITBXy would promote faster rates of substrate dissociation compared to SIMes as the *tert*-butyl groups in the *para* position on the phenyl ring contribute towards the increased electron density on the iridium centre, resulting in weaker iridium-substrate associations and hence, faster substrate dissociation. This is demonstrated via the TEP values for SIMes (2051.5 cm^{-1}) and ITBXy (2049.6 cm^{-1}) shown in Figure 79. Conversely, it was predicted that IMes^{Cl} would strengthen the iridium-substrate interaction compared to SIMes as the chlorides on the imidazole pull electron density away from the iridium centre resulting in slow substrate dissociation. This is also shown in Figure 79 where the TEP value for IMes^{Cl} is 2052.8 cm^{-1} compared to 2051.5cm^{-1} for SIMes.

3.7.1 Gibbs Free Energy in $[Ir(H)_2(NHC)(sub)_3]Cl$

The rates of substrate dissociation at different temperatures were used to determine the Gibbs free energy of dissociation for each of the catalyst/substrate combinations (Figure 80).

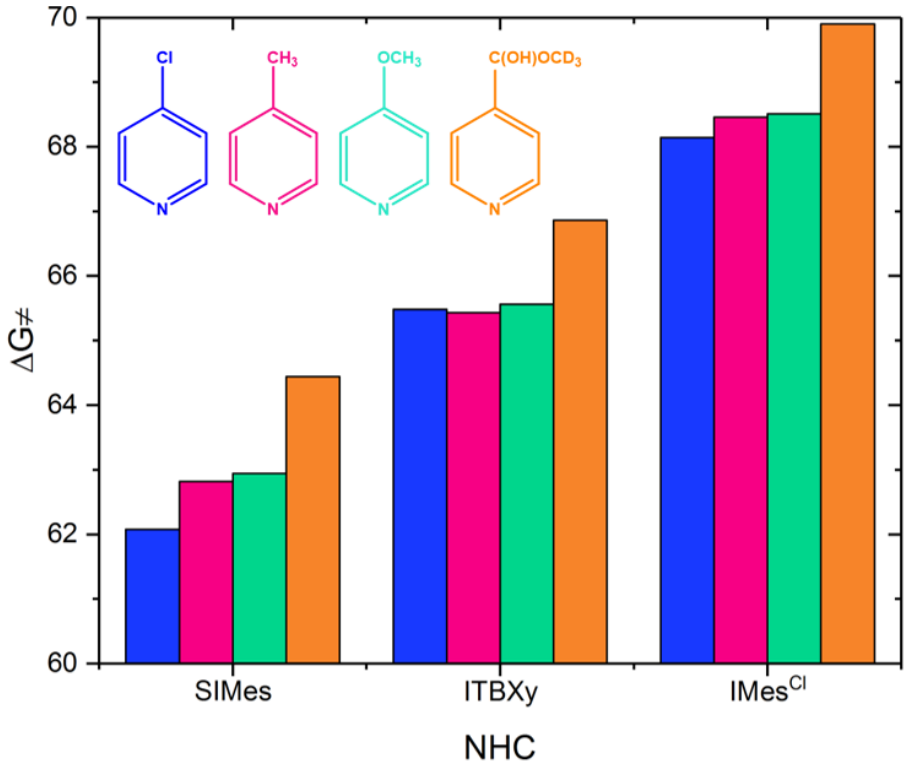

Figure 80 – The Gibbs free energy $\Delta G^{\neq}_{298K}$ as a function of the NHC in the SABRE active species, $[Ir(H)_2(NHC)(sub)_3]Cl$ for the substrates shown.

	***p*-substituent**	**Cl**	**CH_3**	**OCH_3**	**CHO**
	pK_a	2.00	4.02	4.89	3.12
$\Delta G^{\neq}_{(298)}$ ***(kJmol^{-1})***	SIMes	62.08	62.82	62.94	64.44
	ITBXy	65.64	65.43	65.56	66.86
	$IMes^{Cl}$	68.14	68.46	68.51	69.90

Table 12 – $\Delta G^{\neq}_{(298)}$ values for each of the substrate/catalyst combinations. The errors in the $\Delta G^{\neq}$ values were calculated using the method described in in Chapter 6, Section 6.2.7.3 Calculation of Gibbs free energy and associated errors. As the errors are very small they are not listed in this table but they can be found in Appendix B.

Figure 80 compares the $\Delta G^{\neq}_{298K}$ values calculated for each substrate/NHC combination. Similar trends are observed for SIMes and $IMes^{Cl}$ where 4-chloropyridine has the lowest value of $\Delta G^{\neq}_{298K}$ followed by 4-methylpyridine, 4-methoxypyridine and 4-pyridinecarboxaldehyde. If the NHC ITBXy is employed, 4-methylpyridine has the lowest value of $\Delta G^{\neq}_{298K}$ (65.43 $kJmol^{-1}$) followed by 4-methoxypyridine (65.56 $kJmol^{-1}$), 4-chloropyridine (65.64 $kJmol^{-1}$) and 4-

pyridinecarboxaldehyde (66.86 kJmol^{-1}). 4-pyridinecarboxaldehyde consistently has the highest value of $\Delta G^{\neq}_{298K}$ regardless of the NHC used. This contradicts the hypothesis that the lower the pK_a, the weaker the iridium-substrate association and therefore the lower the value of $\Delta G^{\neq}_{298K}$. This stronger interaction has been attributed to the increased π-backdonation that occurs from the metal centre to the ligand as a consequence of the electron withdrawing hemiacetal group which removes electron density from the pyridine ring.

As predicted, IMes^{Cl} encourages stronger iridium-substrate associations in all the substrates as the $\Delta G^{\neq}_{(298)}$ value increased from 62.08 kJmol^{-1} to 68.14 kJmol^{-1} for 4-chloropyridine and 64.44 kJmol^{-1} to 69.90 kJmol^{-1} for 4-pyridinecarboxaldehyde. It was anticipated that the catalyst modification ITBXy would encourage weaker iridium-substrate associations as the *tert*-butyl groups in the *para* position on the mesityl group increase the electron density on the iridium resulting in faster substrate dissociation. This is demonstrated in Figure 79 by the TEP values for SIMes (2051.5 cm^{-1}) and ITBXy (2049.6 cm^{-1}). However, Figure 80 shows that ITBXy instead favours the formation of stronger associations as the $\Delta G^{\neq}_{(298)}$ values are higher than those of SIMes. For example, the $\Delta G^{\neq}_{(298)}$ value increased from 62.08 kJ to 65.64 kJ for 4-chloropyridine. If the steric contribution for each of the catalyst modifications are considered, the buried volume for ITBXy (31.7%) is smaller than for SIMes (36.9%), meaning it is less sterically encumbered (Figure 79). As SIMes is bulkier, it pushes the substrate further away from the iridium centre weakening this association and culminating in faster substrate dissociation. Therefore, when SIMes is compared to ITBXy, sterics are a vital aspect when considering iridium-substrate ligation.

3.7.2 Relaxation Effects in $[Ir(H)_2(NHC)(sub)_3]Cl$

The T_1 relaxation data was measured using the process described in Chapter 6 (Section 6.2.7.2.1 T_1 Relaxation Measurements), for each of the substrate/catalyst combinations. As binding to iridium promotes relaxation, it was predicted that the T_1 values measured for ITBXy and IMes^{Cl} would be shorter compared to SIMes.

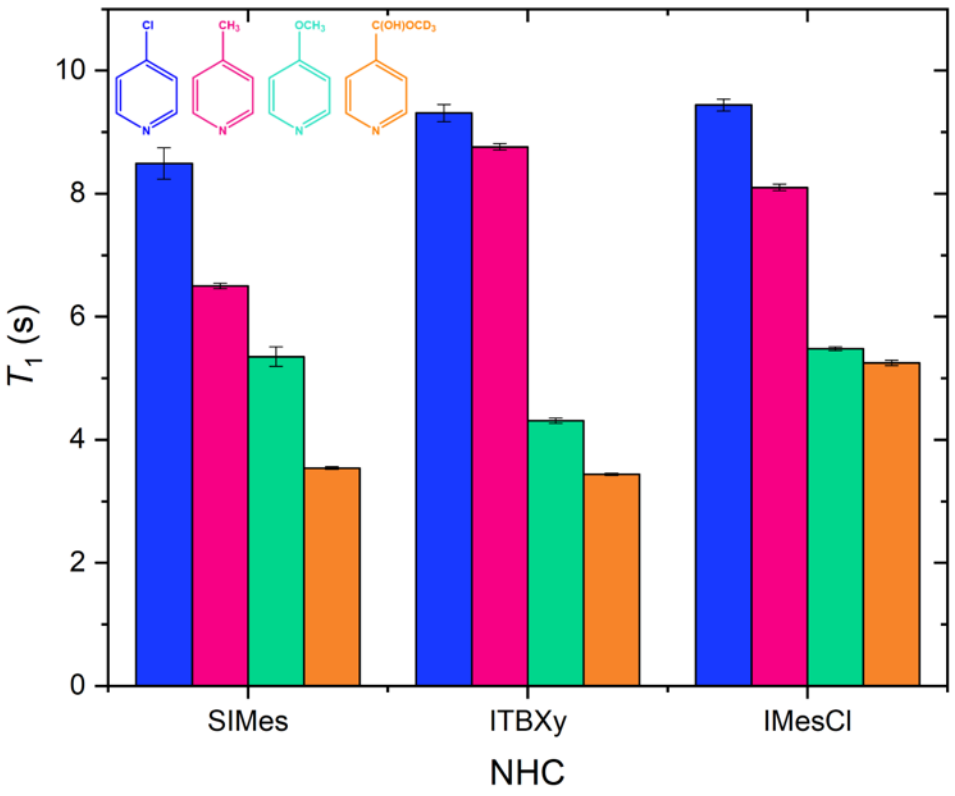

Figure 81 – T_1 as a function of the NHC in the SABRE active species, $[Ir(H)_2(NHC)(sub)_3]Cl$ for the substrates shown. The T_1 is for the *ortho*-proton in the free substrate. The errors in the T_1 values are calculated from fitting the T_1 curves shown in Appendix B.

Figure 81 shows that as the T_1 decreases with the substrate $\Delta G^{\neq}_{(298)}$ irrespective of the NHC used. For example, for SIMes the T_1 values vary from 8.49 s (4-chloropyridine) to 3.54 s (4-pyridinecarboxaldehyde), for ITBXy they range from 9.31 s to 4.31 s, finally for $IMes^{Cl}$ they vary from 9.45 s to 5.25 s. As the catalyst modifications ITBXy and $IMes^{Cl}$ encouraged stronger iridium-substrate associations and it is well established that binding to iridium promotes relaxation, it was expected that the corresponding T_1 values would be shorter compared to SIMes. Whilst this is the case for 4-methoxypyridine and 4-pyridinecarboxaldehyde combined with ITBXy, longer T_1 values are observed for 4-chloropyridine and 4-methylpyridine. When $IMes^{Cl}$ is considered, longer T_1 values are observed for all four of the substrates. In this catalyst modification, the replacement of the hydrogens on the imidazolydine backbone with chlorides is thought to remove a scalar coupling route to relaxation, hence T_1 values are longer. [28]

3.7.3 Enhancement in $[Ir(H)_2(NHC)(sub)_3]Cl$

All enhancements were measured with the manual shaking method using the stray field of the spectrometer, using 4 bar (absolute) pressure of 99.9% *p*-H_2. However, when ITBXy was used with 4-methylpyridine, antiphase peaks were observed (Figure 82) which are characteristic of radiation damping. Radiation damping is typically observed at high field and in the presence of protonated solvents. As these samples are highly concentrated (proton rich), when a pulse is applied, placing the protons in the transverse (xy plane), a rotating electromotive force is induced in the RF coil. This produces an additional magnetic field in the sample, leading to peak broadening, peak asymmetry, phase shifting and residual signals.[37-39] In some SABRE experiments, the intensity of the hyperpolarised signals has been seen to induce similar affects.[40]

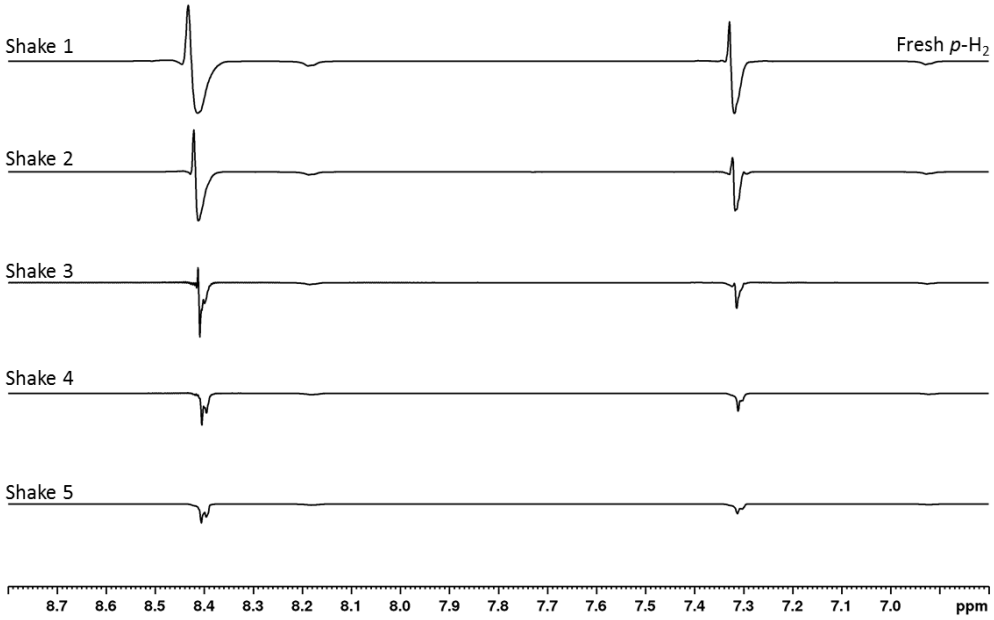

Figure 82 - Radiation dampening observed during repeating manual shaking using the stray field of the spectrometer, with 4-methylpyridine, ITBXy and 99% *p*-H_2

In Figure 82 it was observed that with continued shaking without refreshing the *p*-H_2, the hyperpolarised signals eventually became in-phase once the signal reaches a certain level (see Shakes 4 and 5). In 2018, Richardson et *al.*[40] measured the level of substrate enhancement as a function of *p*-H_2 enrichment. It was found that there was a linear relationship between these variables for a range of molecules, catalysts and

NMR detection fields. It was thought that using a lower level of enrichment here could also be employed to overcome the radiation damping problem presented in Figure 82 where the enhancements could be calculated at different concentrations of *p*-H_2 in order to predict the enhancement at 99.9 %. The concentrations selected were 40, 50 and 60 % *p*-H_2 and once these had been plotted against the relative enhancements, the enhancement at 99.9 % could be calculated using a linear model (Figure 83).[40]

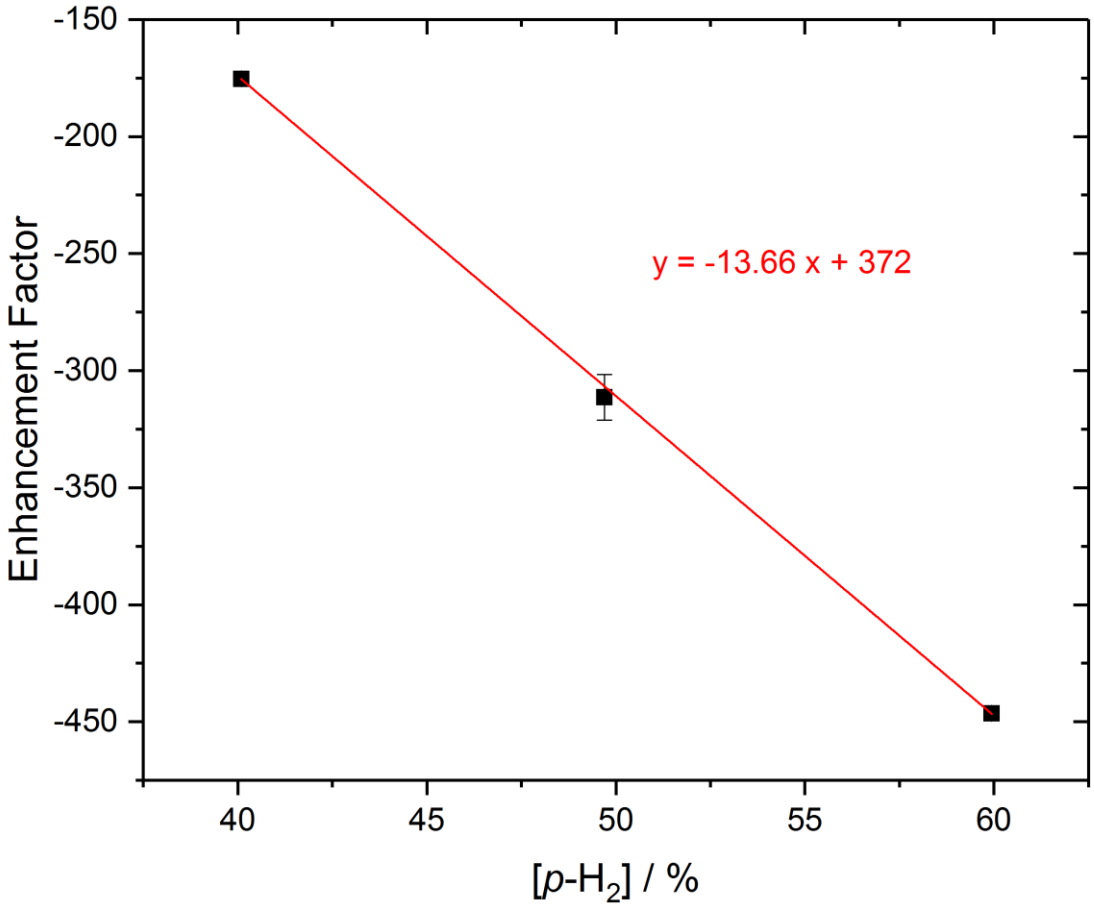

Figure 83 - Plot of enhancements against *p*-H_2 percentage

Predicting the enhancement in this way gave rise to the largest signal enhancement out of all the substrate/catalyst combinations (−980 ± 10-fold for 4-methylpyridine and ITBXy). The largest measured enhancement was −756 ± 18-fold for 4-methoxypyridine and $IMes^{Cl}$ (Figure 84). As the NHC influences the iridium-substrate association, each substrate produced the largest enhancement for different NHCs. For example, 4-pyridinecarboxaldehyde has been seen to form strong associations

with SIMes, therefore when these associations are further strengthened via the NHC modifications ITBXy and $IMes^{Cl}$, substrate dissociation is even slower and relaxation effects are stronger, resulting in lower enhancements. It seems that the largest enhancements are observed when the $\Delta G^{\neq}_{(298)}$ value lies between 64.44 kJ (4-pyridinecarboxaldehyde + SIMes) and 65.56 kJ (4-methoxypyridine + ITBXy).

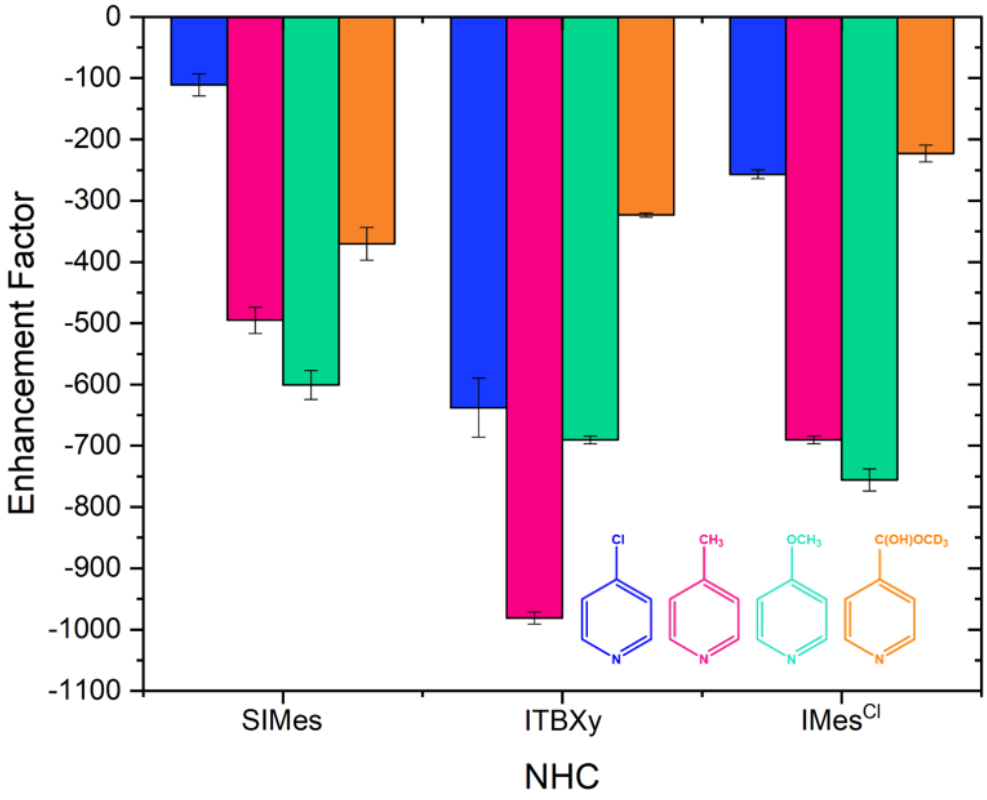

Figure 84 – Enhancement factor as a function of the NHC in the SABRE active species, $[Ir(H)_2(NHC)(sub)_3]Cl$ for the substrates shown. The enhancements were observed using the manual shaking method. The experiment was repeated five times and the ^1H signal enhancements at the *ortho* proton were averaged. The error bars indicate the standard error of the experiment.

3.7.3.1 NHC Deuteration

As the combination of 4-methylpyridine and catalyst ITBXy yielded the largest enhancement of −980 ± 10-fold, the deuterated analogue of the NHC was also tested. Instead of using the traditional manual shaking method involving the stray field of spectrometer, this was tested using the 65 G shaker. Furthermore, five [*p*-H_2] concentrations were chosen rather than three in order to accurately predict the enhancement level at 99.9% *p*-H_2.

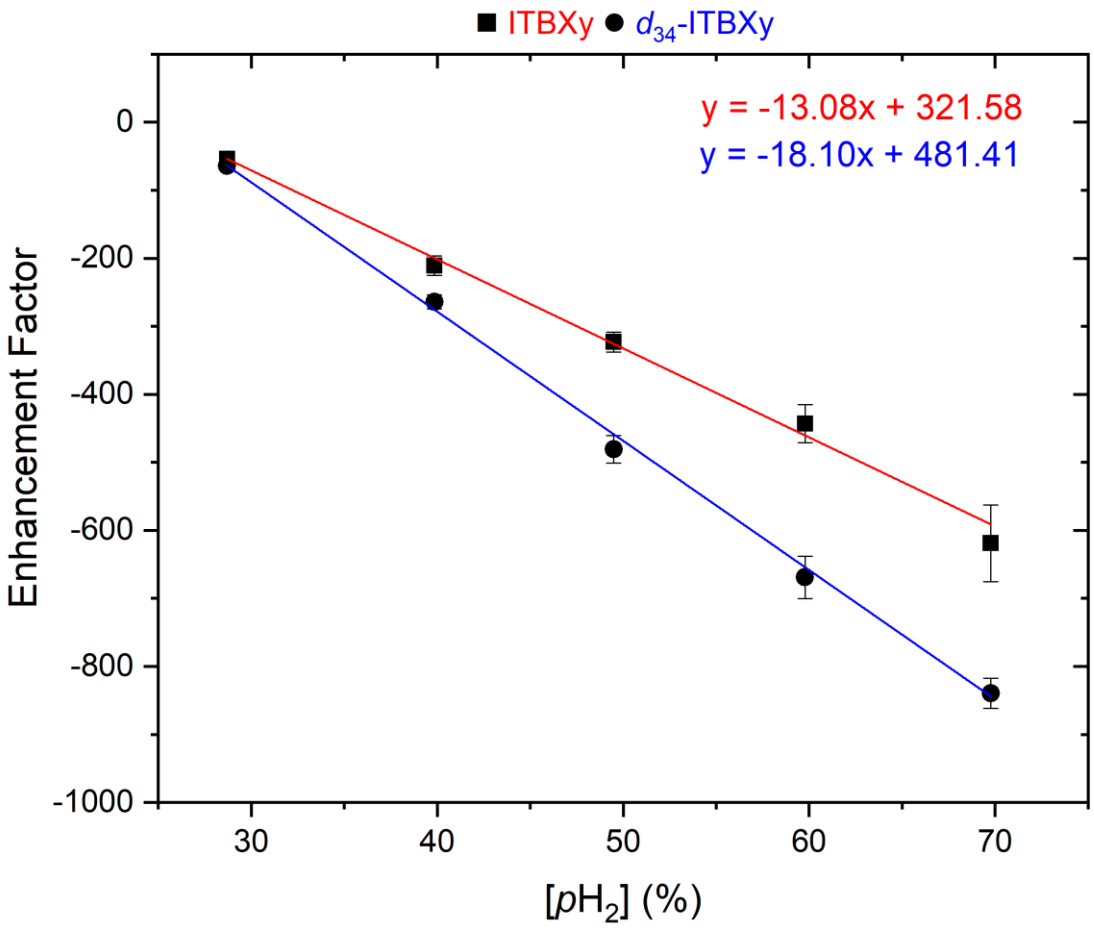

Figure 85 - Variation in enhancement factor with [*p*-H_2] for ITBXy and its deuterated isotopologue d_{34}-ITBXy

Enhancement levels with d_{34}-ITBXy were larger compared to the non-deuterated analogue. For example, at 70% *p*-H_2, the signal enhancement was −619 ± 56-fold for ITBXy compared to −839 ± 22-fold for d_{34}-ITBXy which corresponds to a 36% increase. By using the straight-line equations, it was predicted that enhancements of −990 ± 65-fold would be observed for ITBXy and −1411 ± 40-fold for d_{34}-ITBXy at 99% *p*-H_2.

3.8 Summary

In this chapter, the strength of the iridium-substrate ligation in the SABRE-active species and consequently the SABRE response was investigated. The strength of this ligation was probed by a range of *para* substituted pyridines. This topic is of high importance in the optimisation of the SABRE approach as a lot of work goes into the optimisation of each individual system, therefore this work could lead to some insight into predicting substrate-catalyst behaviour.

Substitution at the *para* position is known to have the greatest effect on the activity of pyridine which can be expressed in terms of pK_a. The substrates selected for this study were 4-chloropyridine, 4-pyridinecarboxaldehyde, 4-methylpyridine and 4-methoxypyridine which have corresponding pK_a values of 2.00, 3.12, 4.02 and 4.89. It was predicted that the higher the substrate pK_a, the stronger the substrate would associate to the metal centre. This hypothesis was validated using the rate of substrate dissociation and the rate of relaxation. It was postulated that strong substrate-iridium ligations would result in slow substrate dissociation and shorter T_1 values. Conversely, weak ligations would be demonstrated by fast rates of substrate dissociation and longer T_1 values.

The SABRE enhancements of the SABRE-active species for the four substrates were determined. 4-Methylpyridine yielded the largest enhancement of −767 ± 8-fold compared to −340 ± 2-fold (4-chloropyridine), −571 ± 41-fold (4-pyridinecarboxaldehyde) and −680 ± 11-fold (4-methoxypyridine). This means that 4-methylpyridine binds to iridium such that relaxation effects are not induced whilst sufficient polarisation is transferred from the hydrides before substrate dissociation occurs.

The rate of substrate dissociation was determined over a range of different temperatures for each of the substrates. It was observed that 4-chloropyridine had the fastest rate of dissociation followed by 4-methylpyridine, 4-methoxypyridine and 4-pyridinecarboxaldehyde. It was expected that the rate of dissociation would become slower as the substrate pK_a increased. It was observed that 4-pyridinecarboxaldehyde had the slowest rate of dissociation compared to the other substrates, suggesting it forms stronger associations to the metal centre. Previous works have suggested that the optimum dissociation rate for SABRE is 4.5 s^{-1}.[27, 28] According to the Arrhenius equation, the rate of dissociation is temperature dependent and therefore SABRE efficiency must also vary with temperature. It was predicted that the optimum temperatures for SABRE (where k_d = 4.5 s^{-1}) were 281.1 K, 282.7 K, 285.0 K and 288.2 K across the substrate series. The effect of temperature on SABRE efficiency was measured using a variable temperature flow system. The

SABRE enhancements were then plotted as a function of the temperature and fitted with a gauss curve to determine the precise temperature for optimum SABRE catalysis. These were 281.8 K (4-chloropyridine), 285 K (4-methylpyridine), 284.5 K (4-methoxypyridine) and 287.4 K (4-pyridinecarboxaldehyde), confirming that the stronger the iridium-substrate association, the higher the temperature required for optimum SABRE efficiency. The corresponding rates of dissociation were also calculated as 4.86 ± 0.79 s^{-1}, 6.23 ± 1.01 s^{-1}, 5.15 ± 0.25 s^{-1} and 3.96 ± 0.25 s^{-1} which whilst statistically different from one another, are all comparable to the predicted optimum of 4.5 s^{-1}.

Further analysis of the rate of dissociation via the Eyring-Polanyi equation allowed for the Gibbs free energy of dissociation to be calculated. The Gibbs free energy describes the stability of the iridium-substrate ligation. 4-Chloropyridine had the highest value of $\Delta G^{\neq}_{298K}$ at 62.08 $kJmol^{-1}$ compared to 62.82 $kJmol^{-1}$ (4-methylpyridine), 62.94 $kJmol^{-1}$ (4-methoxypyridine) and 64.44 $kJmol^{-1}$ (4-pyridinecarboxaldehyde). It was expected that $\Delta G^{\neq}_{298K}$ would increase with the substrate pK_a, however the strongest iridium-substrate interaction was observed for 4-pyridinecarboxaldehyde (pK_a = 3.12) as it exhibits the highest $\Delta G^{\neq}_{298K}$ value of the series. This stronger association explains why 4-pyridinecarboxaldehyde has the slowest rate of dissociation compared to the other three substrates. As 4-pyridinecarboxaldehyde contains an electron withdrawing group, π-backdonation occurs from the metal centre to the pyridine to stabilise the metal-ligand interaction. This means that this interaction is more stable compared to those observed with 4-chloropyridine, 4-methlypyridine and 4-methoxypyridine. The $\Delta G^{\neq}_{298K}$ values were also determined at the optimum SABRE temperatures. Comparison of these values with the corresponding enhancements at 298 K and the optimum SABRE temperature suggested that for optimum SABRE the $\Delta G^{\neq}$ value must lie between 62.94 $kJmol^{-1}$ and 63.29 $kJmol^{-1}$.

The pseudo transfer couplings ($^4J_{HH}$) between the hydride and the substrate protons were also determined. Whilst there was no clear relationship to substrate pK_a, it was observed that this coupling increased with the strength of the substrate-iridium

ligation, as observed via $\Delta G^{\neq}_{298K}$. For example, 4-pyridinecarboxaldehyde had the largest value of value of $\Delta G^{\neq}_{298K}$ (64.44 kJ) and the largest corresponding pseudo transfer coupling of 1.38 Hz. This compares to 4-chloropyridine that formed the weakest ligations to iridium ($\Delta G^{\neq}_{298K}$ =) and exhibited the smallest value of $^4J_{HH}$ (Hz). It was assumed that the larger the pseudo coupling, the more efficient the polarisation transfer into the substrate. However, the largest enhancements were observed with 4-methylpyridine (−767 ± 8-fold) which has a transfer coupling of 1.11 Hz. 4-pyridinecarboxaldehyde however, yielded a smaller enhancement of −571 ± 41-fold, suggesting that relaxation effects are another important consideration of SABRE efficiency.

The T_1 values were also measured at 298 K for the free and bound substrate in the SABRE active species $[Ir(H)_2(SIMes)(sub)_3]Cl$ for the four substrates. Ligation to the metal centre promotes relaxation of the substrate resulting in shorter T_1 values. This was observed when the effective T_1 values were compared to axial substrate bound *trans* to the NHC which doesn't exchange on the timescale of the NMR experiment. For instance, the free *ortho* T_1 of 4-chloropyridine was 8.49 s compared to 3.04 s in the axial bound substrate. This also meant that 4-pyridinecarboxaldehyde which forms the strongest associations to iridium had the shortest T_1 values from the series (3.54 s in the free substrate and 1.81 s in the axially bound substrate). The effective T_1 values were also measured for the free substrate at the SABRE optimum temperatures of 281.8 K (4-chloropyridine), 285 K (4-methylpyridine), 284.5 K (4-methoxypyridine) and 287.4 K (4-pyridinecarboxaldehyde). These were measured as 5.63 ± 0.07 s, 4.07 ± 0.07 s 3.3 ± 0.3 s and 2.6 ± 0.2 s, respectively. When these data points are plotted against the corresponding enhancement maxima it seems that once the rate of substrate dissociation is removed from consideration, the T_1 becomes the dominant factor controlling the level of SABRE enhancement. Furthermore, the data points can be fitted to a single exponential suggesting that there is a limit to this T_1 effect.

To compliment previous works, these measurements were expanded to include two additional NHCs; 1,3-bis(4-tert-butyl-2,6-dimethylphenyl)imidazole-2-ylidine (ITBXy)

and 1,3-bis(2,4,6-trimethylphenyl)-4,5-dichloroimidazol-2-ylidine ($IMes^{Cl}$). It was predicted that ITBXy would encourage formation of weaker substrate associations whilst $IMes^{Cl}$ would favour stronger associations. However, analysis of the $\Delta G^{\neq}_{298K}$ data showed that ITBXy stronger substrate-iridium associations existed. The buried ligand volumes showed that SIMes is more sterically hindered; hence it promotes weaker substrate associations. The $\Delta G^{\neq}_{298K}$ values for ITBXy and $IMes^{Cl}$ followed a similar trend to those of SIMes where 4-chloropyridine had the smaller value of $\Delta G^{\neq}_{298K}$ and 4-pyridinecarboxaldehyde had the highest. Furthermore, the T_1 value of the substrate decreased with substrate $\Delta G^{\neq}_{298K}$. The NHC was seen to critically influence the level of ^{1}H SABRE enhancement observed. The largest enhancement of −980 ± 10-fold was detected for 4-methylpyridine and the NHC; ITBXy. As 4-pyridinecarboxaldehyde had been shown to form strong associations with SIMes, further strengthening these associations via the ITBXy and $IMes^{Cl}$ modifications lead to smaller enhancements.

3.9 References

1. D. A. Barskiy, K. V. Kovtunov, I. V. Koptyug, P. He, K. A. Groome, Q. A. Best, F. Shi, B. M. Goodson, R. V. Shchepin, A. M. Coffey, K. W. Waddell and E. Y. Chekmenev, *J. Am. Chem. Soc.*, 2014, **136**, 3322-3325.
2. R. W. Adams, J. A. Aguilar, K. D. Atkinson, M. J. Cowley, P. I. Elliott, S. B. Duckett, G. G. Green, I. G. Khazal, J. Lopez-Serrano and D. C. Williamson, *Science*, 2009, **323**, 1708-1711.
3. H. Szatylowicz, O. A. Stasyuk and T. M. Krygowski, in *Adv. Heterocycl. Chem.*, eds. E. F. V. Scriven and C. A. Ramsden, Academic Press, 2015, vol. 116, pp. 137-192.
4. M. Palusiak, *J. Organomet. Chem.*, 2007, **692**, 3866-3873.
5. M. J. Schneider, in *Alkaloids: Chemical and Biological Perspectives*, ed. S. W. Pelletier, Pergamon, 1996, vol. 10, pp. 155-299.
6. C. H. McAteer, M. Balasubramanian and R. Murugan, in *Comprehensive Heterocyclic Chemistry III*, eds. A. R. Katritzky, C. A. Ramsden, E. F. V. Scriven and R. J. K. Taylor, Elsevier, Oxford, 2008, pp. 309-336.
7. A. A. Altaf, A. Shahzad, Z. Gul, N. Rasool, A. Badshah, B. Lal and E. Khan, *J. Drug Des. Med. Chem*, 2015, **1**, 1-11.
8. M. Baumann and I. R. Baxendale, *Beilstein J. Org. Chem.*, 2013, **9**, 2265-2319.
9. E. Lukevits, *Chem. Heterocycl. Compd.*, 1995, **31**, 639-650.
10. E. Klingsberg, *Pyridine and Its Derivatives*, Wiley, 2009.
11. K. Heclik and J. C. Dobrowolski, *J. Phys. Org. Chem.*, 2017, **30**, e3656.
12. K. Heclik, B. Debska and J. C. Dobrowolski, *RSC Adv.*, 2014, **4**, 17337-17346.
13. W. P. Ozimiński and J. C. Dobrowolski, *J. Phys. Org. Chem.*, 2009, **22**, 769-778.

14. R. E. Mewis, M. Fekete, G. G. Green, A. C. Whitwood and S. B. Duckett, *Chem. Commun.*, 2015, **51**, 9857-9859.
15. P. J. Rayner, M. J. Burns, A. M. Olaru, P. Norcott, M. Fekete, G. G. R. Green, L. A. R. Highton, R. E. Mewis and S. B. Duckett, *Proc. Natl. Acad. Sci. U. S. A.*, 2017, **114**, E3188-E3194.
16. R. V. Shchepin, M. L. Truong, T. Theis, A. M. Coffey, F. Shi, K. W. Waddell, W. S. Warren, B. M. Goodson and E. Y. Chekmenev, *J. Phys. Chem. Lett.*, 2015, **6**, 1961-1967.
17. S. Zhang, *J. Comput. Chem.*, 2012, **33**, 2469-2482.
18. R. Casasnovas, J. Frau, J. Ortega-Castro, A. Salvà, J. Donoso and F. Muñoz, *Journal of Molecular Structure: THEOCHEM*, 2009, **912**, 5-12.
19. C. S. Handloser, M. R. Chakrabarty and M. W. Mosher, *J. Chem. Educ.*, 1973, **50**, 510.
20. T. Kameda, N. Takeda, S. Kuroki, H. Kurosu, S. Ando, I. Ando, A. Shoji and T. Ozaki, *J. Mol. Struct.*, 1996, **384**, 17-23.
21. S. Knecht, A. N. Pravdivtsev, J. B. Hovener, A. V. Yurkovskaya and K. L. Ivanov, *RSC Adv.*, 2016, **6**, 24470-24477.
22. P. Norcott, P. J. Rayner, G. G. R. Green and S. B. Duckett, *Chemistry*, 2017, **23**, 16990-16997.
23. K. M. Appleby, R. E. Mewis, A. M. Olaru, G. G. R. Green, I. J. S. Fairlamb and S. B. Duckett, *Chem. Sci.*, 2015, **6**, 3981-3993.
24. J. G. Małecki and P. Zwoliński, *Polyhedron*, 2012, **39**, 85-90.
25. M. J. Cowley, R. W. Adams, K. D. Atkinson, M. C. Cockett, S. B. Duckett, G. G. Green, J. A. Lohman, R. Kerssebaum, D. Kilgour and R. E. Mewis, *J. Am. Chem. Soc.*, 2011, **133**, 6134-6137.
26. L. S. Lloyd, A. Asghar, M. J. Burns, A. Charlton, S. Coombes, M. J. Cowley, G. J. Dear, S. B. Duckett, G. R. Genov, G. G. R. Green, L. A. R. Highton, A. J. J. Hooper, M. Khan, I. G. Khazal, R. J. Lewis, R. E. Mewis, A. D. Roberts and A. J. Ruddlesden, *Catal. Sci. Technol.*, 2014, **4**, 3544-3554.
27. D. A. Barskiy, A. N. Pravdivtsev, K. L. Ivanov, K. V. Kovtunov and I. V. Koptyug, *Phys. Chem. Chem. Phys.*, 2016, **18**, 89-93.
28. P. J. Rayner, P. Norcott, K. M. Appleby, W. Iali, R. O. John, S. J. Hart, A. C. Whitwood and S. B. Duckett, *Nat Commun*, 2018, **9**, 4251.
29. L. S. Lloyd, R. W. Adams, M. Bernstein, S. Coombes, S. B. Duckett, G. G. Green, R. J. Lewis, R. E. Mewis and C. J. Sleigh, *J. Am. Chem. Soc.*, 2012, **134**, 12904-12907.
30. R. E. Mewis, K. D. Atkinson, M. J. Cowley, S. B. Duckett, G. G. Green, R. A. Green, L. A. Highton, D. Kilgour, L. S. Lloyd, J. A. Lohman and D. C. Williamson, *Magn. Reson. Chem.*, 2014, **52**, 358-369.
31. L. Buljubasich, M. B. Franzoni, H. W. Spiess and K. Munnemann, *J. Magn. Reson.*, 2012, **219**, 33-40.
32. K. L. Ivanov, A. N. Pravdivtsev, A. V. Yurkovskaya, H.-M. Vieth and R. Kaptein, *Prog. Nucl. Magn. Reson. Spec.*, 2014, **81**, 1-36.
33. N. Eshuis, R. L. Aspers, B. J. van Weerdenburg, M. C. Feiters, F. P. Rutjes, S. S. Wijmenga and M. Tessari, *J. Magn. Reson.*, 2016, **265**, 59-66.
34. D. A. Barskiy, S. Knecht, A. V. Yurkovskaya and K. L. Ivanov, *Prog. Nucl. Magn. Reson. Spec.*, 2019, **114-115**, 33-70.

35. P. J. Rayner and S. B. Duckett, *Angew. Chem. Int. Ed.*, 2018, **57**, 6742-6753.
36. B. J. van Weerdenburg, S. Gloggler, N. Eshuis, A. H. Engwerda, J. M. Smits, R. de Gelder, S. Appelt, S. S. Wymenga, M. Tessari, M. C. Feiters, B. Blumich and F. P. Rutjes, *Chem. Commun.*, 2013, **49**, 7388-7390.
37. V. V. Krishnan and N. Murali, *Prog. Nucl. Magn. Reson. Spectrosc.*, 2013, **68**, 41-57.
38. S. Bloom, *J. Appl. Phys.*, 1957, **28**, 800-805.
39. N. Bloembergen and R. V. Pound, *Phys. Rev.*, 1954, **95**, 8-12.
40. P. M. Richardson, R. O. John, A. J. Parrott, P. J. Rayner, W. Iali, A. Nordon, M. E. Halse and S. B. Duckett, *Phys. Chem. Chem. Phys.*, 2018, **20**, 26362-26371.

Chapter 4 SABRE Optimisation for Oxygen-Bound Pyridines

4.1 The Substrates

The previous chapter compared the SABRE efficiency of a series of *para*-substituted pyridine derivatives. 4-hydroxypyridine and isoniazid were originally selected for this study as they also reflect readily available *para*-substituted pyridines with low pK_a values (3.20 and 1.82 respectively). However, upon reaction with H_2 and [IrCl(COD)(SIMes)], rather than form a *tris*-substituted SABRE-active species typically observed (see previous chapter), they each formed a *bis*-substituted complex. These complexes proved to contain a substrate ligand bound to iridium via the secondary functional group rather than the pyridine nitrogen. Both complexes have been shown to enhance under SABRE conditions.

These structures have been fully characterised by ^{1}H, ^{13}C and ^{15}N-NMR methods. Furthermore, their SABRE suitability has also been explored. These results are now discussed.

4.1.1 4-Hydroxypyridine

At first glance, 4-hydroxypyridine presents itself as a simple alcohol derivative of pyridine where the functional group is located in the *para*-position. However, the proton of the alcohol functional group is acidic meaning that tautomerism results in both enol (4-hydroxypyridine) and keto equivalent forms (4-pyridone).[1] This tautomerism has been studied extensively as it is of considerable importance in both chemical and biochemical processes.[2] For example, this tautomeric equilibria can provide a rationale for the structure-function relationships exhibited by nucleotides, the mechanism of enzyme catalysis and substrate-receptor interactions.[3]

4.1.1.1 Tautomerism

The tautomeric equilibria between 4-hydroxypyridine and 4-pyridone is shown in Figure 86. This interaction has been heavily scrutinised and can be influenced by the phase, solvent, temperature and substitution around the pyridine ring.

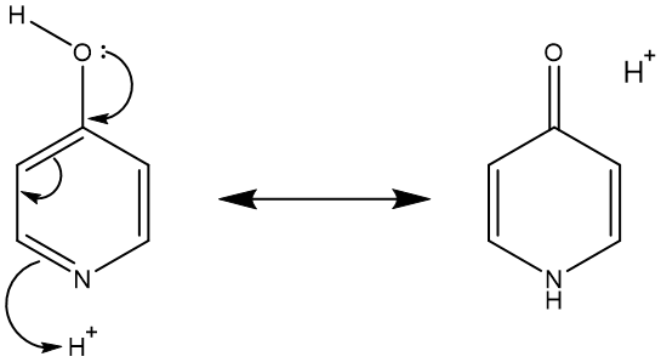

Figure 86 - Tautomerism of 4-hydroxpyridine to 4-pyridone

In 1999, Murguly *et al*.[4] studied the tautomerism of 4-hydroxyterpyridine in the solid, solution and gas phases via infrared (IR) and nuclear magnetic resonance (NMR) spectroscopy. They established that in the gaseous phase, 4-hydroxypyridine exists exclusively in the enol form. This was evident by IR spectroscopy, where an isolated O-H stretch was observed at 3640 cm^{-1}. In the solid phase, the keto form is predominant. This is indicated by the presence of an N-H IR stretch at 3280 cm^{-1}. In polar solvents, such as chloroform or methanol, 4-pyridone is favoured as the IR spectrum now shows an N-H stretching band at 3310 cm^{-1} and a C=O stretch at 1635 cm^{-1}. In solution with dichloromethane, however, a mixture of both tautomers is indicated according to ^{1}H-NMR spectroscopy at 25°C, in a ratio of 6:1 (keto/enol). The proportion of the enol tautomer was shown to increase at lower temperatures. This result was surprising as the dielectric constant of CD_2Cl_2 increases upon cooling[5] and larger dielectric constants favour polar tautomers,[6] hence it was assumed that the more polar keto tautomer would exist exclusively at these temperatures.

The predominance of the keto tautomer; 4-pyridone in the crystalline form and in solution with polar solvents was also supported by Albert *et al*.[1] who used Raman

and IR spectroscopy to analyse this tautomerism. Vogeli *et al*.[7] also observed similar findings using ^{13}C and ^{1}H NMR techniques.

Katritzky *et al*.[8-10] has investigated the effect of substituents on 4-hydroxypyridine/4-pyridone tautomerism in a number of papers. He found that placing electron withdrawing groups, such as chlorine, α (*ortho*) to the pyridine nitrogen atom favours the enol form, 4-hydroxy-2-chloro-pyridine. This is because the chlorine increases the acidity of the amine group in the pyridine form and decreases the basicity of the nitrogen in the hydroxy form thereby pushing the equilibrium to favour 4-hydroxypyridine.[9] In contrast, electron donating groups in the *ortho*-position were shown to favour the keto form, 4-pyridone.[8] Placing either group in the β-position (*meta*) had little effect on the equilibrium position.

Before 4-hydroxypyridine was used in SABRE experiments, it was first characterised by FTIR and NMR methods.

4.1.1.1.1 Fourier Transform Infra-Red Spectroscopy

Due to the tautomerism of 4-hydroxypyridine to 4-pyridone, a number of samples of 4-hydroxypyridine were analysed via FTIR. First the solid, then a solution of 4-hydroxypyridine in dichloromethane-d_2 and a second solution in methanol-d_4. Deuterated solvents were used as the same samples were used for the NMR experiments. The FTIR spectra were measured using a Bruker Tensor 37 FTIR spectrometer, the solid sample was placed directly onto the diamond crystal whereas the solution FTIR samples were measured using the diamond fibre optic probe submersed in < 1 mL solution in a sample vial.

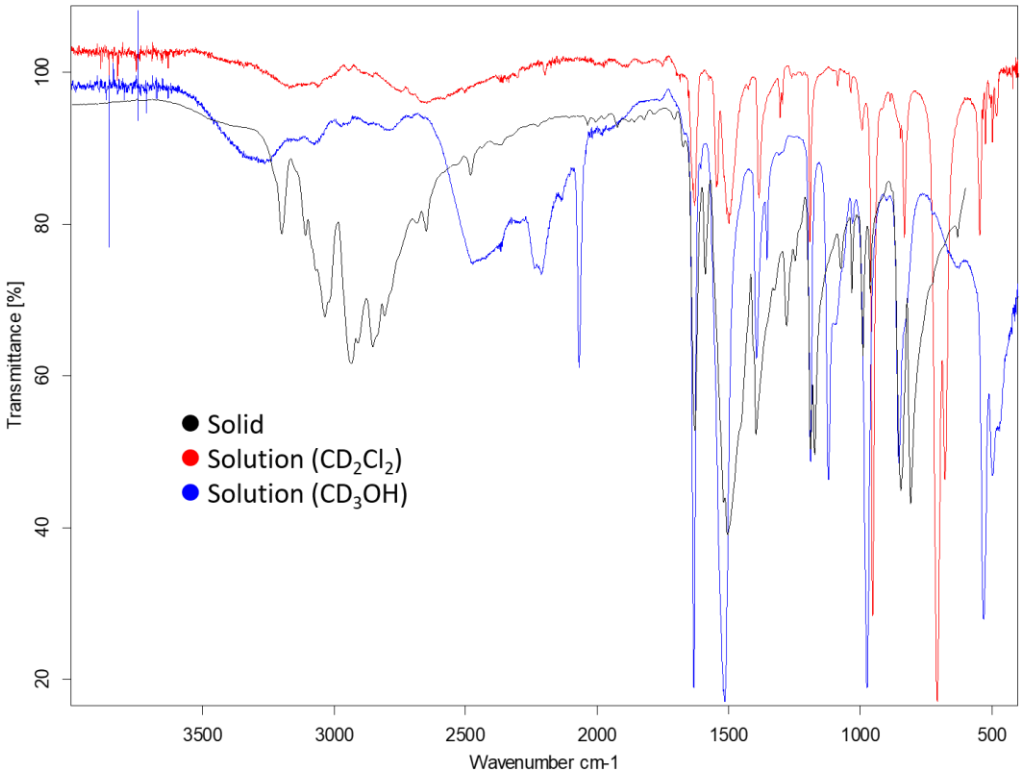

Figure 87 - FTIR spectra of 4-hydroxypyridine solid (black), dissolved in dichloromethane-d_2 (red) and dissolved in methanol-d_4 (blue). Solid FTIR was measured where a <1 mg of substrate was placed directly onto the diamond crystal. Solution FTIR was measured using the diamond fibre optic probe submersed into a vial containing the sample.

Figure 87 shows the FTIR spectra for the solid sample (black) compared to the two solutions in methanol-d_4 (blue) and dichloromethane-d_2 (red). The solid sample shows an absorbance at 3035 cm^{-1} which is indicative of an N-H stretch. The N-H bending mode is observed at 1504 cm^{-1}. A C=O stretch is observed at 1629 cm^{-1}. An O-H stretch which spans a wide range of absorbance frequencies (3300-2250 cm^{-1}) is due to intermolecular H-bonding via the carbonyl group. This confirms that the solid form exists exclusively as the keto tautomer. In methanol-d_4, the keto tautomer is also observed via absorbances at 3267 cm^{-1} and 1632 cm^{-1} which indicate the N-H and C=O stretching modes respectively. 4-Pyridone is shown to form in d_2-dichloromethane by the presence of the N-H stretch at 3172 cm^{-1} and the C=O stretch at 1629 cm^{-1}.

4.1.1.1.2 Temperature Dependence

In 1999 Murguly *et al.*[4] discovered that the keto/enol tautomerism of 4-hydroxypyridine in dichloromethane-d_2 was affected by temperature. They found that as they lowered the temperature from 25°C to -80°C, the proportion of the enol tautomer increased.

To investigate the effect of temperature on the keto/enol tautomerism, 4-hydroxypyridine (< 1 mg) was dissolved in dichloromethane-d_2 (0.6 mL). The sample was then cooled to 203 K in a 500 MHz Bruker Spectrometer before the spectrum was acquired. The temperature was then increased in 10 K increments up to 303 K and a ^{1}H spectra was acquired at each temperature (see Figure 88).

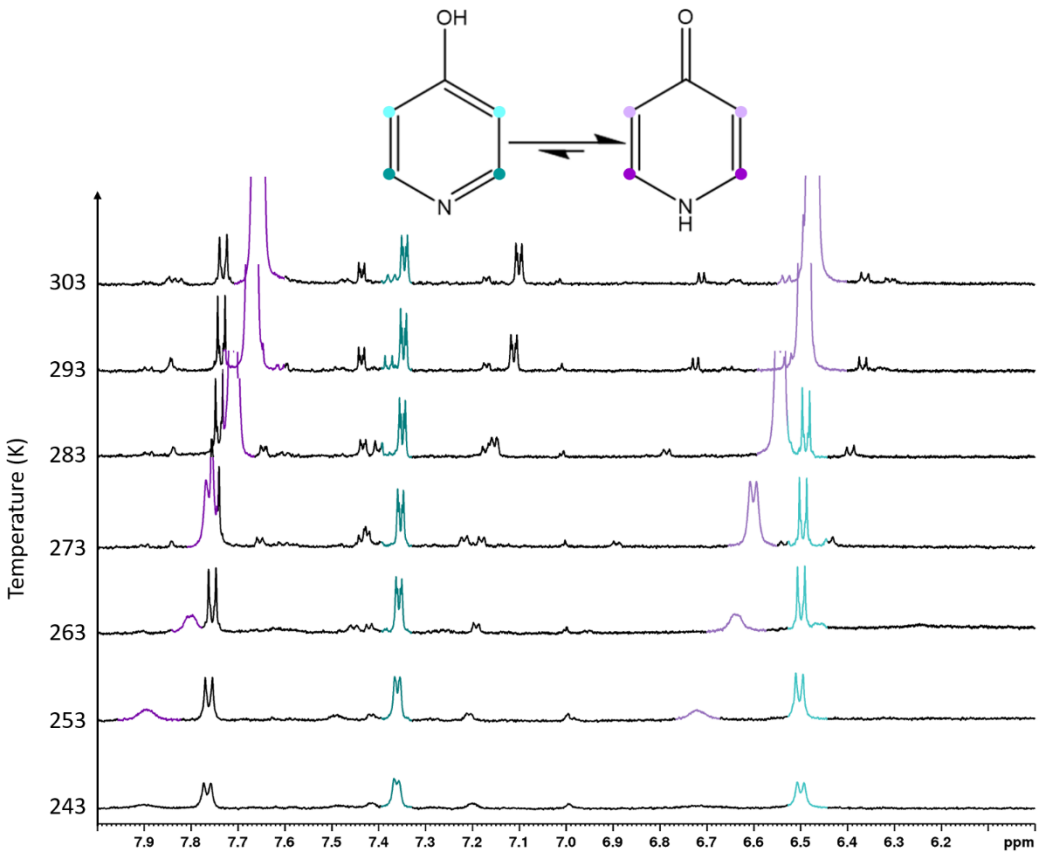

Figure 88 - ^{1}H NMR spectra as a function of temperature for a solution of 4-hydroxypyridine in dichloromethane-d_2. The enol tautomer is represented by the resonances highlighted in teal and the keto tautomer is indicated by the purple resonances. The darker colour represents the *ortho* ^{1}H resonance and the lighter colour the *meta* ^{1}H resonance. The samples were measured on the 500 MHz spectrometer.

Temperature (K)	Enol:Keto
<243	1:0
253	1:1
263	1:1
273	1:2
283	1:6
293	1:16
303	1:27

Table 13 - Table of the enol:keto ratio in the 4-hydroxypyridine/4-pyridone tautomerism as a function of sample temperature for the resonances shown in Figure 88

Figure 88 shows the corresponding ^{1}H-NMR spectra as a function of temperature for 4-hydroxypyridine. The teal colour is used to indicate the presence of the enol tautomer whilst the purple highlights the keto tautomer; 4-pyridone. The darker colours are used to represent the *ortho* ^{1}H resonance and the lighter colour the *meta* resonance. From 203 K to 243 K (not shown), the enol tautomer is predominant as no peaks from the keto tautomer are observed. At 253 K, small peaks at 7.90 and 6.72 ppm reveal the *ortho* and *meta* resonances of the keto tautomer. At this temperature the ratio of enol:keto is 2:1, at 263 K, the abundance of the enol tautomer is equal to that of the keto tautomer. As the temperature increases, the resonances for the keto tautomer increase as the tautomerism shifts to favour 4-pyridone, for example at 303 K, the ratio of enol:keto becomes 1:27 (Table 13).

According to the Van't Hoff equation, the equilibrium constant, K_{eq} of a chemical transformation is related to the change in temperature.[11] For a reversible reaction, the linear form of the Van't Hoff equation (Equation 17) can be used to find the enthalpy and entropy of the reaction where, $\ln(K_{eq})$ is plotted against $\frac{1}{T}$.[12]

$$lnK_{eq} = -\frac{\Delta H^{\theta}}{RT} + \frac{\Delta S^{\theta}}{R}$$

Equation 17, where K_{eq} is the equilibrium constant, ΔH^{θ} is the enthalpy, ΔS^{θ} is the entropy. T is the temperature and R is the gas constant

The enthalpy can then be calculated from the gradient ($-\frac{\Delta H^{\theta}}{RT}$) and the entropy from the intercept ($\frac{\Delta S^{\theta}}{R}$).

Using the ratio of the ketone tautomer from Table 15 as K_{eq}, the natural log of these values can be plotted against the reciprocal of the temperature

This equation can be applied to the data in Table 15, where the ratio of the pyridone tautomer is used as K_{eq}.

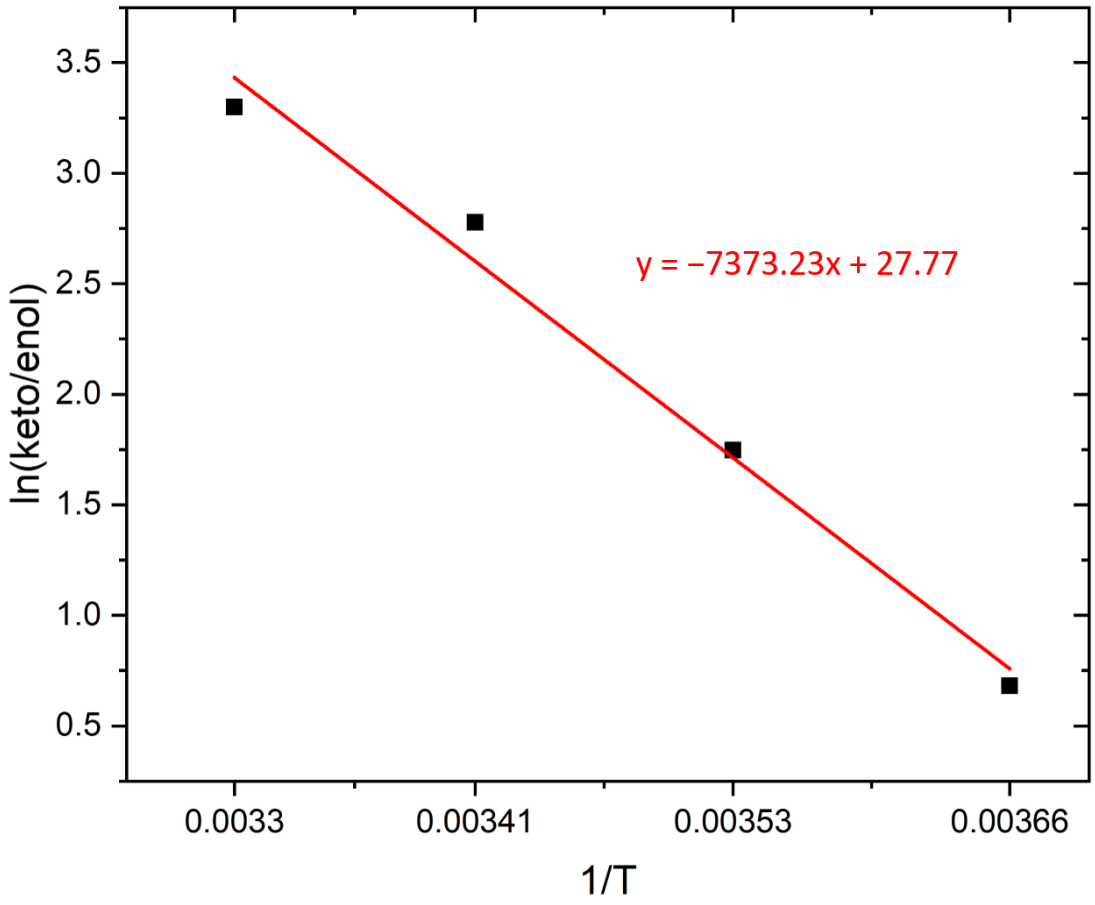

Figure 89 - plot of ln(keto/enol) as a function of 1/T according to the linear form of the Van't Hoff equation in Equation 17

The plot in Figure 89 shows that the formation of the pyridone tautomer is an endothermic reaction. This is why this tautomer is favoured at higher temperatures, as heat is absorbed, meaning that the net enthalpy change is positive. The enthalpy of this transformation is 887 $Jmol^{-1}$ and the entropy is 3.34 $JK^{-1}mol^{-1}$.

4.1.2 Isoniazid

Isoniazid, also known as isonicotinylhydrazide, is a derivative of pyridine containing a hydrazide functional group in the *para* position of the aromatic ring. It has received significant attention in the scientific community due to its use as an antibiotic in the treatment of tuberculosis (TB). It has also been included on the World Health Organisation's list of essential medicines since 1977.[13-15] The reactivity of isoniazid is also of interest as they can form stable complexes with transition metals behaving as mono-, bi- and even poly-dentate ligands,[16, 17] a number of which also possess anti-TB activity.[18]

In 2000, Bottari *et al.*[18] investigated and characterised a number of isoniazid-related transition metal complexes. They found that copper (II) and nickel (II) formed octahedral complexes where the four equatorial coordination sites were occupied by two molecules of isonicotinylhydrazone enolate (see Figure 90a)). The formation of this complex was detected using infrared spectroscopy where the most significant absorbances were observed at 1060 cm^{-1} and 1545 cm^{-1}. The former indicates the C-O stretch in enolate coordination and the latter represents the isonicotinic skeleton ring stretch which illustrates that the pyridine nitrogen does not participate in coordination to the metal centre. Similar complexes where the isoniazid coordinates via the oxygen and nitrogen in the hydrazide group have been observed by Stringer *et al*.[19] and Akinyele *et al.*[20], these complexes are shown in Figure 90.

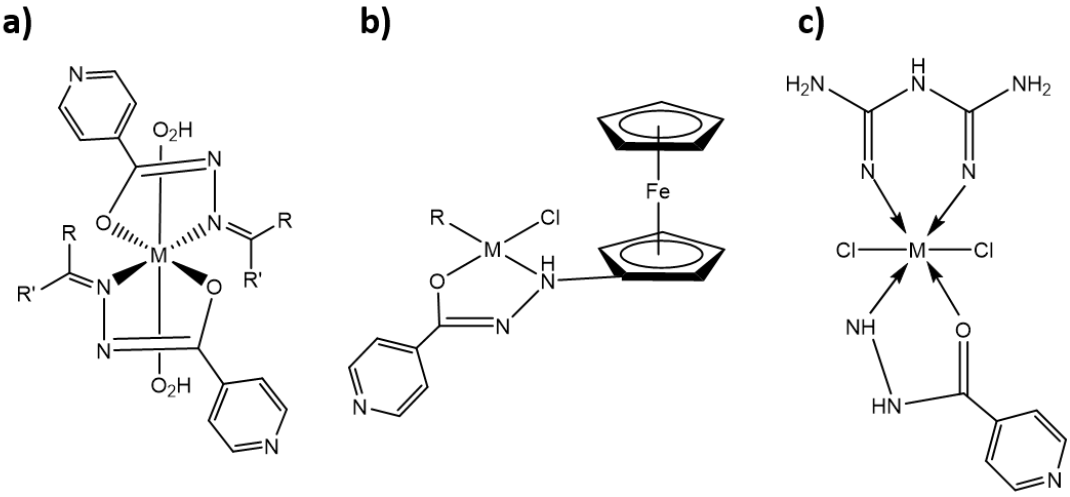

Figure 90 - Metal complexes formed with isoniazid. a) adapted with permissions from B. Bottari et *al.* [18] b) adapted with permissions from T. Stringer et *al.* [19] c) adapted with permissions from O. Akinyele et *al.* [20]

Isoniazid has previously been assessed as a SABRE candidate, first in 2013 by Zeng *et al*.[21] and again in 2017 by Norcott *et al*.[22] In the first paper, Zeng *et al*.[21] investigated the SABRE hyperpolarisation of isoniazid and its suitability for in vivo applications. They found that the maximum enhancement was −220-fold at the *ortho* proton at 46.1°C and 65 G using the iridium catalyst [IrCl(COD)(IMes)]. In 2017, Norcott *et al*.[22] explored a number of different TB drug scaffolds, including their deuterated analogues, and compared their SABRE enhancements and lifetimes. It was discovered that polarisation levels of 20% were possible using a deuterated analogue of isoniazid combined with the deuterated form of IMes (d_{24}-IMes). In both studies, it was assumed that isoniazid bound into the iridium metal centre via the pyridine nitrogen. However, this structure was never confirmed via characterisation.

4.2 Formation of the SABRE pre-catalyst

In the first step of SABRE, the substrate is added to [IrCl(COD)(NHC)]. Typically this induces the displacement of the chloride ligand to form the 16 electron, square planar species; [Ir(COD)(NHC)(sub)]Cl which is termed the 'SABRE pre-catalyst'. Examples of this complex can be found in the previous chapter (see Figure 57). The complexes that form upon reaction of [IrCl(COD)(SIMes)] with 4-hydroxypyridine and isoniazid have been fully characterised by ^{1}H, ^{13}C and ^{15}N-NMR, full details of which can be found below.

4.2.1 [Ir(COD)(SIMes)(4-Hydroxypyridine)]Cl

Despite tautomerism of 4-hydroxypyridine to 4-pyridone, upon reaction with [IrCl(COD)(SIMes], the precatalyst [Ir(COD)(SIMes)(4-hydroxypyridine)]Cl forms.

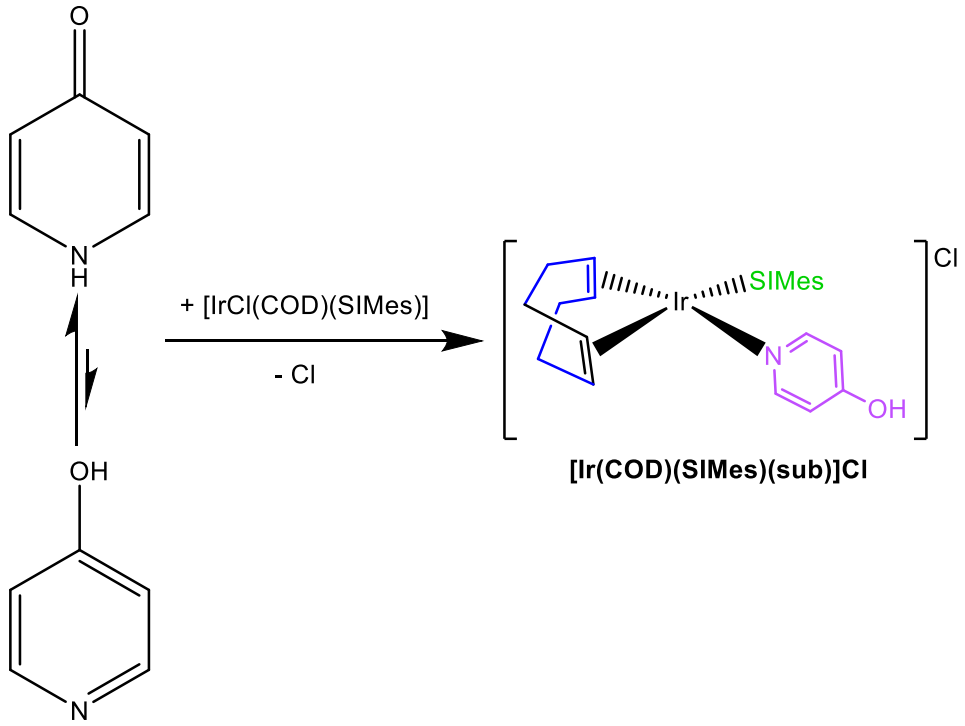

Figure 91 - Schematic diagram of the formation of the SABRE precatalyst [Ir(COD)(SIMes)(sub)]Cl with the substrate 4-hydroxypyridine

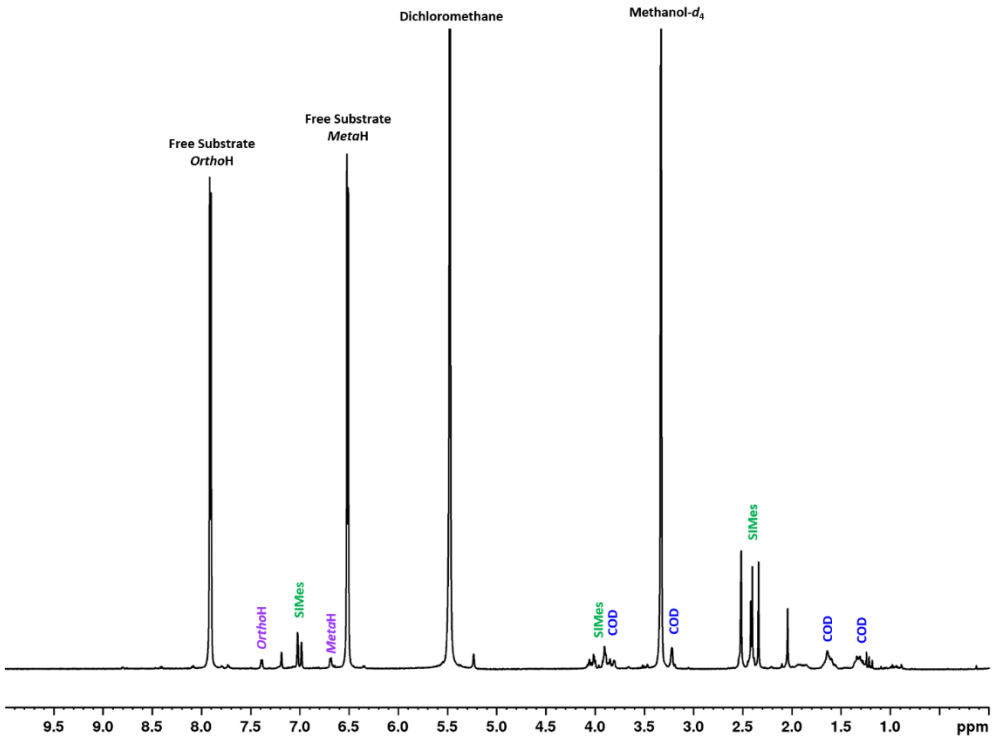

Figure 92 - ^{1}H NMR spectra of the SABRE precatalyst; [Ir(COD)(SIMes)(4-hydroxypyridine)]Cl. The sample contained [IrCl(COD)(SIMes)] (5 mM) and 4-hydroxypyridine (50 mM) dissolved in methanol-d_4 (0.6 mL). The NMR spectrum was acquired at 235 K and 500 MHz.

Position	**^{1}H-NMR**	**^{13}C-NMR**	**^{15}N-NMR**
Free*ortho*H	7.910 J_{HH} = 7.2 Hz	139.1	152.8
Free*meta*H	6.515 J_{HH} = 7.2 Hz	116.5	
Free*para*C=O	-	180.2	
Position	**^{1}H-NMR**	**^{13}C-NMR**	**^{15}N-NMR**
*ortho*H^{sub}	7.389 J_{HH} = 5.95 Hz		207.9
*meta*H^{sub}	6.687 J_{HH} = 5.95 Hz	113.1	
CH^{Ar,Mes}	7.187 6.984	129.8 129.2	
N-CH$_2$-CH$_2$-N	4.037	52.1	
CH^{COD}	3.905 3.220	63.4 51.6	
*ortho*CH$_3^{Mes}$	2.515 2.417	19.9	

$para\mathrm{CH_3}^{\mathrm{Mes}}$	2.043	17.4
$\mathrm{CH_2}^{\mathrm{COD}}$	1.627 1.312	29.7 26.4

Table 14 - NMR resonances for the product formed by reaction of [IrCl(COD)(SIMes)] (5 mM) and 4-hydroxypyridine (50 mM) in methanol-d_4. ^{1}H at 500 MHz, ^{13}C at 125 MHz and ^{15}N at 51 MHz at 235 K.

Confirmation of the binding of 4-hydroxypyridine via the pyridine nitrogen is clearly evident in the ^{15}N-NMR spectrum (Figure 93). The free substrate ^{15}N resonance for the pyridine nitrogen can be found at 152.8 ppm. This resonance is shifted upfield compared to the free pyridine ^{15}N resonance in 4-methylpyridine because in the free solution, 4-hydroxypyridine exists predominantly in the keto form as 4-pyridone. Upon ligation to the iridium centre, this resonance shifts to 207.9 ppm. Further confirmation can be found in the ^{13}C-NMR spectrum where the ^{13}C resonance that corresponds to C-OH in 4-hydroxypyridine or C=O in 4-pyridone can be readily differentiated. In the free solution, this can be found at 180.2 ppm, indicating the presence of 4-pyridone. In the bound substrate, this shifts to 152 ppm corresponding to C-OH in 4-hydroxypyridine.

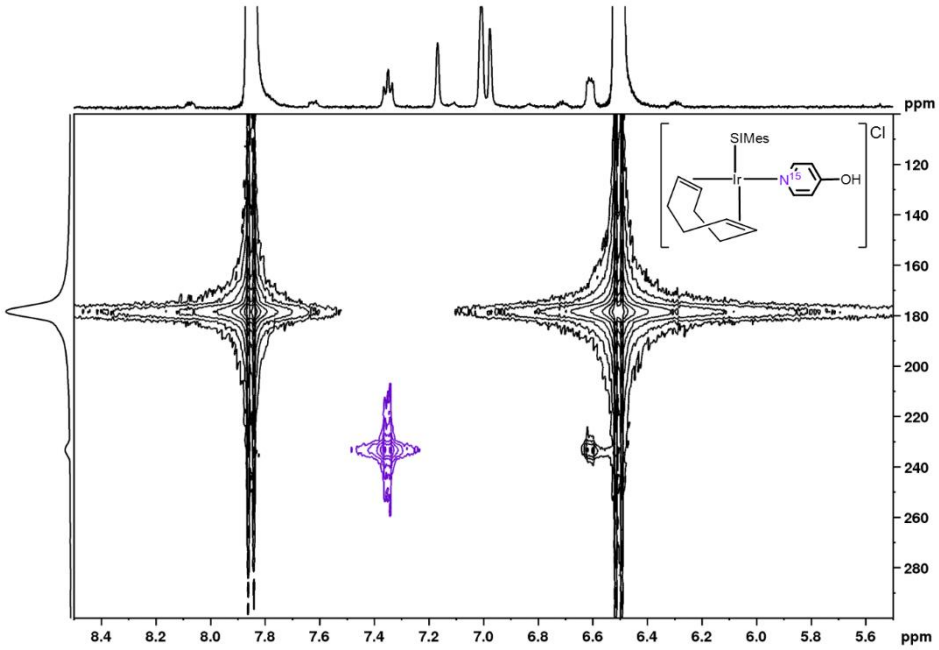

Figure 93 - ^{15}N/^{1}H HMQC NMR spectrum of a solution containing [IrCl(COD)(SIMes)] (5 mM) and ^{15}N-labelled 4-hydroxypyridine (50 mM) in methanol-d_4 at 9.4 T and 253 K. The purple highlighted resonance indicates the

^{15}N-labelled pyridine nitrogen in the bound 4-hydroxypyridine in the SABRE precatalyst; [Ir(COD)(SIMes)(sub)]Cl.

4.2.1.1 In dichloromethane-d_2

It was previously observed that upon dissolution of 4-hydroxypyridine in dichloromethane-d_2, a mixture of both enol/keto tautomers are present in solution (see Section 4.1.1.1.2). The ratio of these tautomers has been shown to be temperature dependent (Figure 88). To observe this effect on the SABRE-precatalyst, 4-hydroxypyridine (50 mM) was added to [IrCl(COD)(SIMes)] (5 mM) in dichloromethane-d_2. This reaction produced a mixture of species in solution. The first species contained the enol tautomer bound to iridium through the pyridine nitrogen and the second the keto tautomer bound via the oxygen. The ratio of these species was also temperature dependent (Figure 94).

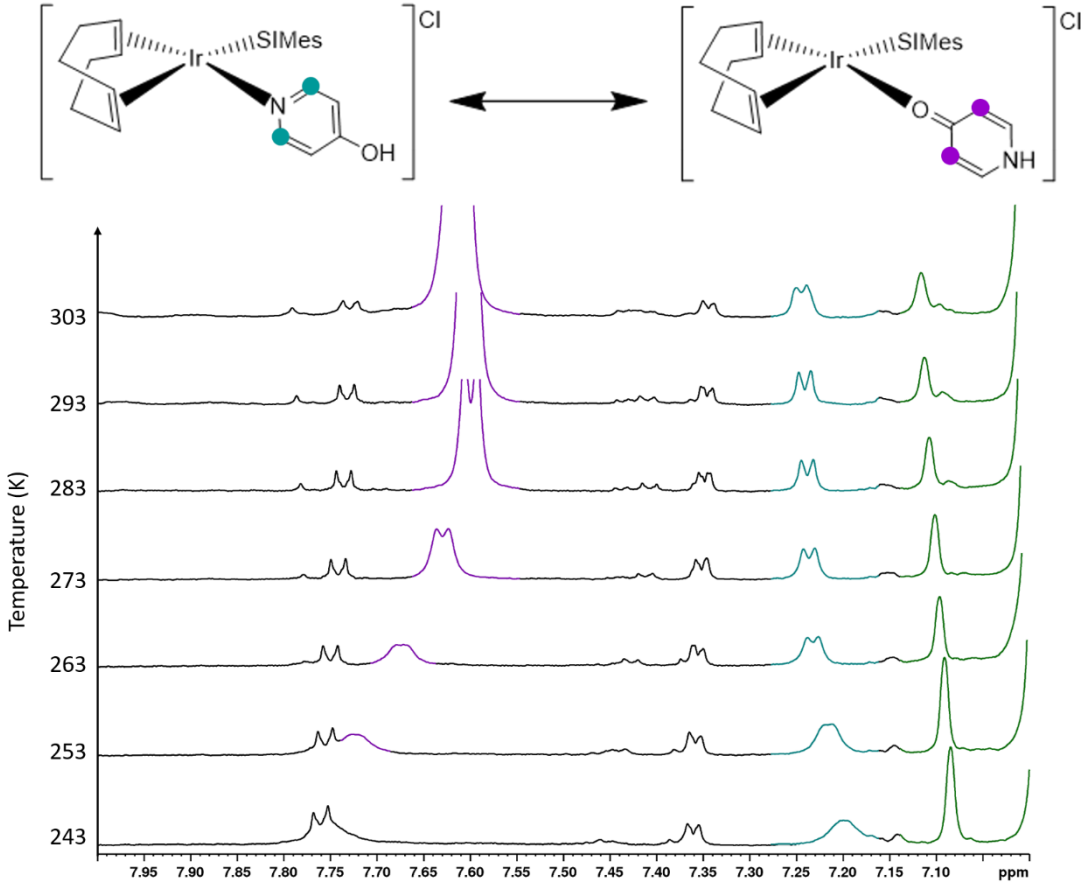

Figure 94 - ^{1}H NMR spectra as a function of temperature for a solution of 4-hydroxypyridine (40 mM) and [IrCl(COD)(SIMes)]Cl (4 mM) in dichloromethane-d_2. The enol tautomer is represented by the resonances highlighted in teal and the keto tautomer is indicated by the purple resonances. Only the resonances at the *ortho* proton are shown. These spectra were measured on a 500 MHz spectrometer.

Temperature (K)	Enol:Keto
<243	1:0
253	2:1
263	1:1
273	1:2
283	1:6
293	1:10
303	1:14

Table 15 - Table of the enol:keto ratio in the 4-hydroxypyridine/4-pyridone tautomerism as a function of sample temperature for the resonances shown in Figure 94

Figure 94 shows a very similar trend to that of Figure 88 where at temperatures below 253 K (not shown) the enol isomer is predominant. At 253 K, the keto tautomer emerges as a broad resonance at 7.72 ppm. At 263 K the enol and keto tautomer are equally present in solution. From 273 – 303 K, the keto tautomer becomes the predominant species in solution. This form has been characterised by ^{13}C NMR where the keto carbon can be observed at 198 ppm. This compares to the free substrate (4-pyridone) where this carbon is detected at 208.8 ppm. The shift in the pre-catalyst [Ir(COD)(SIMes)(4-pyridone)] is due to ligation to iridium.

The ratio of the keto tautomer in Table 15 can be used to generate a Van't Hoff plot where ln(keto/enol) is plotted as a function of $\frac{1}{T}$. The enthalpy (ΔH^{θ}) and entropy (ΔS^{θ}) can then be calculated using the gradient and the intercept.

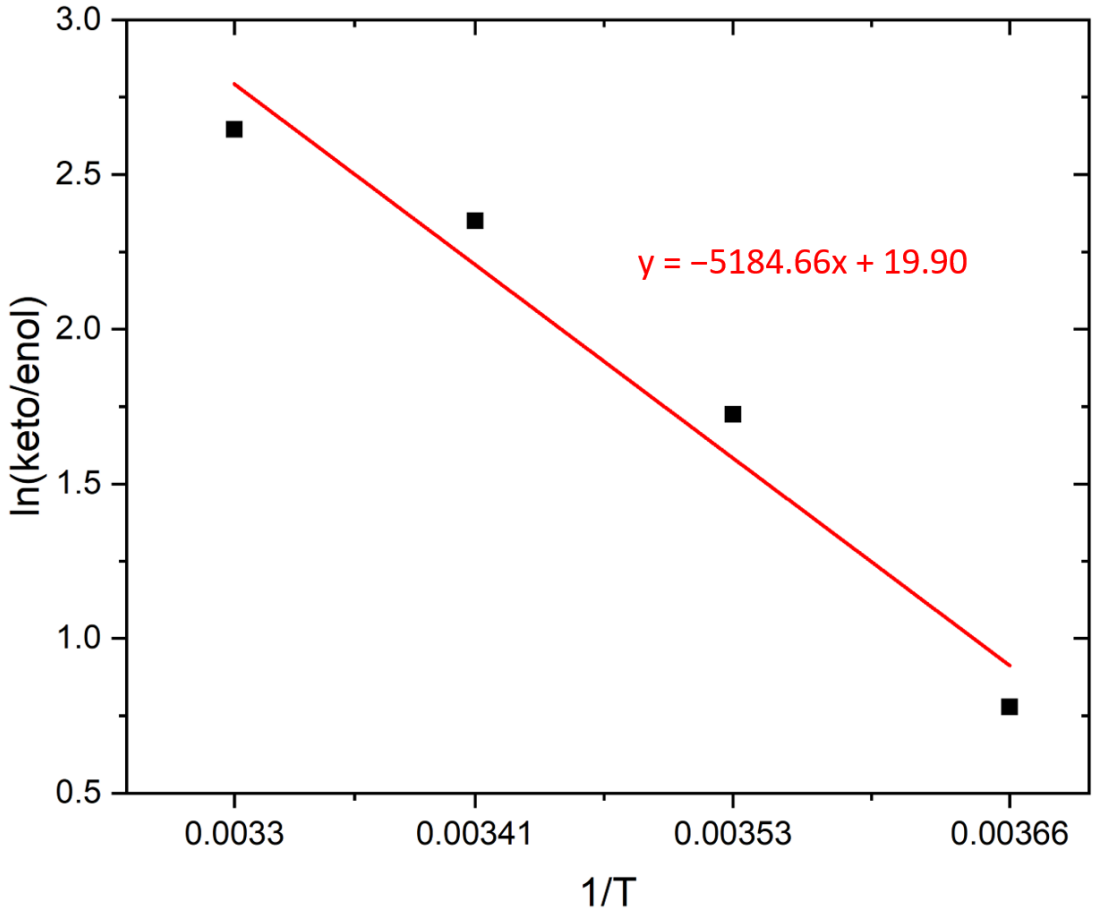

Figure 95 - plot of ln(keto/enol) as a function of 1/T according to the linear form of the Van't Hoff equation in Equation 1

Similarly to Figure 89, the plot in Figure 95 also shows that the formation of the pyridone tautomer is an endothermic reaction. The enthalpy in this case is 624 $Jmol^{-1}$ and the entropy is 2.39 $JK^{-1}mol^{-1}$ which are smaller than the corresponding values in the substrate; 887 $Jmol^{-1}$ and 3.34 $JK^{-1}mol^{-1}$ respectively (Figure 89). This means that formation of the pyridone tautomer is more favourable with [Ir(COD)(SIMes)(4-hydroxypyridine)]Cl.

4.2.2 [Ir(COD)(SIMes)(Isoniazid)]Cl

Upon addition of isoniazid to [IrCl(COD)(SIMes)], two products form in a 2:1 ratio. In the major species ligation occurs via the oxygen atom of the hydrazide group. In the minor species, isoniazid binds in the traditional way, via the pyridine nitrogen atom.

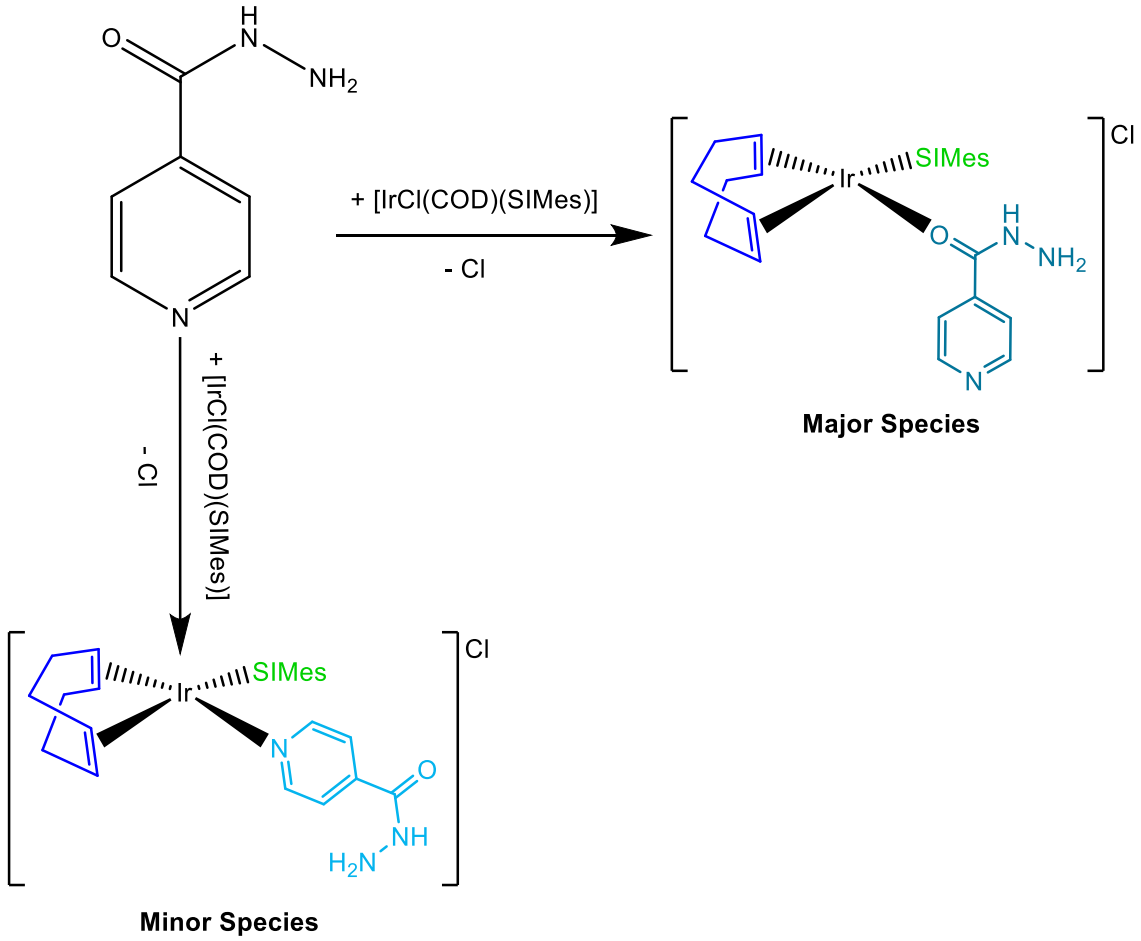

Figure 96 - Schematic diagram for the formation of the SABRE precatalst [Ir(COD)(SIMes)(sub)]Cl for the substrate isonaizid showing the major and minor forms. The major species binds to the iridium via the oxygen in the hydrazide group and the minor binds via the pyridine nitrogen.

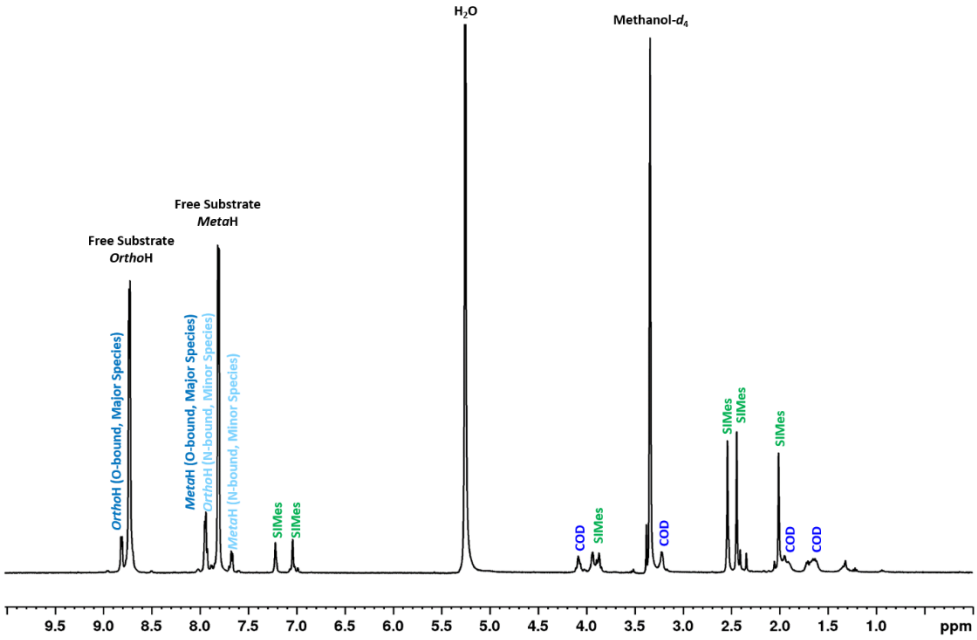

Figure 97 - ^{1}H NMR spectrum of the SABRE precatalyst [Ir(COD)(SIMes)(isoniazid)]Cl. Sample initially contained [IrCl(COD)(SIMes)(sub)] (5 mM) and isoniazid (50 mM) in methanol-d_4 (0.6 mL) and was measured at 500 MHz and 235 K.

Position	***^{1}H-NMR***	***^{13}C-NMR***	***^{15}N-NMR***
Free*ortho*H	8.730 J_{HH} = 5.3 Hz	149.7	308.2
Free*meta*H	7.809 J_{HH} = 5.3 Hz	121.7	
FreeC-CONHNH$_2$	-	165.6	
	MAJOR SPECIES Oxygen Bound Isoniazid		
Position	**^{1}H-NMR**	**^{13}C-NMR**	**^{15}N-NMR**
*ortho*H^{sub}	8.812 J_{HH} = 5.3 Hz	151.7	311.0
*meta*H^{sub}	7.929 J_{HH} = 5.3 Hz	123.5	
CH^{Ar,Mes}	7.219 7.041	136.0 129.7	
N-CH$_2$-CH$_2$-N	4.084 3.870	52.3	
CH^{COD}	3.935 3.219	64.4 83.2	

orthoCH_3^{Mes}	2.539 2.445	19.9	
paraCH_3^{Mes}	2.010	17.3	
CH_2^{COD}	1.907 1.653	32.2 28.8	
	MINOR SPECIES **Pyridine Bound Isoniazid**		
orthoH^{sub}	7.945 J_{HH} = 6.1 Hz	151.7	248.5
metaH^{sub}	7.669 J_{HH} = 6.1 Hz	122.9	
$CH^{Ar,Mes}$	7.219 7.041	136.0 129.4	
N-CH_2-CH_2-N	4.084 3.870	52.14	
CH^{COD}	3.935 3.219	64.4 83.0	
orthoCH_3^{Mes}	2.526 2.408	18.9	
paraCH_3^{Mes}	2.345	17.1	
CH_2^{COD}	1.907 1.653	31.8 28.7	

Table 16 - Table of NMR Resonances for the SABRE precatalyst [Ir(H)$_2$(SIMes)(Isoniazid)$_2$Cl] in methanol-d_4. ^{1}H resonances measured at 500 MHz, ^{13}C at 125 MHz and ^{15}N at 51 MHz at 235 K.

Confirmation of these structures comes from the ^{15}N-NMR data. In the major species, the pyridine nitrogen can be found at 311 ppm which is close to the ^{15}N resonance of the free substrate in solution (308.2 ppm). In the minor species, this shifts to 248 ppm due to ligation to the iridium centre.

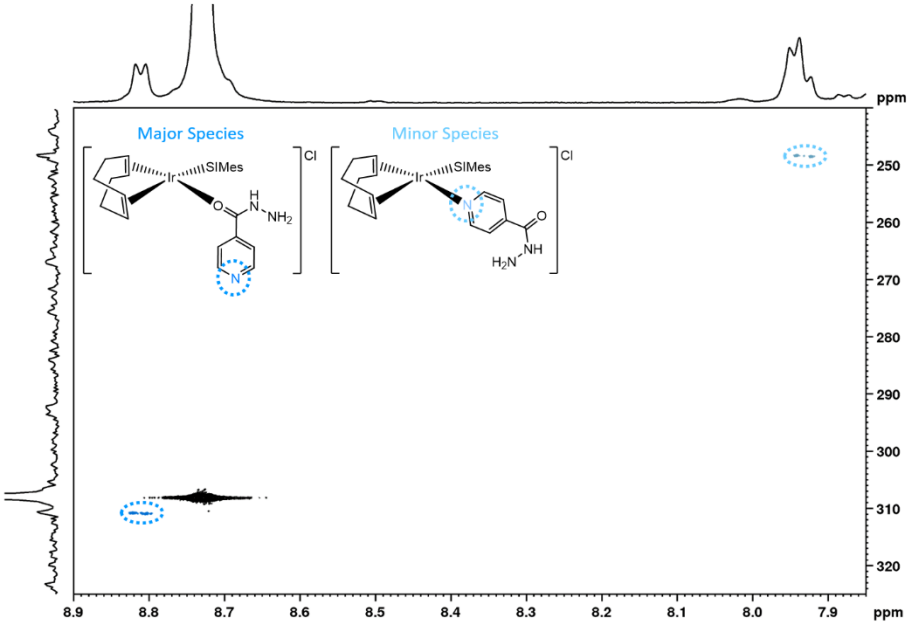

Figure 98 - $^{1}H/^{15}N$ HMQC NMR spectrum of a solution of [IrCl(COD)(SIMes)] (5 mM) and isoniazid (50 mM) in methanol-d_4 at 9.4 T and 263 K.

To confirm that binding to iridium in isoniazid does not occur via the hydrazide nitrogen atom, the ^{15}N resonances for this functional group were also measured. These were shown to be very similar to the ^{15}N chemical shifts of the free substrate and therefore show that ligation must occur via the lone pair on the oxygen atom.

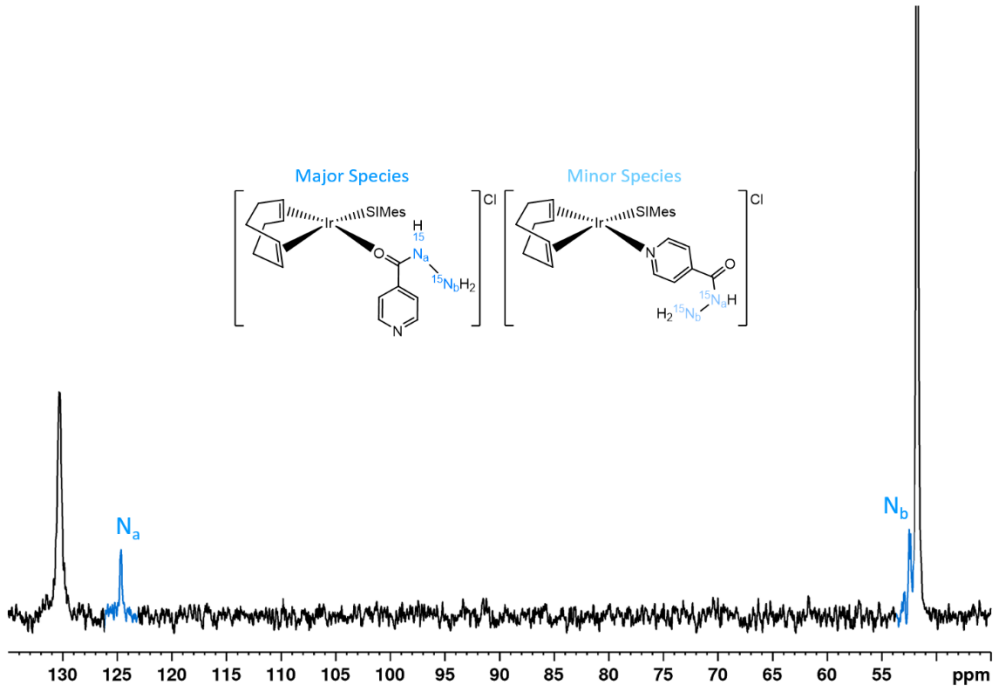

Figure 99 - ^{15}N NMR spectrum of the SABRE precatalyst [Ir(COD)(SIMes)(isoniazid)]Cl with i^{15}N-labelled labelled isoniazid. ^{15}N NMR spectrum measured at 40.56 MHz and 263 K. The strong signals are due to the free ligand

^{15}N-NMR	Free Substrate	Oxygen Bound
N_{py}	308.2	311.0
N_a	130.7	124.9
N_b	51.8	52.5

Table 17 - Table of ^{15}N NMR hydrazide functional group resonances for the SABRE precatalyst [Ir(COD)(SIMes)(isoniazid)]Cl in methanol-d_4 measured at 40.56 MHz and 263 K.

4.3 Formation of the SABRE-Active Catalyst

A SABRE-active catalyst is formed upon addition of *p*-H_2 to the precatalyst. Typically this forms an octahedral complex of the form $[Ir(H)_2(SIMes)(sub)_3]Cl$ where two substrate ligands lie in the equatorial plane *trans* to two hydride ligands. The third substrate is bound *trans* to the NHC in the axial position. Examples of this *tris*-substituted species can be found in the previous chapter (see Figure 26).

The complexes that form with 4-hydroxypyridine and isoniazid have been fully characterised by ^{1}H, ^{13}C and ^{15}N-NMR, full details of which can be found below.

4.3.1 [IrCl(H)$_2$(SIMes)(κ-O-4-pyridone)(κ-N-4-hydroxypyridine)]

When 4-hydroxypyridine is used as the substrate of interest, a neutral *bis*-substituted complex [IrCl(H)$_2$(SIMes)(κ-O-4-pyridone)(κ-N-4-hydroxypyridine)] forms (NMR data Table 18).

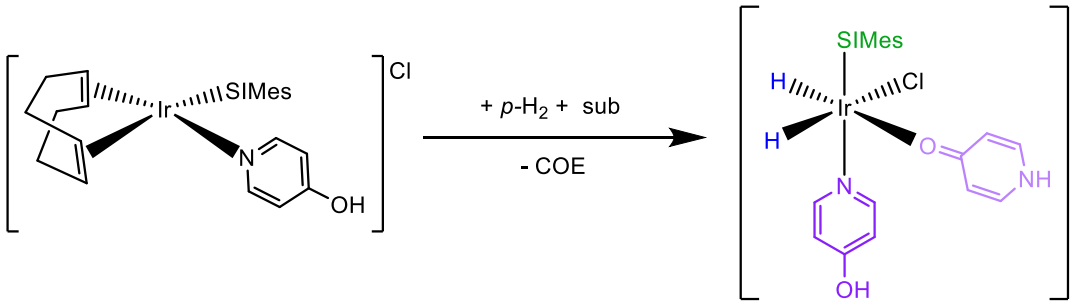

Figure 100 - Schematic diagram showing the formation of the SABRE-active species [IrCl(H)$_2$(SIMes)(κ-O-4-pyridone)(κ-N-4-hydroxypyridine)] from the precatalyst [Ir(COD)(SIMes)(4-hydroxypyridine)]Cl

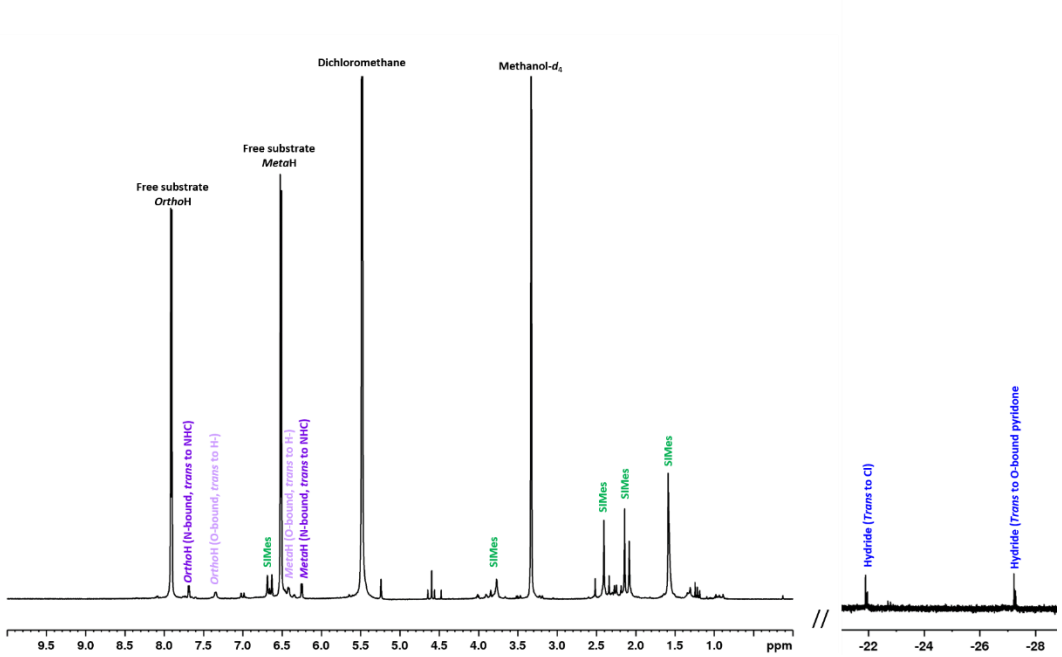

Figure 101 - ^{1}H NMR spectrum of the SABRE-active species [IrCl(H)$_2$(SIMes)(κ-O-4-pyridone)(κ-N-4-hydroxypyridine)] . Sample contains [IrCl(COD)(SIMes)] (5 mM), 4-hydroxpyridine (50 mM) and *p*-H$_2$ (4 bar) dissolved in methanol-*d*$_4$ (0.6 mL) in a young's tap NMR tube. Sample was measured at 500 MHz and 235 K.

Position	^{1}H-NMR	^{13}C-NMR	^{15}N-NMR
Free*ortho*H	7.912 J_{HH} = 7.3 Hz	139.0	152.9
Free*meta*H	6.516 J_{HH} = 7.3 Hz	116.5	

*Free*paraC=O		180.3	
Position	**^{1}H-NMR**	**^{13}C-NMR**	**^{15}N-NMR**
orthoH^{sub} (trans to H^{-})	7.348	136.1	148.8
orthoH^{sub} (trans to NHC)	7.688 J_{HH} = 6.5 Hz	154.5	215
metaH^{sub} (trans to H^{-})	6.418	117.8	
metaH^{sub} (trans to NHC)	6.251 J_{HH} = 6.5 Hz	111.8	
$CH^{Ar,Mes}$	6.689 6.630	128.1	
N-CH_2-CH_2-N	3.769	50.2	
orthoCH_3^{Mes}	2.405 2.142	19.8	
paraCH_3^{Mes}	2.082	17.1	
H	-21.24 -27.24	-	

Table 18 - Table of NMR Resonances for [IrCl(H)$_2$(SIMes)(κ-O-4-pyridone)(κ-N-4-hydroxypyridine)] in methanol-d_4. ^{1}H at 400 MHz and 253 K, ^{13}C at 125 MHz and 235 K and ^{15}N at 41 MHz at 253 K.

These NMR data suggest that the SABRE-active species for 4-hydroxypyridine is of the form [IrCl(H)$_2$(SIMes)(sub)$_2$] where the chloride ligands lies *trans* to hydride. This hydride resonance is observed at −21.24 ppm. Iali *et al*.[23] and Tickener *et al*.[24] have both reported similar hydrides which are bound *trans* to chloride at -21.53. The second hydride is bound *trans* to the keto tautomer of 4-hydroxypyridine, 4-pyridone, which ligates to iridium via the oxygen in the ketone group. This hydride resonance is found at −27.24 ppm. SABRE complexes involving an oxygen bound substrate have been described by Iali *et al*.[23] using pyruvate. They observed hydride resonances *trans* to oxygen at −27 and −29 ppm. In 2019, Tickener *et al.*[25, 26] also characterised hydride ligands *trans* to oxygen using an α-carboxyimine coligand. These were found at −28.5 ppm. The second substrate binds in the axial position *trans* to the NHC. This ligand binds in the traditional way, through the pyridine nitrogen lone pair.

Confirmation of this structure can also be found in the ^{13}C-NMR resonances of the keto/enol carbon. The carbon for the oxygen bound, keto substrate (*trans* to hydride) is located at 180 ppm. The substrate *trans* to SIMes is observed at 164 ppm which is

indicative of the enol tautomer which is bound through the pyridine nitrogen lone pair (Figure 102).

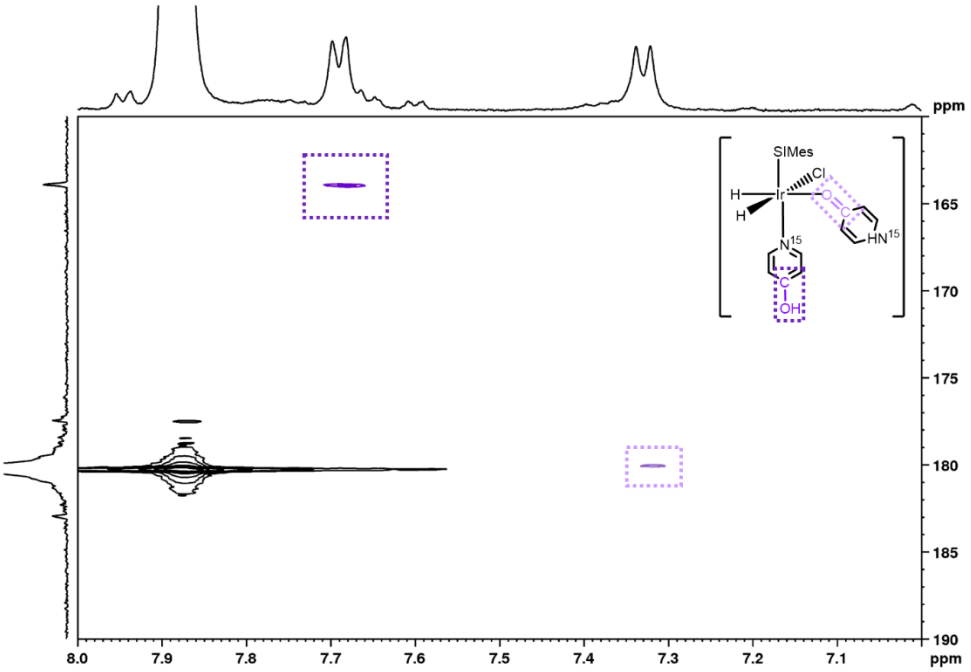

Figure 102 - $^{1}H/^{13}C$ -HMQC NMR spectrum of [IrCl(H)$_2$(SIMes)(κ-O-4-pyridone)(κ-N-4-hydroxypyridine)]. Sample containing [IrCl(COD)(SIMes)] (5 mM), 4-hydroxypyridine (50 mM) and *p*-H$_2$ (4 bar) dissolved in methanol-d_4 measured at 11.74 T at 235 K. Resonance for the keto carbon shown at 180 ppm (^{13}C)/7.35 ppm (^{1}H) is highlighted in lilac and resonance for the enol carbon shown at 164 ppm (^{13}C)/7.69 ppm (^{1}H) highlighted in purple.

The ^{15}N isotopologues of 4-hydroxypyridine were used to confirm the binding modes of the two substrate ligands in the SABRE-active species via $^{1}H/^{15}N$-HMQC (Figure 103). The ^{15}N resonance for the substrate bound *trans* to the NHC is observed at 215 ppm. This suggests the enol tautomer is binding via the pyridine nitrogen. This compares to the substrate *trans* to the hydride where the pyridine nitrogen is detected at 148 ppm. This indicates an amino-nitrogen and suggests binding via the ketone oxygen atom in 4-pyridone.[27]

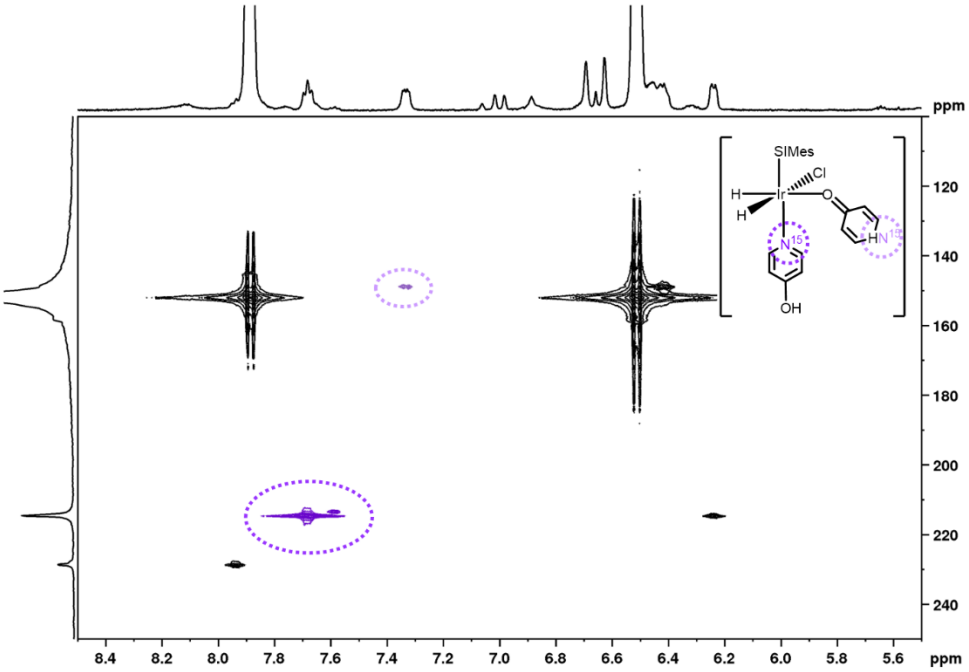

Figure 103 –^{1}H/^{15}N -HMQC of [IrCl(H)$_2$(SIMes)(κ-O-4-pyridone)(κ-N-4-hydroxypyridine)]. Sample containing [IrCl(COD)(SIMes)] (5 mM), 4-hydroxypyridine (50 mM) and *p*-H$_2$ (4 bar) dissolved in methanol-*d*$_4$ measured at 500 MHz (^{1}H) and 51 MHz (^{15}N) at 235 K. Resonance for the nitrogen in the keto tautomer shown at 215 ppm (^{15}N)/7.35 ppm (^{1}H) is highlighted in lilac and the resonance for the nitrogen in the enol form is shown at 148.8 ppm (^{15}N)/7.69 ppm (^{1}H) highlighted in purple.

Whilst the pre-catalyst was also characterised in *d*$_2$-dichloromethane (Section 4.2.1.1), addition of *p*-H$_2$ did not promote the formation of a SABRE-active species.

4.3.2 [Ir(H)$_2$(SIMes)(κ-N-isonicotinylhydrazide)(isonicotinyl-κ-O-κ-N-hydrazide]Cl

When isoniazid reacts with [IrCl(COD)(SIMes)] a major and minor species form in solution; in the major species isoniazid binds via the oxygen in the hydrazide group, while in the minor species it binds through the pyridine nitrogen atom. Upon reaction with *p*-H$_2$, a *bis*-substituted complex forms whereby one isoniazid chelates to the iridium via the oxygen and nitrogen in the hydrazide group and a second ligates through the pyridine nitrogen. This complex has been fully characterised by ^{1}H, ^{13}C and ^{15}N-NMR methods.

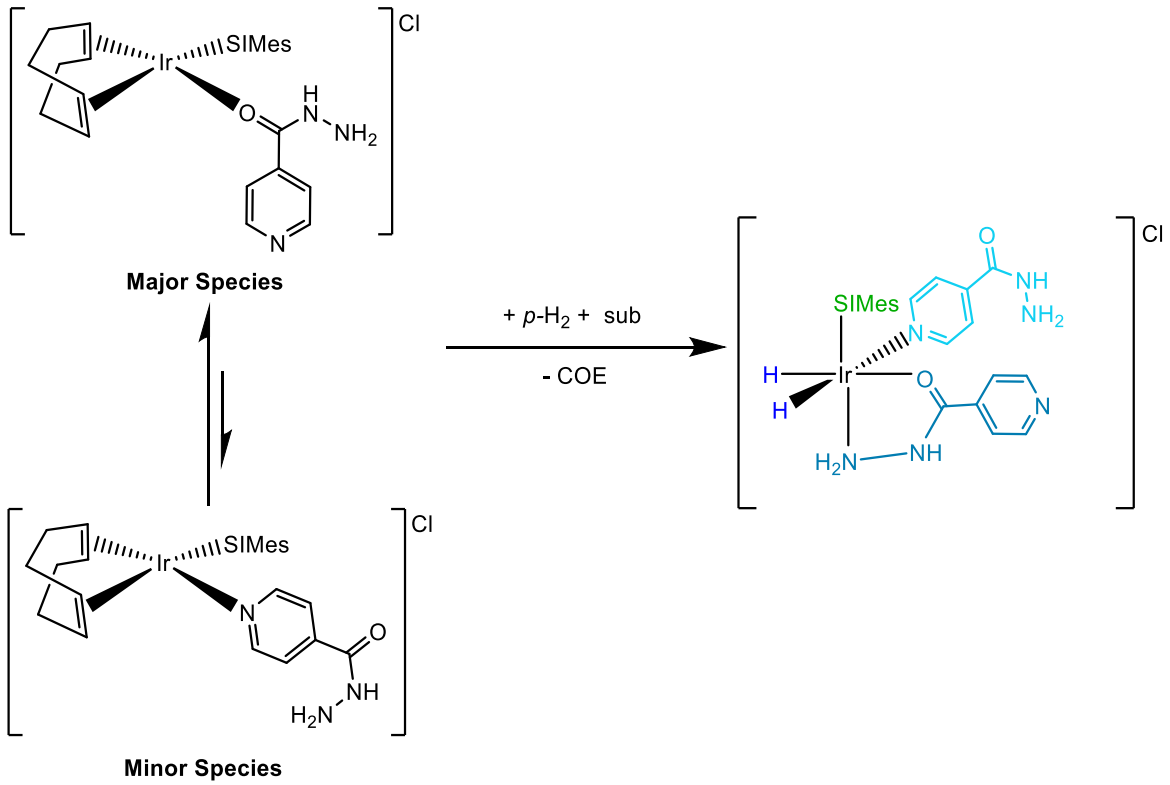

Figure 104 - Schematic diagram showing the formation of the SABRE-active species $[Ir(H)_2(SIMes)(\kappa\text{-}N\text{-}isonicotinylhydrazide)(isonicotinyl\text{-}\kappa\text{-}O\text{-}\kappa\text{-}N\text{-}hydrazide]Cl$ from the pre-catalyst [Ir(COD)(SIMes)(sub)]Cl.

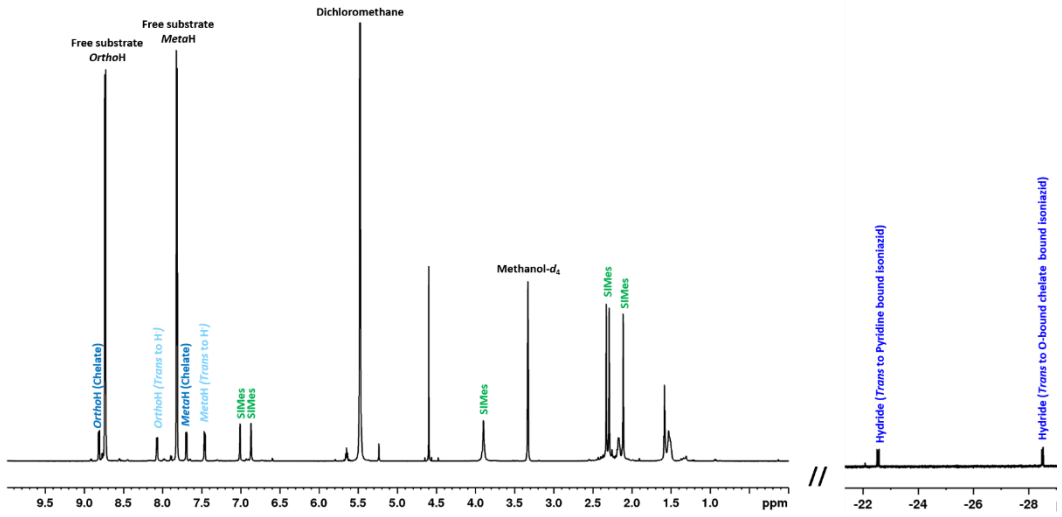

Figure 105 - ^1H NMR spectra of the SABRE-active catalyst formed upon the reaction of [IrCl(COD)(SIMes)] (5 mM) with isoniazid (50 mM) and $p\text{-}H_2$ (4 bar) in methanol-d_4 (0.6 mL). Spectra measured at 500 MHz and 235 K.

Position	***^{1}H-NMR***	***^{13}C-NMR***	***^{15}N-NMR***
Free*ortho*H	8.698	149.5	308.6
Free*meta*H	7.783	121.6	
Free*para*CONHNH$_2$	-	141.3	
FreeCONHNH$_2$	-	165.4	
Position	**^{1}H-NMR**	**^{13}C-NMR**	**^{15}N-NMR**
*ortho*H (chelate bound)	8.81	149.87	311.7
*ortho*H (N$_{py}$ -bound)	8.07	154.04	261.1
*meta*H (chelate bound)	7.70	121.86	
*meta*H (N$_{py}$ -bound)	7.46	123.83	
*para*CONHNH$_2$ (chelate bound)	-	140.3	
*para*CONHNH$_2$ (N$_{py}$-bound)		139.9	
CONHNH$_2$ (chelate bound)	-	169.9	
CONHNH$_2$ (N$_{py}$-bound)		165.5	
CH^{Ar,Mes}	6.89 7.01	128.75	
N-CH$_2$-CH$_2$-N	3.91		
*ortho*CH$_3^{Mes}$	2.33 2.29	19.98 17.43	
*para*CH$_3^{Mes}$	2.11	16.93	
H$^-$	-22.57 -28.52		

Table 19 - Table of NMR Resonances for [Ir(H)$_2$(SIMes)(κ-N-isonicotinylhydrazide)(isonicotinyl-κ-O-κ-N-hydrazide]Cl in methanol-*d*$_4$. ^{1}H measured at 400 MHz and 253 K, ^{13}C at 125 MHz and 235 K and ^{15}N at 41 MHz at 253 K.

The hydride ligand signals observed in the ^{1}H NMR spectrum of the product formed upon reaction of isoniazid and [IrCl(COD)(SIMes)] with H_2 are similar to those detected for 4-hydroxypyridine. The hydride resonance observed at -28.52 ppm is indicative of being *trans* to an Ir-O binding mode.[23-26, 28, 29] Isoniazid contains three

different sites capable of ligation to iridium; the nitrogen within the pyridine ring and the oxygen and nitrogen in the hydrazide group. The presence of two binding sites within the hydrazide group means that isoniazid can chelate to the iridium with the oxygen binding *trans* to the hydride at −28.52 ppm. The second hydride signal at −22.57 ppm is similar in chemical shift to those of the *tris*-substituted species produced with 4-methylpyridine, 4-methoxypyridine and 4-pyridinecarboxaldehyde (see previous chapter).[30] Therefore, the second substrate ligand binds to iridium through the nitrogen within the pyridine ring *trans* to the hydride at −22.57 ppm.

Further evidence for these two ligation motifs is observed through the ^{13}C chemical shift of the carbon resonances in the hydrazide group. The signal giving a ^{13}C NMR shift at 164.65 ppm is very close to that of the free substrate in solution (165.45 ppm) whereas the second peak at 169.96 ppm is shifted, suggesting chelation between the hydrazide oxygen and iridium (Figure 107). A similar complex was characterised by Stringer *et al*.[19] (Figure 90b), where the same carbon atom in the chelated isoniazid was detected at 158.91 ppm.

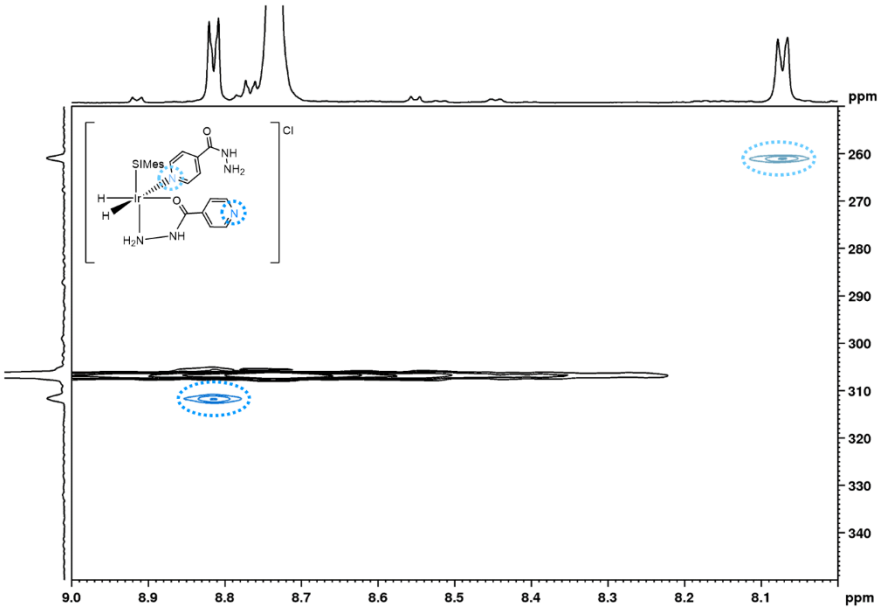

Figure 106 – $^{1}H/^{15}N$-HMQC NMR spectrum of the product formed when [IrCl(COD)(SIMes)] (5 mM), isoniazid (50 mM) and *p*-H_2 (4 bar) react together in methanol-d_4 (0.6 mL), measured at 500 MHz (^{1}H) and 51 MHz (^{15}N)

and 235 K. The ^{15}N resonance of the pyridine bound isoniazid ligand is highlighted at 261.1 ppm (^{15}N)/8.07 ppm (^{1}H) in light blue and the resonance for the chelate bound isoniazid is shown at 311 ppm (^{15}N)/8.81 ppm (^{1}H) in dark blue.

The ^{15}N-HMQC data revealed a distinct difference in chemical shift of the two pyridine-based nitrogen atoms. The resonance at 311 ppm is very close to the resonance of the free substrate in solution (306.9 ppm), justifying that this pyridine nitrogen does not ligate to the iridium in the SABRE-active species. The second resonance appears at 261 ppm which is distinctive of Ir-$N_{(pyridine)}$ coordination. This shift is similar to the ^{15}N chemical shift observed for the *tris*-substituted SABRE-active species formed by 4-methylpyridine where the pyridine nitrogen is observed at 247 ppm (see previous chapter for more details).

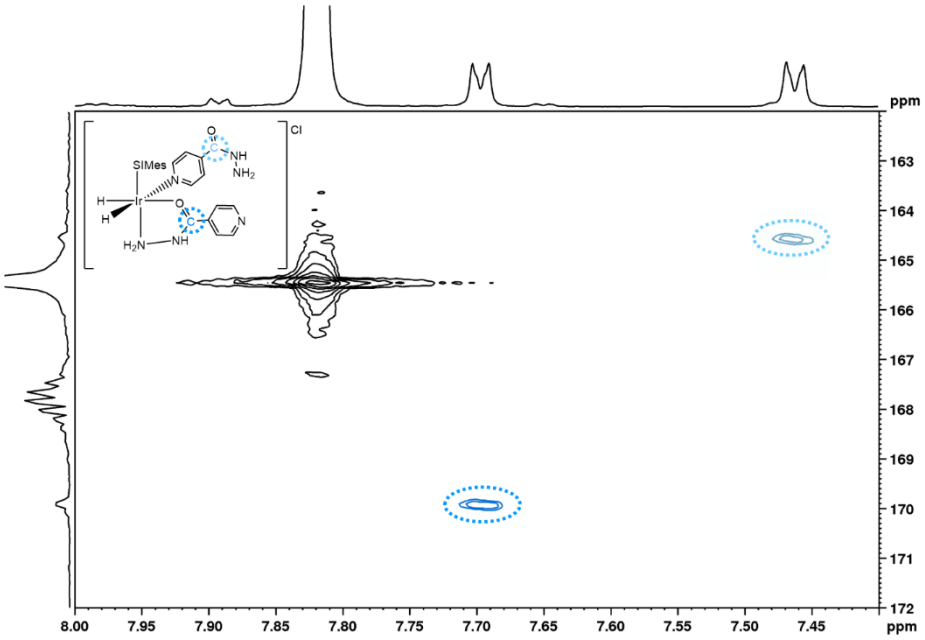

Figure 107 – ^{1}H/^{13}C-HMQC NMR spectrum of the product formed when [IrCl(COD)(SIMes)] (5 mM), isoniazid (50 mM) and *p*-H_2 (4 bar) react in methanol-d_4 (0.6 mL). Measured at 500 MHz (^{1}H) and 125 MHz (^{13}C) and 235 K. The ^{13}C resonance of pyridine bound isoniazid is highlighted at 165 ppm (^{13}C)/8.07 ppm (^{1}H) in light blue and the resonance for the chelate bound isoniazid is shown at 170 ppm (^{13}C)/8.81 ppm (^{1}H) in dark blue.

The ^{1}H/^{15}N-HMQC NMR spectrum of Figure 106 does not show signals for the nitrogen atoms in the hydrazide functional group for either isoniazid ligand in the

product. To observe these resonances, isoniazid was ^{15}N-isotopically labelled at these sites. The SABRE-active species was then analysed by ^{15}N-NMR spectroscopy (Figure 108).

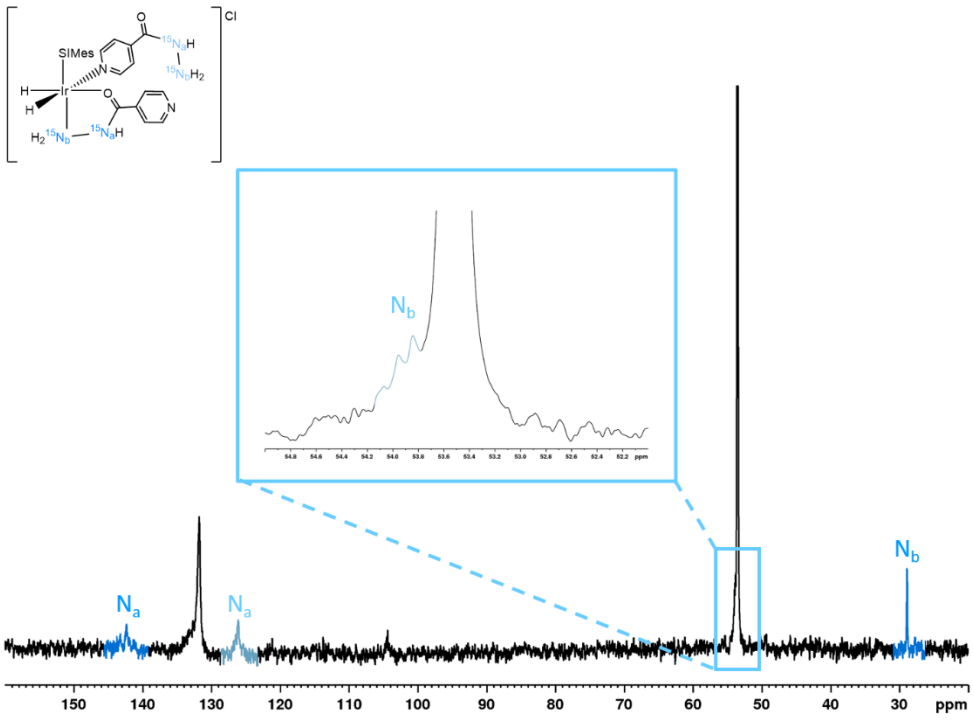

Figure 108 – ^{15}N NMR spectrum of ^{15}N labelled isoniazid measured at 41 MHz and 298 K for a sample containing [IrCl(COD)(SIMes) (5 mM), isoniazid (50 mM) and *p*-H_2 (4 bar) in methanol-d_4 (0.6 mL). ^{15}N resonances for the pyridine bound hydrazide nitrogen atoms are highlighted in light blue while those for the chelate bound form are shown in dark blue.

^{15}N-NMR	Free Substrate	N_{py}-Bound	Chelate-Bound
N_{py}	309.6	265.3	315.1
N_a	131.5 J_{NN} = 5.6 Hz	141.6	125.8
N_b	53.7 J_{NN} = 5.6 Hz	54.1	29.3

Table 20 - Table of ^{15}N resonances for [Ir(H)$_2$(SIMes)(κ-N-isonicotinylhydrazide)(isonicotinyl-κ-O-κ-N-hydrazide]Cl containing ^{15}N-labelled isoniazid measured at 41 MHz and 298 K.

The NMR spectrum of [Ir(H)$_2$(SIMes)(κ-N-isonicotinylhydrazide)(isonicotinyl-κ-O-κ-N-hydrazide]Cl shown in Figure 108, depicts the ^{15}N resonances of the two hydrazide nitrogen atoms, labelled as N_a and N_b for each of the ligands bound to iridium. It has

been suggested that the chelated substrate ligates to iridium through the terminal N-atom of the hydrazide functional group (N_b) and the oxygen atom. In the free substrate, the signal for this nitrogen is observed at 53.7 ppm and overlaps with a signal from the pyridine bound isoniazid ligand. The corresponding signal the proposed chelated form appears at 29.3 ppm, this shift to a lower ppm is due to the nitrogen environment becoming more shielded due to ligation to the iridium.

4.3.3 SABRE Enhancements in the SABRE-Active Catalyst

Once the SABRE-active species has been formed with both 4-hydroxypyridine and isoniazid, the sample is ready for hyperpolarisation measurements. To do these, *p*-H_2 is added to the sample and the sample is shaken within the stray field of the spectrometer (65 G) to promote dissolution of the gas. Magnetism transfer then ensues from the *p*-H_2 derived hydrides to the substrate before the sample is quickly 'dropped' into the spectrometer for detection. Examples of these hyperpolarised spectra are shown in Figure 109. The thermal, non-hyperpolarised control NMR spectra are shown in black and have been magnified 32 times so that they can be viewed alongside the hyperpolarised spectra. The hyperpolarised NMR spectra for 4-hydroxypyridine (dominant in methanol) is depicted in purple and that of isoniazid in blue. Whilst these spectra are shown on similar scales alongside one another, the enhancement yielded for isoniazid is −183-fold compared to −34-fold at the *ortho*-proton resonance. At the *meta*-proton resonance the enhancements are −40-fold and −6-fold respectively.

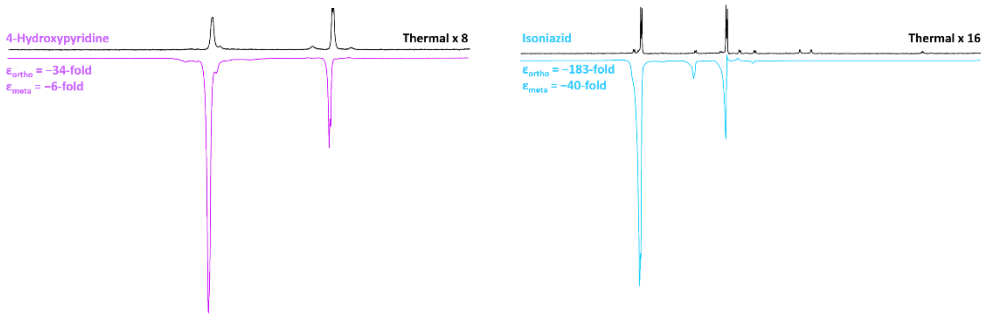

Figure 109 - Thermal ^{1}H-NMR spectrum under Boltzmann conditions (black) compared to a hyperpolarised spectrum where the sample was shaken for 10 s in the stray field (65 G) of the spectrometer (400 MHz) (purple = 4-hydroxypyridine, blue = isoniazid). These spectra were measured using a sample containing the substrate (40 mM), [IrCl(COD)(SIMes)] (4 mM) and *p*-H_2 (4 bar) in methanol-d_4 (0.6 mL). The thermal spectrum has been magnified 8 times for 4-hydroxypyridine and 16 times for isoniazid in the stacked spectra. The enhancements at the *ortho* and *meta* resonances have been calculated.

The NMR signal enhancements exhibited by 4-hydroxypyridine proved to be much lower than those for isoniazid (and the substrates investigated in the previous chapter). SABRE enhancements are known to be concentration dependent,[30] therefore the amount of SABRE-active species for both isoniazid and 4-hydroxypyridine were optimised in order to improve the corresponding enhancements. 4-methylpyridine was also included in this study for comparison.

To do this a number of samples were formulated, each containing different concentrations of substrate. These concentrations were varied from 20-100 mM, whilst the concentration of [IrCl(COD)(SIMes)] was maintained at 4 mM. The same pressure of *p*-H_2 (4-bar) was used and the samples were each shaken for 10 seconds at 65 G using the stray field of the spectrometer (400 MHz). This method of manual shaking was repeated five times to allow an average result to be recorded and the corresponding standard error was calculated. The results of this investigation are shown in Figure 110.

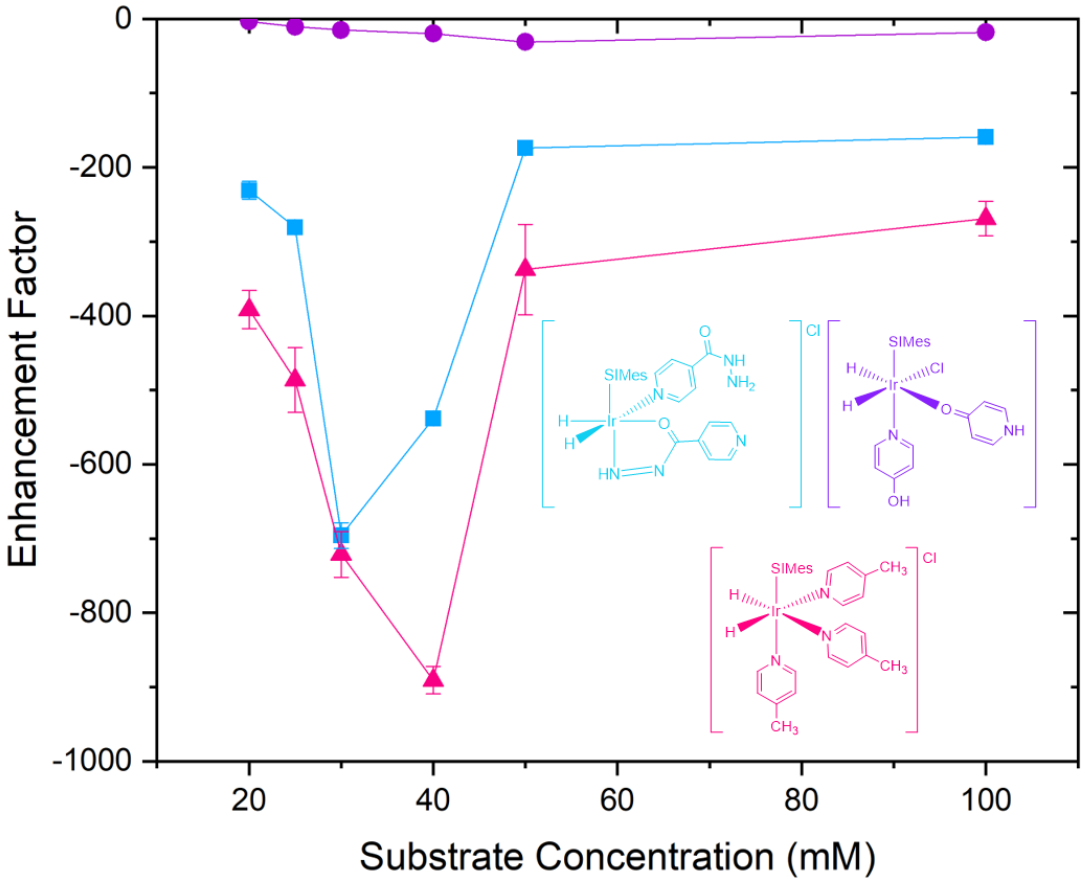

Figure 110 – ^{1}H NMR signal Enhancement factor as a function of substrate enhancement for the SABRE-Active species containing 4-methylpyridine, 4-hydroxypyridine and isoniazid in methanol-d_4 measured at 400 MHz and 298 K.

Figure 110 compares the SABRE enhancements of isoniazid, 4-hydroxypyridine and 4-methylpyridine as a function of substrate concentration. It is clear that 4-hydroxypyridine consistently yields very low SABRE enhancements when compared to the other two substrates. The highest enhancement level is −31 ± 1-fold and was observed when a concentration of 50 mM of substrate was used. This compares to isoniazid which produced the largest signal enhancement of −696 ± 17-fold when the substrate excess was 30 mM. 4-Methylpyridine yielded the largest enhancements compared to the other substrates. The optimum concentration of this substrate was shown to be 40 mM where an enhancement of −891 ± 18-fold was calculated. This trend must link to the ligand binding mode and will be discussed later.

4.4 Diffusion Ordered Spectroscopy in the SABRE-Active Catalyst

The substrates 4-hydroxypyridine and isoniazid have been shown to form atypical SABRE-active species. As both of these complexes contain a 'free' pyridine nitrogen, it is possible that another equivalent of the SABRE catalyst could ligate via this atom. An example of such dimers can be found in Figure 111. Diffusion ordered spectroscopy (DOSY) can be used to observe whether such species form via the diffusion constant that can be used to estimate the size of a molecular species.

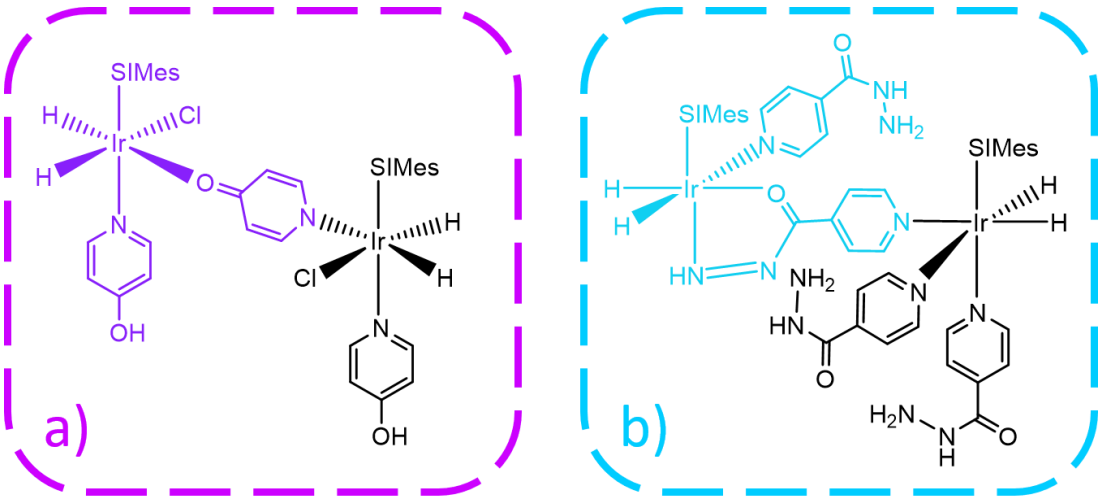

Figure 111 - Suggested dimer structures for the SABRE active species for (a) 4-hydroxypyridine and (b) isoniazid

Self-diffusion describes the random translational (often called Brownian) motion of molecules that is driven by internal thermal energy.[31] This motion is a fundamental form of mass transport and underpins almost all chemical processes as reacting species must collide for the reaction to occur.[32] Additionally, diffusion coefficients can provide information on the size and shape of these molecular species. The connection between diffusion and structural properties arises as the diffusion coefficient (D) depends on friction factors (f_T) and electrophoretic mobilities (μ).[33] This is observed through the Debye-Einstein theory:

$$D = \frac{k_B T}{f_T}$$

Equation 18

Where k_B is the Boltzmann constant, T is the absolute temperature and f_T is the friction factor.

For an idealised case of a diffusing sphere of hydrodynamic radius (r_H) and solvent viscosity (η), the friction factor is provided by:[34]

$$f_T = 6\pi\eta r_H$$

Equation 19

Combining Equation 18 with Equation 19 gives the Stokes-Einstein equation:

$$D = \frac{k_B T}{6\pi\eta r_H}$$

Equation 20

The Stokes-Einstein equation (Equation 20) demonstrates that the diffusion coefficient is inversely related to the radius of the diffusing species. This means that larger molecules or complexes exhibit smaller diffusion coefficients. However, it is important to note that the Stokes-Einstein equation is limited to how well the shape of the molecule can be approximated to that of a sphere. More realistic models for the friction factor represent ellipsoids of revolution or collections of spherical subunits and are described by Perrin's ellipsoid expressions.[35-37]

Pulsed-field gradient NMR (PFG-NMR) is an excellent method to determine the self-diffusion coefficient of a molecule in solution. Often referred to as diffusion-ordered spectroscopy (DOSY), it can also be used to identify different molecular components of mixtures, including any impurities and characterise the size of aggregates or the degree of polymerisation.[38] DOSY is particularly useful for the analysis of mixtures, where NMR signals can be overlapped, however, can be separated according to the

translational diffusion coefficients of the corresponding molecules. The resulting 2D spectra where chemical shift is displayed along the x-axis and the relative self-diffusion coefficient on the y-axis, appears as a virtual form of chromatography.[39] The spectra allows correlation of signals lacking mutual couplings which are difficult to identify as originating from the same molecule via other NMR experiments.[40]

DOSY is achieved by combining radiofrequency pulses with magnetic field gradients that encode spatial information. By using magnetic field gradients, molecules can be spatially labelled according to their position in the sample tube. After a short diffusion time, typically on the order of 10 ms, a second magnetic field gradient pulse is applied to remove the spatial encoding. If the molecules move after the initial encoding step during the diffusion time, the signal will have attenuated. There are four main PFG-NMR pulse sequences for measuring a DOSY spectrum: pulsed gradient spin echo (PFG-SE), pulse field gradient stimulated spin echo (PFG-SSE), bipolar pulse longitudinal eddy current delay (BPP-LED) and asymmetric bipolar PFG-SSE or 'one shot' experiment.[33, 34, 41] In this chapter, we have used the BPP-LED pulse sequence.

The simplest of these methods is the pulsed field gradient spin echo (PFG-SE) which was first proposed by Stejskal and Tanner in 1965.[41] During this sequence, the magnetisation is excited into the xy plane using a 90° pulse which is then dispersed using a magnetic field gradient pulse of duration, δ. After a time period of $\frac{\Delta}{2}$, a 180° radiofrequency pulse is applied which inverts the dispersed magnetisation such that the after a period of Δ, the magnetisation is the inverse direction of what it was following the gradient pulse. Finally, a second gradient pulse is applied to remove the spatial encoding (see Figure 112).

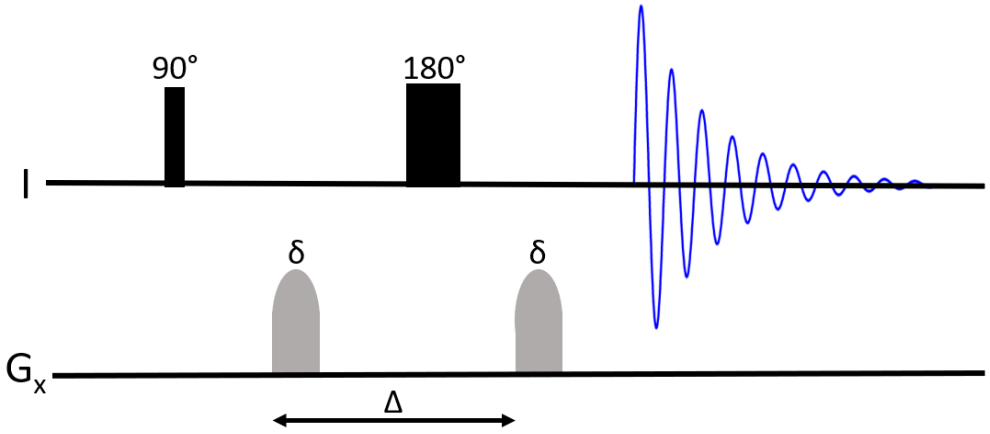

Figure 112 - The PFG-SE pulse sequence

The pulse sequence is iterated, each time incrementing the gradient strength (G) whilst keeping the delays (δ and Δ) constant. The intensity (I) can then be plotted against the gradient strength and the diffusion constant extracted using a non-linear curve fit to the resulting decay.

$$I = I_0 e^{\left[-\gamma^2 G^2 \delta^2 D\left(\Delta - \frac{\delta}{3}\right)\right]}$$

Equation 21 – The Stejskal Tanner Equation, where γ is the gyromagnetic ratio, G is the gradient strength, δ and Δ are delays and D is the diffusion constant.[41,42]

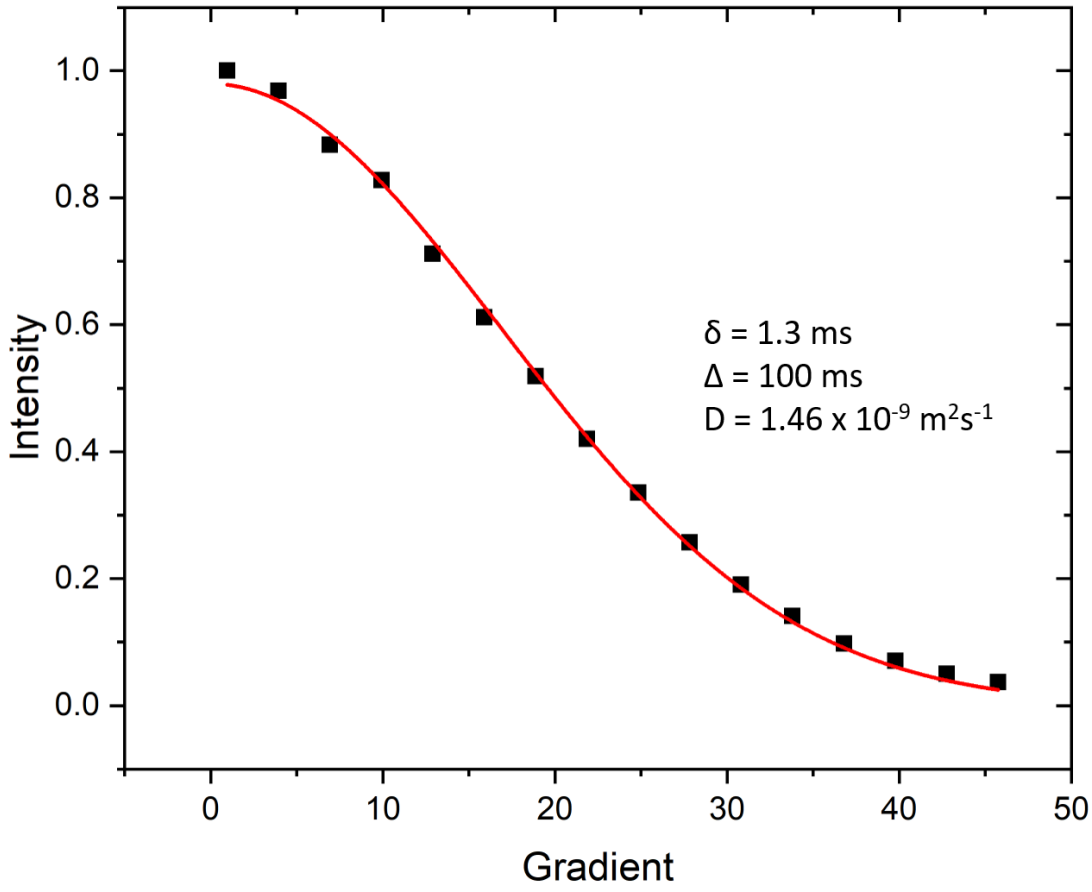

Figure 113 - Signal intensity as a function of the gradient strength. The data has been plotted according to Equation 21. The delays used for δ and Δ have been indicated alongside the calculated diffusion coefficient (D)

The PFG-SE pulse is limited by relaxation as the magnetisation is present in the xy plane during the diffusion period, therefore signal relaxation is dominated by transverse relaxation (T_2). Transverse magnetisation can also be subject to *J*-modulation (coupling evolution) which causes undesirable signal distortion, particularly in strongly-coupled systems.[34] The PFG-STE pulse sequence contains two 90° pulses, rather than the 180° pulse in Figure 112.[43] This means that magnetisation is transverse during the short gradient encoding periods (δ) but longitudinal for the remainder of the diffusion time. Consequently, any signal losses are caused by the slower T_1 relaxation rate. After the diffusion period, the magnetisation is returned to the transverse place by the third 90° pulse for refocusing and subsequent detection. The BPP-LED approach uses bipolar gradient pulse pairs. These replace the single gradient pulses in the SE (Figure 112) and STE approach with two pulses of half the duration and opposing signs separated by a non-selective (hard) 180° pulse. This

imposes a net additive dephasing effect and mirrors the effect of a single pulse and has the purpose of removing any background magnetic field gradients arising from imperfections in the hardware. This pulse sequence also employs an eddy current delay period in which the magnetisation is stored longitudinally prior to detection which allows any eddy currents to decay.[44-46]

Here DOSY has been employed to determine whether dimers have also been formed in these studies for the atypical SABRE-active species for 4-hydroxypyridine and isoniazid. In these cases, dimers can form due to ligation from the lone pair situated on the pyridine nitrogen to iridium (Figure 111). In order to compare these structures, the SABRE active species for 4-methylpyridine was also considered.

4.4.1 $[Ir(H)_2(SIMes)(4\text{-methylpyridine})_3]Cl$

The tris-substituted SABRE active species for 4-methylpyridine was assessed as a control for this experiment. 4-methylpyridine is incapable of dimerization upon complexation with iridium as it contains no other coordination site to the pyridine nitrogen. Therefore, this complex serves as a good comparison against the SABRE-active species for the other substrates.

The diffusion coefficients were measured at 298 K and 273 K. The DOSY experiment was conducted at two different temperatures as from the Stokes-Einstein equation (Equation 20) it is clear that diffusion is temperature dependent.[31] Whilst Figure 114 shows the 2D-DOSY plot from topspin, the diffusion constants were not extracted from this plot. Instead the raw data (peak intensity and the gradient strength) was plotted in origin and fitted using equation 21 to calculate the diffusion constant for each of the ^1H resonances in Table 21. These plots can be found in Appendix C. This method was also used to calculate the diffusion constants for $[IrCl(H)_2(SIMes)(\kappa\text{-O-4-pyridone})(\kappa\text{-N-4-hydroxypyridine})]$ and $[Ir(H)_2(SIMes)(\kappa\text{-N-isonicotinylhydrazide})(\text{isonicotinyl-}\kappa\text{-O-}\kappa\text{-N-hydrazide}]Cl$ in sections 4.2.2 and 4.2.3.

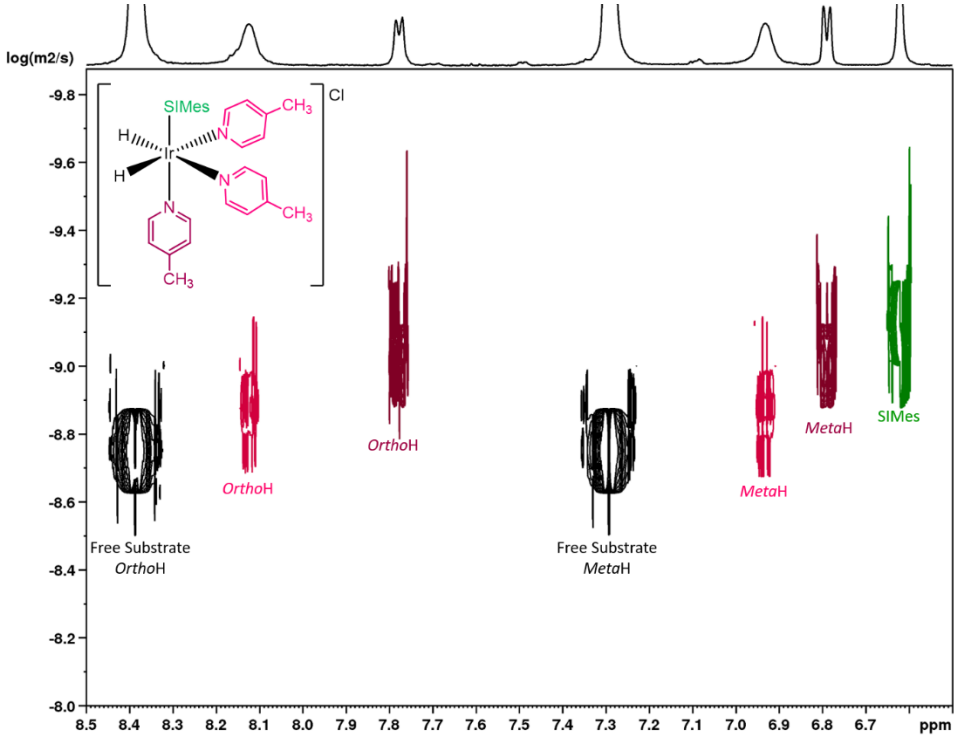

Figure 114 - 2D DOSY spectra of $[Ir(H)_2(SIMes)(4\text{-methylpyridine})_3]Cl$. Sample contained [IrCl(COD)(SIMes)] (5 mM), 4-methylpyridine (50 mM)), *p*-H_2 (4 bar absolute) dissolved in methanol-d_4 (0.6 mL) measured at 400 MHz and 298 K. This figure is used for illustrative purposes only.

	Diffusion Constant (m^2s^{-1})	Hydrodynamic Radius (m)
Free	1.46×10^{-9}	2.47×10^{-10}
Trans to H^-	7.38×10^{-10}	4.88×10^{-10}
Trans to NHC	6.20×10^{-10}	5.81×10^{-10}
SIMes	6.27×10^{-10}	5.74×10^{-10}
Average on the catalyst	$6.24 \times 10^{-10} \pm 3.65 \times 10^{-12}$	$5.77 \times 10^{-10} \pm 3.38 \times 10^{-12}$

Table 21 - Table of the diffusion constant for $[Ir(H)_2(SIMes)(4\text{-methylpyridine})_3]Cl$ at 298 K. The diffusion constants were extracted from the raw data plots in Appendix C. The Spherical radius was then calculated using the Stokes-Einstein equation in Equation 20

Figure 114 shows a 2D DOSY plot where the diffusion coefficients correspond to those displayed in Table 21. The plot in Figure 114 compares the diffusion coefficients for the free substrate (black), the substrate bound *trans* to the hydride (pink), the substrate *trans* to SIMes (dark pink) and the catalyst (green). The diffusion coefficient

for the free substrate is larger than the SABRE-active complex. This is expected as the free substrate is smaller than the complex and therefore can diffuse faster than the complex. The diffusion coefficients for SIMes and the slow exchanging substrate ligand *trans* to it are very similar in magnitude. The substrate *trans* to hydride however undergoes exchange on the timescale of these measurements with the free material. Consequently, the diffusion coefficient for these ligands moves towards that of the smaller free material.

The diffusion coefficient can be used to calculate molecular size by rearranging the Stokes-Einstein equation (Equation 20) to make the Van der Waals or hydrodynamic radius, r, the subject. To do this, the viscosity (η) and temperature must also be known. Whilst the temperature was known to be 298 K for this experiment, the viscosity was not measured. Instead a value of 6.06×10^{-4} Pa S was taken from the literature.[37] The spherical radius was calculated to be 2.47×10^{-10} m for the free substrate compared to 5.77×10^{-10} m for the iridium complex. As expected, the free substrate is smaller than the complex. It must be noted that the Stokes-Einstein equation assumes a perfect diffusing sphere, furthermore, the viscosity of the solution has not been measured. Therefore these values for the hydrodynamic radii are estimated and henceforth they should not be used quantitatively but could be used comparatively.

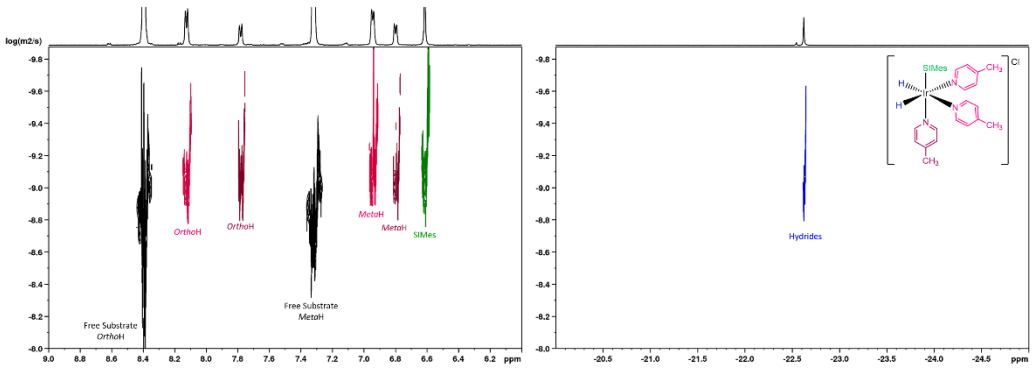

Figure 115 - 2D DOSY ^{1}H NMR spectra of $[Ir(H)_2(SIMes)(4\text{-methylpyridine})_3]Cl$. Sample contained $[IrCl(COD)(SIMes)]$ (5 mM), 4-methylpyridine (50 mM)), p-H_2 (4 bar) dissolved in methanol-d4 (0.6 mL) measured at 400 MHz and 273 K. This figure is used for illustrative purposes only.

	Diffusion Constant (m^2s^{-1})	Spherical Radius (m)
Free	1.53×10^{-9}	1.68×10^{-10}
Trans to H^-	6.44×10^{-10}	3.98×10^{-10}
Trans to NHC	6.20×10^{-10}	4.14×10^{-10}
SIMes	6.22×10^{-9}	4.12×10^{-10}
Average on the catalyst	$6.21 \times 10^{-10} \pm 1.00 \times 10^{-12}$	$4.13 \times 10^{-10} \pm 6.53 \times 10^{-13}$

Table 22 - Table of the diffusion constant for $[Ir(H)_2(SIMes)(4\text{-methylpyridine})_3]Cl$ at 273 K. The diffusion constants were extracted from the raw data plots in Appendix C. The Spherical radius was then calculated using the Stokes-Einstein equation in Equation 20

Figure 115 shows the 2D DOSY plot for [Ir(H)2(SIMes)(4-methylpyridine)3]Cl at 273 K. The corresponding diffusion coefficients and calculated spherical radii are shown in Table 22. Similarly to Figure 114, the diffusion coefficient for the free substrate is faster than the bound species. However, now as the rate of ligand exchange is slowed, the coefficients for the bound ligands and SIMes group as much closer in size. The spherical radii for the free substrate are smaller than the SABRE-active complex and therefore can translate a larger distance than the bound species during the delay time, Δ. The diffusion coefficients at 273 K are slightly slower than at 298 K. This is observed as the diffusion coefficient for the SABRE-active complex at 298 K is 6.24×10^{-10} m^2s^{-1} compared to 6.21×10^{-10} m^2s^{-1} at 273 K. This is to be expected as according to the Stokes-Einstein equation (Equation 20), diffusion is inversely proportional to the temperature. For example, at higher temperatures, molecules have more energy and can therefore they diffuse faster as the movement of the molecules in solution increases.

The hydride region is also visible on the 2D DOSY plot, however, the signals for this resonance are very weak and therefore extracting the corresponding diffusion coefficient was very difficult. However, as they are bound to the iridium complex,

they are similar to those of the bound ligands in the iridium complex (average = 6.21 × 10^{-10} m^2s^{-1}).

4.4.2 [IrCl(H)$_2$(SIMes)(κ-O-4-pyridone)(κ-N-4-hydroxypyridine)]

The SABRE active species containing 4-hydroxypyridine has been shown to form a *bis*-substituted complex of the form; [IrCl(H)$_2$(SIMes)(κ-O-4-pyridone)(κ-N-4-hydroxypyridine)]. This species contains one substrate bound via the terminal oxygen as 4-pyridone and another bound through the pyridine nitrogen. The equatorial plane contains two inequivalent hydrides, one bound *trans* to chloride and the other *trans* to the oxygen bound substrate. As 4-hydroxypyridine clearly contains two binding sites, it may have the ability to form dimers to iridium, as shown in Figure 111. DOSY can be used to characterise the formation of aggregates including dimers and trimers in solution.[32, 37] Similarly to [Ir(H)$_2$(SIMes)(4-methylpyridine)$_3$]Cl, the experiment was repeated at two temperatures; 298 K and 253 K. The DOSY experiment was attempted at 273 K, however, the signal was too weak for the

complex to be fully analysed at this temperature.

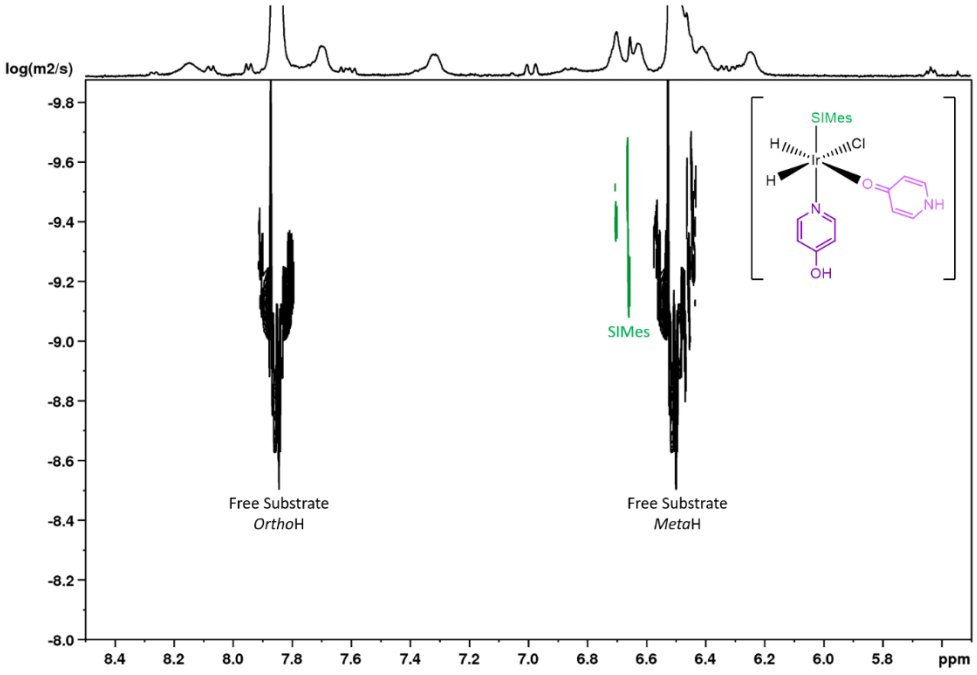

Figure 116 - 2D DOSY ^{1}H NMR spectra of [IrCl(H)$_2$(SIMes)(κ-O-4-pyridone)(κ-N-4-hydroxypyridine)] . Sample contained [IrCl(COD)(SIMes)] (5 mM), 4-hydroxypyridine (50 mM) and p-H2 (4 bar) dissolved in methanol-d4 (0.6 mL) measured at 400 MHz and 298 K. This figure is used for illustrative purposes only.

	Diffusion Constant (m^2s^{-1})	Spherical Radius (m)
Free	1.12×10^{-9}	3.21×10^{-10}
SIMes	6.27×10^{-10}	5.75×10^{-10}

Table 23 - Table of the diffusion constant calculated from Equation 4 for [IrCl(H)$_2$(SIMes)(4-hydroxypyridine)$_2$] at 298 K. The diffusion constants were extracted from the raw data plots in Appendix C. The Spherical radius was then calculated using the Stokes-Einstein equation in Equation 3

Figure 116 shows the 2D DOSY plot for [IrCl(H)$_2$(SIMes)(κ-O-4-pyridone)(κ-N-4-hydroxypyridine)]. The corresponding diffusion values and calculated spherical radii are shown in Table 23. The bound substrate forms could not be observed at this temperature, however the SIMes ligand is visible and therefore this is used to represent the complex form. 4-Hydroxypyridine/4-pyridone exchanges rapidly at 298 K and therefore this could explain why it could not be observed at this temperature.

The diffusion constant for the free form is very similar to the free form of 4-methylpyridine. The diffusion coefficient for free 4-hydroxypyridine is 1.12×10^{-9} m^2s^{-1} compared to 1.46×10^{-9} m^2s^{-1} for 4-methylpyridine. Both substrates are simple *para* substituted derivatives of pyridine and therefore it was expected that they would diffuse at a similar rate. The SABRE-active species for both 4-hydroxypyridine and 4-methylpyridine are also very similar. $[Ir(H)_2(SIMes)(4\text{-methylpyridine})_3]Cl$ has a diffusion coefficient of 6.24×10^{-10} m^2s^{-1} compared to 6.27×10^{-10} m^2s^{-1} for $[IrCl(H)_2(SIMes)(\kappa\text{-O-4-pyridone})(\kappa\text{-N-4-hydroxypyridine})]$. The calculated spherical radii are also similar, 5.77×10^{-10} m for $[Ir(H)_2(SIMes)(4\text{-methylpyridine})_3]Cl$ and 5.75×10^{-10} m for the SABRE-active complex containing 4-hydroxypyridine. As 4-methylpyridine is unable to dimerise and exhibits a similar diffusion coefficient, and spherical radii, to 4-hydroxypyridine, it could be assumed that $[IrCl(H)_2(SIMes)(4\text{-hydroxypyridine})_2]Cl$ also does not form dimers at this temperature.

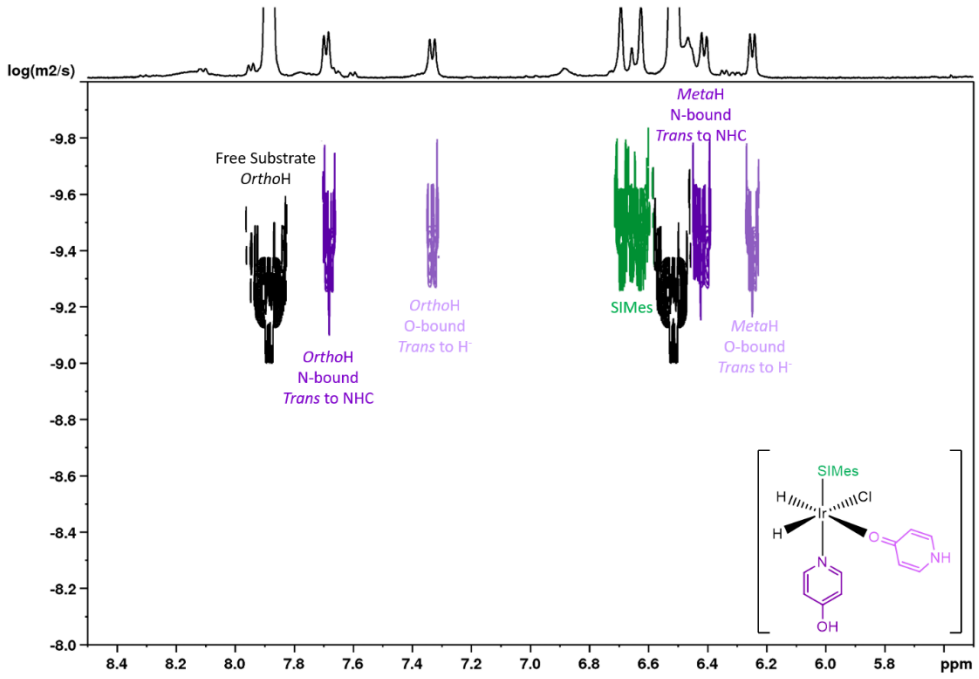

Figure 117 – 2D DOSY ^{1}H NMR spectra of $[IrCl(H)_2(SIMes)(\kappa\text{-O-4-pyridone})(\kappa\text{-N-4-hydroxypyridine})]$. Sample contained $[IrCl(COD)(SIMes)]$ (5 mM), 4-hydroxypyridine (50 mM) and *p*-H_2 (4 bar) dissolved in methanol-d_4 (0.6 mL) measured at 400 MHz and 253 K. This figure is used for illustrative purposes only.

	Diffusion Constant (m^2s^{-1})	Spherical Radius (m)

Free	4.81×10^{-10}	3.47×10^{-10}
N-bound	2.40×10^{-10}	6.94×10^{-10}
O-bound	2.58×10^{-10}	6.46×10^{-10}
SIMes	2.52×10^{-10}	6.63×10^{-10}
SIMes	2.67×10^{-10}	2.25×10^{-10}
Average on the catalyst	$2.53 \times 10^{-10} \pm 7.74 \times 10^{-12}$	$6.61 \times 10^{-10} \pm 2.01 \times 10^{-11}$

Table 24 - Table of the diffusion constant calculated from Equation 4 for [IrCl(H)$_2$(SIMes)(κ-O-4-pyridone)(κ-N-4-hydroxypyridine)] at 253 K. The diffusion constants were extracted from the raw data plots in Appendix C. The Spherical radius was then calculated using the Stokes-Einstein equation in Equation 3

Figure 117 shows the 2D DOSY plot for [IrCl(H)$_2$(SIMes)(κ-O-4-pyridone)(κ-N-4-hydroxypyridine)] at 253 K. The corresponding diffusion coefficients and calculated values for the spherical radii are shown in Table 24. Lowering the temperature to 253 K means that the diffusion for the bound forms of the substrate are also visible on the 2D DOSY plot. The slow exchanging pyridine bound ligand has been averaged with those of the SIMes ligand to give the overall complex diffusion of 2.53×10^{-10} m^2s^{-1}. As expected, this is slower than the diffusion observed at 298 K (6.27×10^{-10} m^2s^{-1}).

4.4.3 [Ir(H)$_2$(SIMes)(κ-N-isonicotinylhydrazide)(isonicotinyl-κ-O-κ-N-hydrazide]Cl

The SABRE-active species containing isoniazid also forms a bis-substituted species of the form; [Ir(H)$_2$(SIMes)(κ-N-isonicotinylhydrazide)(isonicotinyl-κ-O-κ-N-hydrazide]Cl. This complex contains one isoniazid ligand bound via the pyridine nitrogen in the equatorial plane *trans* to hydride. The other isoniazid ligand chelates to iridium through the oxygen and nitrogen in the hydrazide group. This means that the pyridine nitrogen in this substrate is free to coordinate to iridium as the dimer suggested in Figure 111.

The DOSY experiment was conducted at 298 K and 273 K. The results were then compared to [Ir(H)$_2$(SIMes)(4-methylpyridine)$_3$]Cl which is known not to form dimers.

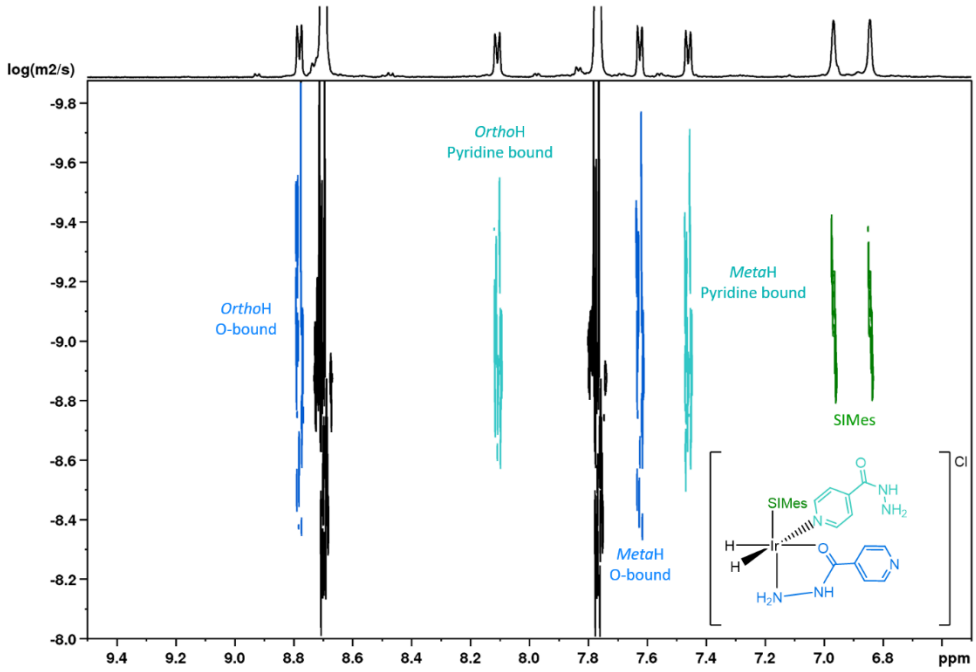

Figure 118 - 2D DOSY ^{1}H NMR spectra of [Ir(H)$_2$(SIMes)(κ-N-isonicotinylhydrazide)(isonicotinyl-κ-O-κ-N-hydrazide]Cl Sample contained [IrCl(COD)(SIMes)] (5 mM), isoniazid (50 mM) and p-H2 (4 bar) dissolved in methanol-d4 (0.6 mL) measured at 400 MHz and 298 K. This figure is used for illustrative purposes only.

	Diffusion Constant (m^2s^{-1})	Spherical Radius (m)
Free	1.33×10^{-9}	2.72×10^{-10}
Chelate	7.27×10^{-10}	4.95×10^{-10}
Pyridine bound	7.06×10^{-10}	5.10×10^{-10}
SIMes	6.73×10^{-10}	5.35×10^{-10}
SIMes	5.87×10^{-10}	6.13×10^{-10}
Average on the catalyst	$6.62 \times 10^{-10} \pm 4.08 \times 10^{-11}$	$5.48 \times 10^{-10} \pm 3.48 \times 10^{-11}$

Table 25 – Table of the diffusion constant calculated from Equation 4 for [Ir(H)$_2$(SIMes)(κ-N-isonicotinylhydrazide)(isonicotinyl-κ-O-κ-N-hydrazide]Cl at 298 K. The diffusion constants were extracted from the raw data plots in Appendix C. The Spherical radius was then calculated using the Stokes-Einstein equation in Equation 3

Figure 118 shows the 2D DOSY plot for [Ir(H)$_2$(SIMes)(κ-N-isonicotinylhydrazide)(isonicotinyl-κ-O-κ-N-hydrazide]Cl at 298 K. The corresponding

diffusion coefficients and calculated spherical radii are shown in Table 25. The diffusion coefficient for the SABRE-active species is very similar to those containing 4-methylpyridine and 4-hydroxypyridine. When isoniazid is used as the substrate the diffusion coefficient is 6.62 × 10^{-10} m^2s^{-1} compared to 6.24 × 10^{-10} m^2s^{-1} for 4-methylpyridine and 6.27 × 10^{-10} m^2s^{-1} for 4-hydroxypyridine. This suggests that isoniazid does not form dimers upon complexation with iridium. $[Ir(H)_2$(SIMes)(κ-N-isonicotinylhydrazide)(isonicotinyl-κ-O-κ-N-hydrazide]Cl has a slightly larger diffusion coefficient and therefore a smaller spherical radius (5.48 × 10^{-10} m) compared to the other two substrates. This is followed by $[IrCl(H)_2$(SIMes)(κ-O-4-pyridone)(κ-N-4-hydroxypyridine)] which has a spherical radius of 5.75 × 10^{-10} m and finally, $[Ir(H)_2$(SIMes)(4-methylpyridine)$_3$]Cl which has a spherical radius of 5.77 × 10^{-10} m. 4-Methylpyridine forms a slightly larger SABRE-active species as it forms a *tris*-substituted complex compared to 4-hydroxypyridine and isoniazid which form complexes containing only two substrate ligands.

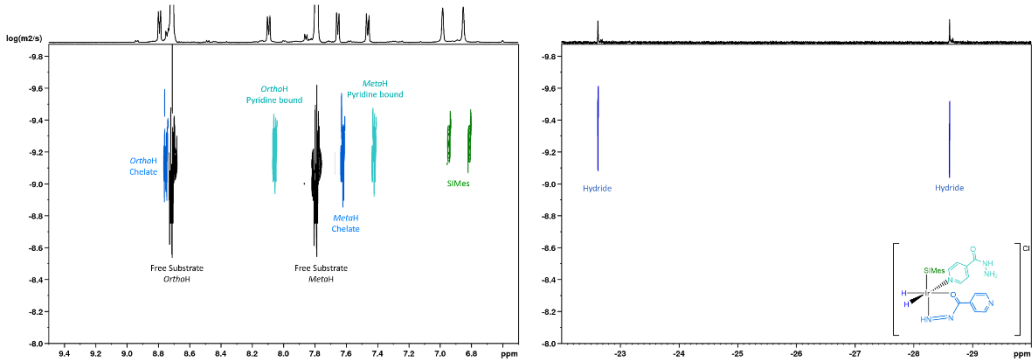

Figure 119 – 2D DOSY ^{1}H NMR spectra of $[Ir(H)_2$(SIMes)(κ-N-isonicotinylhydrazide)(isonicotinyl-κ-O-κ-N-hydrazide]Cl. Sample contained [IrCl(COD)(SIMes)] (5 Mm), isoniazid (50 Mm) and p-H2 (4 bar) dissolved in methanol-d4 (0.6 Ml) measured at 400 MHz and 273 K. This figure is used for illustrative purposes only.

	Diffusion Constant (m^2s^{-1})	Spherical Radius (m)
Free	8.19 × 10-10	3.13 × 10^{-10}
Chelate	4.88 × 10^{-10}	5.26 × 10^{-10}
Pyridine bound	4.54 × 10^{-10}	5.65 × 10^{-10}
SIMes	3.89 × 10^{-10}	6.60 × 10^{-10}

SIMes	3.91×10^{-10}	6.56×10^{-10}
Average on the catalyst	$4.22 \times 10^{-10} \pm 3.26 \times 10^{-11}$	$6.14 \times 10^{-10} \pm 4.40 \times 10^{-11}$

Table 26 - Table of the diffusion constant calculated from Equation 4 for $[Ir(H)_2(SIMes)(\kappa\text{-}N\text{-}isonicotinylhydrazide)(isonicotinyl\text{-}\kappa\text{-}O\text{-}\kappa\text{-}N\text{-}hydrazide]Cl$ at 273 K. The diffusion constants were extracted from the raw data plots in Appendix C. The Spherical radius was then calculated using the Stokes-Einstein equation in Equation 3

Figure 119 shows the diffusion of $[Ir(H)_2(SIMes)(\kappa\text{-}N\text{-}isonicotinylhydrazide)(isonicotinyl\text{-}\kappa\text{-}O\text{-}\kappa\text{-}N\text{-}hydrazide]Cl$ at 273 K. The 2D DOSY plot also shows the diffusion of the hydrides which appears on the same level as the rest of the SABRE-active species. The diffusion of the SABRE complex is 4.22×10^{-10} m^2s^{-1} at 273 K which is slower than the diffusion at 298 K (6.62×10^{-10} m^2s^{-1}). It is also much slower than the diffusion constant of $[Ir(H)_2(SIMes)(4\text{-methylpyridine})_3]Cl$ which was 6.21×10^{-10} m^2s^{-1}.

4.5 Ligand exchange within these SABRE-active catalysts

Despite 4-hydroxypyridine and isoniazid forming alternative octahedral complexes (Figure 100 and Figure 104) to the typical *tris*-substituted SABRE-active species (Figure 26), both these complexes enhance under SABRE conditions (Figure 109). This means that both $[IrCl(H)_2(SIMes)(\kappa\text{-}O\text{-}4\text{-pyridone})(\kappa\text{-}N\text{-}4\text{-hydroxypyridine})]$ and $[Ir(H)_2(SIMes)(\kappa\text{-}N\text{-}isonicotinylhydrazide)(isonicotinyl\text{-}\kappa\text{-}O\text{-}\kappa\text{-}N\text{-}hydrazide]Cl$ must undergo exchange. These hyperpolarised signals result from dissociation of the hyperpolarised bound substrate into bulk solution (Figure 14). When a sample containing the SABRE-active complex and *p*-H_2 is shaken in the stray field of the spectrometer (65 G), *p*-H_2 binds to the metal as two hydrides. Magnetism is then transferred from these *p*-H_2 derived hydrides to the substrate protons via the *J*-coupled network (Figure 16). The now hyperpolarised substrate then dissociates into the free solution leaving a vacant site on the metal centre, allowing for a new substrate from the bulk solution to bind for magnetism transfer. This cycle of hyperpolarisation and dissociation continues until all of the *p*-H_2 has been used.

Substrate dissociation was observed in these species using the EXSY technique described in Chapter 6, Section 6.2.7 Exchange Spectroscopy.

The rates of dissociation have been plotted as a function of temperature for the substrates 4-hydroxypyridine and 4-isoniazid and are shown in Figure 120. The exchange rate of 4-methylpyridine has also been shown in order to compare the behaviour of the *tris*-species to the active species for 4-hydroxypyridine and isoniazid.

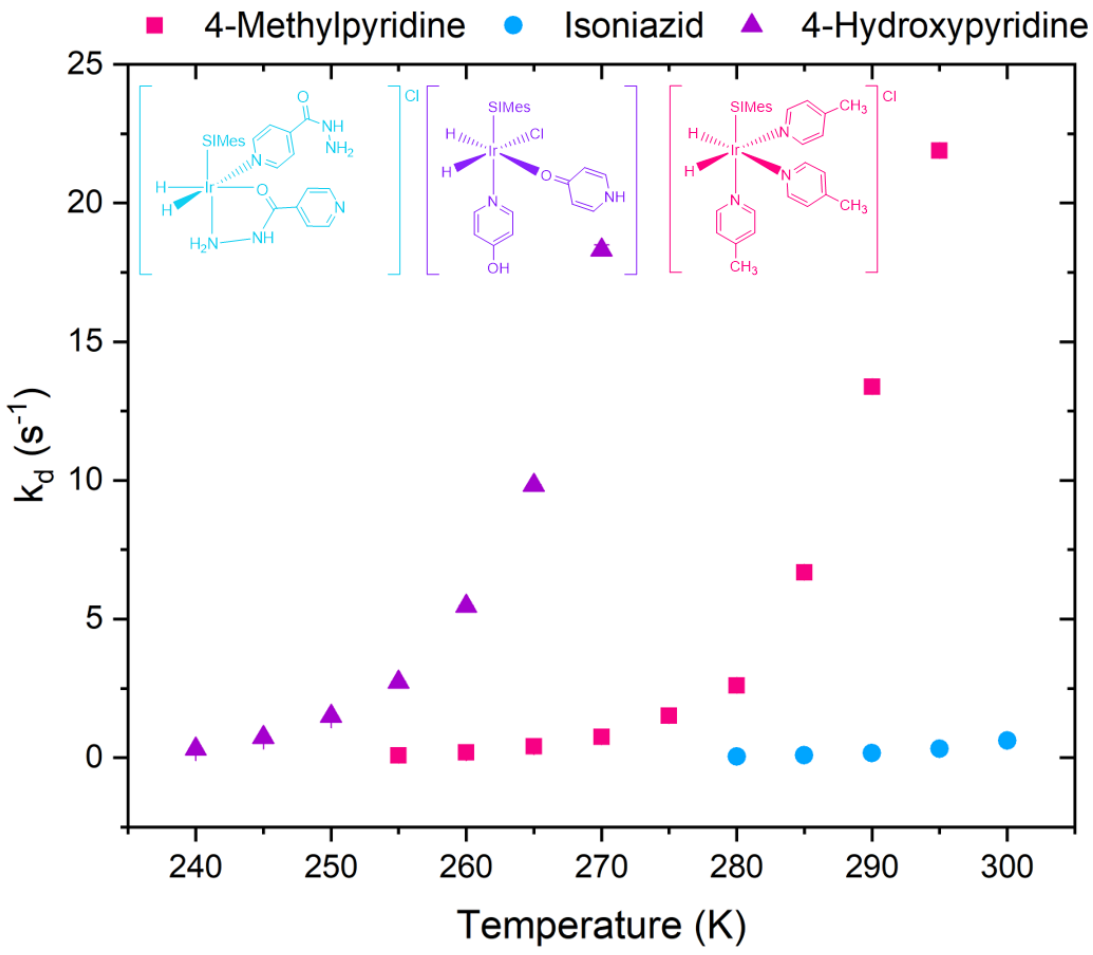

Figure 120 – Rate of ligand dissociation (k_d) as a function of temperature for the complexes form when [IrCl(COD)(SIMes)]Cl (5 mM), the indicated substrate (50 Mm) and *p*-H_2 (4 bar) are probed in methanol-d_4 (0.6 mL) at 500 MHz. Data points corresponding to isoniazid are shown in blue squares, 4-hydroxypyridine are represented by purple circles and 4-methylpyridine are shown by pink triangles. The error bars indicate the error associated with k_d calculated using the Jacknife method described in Chapter 6, Section 6.2.7.2 Associated errors in the calculation of k_d. A table of the associated errors can be found in Appendix C.

The data in Figure 120 shows that the exchange of 4-hydroxypyridine (k_d = 18.31 ± 0.19 s^{-1} at 270 K) occurs on a faster timescale compared to isoniazid (k_d = 0.04 ± 1.79

$\times 10^{-4}$ s^{-1} at 280 K) and 4-methylpyridine (k_d = 0.75 ± 1.53 × 10^{-3} s^{-1} at 270 K and 2.61 ± 2.71 × 10^{-3} s^{-1} at 280 K). Exchange is observed in the substrate bound *trans* to hydride. In the SABRE-active species containing 4-hydroxypyridine, this substrate ligand is bound through the oxygen as its 4-pyridone tautomer. Ligand association is clearly weaker when compared to the other substrates which bind through the pyridine nitrogen. The exchange of isoniazid is very slow by comparison. In this case, the substrate bound *trans* to the hydrides is bound through the pyridine nitrogen. This slower exchange (compared to 4-methylpyridine) must therefore be a consequence of the electronic effect of the chelate (Table 19). Exchange was not observed in the chelated isoniazid ligand in [$Ir(H)_2$(SIMes)(κ-N-isonicotinylhydrazide)(isonicotinyl-κ-O-κ-N-hydrazide]Cl or in the pyridine bound 4-hydroxypyridine ligand in [$IrCl(H)_2$(SIMes)(κ-O-4-pyridone)(κ-N-4-hydroxypyridine)].

4.5.1 Gibbs Free Energy

To further understand the interaction between the substrate and the metal centre, the activation parameters for ligand loss ($\Delta G^{\neq}_d$) can be calculated. As isoniazid loss is much slower, compared to both 4-hydroxypyridine and 4-methylpyridine, it was assumed that this substrate would exhibit the highest barrier.

These data were calculated using an Eyring plot where $\ln\frac{k}{T}$ is plotted as a function of $\frac{1}{T}$ (Figure 121). The enthalpy can then be determined from the gradient: $\left(-\frac{\Delta H^{\neq}}{R}\right)$ and the entropy from the intercept: $\ln\left(\frac{k_B}{h}+\frac{\Delta S^{\neq}}{R}\right)$. The results of these calculations are shown in Table 27.

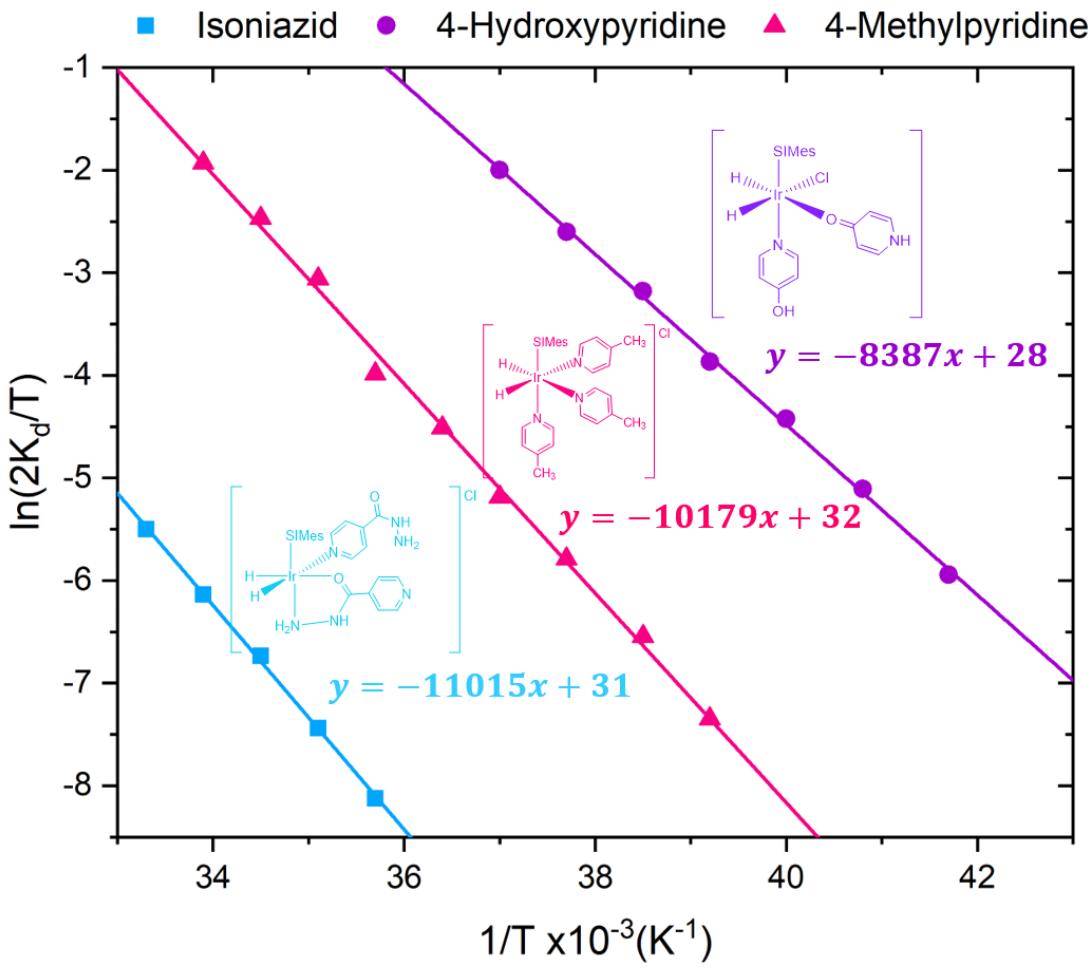

Figure 121 - Eyring polanyi plot for the SABRE-active species containing 4-hydroxypyridine, isoniazid and 4-methylpyridine.

	4-Methylpyridine	4-Hydroxypyridine	Isoniazid
$\Delta H^{\neq}$ (kJmol^{-1})	84.6 ± 3.6	69.7 ± 2.7	91.6 ± 2.9
$\Delta S^{\neq}$ (JK^{-1}mol^{-1})	73.2 ± 13.1	44.1 ± 10.6	62.0 ± 9.8
$\Delta G^{\neq}_{298K}$ (kJmol^{-1})	62.82 ± 0.01	56.58 ± 0.14	73.10 ± 3.13

Table 27 - Table of values calculated for the enthalpy and entropy of dissociation ($\Delta H^{\neq}$ & $\Delta S^{\neq}$) for the SABRE-active species containing isoniazid and 4-hydroxypyridine, which have then been used to calculate the Gibbs free energy of dissociation at 298 K. Data for 4-methylpyridine has been displayed for comparison. $\Delta H^{\neq}$ is calculated from the gradient (m) and $\Delta S^{\neq}$ is calculated from the intercept (c) using the straight-line equations shown in Figure 121 above. $\Delta H^{\neq}$ & $\Delta S^{\neq}$ were subsequently used to calculate the Gibbs free energy of dissociation. The calculations for the errors in $\Delta H^{\neq}$, $\Delta S^{\neq}$ & $\Delta G^{\neq}$ are explained in Chapter 6, Section 6.2.7.3 Calculation of Gibbs free energy and associated errors.

The entropy ($\Delta S^{\neq}$) is positive which is consistent with a dissociative pathway. 4-Hydroxypyridine has the smallest entropy value of 44.1 JK^{-1}mol^{-1} which reflects the

weaker bond between the oxygen bound pyridone tautomer and the metal complex. This means this complex has the most freedom out of the series. The enthalpy ($\Delta H^{\neq}$) indicates the bond strength for dissociative change. Isoniazid has the highest enthalpy value of 91.6 kJmol^{-1} which reflects the stronger bond between the pyridine bound ligand and the metal. This is induced by the chelate bound isoniazid ligand which donates electron density into the metal complex, rendering the metal electron rich. The entropy and enthalpy can be used to calculate the Gibbs free energy of dissociation which have been plotted as a function of the substrate below.

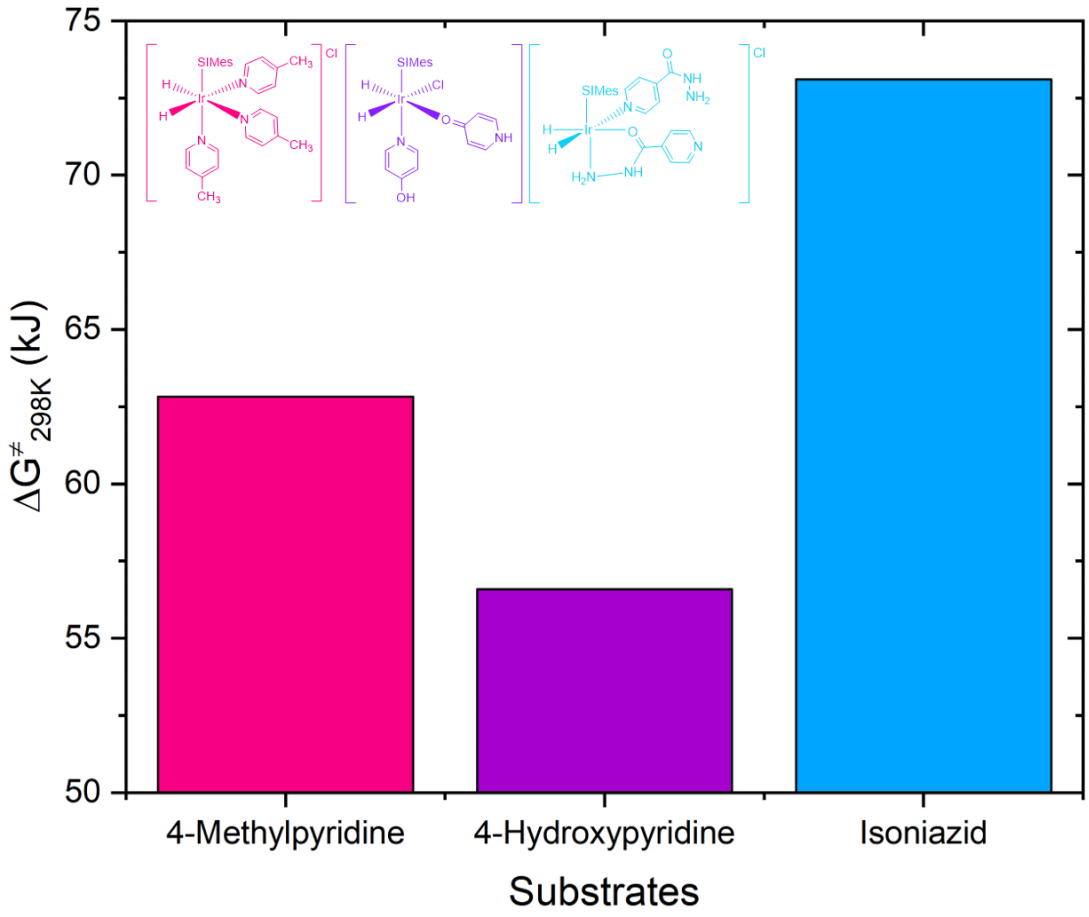

Figure 122 – Gibbs free energy as a function of substrate in the SABRE-active species.

The Gibbs free energy shown in Table 27 and Figure 122 illustrates that, as predicted, the ligation between isoniazid and the metal centre is stronger than the other two examples. Interestingly, the Gibbs free energy of isoniazid (73.1 kJmol^{-1}) is also much larger than that seen for 4-pyridinecarboxaldehyde (64.4 kJmol^{-1}) in the previous chapter. It is thought that the substrate ligand that chelates to the metal centre

donates a large amount of electron density to the iridium. As the iridium centre is now incredibly electron rich, ligation to the pyridine bound isoniazid is much stronger. The Gibbs free energy for 4-hydroxypyridine (56.6 kJ mol^{-1}) is much smaller compared to all of the substrates tested previously, including 4-chloropyridine (62.08 kJ mol^{-1}). This proves that ligation between the oxygen bound pyridone species is far weaker compared to substrates which bind through the pyridine nitrogen atom.

4.6 Relaxation Effects in the SABRE-Active Catalyst

4.6.1 T_1 Relaxation Measurements

The relaxation (T_1) of the associated resonances in these systems were measured according to the procedure described in Chapter 6, Section 6.2.7.2.1 T_1 Relaxation Measurements. These resonances are due to the free substrate, the chelate bound substrate and the pyridine bound substrate (*trans* to H^-) in isoniazid and for the oxygen-bound and nitrogen bound substrate in 4-hydroxypyridine. It was postulated that as isoniazid requires the most energy to dissociate from the metal centre, the T_1 of the substrate *trans* to the hydride would be much shorter compared to the free substrate. The results of this investigation are shown in Figure 123.

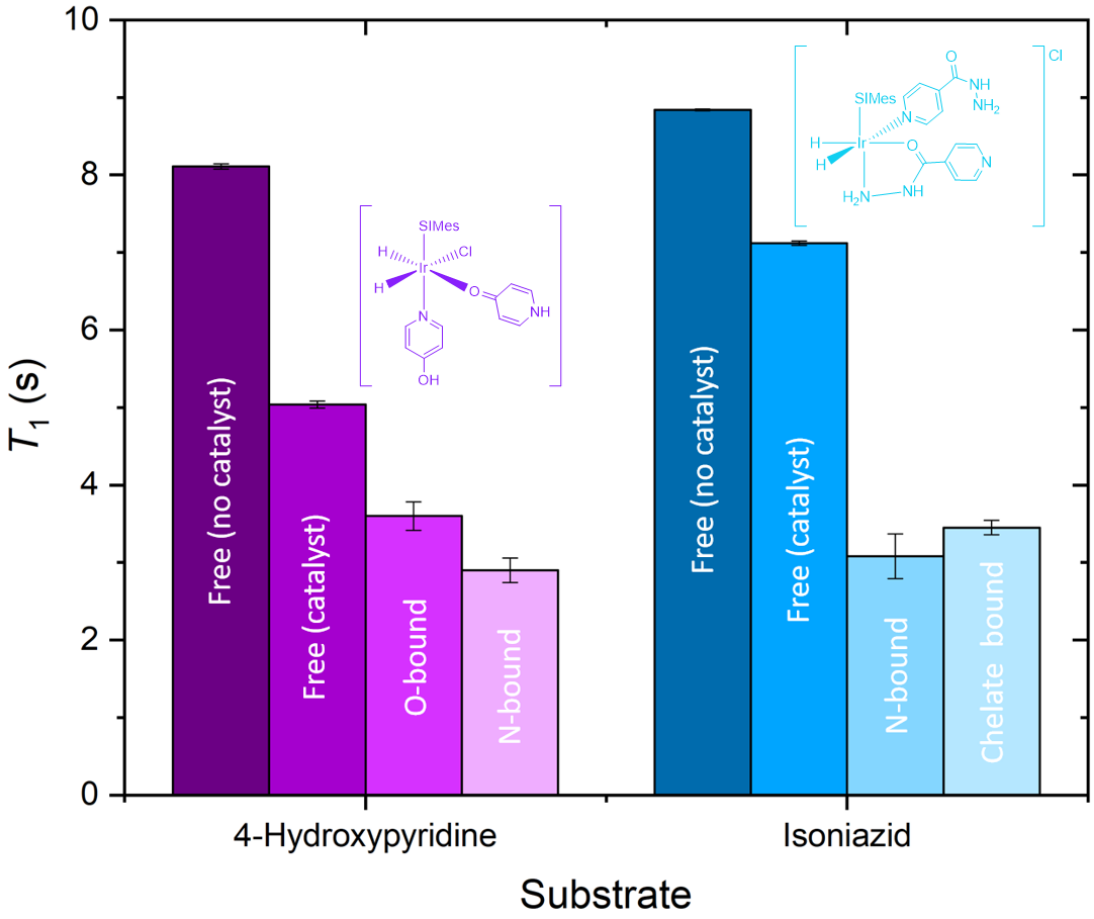

Figure 123 – Comparison of the *Ortho*H T_1 values for 4-hydroxypyridine (purple) and isoniazid (blue). The T_1 for the substrate without catalyst was measured using at 40 mM in methanol-d_4. The T_1 in the presence of catalyst was measured using a sample containing [IrCl(COD)(SIMes)] (4 mM), substrate (40 mM) and *p*-H_2 (4 bar) in methanol-d_4. All measurements were taken at 298 K and 400 MHz. The error bars indicate the fitting error for the T_1 curves shown in Appendix C.

T_1 (s)	4-Hydroxypyridine	Isoniazid
Free	8.11 ± 0.03	8.84 ± 0.01
$Free^{Cat}$	5.04 ± 0.05	7.12 ± 0.03
$N\text{-}bound^{Cat}$	2.90 ± 0.16	3.08 ± 0.29
$O\text{-}bound/chelate\ bound^{Cat}$	3.60 ± 0.18	3.45 ± 0.09

Table 28 - Table of T_1 values at the *ortho* proton resonance in the substrate of interest corresponding to Figure 123. The errors in the T_1 values are calculated from fitting the T_1 curves shown in Appendix C.

Figure 123 shows the T_1 at the *ortho* proton resonance in the free substrate both in the presence of catalyst and without compared to the bound substrate in the SABRE-active species for 4-hydroxypyridine and isoniazid. The corresponding values are

shown in Table 28. The free substrate T_1 without catalyst is 8.11 ± 0.03 s for 4-hydroxypyridine compared to 8.84 ± 0.01 s for isoniazid. Binding to iridium is known to decrease substrate T_1. This effect is observed in the free substrate in the presence of the SABRE catalyst which reduces the T_1 by almost three seconds to 5.04 ± 0.05 s for 4-hydroxypyridine. The presence of the catalyst has a lesser effect on isoniazid where the T_1 is reduced to 7.12 ± 0.03 s. This effect is more pronounced in the bound species, where the pyridine nitrogen bound substrate has a T_1 of 2.90 ± 0.16 s in [IrCl(H)$_2$(SIMes)(κ-O-4-pyridone)(κ-N-4-hydroxypyridine)] compared to 3.08 ± 0.29 s for [Ir(H)$_2$(SIMes)(κ-N-isonicotinylhydrazide)(isonicotinyl-κ-O-κ-N-hydrazide]Cl. The oxygen bound tautomer in [IrCl(H)$_2$(SIMes)(κ-O-4-pyridone)(κ-N-4-hydroxypyridine)] has a T_1 of 3.60 ± 0.18s. This substrate undergoes rapid dissociation with the free material. In the previous chapter it was observed that due to dissociation, the substrate ligand *trans* to hydride has a T_1 value close to that of the free substrate compared to the substrate *trans* to SIMes which has a much lower T_1.

The chelate bound substrate in [Ir(H)$_2$(SIMes)(κ-N-isonicotinylhydrazide)(isonicotinyl-κ-O-κ-N-hydrazide]Cl has a larger T_1 (3.45 ± 0.09 s) than the pyridine bound ligand (3.08 ± 0.29s). This could be attributed to the fact that the *ortho* proton is situated further away from the binding site and therefore is closer to the free T_1.

As the free T_1 in isoniazid is much higher than 4-hydroxypyridine and 4-methylpyridine (6.50 ± 0.04 s for the free substrate in presence of catalyst) it can yield larger enhancements. Hyperpolarisation is lost via relaxation effects, therefore as the T_1 of 4-hydroxypyridine is very small, this effect will reduce the detected signal enhancements.

4.7 Summary

4-Hydroxypyridine and isoniazid were initially selected for SABRE as they are simple *para*-substituted pyridines with low p*K*a values. These substrates were to be included as part of the study in Chapter 3, however, 4-hydroxypyridine readily tautomerizes

to 4-pyridone in solution and isoniazid has been seen to form chelated metal species. This causes them to form atypical SABRE-active species.

In the crystalline form, 4-hydroxypyridine is predominantly found as its 4-pyridone tautomer. It is also the dominant tautomer in polar solvents, the enol tautomer (4-hydroxypyridine) is predominant in the gaseous phase and non-polar solvents. In d_2-dichloromethane, a mixture of both tautomers was found in solution. The ratio of this was found to be temperature dependent. At low temperatures (below 253 K), the enol tautomer was the dominant form. At temperatures above 253 K, the keto tautomer rapidly became the favoured form. A Van't Hoff plot showed the formation of the 4-pyridone tautomer to be an endothermic reaction. The enthalpy was calculated as 886.85 $Jmol^{-1}$ and the entropy was 3.34 $JK^{-1}mol^{-1}$.

The SABRE efficiency of isoniazid has previously been published; however the structure of this complex has been overlooked. It was assumed that this substrate formed the *tris*-substituted complex ($[Ir(H)_2(SIMes)(sub)_3]Cl$), typical in SABRE experiments (see previous chapter). However, analysis in the literature showed that can chelate to metal centres via the oxygen and terminal nitrogen in the hydrazide group.

Reaction of 4-hydroxypyridine with [IrCl(COD)(SIMes)] formed [Ir(COD)(SIMes)(κ-N-4-hydroxypyridine)]Cl, where the substrate ligates to iridium via the pyridine nitrogen as the enol tautomer. This was characterised in the ^{15}N-NMR spectrum where the free pyridine nitrogen is observed at 152.8 ppm compared to 207.9 ppm in the bound form. This upfield shift is similar to those observed for the free and bound forms of 4-methylpyridine in the previous chapter. In d_2-dichloromethane, the keto tautomer was also found to bind to iridium in [Ir(COD)(SIMes)(κ-O-4-pyridone)]Cl. The ratio of the enol:keto tautomers was again shown to be temperature dependent. Below 253 K, the enol form was the predominant tautomer compared to higher temperatures where the keto tautomer dominated. The enthalpy and entropy were calculated from a Van't Hoff plot. The enthalpy in this case is 623.61 $Jmol^{-1}$ and the entropy is 2.39 $JK^{-1}mol^{-1}$ which are smaller than the

corresponding values in the substrate, meaning that formation of the pyridone tautomer is more favourable with [Ir(COD)(SIMes)(4-hydroxypyridine)]Cl.

Reaction of isoniazid with [IrCl(COD)(SIMes)] formed a mixture of species in solution. The major species formed where the substrate bound to iridium via the oxygen in the hydrazide group. This formed in a 2:1 ratio with the minor species where the substrate bound to iridium via the pyridine nitrogen. The ^{15}N-NMR chemical shift showed that the pyridine nitrogen in the major species (311.0 ppm) was close to the ^{15}N chemical shift of the free substrate (308.2 ppm). The equivalent chemical shift in the minor species was 248.5 ppm, this upfield shift is characteristic of a pyridine nitrogen bound to metal (see previous chapter).

The SABRE-active catalyst is typically a *tris*-substituted species of the form: $[Ir(H)_2(SIMes)(substrate)_3]Cl$. Upon reaction with the iridium pre-catalyst, 4-hydroxypyridine and isoniazid each form a *bis*-substituted species. When 4-hydroxypyridine is used as the catalyst this takes the form$[IrCl(H)_2(SIMes)$(κ-O-4-pyridone)(κ-N-4-hydroxypyridine)]. This species contains two inequivalent hydrides in the equatorial plane, one *trans* to chloride and the other *trans* to the 4-pyridone tautomer of 4-hydroxypyridine which binds via the oxygen in the keto functional group. The second substrate ligand lies *trans* to SIMes in the axial position. This substrate binds to iridium via the pyridine nitrogen as the enol tautomer (4-hydroxypyridine). When isoniazid is used as the SABRE target, the SABRE-active species takes the form $[Ir(H)_2(SIMes)$(κ-N-isonicotinylhydrazide)(isonicotinyl-κ-O-κ-N-hydrazide]Cl . One substrate ligates to iridium in the traditional way, via the pyridine nitrogen, the other binds as a chelate via the nitrogen and oxygen in the hydrazide group. This results in two inequivalent hydrides as one is *trans* to the pyridine bound isoniazid ligand and the other *trans* to the oxygen binding site of the chelate. These structures have been confirmed via ^{1}H, ^{13}C and ^{15}N-NMR characterisation techniques. Despite forming these unusual SABRE-active species, both structures have been shown to be SABRE-active as they exhibit enhancements under SABRE-conditions of 4 bar *p*-H_2. $[IrCl(H)_2(SIMes)$(κ-O-4-pyridone)(κ-N-4-hydroxypyridine)]exhibits the lowest enhancements of −31 ± 1-fold when a substrate

concentration of 50 mM is used. $[Ir(H)_2(SIMes)(\kappa\text{-}N\text{-}isonicotinylhydrazide)(isonicotinyl\text{-}\kappa\text{-}O\text{-}\kappa\text{-}N\text{-}hydrazide]Cl$ yields much larger enhancements compared to 4-hydroxypyridine. The largest enhancement yielded was −696 ± 17-fold when a substrate concentration of 30 mM was used.

4-Hydroxypyridine and isoniazid form unusual SABRE-active species, each containing a substrate ligand which binds through the functional group in the *para*-position of the pyridine ring, either as a chelate (isoniazid) or via the oxygen as 4-pyridone (4-hydroxypyridine). This means that the lone pair on the nitrogen is free and could potentially bind to iridium, forming dimers in solution. To establish the formation of aggregates in solution, diffusion ordered spectroscopy (DOSY) can be employed. The results for 4-hydroxypyridine and isoniazid were compared to $[Ir(H)_2(SIMes)(4\text{-}methylpyridine)_3]Cl$ which is known to not form dimers in solution. The diffusion coefficients for each of the SABRE-active species were found to be very similar. For $[Ir(H)_2(SIMes)(4\text{-}methylpyridine)_3]Cl$ the diffusion coefficient was 6.24×10^{-10} m^2s^{-1} compared to 6.27×10^{-10} m^2s^{-1} for $[IrCl(H)_2(SIMes)(\kappa\text{-}O\text{-}4\text{-}pyridone)(\kappa\text{-}N\text{-}4\text{-}hydroxypyridine)]$ and 6.62×10^{-10} m^2s^{-1} for $[Ir(H)_2(SIMes)(\kappa\text{-}N\text{-}isonicotinylhydrazide)(isonicotinyl\text{-}\kappa\text{-}O\text{-}\kappa\text{-}N\text{-}hydrazide]Cl$. This suggests that reaction of 4-hydroxypyridine and isoniazid does not encourage the formation of dimers or any other aggregates in solution. The diffusion coefficient can be used to calculate the spherical radii using the Stokes-Einstein equation. However, this assumes a perfect spherical molecule, furthermore the calculation requires the viscosity of the solution is known. This was not measured and therefore a value from the literature was used, therefore these values cannot be used quantitatively but can be used for comparative purposes. $[Ir(H)_2(SIMes)(4\text{-}methylpyridine)_3]Cl$ was shown to have the largest spherical radius, followed by $[IrCl(H)_2(SIMes)(\kappa\text{-}O\text{-}4\text{-}pyridone)(\kappa\text{-}N\text{-}4\text{-}hydroxypyridine)]$ and $[Ir(H)_2(SIMes)(\kappa\text{-}N\text{-}isonicotinylhydrazide)(isonicotinyl\text{-}\kappa\text{-}O\text{-}\kappa\text{-}N\text{-}hydrazide]Cl$. This is because the SABRE-active species containing 4-methylpyridine is a *tris*-substituted complex whereas $[IrCl(H)_2(SIMes)(\kappa\text{-}O\text{-}4\text{-}pyridone)(\kappa\text{-}N\text{-}4\text{-}hydroxypyridine)]$ and $[Ir(H)_2(SIMes)(isoniazid)_2]Cl$ contain two substrate ligands.

Exchange between the bound and free substrate is a critical feature of the SABRE process as it allows for the hyperpolarised substrate to build up in the bulk solution. Hyperpolarisation is transferred from the *p*-H_2 derived hydrides to the substrate nuclei via the scalar coupling. The substrate then dissociates from the complex leaving a vacant site. A substrate from the bulk solution then binds to the catalyst for hyperpolarisation transfer. As 4-hydroxypyridine and isoniazid yield SABRE enhancements, they must undergo substrate dissociation.

The fastest exchange rate was observed for $[IrCl(H)_2(SIMes)(\kappa\text{-O-4-pyridone})(\kappa\text{-N-4-hydroxypyridine})]$. Substrate dissociation was observed between 240 K and 270 K where k_d was 0.31 s^{-1} and 18.31 s^{-1} respectively. This rate of dissociation was too rapid for efficient SABRE, hence why $[IrCl(H)_2(SIMes)(\kappa\text{-O-4-pyridone})(\kappa\text{-N-4-hydroxypyridine})]$ yields small enhancements.

$[Ir(H)_2(SIMes)(\kappa\text{-N-isonicotinylhydrazide})(\text{isonicotinyl-}\kappa\text{-O-}\kappa\text{-N-hydrazide}]Cl$
exhibited much slower substrate dissociation between 280 K and 300 K. Where the k_d value ranged from 0.04 s^{-1} and 0.61 s^{-1} respectively. These substrate dissociation for these complexes was compared to $[Ir(H)_2(SIMes)(4\text{-methylpyridine})_3]Cl$ which had a substrate dissociation of 0.08 s^{-1} at 255 K and 21.46 s^{-1} at 295 K. Exchange is observed in the substrate that lies *trans* to the hydride. In $[IrCl(H)_2(SIMes)(\kappa\text{-O-4-pyridone})(\kappa\text{-N-4-hydroxypyridine})]$ this is the oxygen bound 4-pyridone tautomer. As binding to iridium via oxygen is assumed to be weaker than binding via the pyridine nitrogen, this will result in rapid substrate exchange. In $[Ir(H)_2(SIMes)(\kappa\text{-N-isonicotinylhydrazide})(\text{isonicotinyl-}\kappa\text{-O-}\kappa\text{-N-hydrazide}]Cl$, the substrate *trans* to hydride is bound via the pyridine nitrogen. Therefore, the slower exchange must be a consequence of the chelated substrate.

The Gibbs free energy ($\Delta G^{\neq}$) was calculated using an Eyring-Polanyi plot where $\ln\frac{k}{T}$ is plotted as a function of $\frac{1}{T}$. The enthalpy ($\Delta H^{\neq}$) can then be extracted from the gradient and the entropy ($\Delta S^{\neq}$) from the intercept. The entropy for $[IrCl(H)_2(SIMes)(\kappa\text{-O-4-pyridone})(\kappa\text{-N-4-hydroxypyridine})]$ and $[Ir(H)_2(SIMes)(\kappa\text{-N-isonicotinylhydrazide})(\text{isonicotinyl-}\kappa\text{-O-}\kappa\text{-N-hydrazide}]Cl$ is positive which is

consistent with a dissociative pathway. 4-hydroxypyridine had the smallest entropy and enthalpy values of 44.1 $JK^{-1}mol^{-1}$ and 69.7 $kJmol^{-1}$ which reflected the weaker bond between the oxygen bound pyridone tautomer and the metal complex. Isoniazid had higher entropy and enthalpy values of 62 $JK^{-1}mol^{-1}$ and 91.6 $kJmol^{-1}$ which reflects the stronger bond between the pyridine bound ligand and the metal. $\Delta G^{\neq}$ can calculated from $\Delta S^{\neq}$ and $\Delta H^{\neq}$ and be used to quantify the strength of iridium-substrate ligation. As 4-hydroxypyridine demonstrated the fastest substrate dissociation, it was shown to have the weakest ligation to iridium. The $\Delta G^{\neq}_{(298\ K)}$ value was 56.58 $kJmol^{-1}$, which was smaller than 4-chloropyridine which had the weakest iridium-substrate ligation in the previous chapter ($\Delta G^{\neq}_{(298\ K)}$ = 62.08 kJ mol^{-1}). Isoniazid displayed the highest $\Delta G^{\neq}$ value of all of the substrates discussed in this thesis. The $\Delta G^{\neq}_{(298\ K)}$ value was 73.10 $kJmol^{-1}$ compared to 4-pyridinecarboxaldehyde which had a $\Delta G^{\neq}_{(298\ K)}$ of 64.44 $kJmol^{-1}$ in the previous chapter. This is attributed to the chelate ligand which donates electron density to the iridium metal centre. As the iridium is now very electron rich, ligation to the pyridine bound isoniazid is much stronger.

Relaxation (T_1) is another limiting factor of SABRE efficiency as hyperpolarisation can be lost via relaxation effects. This is because binding to iridium promotes relaxation, this is observed when the free substrate *ortho* T_1 in the absence of catalyst is compared to the free substrate in the presence in catalyst. For example, 4-hydroxypyridine has an *ortho* T_1 of 8.11 s which is reduced to 5.04 s in the presence of the SABRE-active species. This effect is much weaker when isoniazid is considered. In the absence of catalyst, the *ortho* T_1 is 8.84 s which is lowered to 7.12 s in the presence of catalyst. As the T_1 of isoniazid is larger than 4-hydroxypyridine, less hyperpolarisation is lost before substrate dissociation occurs. This means that larger signal enhancements can be yielded using isoniazid. This is unexpected as isoniazid has a higher $\Delta G^{\neq}$ value and therefore it was assumed that it would experience a larger T_1 effect from ligation to iridium compared to 4-hydroxypyridine.

4.8 References

1. A. Albert and E. Spinner, *J. Chem. Soc.*, 1960, 1221-1226.

2. M. T. Chenon, R. J. Pugmire, D. M. Grant, R. P. Panzica and L. B. Townsend, *J. Am. Chem. Soc.*, 1975, **97**, 4636-4642.
3. H. B. Schlegel, P. Gund and E. M. Fluder, *J. Am. Chem. Soc.*, 1982, **104**, 5347-5351.
4. E. Murguly, T. B. Norsten and N. Branda, *J. Chem. Soc., Perkin Trans. 2*, 1999, DOI: DOI 10.1039/a904323c, 2789-2794.
5. R. Diguet, R. Deul and E. U. Franck, *Berichte der Bunsengesellschaft für physikalische Chemie*, 1985, **89**, 800-804.
6. J. Wang and R. J. Boyd, *J. Phys. Chem.*, 1996, **100**, 16141-16146.
7. U. Vögeli and W. von Philipsborn, *Org. Magn. Reson.*, 1973, **5**, 551-559.
8. A. Gordon, A. Katritzky and S. Roy, *Journal of the Chemical Society B: Physical Organic*, 1968, 556-561.
9. A. Katritzky, J. Rowe and S. Roy, *Journal of the Chemical Society B: Physical Organic*, 1967, 758-761.
10. A. R. Katritzky and J. M. Lagowski, in *Adv. Heterocycl. Chem.*, ed. A. R. Katritzky, Academic Press, 1963, vol. 1, pp. 311-338.
11. H. Kemp, *J. Chem. Educ.*, 1987, **64**, 482.
12. H. Naghibi, A. Tamura and J. M. Sturtevant, *Proc. Natl. Acad. Sci.*, 1995, **92**, 5597.
13. W. H. Organization, 2020.
14. W. H. Organization, *World Health Organization model list of essential medicines: 21st list 2019*, World Health Organization, 2019.
15. N. Persaud, M. Jiang, R. Shaikh, A. Bali, E. Oronsaye, H. Woods, G. Drozdzal, Y. Rajakulasingam, D. Maraj, S. Wadhawan, N. Umali, R. Wang, M. McCall, J. K. Aronson, A. Plüddemann, L. Moja, N. Magrini and C. Heneghan, *Bull World Health Organ*, 2019, **97**, 394-404C.
16. P. S. S. J. Sastry, R. K. Lonibala and T. R. Rao, *Synth. React. Inorg. Met. Org. Chem.*, 1995, **25**, 1261-1278.
17. K. K. Narang, M. K. Singh, M. R. Goyle and K. Bhuvaneshwari, *Synth. React. Inorg. Met.-Org. Chem.*, 1991, **21**, 1569-1585.
18. B. Bottari, R. Maccari, F. Monforte, R. Ottana, E. Rotondo and M. G. Vigorita, *Bioorg. Med. Chem. Lett.*, 2000, **10**, 657-660.
19. T. Stringer, R. Seldon, N. Liu, D. F. Warner, C. Tam, L. W. Cheng, K. M. Land, P. J. Smith, K. Chibale and G. S. Smith, *Dalton Trans.*, 2017, **46**, 9875-9885.
20. O. Akinyele, E. Fakola, L. Durosinmi, T. Ajayeoba and A. Ayeni, *Ife Journal of Science*, 2019, **21**, 184-192.
21. H. Zeng, J. Xu, J. Gillen, M. T. McMahon, D. Artemov, J. M. Tyburn, J. A. Lohman, R. E. Mewis, K. D. Atkinson, G. G. Green, S. B. Duckett and P. C. van Zijl, *J. Magn. Reson.*, 2013, **237**, 73-78.
22. P. Norcott, P. J. Rayner, G. G. R. Green and S. B. Duckett, *Chemistry*, 2017, **23**, 16990-16997.
23. W. Iali, S. S. Roy, B. J. Tickner, F. Ahwal, A. J. Kennerley and S. B. Duckett, *Angew. Chem. Int. Ed.*, 2019, **58**, 10271-10275.
24. B. J. Tickner, J. S. Lewis, R. O. John, A. C. Whitwood and S. B. Duckett, *Dalton Trans.*, 2019, **48**, 15198-15206.
25. B. J. Tickner, W. Iali, S. S. Roy, A. C. Whitwood and S. B. Duckett, *Chem. Phys. Chem.*, 2019, **20**, 241-245.

26. B. J. Tickner, R. O. John, S. S. Roy, S. J. Hart, A. C. Whitwood and S. B. Duckett, *Chem. Sci.*, 2019, **10**, 5235-5245.
27. P. Beltrame, E. Cadoni, C. Floris, G. Gelli and A. Lai, *Spectrochimica Acta Part A: Molecular and Biomolecular Spectroscopy*, 2002, **58**, 2693-2697.
28. A. J. Ruddlesden, R. E. Mewis, G. G. Green, A. C. Whitwood and S. B. Duckett, *Organometallics*, 2015, **34**, 2997-3006.
29. A. J. Ruddlesden and S. B. Duckett, *Chem. Commun.*, 2016, **52**, 8467-8470.
30. L. S. Lloyd, A. Asghar, M. J. Burns, A. Charlton, S. Coombes, M. J. Cowley, G. J. Dear, S. B. Duckett, G. R. Genov, G. G. R. Green, L. A. R. Highton, A. J. J. Hooper, M. Khan, I. G. Khazal, R. J. Lewis, R. E. Mewis, A. D. Roberts and A. J. Ruddlesden, *Catal. Sci. Technol.*, 2014, **4**, 3544-3554.
31. K. Nicolay, K. P. J. Braun, R. A. d. Graaf, R. M. Dijkhuizen and M. J. Kruiskamp, *NMR Biomed.*, 2001, **14**, 94-111.
32. R. Evans, *Prog. Nucl. Magn. Reson. Spec.*, 2019, DOI: https://doi.org/10.1016/j.pnmrs.2019.11.002.
33. C. S. Johnson, *Prog. Nucl. Magn. Reson. Spec.*, 1999, **34**, 203-256.
34. T. D. W. Claridge, *High-Resolution NMR Techniques in Organic Chemistry*, Elsevier Science, 2016.
35. C. R. Cantor and P. R. Schimmel, *Biophysical chemistry: Part II: Techniques for the study of biological structure and function*, Macmillan, 1980.
36. W. A. Wegener, V. J. Koester and R. M. Dowben, *Proc. Natl. Acad. Sci.*, 1979, **76**, 6356-6360.
37. R. Evans, G. Dal Poggetto, M. Nilsson and G. A. Morris, *Anal. Chem.*, 2018, **90**, 3987-3994.
38. K. F. Morris and C. S. Johnson, *J. Am. Chem. Soc.*, 1992, **114**, 3139-3141.
39. L. Guduff, D. Kurzbach, C. van Heijenoort, D. Abergel and J. N. Dumez, *Chemistry*, 2017, **23**, 16722-16727.
40. I. Reile, R. Aspers, J. M. Tyburn, J. G. Kempf, M. C. Feiters, F. Rutjes and M. Tessari, *Angew. Chem. Int. Ed.*, 2017, **56**, 9174-9177.
41. E. O. Stejskal and J. E. Tanner, *J. Chem. Phys.*, 1965, **42**, 288-292.
42. D. Sinnaeve, Concepts in Magnetic Resonance Part A, 2012, 40A, 39-65.
43. R. M. Cotts, M. J. R. Hoch, T. Sun and J. T. Markert, *Journal of Magnetic Resonance (1969)*, 1989, **83**, 252-266.
44. R. F. Karlicek and I. J. Lowe, *Journal of Magnetic Resonance (1969)*, 1980, **37**, 75-91.
45. S. J. Gibbs and C. S. Johnson, *J. Magn. Reson.*, 1991, **93**, 395-402.
46. D. Wu, A. Chen and C. S. Johnson, *J. Magn. Reson.,* 1995, **115**, 260-264.
47. J. D. Isdale, A. J. Easteal and L. A. Woolf, *Int. J. Thermophys.*, 1985, **6**, 439-450.

Chapter 5 Conclusions and Further Work

As illustrated in this work, signal amplification by reversible exchange (SABRE) is a hyperpolarisation technique that dramatically increases the sensitivity of the nuclear magnetic resonance (NMR) experiment. SABRE employs an inorganic, iridium catalyst and *p*-H_2 for the enhanced detection of a target molecule (substrate). In the SABRE experiment, an iridium complex catalyses the polarisation transfer from *p*-H_2 to the substrate. Polarisation is then transferred via the *J*-coupled network within the iridium complex. However, whilst the catalyst facilitates polarisation transfer, it also provides a route to depolarisation via relaxation processes and the oscillatory nature of the transfer. Substrate dissociation and association mechanisms then allow for net polarisation to build up (equilibrate) in the bulk solution, generating large signal enhancements. Typically, SABRE targets are pyridine derivatives as coordination via the ring nitrogen to the iridium centre allows for substrate exchange to occur on a suitable timescale to allow polarisation transfer. Additionally, pyridine rings are heavily prevalent in biological processes making them excellent candidates for SABRE-MRI.

Three different SABRE methods for polarisation transfer experiments were investigated in this thesis: manual shaking using the stray field of the spectrometer, manual shaking using a handheld magnetic array and an automated flow system. It was established that the automated flow system was the most reproducible method, but the manual shaking methods yielded larger signal enhancements. The manual shaking method using the stray field approach yielded the largest signal enhancements and smallest errors compared to the other two methods. This was surprising at it contradicted the findings of Richardson *et al*.[1] who established that using the handheld magnetic array provided larger signal enhancements coupled with much smaller errors. The differences between the literature and the results of Chapter 2 were attributed to longer sample transfer times, and the clear challenge in using this method. Differences were established between two 400 MHz spectrometers, one of which was a narrow bore instrument (**a**) whilst the other was a wide bore instrument (**b**) to allow for imaging capabilities. It was found that

instrument A produced the largest and most reproducible signal enhancements. The differences between these two spectrometers were assumed to result from the longer sample transfer times associated with the utilisation of spectrometer **b** as a consequence of the instrument being situated further away from the computer compared to spectrometer **a**. Therefore this spectrometer was utilised for all subsequent SABRE experiments. This observation is itself illuminating as it details how careful an operator needs to be if optimum polarisation levels are to be achieved.

A number of *para*-substituted pyridine rings were selected for SABRE scrutiny: 4-chloropyridine, 4-methylpyridine, 4-methoxypyridine and 4-pyridinecarboxaldehyde. These substrates were shown to form *tris*-substituted SABRE active complexes of the form $[Ir(H)_2(SIMes)(substrate)_3]Cl$. Initially, the properties of these systems were classed according to their pK_a and it was hypothesised that substrates with high pK_a values would form strong associations to the iridium SABRE-active catalyst due to the increased basicity at the pyridine nitrogen. The effective pK_a values were then measured in methanol solution such that 4-chloropyridine had the lowest pK_a value of 2.00, followed by 4-pyridinecarboxaldehyde (3.12), 4-methylpyridine (4.02) and finally 4-methoxypyridine (4.89). Therefore, it was predicted that 4-methoxypyridine would form the strongest substrate-iridium ligations. Instead, 4-pyridinecarboxaldehyde was shown to form the strongest associations to the metal complex. This was observed by slow substrate dissociation rates and high values of enthalpy of activation of ligand loss (92.84 kJ mol^{-1}) and related Gibbs free energy values (64.44 kJ mol^{-1}), which indicate strong and stable bonds. As a consequence of these strong bonds and longer catalyst residence times, 4-pyridinecarboxaldehyde proved to exhibit the shortest ^1H T_1 values in solution due to contributions from the strongly ligations to the iridium centre. Conversely, 4-chloropyridine was found to undergo rapid substrate dissociation and therefore formed the weakest iridium-substrate associations this resulted in a reduced reduction in ^1H T_1 values. 4-Chloropyridine proved to yield the smallest signal enhancements of (−340-fold) compared to the other substrates. Therefore, in this case, substrate dissociation occurs too rapidly for

efficient polarisation transfer prior to its dissociation. Similar trends in SABRE behaviour to those observed with [IrCl(COD)(SIMes)] were also observed when related investigations were performed in conjunction with the catalyst precursors [IrCl(COD)(ITBXy)] and [IrCl(COD)(IMes^{Cl})]. The optimum rate of substrate dissociation has been suggested to be 4.5 s^{-1} according to the literature in such systems.[2] This meant that is was possible to define the temperature for optimum SABRE performance in theses [Ir(H)$_2$(SIMes)(substrate)$_3$]Cl catalysts. Unsurprisingly, it was established that the stronger the iridium-substrate associations, the higher the temperature required for optimal SABRE performance. In this idealised scenario, where the rate of substrate dissociation on SABRE efficiency was removed from consideration, the T_1 became the dominant factor controlling the level of signal enhancement. These findings were published in *Catalysis Science and Technology* in 2019.[3]

When the substrates isoniazid and 4-hydroxypyridine were investigated for their SABRE hyperpolarisation, both proved to form *bis*-substituted species where one substrate ligand binds to iridium via the pyridine nitrogen and the second ligates via an alternative binding mode according to the functional group that is located in the *para* position. Analysis by diffusion ordered spectroscopy (DOSY) showed that despite both complexes containing free pyridine nitrogen atoms available for binding, no dimers were formed in solution. Furthermore, the SABRE-active complexes of 4-hydroxypyridine and isoniazid were found to hyperpolarise under SABRE conditions. 4-Hydroxypyridine readily tautomerises to 4-pyridone and both tautomers were found to bind to iridium in the SABRE-active complex which takes the form: [IrCl(H)$_2$(SIMes)(κ-O-4-pyridone)(κ-N-4-hydroxypyridine)]. The 4-pyridone tautomer binds to iridium via the oxygen in the ketone functional group and is located *trans* to hydride. It is this substrate ligand that receives optimal polarisation during transfer from the *para*hydrogen derived hydride ligands. This ligand also undergoes fast substrate dissociation which, coupled with the $^5J_{HH}$ propagator results in small signal enhancements when compared to the other substrates discussed in this thesis. Small values of enthalpy of activation (69.7 kJ mol^{-1}) and Gibbs free energy of activation (56.58 kJ mol^{-1}) are characteristic of dissociation and illustrate the

weaker ligation between the oxygen-bound 4-pyridone tautomer and iridium. In contrast, isoniazid forms the SABRE-active species $[Ir(H)_2(SIMes)(\kappa\text{-}N\text{-}isonicotinylhydrazide)(isonicotinyl\text{-}\kappa\text{-}O\text{-}\kappa\text{-}N\text{-}hydrazide]Cl$ upon reaction with [IrCl(COD)(SIMes)] and *para*hydrogen. This species contains one substrate ligand that chelates to the iridium via the terminal nitrogen and oxygen in the hydrazide functional group. The pyridine-bound isoniazid ligand lies *trans* to hydride and undergoes slow substrate dissociation and was found to form strong associations to the metal centre. This was evidenced by high values of enthalpy of activation (91.6 kJ mol^{-1}) and Gibbs free energy of activation (73.1 kJ mol^{-1}). Despite the slower substrate dissociation rate, the signal enhancements yielded for isoniazid (−696-fold) were comparable to those observed for 4-methylpyridine (−891-fold). Whilst these novel complexes have not yet been published, previous literature has overlooked the formation of these *bis*-substituted species.[4, 5]

5.1 Further Work

The effect of *para*-substituents on the iridium-substrate binding modes were thoroughly investigated. This included the initial study comparing the binding potential of 4-chloropyridine, 4-pyridinecarboxaldehyde, 4-methylpyridine and 4-methoxypyridine. It was established that the optimal conditions for SABRE occur when the iridium-substrate ligations allow for sufficient polarisation transfer before relaxation mechanisms begin to take effect, thus limiting the observed signal enhancement. As an extension of this study, it would be interesting to analyse mixtures of these substrates in solution and observe which substrate preferentially binds to the iridium complex. Studies of SABRE hyperpolarised mixtures of substrates have been published using single-scan DOSY NMR.[6] Furthermore, it would be interesting to understand whether specific substrate combinations could be used to enhance the signal enhancements of the least SABRE efficient substrates (eg 4-chloropyridine).

In the second investigation, it was observed that 4-hydroxypyridine and isoniazid form the following *bis*-substituted SABRE-active species: $[IrCl(H)_2(SIMes)(\kappa\text{-}O\text{-}4\text{-}$

pyridone)(κ-N-4-hydroxypyridine)] and [Ir(H)$_2$(SIMes)(κ-N-isonicotinylhydrazide)(isonicotinyl-κ-O-κ-N-hydrazide]Cl. Although these complexes were fully characterised by ^{13}C, ^{15}N and ^{1}H-NMR methods, analysing these via x-ray crystallography would provide a clear picture of the complex structures. To do this, crystals of the SABRE-active species would need to be grown in a controlled environment. Although similar oxygen-bound and chelated iridium SABRE species have been published,[7-9] the species associated with 4-hydroxypyridine and isoniazid have not yet been scrutinised. Furthermore, the data presented in Chapter 4 demonstrates a full and comprehensive study of the SABRE efficiency of these catalysts. [Ir(H)$_2$(SIMes)(κ-N-isonicotinylhydrazide)(isonicotinyl-κ-O-κ-N-hydrazide]Cl was shown to yield larger signal enhancements, comparable to 4-methylpyridine and 4-methoxypyridine. Therefore, isoniazid could potentially be used as a co-ligand to enhance the detection of less efficient SABRE substrate (e.g. 4-chloropyridine or 4-hydroxypyridine). Co-ligands such as acetonitrile and dimethoxy sulfoxide have previously been reported for the enhanced SABRE hyperpolarisation of a number of substrates including [1-^{13}C]-pyruvate.[8, 10-12] Finally, as [IrCl(H)$_2$(SIMes)(κ-O-4-pyridone)(κ-N-4-hydroxypyridine)] contains oxygen-bound 4-pyridone it may be possible to observe signal enhancements using ^{13}C-NMR. Hyperpolarisation of ^{13}C nuclei via SABRE is beneficial as this nucleus has been shown to exhibit longer hyperpolarisation lifetimes compared to ^{1}H.[13, 14]

5.2 References

1. P. M. Richardson, S. Jackson, A. J. Parrott, A. Nordon, S. B. Duckett and M. E. Halse, *Magn. Reson. Chem.*, 2018, **56**, 641-650.
2. D. A. Barskiy, A. N. Pravdivtsev, K. L. Ivanov, K. V. Kovtunov and I. V. Koptyug, *Phys. Chem. Chem. Phys.*, 2016, **18**, 89-93.
3. E. V. Stanbury, P. M. Richardson and S. B. Duckett, *Catal. Sci. Technol.*, 2019, **9**, 3914-3922.
4. P. Norcott, P. J. Rayner, G. G. R. Green and S. B. Duckett, *Chemistry*, 2017, **23**, 16990-16997.
5. H. Zeng, J. Xu, J. Gillen, M. T. McMahon, D. Artemov, J. M. Tyburn, J. A. Lohman, R. E. Mewis, K. D. Atkinson, G. G. Green, S. B. Duckett and P. C. van Zijl, *J. Magn. Reson.*, 2013, **237**, 73-78.
6. L. Guduff, P. Berthault, C. van Heijenoort, J.-N. Dumez and G. Huber, *Chem. Phys. Chem.*, 2019, **20**, 392-398.

7. A. J. Ruddlesden, R. E. Mewis, G. G. Green, A. C. Whitwood and S. B. Duckett, *Organometallics*, 2015, **34**, 2997-3006.
8. B. J. Tickner, W. Iali, S. S. Roy, A. C. Whitwood and S. B. Duckett, *Chem. Phys. Chem.*, 2019, **20**, 241-245.
9. B. J. Tickner, J. S. Lewis, R. O. John, A. C. Whitwood and S. B. Duckett, *Dalton Trans.*, 2019, **48**, 15198-15206.
10. R. E. Mewis, R. A. Green, M. C. Cockett, M. J. Cowley, S. B. Duckett, G. G. Green, R. O. John, P. J. Rayner and D. C. Williamson, *J. Phys. Chem. B*, 2015, **119**, 1416-1424.
11. W. Iali, S. S. Roy, B. J. Tickner, F. Ahwal, A. J. Kennerley and S. B. Duckett, *Angew. Chem. Int. Ed.*, 2019, **58**, 10271-10275.
12. B. J. Tickner, R. O. John, S. S. Roy, S. J. Hart, A. C. Whitwood and S. B. Duckett, *Chem. Sci.*, 2019, **10**, 5235-5245.
13. P. M. Richardson, W. Iali, S. S. Roy, P. J. Rayner, M. E. Halse and S. B. Duckett, *Chem. Sci.*, 2019, **10**, 10607-10619.
14. P. M. Richardson, A. J. Parrott, O. Semenova, A. Nordon, S. B. Duckett and M. E. Halse, *Analyst*, 2018, **143**, 3442-3450.

Chapter 6 Experimental

6.1 Instrumentation

6.1.1 Nuclear Magnetic Resonance

NMR characterisation was conducted on Bruker Avance III 400 and 500 MHz spectrometers, where the ^{1}H NMR frequency was 400.1 or 500.1 MHz respectively. The ^{13}C frequency was 100.6 or 125.8 MHz and the ^{15}N frequency at 40.5 or 50.7 MHz. The hyperpolarisation measurements were conducted on Bruker Avance III 400 MHz spectrometers, where the ^{1}H NMR frequency was 400.1 MHz. Bruker Topspin 3.5 was used for data acquisition and processing.

Chemical shifts are provided in parts per million (ppm) with respect to the associated residual solvent signal. The NMR solvents used were: methanol-d_4, methanol-d_2 and dichloromethane-d_2. These have been specified in the figure and table captions throughout the results chapters. Couplings are given in Hz.

6.1.1.1 Pulse Sequences/Experiments

A number of advanced NMR methods were used in this work.

^{1}H/^{13}C-HMQC and ^{1}H/^{15}N-HMQC spectra were used for the characterisation of the SABRE precatalyst and the SABRE-active species described in Chapters 3 and 4. These were collected using the hmqcgpqf pulse sequence (see Figure 1). The delay, d2, is set according to the reciprocal of the coupling between the proton and heteronucleus. Couplings constants of 145 Hz and 12 Hz were chosen for ^{13}C as these correspond to the typical $^{2}J_{CH}$ ≈ 12 Hz and $^{1}J_{CH}$ ≈120-160 Hz.[1] A value of 8 Hz was used for ^{15}N as this corresponds to $^{1}J_{NH}$.[2]

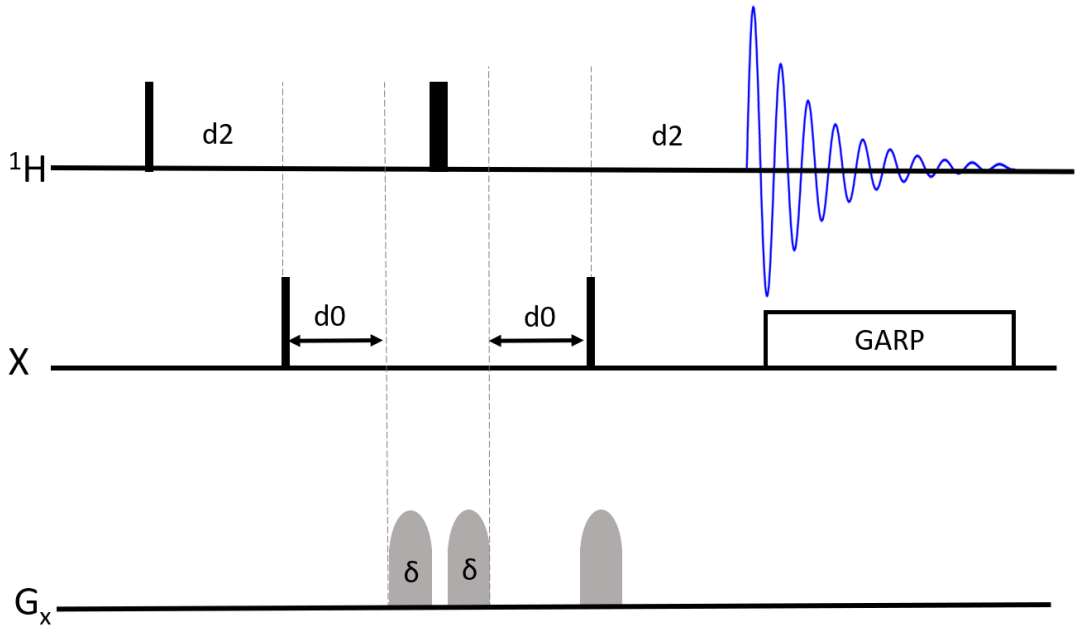

Figure 124 - hmqcgpqf pulse sequence

The ^{15}N characterisation spectra in Chapter 4 were collected using the zgig pulse sequence of Figure 2.

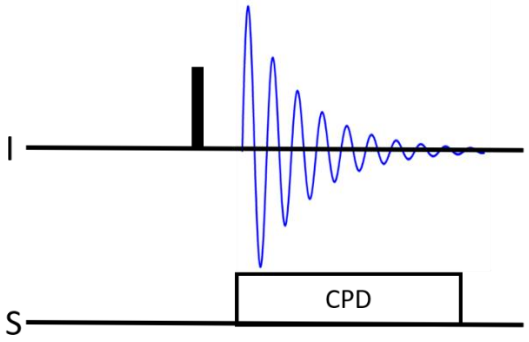

Figure 125 - zgig pulse sequence

Hyperpolarised NMR data was collected using standard 1D pulse sequence (Figure 3) involving a single scan with receiver gain 1 and a π/4 pulse. This pulse sequence was used for any of the SABRE experiments conducted throughout Chapters 2, 3 and 4.

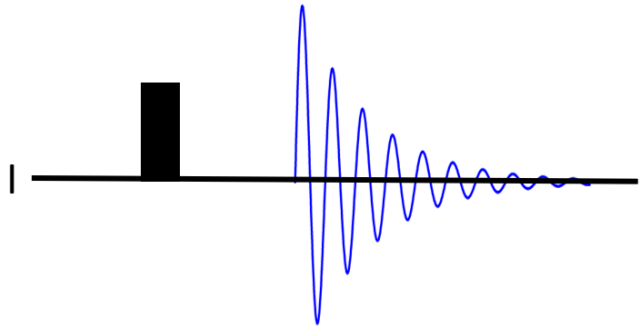

Figure 126 - standard zg pulse sequence

The rate and nOe data were collected using the EXSY sequence (Figure 4) which involves selective excitation. D8 is the mixing time used to encode exchange or build-up nOe transfer. This sequence was used for the exchange measurements described in Chapters 3 and 4.

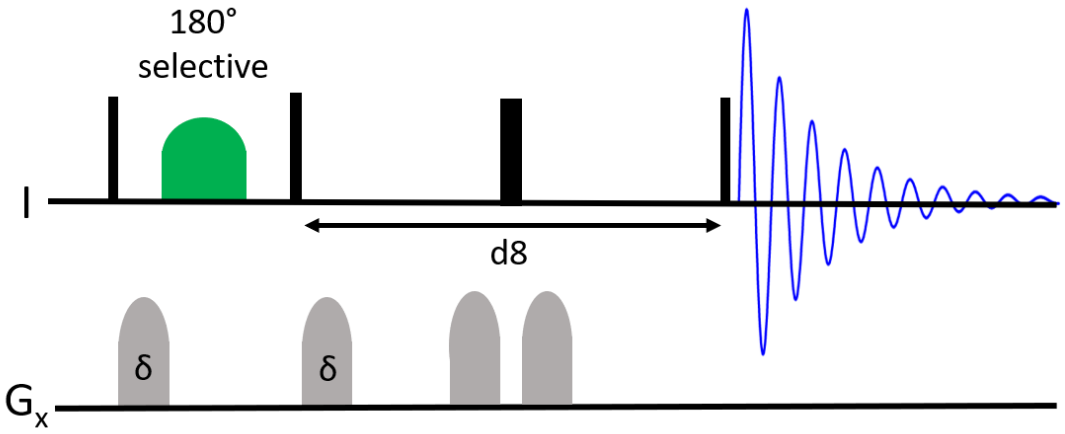

Figure 127 - selnogp pulse sequence

The $^{4}J_{HH}$ couplings measured in Chapter 3 that are reported were determined using a measured using a selective 1D COSY pulse program (Figure 5). This pulse sequence is described in more detail within the chapter.

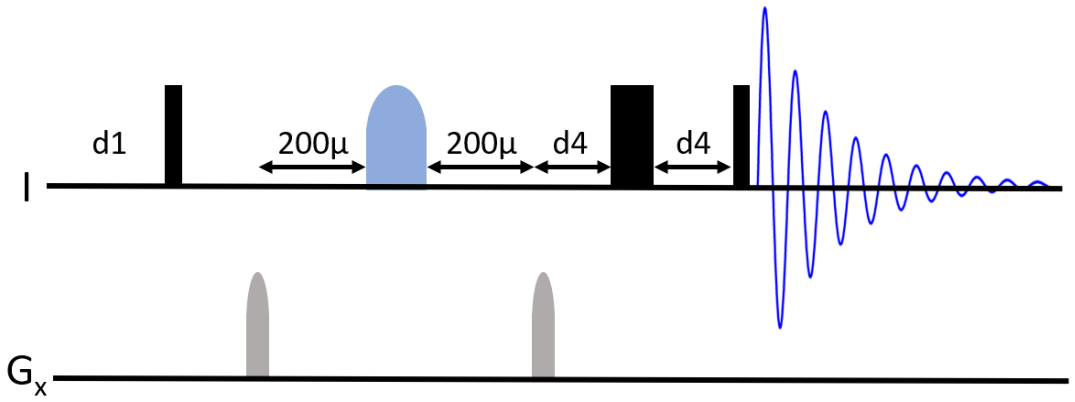

Figure 128 - selcogp pulse sequence

The DOSY measurements described in Chapter 4 were measured using a bipolar LED pulse sequence (Figure 6). In this experiment D20 is the diffusion time and d21 is the eddy-current delay time. This pulse sequence is described in more detail within the chapter.

For the experiments in the chapter values between 1.3 and 1 and 10 ms were used for δ and 99.9 and 100 ms for Δ were used. These values were optimised for each sample and each temperature used.

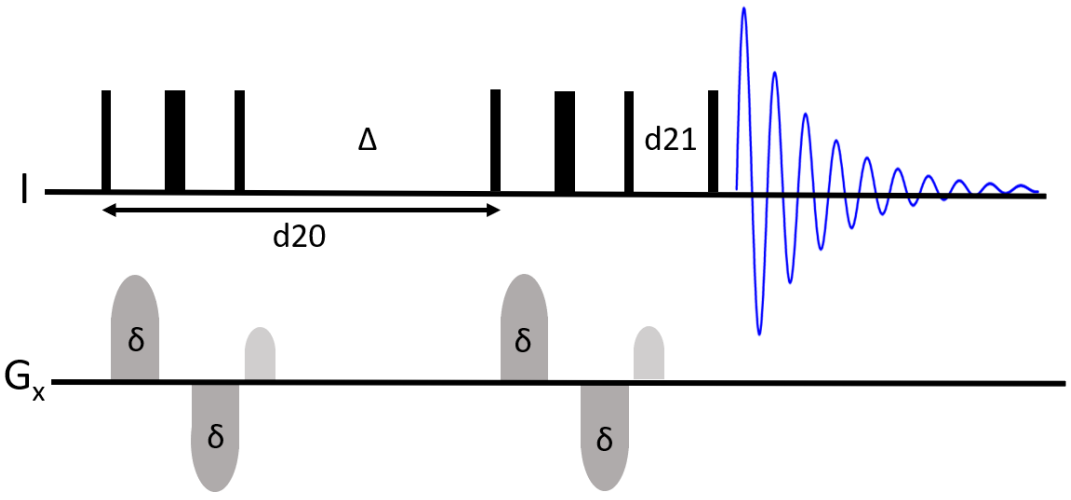

Figure 129 - ledbpgp2s pulse sequence

T_1 relaxation was measured using the saturation recovery pules sequence illustrated in Figure 7. This sequence was used for the measurements of T_1 relaxation described in Chapters 3 and 4.

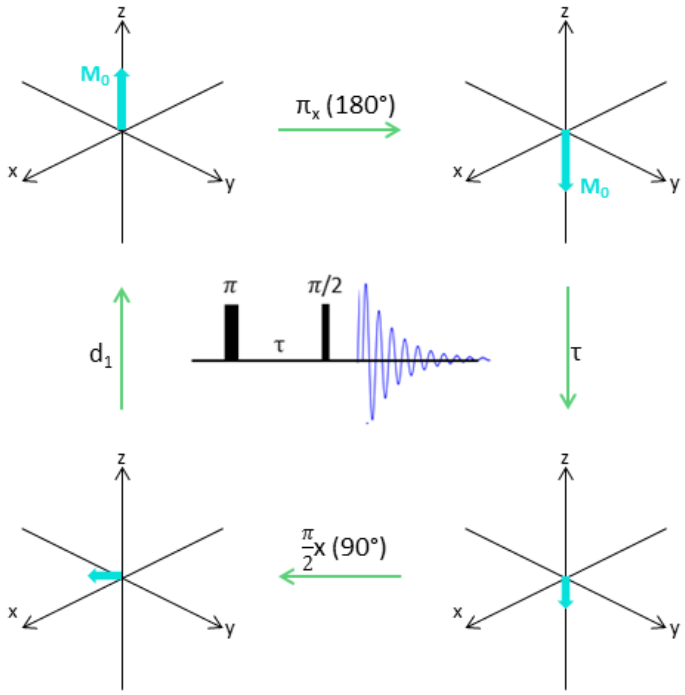

Figure 130 - invrec pulse sequence

6.1.2 *Para*hydrogen Rig

A *p*-H_2 rig was used to generate *p*-H_2 of 99% purity. In brief, hydrogen gas is cooled to 30 K using a closed cycle helium refrigeration unit before being passed over *para*magnetic iron oxide (Fe_2O_3), permitting the conversion of *o*-H_2 to *p*-H_2. Pressures of 4 bar *p*-H_2 was used for SABRE hyperpolarisation experiments, unless otherwise stated.[3] The *p*-H_2 rig is explained in more detail in Chapter 1.4.2.

The *p*-H_2 enrichment used for SABRE hyperpolarisation experiments was typically 99 %. However, in some cases the concentration of *p*-H_2 was changed so that the theoretical enhancement at 99 % purity could be calculated. This is because Richardson *et al.*[3] found that the substrate enhancement is directly proportional to the *p*H_2 purity. This linear relationship between these two variables was observed for a range of molecules, catalysts, and NMR detection fields. In Chapter 3 this method

was used to overcome radiation dampening that was observed for the hyperpolarised SABRE sample containing $[Ir(H)_2(ITBXy)(4\text{-methylpyridine})_3]Cl$ and *p*-H_2.

6.1.3 Flow System

A custom-built flow system was used in these studies.[4] It comprises of a Bruker *p*-H_2 generator which electrolyses water to produce hydrogen. The hydrogen is then cooled to 38 K in the presence of an activated charcoal catalyst to provide a predicted 92% purity *p*-H_2.

The *p*-H_2 generator is connected to a flow cell containing the sample solution, which is introduced into the sample via a porous frit positioned at the base of the cell. The cell is encased in a copper coil solenoid which is used to generate a controlled magnetic environment between −150 G and 150 G in order to provide the required polarisation transfer field. The hyperpolarised sample is then transferred pneumatically under a flow of N_2 gas (3.2 bar) to the flow probe which is integrated within the NMR spectrometer.[4]

The transfer time for shutting of the hyperpolarised sample into the spectrometer is between 1-2 seconds. Each time the system was used, the transfer pressures and timings were adjusted to ensure the flow cell was completely filled with the sample solution. Filling of the sample chamber was observed using a gradshim pulse program.

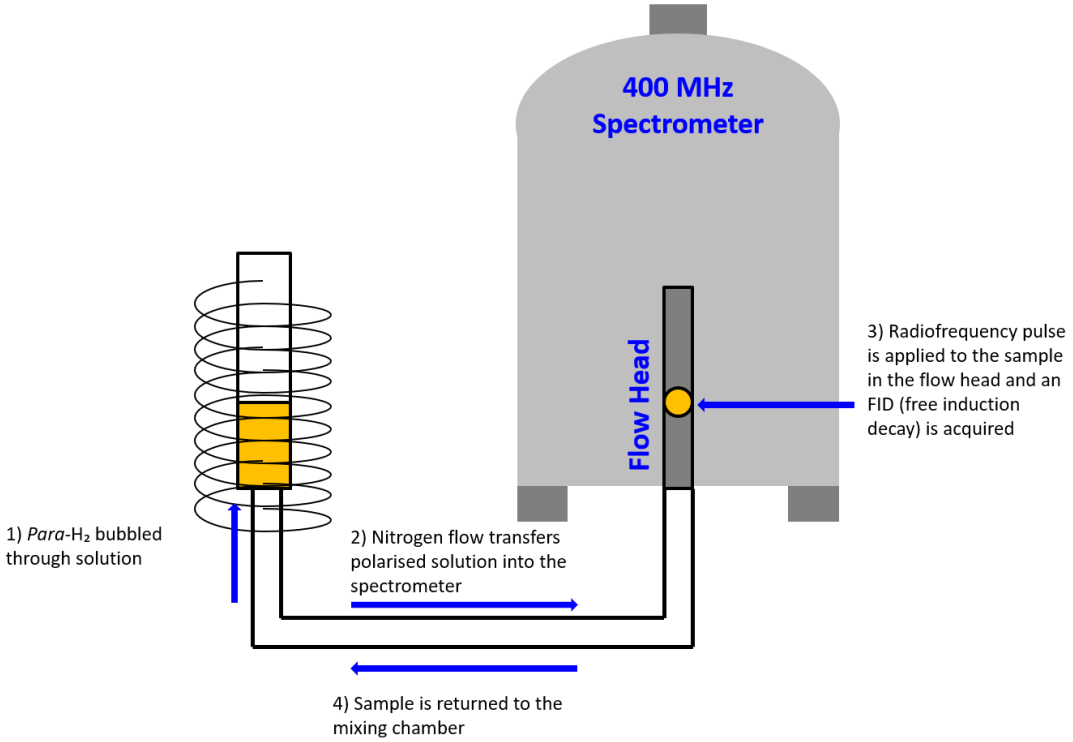

Figure 131 – Schematic diagram of the automated flow probe. 1) A sample of $[Ir(H)_2(SIMes)(sub)_3]Cl$ in methanol-d_4 is contained in a flow cell where pH_2 (4 bar) is bubbled through the solution, 2) The hyperpolarised sample is transferred into the spectrometer via a nitrogen flow, 3) The hyperpolarised spectrum is acquired using the one-shot pulse sequence described in Figure 28, 4) The sample is transferred from the spectrometer back to the flow cell using a nitrogen flow. Image adapted with permissions R. E. Mewis, K. D. Atkinson, M. J. Cowley, S. B. Duckett, G. G. Green, R. A. Green, L. A. Highton, D. Kilgour, L. S. Lloyd, J. A. Lohman and D. C. Williamson, *Magn. Reson. Chem.*, 2014, 52, 358-369.[6]

6.1.3.1 Variable Temperature

The variable temperature experiments described in Chapter 3 using the optimum rate of dissociation were conducted using a variation of the flow system. In this modification, the sample chamber is surrounded by a water jacket connected to a variable temperature water bath capable of reaching temperatures between 277-373 K. Water was used as the coolant in these experiments, however this temperature range could be extended by using alternative coolants. The temperature of the NMR spectrometer was also set to match that of the water bath. For the measurements described in Chapter 3.4.1.1, the temperature was varied from 280-300 K using 5 K increments.

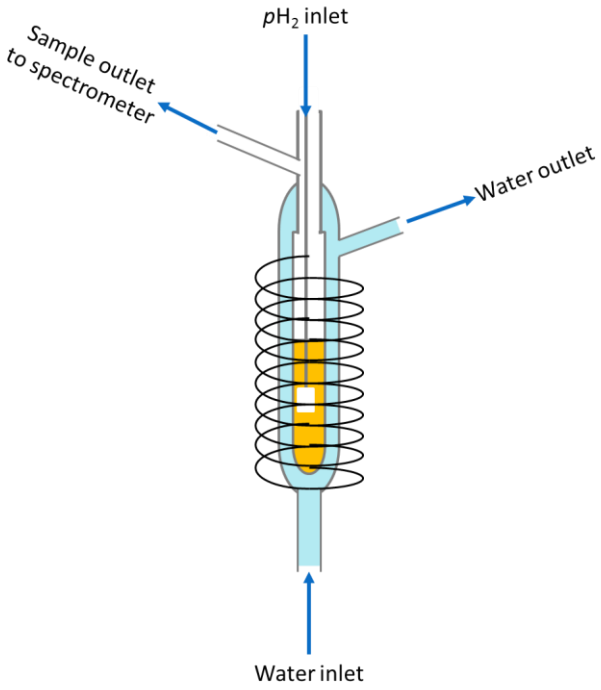

Figure 132 – The modified flow cell used to study the temperature dependence of SABRE

6.1.4 Fourier Transform Infrared (FTIR)

All FTIR spectra were measured using a Bruker Tensor 37 FTIR spectrometer with ATR and fibre optic probe attachment. Data was collected and processed using Bruker OPUS software. A 'background' reference spectrum was collected and then subtracted from the sample spectrum. Sample spectra were collected between 4000 and 500 wavenumbers (cm^{-1}) and is shown in transmission (%) mode.

6.2 General Experimental Procedures

6.2.1 Synthesis of [IrCl(COD)(NHC)] and Isotopically Labelled Substrates

The synthesis of [IrCl(COD)(NHC)] was completed by Dr Peter Rayner and Dr Vicky Annis using the synthetic procedures detailed in published literature records.[5, 6]

The synthesis of isotopically labelled ^{15}N-4-hydroxypyridine and ^{15}N-isoniazid were completed by Dr Phil Norcott.

The substrates used in this thesis were used as purchased. 4-Chloropyridine hydrochloride, 4-pyridinecarboxaldehyde, 4-hydroxypyridine and isoniazid were purchased from Sigma Aldrich. 4-Methylpyridine (4-picoline) was sourced from Alfa Aesar and 4-methoxypyridine from Fluorochem.

6.2.2 NMR Samples

NMR samples were formulated using a substrate (50 mM), [IrCl(COD)(NHC)] (5 mM) and solvent (0.6 mL) in a 5 x 230 mm NMR tube fitted with a J Young valve. Addition of the substrate to the iridium catalyst forms the SABRE precatalyst [Ir(COD)(NHC)(substrate]Cl where the chloride is displaced by the substrate. Formation of this product is indicated by NMR characterisation ad visually by a colour change from yellow to orange. The sample is then degassed using a freeze-pump-thaw procedure using a dry ice acetone bath for methanol-d_4 samples or liquid nitrogen for dichloromethane-d_2 samples.

Hydrogen (4 bar absolute) is then added to activate the catalyst to form the SABRE-active catalyst, which is typically of the form, $[Ir(H)_2(NHC)(substrate)_3]Cl$. Addition of hydrogen promotes hydrogenation of the COD ligand to form COA. Subsequently, 2 substrate ligands from the excess solution bind to the catalyst along with hydrogen to form the octahedral SABRE catalytic species. Formation of this product is usually indicated by a colour change from orange to colourless.

For manual shaking experiments, 4 bar (absolute) *p*-H_2 was added using the *p*-H_2 rig.

6.2.3 Manual Shaking Method

NMR samples were prepared using the procedure outlined above.

P-H_2 (4 bar absolute) was added to the sample using the *p*-H_2 rig described earlier via the Youngs valve. The sample was then shaken using the stray field of the spectrometer (approx. 65 G) for 10 seconds (unless stated otherwise) before being placed in the spectrometer for acquisition. The position for sample shaking was determined using a Hirst GM08 series gaussmeter. This experiment was typically

repeated a minimum of five times in order for the average enhancement and corresponding standard error to be calculated.

For some experiments, a handheld magnetic array (60 G) was used. Once *p*-H_2 (4 bar absolute) has been added to the sample tube, the sample is then placed inside the magnetic array before being shaken for 10 seconds (unless stated otherwise) before being removed and placed in the spectrometer for acquisition. Similarly to the manual shaking method, this experiment was repeated a minimum of five times in order for the average enhancement and corresponding standard error to be calculated.

Hyperpolarised spectra were collected using a single scan experiment with a pulse angle of π/4 and a receiver gain of 1.

More detail on these manual shaking methods and the corresponding advantages and disadvantages can be found in Chapter 2.

6.2.4 Flow System

NMR samples were prepared using substrate (50 mM), [IrCl(COD)(NHC)] (5 mM) and solvent (3 mL) in a sample vial. This was then placed into the reaction cell described in section 6.1.3.

The *p*-H_2 bubble time and the transfer times to and from the flow probe is controlled by the user. A *p*-H_2 pressure of 4 bar (absolute) was used. A single NMR scan was then collected using a receiver gain of 1 and a pulse angle of π/4.

More detail on this method and the corresponding advantages and disadvantages can be found in Chapter 2.

6.2.5 Calculating SABRE Enhancements

SABRE enhancements were calculated using:

$$Enhancement\ Factor, \varepsilon = \frac{Integral\ of\ hyperpolarised\ signal}{Integral\ of\ thermal\ signal}$$

Equation 22

The thermal signal refers to the non-hyperpolarised spectrum. This was collected after the SABRE sample had been left for 10 minutes, allowing for the hyperpolarised signals to relax. The same acquisition parameters were used to collect both the hyperpolarised and thermal signals. The hyperpolarised signals are typically emissive and therefore the corresponding enhancement factors are quoted as negative values.

The corresponding standard errors were calculated using Equation 23.

$$Std\ Error = \frac{Std\ Deviation}{\sqrt{Sample\ size}}$$

Equation 23

6.2.6 Measuring pK_a

The pK_a values of Chapter 3 were measured as follows.

The *para*-substituted substrates were dissolved in methanol-d_4 with added HCl. HCl was used to control the pH of the solution, promoting formation of the acidic form in solution which exists in equilibrium with the basic form.

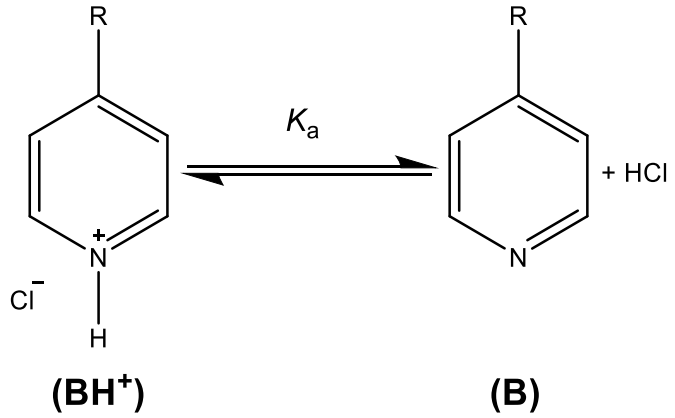

Figure 133 - The two forms of the substituted pyridine in solution with methanol and hydrochloric acid (HCl) used to control the pH of the solution

The ionisation constant, K_a, of these substituted pyridine acids can be described by:

$$K_a = \frac{[\mathrm{HCl}][\mathrm{B}]}{[\mathrm{BH^+}]}$$

Equation 24

The pK_a can then be written as:

$$\mathrm{p}K_a = \mathrm{pH} + \log\left(\frac{[\mathrm{BH^+}]}{[\mathrm{B}]}\right)$$

Equation 25

In NMR, the concentrations of each form can be substituted for the fractional populations ($x_{\mathrm{B}}$and $x_{\mathrm{BH^+}}$), therefore Equation 25 becomes:

$$\mathrm{p}K_a = \mathrm{pH} + \log\left(\frac{x_{\mathrm{BH^+}}}{x_{\mathrm{B}}}\right)$$

Equation 26

NMR cannot detect chemical change that occurs on a faster timescale than the NMR experiment itself, therefore there is only one observed peak which accounts for both forms. The location of this peak reflects the weighted average of the relative

populations and chemical shift of the pure acidic and pure basic forms. If the chemical shift of the protonated form (i.e. in strong acidic conditions, δ_A) and the deprotonated form (i.e. in strong basic conditions, δ_B) are known then the measured chemical shift (δ_m) can be described by Equation 27.

$$\delta_{\mathrm{m}} = x_{\mathrm{BH^+}}\delta_{\mathrm{BH^+}} + x_{\mathrm{B}}\delta_{\mathrm{B}}$$

Equation 27

As $x_{\mathrm{B}}$and $x_{\mathrm{BH^+}}$ are fractional populations, they must sum to 1, therefore the proportion of the deprotonated form can be expressed as in Equation 28.

$$x_{\mathrm{B}} = 1 - x_{\mathrm{BH^+}}$$

Equation 28

The relative population of the protonated form can then be calculated using Equation 29 by substituting Equation 28 into Equation 27.

$$x_{\mathrm{BH^+}} = \frac{\delta_{\mathrm{m}} - \delta_{\mathrm{B}}}{\delta_{\mathrm{A}} - \delta_{\mathrm{B}}}$$

Equation 29

Analogously, the fractional population of the deprotonated form can be expressed as in Equation 30.

$$x_{\mathrm{B}} = \frac{\delta_{\mathrm{A}} - \delta_{\mathrm{m}}}{\delta_{\mathrm{A}} - \delta_{\mathrm{B}}}$$

Equation 30

Finally, substituting Equation 29 and Equation 30 into Equation 26 and rearranging provides an expression for the measured chemical shift as a function of pH in the form of Equation 39.

$$\delta_{\mathrm{m}} = \frac{\delta_{\mathrm{A}} 10^{\mathrm{p}K_{\mathrm{a}}-\mathrm{pH}} + \delta_B}{1 + 10^{\mathrm{p}K_{\mathrm{a}}-\mathrm{pH}}}$$

Equation 31

Therefore, it is possible to measure the chemical shift of a molecule by NMR for solutions of different pH levels and fit the data using Equation 14 to determine the pK_a for the molecule.

6.2.7 Exchange Spectroscopy

6.2.7.1 Calculating the Rate of Dissociation (k_d)

Exchange spectroscopy (EXSY) was used to monitor substrate dissociation from the bound SABRE-active species $[Ir(H)_2(NHC)(substrate)_3]Cl$ into the free solution. The rate of dissociation is an integral SABRE parameter as it can indicate the SABRE efficiency of a system.

The substrate bound *trans* to the hydride was selectively excited using a shaped pulse (Figure 127). The intensity of this signal was then compared to the intensity of the free solution and monitored over time.

The exchange pathway for substrate dissociation is shown in Figure 8.

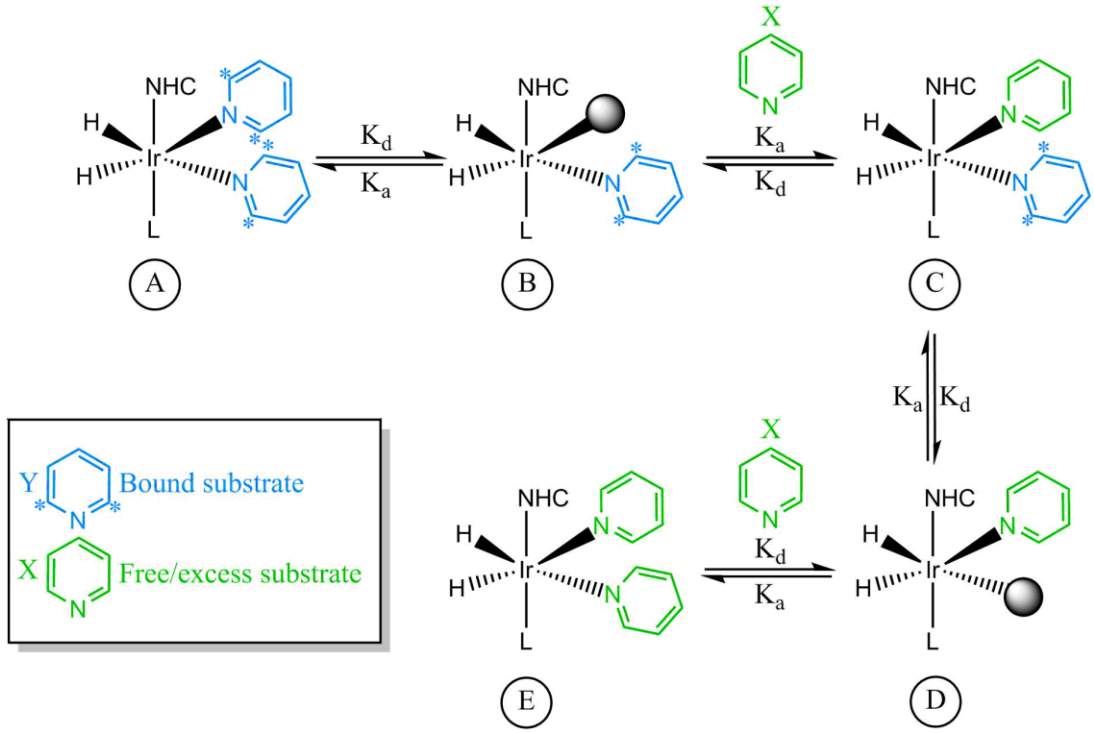

Figure 134 - Exchange species for substrate dissociation in $[Ir(H)_2(NHC)(substrate)_3]Cl$. The asterix, *, is used to denote the ^1H resonance that is selectively excited.

The rate equations for the formation of each of the individual species (A-E, X & Y) were then determined (Equation 32), where k_a is the rate constant of association of the substrate and k_d is the rate constant of dissociation of the substrate.

$$\frac{[A]}{dt} = [A]_0 + k_a[B][Y] - 2k_d[A]$$

$$\frac{[B]}{dt} = [B]_0 + 2k_d[A] - k_a[B][Y] + k_d[C] - k_a[B][X]$$

$$\frac{[C]}{dt} = [C]_0 + k_a[B][X] - k_d[C] + k_a[D][Y] - k_d[C]$$

$$\frac{[D]}{dt} = [D]_0 + k_d[C] - k_a[D][Y] + 2k_d[E] - k_a[D][X]$$

$$\frac{[E]}{dt} = [E]_0 + k_a[D][X] - 2k_d[E]$$

$$\frac{[X]}{dt} = [X]_0 + k_d[C] - k_a[B][X] + 2k_d[E] - k_a[D][X]$$

$$\frac{[Y]}{dt} = [Y]_0 + 2k_d[A] - 2k_a[B][Y] + k_d[C] - k_a[D][Y]$$

Equation 32 - Rate equations for the SABRE exchange species displayed in Figure 134

In substrate dissociation from species [A] to form [B], either of the two excited bound substrate ligands can dissociation with equal probability. In substrate dissociation of [C] to form [B], only the bound, relaxed substrate ligand can dissociate. Therefore the probability of forming species [B] from [C] is half the probability of forming [B] from [A]. Consequently, the net rate of dissociation from [A] to [B] is $2k_d$.

These equations were then inputted into a Microsoft Excel spreadsheet in order to determine the rate of dissociation (k_d). To do this, a simulated data set was created, using the known concentrations of the free substrate ([X]) and the catalyst ([A]) and the delay time (D8). The delay time is the time allowed between measurements. Values of k_d and k_a were then estimated. The percentage intensities of the bound and free species were calculated from the simulated concentration of the different species. These were calculated according to Equation 33 and Equation 34.

$$\%\, bound = \frac{2A + C}{2A + C + Y} \times 100$$

Equation 33

$$\%\, free = \frac{Y}{2A + C + Y} \times 100$$

Equation 34

The experimental data is also added to the same Excel spreadsheet, where the integrals of the interchanging species were converted into a percentage of the overall signal. For example, at the start of the measurement, 100% of the excited signal lies within the bound substrate (species A, B or C, which all contain at least 1 'excited' bound substrate). At the end of the measurement, most of the excited signal (>50%) is observed in the free solution (species X) (Figure 135). Once the experimental data has been tabulated, the difference between this data set and the simulation is calculated. This is achieved using Excel's solver package where each value is assumed

to have to same uncertainty and therefore the unweighted least squares method was used. Solver then minimises the value of the squared residuals, thereby fitting the simulated data set to the experimental data. A plot of the simulation was then compared to the experimental to ensure a suitable fit (Figure 136).[6]

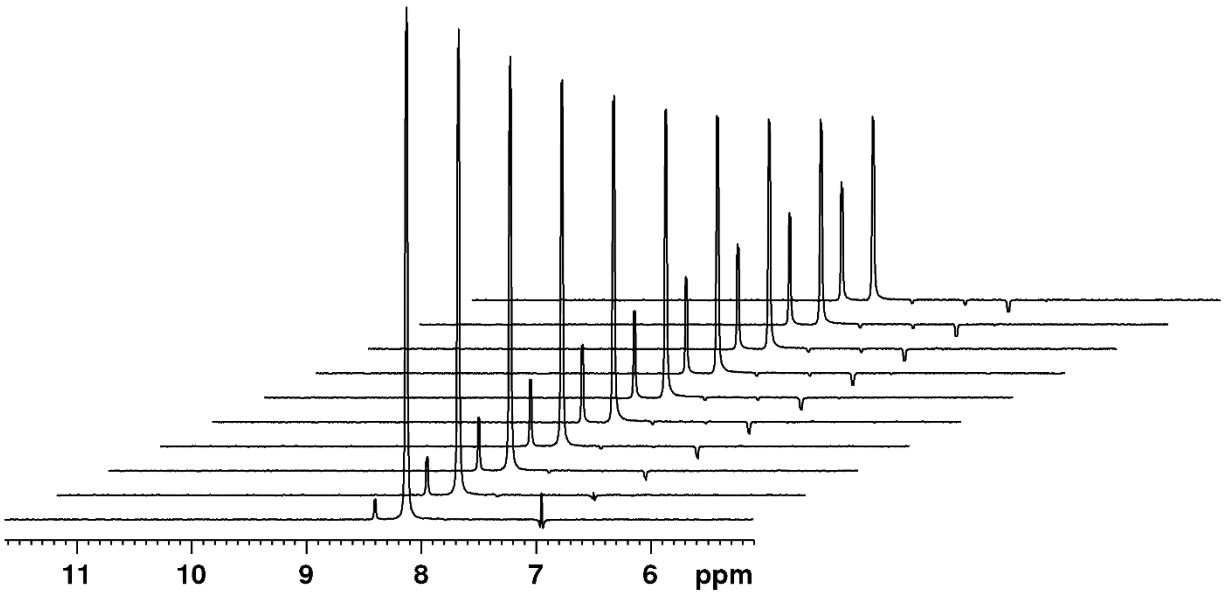

Figure 135 - Movement of excited signal from the bound substrate to the free substrate over time

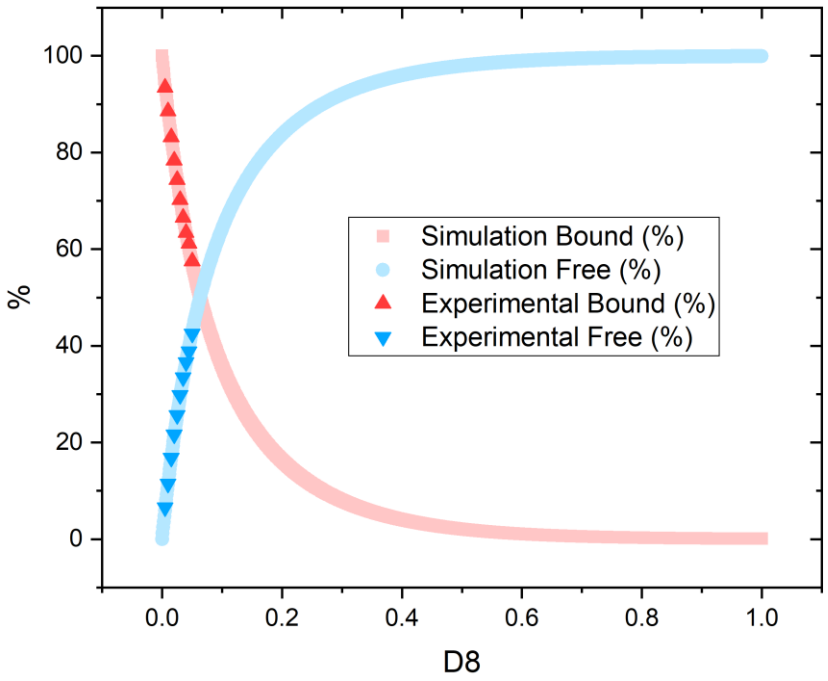

Figure 136 - Percentage signal intensity as a function of the delay time. The diamond and square markers are used to signify the experimental data set and the lines the simulation. Dark blue represents the bound substrate and the light blue signifies the free substrate.

6.2.7.1.1 Calculating Associated Errors in k_d

The errors in k_d wre calculated using the Jackknife method described by Harris in 1998.[7]

k_d was determined for each temperature from 10 separate experiments, each with a different delay time. To calculate the uncertainty, each experimental data point was subsequently deleted before a solution for k_d was found using the solver method described above. This value was then restored before the following data point was deleted and solved to find k_d. Once k_d was calculated for each iteration, the results were tabulated (Figure 148) and the standard error was calculated using the standard deviation and the square root of the sample number.

Experimental Data

D8	Integral of the Free Substrate	Integral of the Bound Substrate	Sum of Integrals	%Free	%Bound	Difference (expt-sim) for Free Sub	Difference (expt-sim) for Bound Sub	Column V^2	Column W^2	Sum (X+Y)
0.005	0.0704	1	1.0704	6.57698	93.423	2.33E-01	-2.33E-01	0.05434	0.054344	0.10869
0.01	0.1293	1	1.1293	11.4496	88.5504	-4.96E-01	4.96E-01	0.24607	0.24607	0.49214
0.015	0.2024	1	1.2024	16.833	83.167	-1.36E-01	1.36E-01	0.01843	0.018431	0.03686
0.02	0.2765	1	1.2765	21.6608	78.3392	1.32E-01	-1.32E-01	0.01745	0.017449	0.0349
0.025	0.3455	1	1.3455	25.6782	74.3218	-2.69E-02	2.69E-02	0.00073	0.000725	0.00145
0.03	0.4245	1	1.4245	29.7999	70.2001	2.46E-01	-2.46E-01	0.06049	0.060493	0.12099
0.035	0.5032	1	1.5032	33.4753	66.5247	3.59E-01	-3.59E-01	0.12897	0.128968	0.25794
0.04	0.577	1	1.577	36.5885	63.4115	1.65E-01	-1.65E-01	0.02738	0.027377	0.05475
0.045	0.6341	1	1.6341	38.8042	61.1958	-6.96E-01	6.96E-01	0.48405	0.484049	0.9681
0.05	0.7399	1	1.7399	42.5254	57.4746	1.57E-01	-1.57E-01	0.02465	0.024649	0.0493
									Total Sum:	2.12511

Uncertainties

Cell Deleted	kd
Z22	13.3354
Z23	13.5266
Z24	13.4303
Z25	13.3292
Z26	13.3849
Z27	13.3357
Z28	13.3515
Z29	13.3827
Z30	13.2606
Z31	13.4309
Std Dev	0.07313
SQRT(n)	3.16228
Std Error	0.02313

Original kd
12.2862

Figure 137 - Table showing how the uncertainties are generated using the Jackknife method alongside the experimental data set.

6.2.7.2 Gibbs Free Energy

The Gibbs Free energy of dissociation ($\Delta G^{\neq}$) defines the amount of energy required to break a bond. Therefore it can be used to quantify the strength of iridium-substrate ligation in SABRE-active species. This has been demonstrated in Chapters 3 and 4.

$\Delta G^{\neq}$ is determined from the enthalpy ($\Delta H^{\neq}$) and entropy ($\Delta S^{\neq}$) of dissociation. These are calculated via an Eyring-Polanyi plot whereby $ln\frac{k}{T}$ (where k = rate of dissociation and T = temperature) is plotted as a function of $\frac{1}{T}$. The enthalpy can then be

determined from the gradient: $\left(-\frac{\Delta H^{\neq}}{R}\right)$ and the entropy from the intercept: $\ln\left(\frac{k_B}{h}+\frac{\Delta S^{\neq}}{R}\right)$.

$\Delta G^{\neq}$ can then be calculated using:

$$\Delta G^{\neq} = \Delta H^{\neq} - T\Delta S^{\neq}$$

Equation 35

6.2.7.2.1 Calculating Associated Errors in $\Delta H^{\neq}$, $\Delta S^{\neq}$ and $\Delta G^{\neq}$

As described above, $\Delta G^{\neq}$ is determined using an Eyring plot. This Eyring plot uses the linear form of the Eyring equation and graphically shows the relationship between the rate of dissociation (k_d) and the reaction temperature. An example plot is shown in Figure 1. The enthalpy ($\Delta H^{\neq}$) and entropy ($\Delta S^{\neq}$) terms for the reaction can then be calculated using the gradient and intercept of the line of best fit that results from the linear regression analysis. The equations used are shown in Figure 1.

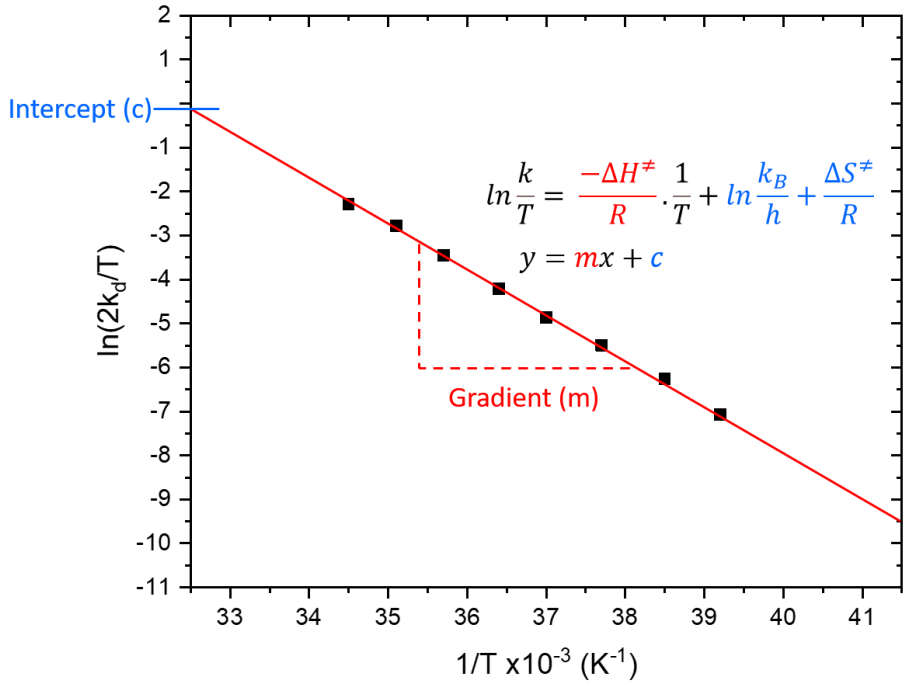

Figure 138 - Eyring plot where ln(2kd/T) is plotted as a function of 1/T. The data is fitted using a linear fit of the form y = mx + c.

The errors in $\Delta H^{\neq}$ and $\Delta S^{\neq}$ are then calculated directly using the 95% confidence limits provided by the linear regression analysis in Excel (Figure 2). The error can be calculated by calculating the minimum and maximum values of $\Delta H^{\neq}$ and $\Delta S^{\neq}$ using the upper and lower 95% limits. These upper and lower limits can then be averaged and the corresponding standard error calculated from the standard deviation.

SUMMARY OUTPUT

Regression Statistics	
Multiple R	0.999537233
R Square	0.99907468
Adjusted R Square	0.99892046
Standard Error	0.055299791
Observations	8

Red = Gradient
Blue = Intercept

ANOVA

	df	*SS*	*MS*	*F*	*Significance F*
Regression	1	19.8109026	19.8109	6478.24373	2.47672E-10
Residual	6	0.018348401	0.003058		
Total	7	19.829251			

	Coefficients	*Standard Error*	*t Stat*	*P-value*	*Lower 95%*	*Upper 95%*
Intercept	32.80250219	0.464516499	70.61644	5.42623E-10	31.66587126	33.93913311
Gradient	-10161.12791	126.2447355	-80.4875	2.47672E-10	-10470.03765	-9852.21817

$$\Delta(\Delta H)^{\neq} = \frac{(lower\ 95\% - upper\ 95\%) \times R}{2}$$

$$\Delta(\Delta S)^{\neq} = \frac{(lower\ 95\% - upper\ 95\%) \times R}{2}$$

$$\Delta(\Delta G)^{\neq} = \frac{((e^{C} \times 298) - (e^{A} \times 298)) - ((e^{C} \times 298) - (e^{B} \times 298))}{2}$$

$$\text{Where, } A = Error\ in\ upper\ 95\%\ of\ ln\frac{k}{T} = \left(\frac{lower\ 95\%}{298}\right) + upper\ 95\%$$

$$B = Error\ in\ lower\ 95\%\ of\ ln\frac{k}{T} = \left(\frac{upper\ 95\%}{298}\right) + lower\ 95\%$$

$$C = ln\frac{k}{T} = \left(\frac{gradient}{298}\right) + intercept$$

Figure 139 - Summary output from the linear regression analysis from the Eyring plot shown in Figure 1. Red is used to indicate numbers relevant to the gradient and blue indicates those related to the intercept. In the equations, R = gas constant and T = temperature (K)

Please note:

$\Delta S^{\neq}$ can be poorly defined using this method as its calculation requires extrapolation away from the experimental data points (where the error is relatively small), therefore the associated error in $\Delta S^{\neq}$ are large. It is therefore important to obtain data over a wide temperature range.

$\Delta H^{\neq}$ is calculated from the gradient which uses the measured data and therefore the error is often smaller than the error in $\Delta S^{\neq}$.

The error in $\Delta G^{\neq}$ is calculated for a particular temperature, e.g. 298 K. It is possible to determine $\Delta G^{\neq}$ using the Gibbs free energy relationship. This would involve propagation of the errors in $\Delta H^{\neq}$, $\Delta S^{\neq}$ and $\Delta G^{\neq}$ resulting in a large error value. A better way to determine the error in $\Delta G^{\neq}$ is to take the upper and lower limits from the 95% confidence plots of the Eyring equation and rearrange it for the determination of $\Delta G^{\neq}$ (as shown in Figure 139). This reflects the fact that we have precisely calculated values for k_d and the associated error. We can be confident that the error in k_d is relatively small as it results from 10 separate measurements. If this approach is used, the error in $\Delta G^{\neq}$ reduces as it is specific for the selected temperature and echoes the real data around the temperature at which $\Delta G^{\neq}$ is calculated.

6.2.8 T_1 Relaxation Measurements

Relaxation quantifies the mechanisms that allow nuclear spins to lose energy and drop from the excited state to the ground state non-radiatively.[8] Two forms of relaxation exist; spin-lattice relaxation and spin-spin relaxation. In spin-lattice relaxation, the spins of a nucleus are permitted to flip between the energy levels, thus establishing the Boltzmann population difference essential to the NMR experiment. As the nuclei return to the equilibrium state, the energy released is dissipated into the surroundings (the 'lattice')[9]. The process of spin-lattice relaxation is necessary to understanding how molecules behave in NMR and is characterised by a time T_1 (spin-lattice relaxation time). There are several different relaxation mechanisms; however for spin $\frac{1}{2}$ nuclei (such as ^{1}H) the most dominant mechanism arises from dipole-dipole interactions. If a nucleus has spin $\frac{1}{2}$ and is exposed to a magnetic field, the population difference between the two states ($m = +\frac{1}{2}\ or\ -\frac{1}{2}$) grows exponentially with time (τ)[9] (Figure 140).

The T_1 values were measured using the inversion recovery pulse shown in Figure 130. In NMR, there exists a bulk magnetisation (M_0) lies along the z-axis at equilibrium. A 180° (π) pulse is used to perturb the magnetisation into the −z orientation. After a variable time (τ), a read pulse (90°) is applied which places the magnetisation into the x-y plane following signal detection. This experiment is repeated several times,

each time iterating the variable time, τ. As the time is increased, the magnetisation returns to thermal equilibrium. The system reaches thermal equilibrium by waiting 5*T_1.

The T_1 relaxation time is then calculated from Equation 36 as shown pictorially in Figure 10.

$$M_{XY} = M_0[1 - 2\exp\left(\frac{-\tau}{T_1}\right)]$$

Equation 36, Where M_{XY} is bulk magnetisation, M_0 is magnetisation at thermal equilibrium, τ is the variable time and T_1 is the spin-lattice relaxation time.

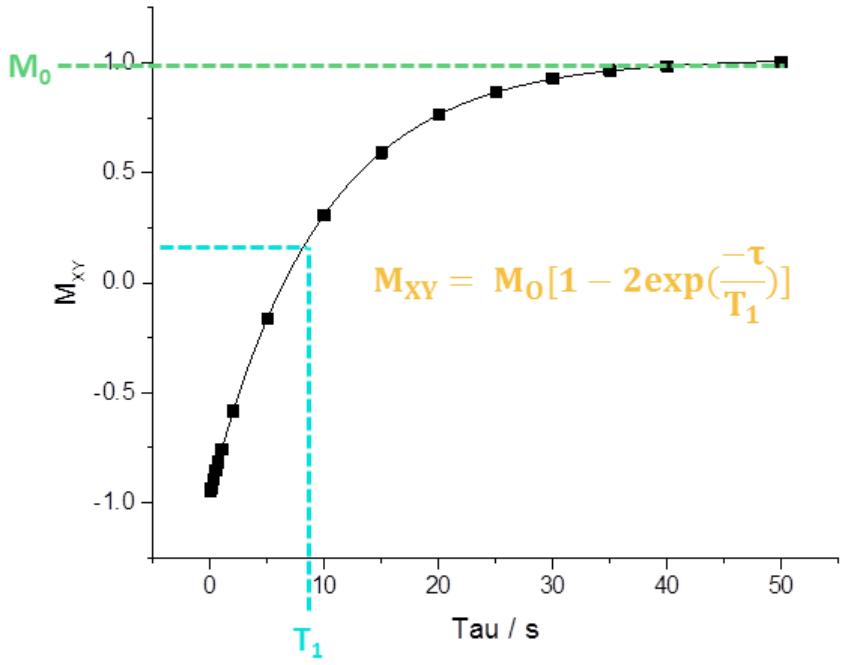

Figure 140 - The magnetisation (M_{XY}) for a spin ½ nuclei as a function of time (τ) after exposure of the system to a magnetic field. M_0 is the magnetisation at thermal equilibrium and T_1 is the spin-lattice/longitudinal relaxation time.

6.2.9 Hyperpolarised T_1 Measurements

The hyperpolarised T_1 value is defined as the exponential decay factor determined from the relaxation of the established hyperpolarised signal built up in solution. It is assumed that the hyperpolarised T_1 and conventional T_1 should be equal due to the same relaxation methods, which, should be independent of the starting

magnetisation. The hyperpolarised T_1 values were measured using a variable flip angle single-shot sequence as described by Semenova *et al*.[10] and Rayner *et al*.[11] and derived from a similar method described by Shchepin *et al*.[12]

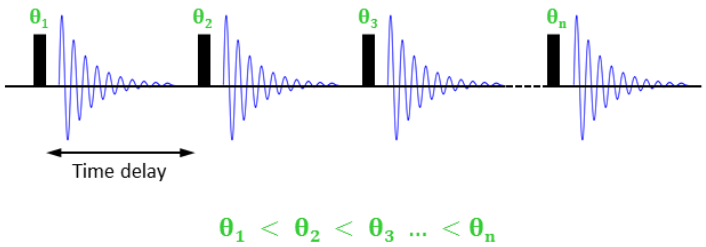

Figure 141 - Single-shot hyperpolarised T_1 variable flip angle pulse sequence

In this method, a series of 'n' FIDs were recorded where each FID was associated with an RF pulse with a unique flip angle. In this thesis, 16 ^{1}H NMR spectra were acquired where the excitation pulse for each individual acquisition was measured using RF pulses of increasing flip angle (θ). The variable flip angles excited an equal fraction of the available magnetisation (M_{xy}) so in the absence of relaxation would give the same intensity each measurement. Therefore, the decrease in signal over time can be attributed to relaxation and quantified by using an exponential fit.

During the variable flip angle pulse sequence, the transverse magnetisation is termed $M_{XY,n}$, this magnetisation retains the same amplitude for the duration of the experiment. The longitudinal magnetisation is termed $M_{z,n}$, which describes the magnetisation that remains along the z-axis before the previous pulse ($M_{z,n-1}$). M_{xy} is defined by Equation 37, where the magnetisation is equal to the magnetisation in the z-axis in the previous pulse multiplied by sin of the flip angle. $M_{z,n}$ is defined by Equation 38, where the remaining magnetisation leftover from the previous pulse is multiplied by the cosine of the flip angle.

$$M_{xy,n} = M_{z,n-1}\sin(\theta_n)$$

Equation 37

$$M_{z,n} = M_{z,n-1}\cos(\theta_n)$$

Equation 38

The effect of variable flip angle can then seen in Equation 39.

$$\theta = \sin^{-1}\left(\frac{M_{xy,n}}{M_{z,n-1}}\right)$$

Equation 39

The pulse duration ($v_{p,n}$) can then be calculated using the duration of a standard 90° pulse length (d90) which is usually optimised prior to the HyperT_1 experiment (Equation 40).

$$v_{p,n} = \frac{\theta_n}{90} \times d90$$

Equation 40

The sequence was optimised, such that the percentage measured at each point left no hyperpolarised magnetisation after the final point, which has the effect of maximising the signal to noise of the experiment. An example of these effects is shown in Table 1.

N	$M_{z,n}$	$M_{xy,n}$	θ_n	$v_{p,n}$
0	100	0	0	0
1	96.82	25.00	14.48	1.93
2	93.54	25.00	14.96	2.00
3	90.14	25.00	15.50	2.07
4	86.60	25.00	16.10	2.15
5	82.92	25.00	16.78	2.24
6	79.06	25.00	17.55	2.34

7	75.00	25.00	18.43	2.46
8	70.71	25.00	19.47	2.60
9	66.14	25.00	20.70	2.76
10	61.24	25.00	22.21	2.96
11	55.90	25.00	24.09	3.21
12	50.00	25.00	26.56	3.54
13	43.30	25.00	30.00	4.00
14	35.36	25.00	35.26	4.70
15	25.00	25.00	45.00	6.00
16	0.13	25.00	89.71	11.96

Table 29 – Calculated parameters for $M_{z,n}$, $M_{xy,n}$, θ_n and $v_{p,n}$ for a d90 value of 12 µs.

The experiment was then conducted using the variable flip angles shown in Table 29 in conjunction with the hyperpolarised sample. A reference (thermal) measurement was also recorded in the absence of *p*-H_2 which was then subtracted from the hyperpolarised spectra prior to T_1 analysis. This ensured that thermal magnetisation was removed from consideration. Henceforth, the resulting T_1 analysis was a true indication of the hyperpolarisation lifetime. The hyperpolarised T_1 relaxation times were determined from an exponential fit of the signal decay using Equation 36.

6.3 Diffusion Ordered Spectroscopy

Diffusion ordered spectroscopy (DOSY) allows the separation of molecules in a system according to their diffusion coefficient. Measurements of this can indicate the size and shape of a molecular species. In Chapter 4, this method was used to examine two *bis*-substituted SABRE species to understand whether dimerization occurred in these systems. The diffusion coefficient is linked to structural properties of a system by the Debeye-Einstein theory:

$$D = \frac{k_B T}{f_T}$$

Equation 41, where D = diffusion coefficient, f_T = friction factors, k_B = Boltzmann constant and T = temperature

For an idealised case of a diffusing sphere of hydrodynamic radius (r_H) and solvent viscosity (η), the friction factor is provided by:

$$f_T = 6\pi\eta r_H$$

Equation 42

Combining the above equations provides the Stokes-Einstein equation (), where the diffusion coefficient is inversely proportional to the radius of the diffusing species. Therefore larger molecules exhibit smaller diffusion coefficients.

$$D = \frac{k_B T}{6\pi\eta r_H}$$

Equation 43

The diffusion coefficients of Chapter 4 were measured using the BPP-LED pulse sequence shown in Figure 129. This sequence was chosen as it removes background magnetic field effects and allows eddy currents to delay.[13-15]

The pulse sequence is iterated such that in each iteration, the gradient strength is incremented whilst the delays δ and Δ are kept constant. These constants were optimised for each of the samples measured and at each temperature. The signal intensity was then plotted against the gradient strength using Origin, allowing the diffusion constant to be calculated using a non-linear curve fit to the resulting decay (using Equation 44).

$$I = I_0 e^{\left[-\gamma^2 G^2 \delta^2 D\left(\Delta - \frac{\delta}{3}\right)\right]}$$

Equation 44, where γ is the gyromagnetic ratio, G is the gradient strength, δ and Δ are delays and D is the diffusion constant.

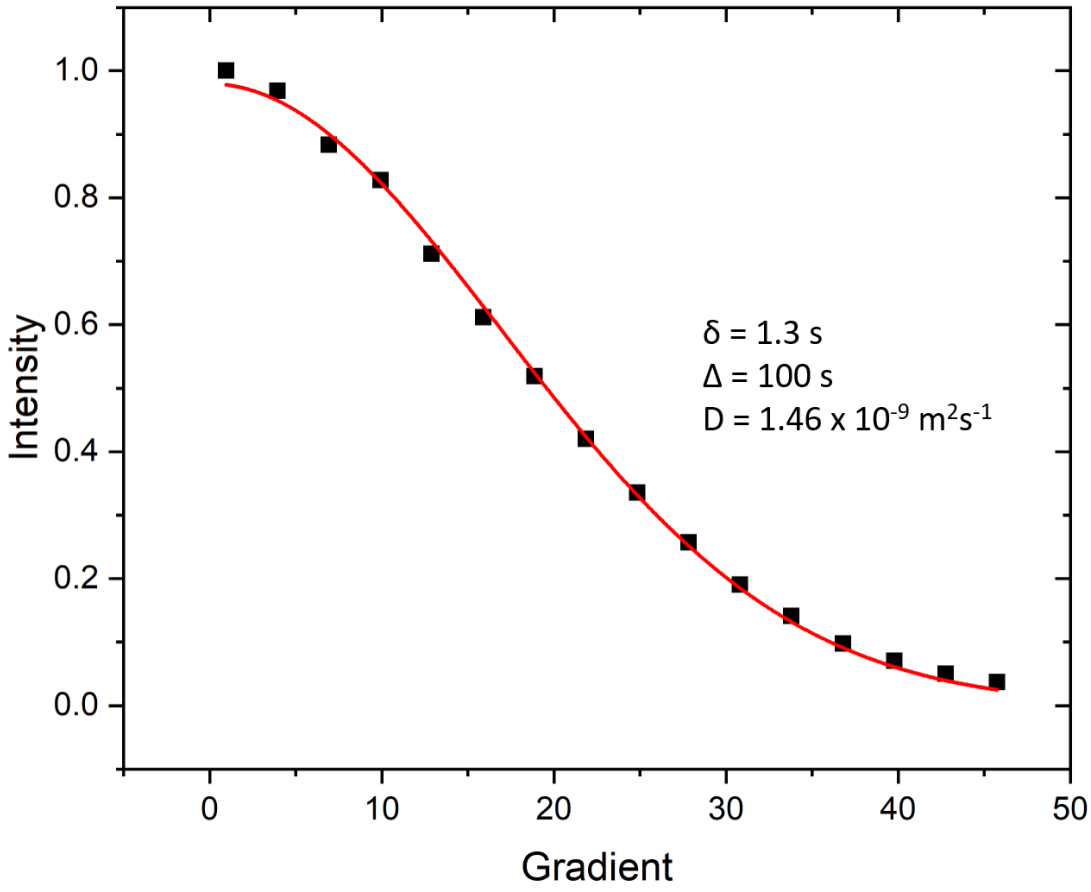

Figure 142 - Signal intensity as a function of the gradient strength. The data has been plotted according to Equation 21. The delays used for δ and Δ have been indicated alongside the calculated diffusion coefficient (D)

6.4 References

1. M. Hansen and H. J. Jakobsen, *J. Magn. Reson.*, 1973, **10**, 74-84.
2. W. Städeli, P. Bigler and W. Von Philipsborn, *Org. Magn. Reson.*, 1981, **16**, 170-172.
3. P. M. Richardson, R. O. John, A. J. Parrott, P. J. Rayner, W. Iali, A. Nordon, M. E. Halse and S. B. Duckett, *Phys. Chem. Chem. Phys.*, 2018, **20**, 26362-26371.
4. R. E. Mewis, K. D. Atkinson, M. J. Cowley, S. B. Duckett, G. G. Green, R. A. Green, L. A. Highton, D. Kilgour, L. S. Lloyd, J. A. Lohman and D. C. Williamson, *Magn. Reson. Chem.*, 2014, **52**, 358-369.
5. L. D. Vazquez-Serrano, B. T. Owens and J. M. Buriak, *Inorg. Chim. Acta*, 2006, **359**, 2786-2797.
6. P. J. Rayner, P. Norcott, K. M. Appleby, W. Iali, R. O. John, S. J. Hart, A. C. Whitwood and S. B. Duckett, *Nat Commun*, 2018, **9**, 4251.
7. D. C. Harris, J. Chem. Educ., 1998, 75, 119-121.
8. J. A. Iggo, *NMR spectroscopy in Inorganic Chemistry*, Oxford University Press New York, 1999.
9. P. J. Hore, *Nuclear Magnetic Resonance (Oxford Chemistry Primers)*, Oxford University Press, USA, 1995.

10. O. Semenova, P. M. Richardson, A. J. Parrott, A. Nordon, M. E. Halse and S. B. Duckett, *Anal. Chem.*, 2019, **91**, 6695-6701.
11. P. J. Rayner, P. M. Richardson and S. B. Duckett, *Angew. Chem.*, 2020, **132**, 2732-2736.
12. R. V. Shchepin, L. Jaigirdar and E. Y. Chekmenev, *J. Phys. Chem. C.*, 2018, **122**, 4984-4996.
13. R. F. Karlicek and I. J. Lowe, *J. Magn. Reson.*, 1980, **37**, 75-91.
14. S. J. Gibbs and C. S. Johnson, *J. Magn. Reson.*, 1991, **93**, 395-402.
15. D. Wu, A. Chen and C. S. Johnson, *J. Magn. Reson.,* 1995, **115**, 260-264.

Appendix A

Manual Shaking Method Using the Stray Field of the Spectrometer

Shake Time (s)	*OrthoH Enhancement Factor*	
	a	**b**
5	-654±34	-542±141
7	-578±37	-782±4
10	-891±18	-842±43
15	-767±25	-257±42

Table 30 – *Ortho*H enhancement factor as a function of the shake time for the manual shaking method using the stray field of the spectrometer

Automated Flow System

Bubble Time (s)	*OrthoH Enhancement Factor*	
	a	**b**
5	-194±5	-178±8
7	-205±7	-190±28
10	-227±8	-135±84
15	-220±8	-264±57
20	-217±10	-61±7
25	-200±7	-133±71
30	-212±14	-100±39

Table 31 - *Ortho*H enhancement factor as a function of the *para*hydrogen bubble time for the automated flow system

Manual Shaking Using a Handheld Magnetic Array

Shake Time (s)	*OrthoH Enhancement Factor*	
	a	**b**
5	-454±16	-356±15
7	-489±15	-339±12
10	-497±28	-339±20
15	-442±11	-344±16

Table 32 - *Ortho*H enhancement factor as a function of the shake time for the manual shaking method using a handheld magnetic array.

Appendix B

Measuring the pK_a for the substrates in Chapter 3

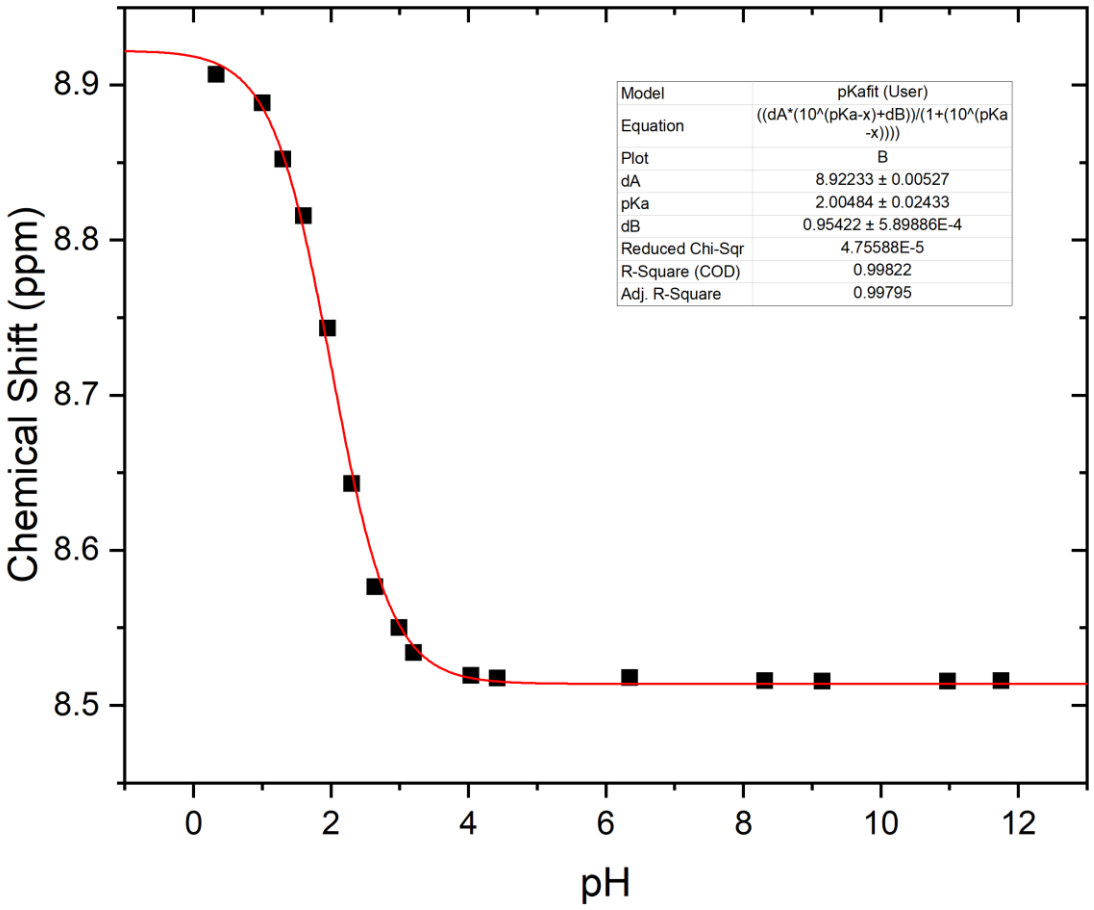

Figure 143 - *Ortho* ^{1}H resonance in 4-Chloropyridine

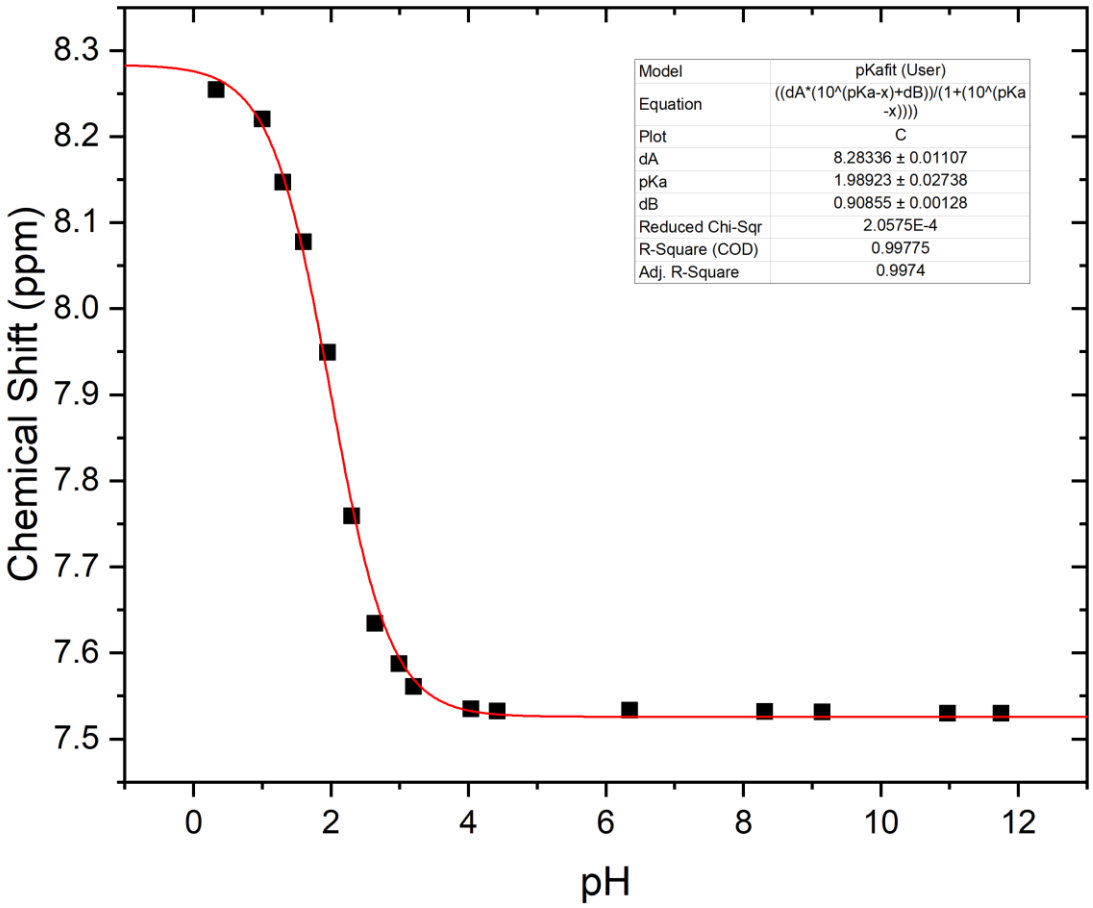

Figure 144 - *Meta* ^{1}H resonance in 4-chloropyridine

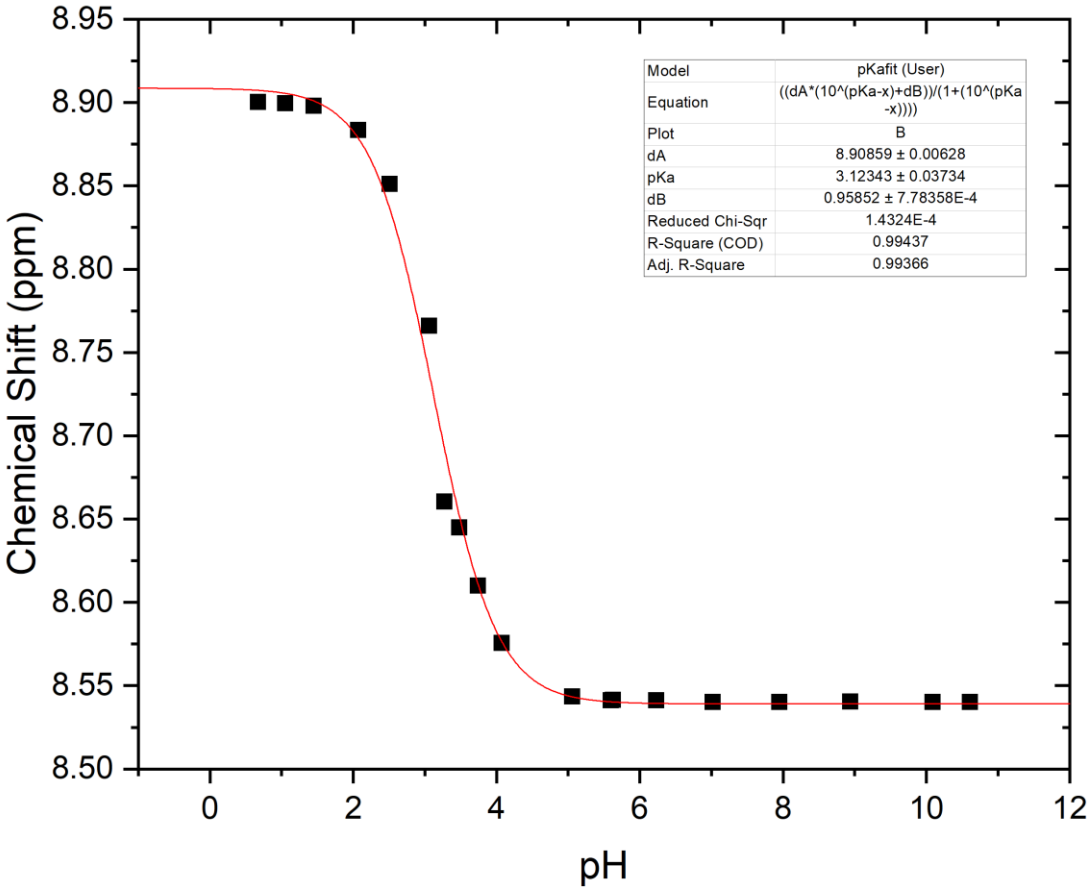

Figure 145 - *Ortho* ^{1}H resonance in 4-pyridinecarboxaldehyde

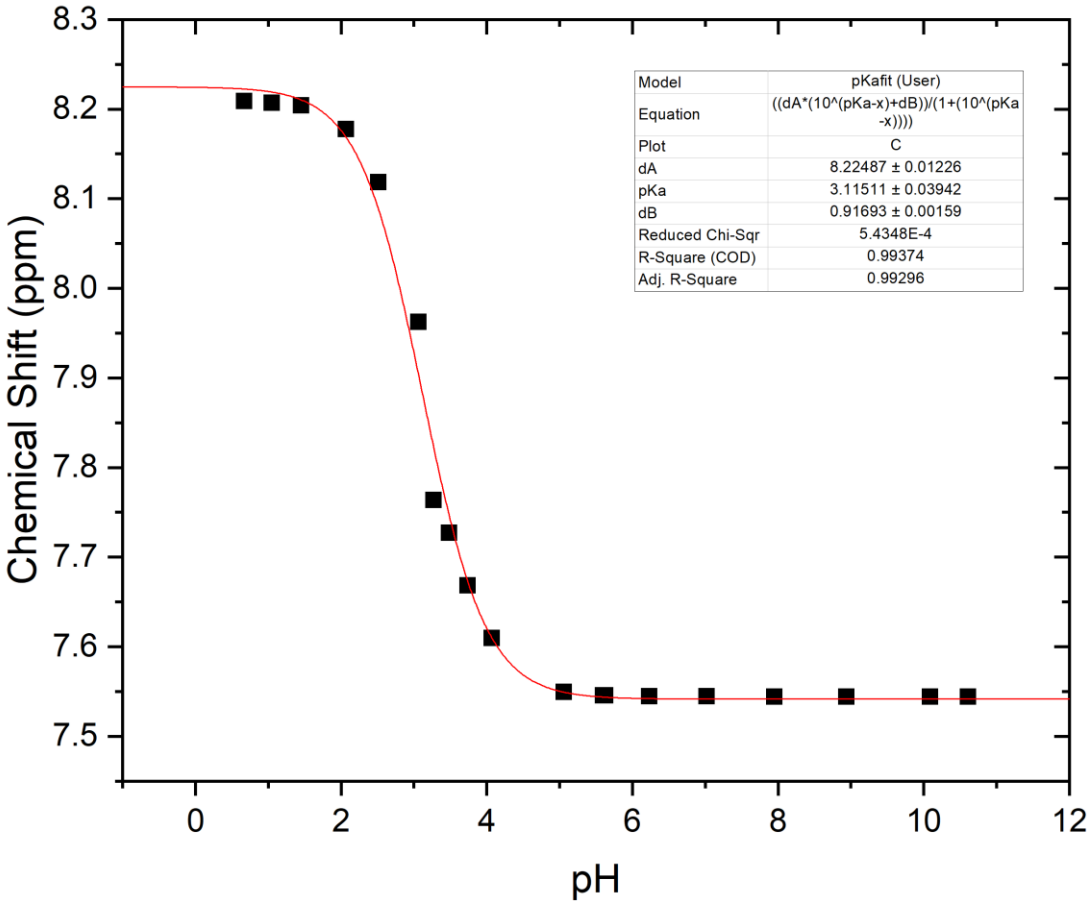

Figure 146 - *Meta* ^{1}H resonance in 4-pyridinecarboxaldehyde

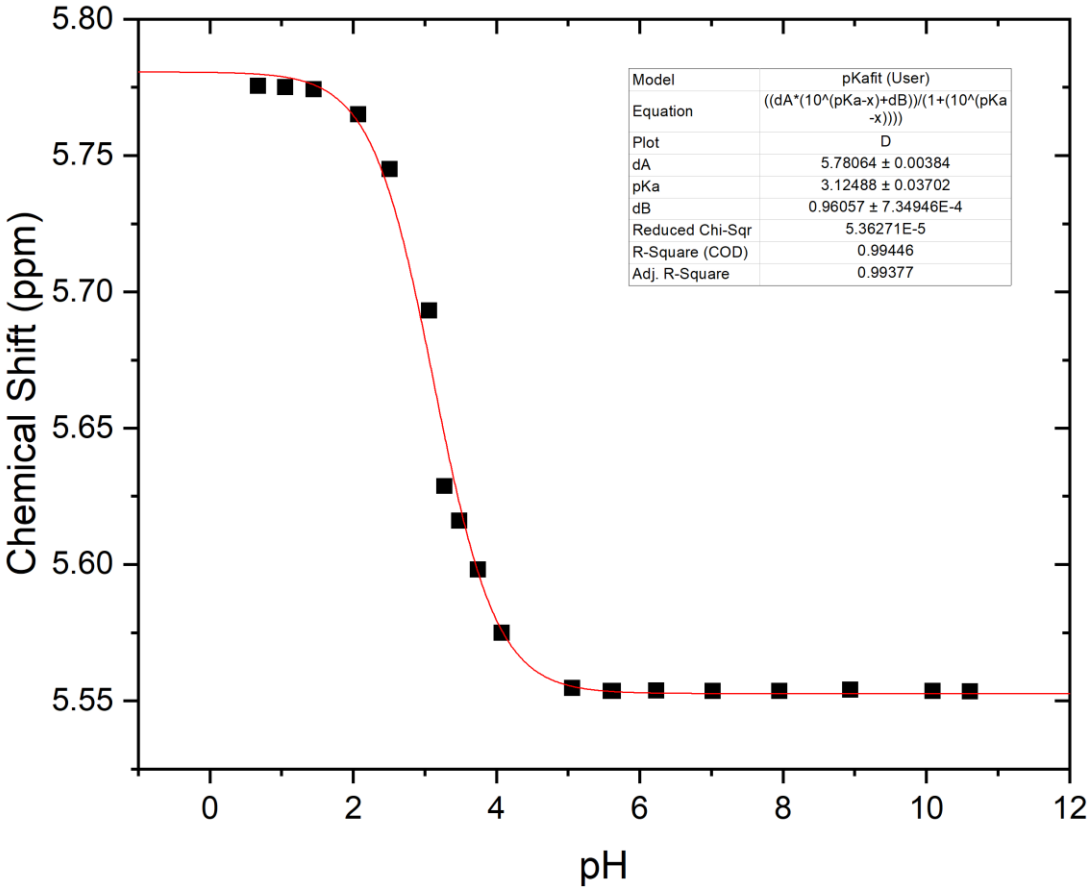

Figure 147 - *Para* ^{1}H resonance in 4-pyridinecarboxaldehyde

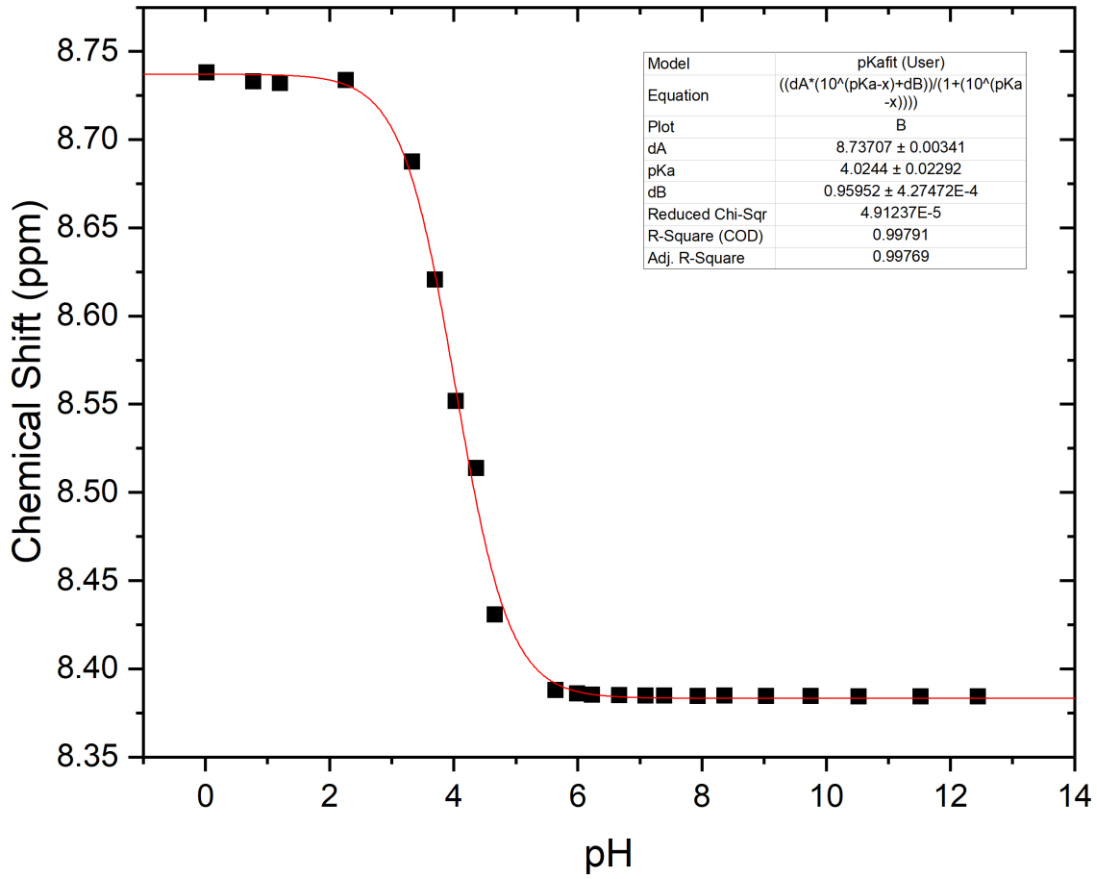

Figure 148 - *Ortho* ^{1}H resonance in 4-methylpyridine

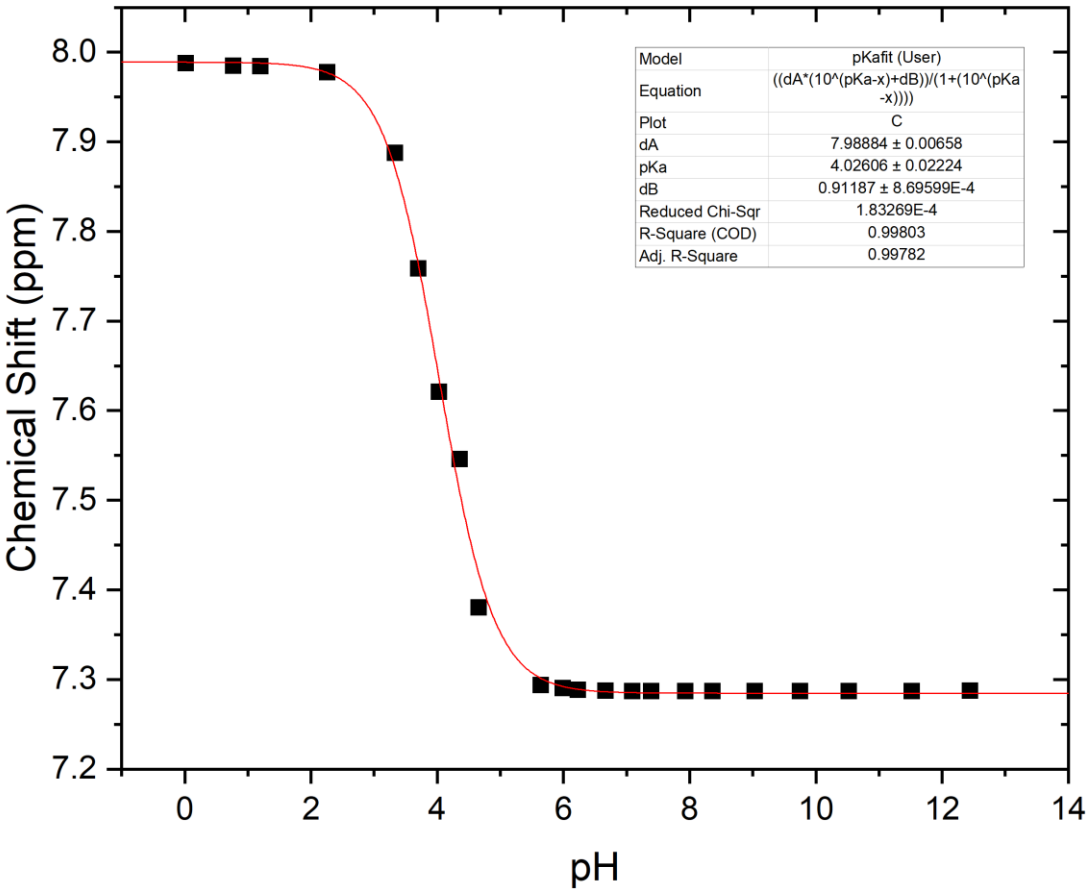

Figure 149 - *Meta* ^{1}H resonance in 4-methylpyridine

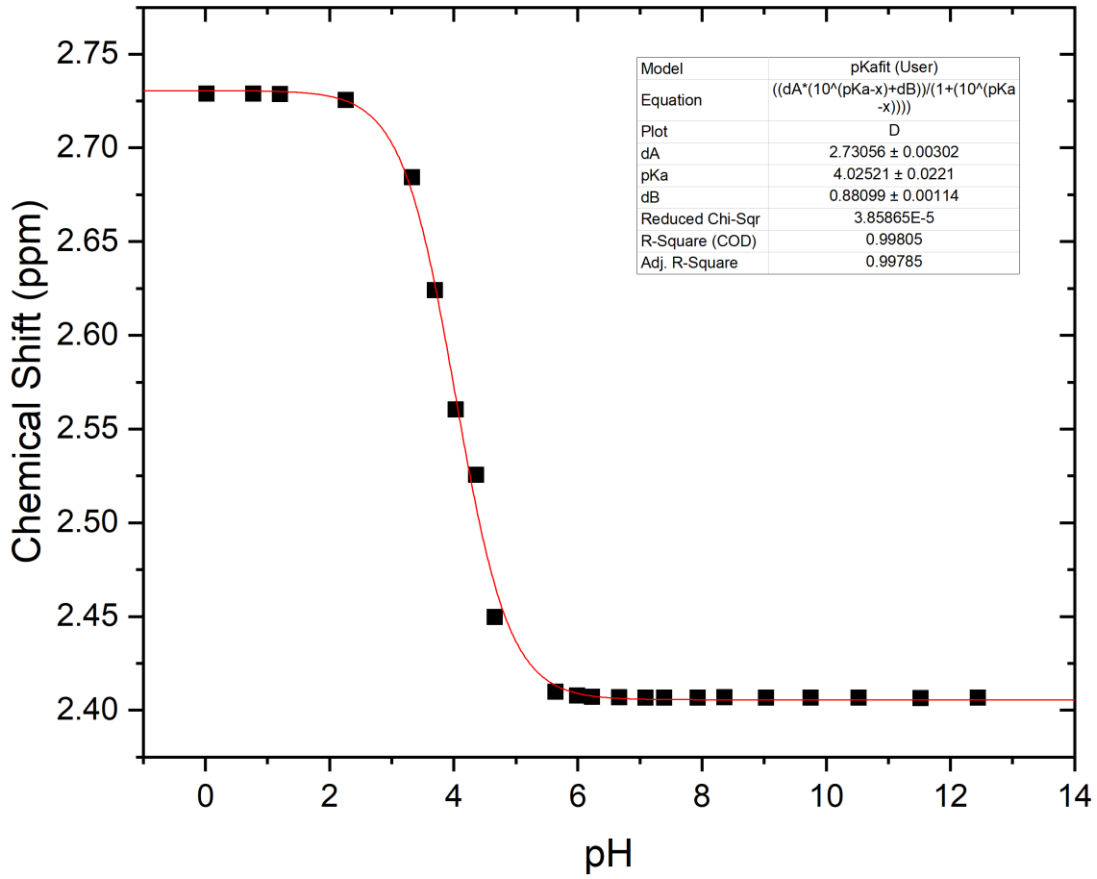

Figure 150 - *Para* ^{1}H resonance in 4-methylpyridine

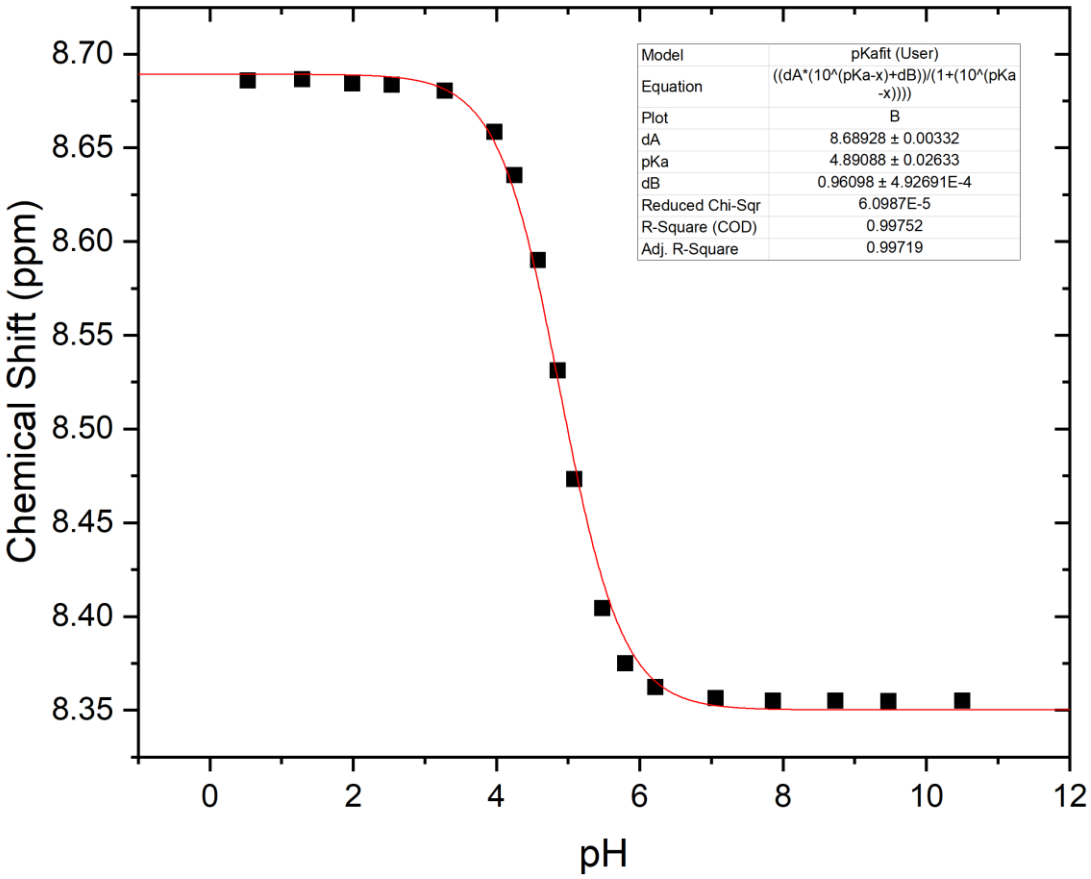

Figure 151 - *Ortho* ^{1}H resonance in 4-methoxypyridine

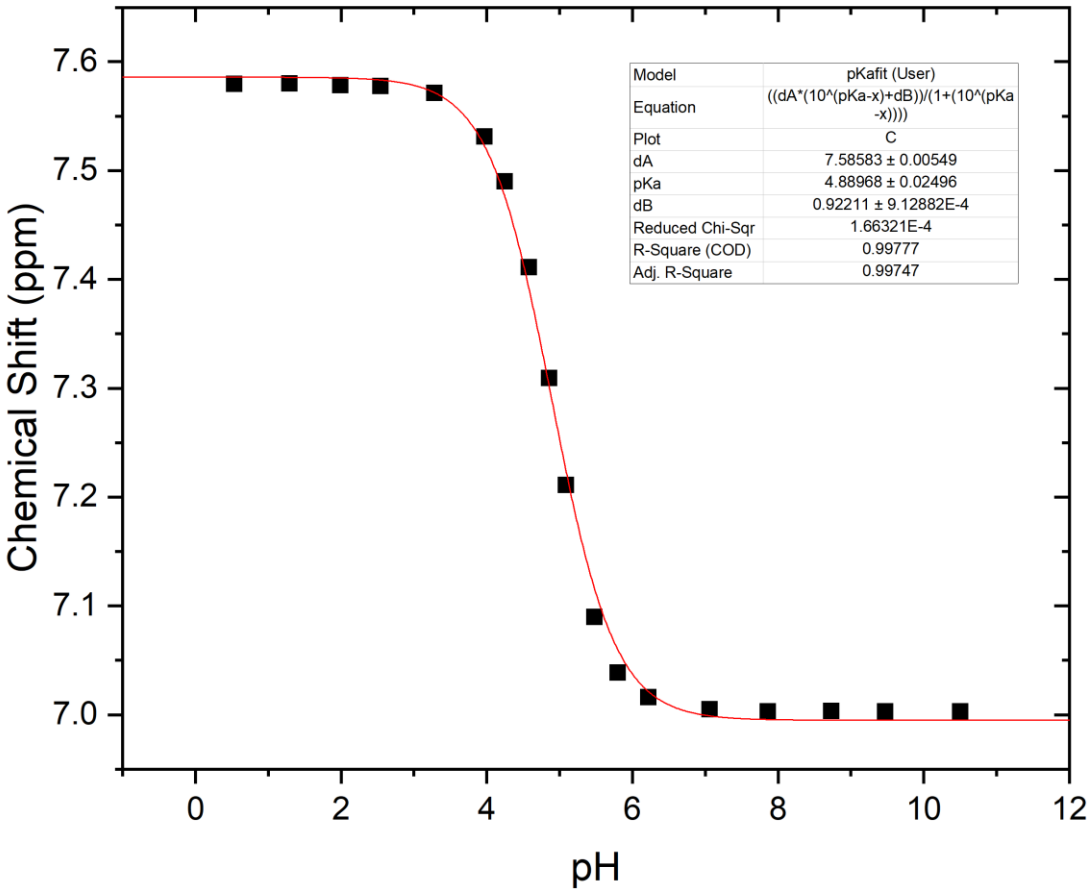

Figure 152 - *Meta* ^{1}H resonance in 4-methoxypyridine

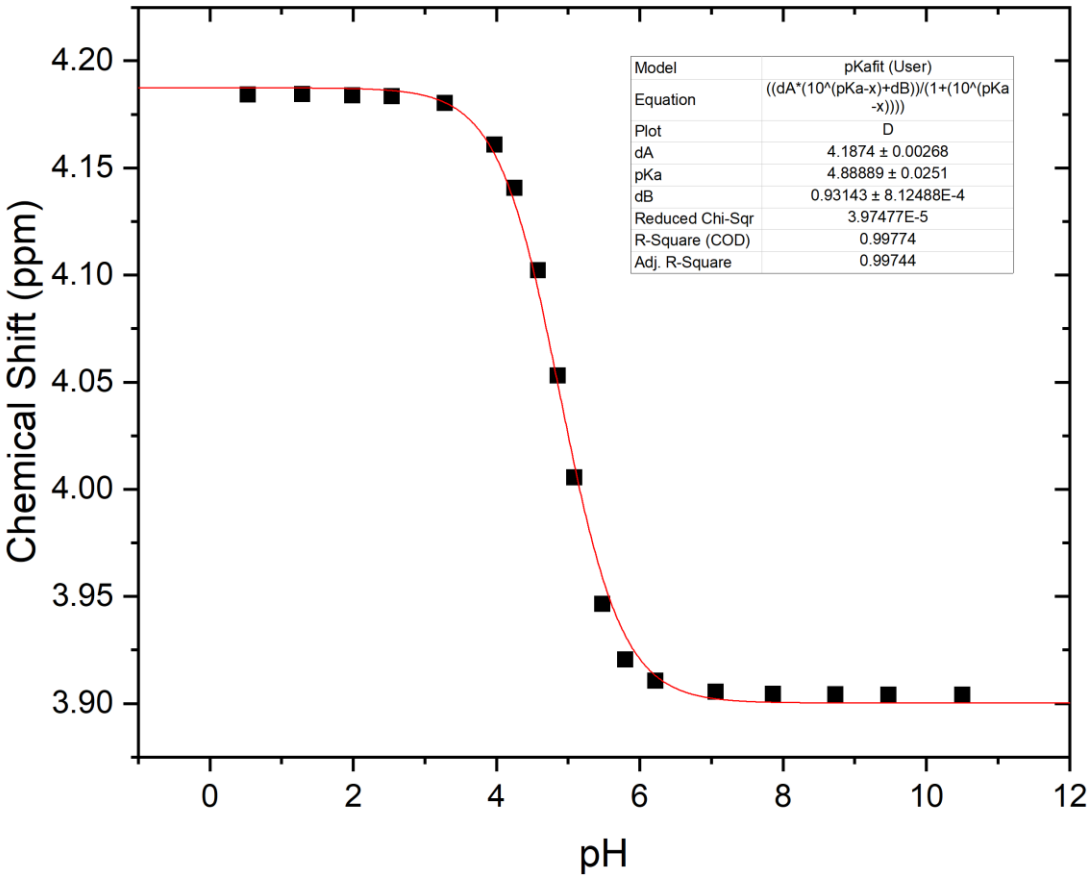

Figure 153 - *Para* ^{1}H resonance in 4-methoxypyridine

Characterisation of Substrates for the Substrates in Chapter 3

4-Chloropyridine

Position	*^{1}H-NMR*	*T_1 (s)*	*^{13}C-NMR*	*^{15}N-NMR*
ortho	8.555 J_{HH} = 4.46 Hz	15.91±0.65	150.1	295.81
meta	7.616 J_{HH} = 4.46 Hz	16.35±1.40	124.9	-
para		-	145.0	-

Table 33 – NMR resonances and T_1 values for the substrate 4-chloropyridine in CD_3OD at 500 MHz spectrometer and 298 K

4-Methylpyridine

Position	*^{1}H-NMR*	*T_1 (s)*	*^{13}C-NMR*	*^{15}N-NMR*
ortho	8.400 J_{HH} = 5.36 Hz	20.52±0.05	148.2	289.2
meta	7.329 J_{HH} = 5.36 Hz	17.70±0.07	125.2	-
para	-	-	-	-
CH_3	2.427	5.91±0.08	19.8	-

Table 34 – NMR resonances and T_1 values for the substrate 4-methylpyridine in CD_3OD at 500 MHz spectrometer and 298 K

4-Methoxypyridine

Position	*^{1}H-NMR*	*T_1 (s)*	*^{13}C-NMR*	*^{15}N-NMR*
ortho	8.356 J_{HH} = 4.7, 1.57 Hz	15.57±0.16	150.1	276.2
Meta	7.007 J_{HH} = 4.7, 1.57 Hz	10.53±0.08	110.4	-
para	-	-	166.8	-
OCH_3	3.908	5.29±0.06	54.6	-

Table 35 – NMR resonances and T_1 values for the substrate 4-methoxypyridine in CD_3OD at 500 MHz and 298 K

4-Pyridinecarboxaldehyde

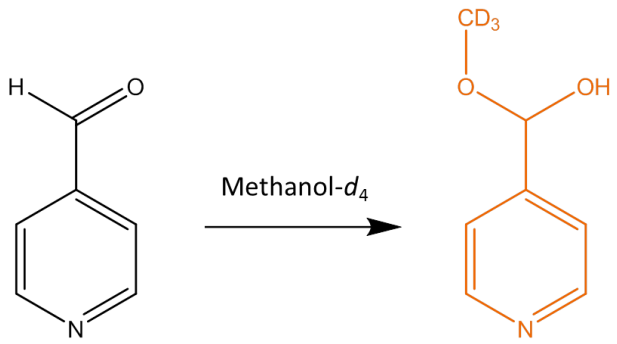

Position	*^{1}H-NMR*	*T_1 (s)*	*^{13}C-NMR*	*^{15}N-NMR*
ortho	8.543 J_{HH} = 6.0 Hz	8.24±0.07	148.5	297.0
meta	7.547 J_{HH} = 6.0 Hz	7.88±0.10	121.5	-
para	-	-	151.4	-
$OHCCD_3$	5.554	-	95.5	-

Table 36 – NMR resonances and T_1 values for the methyl hemiacetal form of 4-pyridinecarboxaldehyde in CD_3OD at 500 MHz spectrometer and 298 K

Characterisation of [Ir(COD)(SIMes)(sub)]Cl for the Substrates in Chapter 3

[Ir(COD)(SIMes)(4-chloropyridine)]Cl

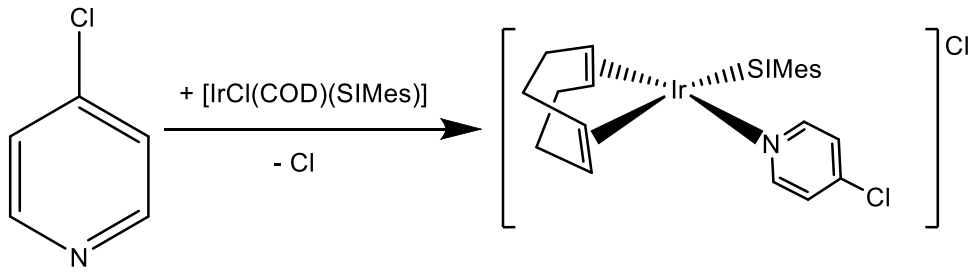

Position	*^{1}H-NMR*	*^{13}C-NMR*	*^{15}N-NMR*
Free*ortho*H	8.547 J_{HH} = 6.2 Hz	150.1	295.1
Free*meta*H	7.616 J_{HH} = 6.2 Hz	124.9	-
FreeparaCCl	-	145.1	-
Position	**^{1}H-NMR**	**^{13}C-NMR**	**^{15}N-NMR**
*ortho*H^{sub}	7.739 J_{HH} = 6.6 Hz	151.8	237.2
*meta*H^{sub}	7.507 J_{HH} = 6.6 Hz	126.1	
$CH^{Ar,Mes}$	7.199 7.027	129.5	
$N\text{-}CH_2\text{-}CH_2\text{-}N$	3.898	51.7	

CH^{COD}	3.890 3.214	65.3 83.1
orthoCH_3^{Mes}	2.518 2.396	20.1
paraCH_3^{Mes}	2.029	17.5
CH_2^{COD}	1.621 1.237	31.9 28.3

Table 37 - NMR Resonances for [Ir(COD)(SIMes)(4-Chloropyridine)]Cl in CD_3OH. ^1H at 500 MHz, ^{13}C at 125 MHz and ^{15}N at 41 MHz at 235 K.

[Ir(COD)(SIMes)(4-methylpyridine)]Cl

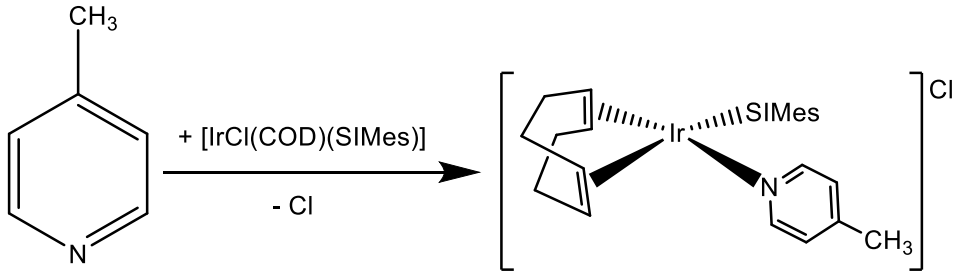

Position	***^{1}H-NMR***	***^{13}C-NMR***	***^{15}N-NMR***
FreeorthoH	8.415 J_{HH} = 6.1 Hz	148.4	288.1
FreemetaH	7.359 J_{HH} = 6.1 Hz	125.4	-
FreeCH₃	2.439	19.8	-
Position	**^{1}H-NMR**	**^{13}C-NMR**	**^{15}N-NMR**
orthoH^{sub}	7.593 J_{HH} = 6.5 Hz	150.4	232.8
metaH^{sub}	7.223	126.4	
$CH^{Ar,Mes}$	7.208 7.035	136.0 129.4	
N-CH₂-CH₂-N	3.862	52.14	
CH^{COD}	4.068 3.206	64.4 83.0	
orthoCH_3^{Mes}	2.439 2.433	19.9	
CH_3^{Sub}	2.528	18.2	

paraCH_3^{Mes}	1.992	17.1
CH_2^{COD}	1.904 1.624	32.2 28.8

Table 38 - NMR Resonances for [Ir(COD)(SIMes)(4-Methylpyridine)]Cl in CD_3OD. ^1H at 500 MHz, ^{13}C at 125 MHz and ^{15}N at 41 MHz at 235 K.

[Ir(COD)(SIMes)(4-methoxypyridine)]Cl

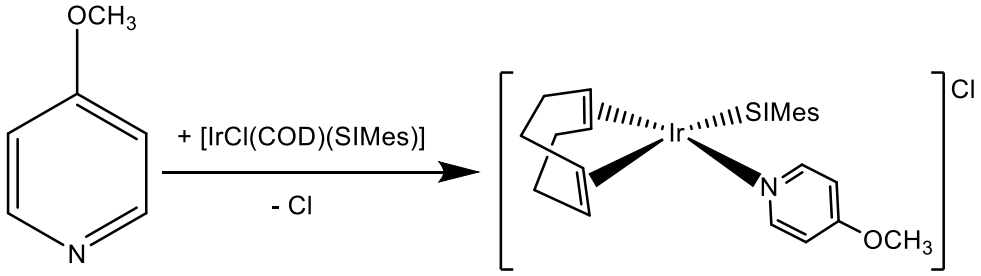

Position	***^{1}H-NMR***	***^{13}C-NMR***	***^{15}N-NMR***
FreeorthoH	8.382 J_{HH} = 6.5 Hz	149.9	273.4
FreemetaH	7.007 J_{HH} = 6.1 Hz	110.5	-
Para	-	166.7	-
FreeCH_3	3.908	54.6	-
Position	**^{1}H-NMR**	**^{13}C-NMR**	**^{15}N-NMR**
orthoH^{sub}	7.560 J_{HH} = 6.5 Hz	151.5	232.8
metaH^{sub}	6.959 J_{HH} = 6.5 Hz	111.7	
$CH^{Ar,Mes}$	7.198 7.041	129.6	
CH_3^{sub}	3.961	55.59	
N-CH_2-CH_2-N	3.845	52.2	
CH^{COD}	3.851 3.206	63.7 82.6	
orthoCH_3^{Mes}	2.526 2.426	19.87	
paraCH_3^{Mes}	2.206	17.4	

CH_2^{COD}	1.904 1.607	31.9 29.0

Table 39 - NMR Resonances for [Ir(COD)(SIMes)(4-Methoxypyridine)]Cl in CD_3OD. ^1H at 500 MHz, ^{13}C at 125 MHz and ^{15}N at 41 MHz at 235 K.

[Ir(COD)(SIMes)(4-pyridinecarboxaldehyde)]Cl

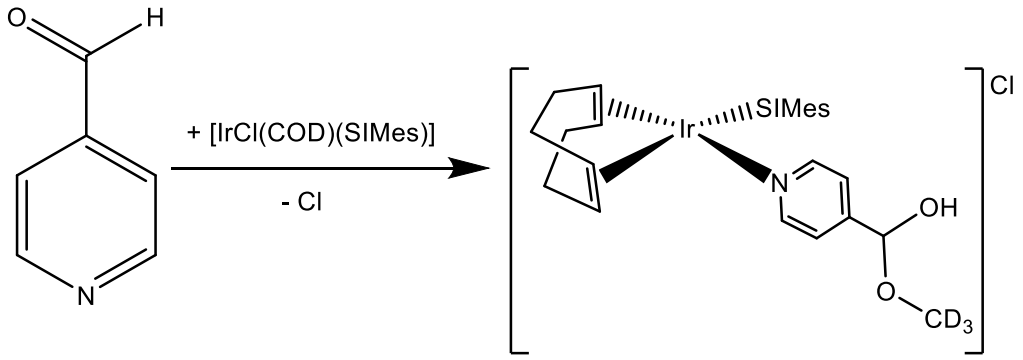

Position	***^{1}H-NMR***	***^{13}C-NMR***	***^{15}N-NMR***
FreeorthoH	8.571 J_{HH} = 6.1 Hz	148.5	294.8
FreemetaH	7.602 J_{HH} = 6.1 Hz	121.8	-
FreeOHCCD₃	-	151.6	-
Position	**^{1}H-NMR**	**^{13}C-NMR**	**^{15}N-NMR**
orthoH^{sub}	7.769 J_{HH} = 6.5 Hz	151.4	239.9
metaH^{sub}	7.418 J_{HH} = 6.5 Hz	122.8	
OHCCD₃	-	151.93	
$CH^{Ar,Mes}$	7.202 7.012	129.4	
N-CH₂-CH₂-N	4.061 3.844	52.2	
CH^{COD}	3.886 3.210	64.6 83.1	
orthoCH_3^{Mes}	2.526 2.429	19.8	
paraCH_3^{Mes}	1.998	17.2	
CH_2^{COD}	1.908 1.639	32.1 28.8	

Table 40 - NMR Resonances for [Ir(COD)(SIMes)(4-Pyridinecarboxaldehyde)]Cl in CD_3OD. ^1H at 500 MHz, ^{13}C at 125 MHz and ^{15}N at 41 MHz at 235 K.

Characterisation of $[Ir(H)_2(SIMes)(sub)_3]Cl$ for the Substrates in Chapter 3

$[Ir(H)_2(SIMes)(4\text{-chloropyridine})_3]Cl$

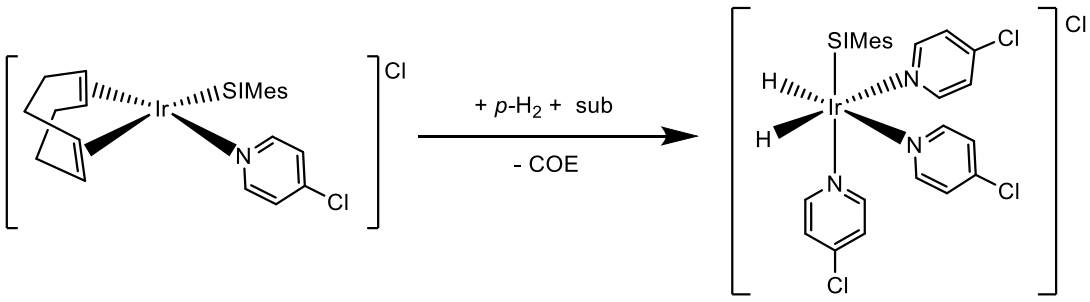

Position	***^{1}H-NMR***	***^{13}C-NMR***	***^{15}N-NMR***
Free*ortho*H	8.548 J_{HH} = 6.4 Hz	150.1	295.0
Free*meta*H	7.614 J_{HH} = 6.4 Hz	124.8	-
*para*CCl	-	145.2	-
Position	**^{1}H-NMR**	**^{13}C-NMR**	**^{15}N-NMR**
orthoH^{sub} *(trans to H^-)*	8.228 J_{HH} = 6.3 Hz	155.1	250.6
orthoH^{sub} *(trans to NHC)*	8.002 J_{HH} = 6.7 Hz	156.2	236.3
metaH^{sub} (*trans* to H^-)	7.263 J_{HH} = 6.3 Hz	125.8	
metaH^{sub} *(trans to NHC)*	7.121 J_{HH} = 6.7 Hz	125.9	
$CH^{Ar,Mes}$	6.638	128.7	
$N\text{-}CH_2\text{-}CH_2\text{-}N$	3.901	50.3	
orthoCH_3^{Mes}	2.248	19.7	
paraCH_3^{Mes}	2.184	17.7	
H^-	-22.53	-	

Table 41 - NMR resonances for $[Ir(H)_2(SIMes)(4\text{-Chloropyridine})_3]Cl$ in CD_3OH at 500 MHz spectrometer and 235 K

$[Ir(H)_2(SIMes)(4\text{-methylpyridine})_3]Cl$

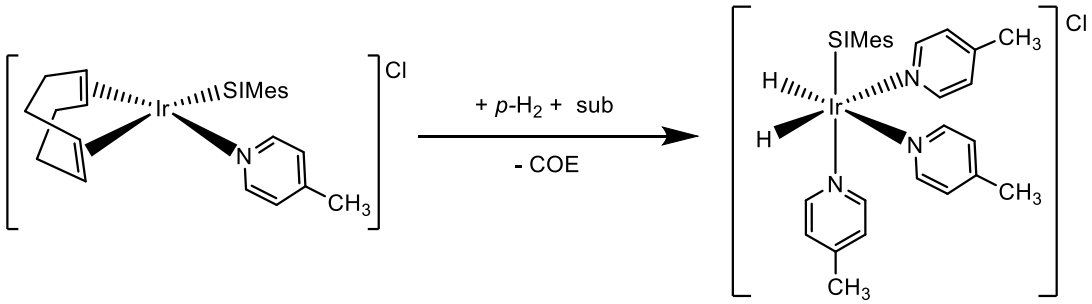

Position	***^{1}H-NMR***	***^{13}C-NMR***	***^{15}N-NMR***
FreeorthoH	8.413 J_{HH} = 6.0 Hz	149.3	288.1
FreemetaH	7.357 J_{HH} = 6.0 Hz	125.3	-
FreeCH₃	2.439	19.8	-
Position	**^{1}H-NMR**	**^{13}C-NMR**	**^{15}N-NMR**
orthoH^{sub} (*trans* to H^-)	8.121 J_{HH} = 5.9 Hz	153.6	247.2
orthoH^{sub} *(trans to NHC)*	7.799 J_{HH} = 5.5 Hz	154.2	233.1
metaH^{sub} (*trans* to H^-)	6.963 J_{HH} = 5.9 Hz	125.9	
metaH^{sub} (*trans to* NHC)	6.814 J_{HH} = 5.5 Hz	125.9	
$CH^{Ar,Mes}$	6.616	128.5	
N-CH₂-CH₂-N	3.869	50.5	
orthoCH_3^{Mes}	2.235	19.83	
CH_3^{Sub} (*trans* to H^-)	2.170	17.67	
CH_3^{Sub} *(trans to NHC)*	2.343	19.52	
paraCH_3^{Mes}	2.157	19.36	
H^-	-22.43	-	

Table 42 - NMR resonances for $[Ir(H)_2(SIMes)(4\text{-Methylpyridine})_3]Cl$ in CD_3OD at 500 MHz spectrometer and 235 K

$[Ir(H)_2(SIMes)(4\text{-methoxypyridine})_3]Cl$

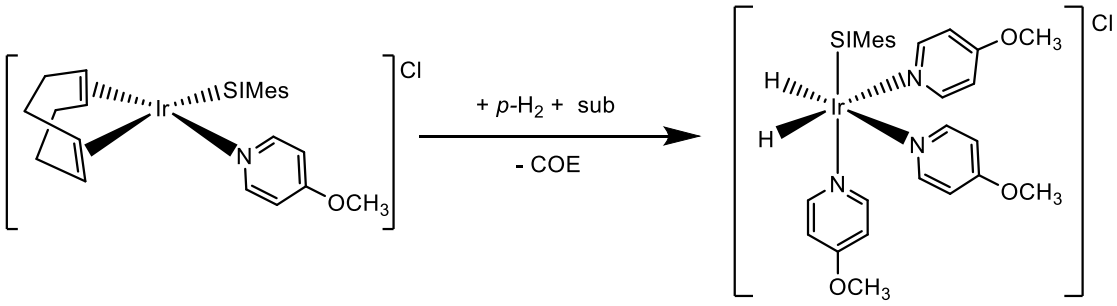

Position	***^{1}H-NMR***	***^{13}C-NMR***	***^{15}N-NMR***
FreeorthoH	8.383 J_{HH} = 6.5 Hz	149.7	273.4
FreemetaH	7.070 J_{HH} = 6.5 Hz	110.2	-
FreeparaC	-	166.8	-
FreeCH_3	3.920	55.6	-
Position	**^{1}H-NMR**	**^{13}C-NMR**	**^{15}N-NMR**
orthoH^{sub} (*trans* to H^-)	8.084 J_{HH} = 6.5 Hz	155.0	232.9
orthoH^{sub} *(trans to NHC)*	7.742 J_{HH} = 6.9 Hz	155.7	218.0
metaH^{sub} (*trans* to H^-)	6.694 J_{HH} = 6.5 Hz	110.9	
metaH^{sub} *(trans to NHC)*	6.556 J_{HH} = 6.9 Hz	110.8	
$CH^{Ar,Mes}$	6.643	128.6	
N-CH_2-CH_2-N	3.864	-	
CH_3^{Sub} (*trans* to H^-)	3.870	50.33	
CH_3^{Sub} (trans to NHC)	3.723	-	
orthoCH_3^{Mes}	2.251	19.8	
paraCH_3^{Mes}	2.172	17.9	
H^-	-23.01	-	

Table 43 - Table of NMR resonances for $[Ir(H)_2(SIMes)(4\text{-Methoxypyridine})_3]Cl$ in CD_3OD at 500 MHz and 235 K

$[Ir(H)_2(SIMes)(4\text{-pyridinecarboxaldehyde})_3]Cl$

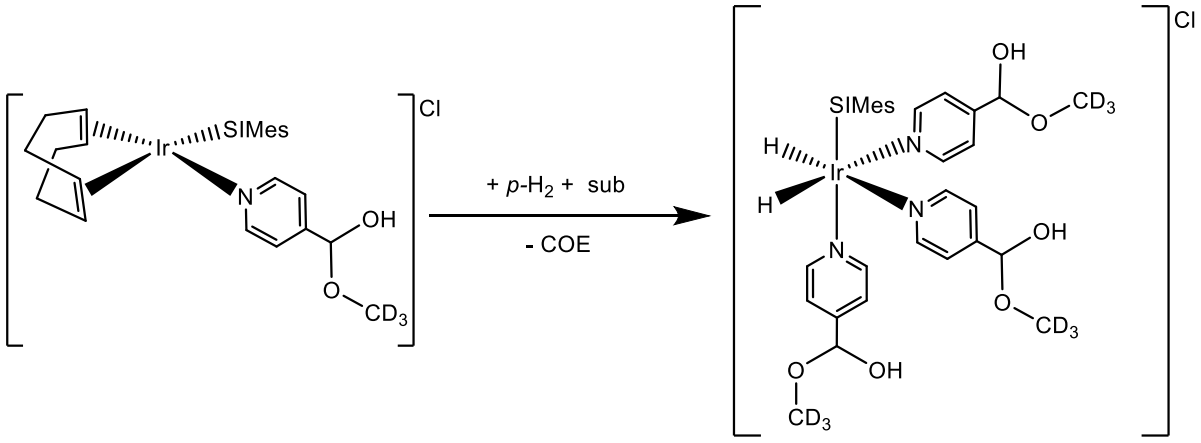

Position	***^{1}H-NMR***	***^{13}C-NMR***	***^{15}N-NMR***
FreeorthoH	8.563 J_{HH} = 4.2 Hz	148.5	295.3
FreemetaH	7.594 J_{HH} = 4.2 Hz	121.8	
FreeOHCCD₃	-	151.6	
Position	**^{1}H-NMR**	**^{13}C-NMR**	**^{15}N-NMR**
orthoH^{sub} (*trans* to H^-)	8.28	150.0	254.4
orthoH^{sub} *(trans to NHC)*	7.97	150.6	240.1
metaH^{sub} (*trans* to H^-)	7.18	122.53	
metaH^{sub} *(trans to NHC)*	7.04	122.59	
OHCCD₃ (*trans* to H^-)	-	154.0	
OHCCD₃ (trans to NHC)	-	154.7	
$CH^{Ar,Mes}$	6.60	128.62	
N-CH₂-CH₂-N	3.89	50.39	
orthoCH_3^{Mes}	2.24	17.86	
paraCH_3^{Mes}	2.16	19.69	

H^-	-22.39	-

Table 44 - Table of NMR Resonances for [Ir(H)2(SIMes)(4-Pyridinecarboxaldehyde)3Cl] in CD3OD at 500MHz and 243 K

Enhancements in $[Ir(H)_2(SIMes)(sub)_3]Cl$ for the Substrates in Chapter 3

p-substituent	*OrthoH Enhancement Factor*	
	SIMes	**d_{22}-SIMes**
Cl	-1340 ± 2	-673 ± 26
CHO	-571 ± 41	-803 ± 14
OMe	-767 ± 8	-915 ± 18
Me	-680 ± 11	-677 ± 10

Table 45

Exchange in $[Ir(H)_2(SIMes)(sub)_3]Cl$ for the Substrates in Chapter 3

Table 46 - Calculated values of K_d for the substrates presented in Chapter 3

Temp (K)	*Cl*	*Std Error*	*Me*	*Std Error*	*OMe*	*Std Error*	*CHO*	*Std Error*
250							0.01015	2.05E-04
255	0.10889	2.05E-04	0.08208	3.91E-04	0.0784	2.88E-04	0.0246	2.05E-04
260	0.24794	2.05E-04	0.18724	7.85E-04	0.17308	6.91E-04	0.05492	2.05E-04
265	0.54294	2.05E-04	0.40524	0.00149	0.39582	0.00109	0.12813	2.05E-04
270	1.04119	2.05E-04	0.75415	0.00153	0.83256	0.00186	0.29161	2.05E-04
275	2.10558	2.05E-04	1.51458	0.00309	1.58881	0.00174	0.64376	2.05E-04
280	4.42317	2.05E-04	2.60901	0.00271	3.29846	0.01112	1.3948	2.05E-04
285	8.87521	2.05E-04	6.6854	0.00367	4.46241	0.01229	2.80014	2.05E-04
290	14.65205	2.05E-04	13.37759	0.02313			5.35469	2.05E-04
295			21.89506	0.20378			10.07181	2.05E-04

300		21.47452	2.05E-04

Table 47 - Calculated values of K_d and associated errors calculated using the Jackknife method for the substrates presented in Chapter 3

Variation in enhancement factor with temperature used to calculate optimum rates of substrate dissociation

	OrthoH Enhancement Factor			
Temp (K)	**Cl**	**Me**	**OMe**	**CHO**
280	-180.54918	-112.25874	-120.77237	-46.25366
285	-171.81386	-127.84909	-126.80681	-51.81213
290	-138.16703	-122.83442	-115.12831	-50.07025
295	-99.30651	-99.93102	-89.04842	-46.3549
300	-39.23032	-66.71993	-54.23912	-37.03337
310	-4.76145	-15.26367	-9.89929	-14.93244
320		-2.69508	-1.12857	-3.41554

Table 48 – *Ortho*H Enhancement Factor at different temperatures

Measuring the $^{4}J_{HH}$ Coupling in $[Ir(H)_2(SIMes)(sub)_3]Cl$

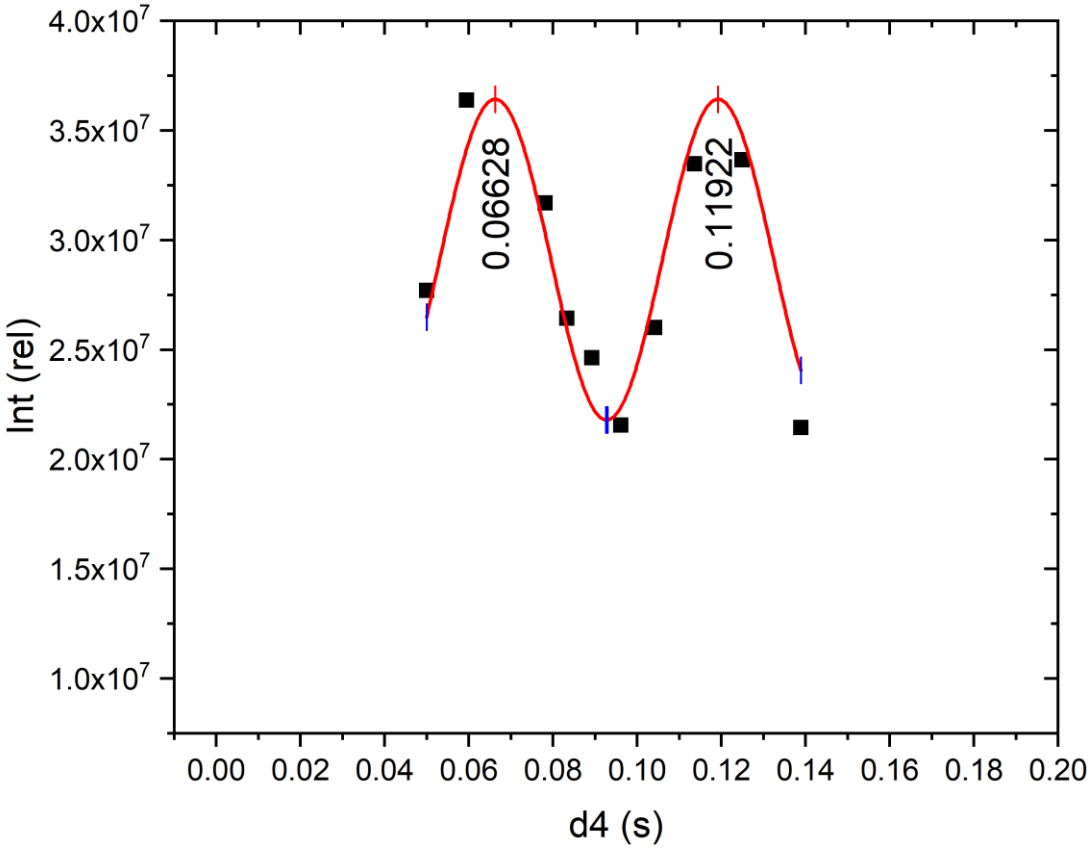

Figure 154 – Oscillation frequency for 4-chloropyridine

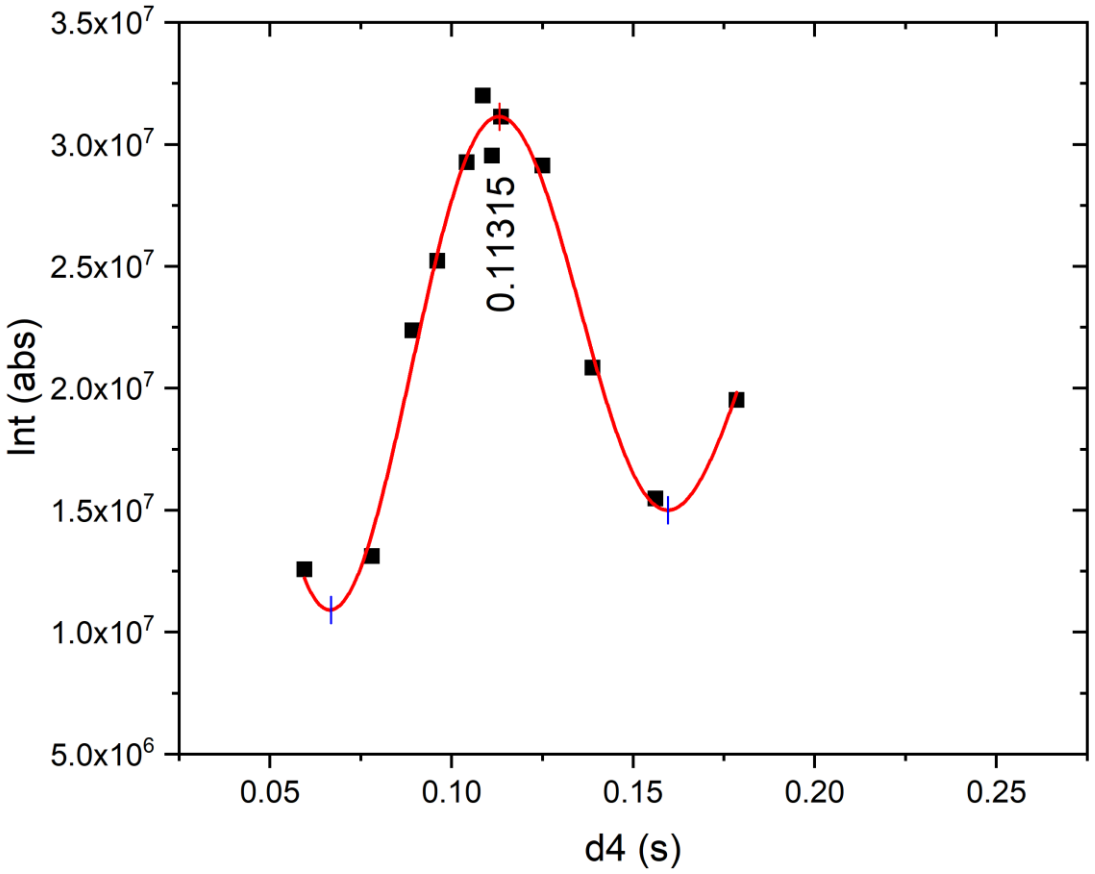

Figure 155 - 4-methylpyridine

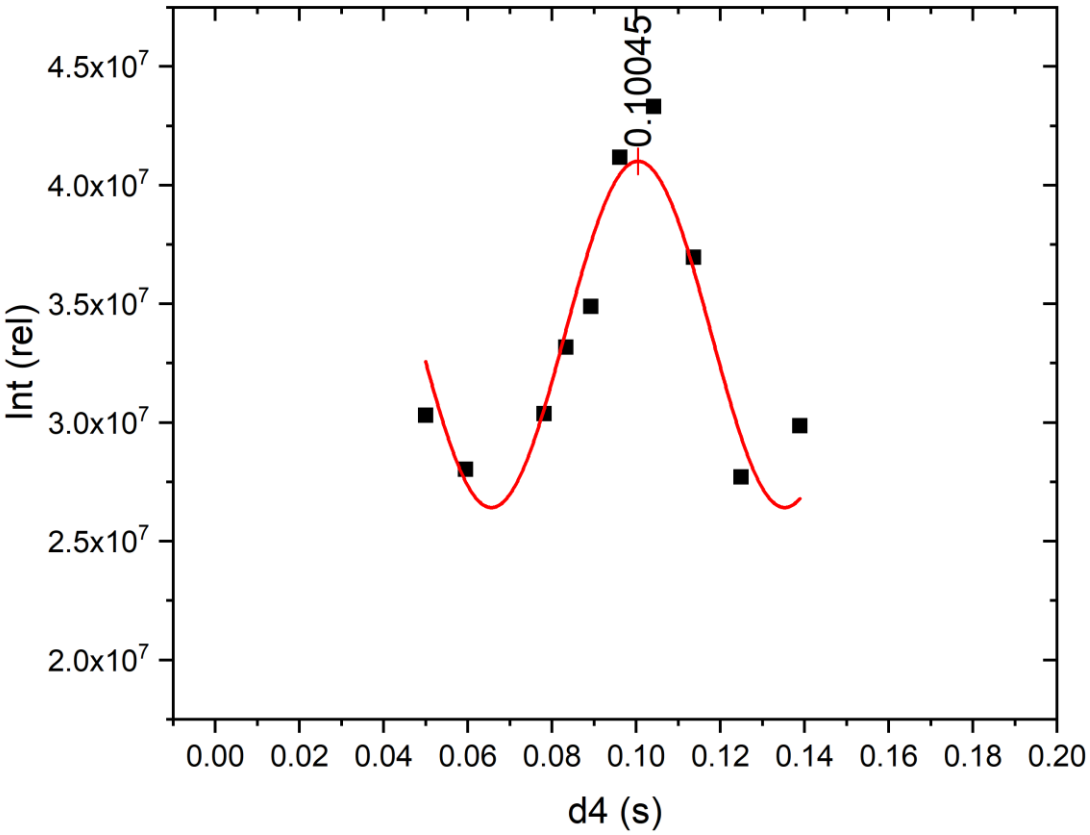

Figure 156 - 4-methoxypyridine

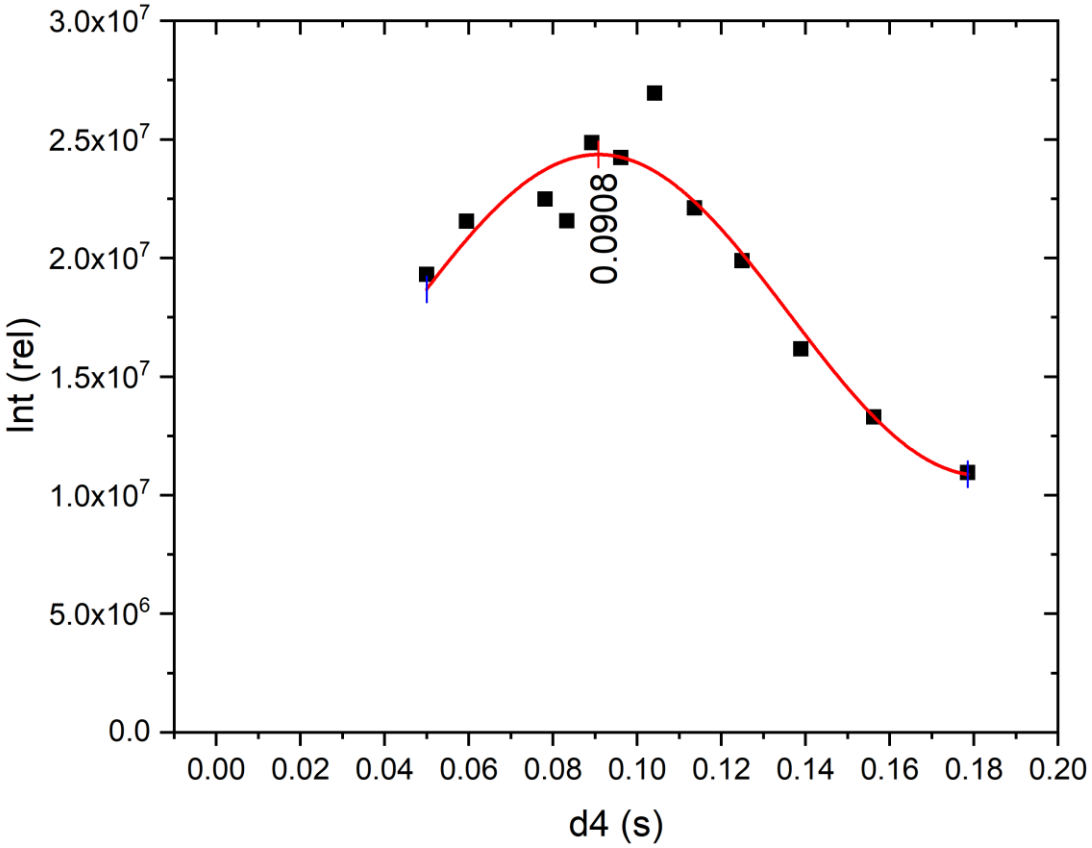

Figure 157 - 4-pyridinecarboxaldehyde

Relaxation effects in $[Ir(H)_2(SIMes)(sub)_3]Cl$ for the substrates in chapter 3

T_1 graphs for $[Ir(H)_2(SIMes)(sub)_3]Cl$

Free Substrate OrthoH

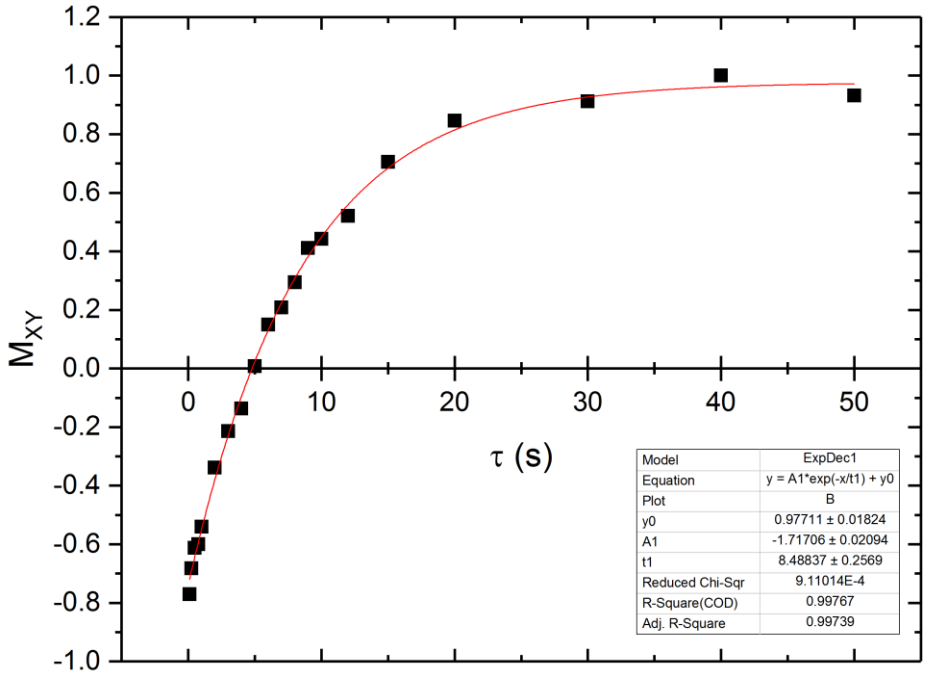

Figure 158 - T_1 for 4-chloropyridine

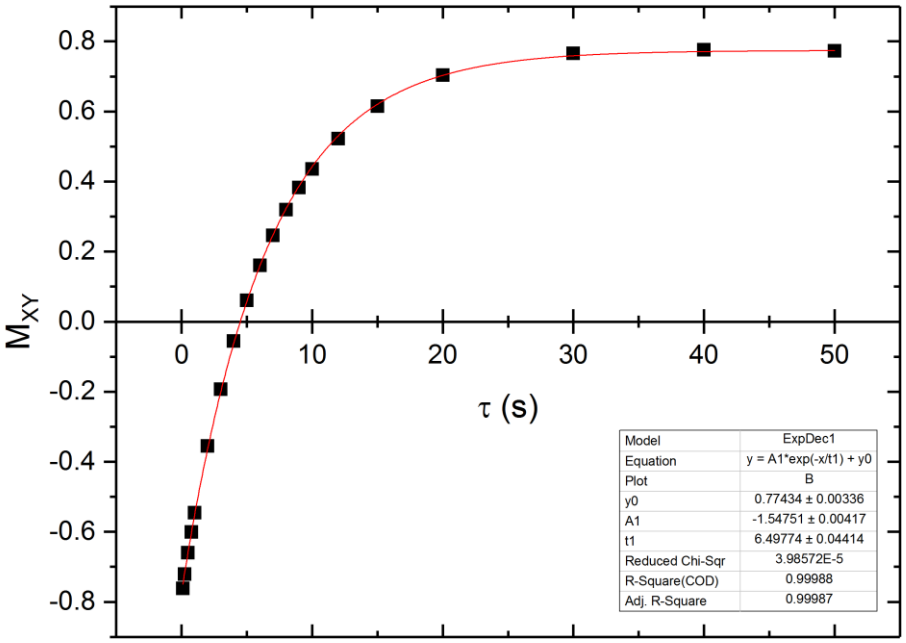

Figure 159 - T_1 for 4-methylpyridine

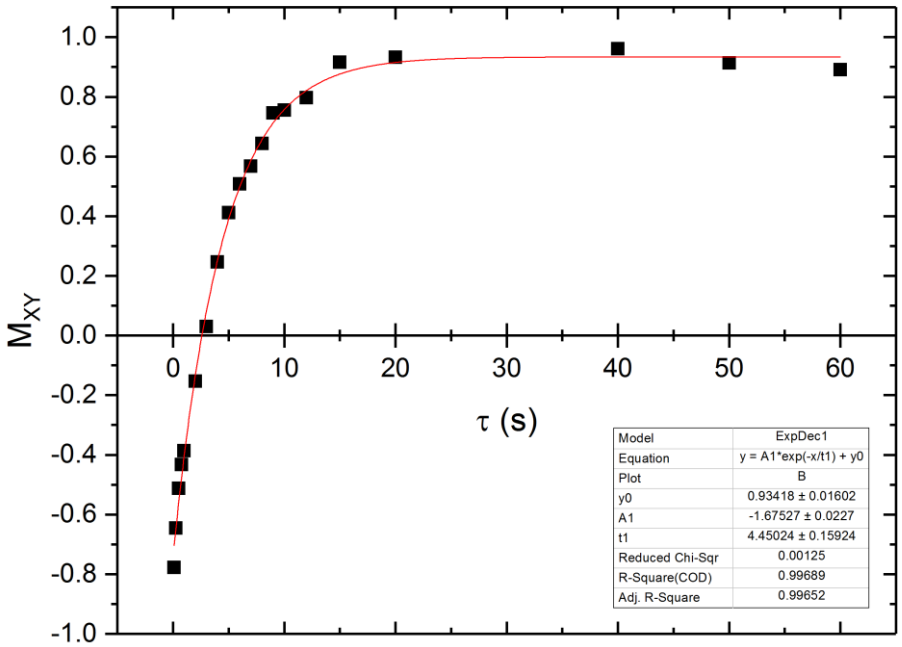

Figure 160 - T_1 for 4-methoxypyridine

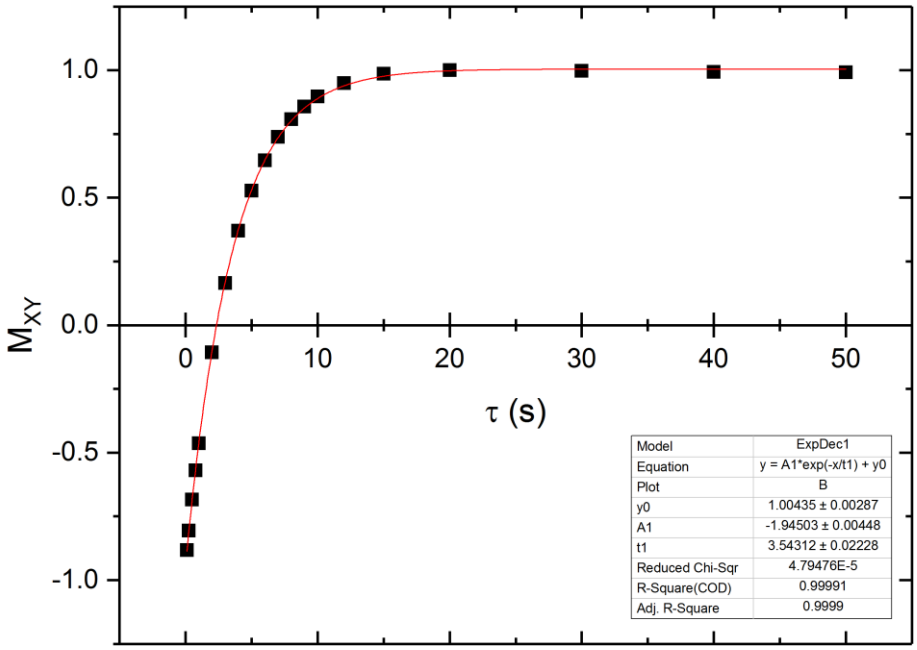

Figure 161 - T_1 for 4-pyridinecarboxaldehyde

Bound Substrate Trans to Hydride

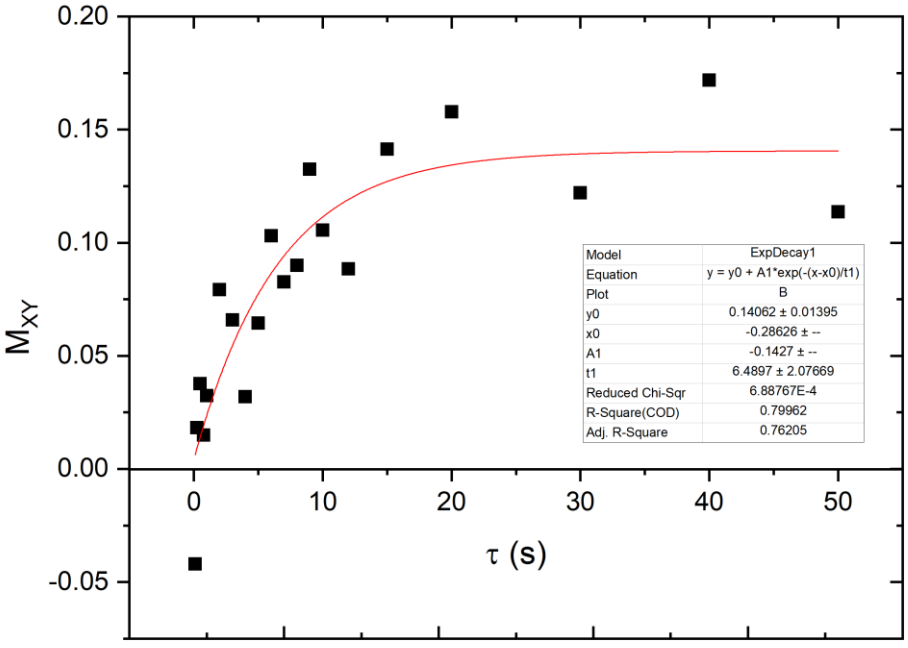

Figure 162 - 4-chloropyridine

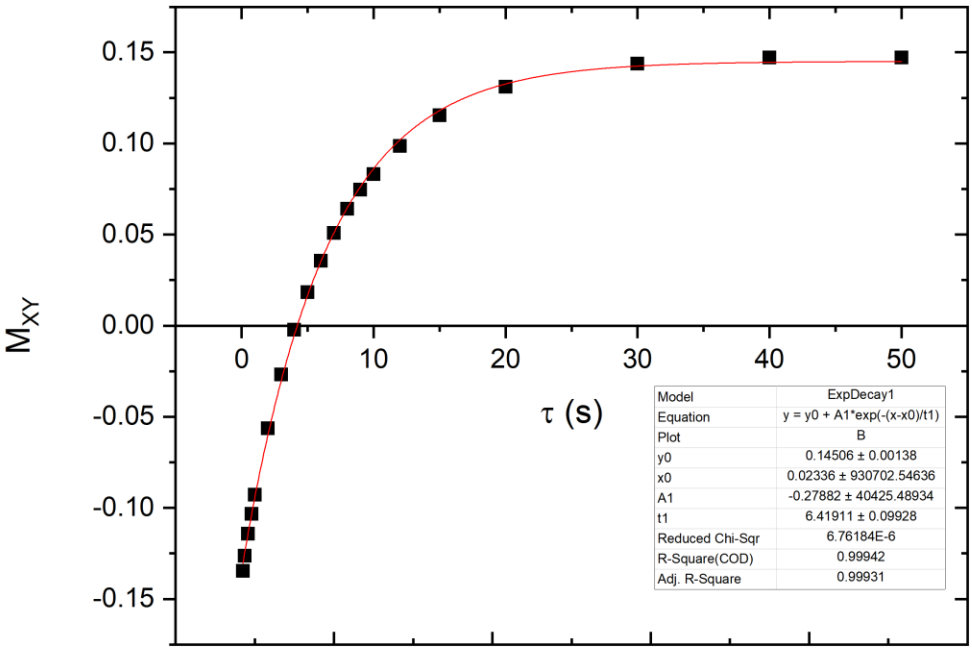

Figure 163 - 4-methylpyridine

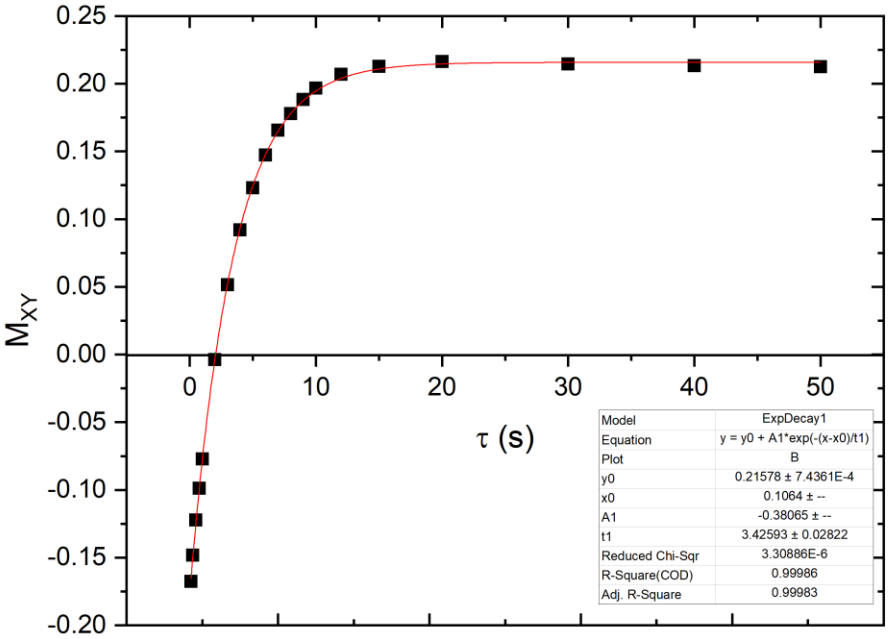

Figure 164 - 4-pyridinecarboxaldehyde

Bound Substrate Trans to NHC

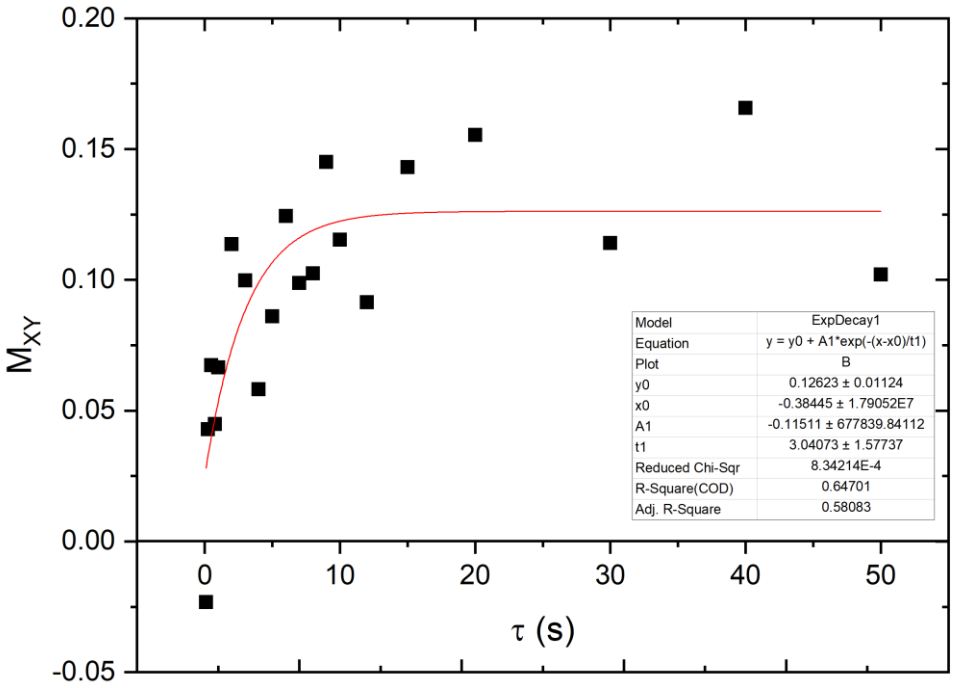

Figure 165 - 4-chloropyridine

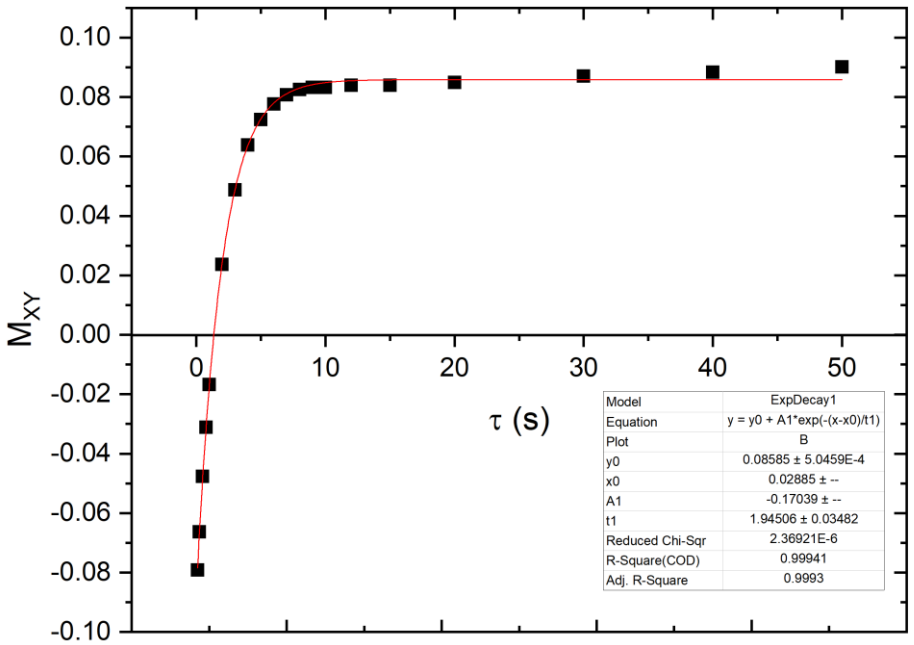

Figure 166 - 4-methylpyridine

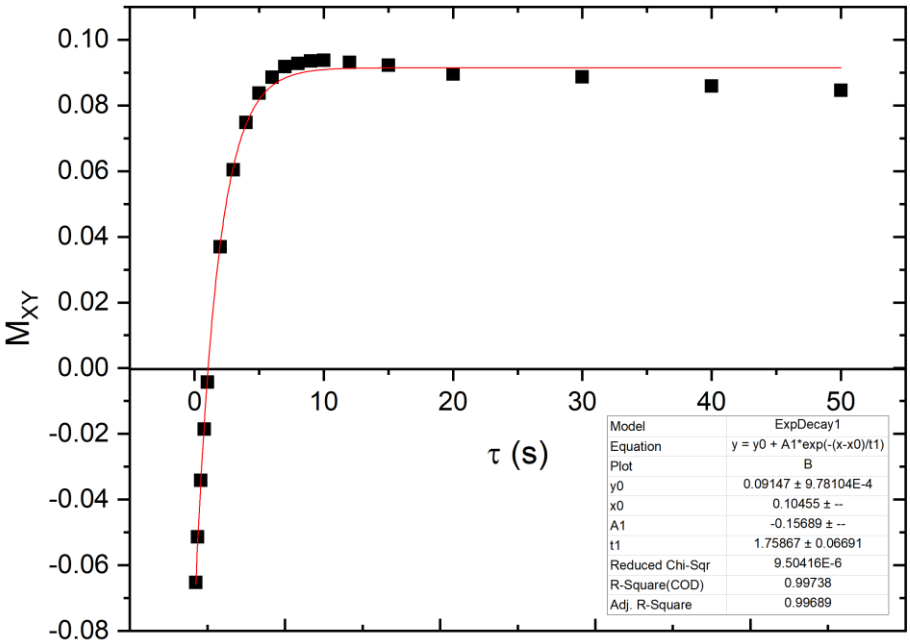

Figure 167 - 4-methoxypyridine

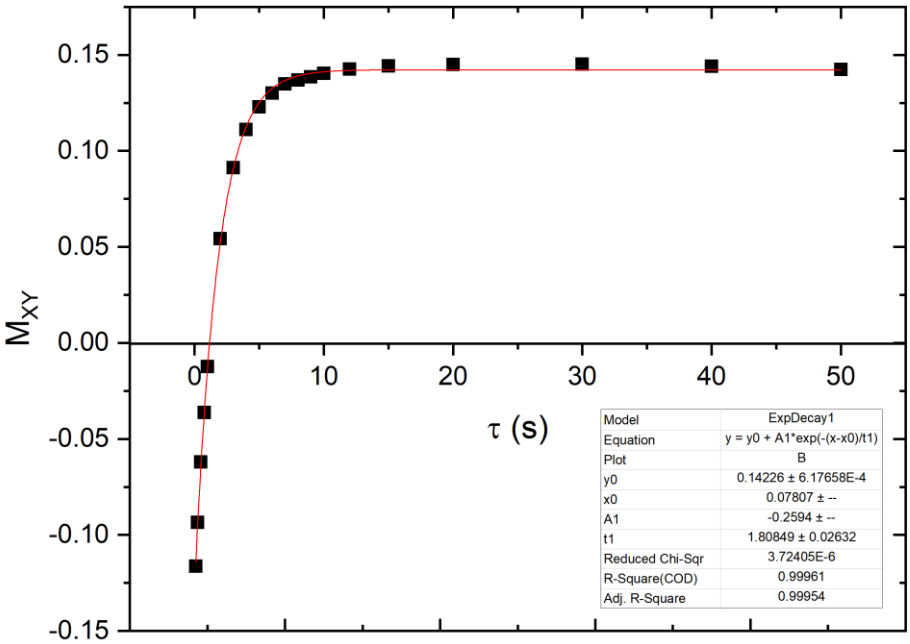

Figure 168 - 4-pyridinecarboxaldehyde

T_1 graphs for [Ir(H)$_2$(d_{22}-SIMes)(sub)$_3$]Cl

Free Substrate OrthoH

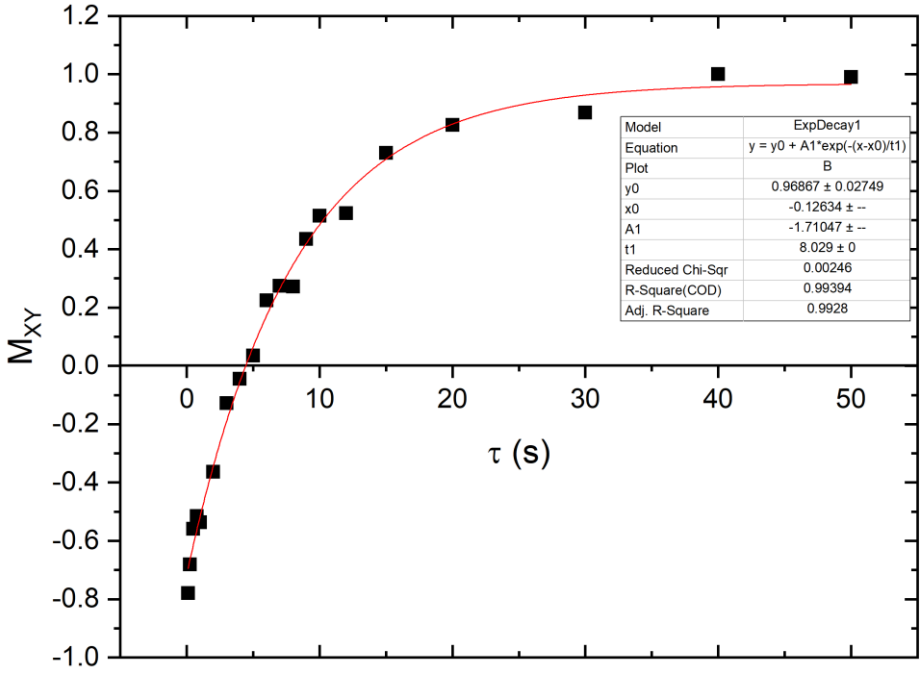

Table 49 – T_1 for 4-chloropyridine

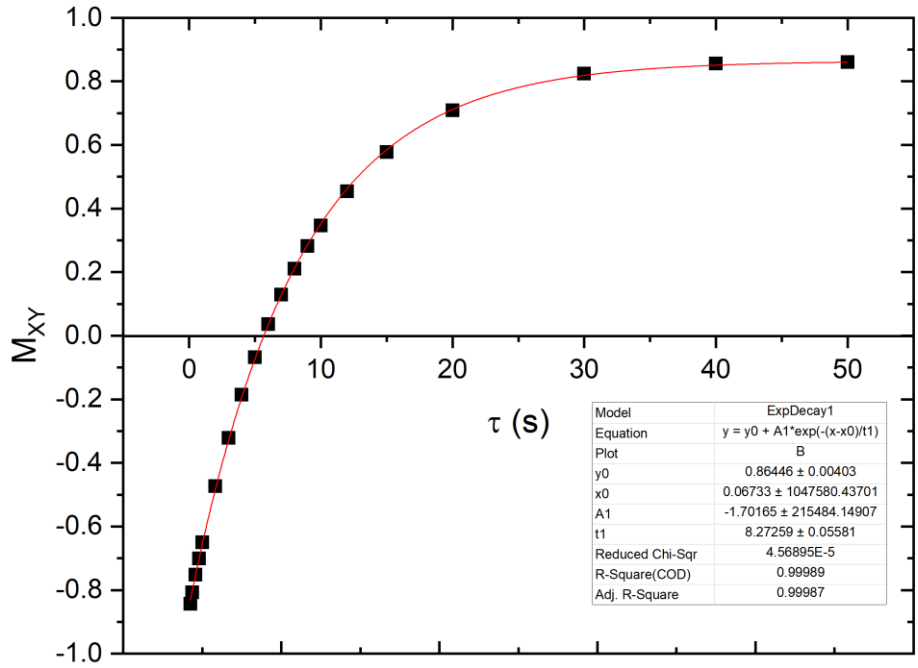

Table 50 – T_1 for 4-methylpyridine

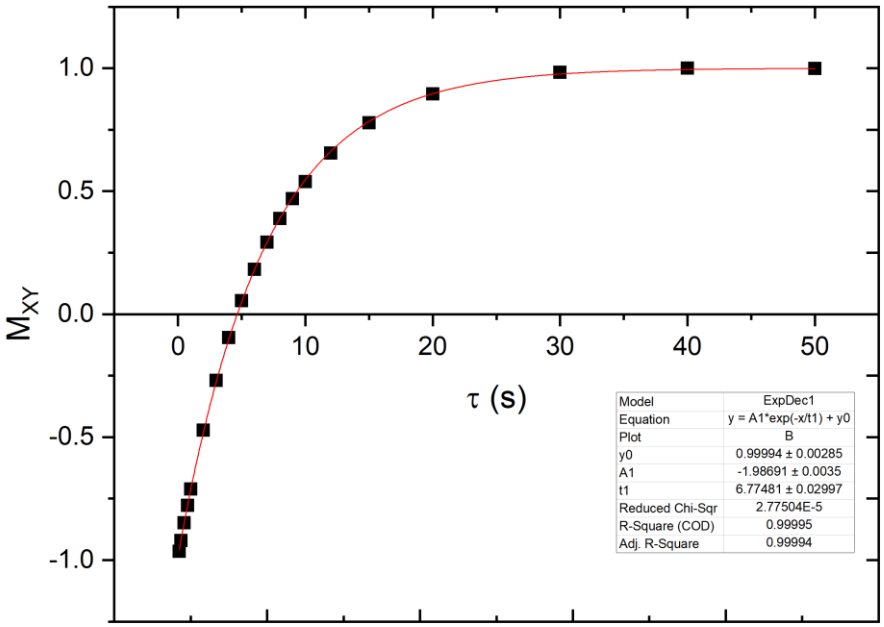

Table 51 – T_1 for 4-methoxypyridine

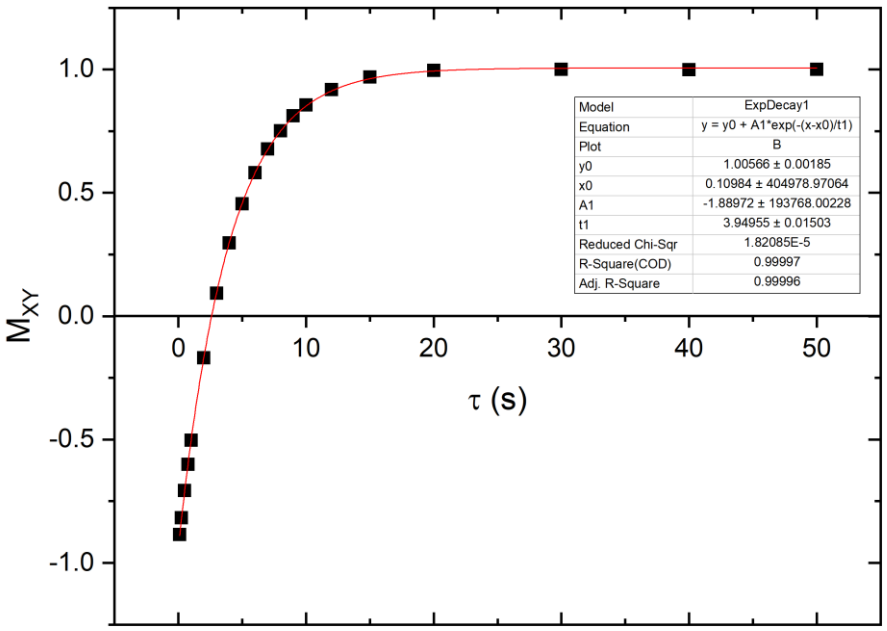

Table 52 – T_1 for 4-pyridinecarboxaldehyde

T_1 graphs at optimum SABRE temperature

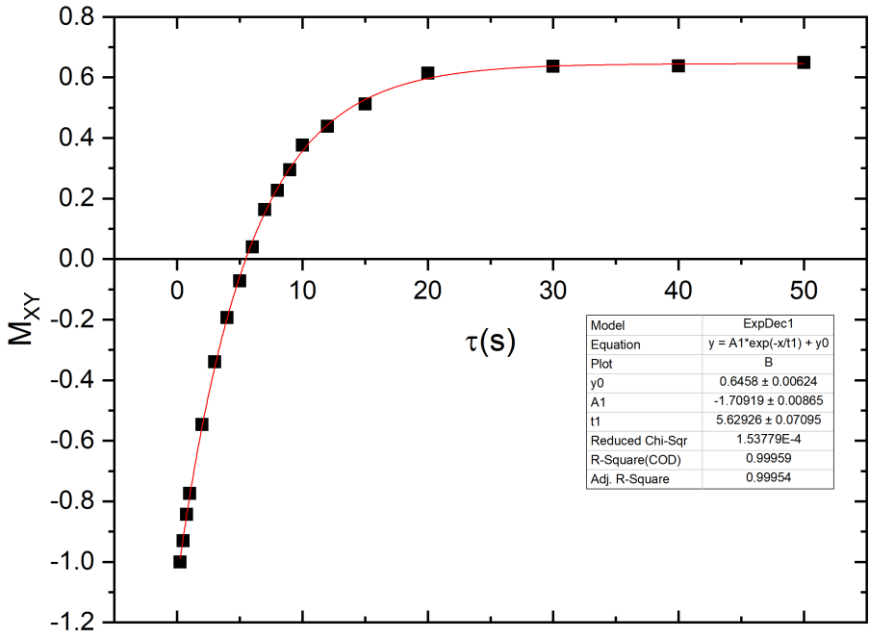

Table 53 – T_1 for 4-chloropyridine

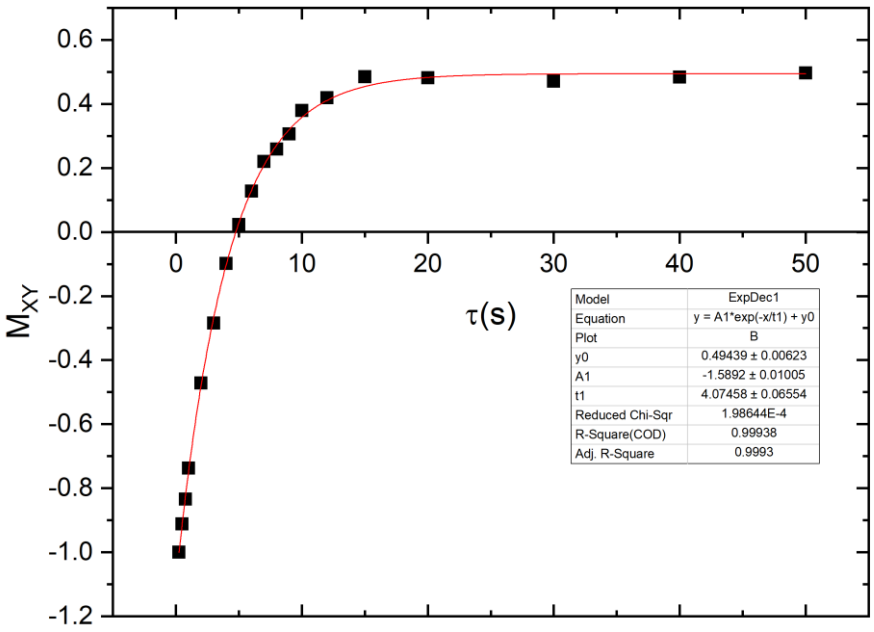

Table 54 – T_1 for 4-methylpyridine

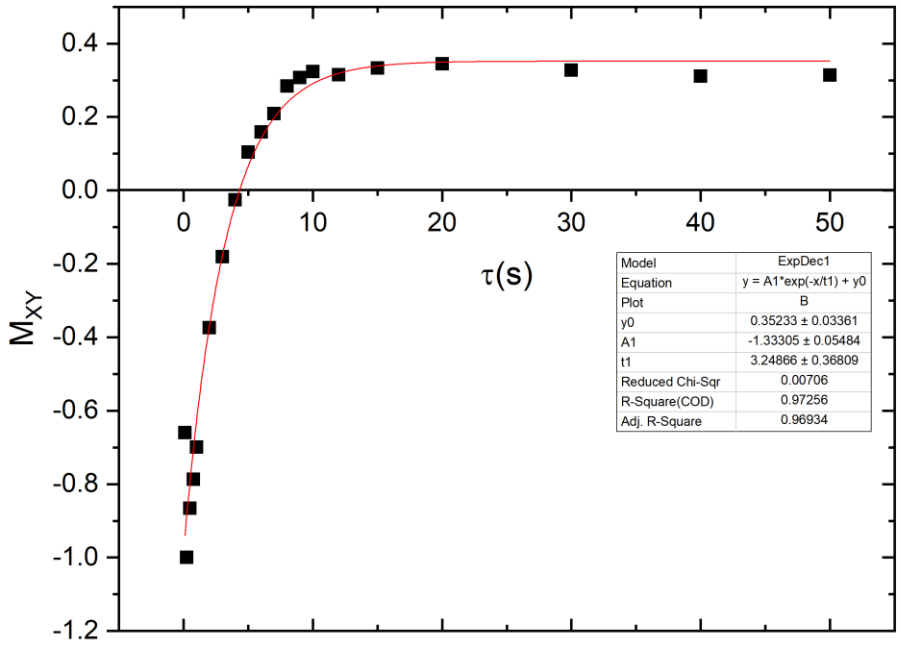

Table 55 – T_1 for 4-methoxypyridine

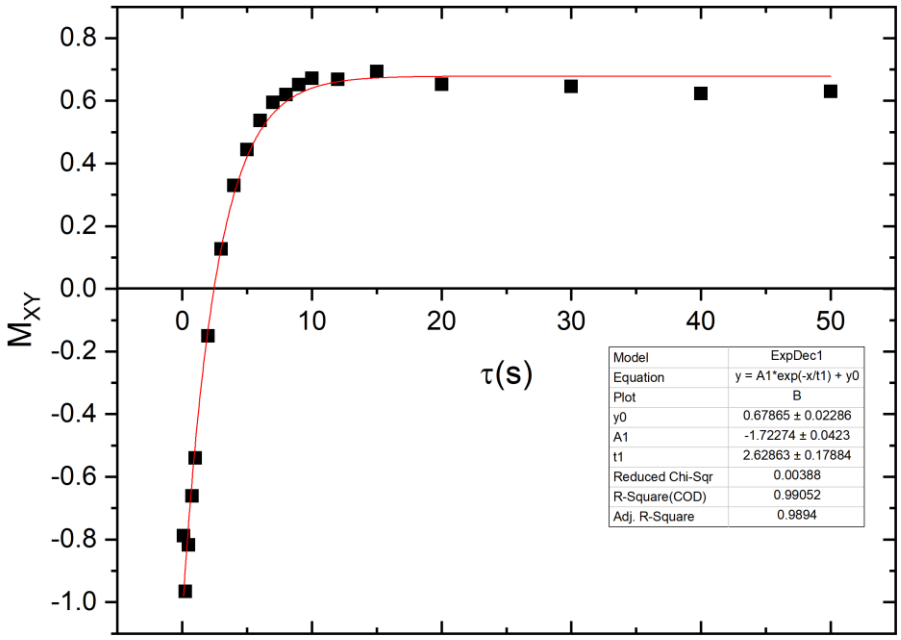

Table 56 – T_1 for 4-pyridinecarboxaldehyde

Changing the NHC for the substrates in chapter 3

Gibbs Free Energy

***p*-substitutent**	$\Delta G^{\neq}_{298K}$		
	SIMes	**ITBXy**	**IMes^{Cl}**
Cl	62.08 ± 0.008	65.64 ± 0.005	68.14 ± 0.003

Me	62.82 ± 0.008	65.43 ± 0.002	68.46 ± 0.0004
OMe	62.94 ± 0.013	65.56 ± 0.003	68.51 ± 0.001
CHO	64.45 ± 0.001	66.86 ± 0.002	69.90 ± 0.001

Table 57 – $\Delta G^{\neq}_{298K}$ for each substrate with the NHC modifications ITBXy and $IMes^{Cl}$ compared to SIMes

Relaxation Effects

ITBXy

Free Substrate *Ortho*H

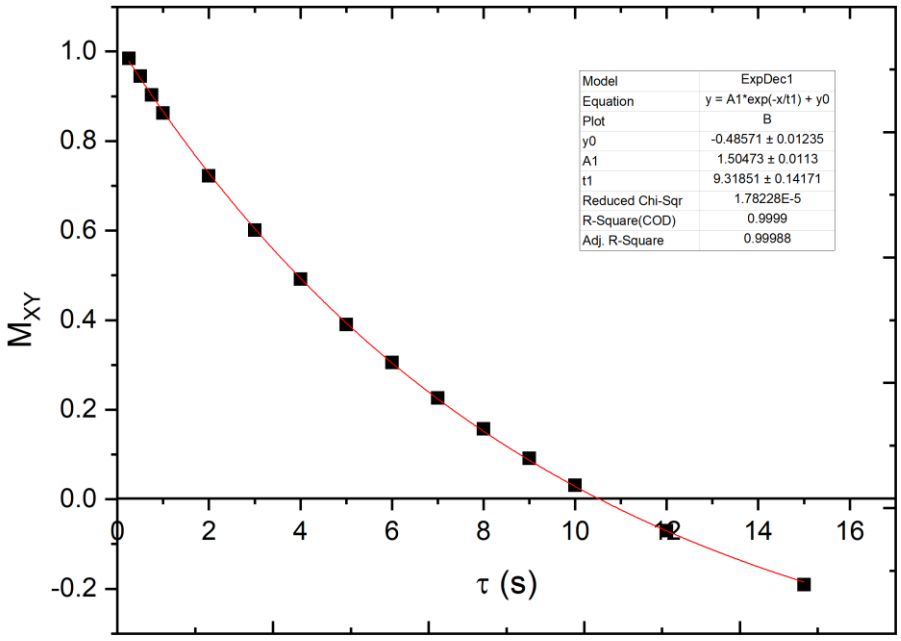

Figure 169 - T_1 for substrate 4-chloropyridine

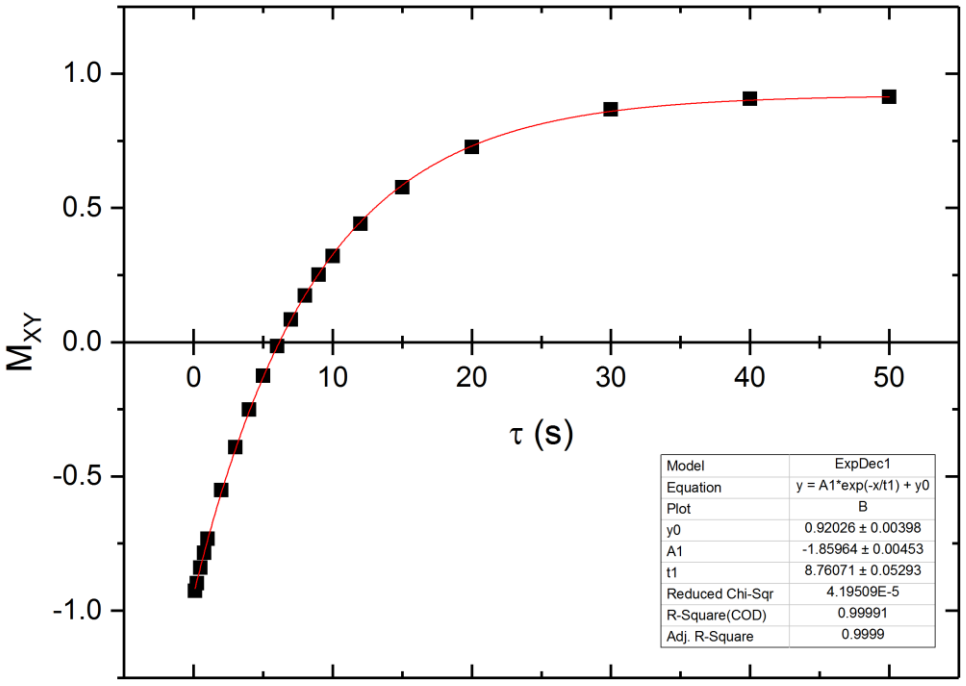

Figure 170 - T_1 for substrate 4-methylpyridine

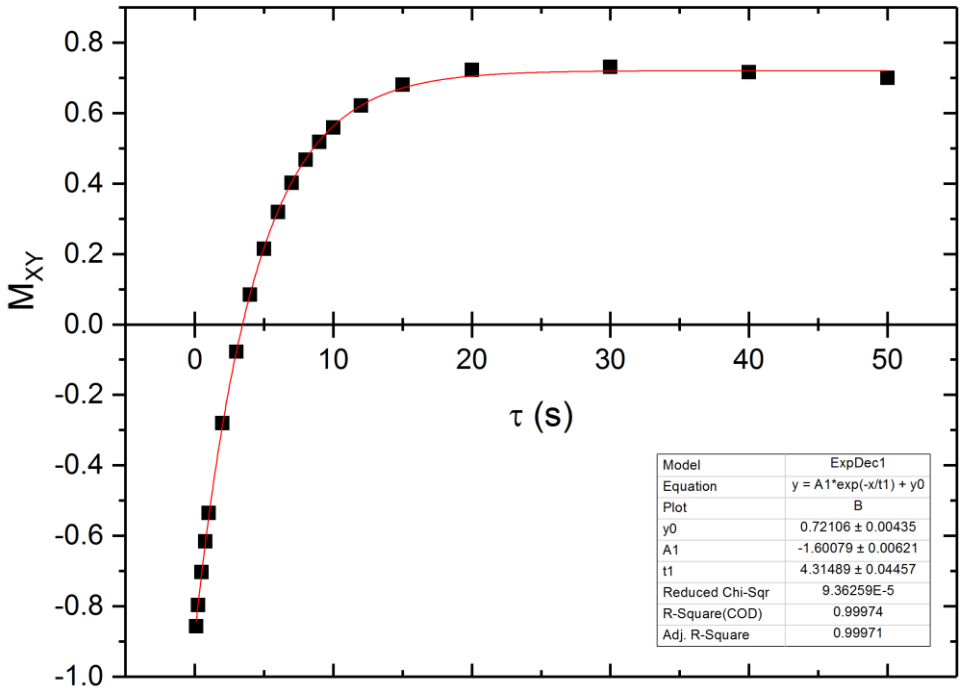

Figure 171 - T_1 for substrate 4-methoxypyridine

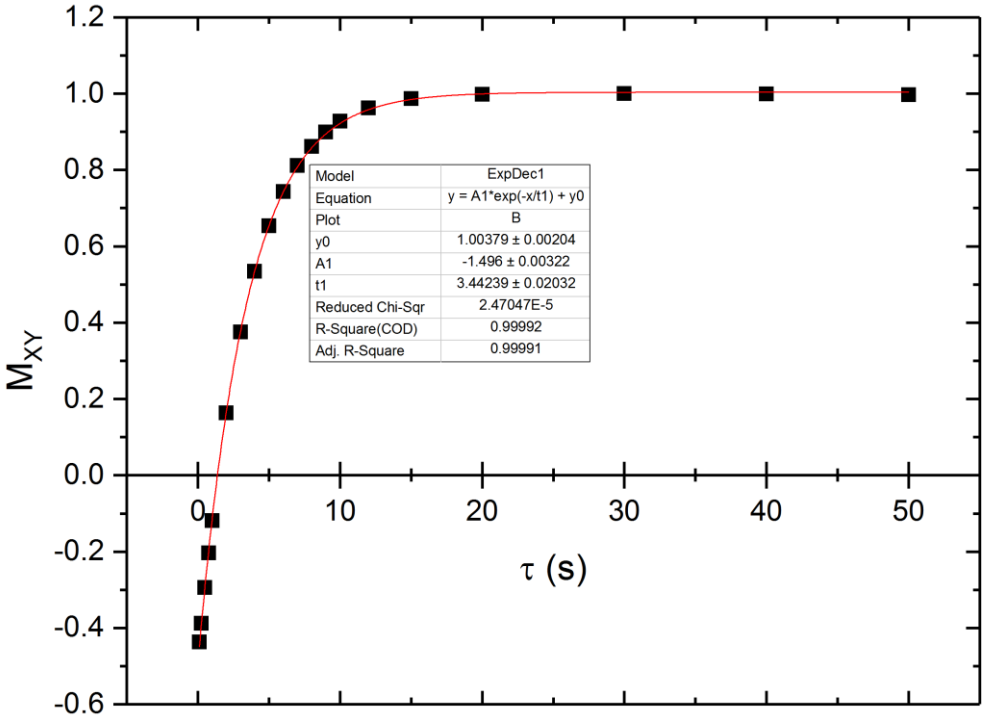

Figure 172 - T_1 for substrate 4-pyridinecarboxaldehyde

$IMes^{Cl}$

The T_1 for 4-chloropyridine was calculated using a Hyperpolarised T_1 pulse program. This is a single-shot experiment where various pulse durations are applied to the sample, yielding different flip angles. The first pulse has a small angle, with subsequent pulses having progressively larger durations. These have been calculated to provide the same signal on each acquisition in the absence of relaxation, meaning the signal decay relates to the decay of the hyperpolarised signal.

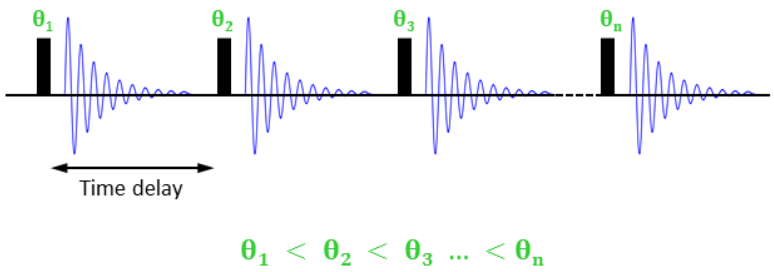

Figure 173 - A single-shot pulse sequence for measuring the lifetime of hyperpolarisation

Time is plotted against the bulk magnetisation of the system, an exponential of the form displayed in Equation 36 is applied and the T_1 is extracted. However, rather than the bulk magnetisation returning to 1 (from -1) as in normal T_1s, the bulk magnetisation for hyperpolarized T_1s instead returns to zero. In SABRE enhancements, the hyperpolarized signal is shown as negative, due to the selective population of the spin states of the proton. Therefore when the hyperpolarised T_1 is measured, the magnetisation becomes less intense as it returns back to thermal equilibrium.

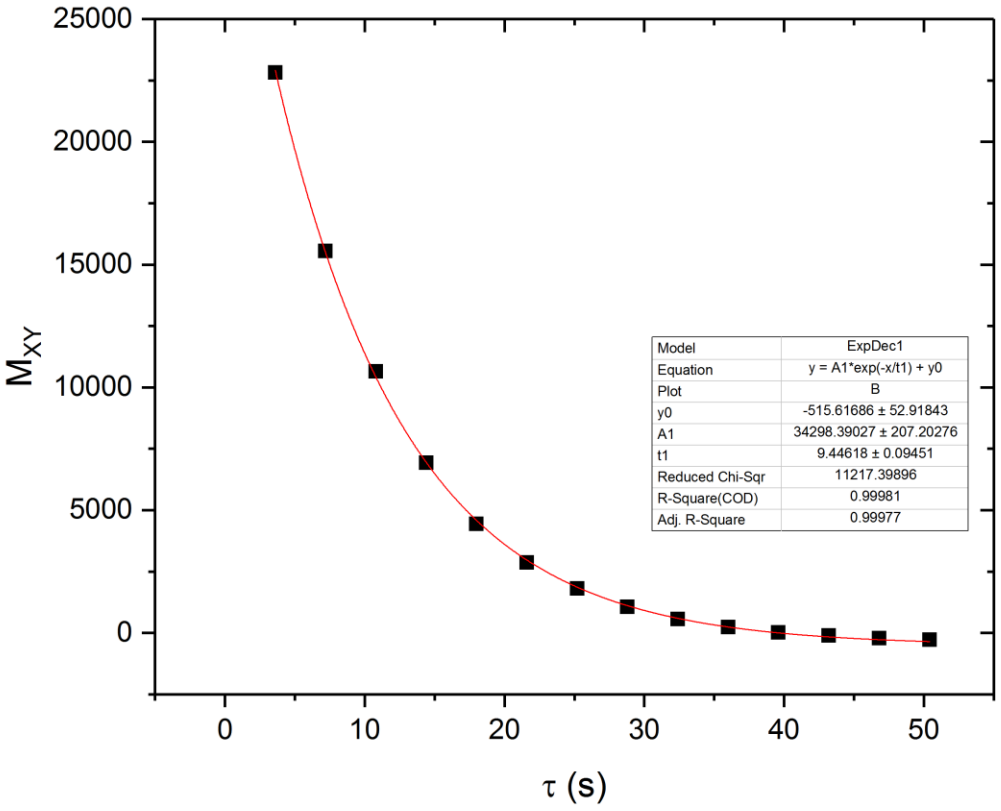

Figure 174 - Hyperpolarised T_1 for substrate 4-chloropyridine

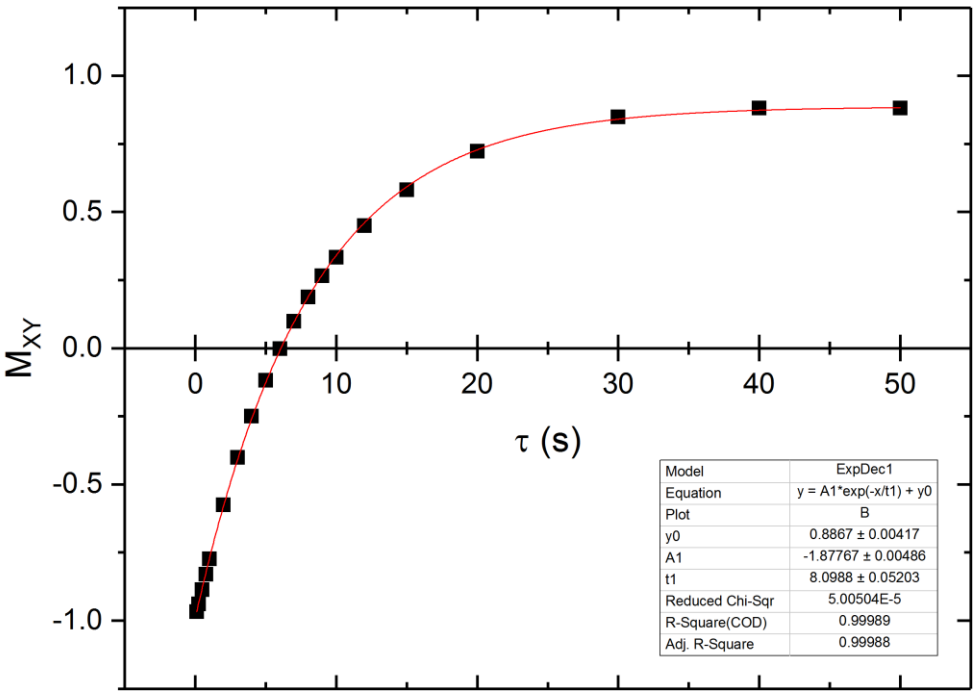

Figure 175 - T_1 for substrate 4-methylpyridine

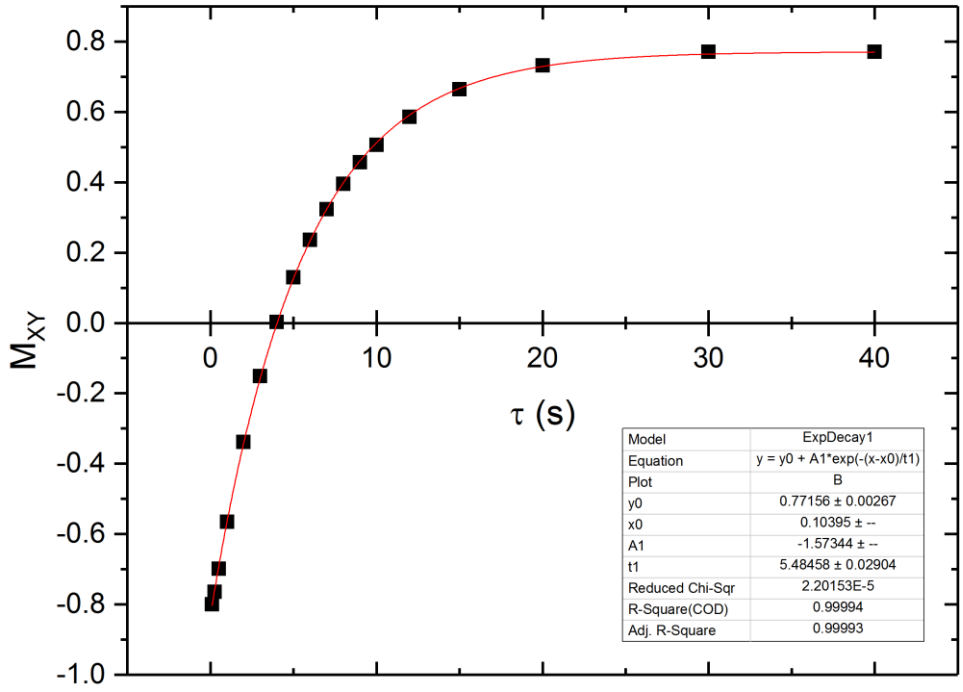

Figure 176 - T_1 for substrate 4-methoxypyridine

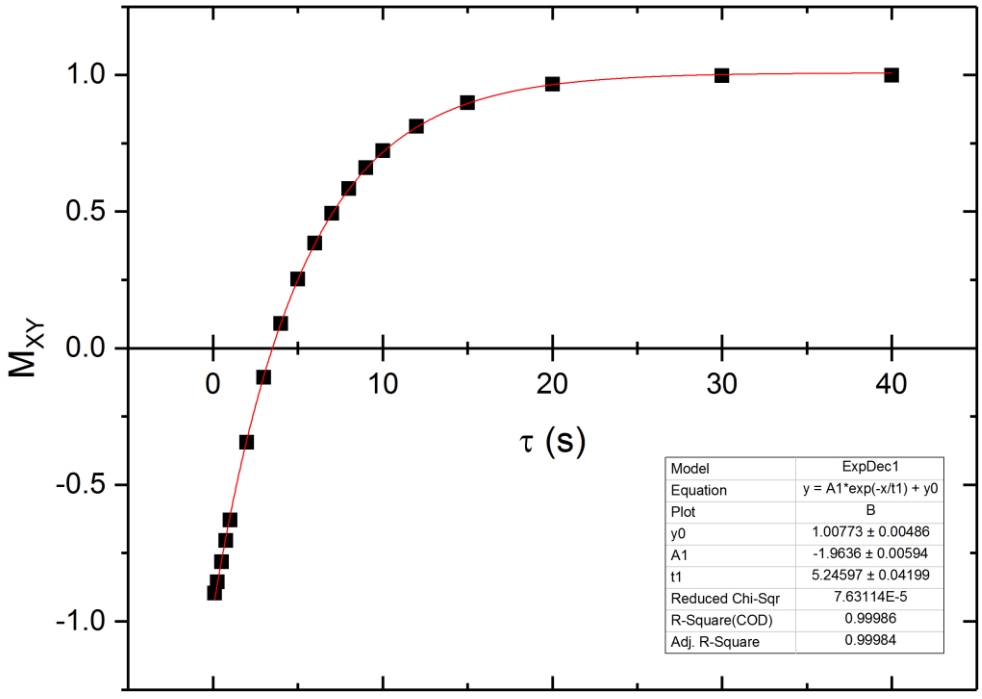

Figure 177 - T_1 for substrate 4-pyridinecarboxaldehyde

Enhancement

	OrthoH Enhancement Factor		
p-substituent	**SIMes**	**ITBXy**	**IMes^{Cl}**
Cl	-111 ± 18	-638 ± 49	-282 ± 10.17
Me	-495 ± 22	-980 ± 10	-500 ± 17
OMe	-601 ± 24	-691 ± 6	-756 ± 18
CHO	-370 ± 27	-323 ± 3	-223 ± 14

Table 58 – Table of *ortho*H enhancement factors for the different NHCs used

Appendix C

Enhancements in [IrCl(H)$_2$(SIMes)(κ-O-4-pyridone)(κ-N-4-hydroxypyridine)] and [Ir(H)$_2$(SIMes)(κ-N-isonicotinylhydrazide)(isonicotinyl-κ-O-κ-N-hydrazide]Cl

Substrate Concentration (mM)	***4-Methyl pyridine***	***4-Hydroxy pyridine***	***Isoniazid***
20	−392 ± 26	−3 ± 0.1	−231 ± 12
25	−486 ± 44	−10 ± 1	−281 ± 10
30	−721 ± 31	−15 ± 20	−696 ± 17
40	−891 ± 18	−20 ± 3	−538 ± 10
50	−338 ± 61	−31 ± 1	−174 ± 8
100	−269 ± 23	−18 ± 1	−159 ± 3

Figure 178 - *ortho*H enhancement factor for different substrate concentrations for the substrates in Chapter 4

Diffusion Ordered Spectroscopy in [Ir(H)$_2$(SIMes)(4-methylpyridine)$_3$]Cl, [IrCl(H)$_2$(SIMes)(κ-O-4-pyridone)(κ-N-4-hydroxypyridine)] and [Ir(H)$_2$(SIMes)(κ-N-isonicotinylhydrazide)(isonicotinyl-κ-O-κ-N-hydrazide]Cl

[Ir(H)$_2$(SIMes)(4-methylpyridine)$_3$]Cl

298K

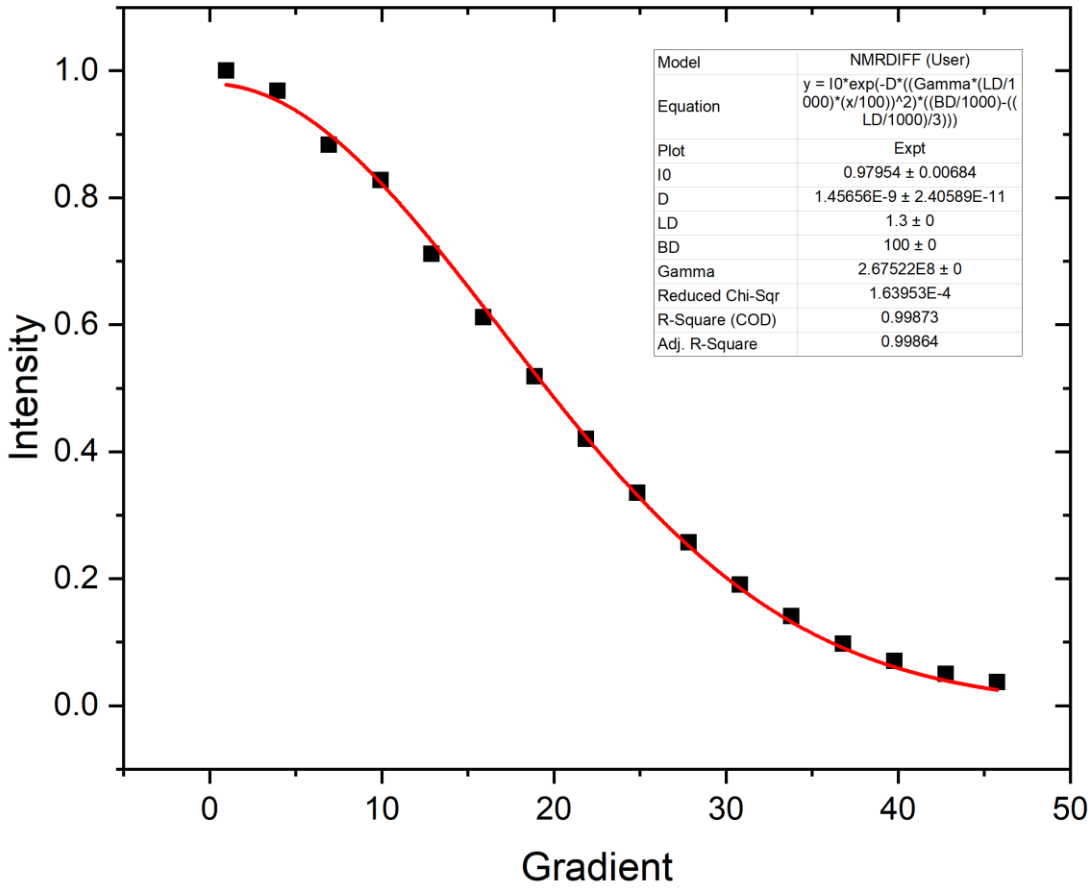

Figure 179 - Free substrate

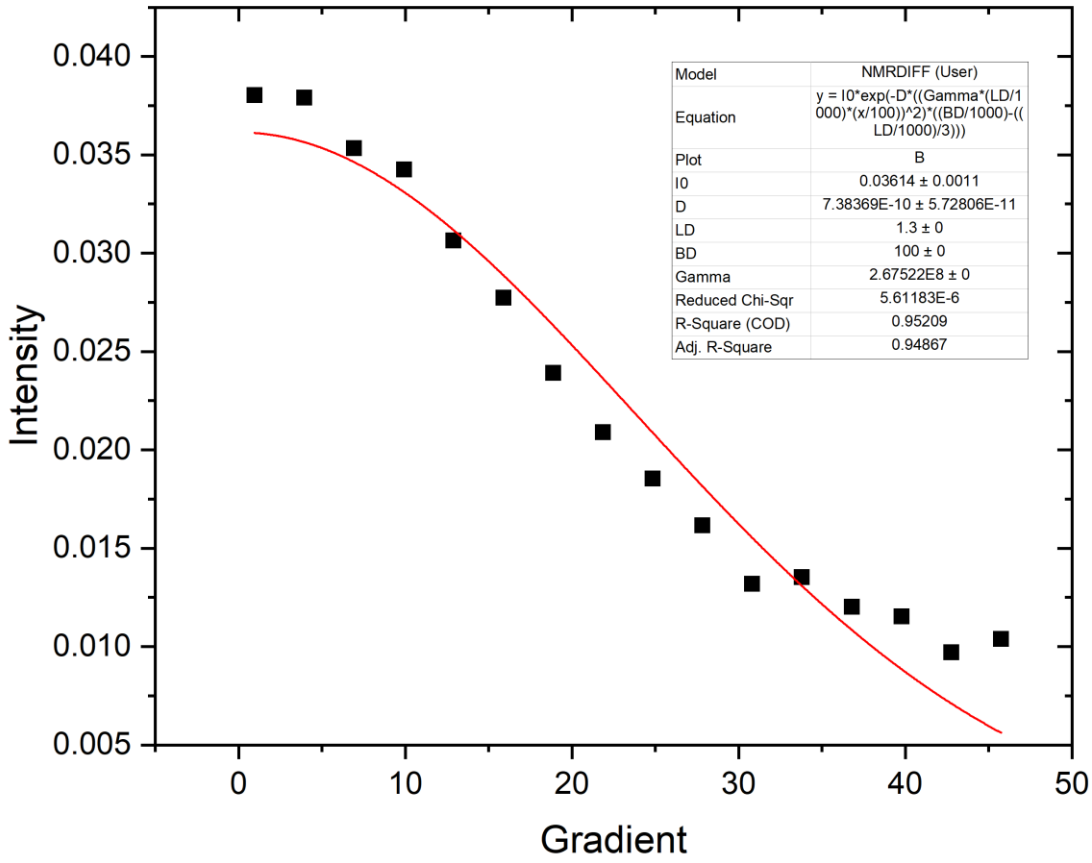

Figure 180 - *Trans* to H^-

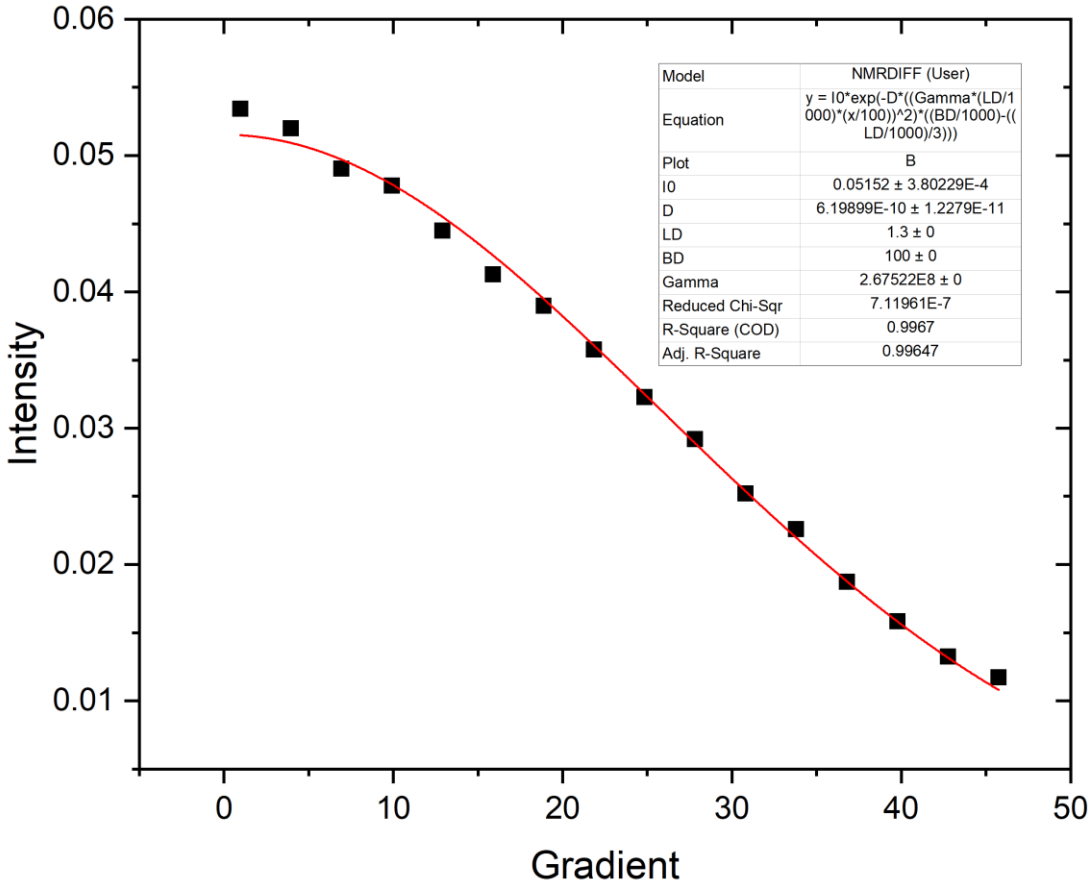

Figure 181 - *Trans* to NHC

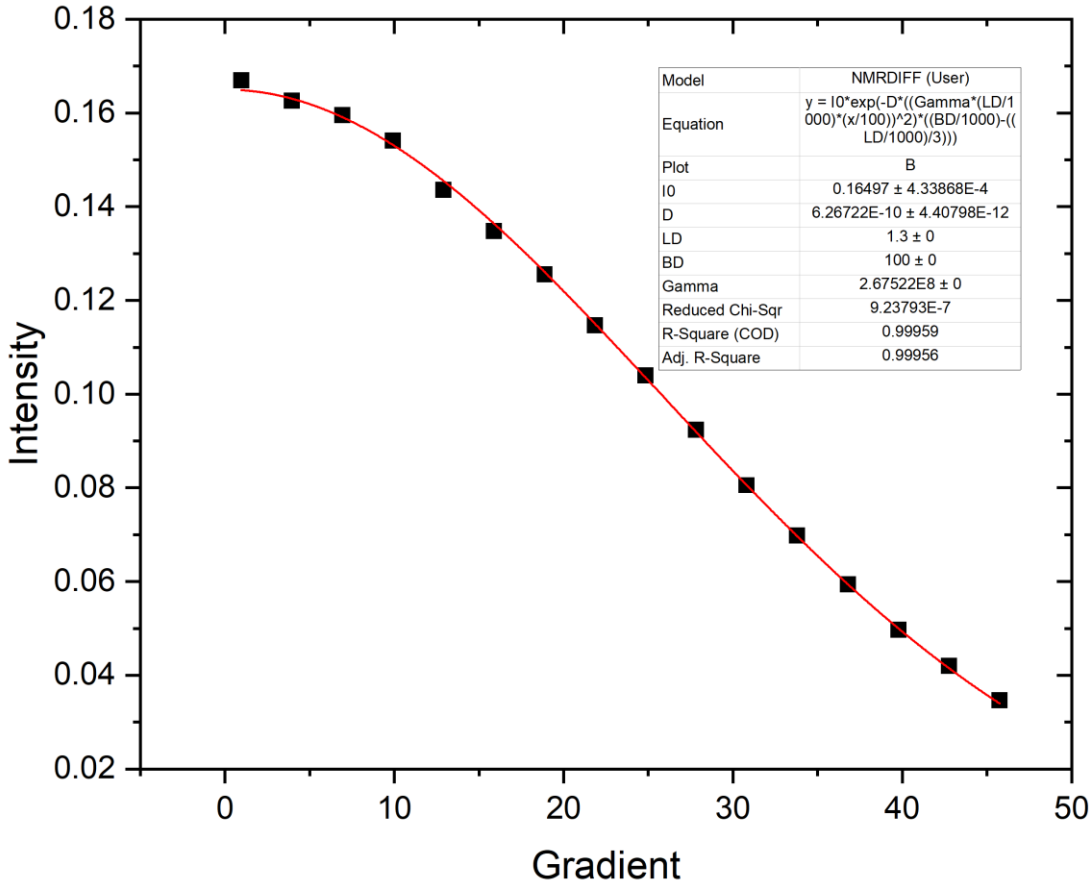

Figure 182 – SIMes

273K

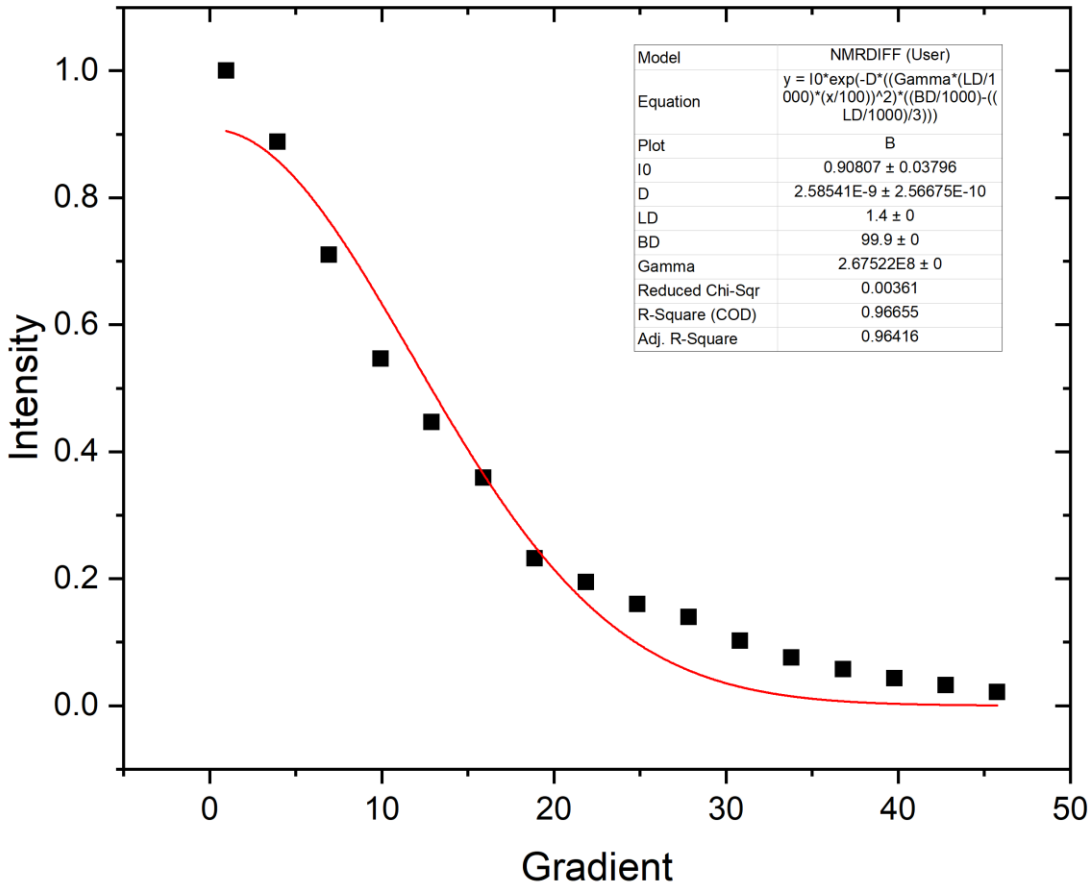

Figure 183 - Free substrate

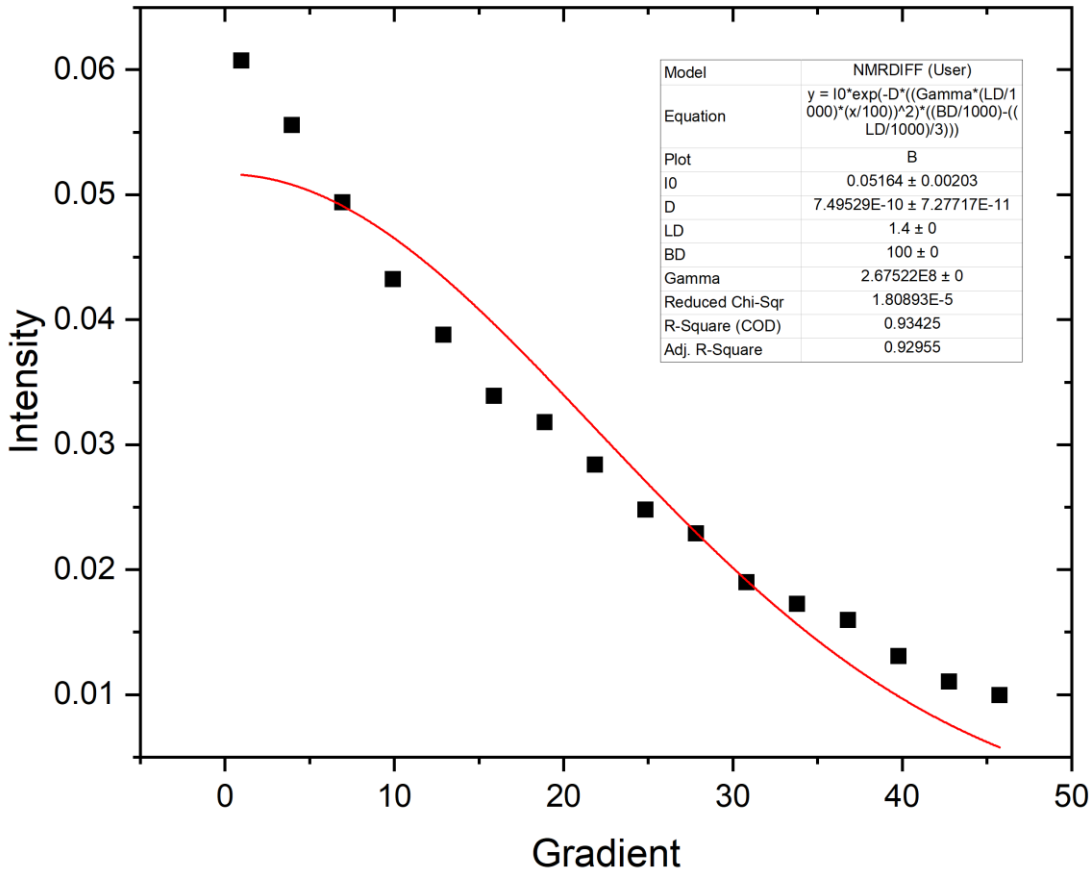

Figure 184 - *Trans* to H^-

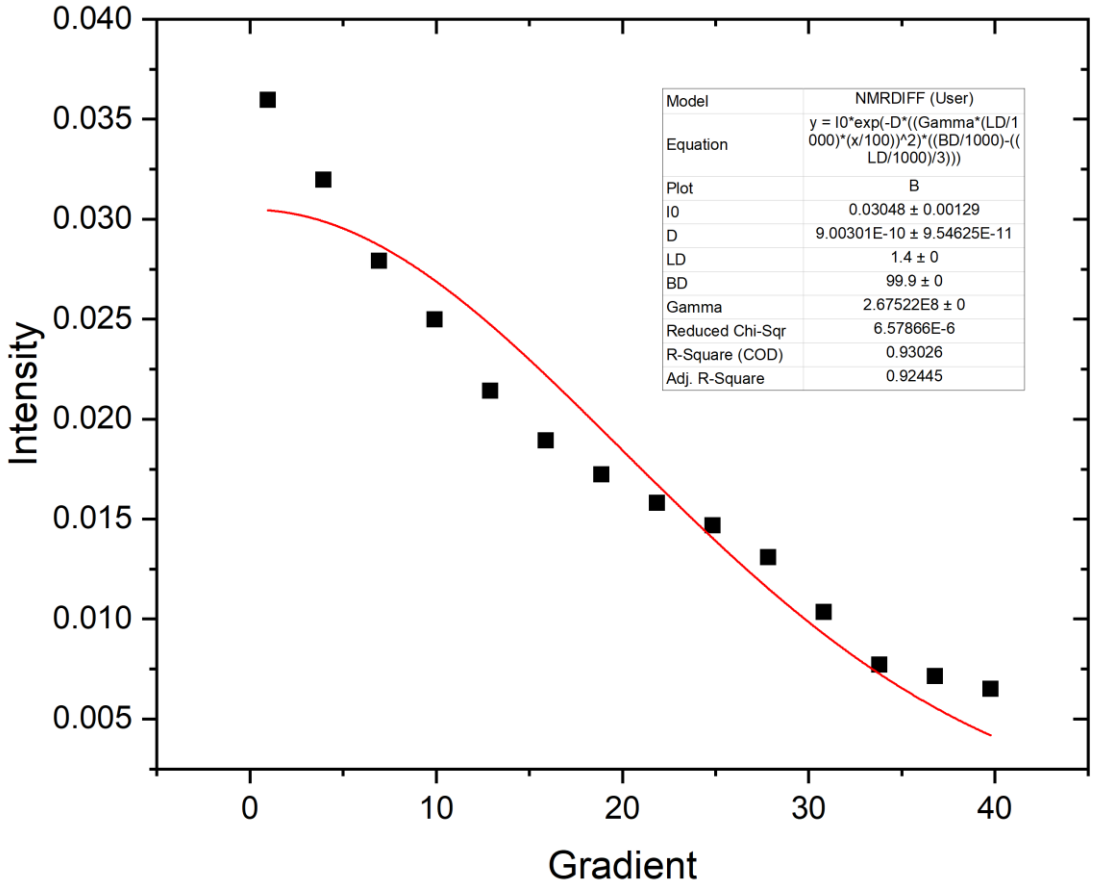

Figure 185 - *Trans* to NHC

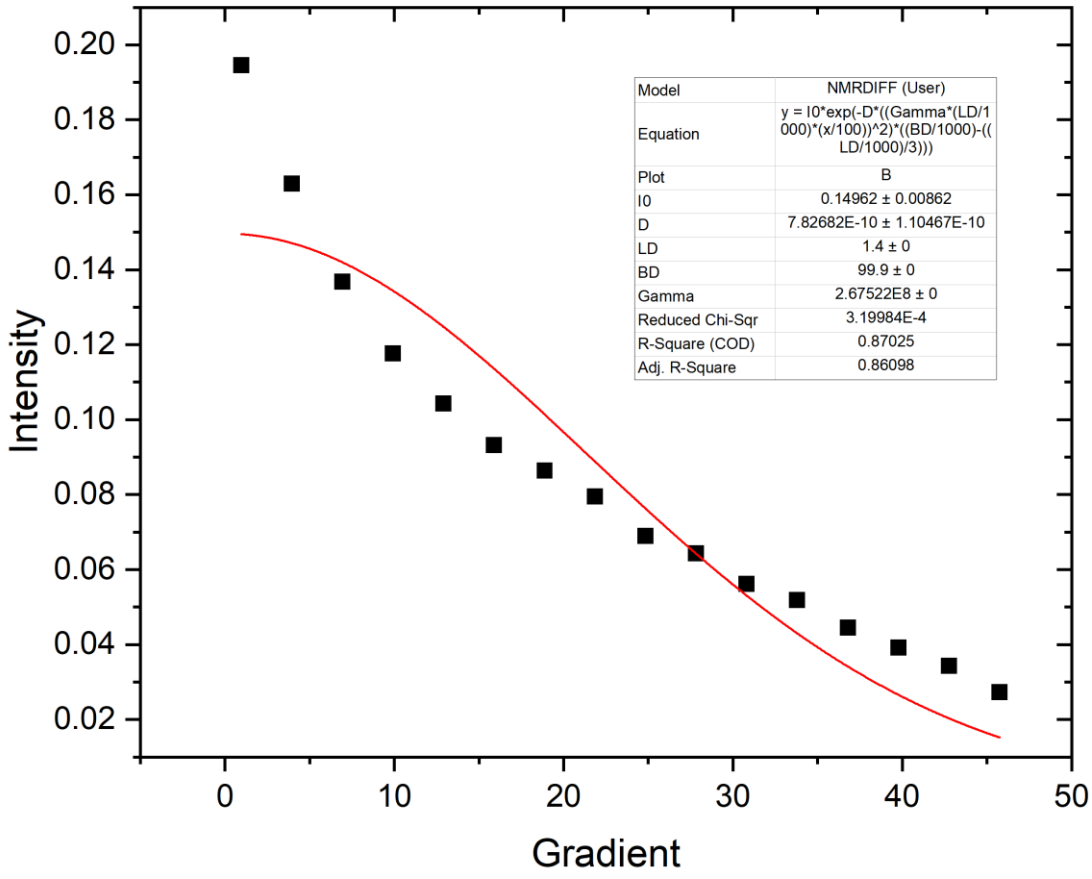

Figure 186 – SIMes

[IrCl(H)$_2$(SIMes)(κ-O-4-pyridone)(κ-N-4-hydroxypyridine)]

298K

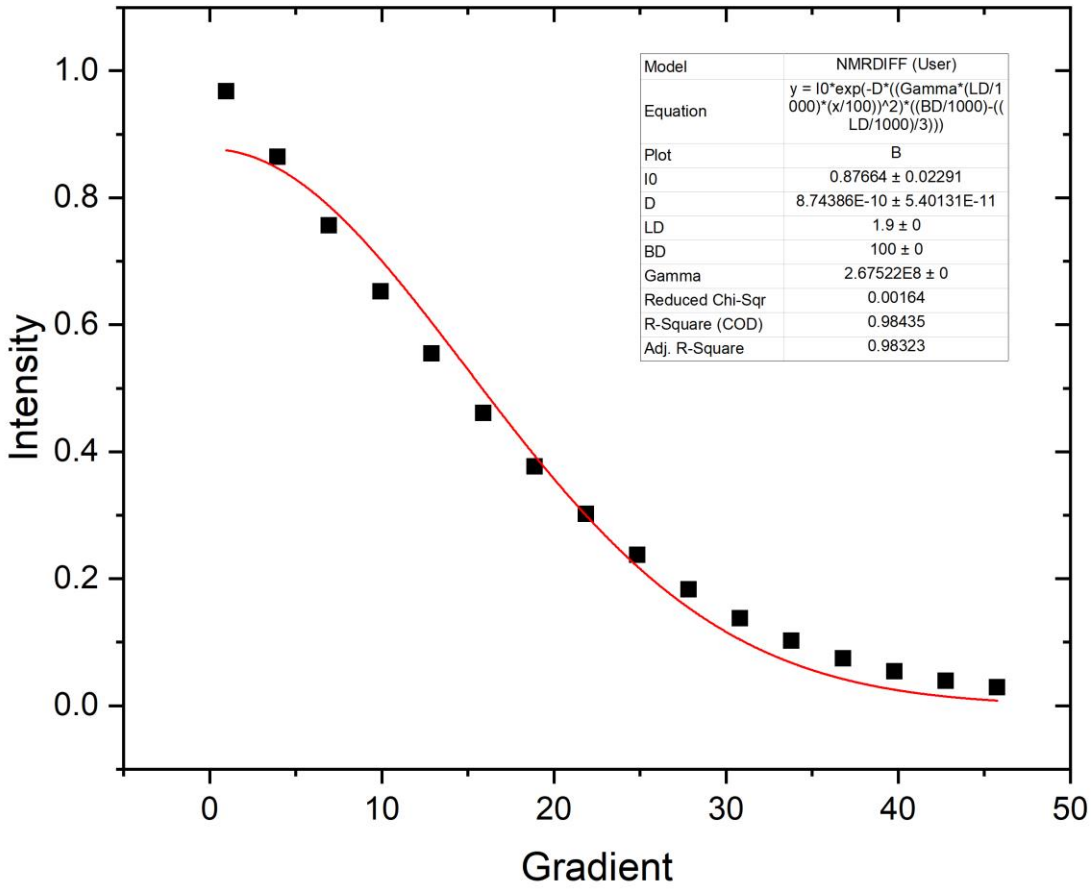

Figure 187 - Free Substrate

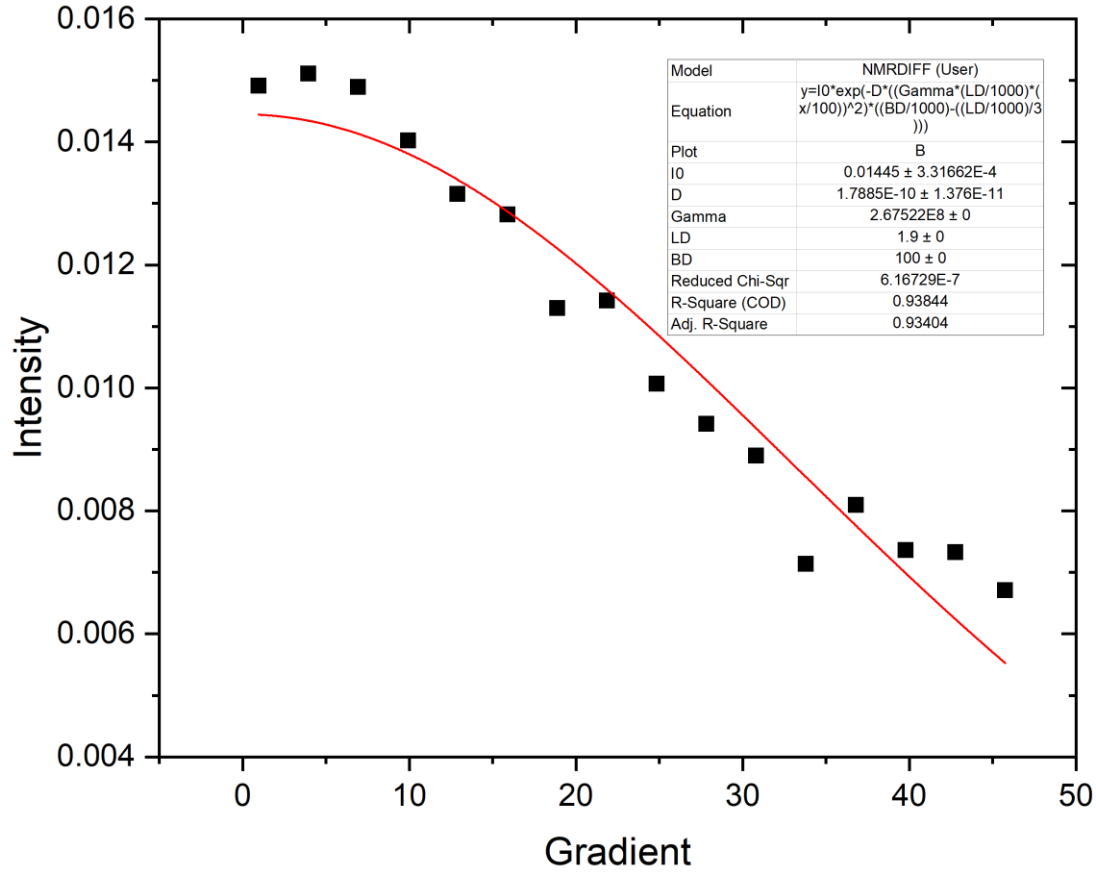

Figure 188 – SIMes

253K

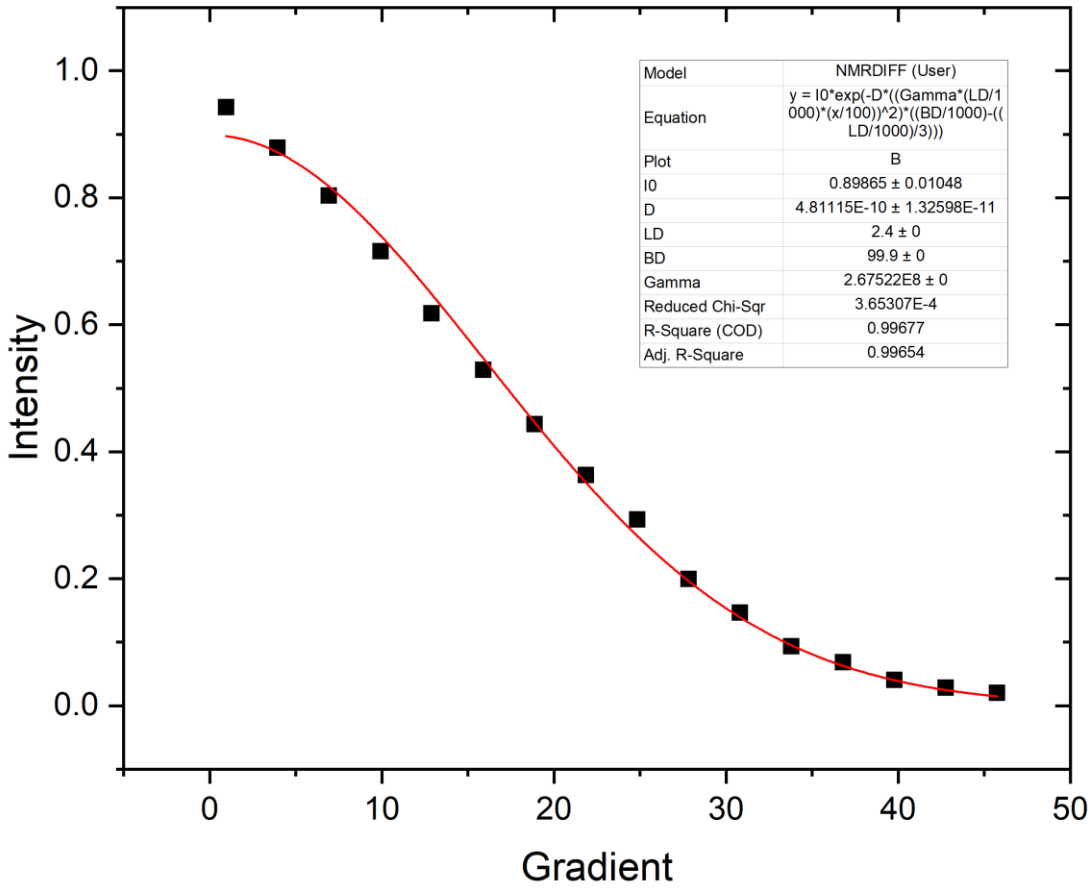

Figure 189 - Free substrate

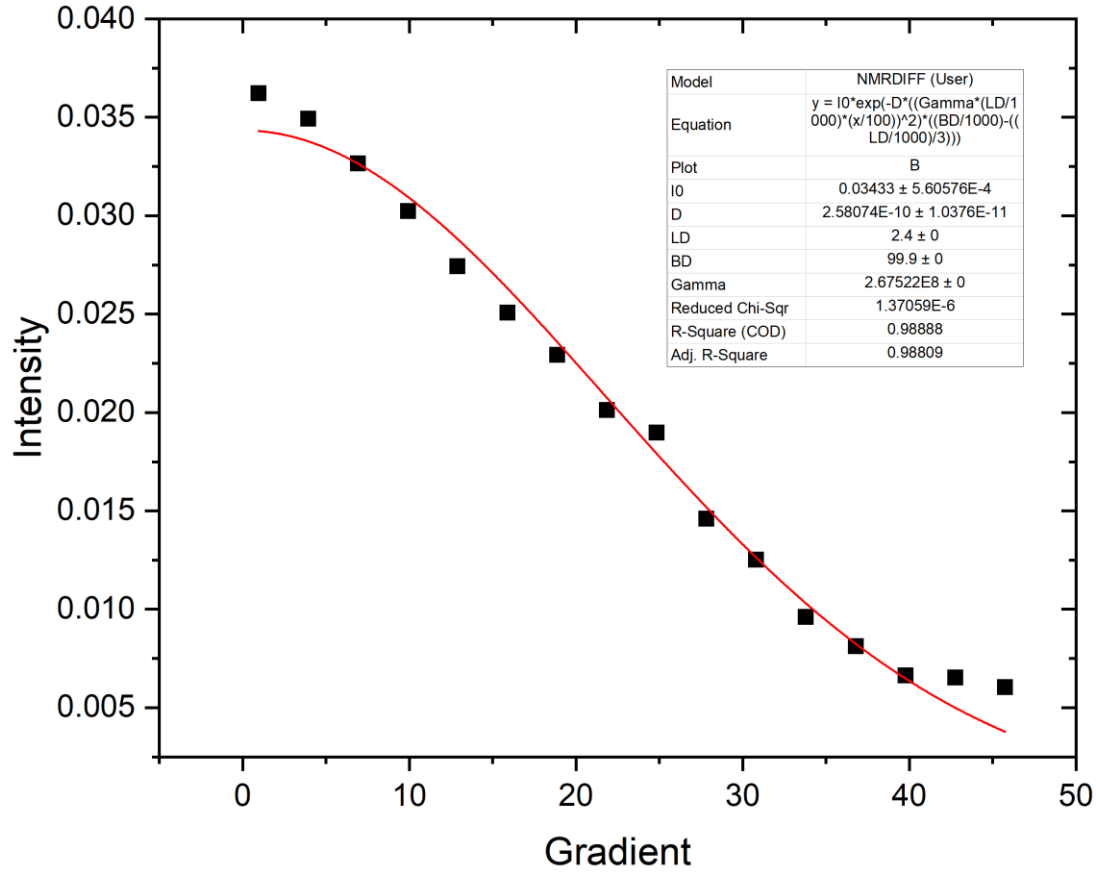

Figure 190 - Nitrogen bound substrate

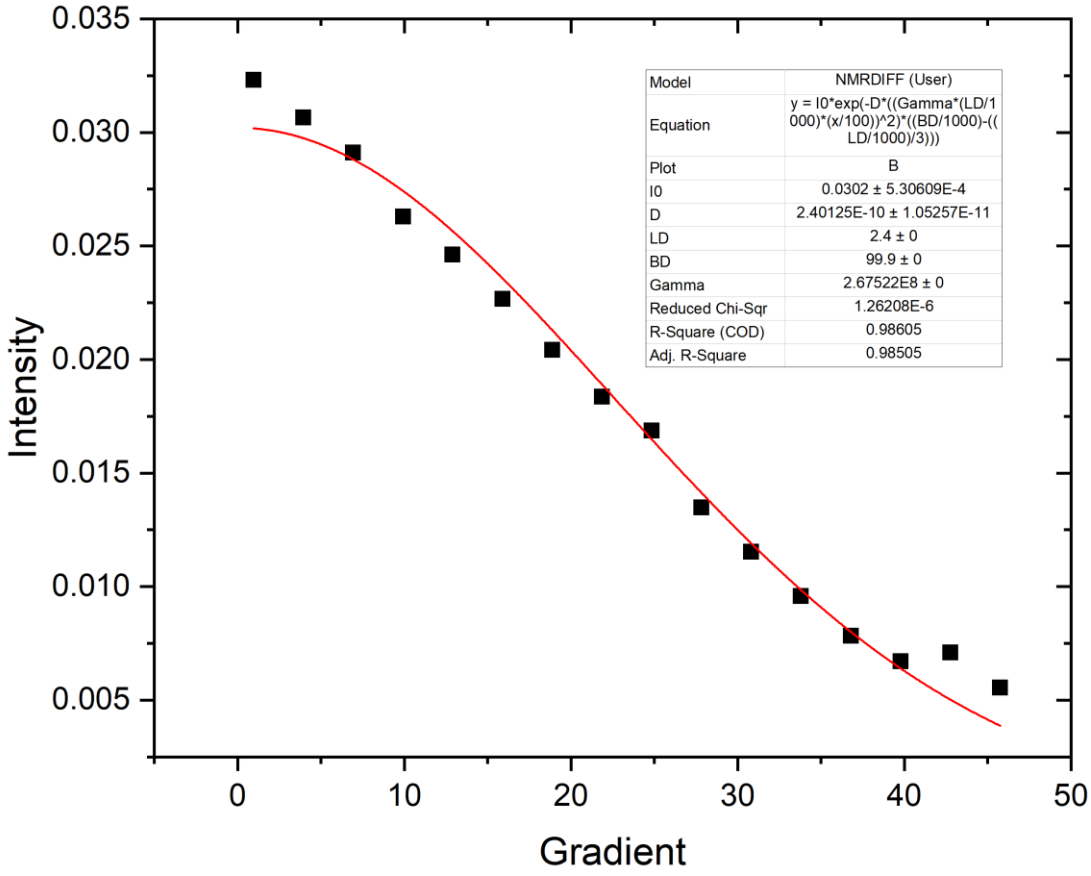

Figure 191 - Oxygen bound substrate

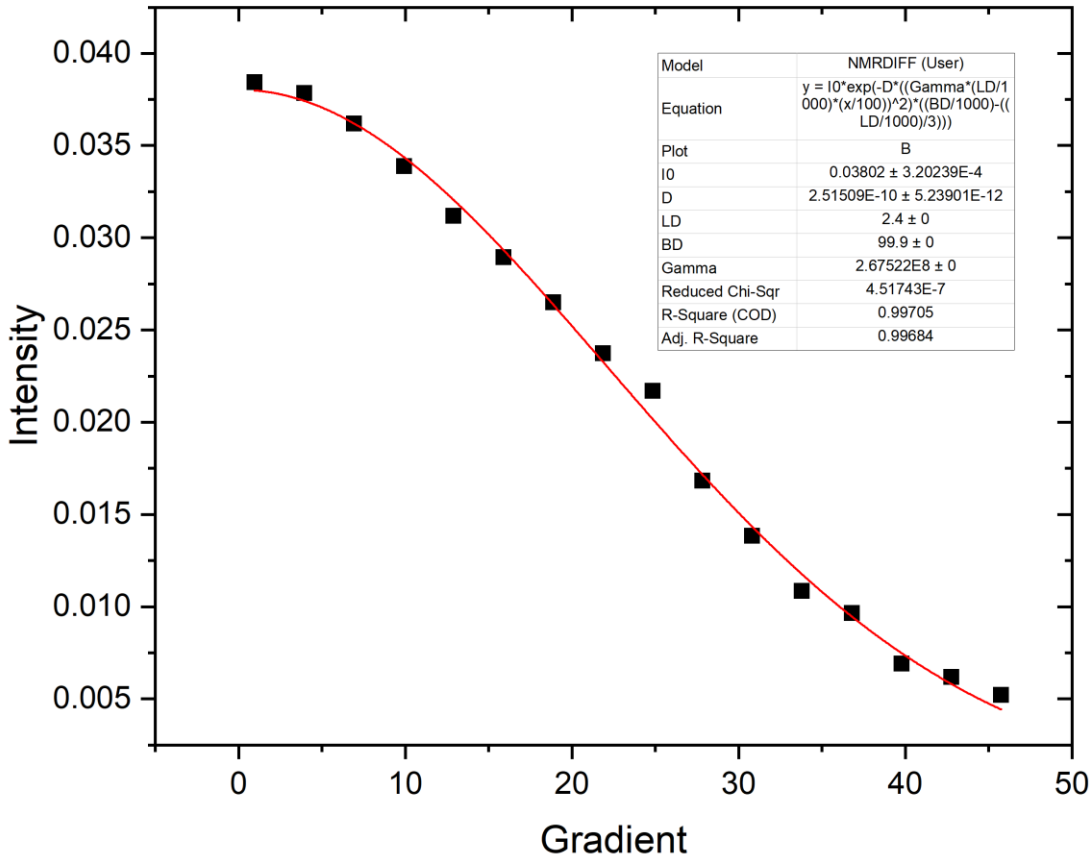

Figure 192 – SIMes

$[Ir(H)_2(SIMes)(\kappa\text{-N-isonicotinylhydrazide})(\text{isonicotinyl-}\kappa\text{-O-}\kappa\text{-N-hydrazide})]Cl$

298K

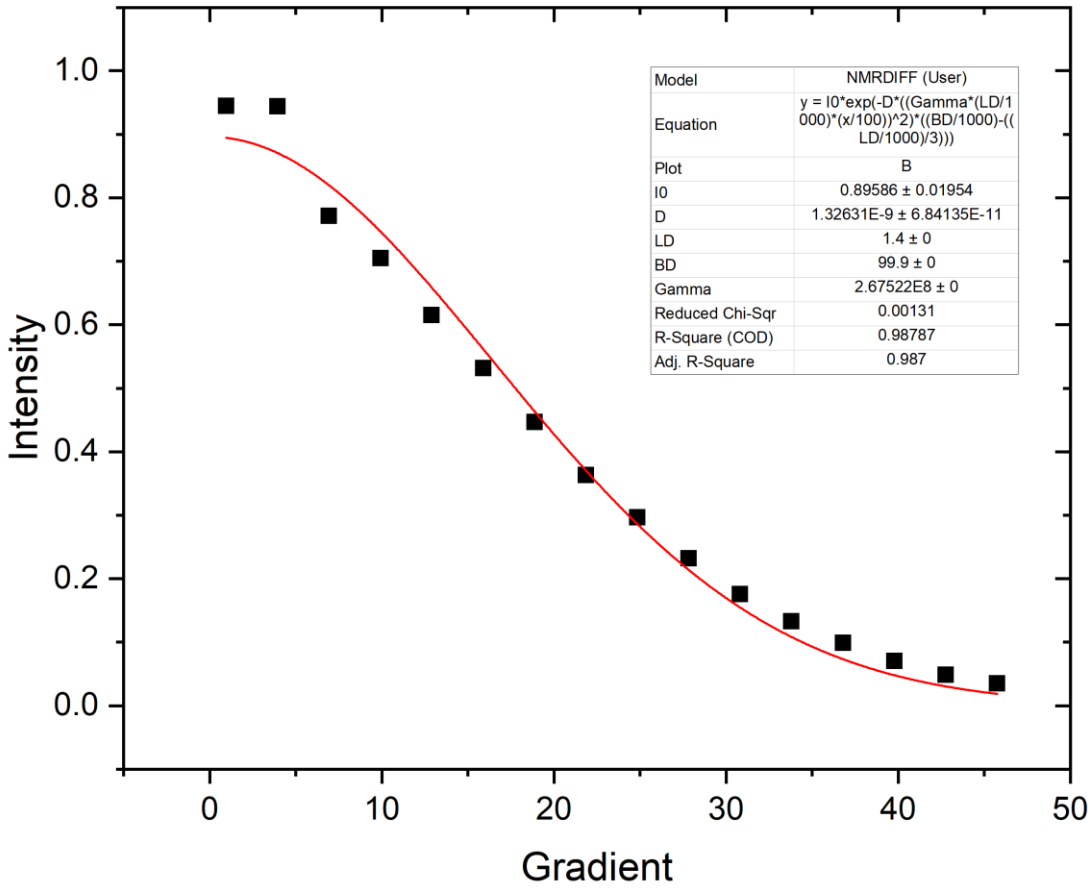

Figure 193 - Free substrate

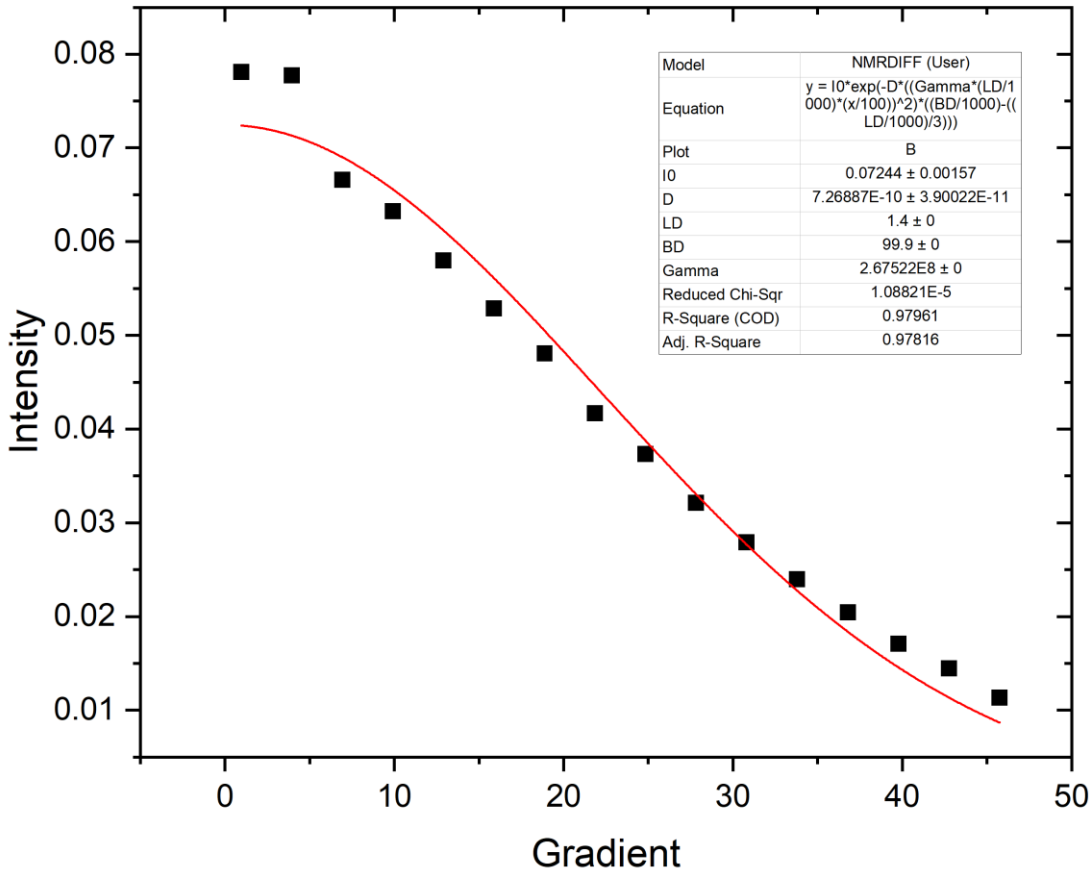

Figure 194 - Chelate bound substrate

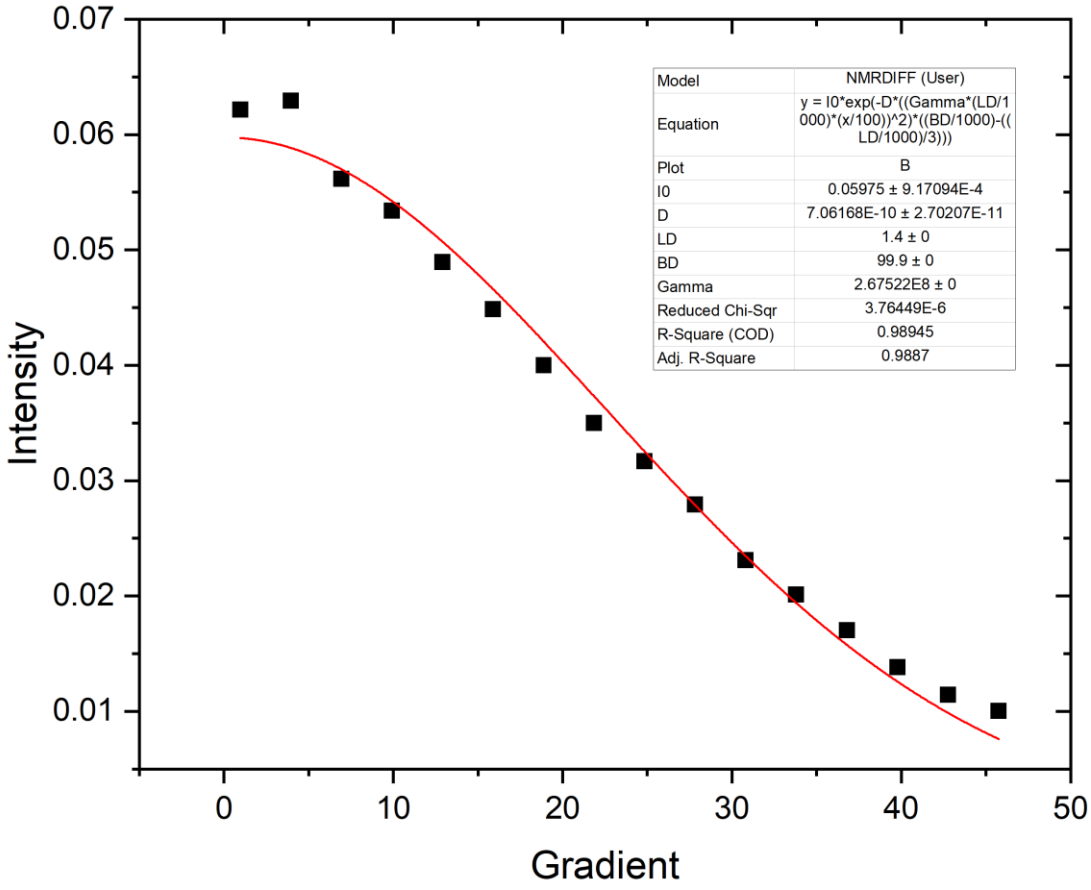

Figure 195 - Pyridine bound substrate

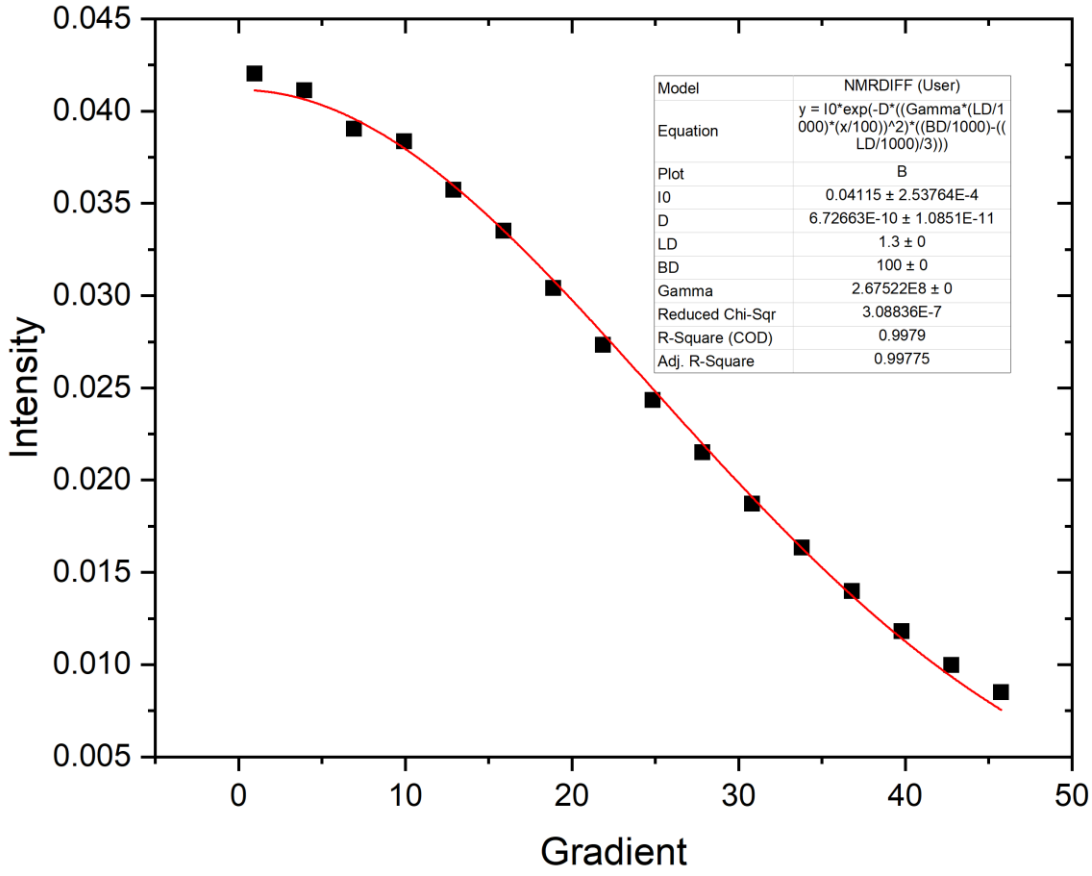

Figure 196 - SIMes

Exchange in [IrCl(H)$_2$(SIMes)(κ-O-4-pyridone)(κ-N-4-hydroxypyridine)] and [Ir(H)$_2$(SIMes)(κ-N-isonicotinylhydrazide)(isonicotinyl-κ-O-κ-N-hydrazide]Cl

Figure 197 - dissociation constant (k_d)

Temp (K)	*Me*	*Std Error*	*Isoniazid*	*Std Error*	*OH*	*Std Error*
240					0.31477	0.00185
245					0.74035	0.00133
250					1.49719	0.00303
255	0.08208	3.91E-04			2.72426	0.01754
260	0.18724	7.85E-04			5.46654	0.01537
265	0.40524	0.00149			9.82456	0.01636
270	0.75415	0.00153			18.31049	0.18583
275	1.51458	0.00309				
280	2.60901	0.00271	0.04149	1.79E-04		
285	6.6854	0.00367	0.08381	4.01E-04		
290	13.37759	0.02313	0.17248	3.72E-04		

295	21.89506	0.20378	0.31892	5.61E-04
300			0.6143	0.00152

Figure 198 - dissociation constant (k_d) and associated errors calculated using the Jackknife method for the substrates in Chapter 4

Relaxation Effects in $[IrCl(H)_2(SIMes)(4\text{-hydroxypyridine})_2]$ and $[Ir(H)_2(SIMes)(Isoniazid)_2]Cl$

Free Substrate (no catalyst)

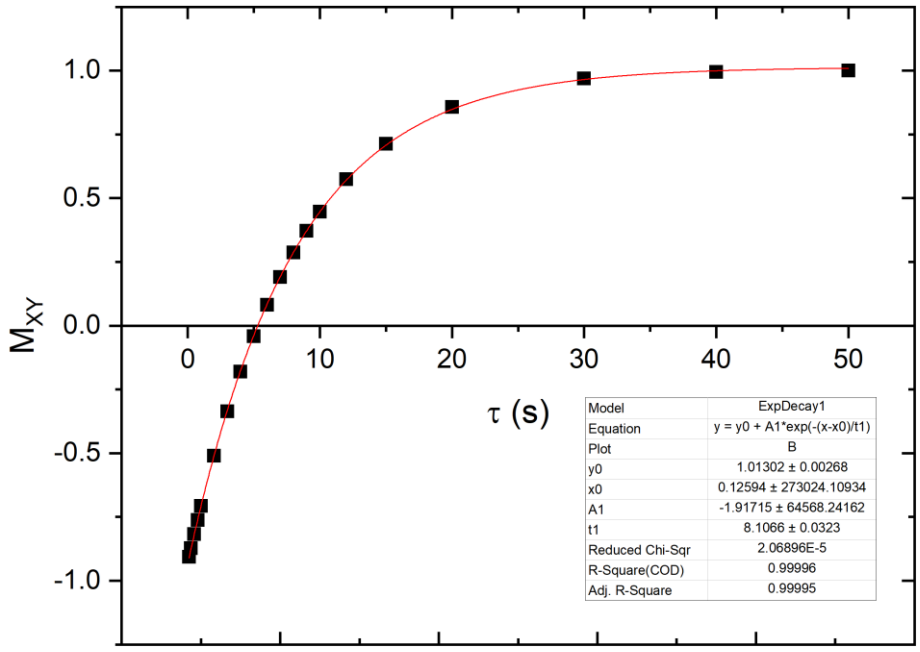

Figure 199 - 4-hydroxypyridine

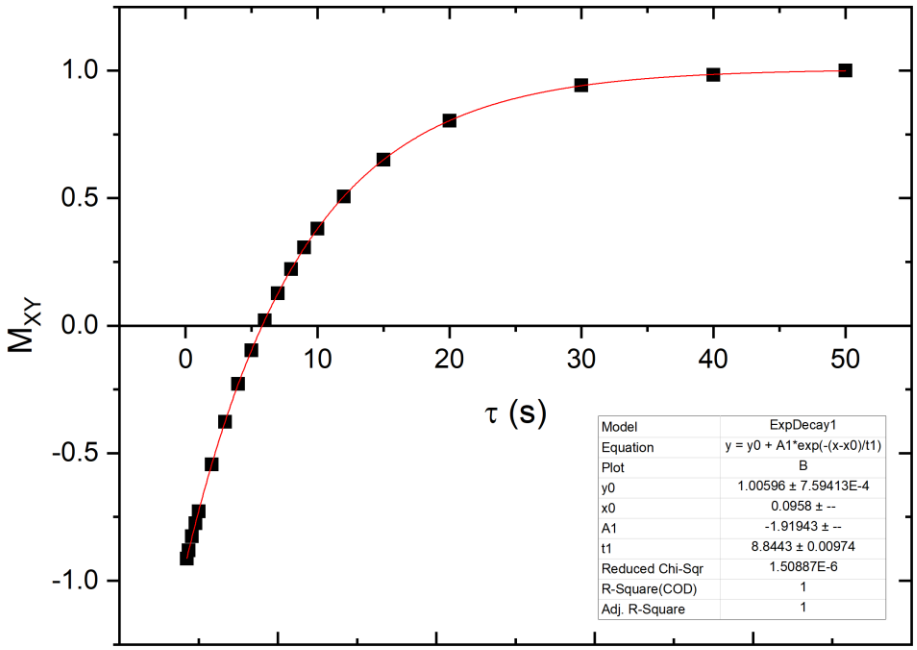

Figure 200 - isoniazid

Free Substrate

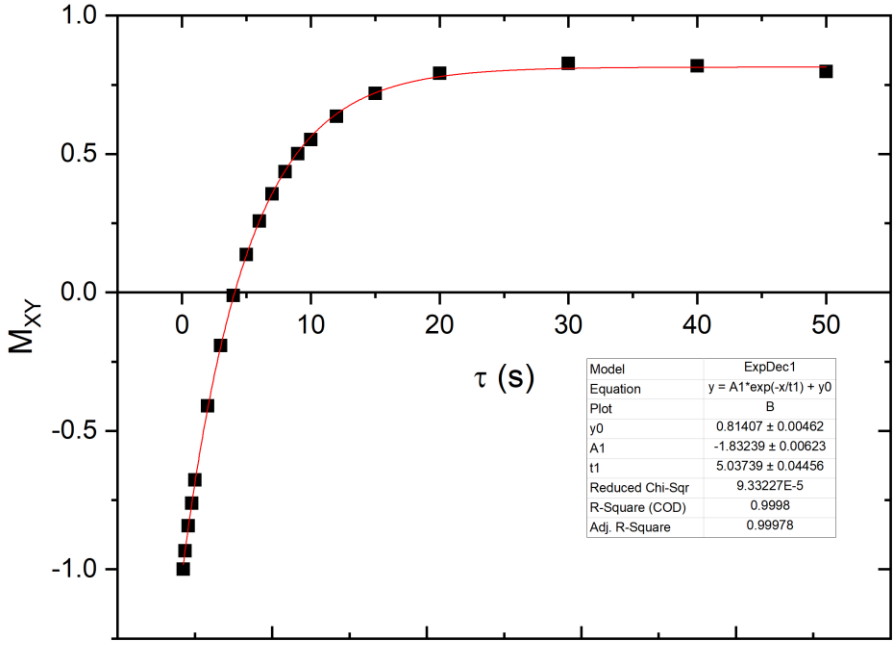

Figure 201 - 4-hydroxypyridine

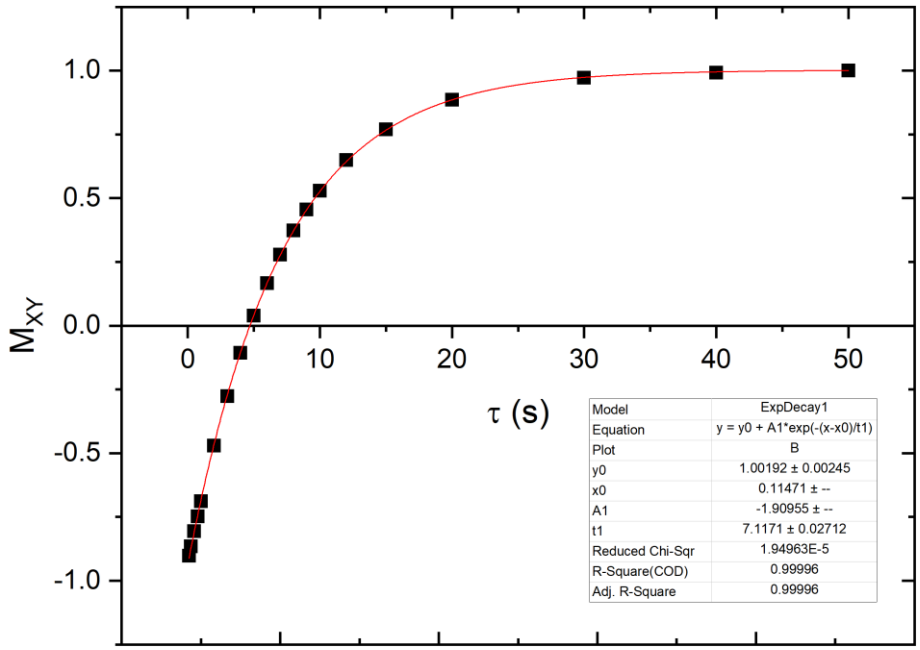

Figure 202 - isoniazid

Bound Substrate *Trans* to Hydride

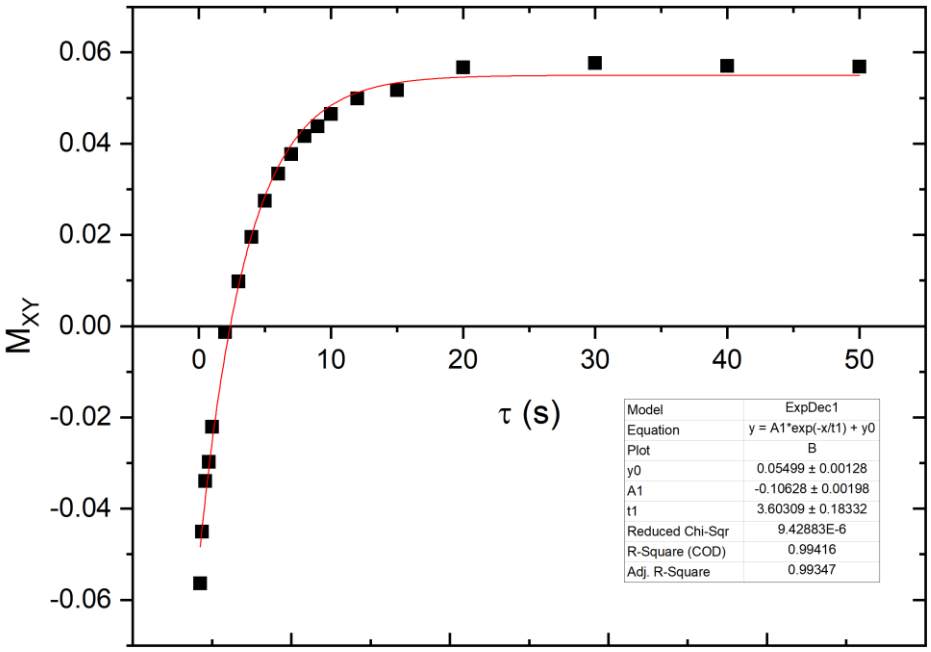

Figure 203 - 4-hydroxypyridine (oxygen bound)

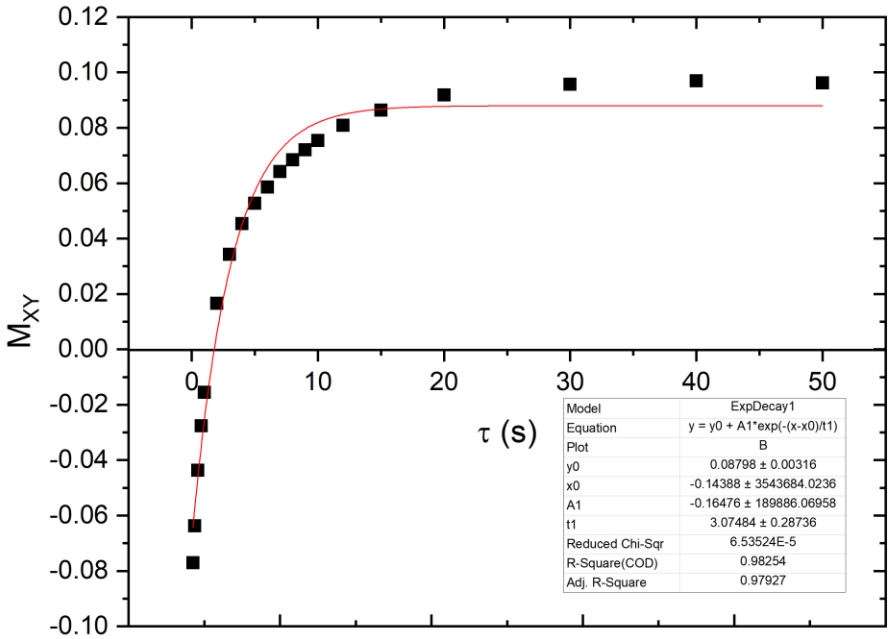

Figure 204 - isoniazid (nitrogen bound)

Bound Substrate *Trans* to NHC

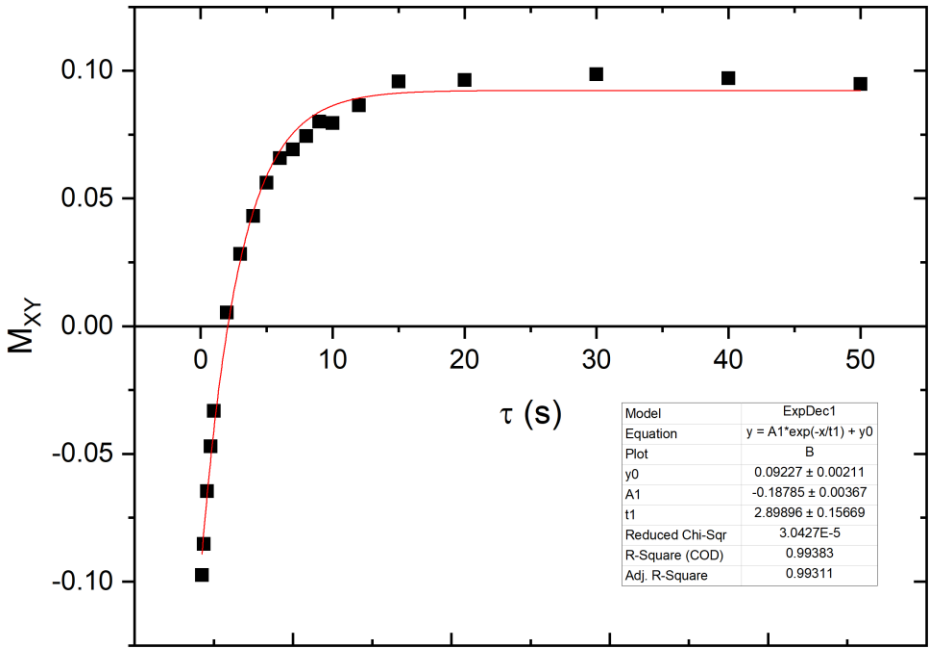

Figure 205 - 4-hydroxypyridine (nitrogen bound)

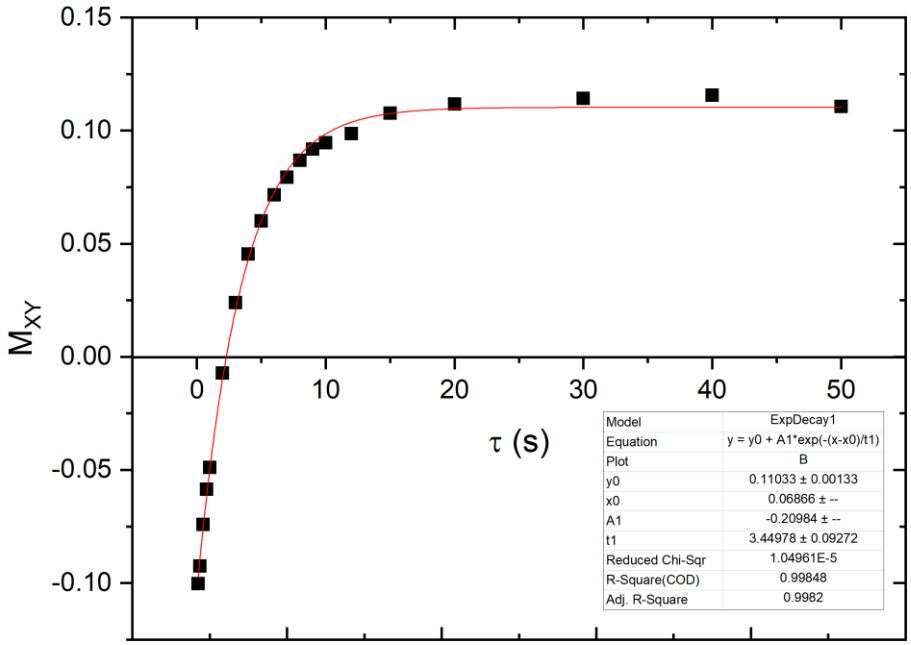

Figure 206 - isoniazid (chelate bound)

Bibliography

A. Abragam and M. Goldman, *Rep. Prog. Phys.*, 1978, **41**, 395-467.

A. Abragam and W. G. Proctor, *Phys. Rev.*, 1958, **109**, 1441-1458.

A. Abragam and W. G. Proctor, *C. R. Acad. Sci.*, 1958, 246.

M. Abraham, M. A. H. Mccausland and F. N. H. Robinson, *Phys. Rev. Lett.*, 1959, **2**, 449-451.

D. Abrams, M. E. Trusheim, D. R. Englund, M. D. Shattuck and C. A. Meriles, *Nano Lett*., 2014, **14**, 2471-2478.

R. W. Adams, J. A. Aguilar, K. D. Atkinson, M. J. Cowley, P. I. Elliott, S. B. Duckett, G. G. Green, I. G. Khazal, J. Lopez-Serrano and D. C. Williamson, *Science*, 2009, **323**, 1708-1711.

R. W. Adams, S. B. Duckett, R. A. Green, D. C. Williamson and G. G. Green, *J. Chem. Phys*., 2009, **131**, 194505.

J. A. Aguilar, R. W. Adams, S. B. Duckett, G. G. Green and R. Kandiah, *J. Magn. Reson.*, 2011, **208**, 49-57.

J. A. Aguilar, P. I. Elliott, J. Lopez-Serrano, R. W. Adams and S. B. Duckett, *Chem. Commun.*, 2007, DOI: 10.1039/b616307f, 1183-1185.

A. Ajoy, U. Bissbort, M. D. Lukin, R. L. Walsworth and P. Cappellaro, *Phys. Rev.*, 2015, **5**, 011001.

A. Ajoy, K. Liu, R. Nazaryan, X. Lv, P. R. Zangara, B. Safvati, G. Wang, D. Arnold, G. Li, A. Lin, P. Raghavan, E. Druga, S. Dhomkar, D. Pagliero, J. A. Reimer, D. Suter, C. A. Meriles and A. Pines, *Sci. Adv.*, 2018, **4**, eaar5492.

O. Akinyele, E. Fakola, L. Durosinmi, T. Ajayeoba and A. Ayeni, *Ife Journal of Science*, 2019, **21**, 184-192.

M. M. Alauddin, *Am. J. Nucl. Med. Mol. Im*, 2012, **2**, 55-76.

A. Albert and E. Spinner, *J. Chem. Soc.*, 1960, DOI: 10.1039/jr9600001221, 1221-1226.

A. A. Altaf, A. Shahzad, Z. Gul, N. Rasool, A. Badshah, B. Lal and E. Khan, *J. Drug Des. Med. Chem.*, 2015, **1**, 1-11.

N. G. Anderson, Practical Process Research and Development: A Guide for Organic Chemists, Elsevier Science, 2012.

K. M. Appleby, R. E. Mewis, A. M. Olaru, G. G. R. Green, I. J. S. Fairlamb and S. B. Duckett, *Chem. Sci.*, 2015, **6**, 3981-3993.

J. Ardenkjaer-Larsen, S. Bowen, J. Raagaard Petersen, O. Rybalko, M. Vinding, M. Ullisch and N. Chr. Nielsen, Cryogen-Free dissolution Dynamic Nuclear Polarization polarizer operating at 3.35 T, 6.70 T and 10.1 T, 2018.

J. H. Ardenkjaer-Larsen, B. Fridlund, A. Gram, G. Hansson, L. Hansson, M. H. Lerche, R. Servin, M. Thaning and K. Golman, *Proc. Natl. Acad. Sci. U. S. A.*, 2003, **100**, 10158-10163.

K. D. Atkinson, M. J. Cowley, S. B. Duckett, P. I. Elliott, G. G. Green, J. Lopez-Serrano, I. G. Khazal and A. C. Whitwood, *Inorg. Chem.*, 2009, **48**, 663-670.

K. D. Atkinson, M. J. Cowley, P. I. Elliott, S. B. Duckett, G. G. Green, J. Lopez-Serrano and A. C. Whitwood, *J. Am. Chem. Soc.*, 2009, **131**, 13362-13368.

V. S. Bajaj, M. K. Hornstein, K. E. Kreischer, J. R. Sirigiri, P. P. Woskov, M. L. Mak-Jurkauskas, J. Herzfeld, R. J. Temkin and R. G. Griffin, *J. Magn. Reson.*, 2007, **189**, 251-279.

G. Balasubramanian, I. Y. Chan, R. Kolesov, M. Al-Hmoud, J. Tisler, C. Shin, C. Kim, A. Wojcik, P. R. Hemmer, A. Krueger, T. Hanke, A. Leitenstorfer, R. Bratschitsch, F. Jelezko and J. Wrachtrup, *Nature*, 2008, **455**, 648-651.

J. Barkemeyer, M. Haake and J. Bargon, *J. Am. Chem. Soc.*, 1995, **117**, 2927-2928.

W. A. Barker, *Rev. Mod. Phys.*, 1962, **34**, 173-&.

A. B. Barnes, G. D. Paepe, P. C. van der Wel, K. N. Hu, C. G. Joo, V. S. Bajaj, M. L. Mak-Jurkauskas, J. R. Sirigiri, J. Herzfeld, R. J. Temkin and R. G. Griffin, *Appl. Magn. Reson.*, 2008, **34**, 237-263.

D. A. Barskiy, L. A. Ke, X. Li, V. Stevenson, N. Widarman, H. Zhang, A. Truxal and A. Pines, *J. Phys. Chem. Lett.*, 2018, **9**, 2721-2724.

D. A. Barskiy, S. Knecht, A. V. Yurkovskaya and K. L. Ivanov, *Prog. Nucl. Magn. Reson. Spec.*, 2019, **114-115**, 33-70.

D. A. Barskiy, K. V. Kovtunov, I. V. Koptyug, P. He, K. A. Groome, Q. A. Best, F. Shi, B. M. Goodson, R. V. Shchepin, A. M. Coffey, K. W. Waddell and E. Y. Chekmenev, *J. Am. Chem. Soc.*, 2014, **136**, 3322-3325.

D. A. Barskiy, A. N. Pravdivtsev, K. L. Ivanov, K. V. Kovtunov and I. V. Koptyug, *Phys. Chem. Chem. Phys.*, 2016, **18**, 89-93.

D. A. Barskiy, R. V. Shchepin, C. P. N. Tanner, J. F. P. Colell, B. M. Goodson, T. Theis, W. S. Warren and E. Y. Chekmenev, *Chem. Phys. Chem.*, 2017, **18**, 1493-1498.

E. Bartholomé, *Zeitschrift für Elektrochemie und angewandte physikalische Chemie*, 1935, **41**, 812-812.

M. Baudin, B. Vuichoud, A. Bornet, G. Bodenhausen and S. Jannin, *J. Magn. Reson*., 2018, **294**, 115-121.

M. Baumann and I. R. Baxendale, Beilstein *J. Org. Chem.*, 2013, **9**, 2265-2319.

C. P. Bean, *Rev. Mod. Phys.*, 1964, **36**, 31.

P. Beltrame, E. Cadoni, C. Floris, G. Gelli and A. Lai, *Spectrochimica Acta Part A: Molecular and Biomolecular Spectroscopy*, 2002, **58**, 2693-2697.

D. Blazina, S. B. Duckett, J. P. Dunne and C. Godard, *Dalton Trans.*, 2004, DOI: 10.1039/B409606A, 2601-2609.

N. Bloembergen and R. V. Pound, *Phys. Rev.*, 1954, **95**, 8-12.

S. Bloom, *J. Appl. Phys.*, 1957, **28**, 800-805.

C. Boehme and G. Frenking, *J. Am. Chem. Soc.*, 1996, **118**, 2039-2046.

V. Boekelheide, *J. Am. Chem. Soc.*, 1961, **83**, 4680-4680.

M. Borghini, *Phys. Rev. Lett.*, 1968, **20**, 419-&.

B. Bottari, R. Maccari, F. Monforte, R. Ottana, E. Rotondo and M. G. Vigorita, *Bioorg. Med. Chem. Lett.*, 2000, **10**, 657-660.

C. R. Bowers, H. W. Long, T. Pietrass, H. C. Gaede and A. Pines, *Chem. Phys. Lett*., 1993, **205**, 168-170.

C. R. Bowers and D. P. Weitekamp, *Phys. Rev. Lett.*, 1986, **57**, 2645-2648.

C. R. Bowers and D. P. Weitekamp, *J. Am. Chem. Soc.*, 1987, **109**, 5541-5542.

D. J. Brown, *The Chemistry of Heterocyclic Compounds, Pyridine Metal Complexes*, John Wiley & Sons, 2009.

L. Buljubasich, M. B. Franzoni, H. W. Spiess and K. Munnemann, *J. Magn. Reson*., 2012, **219**, 33-40.

M. S. Caceci, *Anal. Chem.*, 1989, **61**, 2324-2327.

T. V. Can, Q. Z. Ni and R. G. Griffin, *J. Magn. Reson.*, 2015, **253**, 23-35.

C. R. Cantor and P. R. Schimmel, *Biophysical chemistry: Part II: Techniques for the study of biological structure and function*, Macmillan, 1980.

M. Carravetta, O. G. Johannessen and M. H. Levitt, *Phys. Rev. Lett.*, 2004, **92**, 153003.

T. R. Carver and C. P. Slichter, *Phys. Rev.*, 1953, **92**, 212-213.

R. Casasnovas, J. Frau, J. Ortega-Castro, A. Salvà, J. Donoso and F. Muñoz, *Journal of Molecular Structure: THEOCHEM*, 2009, **912**, 5-12.

E. Cavallari, C. Carrera, S. Aime and F. Reineri, *J. Magn. Reson.*, 2018, **289**, 12-17.

E. Cavallari, C. Carrera, T. Boi, S. Aime and F. Reineri, *J. Phys. Chem. B*, 2015, **119**, 10035-10041.

E. Cavallari, C. Carrera, G. Di Matteo, O. Bondar, S. Aime and F. Reineri, *Frontiers in Oncology*, 2020, **10**.

A. Chaubey and S. Pandeya, *Asian J. Pharm. Clin. Res*., 2011, **4**, 5-8.

J. Y. C. Chen, unpublished work.

Q. Chen, I. Schwarz, F. Jelezko, A. Retzker and M. B. Plenio, *Phys. Rev. B*, 2015, **92**, 184420.

M. T. Chenon, R. J. Pugmire, D. M. Grant, R. P. Panzica and L. B. Townsend, *J. Am. Chem. Soc*., 1975, **97**, 4636-4642.

L. Childress, M. V. Gurudev Dutt, J. M. Taylor, A. S. Zibrov, F. Jelezko, J. Wrachtrup, P. R. Hemmer and M. D. Lukin, *Science*, 2006, **314**, 281-285.

T. D. W. Claridge, *High-Resolution NMR Techniques in Organic Chemistry*, Elsevier Science, 2016.

J. Colell, A. W. Logan, Z. Zhou, J. R. Lindale, R. Laasner, R. Shchepin, E. Chekmenev, V. Blum, W. S. Warren and S. J. Malcolmson, *Chem. Commun*., 2020.

B. Corzilius, *Phys. Chem. Chem. Phys*., 2016, **18**, 27190-27204.

R. M. Cotts, M. J. R. Hoch, T. Sun and J. T. Markert, *J. Magn. Reson.*, 1989, **83**, 252-266.

M. J. Cowley, R. W. Adams, K. D. Atkinson, M. C. Cockett, S. B. Duckett, G. G. Green, J. A. Lohman, R. Kerssebaum, D. Kilgour and R. E. Mewis, *J. Am. Chem. Soc.*, 2011, **133**, 6134-6137.

M. J. Cowley, S. B. Duckett and G. Green, *Abstr. Pap. Am. Chem. Soc*., 2010, **240**.

R. H. Crabtree, H. Felkin and G. E. Morris, *J. Organomet. Chem*., 1977, **141**, 205-215.

R. H. Crabtree, M. F. Mellea, J. M. Mihelcic and J. M. Quirk, *J. Am. Chem. Soc*., 1982, **104**, 107-113.

S. E. Day, M. I. Kettunen, F. A. Gallagher, D. E. Hu, M. Lerche, J. Wolber, K. Golman, J. H. Ardenkjaer-Larsen and K. M. Brindle, *Nat. Med*. (N. Y., NY, U. S.), 2007, **13**, 1382-1387.

S. Díez-González and S. P. Nolan, *Coord. Chem. Rev*., 2007, **251**, 874-883.

R. Diguet, R. Deul and E. U. Franck, *Berichte der Bunsengesellschaft für physikalische Chemie*, 1985, **89**, 800-804.

E. B. Ducker, L. T. Kuhn, K. Munnemann and C. Griesinger, *J. Magn. Reson*., 2012, **214**, 159-165.

S. B. Duckett and D. Blazina, *Eur. J. Inorg. Chem*., 2003, DOI: 10.1002/ejic.200300119, 2901-2912.

S. B. Duckett and R. E. Mewis, *Acc. Chem. Res*., 2012, **45**, 1247-1257.

S. B. Duckett and R. E. Mewis, *Hyperpolarization Methods in NMR Spectroscopy, ed*. L. T. Kuhn, 2013, **338**, 75-103.

S. B. Duckett, C. L. Newell and R. Eisenberg, *J. Am. Chem. Soc*., 1993, **115**, 1156-1157.

S. B. Duckett and N. J. Wood, *Coord. Chem. Rev*., 2008, **252**, 2278-2291.

J. N. Dumez, *Magn. Reson. Chem*., 2017, **55**, 38-46.

M. V. Dutt, L. Childress, L. Jiang, E. Togan, J. Maze, F. Jelezko, A. S. Zibrov, P. R. Hemmer and M. D. Lukin, *Science*, 2007, **316**, 1312-1316.

B. Efron, *Biometrika*, 1981, **68**, 589-599.

B. Efron and G. Gong, *The American Statistician*, 1983, **37**, 36-48.

K. S. Egorova and V. P. Ananikov*, Organometallics*, 2017, **36**, 4071-4090.

T. C. Eisenschmid, R. U. Kirss, P. P. Deutsch, S. I. Hommeltoft, R. Eisenberg, J. Bargon, R. G. Lawler and A. L. Balch, *J. Am. Chem. Soc*., 1987, **109**, 8089-8091.

T. C. Eisenschmid, J. McDonald, R. Eisenberg and R. G. Lawler, *J. Am. Chem. Soc.,* 1989, **111**, 7267-7269.

R. R. Ernst, *Biosci. Rep.*, 1992, **12**, 143-187.

N. Eshuis, R. L. Aspers, B. J. van Weerdenburg, M. C. Feiters, F. P. Rutjes, S. S. Wijmenga and M. Tessari, *J. Magn. Reson*., 2016, **265**, 59-66.

N. Eshuis, N. Hermkens, B. J. van Weerdenburg, M. C. Feiters, F. P. Rutjes, S. S. Wijmenga and M. Tessari, *J. Am. Chem. Soc*., 2014, **136**, 2695-2698.

N. Eshuis, B. J. van Weerdenburg, M. C. Feiters, F. P. Rutjes, S. S. Wijmenga and M. Tessari, *Angew. Chem. Int. Ed*., 2015, **54**, 1481-1484.

R. Evans, *Prog. Nucl. Magn. Reson. Spec.,* 2019, DOI:https://doi.org/10.1016/j.pnmrs.2019.11.002.

R. Evans, G. Dal Poggetto, M. Nilsson and G. A. Morris, *Anal. Chem.*, 2018, **90**, 3987-3994.

C. T. Farrar, D. A. Hall, G. J. Gerfen, S. J. Inati and R. G. Griffin, *J. Chem. Phys.*, 2001, **114**, 4922-4933.

C. M. A. Farrow, G. R. Akien, N. R. Halcovitch, J. A. Platts and M. P. Coogan, *Dalton Trans*., 2018, **47**, 3906-3912.

M. Fekete, O. W. Bayfield, S. B. Duckett, S. Hart, R. E. Mewis, N. Pridmore, P. J. Rayner and A. Whitwood, *Inorg. Chem.*, 2013, **52**, 13453-13461.

M. Fekete, C. Gibard, G. J. Dear, G. G. Green, A. J. Hooper, A. D. Roberts, F. Cisnetti and S. B. Duckett, *Dalton Trans*., 2015, **44**, 7870-7880.

M. Fekete, P. J. Rayner, G. G. R. Green and S. B. Duckett, *Magn. Reson. Chem.*, 2017, **55**, 944-957.

B. Feng, A. M. Coffey, R. D. Colon, E. Y. Chekmenev and K. W. Waddell, *J. Magn. Reson.*, 2012, **214**, 258-262.

P. Fernandez-Acebal, O. Rosolio, J. Scheuer, C. Muller, S. Muller, S. Schmitt, L. P. McGuinness, I. Schwarz, Q. Chen, A. Retzker, B. Naydenov, F. Jelezko and M. B. Plenio, *Nano Lett*., 2018, **18**, 1882-1887.

M. Foroozandeh, R. W. Adams, M. Nilsson and G. A. Morris, *J. Am. Chem. Soc*., 2014, **136**, 11867-11869.

M. B. Franzoni, L. Buljubasich, H. W. Spiess and K. Münnemann, *J. Am. Chem. Soc.*, 2012, **134**, 10393-10396.

L. J. Friedman, P. J. Millet and R. C. Richardson, *Phys. Rev. Lett.*, 1981, **47**, 1078-1081.

L. Frydman, *Nat Chem*, 2009, **1**, 176-178.

D. G. Gadian, K. S. Panesar, A. J. Linde, A. J. Horsewill, W. Kockenberger and J. R. Owers-Bradley, *Phys. Chem. Chem. Phys.*, 2012, **14**, 5397-5402.

D. Gajan, A. Bornet, B. Vuichoud, J. Milani, R. Melzi, H. A. van Kalkeren, L. Veyre, C. Thieuleux, M. P. Conley, W. R. Gruning, M. Schwarzwalder, A. Lesage, C. Coperet, G. Bodenhausen, L. Emsley and S. Jannin, *Proc. Natl. Acad. Sci. U. S. A.*, 2014, **111**, 14693-14697.

J. L. Gao and L. Shao, *J. Phys. Chem.*, 1994, **98**, 13772-13779.

L. Garrido, N. Beckmann and W. Price, *New Applications of NMR in Drug Discovery and Development*, Royal Society of Chemistry, 2013.

S. J. Gibbs and C. S. Johnson, *J. Magn. Reson.,* 1991, **93**, 395-402.

T. Gilchrist, New York, 1997.

K. Golman, R. I. Zandt, M. Lerche, R. Pehrson and J. H. Ardenkjaer-Larsen, *Cancer Res*., 2006, **66**, 10855-10860.

B. M. Goodson, B. Kidd, J.B. Hövener, L. Schröder, T. Theis, N. Whiting and E. Y. Chekmenev, 2018.

A. Gordon, A. Katritzky and S. Roy, *J. Chem. Soc. B: Phys. Org*., 1968, 556-561.

B. L. Green, B. G. Breeze, G. J. Rees, J. V. Hanna, J. P. Chou, V. Ivady, A. Gali and M. E. Newton, *Phys. Rev. B*, 2017, **96**, 054101.

R. A. Green, R. W. Adams, S. B. Duckett, R. E. Mewis, D. C. Williamson and G. G. Green, *Prog. Nucl. Magn. Reson. Spectrosc*., 2012, **67**, 1-48.

A. Gruber, A. Drabenstedt, C. Tietz, L. Fleury, J. Wrachtrup and C. vonBorczyskowski, *Science*, 1997, **276**, 2012-2014.

L. Guduff, P. Berthault, C. van Heijenoort, J.-N. Dumez and G. Huber, *Chem. Phys. Chem*., 2019, **20**, 392-398.

L. Guduff, I. Kuprov, C. van Heijenoort and J. N. Dumez, Chem *Commun (Camb)*, 2017, **53**, 701-704.

L. Guduff, D. Kurzbach, C. van Heijenoort, D. Abergel and J. N. Dumez, *Chemistry*, 2017, **23**, 16722-16727.

H. Gutte, A. E. Hansen, H. H. Johannesen, A. E. Clemmensen, J. H. Ardenkjær-Larsen, C. H. Nielsen and A. Kjær, *Am. J. Nucl. Med. Mol. Im*, 2015, **5**, 548-560.

M. Haake, J. Barkemeyer and J. Bargon, *J. Phys. Chem*., 1995, **99**, 17539-17543.

E. L. Hahn, *Phys. Rev*., 1950, **77**, 297-299.

K. Halbach, *Nuclear Instruments & Methods*, 1980, **169**, 1-10.

C. S. Handloser, M. R. Chakrabarty and M. W. Mosher, *J. Chem. Educ.*, 1973, **50**, 510.

M. Hansen and H. J. Jakobsen, *J. Magn. Reson.,* 1973, **10**, 74-84.

D. C. Harris, *J. Chem. Educ.*, 1998, **75**, 119-121.

K. Hashi, S. Ohki, S. Matsumoto, G. Nishijima, A. Goto, K. Deguchi, K. Yamada, T. Noguchi, S. Sakai, M. Takahashi, Y. Yanagisawa, S. Iguchi, T. Yamazaki, H. Maeda, R. Tanaka, T. Nemoto, H. Suematsu, T. Miki, K. Saito and T. Shimizu, *J. Magn. Reson*., 2015, **256**, 30-33.

K. Heclik, B. Debska and J. C. Dobrowolski, *RSC Adv*., 2014, **4**, 17337-17346.

K. Heclik and J. C. Dobrowolski, *J. Phys. Org. Chem*., 2017, **30**, 3656.

A. Henstra, T. S. Lin, J. Schmidt and W. T. Wenckebach, *Chem. Phys. Lett*., 1990, **165**, 6-10.

N. K. J. Hermkens, M. C. Feiters, F. Rutjes, S. S. Wijmenga and M. Tessari, *J. Magn. Reson*., 2017, **276**, 122-127.

W. A. Herrmann, *Angew. Chem. Int. Ed*., 2002, **41**, 1290-1309.

M. L. Hirsch, N. Kalechofsky, A. Belzer, M. Rosay and J. G. Kempf, *J. Am. Chem. Soc.*, 2015, **137**, 8428-8434.

M. L. Hirsch, B. A. Smith, M. Mattingly, A. G. Goloshevsky, M. Rosay and J. G. Kempf, *J. Magn. Reson*., 2015, **261**, 87-94.

A. J. Holmes, P. J. Rayner, M. J. Cowley, G. G. R. Green, A. C. Whitwood and S. B. Duckett, *Dalton Trans*., 2015, **44**, 1077-1083.

P. J. Hore, *Nuclear Magnetic Resonance (Oxford Chemistry Primers)*, Oxford University Press, USA, 1995.

D. I. Hoult and B. Bhakar, *Concepts in Magnetic Resonance*, 1997, **9**, 277-297.

J. B. Hovener, S. Bar, J. Leupold, K. Jenne, D. Leibfritz, J. Hennig, S. B. Duckett and D. von Elverfeldt, *NMR Biomed*., 2013, **26**, 124-131.

J. B. Hovener, A. N. Pravdivtsev, B. Kidd, C. R. Bowers, S. Gloggler, K. V. Kovtunov, M. Plaumann, R. Katz-Brull, K. Buckenmaier, A. Jerschow, F. Reineri, T. Theis, R. V. Shchepin, S. Wagner, P. Bhattacharya, N. M. Zacharias and E. Y. Chekmenev, *Angew. Chem. Int. Ed*., 2018, **57**, 11140-11162.

J. B. Hovener, N. Schwaderlapp, R. Borowiak, T. Lickert, S. B. Duckett, R. E. Mewis, R. W. Adams, M. J. Burns, L. A. Highton, G. G. Green, A. Olaru, J. Hennig and D. von Elverfeldt, *Anal. Chem*., 2014, **86**, 1767-1774.

J. B. Hovener, N. Schwaderlapp, T. Lickert, S. B. Duckett, R. E. Mewis, L. A. Highton, S. M. Kenny, G. G. Green, D. Leibfritz, J. G. Korvink, J. Hennig and D. von Elverfeldt, *Nat Commun*, 2013, **4**, 2946.

K. N. Hu, *Solid State Nucl. Magn. Reson*., 2011, **40**, 31-41.

P. S. Hubbard, *Phys. Rev.,* 1963, **131**, 1155-&.

W. Iali, G. G. R. Green, S. J. Hart, A. C. Whitwood and S. B. Duckett, *Inorg. Chem*., 2016, **55**, 11639-11643.

W. Iali, A. M. Olaru, G. G. R. Green and S. B. Duckett, *Chemistry*, 2017, **23**, 10491-10495.

W. Iali, P. J. Rayner, A. Alshehri, A. J. Holmes, A. J. Ruddlesden and S. B. Duckett, *Chem. Sci*., 2018, **9**, 3677-3684.

W. Iali, P. J. Rayner and S. B. Duckett, *Sci. Adv*., 2018, **4**, eaao6250.

W. Iali, S. S. Roy, B. J. Tickner, F. Ahwal, A. J. Kennerley and S. B. Duckett, *Angew. Chem. Int. Ed.*, 2019, **58**, 10271-10275.

J. A. Iggo, *NMR spectroscopy in Inorganic Chemistry*, Oxford University Press New York, 1999.

J. D. Isdale, A. J. Easteal and L. A. Woolf, *Int. J. Thermophys*., 1985, **6**, 439-450.

K. L. Ivanov, A. N. Pravdivtsev, A. V. Yurkovskaya, H.-M. Vieth and R. Kaptein, *Prog. Nucl. Magn. Reson. Spec.*, 2014, **81**, 1-36.

S. Jannin, A. Bornet, R. Melzi and G. Bodenhausen, *Chem. Phys. Lett.*, 2012, **549**, 99-102.

F. Jelezko, T. Gaebel, I. Popa, M. Domhan, A. Gruber and J. Wrachtrup, *Phys. Rev. Lett*., 2004, **93**, 130501.

F. Jelezko, T. Gaebel, I. Popa, A. Gruber and J. Wrachtrup, *Phys. Rev. Lett*., 2004, **92**, 076401.

F. Jelezko and J. Wrachtrup, *Physica Status Solidi a-Applications and Materials Science*, 2006, **203**, 3207-3225.

A. Jerschow and N. Muller, *J. Magn. Reson*., 1997, **125**, 372-375.

X. Ji, A. Bornet, B. Vuichoud, J. Milani, D. Gajan, A. J. Rossini, L. Emsley, G. Bodenhausen and S. Jannin, *Nat Commun*, 2017, **8**, 13975.

S. Jochen, S. Ilai, C. Qiong, S.S. David, C. Patrick, H. Peter, R. Alexander, S. Hitoshi, I. Junichi, L. Burkhard, B. P. Martin, N. Boris and J. Fedor, *New J. Phys*., 2016, **18**, 013040.

H. Jóhannesson, S. Macholl and J. H. Ardenkjaer-Larsen, *J. Magn. Reson*., 2009, **197**, 167-175.

C. S. Johnson, *Prog. Nucl. Magn. Reson. Spec*., 1999, **34**, 203-256.

T. Kameda, N. Takeda, S. Kuroki, H. Kurosu, S. Ando, I. Ando, A. Shoji and T. Ozaki*, J. Mol. Struct*., 1996, **384**, 17-23.

R. F. Karlicek and I. J. Lowe, *J. Magn. Reson.*, 1980, **37**, 75-91.

A. Kastler, *J. Phys. Radium*, 1950, **11**, 255-265.

A. Kastler, *J. Opt. Soc. Am*., 1957, **47**, 460-465.

A. Katritzky, J. Rowe and S. Roy, *J. Chem. Soc. B: Physical Organic*, 1967, 758-761.

A. R. Katritzky and J. M. Lagowski, *Adv. Heterocycl. Chem., ed.* A. R. Katritzky, Academic Press, 1963, vol. 1, pp. 311-338.

R. Kaur, P. Kaur, S. Sharma, G. Singh, S. Mehndiratta, P. MS Bedi and K. Nepali, *Recent Pat. Anti-Cancer Drug Discovery*, 2015, **10**, 23-71.

H. Kemp, *J. Chem. Educ.*, 1987, **64**, 482.

K. R. Keshari and D. M. Wilson, *Chem Soc Rev*, 2014, **43**, 1627-1659.

G. J. Kharadi, J. R. Patel and B. Z. Dholakiya, *Appl. Organomet. Chem*., 2010, **24**, 821-827.

B. E. Kidd, J. L. Gesiorski, M. E. Gemeinhardt, R. V. Shchepin, K. V. Kovtunov, I. V. Koptyug, E. Y. Chekmenev and B. M. Goodson, *J. Phys. Chem. C*., 2018, **122**, 16848-16852.

B. E. Kidd, J. A. Mashni, M. N. Limbach, F. Shi, E. Y. Chekmenev, Y. Hou and B. M. Goodson, *Chemistry*, 2018, **24**, 10641-10645.

R. Kimmich, W. Nusser and F. Winter, *Phys. Med. Biol*., 1984, **29**, 593.

R. U. Kirss, T. C. Eisenschmid and R. Eisenberg, *J. Am. Chem. Soc*., 1988, **110**, 8564-8566.

A. Kiswandhi, P. Niedbalski, C. Parish, Q. Wang and L. Lumata, *Magn. Reson. Chem*., 2017, **55**, 846-852.

C. Kittel, *Phys. Rev*., 1949, **76**, 743.

P. Kiuru and J. Yli-Kauhaluoma, *Heterocycl. Nat. Prod. Synth*., 2011, 267-297.

E. Klingsberg, *Pyridine and Its Derivatives*, Wiley, 2009.

S. Knecht, A. N. Pravdivtsev, J. B. Hovener, A. V. Yurkovskaya and K. L. Ivanov, *RSC Adv*., 2016, **6**, 24470-24477.

B. L. Koelsch, K. R. Keshari, T. H. Peeters, P. E. Z. Larson, D. M. Wilson and J. Kurhanewicz, *Analyst*, 2013, **138**, 1011-1014.

H. Kovacs, D. Moskau and M. Spraul, *Prog. Nucl. Magn. Reson. Spec*., 2005, **46**, 131-155.

K. V. Kovtunov, D. A. Barskiy, O. G. Salnikov, R. V. Shchepin, A. M. Coffey, L. M. Kovtunova, V. I. Bukhtiyarov, I. V. Koptyug and E. Y. Chekmenev, *RSC Adv*, 2016, **6**, 69728-69732.

K. V. Kovtunov, L. M. Kovtunova, M. E. Gemeinhardt, A. V. Bukhtiyarov, J. Gesiorski, V. I. Bukhtiyarov, E. Y. Chekmenev, I. V. Koptyug and B. M. Goodson, *Angew. Chem. Int. Ed*., 2017, **56**, 10433-10437.

K. V. Kovtunov, E. V. Pokochueva, O. G. Salnikov, S. F. Cousin, D. Kurzbach, B. Vuichoud, S. Jannin, E. Y. Chekmenev, B. M. Goodson, D. A. Barskiy and I. V. Koptyug, *Chem. Asian. J*., 2018, **13**, 1857-1871.

V. V. Krishnan and N. Murali, *Prog. Nucl. Magn. Reson. Spectrosc*., 2013, **68**, 41-57.

E. V. Krjukov, J. D. O'Neill and J. R. Owers-Bradley, J. *Low Temp. Phys*., 2005, **140**, 397-408.

J. Kurhanewicz, D. B. Vigneron, K. Brindle, E. Y. Chekmenev, A. Comment, C. H. Cunningham, R. J. DeBerardinis, G. G. Green, M. O. Leach and S. S. Rajan, *Neoplasia*, 2011, **13**, 81-97.

K. J. Laidler and M. C. King, *J. Phys. Chem*., 1983, **87**, 2657-2664.

R. G. Lawler, *J. Am. Chem. Soc*., 1967, **89**, 5519.

D. Lee, H. Takahashi, A. S. L. Thankamony, J. P. Dacquin, M. Bardet, O. Lafon and G. De Paepe, *J. Am. Chem. Soc*., 2012, **134**, 18491-18494.

Y. Lee, *Appl. Spectrosc. Rev*., 2016, **51**, 210-226.

M. H. Levitt, *Spin Dynamics: Basics of Nuclear Magnetic Resonance*, Wiley, 2013.

Y. J. Lin and A. P. Koretsky, *Magn. Reson. Med*., 1997, **38**, 378-388.

N. Lisitza, I. Muradian, E. Frederick, S. Patz, H. Hatabu and E. Y. Chekmenev, *J. Chem. Phys*., 2009, **131**, 044508.

M. Liu, R. D. Farrant, J. M. Gillam, J. K. Nicholson and J. C. Lindon, *J. Magn. Reson*., 1995, **109**, 275-283.

L. S. Lloyd, R. W. Adams, M. Bernstein, S. Coombes, S. B. Duckett, G. G. Green, R. J. Lewis, R. E. Mewis and C. J. Sleigh, *J. Am. Chem. Soc*., 2012, **134**, 12904-12907.

L. S. Lloyd, A. Asghar, M. J. Burns, A. Charlton, S. Coombes, M. J. Cowley, G. J. Dear, S. B. Duckett, G. R. Genov, G. G. R. Green, L. A. R. Highton, A. J. J. Hooper, M. Khan, I. G. Khazal, R. J. Lewis, R. E. Mewis, A. D. Roberts and A. J. Ruddlesden, *Catal. Sci. Technol*., 2014, **4**, 3544-3554.

I. Lovchinsky, A. O. Sushkov, E. Urbach, N. P. de Leon, S. Choi, K. De Greve, R. Evans, R. Gertner, E. Bersin, C. Muller, L. McGuinness, F. Jelezko, R. L. Walsworth, H. Park and M. D. Lukin, *Science*, 2016, **351**, 836-841.

E. Lukevits, *Chem. Heterocycl. Compd*., 1995, **31**, 639-650.

M. MacCoss and M. Robins, *The Chemistry of antitumour agents*, Springer, 1990, pp. 261-298.

A. L. MacKinnon and J. Taunton, *Current Protocols in Chemical Biology*, 2009, **1**, 55-73.

J. G. Małecki and P. Zwoliński, *Polyhedron*, 2012, **39**, 85-90.

A. Manoharan, P. J. Rayner, M. Fekete, W. Iali, P. Norcott, V. Hugh Perry and S. B. Duckett, *Chem. Phys. Chem*., 2019, **20**, 285-294.

A. Manoharan, P. J. Rayner, W. Iali, M. J. Burns, V. H. Perry and S. B. Duckett, *Chem. Med. Chem.*, 2018, **13**, 352-359.

N. Marco, A. A. Souza, P. Nolis, C. Cobas, R. R. Gil and T. Parella, *J. Org. Chem*., 2017, **82**, 2040-2044.

I. Marco-Rius, M. C. Tayler, M. I. Kettunen, T. J. Larkin, K. N. Timm, E. M. Serrao, T. B. Rodrigues, G. Pileio, J. H. Ardenkjaer-Larsen and M. H. Levitt, *NMR Biomed*., 2013, **26**, 1696-1704.

J. R. Maze, P. L. Stanwix, J. S. Hodges, S. Hong, J. M. Taylor, P. Cappellaro, L. Jiang, M. V. Dutt, E. Togan, A. S. Zibrov, A. Yacoby, R. L. Walsworth and M. D. Lukin, *Nature*, 2008, **455**, 644-647.

C. H. McAteer, M. Balasubramanian and R. Murugan, *Comprehensive Heterocyclic Chemistry III*, eds. A. R. Katritzky, C. A. Ramsden, E. F. V. Scriven and R. J. K. Taylor, Elsevier, Oxford, 2008, 309-336.

R. E. Mewis, *Magn. Reson. Chem*., 2015, **53**, 789-800.

R. E. Mewis, K. D. Atkinson, M. J. Cowley, S. B. Duckett, G. G. Green, R. A. Green, L. A. Highton, D. Kilgour, L. S. Lloyd, J. A. Lohman and D. C. Williamson, *Magn. Reson. Chem*., 2014, **52**, 358-369.

R. E. Mewis, M. Fekete, G. G. Green, A. C. Whitwood and S. B. Duckett, *Chem. Commun*., 2015, **51**, 9857-9859.

R. E. Mewis, R. A. Green, M. C. Cockett, M. J. Cowley, S. B. Duckett, G. G. Green, R. O. John, P. J. Rayner and D. C. Williamson*, J. Phys. Chem. B*, 2015, **119**, 1416-1424.

K. F. Morris and C. S. Johnson, *J. Am. Chem. Soc*., 1992, **114**, 3139-3141.

K. Motiram-Corral, M. Perez-Trujillo, P. Nolis and T. Parella, *Chem Commun (Camb)*, 2018, **54**, 13507-13510.

C. J. Moulton and B. L. Shaw, *J. Chem. Soc., Dalton Transactions*, 1976, DOI: 10.1039/DT9760001020, 1020-1024.

E. Murguly, T. B. Norsten and N. Branda, *J. Chem. Soc*., Perkin Trans. **2**, 1999, DOI: DOI 10.1039/a904323c, 2789-2794.

H. Naghibi, A. Tamura and J. M. Sturtevant, *Proc. Natl. Acad. Sci*., 1995, **92**, 5597.

K. K. Narang, M. K. Singh, M. R. Goyle and K. Bhuvaneshwari, *Synth. React. Inorg. Met.-Org. Chem*., 1991, **21**, 1569-1585.

J. Natterer and J. Bargon, *Prog. Nucl. Magn. Reson. Spec*., 1997, **31**, 293-315.

K. Nicolay, K. P. J. Braun, R. A. d. Graaf, R. M. Dijkhuizen and M. J. Kruiskamp, *NMR Biomed*., 2001, **14**, 94-111.

P. Nikolaou, B. M. Goodson and E. Y. Chekmenev, *Chem.Eur. J*., 2015, **21**, 3156-3166.

P. Norcott, M. J. Burns, P. J. Rayner, R. E. Mewis and S. B. Duckett, *Magn. Reson. Chem*., 2018, **56**, 663-671.

P. Norcott, P. J. Rayner, G. G. R. Green and S. B. Duckett, *Chemistry*, 2017, **23**, 16990-16997.

A. M. Olaru, M. J. Burns, G. G. R. Green and S. B. Duckett, *Chem. Sci*. , 2017, **8**, 2257-2266.

A. M. Olaru, A. Burt, P. J. Rayner, S. J. Hart, A. C. Whitwood, G. G. R. Green and S. B. Duckett, *Chem Commun (Camb)*, 2016, **52**, 14482-14485.

A. M. Olaru, T. B. R. Robertson, J. S. Lewis, A. Antony, W. Iali, R. E. Mewis and S. B. Duckett, *Chemistry Open*, 2017, **7**, 97-105.

A. M. Olaru, S. S. Roy, L. S. Lloyd, S. Coombes, G. G. Green and S. B. Duckett, *Chem Commun (Camb)*, 2016, **52**, 7842-7845.

W. H. Organization, *World Health Organization model list of essential medicines: 21st list 2019*, World Health Organization, 2019.

W. H. Organization, 2020.

A. W. Overhauser, *Phys. Rev.*, 1953, **92**, 411-415.

J. R. Owers-Bradley, A. J. Horsewill, D. T. Peat, K. S. Goh and D. G. Gadian, *Phys. Chem. Chem. Phys.*, 2013, **15**, 10413-10417.

W. P. Ozimiński and J. C. Dobrowolski, *J. Phys. Org. Chem.*, 2009, **22**, 769-778.

A. Padwa, S. Murphree, G. Gribble and T. Gilchrist, *Prog. Hetero. Chem.*, 2002.

M. Palusiak, *J. Organomet. Chem.*, 2007, **692**, 3866-3873.

T. Parella, *Magn. Reson. Chem.*, 1998, **36**, 467-495.

T. Parella, *Magn. Reson. Chem.*, 2018, **56**, 230-250.

L. Paudel, R. W. Adams, P. Kiraly, J. A. Aguilar, M. Foroozandeh, M. J. Cliff, M. Nilsson, P. Sandor, J. P. Waltho and G. A. Morris, *Angew. Chem. Int. Ed.,* 2013, **52**, 11616-11619.

D. T. Peat, M. L. Hirsch, D. G. Gadian, A. J. Horsewill, J. R. Owers-Bradley and J. G. Kempf, *Phys. Chem. Chem. Phys.*, 2016, **18**, 19173-19182.

D. T. Peat, A. J. Horsewill, W. Kockenberger, A. J. Perez Linde, D. G. Gadian and J. R. Owers-Bradley, *Phys. Chem. Chem. Phys.*, 2013, **15**, 7586-7591.

N. Persaud, M. Jiang, R. Shaikh, A. Bali, E. Oronsaye, H. Woods, G. Drozdzal, Y. Rajakulasingam, D. Maraj, S. Wadhawan, N. Umali, R. Wang, M. McCall, J. K. Aronson, A. Plüddemann, L. Moja, N. Magrini and C. Heneghan, *Bull World Health Organ*, 2019, **97**, 394-404C.

T. Pietrass, *Colloid Surf. A. Physicochem. Eng. Asp.*, 1999, **158**, 51-57.

T. Pietrass and H. C. Gaede, *Adv. Mater.*, 1995, **7**, 826.

A. N. Pravdivtsev, A. V. Yurkovskaya, P. A. Petrov, H. M. Vieth and K. L. Ivanov, *Appl. Magn. Reson.*, 2016, **47**, 711-725.

A. N. Pravdivtsev, A. V. Yurkovskaya, H. M. Vieth, K. L. Ivanov and R. Kaptein, *Chem. Phys. Chem.*, 2013, **14**, 3327-3331.

A. N. Pravdivtsev, A. V. Yurkovskaya, H.-M. Vieth and K. L. Ivanov*, J. Phys. Chem. B*, 2015, **119**, 13619-13629.

M. G. Pravica and D. P. Weitekamp, *Chem. Phys. Lett*., 1988, **145**, 255-258.

D. Raftery, L. Reven, H. Long, A. Pines, P. Tang and J. Reimer, *J. Phys. Chem*., 1993, **97**, 1649-1655.

P. J. Rayner, M. J. Burns, A. M. Olaru, P. Norcott, M. Fekete, G. G. R. Green, L. A. R. Highton, R. E. Mewis and S. B. Duckett, *Proc. Natl. Acad. Sci. U. S. A.,* 2017, **114**, E3188-E3194.

P. J. Rayner and S. B. Duckett, *Angew. Chem. Int. Ed*., 2018, **57**, 6742-6753.

P. J. Rayner, P. Norcott, K. M. Appleby, W. Iali, R. O. John, S. J. Hart, A. C. Whitwood and S. B. Duckett, *Nat Commun*, 2018, **9**, 4251.

P. J. Rayner, P. M. Richardson and S. B. Duckett, *Angew. Chem*., 2020, **132**, 2732-2736.

I. Reile, R. Aspers, J. M. Tyburn, J. G. Kempf, M. C. Feiters, F. Rutjes and M. Tessari, *Angew. Chem. Int. Ed*., 2017, **56**, 9174-9177.

J. C. Richardson, R. W. Bowtell, K. Mäder and C. D. Melia, *Adv. Drug Delivery Rev*., 2005, **57**, 1191-1209.

P. M. Richardson, Ph.D., University of Leeds, 2013.

P. M. Richardson, W. Iali, S. S. Roy, P. J. Rayner, M. E. Halse and S. B. Duckett, *Chem. Sci*., 2019, **10**, 10607-10619.

P. M. Richardson, S. Jackson, A. J. Parrott, A. Nordon, S. B. Duckett and M. E. Halse, *Magn. Reson. Chem*., 2018, **56**, 641-650.

P. M. Richardson, R. O. John, A. J. Parrott, P. J. Rayner, W. Iali, A. Nordon, M. E. Halse and S. B. Duckett, *Phys. Chem. Chem. Phys*., 2018, **20**, 26362-26371.

P. M. Richardson, A. J. Parrott, O. Semenova, A. Nordon, S. B. Duckett and M. E. Halse, *Analyst*, 2018, **143**, 3442-3450.

L. D. Roberts and J. W. T. Dabbs, *Annu. Rev. Nucl. Sci*., 1961, **11**, 175-212.

T. B. R. Robertson and R. E. Mewis, *Annual Reports on NMR Spectroscopy*, Vol 93, ed. G. A. Webb, 2018, vol. 93, pp. 145-212.

P. Rovedo, S. Knecht, T. Baumlisberger, A. L. Cremer, S. B. Duckett, R. E. Mewis, G. G. Green, M. Burns, P. J. Rayner, D. Leibfritz, J. G. Korvink, J. Hennig, G. Putz, D. von Elverfeldt and J. B. Hovener, *J. Phys. Chem. B*, 2016, **120**, 5670-5677.

S. S. Roy, K. M. Appleby, E. J. Fear and S. B. Duckett, *J. Phys. Chem. Lett*., 2018, **9**, 1112-1117.

S. S. Roy, P. Norcott, P. J. Rayner, G. G. Green and S. B. Duckett, *Angew. Chem. Int. Ed*., 2016, **55**, 15642-15645.

S. S. Roy, P. Norcott, P. J. Rayner, G. G. R. Green and S. B. Duckett, *Chemistry*, 2017, **23**, 10496-10500.

S. S. Roy, P. J. Rayner, P. Norcott, G. G. R. Green and S. B. Duckett, *Phys. Chem. Chem. Phys*., 2016, **18**, 24905-24911.

S. S. Roy, G. Stevanato, P. J. Rayner and S. B. Duckett, *J. Magn. Reson*., 2017, **285**, 55-60.

A. J. Ruddlesden and S. B. Duckett, *Chem. Commun*., 2016, **52**, 8467-8470.

A. J. Ruddlesden, R. E. Mewis, G. G. Green, A. C. Whitwood and S. B. Duckett, *Organometallics*, 2015, **34**, 2997-3006.

P. S. S. J. Sastry, R. K. Lonibala and T. R. Rao, *Synth. React. Inorg. Met. Org. Chem*., 1995, **25**, 1261-1278.

Y. Sato, Y. Kayaki and T. Ikariya, *Organometallics*, 2016, **35**, 1257-1264.

J. F. Schenck, *Medical physics*, 1996, **23**, 815-850.

H. B. Schlegel, P. Gund and E. M. Fluder, *J. Am. Chem. Soc*., 1982, **104**, 5347-5351.

S. Schmitt, T. Gefen, F. M. Sturner, T. Unden, G. Wolff, C. Muller, J. Scheuer, B. Naydenov, M. Markham, S. Pezzagna, J. Meijer, I. Schwarz, M. Plenio, A. Retzker, L. P. McGuinness and F. Jelezko, *Science*, 2017, **356**, 832-837.

M. J. Schneider, *Alkaloids: Chemical and Biological Perspectives*, ed. S. W. Pelletier, Pergamon, 1996, vol. 10, pp. 155-299.

D. Schott, C. J. Sleigh, J. P. Lowe, S. B. Duckett, R. J. Mawby and M. G. Partridge, *Inorg. Chem*., 2002, **41**, 2960-2970.

O. Semenova, P. M. Richardson, A. J. Parrott, A. Nordon, M. E. Halse and S. B. Duckett, *Anal. Chem*., 2019, **91**, 6695-6701.

I. A. Shaaban, T. A. Mohamed, W. M. Zoghaib, L. D. Wilson, R. S. Farag, M. S. Afifi and Y. A. Badr, *J. Mol. Struct*., 2013, **1043**, 52-67.

R. V. Shchepin, L. Jaigirdar and E. Y. Chekmenev, *J. Phys. Chem. C*, 2018, **122**, 4984-4996.

R. V. Shchepin, M. L. Truong, T. Theis, A. M. Coffey, F. Shi, K. W. Waddell, W. S. Warren, B. M. Goodson and E. Y. Chekmenev, *J. Phys. Chem. Lett*., 2015, **6**, 1961-1967.

K. Shen, A. W. J. Logan, J. F. P. Colell, J. Bae, G. X. Ortiz Jr., T. Theis, W. S. Warren, S. J. Malcolmson and Q. Wang, *Angew. Chem. Int. Ed.*, 2017, **56**, 12112-12116.

F. Shi, A. M. Coffey, K. W. Waddell, E. Y. Chekmenev and B. M. Goodson, *Angew. Chem. Int. Ed*., 2014, **53**, 7495-7498.

F. Shi, A. M. Coffey, K. W. Waddell, E. Y. Chekmenev and B. M. Goodson, *J. Phys. Chem. C*, 2015, **119**, 7525-7533.

F. Shi, P. He, Q. A. Best, K. Groome, M. L. Truong, A. M. Coffey, G. Zimay, R. V. Shchepin, K. W. Waddell, E. Y. Chekmenev and B. M. Goodson, *J. Phys. Chem. C.,* 2016, **120**, 12149-12156.

I. V. Skovpin, A. Svyatova, N. Chukanov, E. Y. Chekmenev, K. V. Kovtunov and I. V. Koptyug, *Chem. Eur. J*., 2019, **25**, 12694-12697.

M. Solimannejad, M. Malekani and I. Alkorta, *J. Phys. Chem. A*, 2013, **117**, 5551-5557.

P. Spannring, I. Reile, M. Emondts, P. P. M. Schleker, N. K. J. Hermkens, N. G. J. van der Zwaluw, B. J. A. van Weerdenburg, P. Tinnemans, M. Tessari, B. Blümich, F. P. J. T. Rutjes and M. C. Feiters, *Chem. Eur. J.,* 2016, **22**, 9277-9282.

W. Städeli, P. Bigler and W. Von Philipsborn, *Org. Magn. Reson*., 1981, **16**, 170-172.

E. V. Stanbury, P. M. Richardson and S. B. Duckett, *Catal. Sci. Technol*., 2019, **9**, 3914-3922.

E. O. Stejskal and J. E. Tanner, *J. Chem. Phys*., 1965, **42**, 288-292.

N. J. Stewart, G. Norquay, P. D. Griffiths and J. M. Wild, *Magn. Reson. Med*., 2015, **74**, 346-352.

T. Stringer, R. Seldon, N. Liu, D. F. Warner, C. Tam, L. W. Cheng, K. M. Land, P. J. Smith, K. Chibale and G. S. Smith, *Dalton Trans*., 2017, **46**, 9875-9885.

H. Szatylowicz, O. A. Stasyuk and T. M. Krygowski, *Adv. Heterocycl. Chem*., eds. E. F. V. Scriven and C. A. Ramsden, Academic Press, 2015, vol. 116, pp. 137-192.

C. Terenzi, S. Bouguet-Bonnet and D. Canet, *J. Chem. Phys*., 2017, **146**, 154203.

T. Theis, G. X. Ortiz, Jr., A. W. Logan, K. E. Claytor, Y. Feng, W. P. Huhn, V. Blum, S. J. Malcolmson, E. Y. Chekmenev, Q. Wang and W. S. Warren, *Sci. Adv*., 2016, **2**, 1501438.

T. Theis, M. Truong, A. M. Coffey, E. Y. Chekmenev and W. S. Warren, *J. Magn. Reson*., 2014, **248**, 23-26.

T. Theis, M. L. Truong, A. M. Coffey, R. V. Shchepin, K. W. Waddell, F. Shi, B. M. Goodson, W. S. Warren and E. Y. Chekmenev, *J. Am. Chem. Soc*., 2015, **137**, 1404-1407.

C. Tian, P. Florent, J. Louise Helene Søgaard, B. Ben van den, C. Arnaud and M. Anders, *IOP Conference Series: Materials Science and Engineering*, 2017, **278**, 012123.

B. J. Tickner, W. Iali, S. S. Roy, A. C. Whitwood and S. B. Duckett, *Chem. Phys. Chem*., 2019, **20**, 241-245.

B. J. Tickner, R. O. John, S. S. Roy, S. J. Hart, A. C. Whitwood and S. B. Duckett, *Chem. Sci*., 2019, **10**, 5235-5245.

B. J. Tickner, J. S. Lewis, R. O. John, A. C. Whitwood and S. B. Duckett, *Dalton Trans*., 2019, **48**, 15198-15206.

C. M. Timperley, M. Bird, S. C. Heard, S. Notman, R. W. Read, J. E. H. Tattersall and S. R. Turner, *J. Fluorine Chem*., 2005, **126**, 1160-1165.

O. Torres, B. Procacci, M. E. Halse, R. W. Adams, D. Blazina, S. B. Duckett, B. Eguillor, R. A. Green, R. N. Perutz and D. C. Williamson, *J. Am. Chem. Soc*., 2014, **136**, 10124-10131.

M. L. Truong, F. Shi, P. He, B. Yuan, K. N. Plunkett, A. M. Coffey, R. V. Shchepin, D. A. Barskiy, K. V. Kovtunov, I. V. Koptyug, K. W. Waddell, B. M. Goodson and E. Y. Chekmenev, *J. Phys. Chem. B*, 2014, **118**, 13882-13889.

M. L. Truong, T. Theis, A. M. Coffey, R. V. Shchepin, K. W. Waddell, F. Shi, B. M. Goodson, W. S. Warren and E. Y. Chekmenev, *J. Phys. Chem. C*., 2015, **119**, 8786-8797.

N. Tsuchida and S. Yamabe, *J. Phys. Chem. A*, 2005, **109**, 1974-1980.

D. D. K. Tyagi and S. Kumar, *IOSR Journal of Applied Chemistry*, 2014, **7**, 13-16.

R. Tycko and J. A. Reimer, *J. Phys. Chem*., 1996, **100**, 13240-13250.

M. E. van der Boom and D. Milstein, *Chem. Rev*. (Washington, DC, U. S.), 2003, **103**, 1759-1792.

B. J. van Weerdenburg, N. Eshuis, M. Tessari, F. P. Rutjes and M. C. Feiters, *Dalton Trans*., 2015, **44**, 15387-15390.

B. J. van Weerdenburg, S. Gloggler, N. Eshuis, A. H. Engwerda, J. M. Smits, R. de Gelder, S. Appelt, S. S. Wymenga, M. Tessari, M. C. Feiters, B. Blumich and F. P. Rutjes, *Chem. Commun*., 2013, **49**, 7388-7390.

L. D. Vazquez-Serrano, B. T. Owens and J. M. Buriak, *Inorg. Chim. Acta*, 2006, **359**, 2786-2797.

L. D. Vázquez-Serrano, B. T. Owens and J. M. Buriak, *Chem. Commun*., 2002, DOI: 10.1039/B208403A, 2518-2519.

P. Vigoureux and G. B. B. M. Sutherland, *Proceedings of the Royal Society of London. Series A. Mathematical and Physical Sciences*, 1962, **270**, 72-89.

U. Vögeli and W. von Philipsborn, *Org. Magn. Reson*., 1973, **5**, 551-559.

T. G. Walker and W. Happer, *Rev. Mod. Phys*. , 1997, **69**, 629-642.

J. Wang and R. J. Boyd, *J. Phys. Chem*., 1996, **100**, 16141-16146.

W. S. Warren, E. Jenista, R. T. Branca and X. Chen, *Science*, 2009, **323**, 1711-1714.

W. A. Wegener, V. J. Koester and R. M. Dowben, *Proc. Natl. Acad. Sci*., 1979, **76**, 6356-6360.

R. Wind, M. Duijvestijn, C. Van Der Lugt, A. Manenschijn and J. Vriend, *Prog. Nucl. Magn. Reson. Spec.*, 1985, **17**, 33-67.

D. S. Wollan*, Phys. Rev. B*, 1976, **13**, 3671.

D. S. Wollan, *Phys. Rev. B*, 1976, **13**, 3686.

C. M. Wong, M. Fekete, R. Nelson-Forde, M. R. D. Gatus, P. J. Rayner, A. C. Whitwood, S. B. Duckett and B. A. Messerle, *Catal. Sci. Technol*., 2018, **8**, 4925-4933.

N. J. Wood, J. A. Brannigan, S. B. Duckett, S. L. Heath and J. Wagstaff, *J. Am. Chem. Soc*., 2007, **129**, 11012-11013.

D. Wu, A. Chen and C. S. Johnson, *J. Magn. Reson. Series A*, 1995, **115**, 260-264.

Y. Wu, F. Jelezko, M. B. Plenio and T. Weil, *Angew. Chem. Int. Ed*., 2016, **55**, 6586-6598.

K. Wuthrich, *Angew. Chem. Int. Ed*., 2003, **42**, 3340-3363.

Y. Xu, D. M. P. Mingos and J. M. Brown, *Chem. Commun*., 2008, 199-201.

M.-L. Yuan, J.-H. Xie, S.-F. Zhu and Q.-L. Zhou, *ACS Catalysis*, 2016, **6**, 3665-3669.

H. Zeng, J. Xu, J. Gillen, M. T. McMahon, D. Artemov, J. M. Tyburn, J. A. Lohman, R. E. Mewis, K. D. Atkinson, G. G. Green, S. B. Duckett and P. C. van Zijl, *J. Magn. Reson*., 2013, **237**, 73-78.

H. Zeng, J. Xu, J. Gillen, M. T. McMahon, D. Artemov, J.-M. Tyburn, J. A. B. Lohman, R. E. Mewis, K. D. Atkinson, G. G. R. Green, S. B. Duckett and P. C. M. van Zijl, *J. Magn. Reson*., 2013, **237**, 73-78.

S. Zhang, *J. Comput. Chem*., 2012, **33**, 2469-2482.

R. Zhou, W. Cheng, L. M. Neal, E. W. Zhao, K. Ludden, H. E. Hagelin-Weaver and C. R. Bowers, *Phys. Chem. Chem. Phys*., 2015, **17**, 26121-26129.

A. L. Zook, B. B. Adhyaru and C. R. Bowers, *J. Magn. Reson*., 2002, **159**, 175-182.